小児歯科学雑誌　39(5) : 959–965　2001

小児歯科領域における抗菌薬添加裏層剤の臨床応用

中村　均　吉田明弘　福島知典
朝田芳信　前田隆秀

要旨：乳歯および幼若永久歯の深部齲蝕に対し，感染歯質を完全に除去することなく歯髄保存処置を可能とする抗菌薬を添加した裏層剤を用いた間接あるいは直接覆髄法における臨床経過を，臨床所見ならびにエックス線写真所見より長期観察したところ，以下の結果を得た。

1．乳歯132歯および幼若永久歯40歯の合計172歯の深部齲蝕処置に対し，抗菌薬を添加した裏層剤を間接覆髄あるいは直接覆髄に用いたところ，臨床成功率は95.3%と高い値を示した。予後不良例では，直接覆髄法がその大部分を占めていた。

2．年齢別臨床成績では，3〜5歳の低年齢で処置後の経過不良が集中していた。

以上のことより，明らかに歯髄処置を要するような深部齲蝕に対し抗菌薬添加裏層剤の応用は有効であり，今後小児の齲蝕治療への応用を検討したい。

Key words：小児歯科，抗菌薬，裏層剤，断髄法，齲蝕

緒　言

齲蝕症の病因，すなわち酸産生，蛋白質分解あるいは蛋白質分解キレーションにはすべての過程に微生物が関与している。その意味から齲蝕に罹患した歯の保存療法に対する基本概念は感染歯質を完全に除去することである。しかしながら，有機質含有量の多い乳歯および幼若永久歯の齲蝕処置では齲蝕進行に伴う軟化が高度に進むため，感染歯質を完全に除去しようとするならば広範囲露髄が頻度として多くなる。機械的な露髄を起こすと，窩洞形成中の発熱による傷害や手用器具によって歯髄に直接圧を伝える事が予後に大きな影響を及ぼすと言われている[1〜3]。

現在のところ，乳歯の歯内療法は，複雑な根管形態や生理的歯根吸収の存在から抜髄法より断髄法が広く用いられている。しかし，歯髄の切断面直下では歯髄組織が慢性炎症に陥りやすく交換期までの長期観察では予後は優れているとは言い難い[4]。

一方，幼若永久歯の深部齲蝕では暫間的間接覆髄法（Indirect Pulp Capping：IPC）が主流をなしているものの，数か月後には再度処置しなければならず患児および保護者の協力が必要となる。

近年，鮎川は[5]歯根完成永久歯の齲蝕処置に対し抗菌薬を加えた裏層剤を用いることで，仮性露髄が疑われる歯に対して感染歯質を完全に除去することなく保存処置が可能であることを報告している。機械的露髄の危険性が高い乳歯や幼若永久歯に対して有機質の蛋白質分解を抑制する抗菌薬添加裏層剤の応用[5]が小児歯科領域へ可能であるかどうかは注目されるところである。そこで，乳歯および幼若永久歯の深部齲蝕に対する抗菌薬添加裏層剤の臨床的効果を検討するため臨床所見ならびにエックス線写真所見による長期的観察下で予後の判定を行ったところ，若干の知見を得たので報告する。

日本大学松戸歯学部小児歯科学教室
千葉県松戸市栄町西2-870-1
（主任：前田隆秀教授）
（2001年7月17日受付）
（2001年10月26日受理）

試料および研究方法

対象者は平成9年4月から平成10年6月までの期間に日本大学松戸歯学部付属歯科病院小児歯科部を受診し，齲蝕を主訴に来院した患児のうち，抗菌薬を用いた歯髄保護処置について説明し了承を得られた3歳から9歳までの109名（男児55名，女児54名）で，定期検診において定期的に経過観察を行うことができ，臨床所見ならびにエックス線写真所見より，栗原ら[6]の基準に則ると歯髄処置が必要と診断された深部齲蝕歯172歯（乳歯132歯，永久歯40歯）を対象とした。

適応基準および処置方法

本研究における対象歯の適応基準は，エックス線写真所見で，歯根膜腔の拡大，歯根周囲に病的透過像，歯根

の異常が認められず，自発痛の無い乳歯および幼若永久歯であり，すべての処置に際しては，局所麻酔奏効後，ラバーダム防湿下にて行った。感染歯質の除去により露髄の恐れのある齲蝕歯には，残存感染歯質を抗菌薬添加裏層剤（間接覆髄用）にて間接覆髄を行った後，通法に従いクリアフィルライナーボンドⅡΣによるボンディング，光重合型レジン（クリアフィル AP-X）にて修復処置を行った。また，感染歯質除去中に露髄を来たした齲蝕歯は，露髄面を 0.5% 次亜塩素酸ナトリウム溶液と 3%過酸化水素水にて交互に洗浄後，抗菌薬裏層剤（直接覆髄用）にて直接覆髄を行い，さらに間接覆髄法と同一の抗菌薬添加裏層剤にて感染歯質を裏層し，前述と同様に修復処置を行った。

抗菌薬添加裏層剤

鮎川の[5]方法による添加薬剤は，メトロニダゾール（MN），セファクロル（CCL），シプロフロキサシン（CPFX）を使用しているが，小児に対する安全性が確立されていないため，CPFX を除いた 2 種混合裏層剤を用いた。2 種混合裏層材は，MN・CCL を力価で 3 : 1 の割合で調合し，直接覆髄用 α-Tricalcium phosphate（ニューアパタイトライナータイプⅠ）および間接覆髄用 α-Tricalcium phosphate ニューアパタイトライナータイプⅡ）に重量比 4% で混合したもの[5]を使用した。

臨床経過の検討

当該歯の臨床所見ならびにエックス線写真所見を経時的に観察し，経過良好，経過不良の判定を行った。処置時から最終観察時までの期間は，最短 10 日で，最長は 31 か月であった。経過良好の判定は，臨床所見に異常が認められず，エックス線写真所見で，歯根膜腔の拡大，歯根周囲に病的透過像，歯根の異常吸収が認められないものとした。経過不良の判定は，臨床所見として，術後の違和感，自発痛，誘発痛の出現，歯肉膿瘍，異常な動揺が認められ，さらにエックス線写真所見で，歯根膜腔の拡大，歯根周囲に病的透過像，歯根の異常吸収が認められるものとした。

結　果

1．臨床総合成績（表 1）

表 1 に示すように，乳歯 132 歯のうち 125 歯（94.7%）が経過良好で，永久歯 40 歯のうち 39 歯（97.5%）が経過良好であった。すべての対象歯 172 歯のうち 164 歯（95.3%）が経過良好で，経過不良歯は 8 歯（4.7%）であった。

2．処置内容による臨床成績（表 2）

1）乳歯：間接覆髄法を行った 100 歯のうち 2 歯（2%）で経過不良がみられた。一方直接覆髄法を行った 32 歯のうち 5 歯（15.6%）で経過不良がみられた。

2）永久歯：間接覆髄法を行った 32 歯のうち 1 歯（3%）で経過不良がみられた。一方直接覆髄法を行った 8 歯はすべて経過良好であった。

表 1　臨床総合成績

	経過良好	経過不良	合計
乳　歯	125	7	132
永久歯	39	1	40
合　計	164	8	172

単位：歯数

表 2　処置内容による臨床成績

		経過良好	経過不良	合計
乳　歯	間接覆髄	98	2	100
	直接覆髄	27	5	32
永久歯	間接覆髄	31	1	32
	直接覆髄	8	0	8
合　計		164	8	172

単位：歯数

3．歯種別による臨床成績（表 3）

1）乳歯：上顎左側乳中切歯および乳側切歯，上顎左側乳犬歯，上顎左側および右側第二乳臼歯，下顎左側第一乳臼歯，下顎右側乳犬歯ではすべての被検歯において経過良好であった。経過不良歯は下顎右側第一乳臼歯で 20 例中 3 歯（15%）と最も多く，次に下顎右側第二乳臼歯が 23 例中 2 歯（8.7%），下顎左側第二乳臼歯で 12 例中 1 歯（8.3%），上顎左側第一乳臼歯で 14 例中 1 歯（7.1%）であった。

2）永久歯：上顎左側中切歯で 3 例中 1 歯（33%）で経過不良がみられた以外，すべての被検歯において経過良好であった。

4．施術年齢別による臨床成績（表 4）

乳歯の経過不良であった 8 歯は，3～5 歳児にすべて集中していた。永久歯の経過不良 1 歯は 12 歳児の処置であった。

5．経過不良歯の内容（表 5）

経過不良であった 8 歯のうち 5 歯は下顎右側に集中し，2 歯は下顎左側乳臼歯，1 歯は上顎左側中切歯であった。経過期間はもっとも短い症例で 10 日（2 歯），長い症例では 11 か月（2 歯）であった。

表3　歯種別による臨床成績

歯式	経過良好	経過不良	合計
A|	2	0	2
B|	0	0	0
C|	1	0	1
D|	9	0	9
E|	12	0	12
|A	1	0	1
|B	2	0	2
|C	4	0	4
|D	13	1	14
|E	16	0	16
|A	15	0	15
|B	11	1	12
|C	2	0	2
|D	17	3	20
|E	21	2	23
1|	3	0	3
2|	2	0	2
6|	2	0	2
7|	2	0	2
|1	2	1	3
|2	4	0	4
|6	4	0	4
|6	6	0	6
6|	10	0	10
7|	3	0	3
合計	164	8	172

単位：歯数

表4　施術年齢別による臨床経過

年齢	乳歯			幼若永久歯			総合計
	経過良好	経過不良	合計	経過良好	経過不良	合計	
3	14	1	15	0	0	0	15
4	44	5	49	0	0	0	49
5	31	2	33	0	0	0	33
6	14	0	14	0	0	0	14
7	4	0	4	5	0	5	9
8	10	0	10	8	0	8	18
9	8	0	8	26	1	27	35
合計	125	8	133	39	1	40	173

単位：歯数

6．経過良好および経過不良歯の経過観察期間（表6）

経過良好であった症例の経過観察期間は，最短の症例は2か月で脱落し，最長の症例は31か月で経過観察継続中である。また，経過不良となった症例の経過観察期間は，最短の症例は10日間で根尖性歯周炎を発症し，最長の症例は11か後に歯髄炎の症状を呈した。

表5　経過不良歯の内容

歯式	年齢	経過期間	露髄の有無	経過不良となった理由
下顎右側第一乳臼歯	5	10か月	有り	根尖性歯周炎
下顎左側第二乳臼歯	3	1か月	有り	根尖性歯周炎
下顎右側第一乳臼歯	4	10日	無し	根尖性歯周炎
下顎右側第二乳臼歯	4	10日	無し	根尖性歯周炎
上顎左側第一乳臼歯	5	7か月	有り	根尖性歯周炎
上顎左側中切歯	9	3か月	無し	歯髄炎
下顎右側第一乳臼歯	4	11か月	無し	歯髄炎
下顎右側第二乳臼歯	4	11か月	無し	歯髄炎

表6　経過良好歯および経過不良歯の経過観察期間

	最短経過観察期間	最長経過観察期間
経過良好歯	2か月 （交換期による脱落）	31か月 （経過観察継続中）
経過不良歯	10日間 （根尖性歯周炎発症）	11か月 （急性歯髄炎発症）

考　察

臨床において永久歯および乳歯の歯髄疾患を正確に病理組織学的レベルでの診断を下す方法は現在のところない。とくに乳歯では対象が小児患者であり行動の点からも診断がいっそう困難となる。一般に乳歯の歯髄処置においては生理的歯根吸収を円滑に進め永久歯との正常な交換のため，できるだけ歯髄を生活させた状態で維持し，可及的に歯髄処置を施さない方法が薦められる。しかしながら，有機質含有量の多い乳歯および幼若永久歯の齲蝕処置では齲蝕進行に伴う有機質の蛋白質分解がおこり軟化が高度に進むため，感染歯質を完全に除去しようとするならば広範囲露髄が頻度として多くなる。

そこで，露髄が生じてしまった場合，処置の選択肢の一つとして，断髄法があげられる。この断髄法は，感染し炎症に陥った歯冠部歯髄組織だけを除去し歯根部歯髄組織に炎症が及ばないようにし，乳歯根の生理的吸収を阻害せず，また幼若永久歯のアペキソジェネーシスを可能とすることから，主に乳歯および幼若永久歯に用いられる。しかしながら，断髄法では高い臨床的成功率に比較し組織学的な検索においては歯髄組織が慢性炎症に陥っていることが報告されている[7]。

中島ら[4]は，断髄法を行った乳歯の予後をエックス線

学的に評価したところ，経過不良と判断されたものが水酸化カルシウム法では26%，ホルモクレゾール（FC）法では60% と報告している。水酸化カルシウムによる直接あるいは間接覆髄および断髄は，修復象牙質による象牙質被蓋の形成を惹起する。しかし，水酸化カルシウムは根管内組織の石灰化や炎症性反応の持続に伴う内部吸収を引き起こす。

一方，FC 法は乳歯断髄法に用いられ臨床的成功率は高いものの，FC は動物実験において象牙質，歯髄，歯根膜および骨に広く拡散することを報告している。また，Messer ら[8]が FC 法により断髄法を乳歯に施したあと，断髄法に用いられた薬剤毒性の影響により，後継永久歯の捻転やエナメル質表面の欠損の発生すると報告している。これらのことから，断髄法が感染歯質除去中に露髄の危険性がある場合や仮性露髄の疑われる場合に最も相応しい処置とは言い難い。

露髄を避けて感染歯質を残す方法としては IPC が知られている。IPC を行った際には，残存感染歯質の除去を IPC 施術後 1 か月から 6 週間後に行うことが Leung ら[12]によって推奨されている。一方，IPC において臨床的に健康象牙質と判断された歯質でも細菌の進入が 36%以上の症例で存在するという報告[10, 11]もあることから，再度の感染歯質完全除去のために窩洞形成が推奨される。これらのことから，IPC を用いる患児及び保護者に対し，理解と協力が不可欠である。不十分な場合には歯の保存が不可能となり，患児及び保護者の信頼を失いかねない。

また，感染歯質除去中に偶発的に歯髄が機械的に露出された症例に直接覆髄法が用いられることがあるが，歯髄を露出させる行為によって組織は押しつぶされ血管が破壊されそのために歯髄内出血が起こり[12]露髄に伴う生理的変化は予後に大きな影響を及ぼすと言われている。さらに，直接覆髄法では直接的に歯髄へ刺激を与えることから炎症性反応が慢性化しやすく，露髄の大きさや位置によっても影響を受けやすく長期にわたる経過観察が必要となる。すなわち，不快症状の発現など臨床症状の経過を一定期間観察した後，永久修復を施すことが一般的である。

近年，岩久ら[9]は口腔齲蝕病巣から分離された細菌叢の詳細な検討から偏性嫌気性菌が圧倒的優勢であることを報告している。さらに，偏性嫌気性菌に有効な抗菌薬であるメトルニダゾール（MN）とシプロフロキサシン（CPFX）ならびに抗生剤であるセファクロール（CCL）を基材の α-TCP セメント（商品名：ニューアパタイトライナー・三金工業社製）に混合した抗菌薬添加裏層剤を用いた永久歯歯根完成歯の間接および直接覆髄処置における臨床成績が非常に良好であることを報告している。基材として用いられている α-TCP セメントはリン酸カルシウム系の材料であり微細な粉末として供給され生理食塩水や弱酸溶液などの溶液と練和することにより 40℃ 以下の低温で加水分解し，ハイドロキシアパタイト転化するためハイドロキシアパタイトの前駆体と呼ばれ，また硬化時間を調整できるため症例に応じた成形が可能である。ハイドロキシアパタイトセメントや β-TCP セメントに比較して溶解度が高く生体への親和性が優れている。

これらのことを踏まえ，自発痛などの自覚症状が無い広範囲齲蝕歯の処置において，感染歯質除去中に露髄する危険性が高い場合や仮性露髄が疑われる症例に対し，感染歯質を完全に除去することなく細菌の増殖抑制および死滅させ炎症反応を鎮静でき，有機質の蛋白質分解を抑制する抗菌薬添加裏層剤を小児歯科領域へ応用が可能であれば，歯髄保存という観点からも最も有効と考えられる。

そこで，今回我々は乳歯および幼若永久歯の深部齲蝕に対する抗菌薬添加裏層剤の臨床効果を検討するため，軟化象牙質除去中に露髄の危険性がある，あるいは一部露髄が認められた乳歯（132 歯）および幼若永久歯（40 歯）の合計 172 歯について抗菌薬添加裏層剤を直接あるいは間接覆髄に用い保存修復処置を行い，臨床所見ならびにエックス線写真所見による長期的観察を行った。その結果，抗菌薬添加裏層剤による間接および直接覆髄処置では，表 1 に示すとおり臨床的成功率が 95.3% と高く，従来までの酸化亜鉛ユージノールセメントや水酸化カルシウムを使用薬剤とした間接および直接覆髄法における臨床的成功率よりも良好な結果が得られた[14, 15]。

一方，10 日から 31 か月の長期予後観察において臨床およびエックス線写真所見から経過不良とされたものが 8 歯で，全体の 4.7% であった。治療内容について見ると表 2 に示すとおり，直接覆髄法での経過不良例が多く見られた。その理由として乳歯歯髄炎の炎症の程度を正確に診断することは困難であり，今回経過不良となった乳歯では処置時すでに，一部性あるいは全部性に炎症が波及していたことが予想される。また，抗菌薬には炎症の減弱や硬組織沈着の促進効果のないことが McWalter ら[16, 17]により報告されており，今回用いた抗菌薬は細菌の増殖抑制ならびに死滅を目的に歯髄感染を軽減させる働きが主になることからも，歯髄の炎症症状を正確に診断することが重要である。

この結果より歯髄保護という観点から可能な限り，偶

発的露髄は避けるべきである。歯種別に臨床成績を検討すると，表3に示すとおり下顎右側に経過不良例が集中している。これは，右利きの小児では下顎右側臼歯のブラッシングは疎かになりやすく齲蝕が重度になりやすいことが考えられる。また，当院では座位診療で処置が行われており，直視が難しい上顎に比べ下顎は直視できる事からむしろ上顎よりも処置後の経過は良好であることが予想される，しかし今回の結果を得た理由としては，すでに述べたように乳歯歯髄炎の炎症の程度を正確に診断することは困難であること，対象者が低年齢児であったため，処置時の行動が影響していること，さらに下顎左側臼歯よりも下顎右側臼歯の処置が行いにくいということが可能性として考えられる。

今回の結果を年齢別に経過を検討してみると，表4で示すとおり，経過不良者が1例を除き5歳以下の患児に集中していることから処置時の行動が大きく影響している可能性を示唆した。また，水酸化カルシウムおよび酸化亜鉛ユージノールを用いた研究の中で施行年齢が増加するに従い成功率が高くなる傾向があると報告されていることからも，処置中の行動が経過に左右するものと考えられる。長期観察の中で，経過期間が10か月，11か月の処置歯における経過不良例がみられた（表5)。その原因の一つとして考えられることは，最終修復物として使用したレジン修復材の破折や接着部位からの辺縁漏洩が考えられる。これらの経過不良例は，表5に示すとおり，4歳および5歳児であり処置時の行動変容が良好でなく，充分な修復操作が行えなかったことが考えられ，結果を左右したのではないかと推定できる。

以上のことから，抗菌薬添加裏層剤は完成永久歯のみならず，乳歯や幼若永久歯においても感染歯質を残した状態での修復処置が充分可能ではあるが，歯髄炎の診断が困難である上に，行動変容が難しい低年齢児に対する抗菌薬添加裏層材の応用後の修復処置を含め慎重を期たす必要性が示唆された。

結　論

乳歯および幼若永久歯の深部齲蝕に対し，感染歯質を完全に除去することなく歯髄保存処置を可能とする抗菌薬を添加した裏層剤を用いた間接あるいは直接覆髄法における臨床経過を，臨床所見ならびにエックス線写真所見より長期観察したところ，以下の結果を得た。

1．乳歯132歯のうち125歯（94.7%）が経過良好で，永久歯40歯のうち39歯（97.5%）が予後良好であった。すべての対象歯172歯のうち164歯（95.3%）が経過良好で，経過不良歯は8歯（4.7%）であった。

2．処置別では乳歯においては間接覆髄法を行った100歯のうち2歯（2%）で経過不良がみられた。一方直接覆髄法を行った32歯のうち5歯（15.6%）で経過不良がみられた。また，永久歯においては間接覆髄法を行った32歯のうち1歯（3%）で経過不良がみられた。一方直接覆髄法を行った8歯はすべて経過良好であった。

3．歯種別では乳歯においては上顎左側乳中切歯および乳側切歯，上顎左側乳犬歯，上顎左側および右側第二乳臼歯，下顎左側第一乳臼歯，下顎右側乳犬歯ではすべての被検歯において経過良好であった。経過不良歯は下顎右側第一乳臼歯で20例中3歯（15%）と最も多く，次に下顎右側第二乳臼歯が23例中2歯（8.7%），下顎左側第二乳臼歯で12例中1歯（8.3%），上顎左側第一乳臼歯で14例中1歯（7.1%）であった。また，永久歯においては上顎左側中切歯で3例中1歯（33%）で経過不良がみられた以外，すべての被検歯において経過良好であった。

4．施術年齢別による臨床成績をみると，乳歯の経過不良であった8歯は，3〜5歳児にすべて集中していた。永久歯の経過不良1歯は12歳児の処置であった。

5．経過不良であった8歯のうち5歯は下顎右側に集中し，2歯は下顎左側乳臼歯，1歯は上顎左側中切歯であった。経過期間はもっとも短い症例で10日（2歯），長い症例では11か月（2歯）であった。

6．経過良好および経過不良歯の経過観察期間は，経過良好であった症例では，最短の症例は2か月で脱落し，最長の症例は31か月で経過観察継続中である。また，経過不良となった症例の経過観察期間は，最短の症例は10日間で根尖性歯周炎を発症し，最長の症例は11か後に歯髄炎の症状を呈した。

以上のことより，明らかに歯髄処置を要するような深部齲蝕に対し抗菌薬添加裏層剤の応用は有効であり，今後小児の齲蝕治療への応用を検討したい。

文　献

1）Paterson, R. C.: Bacterial contamination and the exposed pulp, Brit. Dent. J., 140: 231, 1976.
2）Stenvik, A., Iverson, J. and Mjor, I. A.: Tissue pressure and histology of normal and inflamed tooth pulps in macaque monkeys, Arch. Oral. Biol., 17: 1501, 1972.
3）Watts, A.: Bacterial contamination and the toxicity of silicate and zinc phosphate cements, Brit. Dent. J., 146: 7, 1979.
4）中島正人，信家弘士，三宅雄次郎，長坂信夫：乳歯歯髄切断処置におけるX線学的経過観察－水酸化カルシウ

ム系剤使用例についてー，小児歯誌，26：611–620, 1988.
5）鮎川幸雄：生体親和性抗菌性直接覆髄剤に対するヒト歯髄の反応－混合抗菌剤の改良についてー，日歯保誌，37：643–651, 1994.
6）栗原洋一，林　賢一：新パルパックVによる乳歯生活歯髄切断の臨床成績について，新歯科時報，1，14–17, 1978.
7）Seltzer, S. and Bender, I. B.: Some influences affecting repair of the exposed pulps of dogs'teeth, J. Dent. Res., 37: 678, 1958.
8）Messer, L. B., Cline, J. T. and Korf, N. W.: Long term effects of primary molar pulpotomies on succedaneous bicuspids, J. Dent. Res., 59: 116, 1980.
9）岩久正明，星野悦郎，子田晃一：抗菌剤による新しい歯髄保存法，日本歯科評論社，1996.
10）Shovelton, D. S.: A study of deep carious dentine, Int. Dent. J., 18: 392, 1968.
11）Edwardsson, S.: Bacteriological studies on deep areas of carious dentine, Odont. Revy., 25（Suppl 32）1974.
12）Leung, R. L., Loesche, W. J. and Charbeneau, G. T.: Effect of Dycal on bacteria in deep carious lesions, JADA, 100: 193, 1980.
13）Luostarinen, V.: Dental pulp response to trauma. An experimental study, Suom Hammaslaak Toim 67: Supp 11, 1971.
14）Raymond, H. S.: Dycal capping of exposed pulps in primary teeth, J. Dent. Child., 30: 141–149, 1963.
15）Law, D. B. and Lewis, T. M.: The effect of calcium hydroxide on deep carious lesions: Oral Surg., Oral Med. & Oral Path., 14: 1130–1137, 1961.
16）McWalter, G. M., EI-Kafrawy, A. H. and Mitchell, D. F.: Long-term study of pulp capping in monkeys with three agents, JADA, 93: 105, 1976.
17）McWalter, G. M., El-Kafrawy, A. H. and Mitchell, D. F.: Pulp capping in monkeys with a calcium hydroxide compound, an antibiotic, and a polycarboxylate cement, Oral Surg., 36: 90, 1973.

Clinical Observation on the Pulp Xapping Treatment woth α
——Tricalcium Phosphate Liner mixed antibacterial drugs——

Hitoshi Nakamura, Akihiro Yoshida, Tomonori Fukushima,
Yoshinobu Asada and Takahide Maeda

Department of Pediatric Dentistry, Nihon University School of Dentistry at Matsudo,
(Directar : Prof. Takahide Maeda)

We investigated a radiographic follow up examination and an oral examination in both 132 primary teeth and 40 immature permanent teeth which had been treated by means of pulp capping with antibacterial drugs during the period from April 1997 to June 1998 at the Pediatric Dentistry Clinic of the School of Dentistry at Matsudo, Nihon University.

The results obtained were as follows :

1. At the time of final follow up examination for each treated tooth, there was a number of teeth judged as being successful were 164 (95.3%) and 8 (4.7%) as being unsuccessful. Results we observed especially many teeth judged as being unsuccessful during the period from 18 to 28 months after treatment.
2. For the age of the subjects with unsuccessful results, children aged 3–5 years represented 77 % for the primary tooth treatment.
3. As regards with the successful cases, the ratio of the indirect pulp capping was much higher than that of the direct pulp capping.

These findings suggested that α-Tricalcium Phosphate Liner mixed antibacterial drugs was useful in the pulp capping treatment of both primary teeth and immature permanent teeth.

Key words : Pediatric dentistry, Antimicrobial agents, Antibiotic agents, Lining, Vital amputation of the pulp, Dental caries

小児歯科学雑誌　43(1) : 107–112　2005

エナメル質形成不全症に認められた過剰歯の1例

松根健介　宇治川玲子　三好克実
松永利恵　鈴木久仁博*　前田隆秀

要旨：エナメル質形成不全症は歯の形成，発育の途上でエナメル質の発育が妨げられた結果発症した歯の構造の異常である。全身的異常は認められずエナメル質に限局した障害が発現するものである。今回，エナメル質形成不全症の患児に発現した過剰歯を摘出する機会を得た。その臨床的およびエックス線的所見，ならびに抜去歯の走査型電子顕微鏡におけるエナメル質表面性状について検討したところ，以下のような知見を得た。

1．特発性に発症したエナメル質形成不全症であった。
2．エナメル質形成不全症における過剰歯の発現は稀有であった。
3．患児のエナメル質は形成不全を受けているが，乳歯および永久歯と摘出過剰歯の色調には明らかな違いを認めた。
4．摘出過剰歯のエナメル質表面は，凹凸の激しい粗造感を呈しており，健常児におけるエナメル質表面とは明らかな違いを認めた。

Key words：エナメル質形成不全症，過剰歯，SEM

緒　言

エナメル質形成不全症は歯の形成，発育の途上でエナメル質の発育が妨げられた結果発症する歯の構造の異常である。全身的異常は認められずエナメル質に限局した障害が発現するものである。エナメル質形成不全症の原因による分類は多く報告されている。その分類は，非遺伝的原因すなわち環境要因によるものと，遺伝子因子によるものとの2つに大きく分類される[1]。エナメル質形成不全症におけるエナメル質は，白濁，着色，菲薄，陥没等の異常所見を示し，それらに伴った歯冠形態の異常等が報告されている[2]。また，遺伝性のエナメル質形成不全症は，その臨床的所見や遺伝様式を参考に分類されており，遺伝子レベルでの原因の報告も認める[3~6]。

一方，過剰歯は，歯列のほとんどの部位に発現し，乳歯列期，混合歯列期，永久歯列期のいずれにも認められる[7]。過剰歯の好発部位は上顎切歯部，ついで上下顎小臼歯部，上下顎の大臼歯部であり[8]，形態学的・組織学的報告も数多く認められる[7,9]。しかしながら，エナメル質形成不全症を有する患児に発現した過剰歯の報告は認められない。今回，エナメル質形成不全症の患児に発現した過剰歯を摘出する機会を得た。そこで，その臨床的およびエックス線的所見，ならびに抜去歯の走査型電子顕微鏡におけるエナメル質表面性状について報告し過剰歯の発生を検討した。本論文の発表に際して，患児および保護者の了承を得た。

症　例

患児：8歳5か月男児（初診時4歳，摘出時8歳）
主訴：健診にてエナメル質形成不全を指摘され，その精査加療を希望し来院した。
家族歴：問診の結果，歯の形成不全および過剰歯を有する者は認めなかった。
既往歴：
妊娠分娩歴において，妊娠6か月時にかぜのため薬物を3日間服用した。7か月時に膀胱炎にて薬物を3日間服用した。8か月時から貧血の薬物を出生時まで服用したが，薬剤名は不明である。吸引分娩にて出生した。その他，特記事項は認めなかった。
歯科的既往歴：
1歳6か月児健診にて，エナメル質形成不全を指摘され

日本大学松戸歯学部小児歯科学教室
千葉県松戸市栄町西2丁目870番1
（主任：前田隆秀教授）
*日本大学松戸歯学部解剖学Ⅱ教室
千葉県松戸市栄町西2丁目870番1
（主任：小澤幸重教授）
（2004年12月21日受付）
（2005年1月16日受理）

た。3歳児健診にて再度指摘された。平成8年（初診時4歳）に当歯科病院来院，口腔内所見，パノマエックス線写真像から，乳歯と永久歯全てにエナメル質の低形成が認められ，特発性のエナメル質形成不全症と診断した。その際，2本の正中埋伏過剰歯を認めたが，後継永久歯胚との位置関係より経過観察とした。8歳5か月時にエックス線診査を行い埋伏過剰歯の摘出を行った。

全身所見：

皮膚，頭髪，爪等の外胚葉系器官に異常は認めなかった。

口腔内所見：

患児の乳歯と永久歯の歯冠全体のエナメル質表面は，凹凸感を呈した黄褐色であり，水平方向に槁を認めた。また，凹凸感は認めるものの硬さの異常や異常な粗造感は認めなかった（図1, 2）。

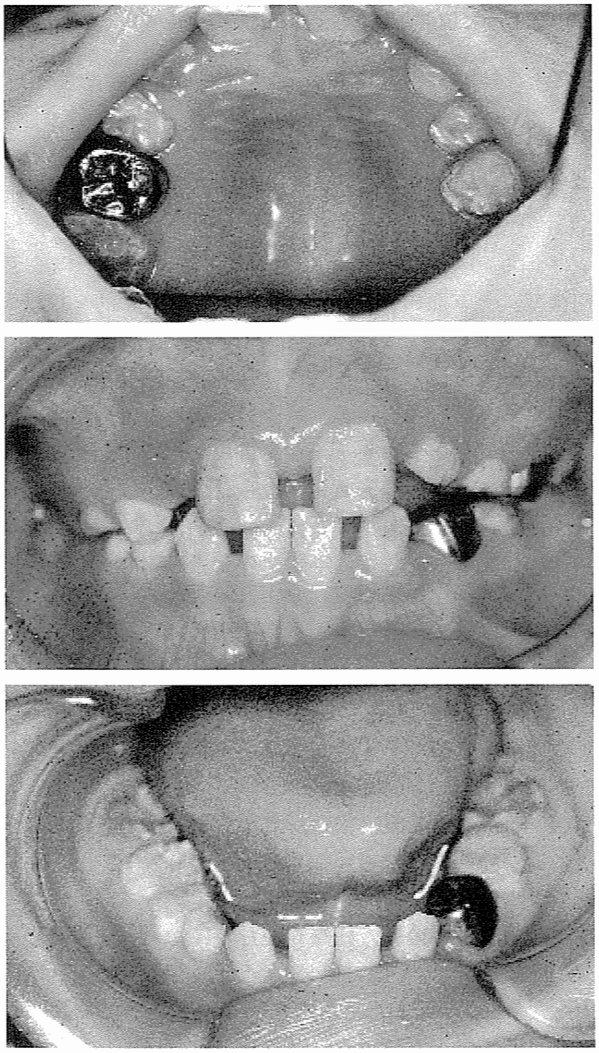

図1　口腔内写真
乳歯と永久歯の歯冠全体のエナメル質表面は，凹凸しており，黄褐色であり，水平方向に槁を認めた。また，凹凸感は認めるものの硬さや粗造感に異常は認めなかった。

エックス線所見：

パノラマエックス線診査の結果，エナメル質に相当する部位の厚さは，健全歯のエナメル質の厚さ[10]と比較し，菲薄感があり，特に乳歯におけるエナメル質と象牙質との境が不明瞭であった（図3）。デンタルエックス線写真において上顎両側中切歯のエナメル質は健常児のそれ[10]に比較し，極めて菲薄であった（図4）。また，上顎中切歯根尖部付近に順生1本，逆生1本，計2本の正中埋伏過剰歯を認めた。過剰歯におけるエナメル質と象牙質は明確な境界を認めなかった。

摘出過剰歯の所見：

1．色調，歯冠形態および歯根形態

本症例における摘出過剰歯（試料1，2）を図5に示す。試料におけるエナメル質表面は白色で，凹凸感はあるものの本患児の乳歯と永久歯に比較しその凹凸感は少なかった。試料1は全長14.00 mm，幅4.78 mmの犬歯型であり歯根彎曲を認め，根未完成であった。試料2は全長10.16 mm，幅4.24 mmの単錐型であり歯根彎曲は認めず，根未完成であった。

2．実体顕微鏡（PHOTOMAKROSKOPM 400, Wild社製）におけるエナメル質表面性状

健常児において摘出された正中埋伏過剰歯をコントロ

		FS	FS						FS	MC		
6	E	D	C		1	1		C	D	E	6	
6	E	D	C	2	1	1	2		D	E	6	
		FS	CR						MC	CR		

図2　口腔内所見
CR；コンポジットレジン充塡，FS；予防塡塞，MC；乳歯冠

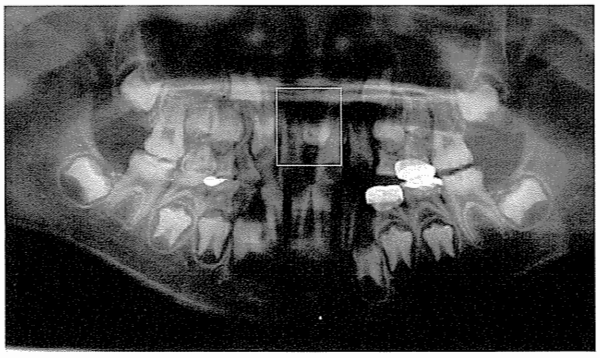

図3　パノラマエックス線写真（8歳5か月時）
乳歯と永久歯全てにエナメル質の低形成が認められた。

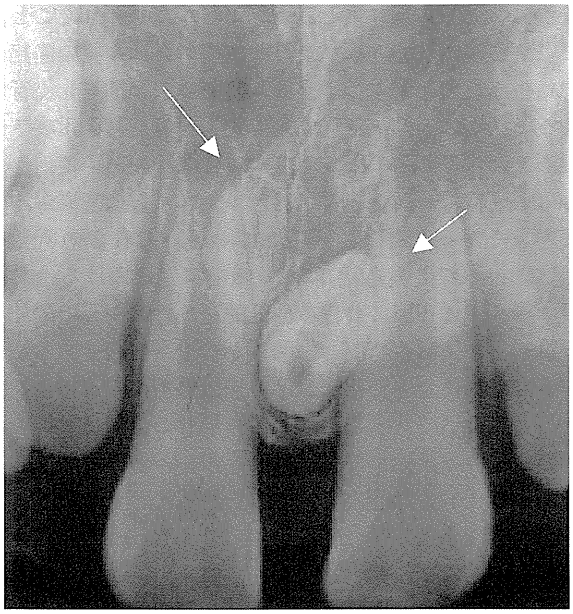

図4　デンタルエックス線写真（8歳5か月時）
2本の正中過剰歯を認めた。

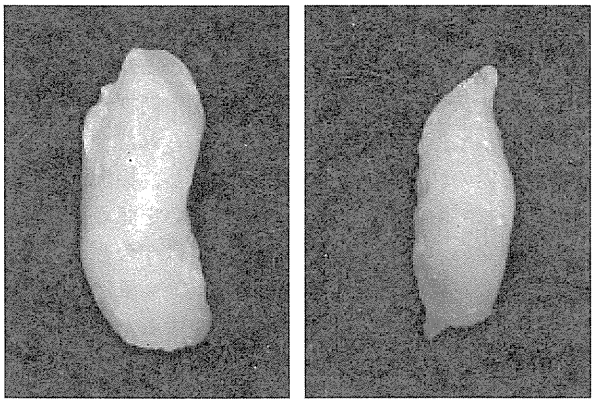

試料1（順生）　　試料2（逆生）

図5　摘出過剰歯
エナメル質表面は，凹凸感はあるものの乳歯と永久歯に比較しその凹凸感は少なく，白色であった。

ールとして比較を行ったところ，コントロールに対しその表面は粗造感と凹凸感が顕著であった（図6）。

3．SEMにおけるエナメル質表面性状

試料1，2はコントロールと比較し表面は著しい凹凸像を示していた。さらに，エナメル質表面のトームス突起の陥凹の形状も不規則であり，部分的に突起の陥凹が認められない部位もあった。また，エナメル質が薄い板状に剥離し，折り重なるような像が認められ，カリフラワー状に隆起したエナメル質の集塊が部分的に認められた。試料の隆起はコントロールに比較し，周囲のエナメル質が不規則で粗造な剥離像を呈し，その出現頻度も高かった（図7）。

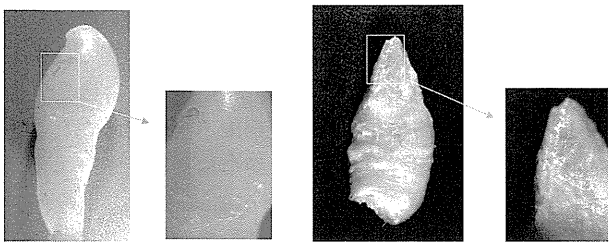

コントロール　　試料（逆生）

図6　エナメル質表面性状
健常児における過剰歯をコントロールとして比較を行ったところ，コントロールに対しその表面は粗造であった。

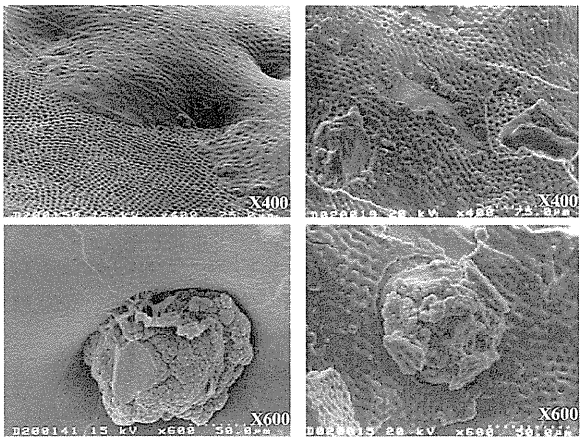

コントロール　　試料（逆生）

図7　エナメル質表面におけるSEM像
摘出過剰歯のエナメル質表面は，凹凸の激しい粗造感を呈しており，健常児におけるエナメル質表面とは明らかな違いを認めた。

考　察

エナメル質形成不全は，特異的にエナメル質の形成が障害される疾患である。遺伝因子によるもの，環境因子すなわち非遺伝的原因によるものとの2つに大別できる[1]。本症例における障害は，乳歯および永久歯に及んでいたため，歯の形成期に局所的な原因が作用して発症したとは考えにくい。既往歴や現症により全身的疾患や外胚葉系の異常，栄養障害や内分泌障害，熱性疾患などにより引き起こされるエナメル質形成不全[1]とも考えにくい。また，母親の妊娠中の問題点も考えられるが，薬剤服用は短期間であり，患児における乳歯および永久歯の両者にエナメル質の形成不全を認めることより，薬剤名は不明であるが妊娠中の問題によってエナメル質の形

成不全が起きたとは考えられない。これらのことより本症例は，環境因子によるエナメル質形成不全症とは考えられない。遺伝性のエナメル質形成不全症には，乳歯列，永久歯列両者にエナメル質形成不全が認められること，また，形成不全が全歯の広範な歯面に広がりエナメル質に限局しているという特徴が挙げられ[2]，本症例においてこの条件は満たされている。従って，遺伝的なエナメル質形成不全症である可能性が示唆された。しかしながら，同時に Witkop は，エナメル質形成不全症には家族的にエナメル質における形成不全が認められることも条件としている[6]。本症例において家族歴を問診したところ，エナメル質形成不全を有する者を明らかにすることは出来なかった。一般に遺伝性疾患における家系調査は，家族の死亡や，散在，家族の十分な協力が困難なことなどにより難しいことが報告されている[1]。本症例においても問診のみによる調査であったため，その家族の詳細な口腔内状況を把握するには到らなかった。より詳細な家族歴を調べることにより遺伝性のエナメル質形成不全症であることを明らかにすることが可能と考えられる。しかし，先に述べたように協力度や遺伝性疾患に対し違和感を持つことなどを考えると，これ以上の家族歴の調査は困難と考えられた。また，姉妹に突然発症する報告[12]があることから，本症例も特発的に引き起こったエナメル質形成不全症であることが示唆された。

過剰歯における形態学的・組織学的検討の報告[7,9]は多く認められるが，エナメル質形成不全症に発現した過剰歯の報告は認められない。過剰歯は，乳歯列期，混合歯列期，永久歯列期のいずれにも認められ，下顎より上顎，部位的には上顎切歯部に好発することが報告されている[8]。その発生頻度は，1.48～5.17% であり，エナメル質形成不全症の発生頻度が 14,000 人に 1 人であることを考えると両者を合わせもった本症例は稀有な症例であることが示唆された。過剰歯は一般的に乳白色のものや淡黄色のもの，およびその中間的な色調を示すことが報告[7]されている。本症例における過剰歯の色調は白色であり，本患児における乳歯および永久歯における黄褐色な色調とは明らかに違うものであった。過剰歯においては，エナメル質表面の性状において部分的な欠如，陥入，粗造感[13]，新産線より表層のエナメル質に石灰化のばらつきを生じることが報告されており，これらのことが色調の変化をもたらす原因の一つと考えられた[7]。SEM におけるエナメル質の観察においては，コントロールに比較し凹凸の著しい像を示していることが明らかになった。さらに，トームス突起の陥凹の不規則さや，突起の陥凹が認められない部位もあった。エナメル質が板状に剝離し，折り重なるような像が認められたこと，また，高い頻度でカリフラワー状のエナメル質の隆起が認められたことから，エナメル質形成が規則正しく行われない，もしくは一部形成が停止した可能性が示唆された。これらのことは，エナメル質形成時において何かしらの形成障害が引き起こされ，エナメル質の形成が均一に起きなかったことを示唆している。これらの所見より，現在までに報告[7]されている健常児における過剰歯のエナメル質表面における部分的なエナメル質の欠如や形成不全による粗造感とは明らかに違うものであることが示唆された。本症例における摘出過剰歯の形態は，犬歯型と円錐型であった。過剰歯の形態の分類において単錐型あるいは円錐型の発現は最も多く，類円錐型を含めるとその大部分を占めていることが報告されており，犬歯型の発現率は非常に低く約 1% であることが報告されている[14]。過剰歯の発生原因としては，歯の発育初期に歯堤が正常の歯数より多くエナメル器を作るためと考えられる[15]。本症例の歯根形成量を考えるとほぼ同時期にエナメル器の過剰な発現が起こったと考えられる。本試料 2 本におけるエナメル質表面の形状は類似しているにも関わらず，歯冠形態が明らかに違った。以上のことから，過剰歯は健常児と同様に過剰なエナメル器の発現が生じ，エナメル質の形成では，他の歯と同様に遺伝子の異常によって形成不全が生じたと考えられた。しかしながら，患児の乳歯ないし永久歯と比較し，摘出過剰歯は白色を呈しており，明らかな色調の違いを認めたことは大変興味深い。この理由について明言は今のところ出来ない。健常児においても過剰歯のエナメル質は，本来形成されるべきではない場において発育するために，正常歯の歯根や歯胚により圧迫をうけ形成不良となる可能性があるとの報告がある[7]。従って，本症例においても萌出歯とは違うエナメル質の形成不良が起こり色調の違いを生む要因となったと考えられた。

過剰歯が及ぼす影響としては，正中離開，切歯の捻転，永久歯の萌出遅延，転移などの報告を認める[16,17]。本症例においても過剰歯が原因と考えられる軽度の正中離開を認める。現在，正中離開を認めるも他に問題点は認めていない。

今後は，エナメル質形成不全部の経過および正中離開の変化を観察していく予定である。

結　論

今回著者らは，エナメル質形成不全症の患児に発現した過剰歯摘出を経験し以下の結論を得た。

1．特発性に発症したエナメル質形成不全症であり，エ

ナメル質形成不全症における過剰歯の発現は稀有である。

2．患児の過剰歯以外の乳歯および永久歯と過剰歯の色調には明らかな違いを認めた。また，摘出過剰歯のエナメル質表面の性状は，健常児におけるエナメル質表面と比較して，凹凸の激しい，粗造感を呈しており，明らかな違いを認めた。

3．エナメル質形成時期に障害を受け，なおかつエナメル質の形成が均一に行われなかったことが示唆された。

文　献

1）吉田忠雄，峰岸秀夫，逢坂亘彦，入江英仁，栗原順吉，五嶋秀男：減形成型をとった遺伝性エナメル質形成不全症の一症例，城歯大紀要，10：315–321, 1981.

2）錦城　香，石川利栄子，蓮井義則，山口公子，西野瑞穂，尾崎和美，松尾敬志：エナメル質形成不全症の1例，小児歯誌，37：620–625, 1999.

3）Darling, A. I.: Some observation on amelogenesis imperfecta and calcication of the dental enamel, Proc. Roy. Soc. Med., 49: 759–765, 1956.

4）Witkop, C. J. Jr.: Genetics and dentistry, Engenics Quart, 5: 15–21, 1958.

5）Witkop, C. J. Jr: Amelogenesis imperfecta, dentinogenesis imperfecta and dentindysplasia revisited: problems in classification, J oral pathol, 17: 547–553, 1989.

6）Wilkop, C. J. Jr. and Rao, S.: Inherited defects in tooth structure, Edited by Bergsma.D., Birth defects: Original article Series. The Williams and wilkins, Baltimore, 1972, pp. 153–184.

7）渡辺直彦：乳歯列前歯部過剰歯の形態ならびに組織構造に関する研究，愛院大歯誌，33：163–181, 1995.

8）藤田恒太郎：人における歯数の異常，口病誌，25：97–106, 1958.

9）渡辺英雄：小児の上顎前歯部過剰歯に関する研究第Ⅱ報抜歯過剰歯，797歯の形態学的観察，愛院大歯誌，24：98–121, 1986.

10）藤田恒太郎：Ⅰ緒論・エナメル質およびセメント質の厚さ，歯の解剖学第21版，金原出版株式会社，東京，1976, pp. 19.

11）前田隆秀：歯の発育と異常，内村　登，前田隆秀，宮澤裕夫，渡辺茂編，スタンダード小児歯科学，学建書院，東京，2001, pp. 37–40.

12）谷口博通：姉妹の全永久歯にみられたエナメル質形成不全症，歯科医学，35：691–697, 1972.

13）長縄弘康，佐々公人，村田格一ほか：下顎前歯部における埋伏過剰歯の2症例，小児歯誌，13：260–265, 1975.

14）杉山乗也，伊藤　明，長縄弘康ほか：上顎前歯部過剰歯に関する研究，小児歯誌，6：118–126, 1968.

15）内村　登，前田隆秀，宮澤裕夫，渡辺　茂：歯の発育と異常，前田隆秀，スタンダード小児歯科学，学建書院，東京，2001, pp. 41–42.

16）長谷川浩三，中澤直美，外木徳子，町田幸雄：上顎正中過剰歯の経年的観察，小児歯誌，29：428–438, 1991.

17）野坂久美子，佐々木勝忠，佐々木仁弘，守口　脩，甘利英一：上顎正中埋伏過剰歯の中切歯歯根形成への影響，小児歯誌，18：502–512, 1980.

A Case Report of Supernumerary Teeth in Patients with Amelogenesis Imperfecta (AI)

Kensuke Matsune, Reiko Ujigawa, Katsumi Miyoshi, Rie Matsunaga
Kunihiro Suzuki* and Takahide Maeda

Department of Pediatric dentistry, Nihon University School of Dentistry at Matsudo
(Director : Prof. Takahide Maeda)
**Department of Anatomy II, Nihon University School of Dentistry at Matsudo, Matsudo,*
(Director : Prof. Yukishige Kozawa)

Amelogenesis imperfecta is a disease that shows up as a defect in tooth structure caused by abnormal enamel development during tooth embryogenesis. The authors experienced a patient who was diagnosed as having amelogenesis imperfecta in this supernumerary teeth based on the results of clinical examination. We then examined the supernumerary teeth of this patient, through clinical examination, radiograph examination and histological examination using a scanning electron microscopy.
The results were as follows :

1. Our patient suffered from of amelogenesis imperfecta and the symptom was seen idiopathically.
2. It was a rare case in that our patient with amelogenesis imperfecta had supernumerary teeth.
3. The color of the enamel of the supernumerary teeth was different from the color of the other teeth of the primary and permanent dentition in this patient.
4. Using a scanning electron microscopy was the surface of the enamel of the supernumerary teeth shown to be rough and uneven compared with the supernumerary teeth in normal patients.

Key words : Amelogenesis imperfecta, Supernumerary teeth, SEM

小児歯科学雑誌　43(4) : 512–517　2005

Nd-YAG レーザーを用いたレーザー溶接の小児歯科領域の有効性の検討（1）

——レーザー照射出力，照射角度と照射回数における変化——

松根健介　丸山明華　荒井清司
岡本春憲　三好克実　清水久美子
渋谷　功*　根本君也*　前田隆秀

要旨：小児歯科臨床において行われる補助弾線の鑞着操作において Nd-YAG レーザーを用いたレーザー溶接の有用性について検討を行った。主線として歯科用コバルトクロム合金サンプラチナ®矯正線直径 0.7 mm を使用し，補助弾線としてステンレススチールワイヤー 0.016 inch を用いレーザー溶接を行った。レーザー溶接は，Nd-YAG レーザーにて行い，レーザー照射出力，照射角度および照射回数を変化させたときの引張り強さの変化を検討した。その結果，レーザー照射出力が 900 mJ，照射角度 45 度から 60 度の条件において引張り強さが有意に高いことが示唆された。さらに，レーザー照射において，レーザー照射時に間隔をあけずに一部レーザー照射部位を重複させると，より強い引張り強さを発揮することが示唆された。また，レーザー溶接は銀鑞着に比較し引張り試験結果は低かったが，日常臨床においてはレーザー溶接による引張り強さで，十分な機能を発揮できると考えられた。さらに，口腔内にて溶接操作が行えるなどの利点もあり，レーザー溶接が有用な方法であることが示された。

Key words：レーザー溶接，補助弾線，Nd-YAG レーザー

緒　言

1960 年に Mainman[1]がルビーを用いてレーザー光の発生に成功して以来，レーザーの種類も豊富になり，歯の切削，耐酸性付与，軟組織の切開や止血といった多岐にわたる症例に有用であることが報告されてきた[2~5]。小児歯科診療においては，レーザーによる歯の削除や耐酸性付与効果の有用性が報告されている[6~8]。また，Nd-YAG レーザーを用いた口腔内溶接や異種金属の溶接については，著者らが報告している[9]。特に，歯科補綴物への応用における基礎研究では，銀鑞着にも劣らない有用性の報告も認める[10, 11]。

一方，小児歯科臨床における鑞着操作は，補助弾線の鑞着やクラウンループの鑞着等において用いられているが，小児歯科領域におけるレーザー溶接の報告は認めない。今回，著者らは小児歯科領域におけるレーザー溶接の有用性を検討すべく補助弾線と主線の溶接において Nd-YAG レーザーの有効性について基礎的，特に照射出力，照射角度と照射回数における引張り強さについて検討を行った。

日本大学松戸歯学部小児歯科学教室
千葉県松戸市栄町西 2 丁目 870 番 1
（主任：前田隆秀教授）
*日本大学松戸歯学部歯科生体材料学教室
千葉県松戸市栄町西 2 丁目 870 番 1
（主任：根本君也教授）
（2005 年 6 月27日受付）
（2005 年 7 月12日受理）

材料および方法

1．試料

本研究では，主線として歯科用コバルトクロム合金サンプラチナ®矯正線（デンツプライ三金社製）直径 0.7 mm を使用し，補助弾線としてステンレススチールワイヤー 0.016 inch（トミー社製）を使用した。

2．方法

1）試験体

3 cm の主線の中央部に補助弾線としての溶接部分が 3 mm となるステンレススチールワイヤーの試験体を作製した。また，ステンレスワイヤーの鑞着部位の別の側の先端に直径 3 mm のループを作製し，溶接あるいは鑞

着部位先端からループまでの距離を3 cmとなるように設定した（図1）。

2）使用レーザー

溶接部位にNd-YAGレーザー（CONTAC LASE™, SLT Japan）を使用し，ファイバー径400 μm（石英　先端加工なし），パルス数を5 pps，照射時間を1秒に設定してレーザー溶接に使用した。照射出力，照射角度および照射回数は変化させた。

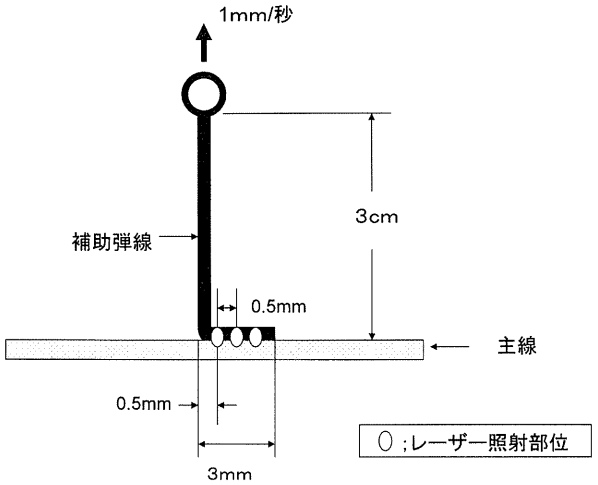

図1　試験体模式図
レーザー溶接部位は3 mmで，3箇所の溶接を行った。

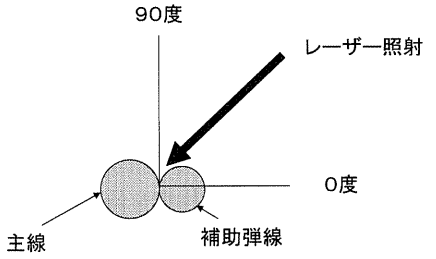

図2　レーザー照射角度模式図
レーザー照射は30, 45, 60, 90度に変化させた。

3）銀鑞着

同一部位に銀鑞着をサンプラチナ®鑞線（デンツプライ三金社製）を用い通法に従って行った。

4）引張り試験

引張り試験は，溶接を行った補助弾線に冶具を介し引張り圧縮試験機TG-5 kN（ミネベア株式会社製）により1 mm/secの速度にて破断時の荷重を測定した。引張り試験は以下に示す2項目について条件を変化させて検討した。

①　照射出力と照射角度の影響について

照射出力は，600・900・1200 mJの3段階，照射角度は，30・45・60・90度の4段階とし，各組み合わせにて設定された試験体を固定し，顕微鏡下にてワイヤーにファイバー先端を接触させ，ハンドピースを固定した状態でレーザー照射を行った（図2）。試験体は各組み合わせに対し10試験体とし，照射間隔は0.5 mmずつ移動させレーザー照射を3点行った。測定値の検定は2次元分散分析と，多重比較にTukeyの検定を用いた。

②　レーザー照射回数の影響について

照射出力を900 mJ，照射角度を45度の条件で設定し，より臨床に近い状態で行うためにハンドピースを手指にて保持し，肉眼にてワイヤーに接触させた状態で照射を行った。レーザー照射回数の変化は，0.5 mm間隔に1・2・3・4点照射した4段階（図3）とし，試験体は各5試験体にて引張り強さを測定した。測定値の検定は一元配置分散分析と，多重比較にTukeyの検定を用いた。対象として銀鑞着試験体をレーザー溶接と同一部位に歯科用銀鑞を用い臨床経験5年以上のドクター5名により作製した。また，間隔の有無における影響については間隔を開けて4点照射した測定値と，レーザー跡を

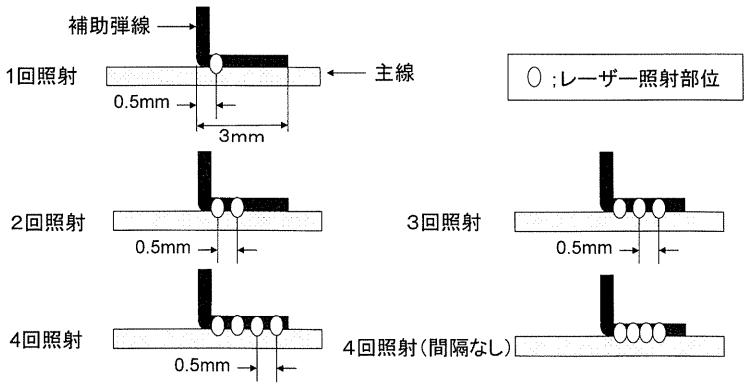

図3　レーザー照射回数模式図
レーザー照射は，間隔をあけて1, 2, 3, 4か所照射した場合と，間隔を開けずに4か所照射した5段階とした。

一部重複させ4点を照射（図3）したときの測定値をt-検定にて比較検討した。

結　果

1）レーザー照射出力と照射角度の影響について

照射出力と照射角度の違いによる引張り試験の結果を表1に示す。

2次元分散分析の結果，照射出力と照射角度に有意な差（$p<0.01$）を認めた。Tukeyの多重比較の結果，600 mJと900 mJとに有意差（$p<0.05$）を認めたが600 mJと1200 mJ，900 mJと1200 mJにおいては有意差を認めなかった。角度においては，30度と45度（$p<0.001$），30度と60度（$p<0.001$），45度と90度（$p<0.001$），60度と90度（$p<0.001$）に有意差を認めた。

2）レーザー照射回数の影響について

レーザー照射回数による引張り試験の結果を表2，3に示す。

照射回数における引張り試験結果は，0.5 mm間隔に照射した場合は有意差を認めなかった。しかしながら，重複させて照射した場合に間隔をあけて照射した場合と比較し有意差（$p<0.01$）を認めた。また，レーザー溶接した場合と銀鑞着した場合の引張り強さには有意差（$p<0.001$）を認めた。

表1　照射角度・照射エネルギーと引張り強さ

n＝120

照射出力	照射角度（度）			
	30	45	60	90
600 mJ	21.1±7.9	35.2±10.2	34.5±7.9	24.9±7.3
900 mJ	33.0±1.2	33.0± 0.9	40.0±0.5	32.0±1.0
1200 mJ	23.3±0.6	39.8± 0.8	37.6±0.8	20.0±0.6

***：30度と45度，30度と60度，60度と90度，900 mJと1200 mJ
*：600 mJと900 mJ
***：600 mJと1200 mJ，900 mJと1200 mJ

平均値±標準偏差，単位：ニュートン（N）
*：$p<0.05$，***：$p<0.001$

表2　照射回数と引張り強さ

n＝25

レーザー溶接回数（回）				
1	2	3	4	銀鑞着
21.7±1.2	20.7±2.2	21.3±1.5	22.7±4.9	85.6±6.7

***：1回と2回，1回と3回，1回と4回，1回と銀鑞着，2回と銀鑞着，3回と銀鑞着，4回と銀鑞着

平均値±標準偏差，単位：ニュートン（N）
***：$p<0.001$

表3　照射間隔と引張り強さ

n＝10

レーザー溶接回数（4回）	
間隔あり	間隔なし
22.7±4.9	33.2±2.3

**：間隔ありと間隔なし

平均値±標準偏差，単位：ニュートン（N）
**：$p<0.01$

考　察

近年，レーザー医学は目覚ましい発展を遂げ，歯科領域におけるレーザーの応用においても診断や診療の新しい手段として多くの期待が寄せられている[12~14]。小児歯科領域における各種レーザーは，歯の切削，エナメル質の耐酸性付与，止血等多岐に用いられている[5, 15~19]。各種レーザーの中でもNd-YAGレーザーの有用性は歯質の耐酸性向上，歯の選択的削除の可能性[20]，さらにレーザー溶接における報告も認める[10, 21]。レーザー溶接に関しては，クラウンブリッジの鑞着や矯正バンドと矯正線における溶接に応用した報告[22, 23]はあるが，小児歯科領域で多用される補助弾線を主線に溶接した報告は認めない。通常，小児歯科臨床における歯の移動に用いる補助弾線は銀鑞で主線に鑞着しているが，火炎中で過熱すると熱変性が生じて弾性を減少させ，弾性限界の低下を惹き起こすことが危惧される。

一方，レーザーによる溶接は，照射された局所が金属の融点に達して蒸散に至っても照射領域が限局されており，暴露時間が短時間であるため照射域外への熱の影響が少ない特徴がある[9]。つまり，補助弾線においてもっとも大切であるワイヤーの弾性力を低下させることなく鑞着をすることが可能であることが考えられた。そこで，著者らは，補助弾線の溶接におけるレーザーの有効性を金属接合部の引張り試験にて検討した。まず，レーザー照射角度について角度を30，45，60，90度の4段階に変化させて影響を検討したところ，30度と90度は45と60度に比べて引張り強さが低下することが明らかになった。また，今回の結果より，45度から60度の範囲に引張り強さのピークが来ることが示され，溶接を行う場合45度から60度間の角度で溶接を行うと補助弾線と主線が密に溶接される可能性が示唆された。Nd-YAGレーザー溶接においては，鏡面研磨された純金や純銀などはビーム吸収率（入射レーザー強度に対する吸収レーザー強度）が非常に低く，溶解しにくい金属であることが言われており，ビーム吸収率は，金属の表面状態，雰囲気，入射角度などによっても影響されることが報告されている[24]。今回の結果からもレーザー溶接がレーザー

入射角度によって影響を強く受けることが示唆された。次に，照射出力においては，600 mJ と 900 mJ に有意差を認め，900 mJ と 1200 mJ 間に有意差を認めなかった。このことは，900 mJ 前後の照射出力であれば十分な引張り強さを獲得できることを示唆している。また，600 mJ と 1200 mJ に有意な差を認めないことにより，900 mJ 前後の照射出力で溶接を行うことが有効である可能性が示唆された。有意差を認めた原因としては，600 mJ では出力が弱すぎるために溶解面積が少なく，1200 mJ では出力が強すぎるために，蒸散した面積が多くなるために溶接面積が減少してしまうため[25]と考えられた。

次に，レーザー溶接回数（間隔）の検討では，0.5 mm 間隔でレーザー照射した試験体の結果間では有意差を認めなかった。しかしながら，間隔を開けずに 4 回照射した結果と間隔をあけて照射を行った時の比較において有意差を認めた。間隔を開けずに連続照射した場合に引張り試験結果に有意差を認めたことを考えると，間隔を開けずにレーザー照射したことによりレーザー溶接部位の重なりが生じ，より多くの連続した溶接領域ができ間隔を開けて照射した場合より広範囲の溶接面積が生じ，強い引張り強さを得ることができたと考えられた。また，銀鑞着の引張り試験結果とレーザー溶接の引張り試験結果間には有意に銀鑞着が強かった。これは，銀鑞着の方が接合部の体積がレーザー溶接に比べ大きいことによると考えられる。

しかし，口腔内において 30 N 以上の引張り力が作用することは考え難いことから，レーザー溶接で十分な強さであるといえる。また，900 mJ で 45 度の照射角度で 3 点照射した場合の結果において，肉眼で行った場合に顕微鏡下で行った時の結果の 70% の引張り強さとなった。これは，手指にてハンドピースを保持した場合，照射時に接触法で行ったとしても手指のわずかな動揺や動きが生じたり，照射時に起こる火花などによる手指のわずかな動きによりワイヤー面から若干チップの先端が浮き上がるためと考えられた。拡散レーザー光は，エネルギー量が距離の自乗に反比例することより，ワイヤー面から若干でも非接触の状態になると，溶接力の低下が生じる可能性が考えられ，今回も若干の非接触状態が生じた結果引張り強さの低下が起こったと考えられた。レーザー溶接は，現在までの歯科技工術式に比較し，熟練をさほど要求しないことが報告されている[24]。

しかしながら，今回の結果のように，レーザー溶接時におこる条件の違いにより，溶接力に変化が生じることが考えられるため，よりレーザーのビーム吸収率を上げるためにワイヤー表面の形態を変化させるなどの工夫を施すことより，より接着力の強い溶接操作条件を検討，確立する必要がある。しかしながら，先に述べたようにレーザーによる溶接においては，ワイヤーが本来持つ弾性を失うことなくワイヤーの鑞着を終了が出来る可能性があり，銀鑞着に比較し歯の移動に対してはより効果を発揮できる可能性が考えられた。また，銀鑞着は，銀部分の腐食の問題や，口腔内での操作が出来ない欠点があるが，レーザー溶接には，照射による暴露時間が非常に短いために火花が飛ぶものの高温になる時間が一瞬であるため，熱さ，痛みを感じないことから口腔内での溶接操作を行うことが出来る可能性が考えられた。さらに，溶接部位の腐食がおきにくいことが考えられた。

一方，小児の口腔内において 900 mJ という高出力を使用する場合には，レーザー照射方向，特に軟組織方向へのレーザー照射における影響が心配となる。Nd-YAG レーザーの卵白を用いた実験において 3～4 W 程度の出力では，卵白に蒸散円錐や膜を作ることがない，つまり，3～4 W 程度の出力では軟組織にレーザーを使用しても，組織を透過してしまいレーザーの影響がおよばないことが報告されている[26]。

今回の結果より 900 mJ，5 pps の照射条件においてレーザー溶接に有効なことが考えられたが，4.5 W の出力であるため軟組織におよぼす影響は少ないことが考えられた。しかしながら，より安全にレーザー溶接を行うには患児の不意な動きなども考慮に入れ確実にハンドピースを固定し，レーザー照射が軟組織方向へ向かわないようにレーザー照射を行うことは大切なことと考えられる。さらに，溶接周辺の軟組織に対しての影響を少なくさせるためには，繰り返しパルス数を下げるなどの検討も必要と考えられた。今回の結果より小児歯科領域での応用では，口腔内で直接クラウンループやディスタルシュー，リンガルアーチ，Nance の装置の溶接を行うことが出来る可能性が考えられ，より適切な部位での溶接によって装置装着の溶接を行うことが出来る可能性が本研究から明らかとなった。

結　論

Nd-YAG レーザーを用いた補助弾線と主線の溶接における引張り強さを検討したところ，溶接操作を照射出力 900 mJ，照射角度 45 度から 60 度，レーザー照射跡を一部重複させて連続照射を行うことでより強いワイヤー間の溶接力を生むことが証明された。このレーザー溶接による引張り強さは銀鑞着より劣るが，口腔内での指溶弾線と主線と引張られる荷重には十分勝ることから臨

床応用が可能であることが示された。

文　献

1）Mainman, T. H.: Stimulated optical radiation in ruby. Nature, 189: 493. 1960.
2）森岡俊夫：歯科領域におけるレーザーの臨床応用　う蝕予防への応用，歯科ジャーナル，39: 251–257, 1994.
3）藤井考人：Nd: YAG レーザーによる軟化象牙質の除去に関する研究－特に墨汁および水性インクの光透過性と蒸散との関係－，日レ歯誌，43: 52–60, 1999.
4）山本憲廣：エルビウムヤグレーザー照射した象牙質とコンポジットレジンの接着性－プライマーの組成とレーザー出力について－，日歯保存誌，43: 1123–1131, 2000.
5）松根健介，前田隆秀：CO_2 レーザーの有用性について，小児歯科臨床，9: 33–39, 2004.
6）山田恵子，桜井　聡，神山紀久男：人口的初期脱灰エナメル質へのレーザー照射と弗化物塗布併用による齲蝕抑制効果に関する実験的研究，小児歯誌，26: 732–741, 1998.
7）涛岡暁子，野坂久美子：幼若永久歯におけるシーラント前処理としての裂溝部清掃へのレーザーの応用，日レ歯誌，12: 21–36, 2001.
8）加藤純二：Er: YAG レーザーの小児歯科領域での応用，小児歯科臨床，9: 17–22, 2004.
9）根本君也，西山典宏，渋谷　功：口腔内におけるレーザー溶接，東京歯会誌，52: 749–755, 2004.
10）南里嶽仁：歯科用レーザー溶接機－歯科用レーザー溶接機はろう付に取って代わることができるか－，Dental Diamond, 8: 84–90, 2000.
11）梶原俊一，辻村　亨：レーザー溶接機“デンタルレーザー DL 2000”の技工操作上の有効性と合理化効果，歯科技工，24: 1423–1432, 1996.
12）Bjelkhagen H, Sundstrom F, Angmar-Mansson B, Ryden H.: Early detection of enamel caries by the luminescence excited by visible laser light, Swed Dent J. 6(1): 1–7, 1982.
13）Attrill D. C., Ashley P. F.: Occlusal caries detection in primary teeth: a comparison of DIAGNOdent with conventional methods, Br Dent J.; 190(8): 440–3, 2001.
14）高森一乗，保刈成志，奥村泰彦，渡部茂：齲蝕診断へのレーザーの応用　フィッシャーシーラント下齲蝕診断への基礎研究，Dental Diamond, 26: 92–94, 2001.
15）加藤純二：Er: YAG レーザーの小児歯科領域での応用，小児歯科臨床，9: 17–22, 2004.
16）加藤純二：He-Ne レーザーの小児歯科領域での応用，小児歯科臨床，9: 23–26, 2004.
17）高森一乗：診断領域のレーザー DIAGNOdent®を中心として，小児歯科臨床，9: 27–32, 2004.
18）神谷　誠：当院のレーザー診療，小児歯科臨床，9: 40–46, 2004.
19）浜田晶子，小田裕子，杉岡千津，田中克明，大野秀夫：成育歯科医療をすすめるためのレーザーの活用，小児歯科臨床，9: 47–58, 2004.
20）松根健介，前田隆秀，渋谷　功，根本君也：Nd-YAG レーザーによるう蝕部の選択的削除，日歯保存誌，46: 139, 2003（抄）.
21）岩崎佳治：金銀パラジウム合金における鑞付とレーザー溶接部の疲労強度－鑞付間隙の影響とレーザー溶接部との比較－，日本歯技，386: 21–33, 2001.
22）渋谷　功，谷本安浩，西山典宏，野村　充，根本君也：口腔内レーザー溶接　第3報　クラウンブリッジの溶接－，歯材器，22: 162, 2003.
23）渋谷　功，谷本安浩，西山典宏，根本君也：口腔内レーザー溶接　第1報　矯正用材料，歯材器，21: 65, 2002.
24）都賀谷紀宏，篠崎照秦：歯科レーザー溶接入門－レーザー溶接を始める人のための基礎知識（1）－，Quintessence of Dental Technology, 24: 740–749, 1999.
25）都賀谷紀宏，篠崎照秦：歯科レーザー溶接入門－レーザー溶接を始める人のための基礎知識（3）－，Quintessence of Dental Technology, 24: 1471–1479, 1999.
26）加藤純二，粟津邦男，篠木　毅，守矢佳代子（編著）：レーザーで遊んでみよう，一からわかるレーザー歯科治療，医歯薬出版株式会社，東京，2003, pp. 8–25.

A Study on Laser Welding using an Nd-YAG Laser for Auxiliary Spring in Pediatric Dental Clinic-Power of the laser, Irradiation angle of laser and irradiation frequency of laser

Kensuke Matsune, Sayaka Maruyama, Kiyoshi Arai, Katsumi Miyoshi
Kumiko Shimizu, Isao Shibuya*, Kimiya Nemoto* and Takahide Maeda

Department of Pediatric dentistry, Nihon University School of Dentistry at Matsudo
(Director : Prof. Takahide Maeda)
**Department of Dental Materiasl, Nihon University School of Dentistry at Matsudo, Matsudo*
(Director : Prof. Kimiya Nemoto)

In pediatric dental clinics, soldering is generally used, but this is not a convenient method as it cannot be used in the oral cavity. Focus is now on recent laser development.

The purpose of this study was to evaluate whether laser welding using an Nd-YAG laser could be used for appliances with an auxiliary spring. It was suggested that the tensile bond strength for laser welding irradiated with a 900 mJ Nd-YAG laser beam and with an irradiation angle of between 45° and 60° was the beat combination compared to other combinations of the 600 mJ and 1200 mJ beams, with angles of 30° and 90°. It was further suggested that the tensile bond strength causes the laser beam to overlap continuously so that the irradiation is effective. The tensile bond strength for laser welding using the Nd-YAG laser was significantly lower than that of argentums soldering using a flame. We feel, however, that the tensile strength of laser welding is sufficient for clinical purposes. In addition, we feel that laser irradiation based on the Nd-YAG laser is useful in clinic because laser welding can be employed for procedures in the oral cavity.

Key words : Laser Welding, Auxiliary spring, Nd-YAG laser

日大口腔科学　28：162～167，2002

《短　報》

鶴天，草食動物の歯で作られた装飾品の顕微フーリエ変換赤外吸収分光分析

砂川一郎　高橋　泰　木村郁子*
鈴木久仁博**　寒河江登志朗**

山梨県立宝石美術専門学校，*富山医科薬科大学薬学部臨床薬理学研究室，
**日本大学松戸歯学部　第II解剖学講座

キーワード：鶴天，装飾品，草食動物，歯，顕微FT-IR

Micro FT-IR Analysis of "Kakuten", An Ornamental Object Fashioned from Tooth of Herbivorous Animal

Ichiro Sunagawa, Yasushi Takahashi, Ikuko Kimura*,
Kunihiro Suzuki**, Toshiro Sakae**

Yamanashi Institute of Gemmology and Jewellery Arts, Kofu, 400-0808, Japan
*Department of Clinical Pharmacology, Toyama Medical and Pharmaceutical University, Toyama, 930-0194, Japan
**Department of Anatomy II, Nihon University School of Dentistry at Matsudo
Matsudo, Chiba 271-8587, Japan

Key words : "Kakuten", ornament, herbivore, tooth, micro FT-IR

Nihon Univ. J. Oral Sci. 28 : 162～167, 2002

緒　言

装飾品の歴史は人類の歴史とともに始まっている。美しい鳥の羽根，猛獣の牙などで首飾りを作り身を飾る風習などは今日でも僻地の原住民の間に残っている。河原で拾った美しい色の鉱物が，今日の宝石の始まりであることも多くの人が納得するところであろう。生物界でできる真珠や象牙も古くから装飾品の重要な素材として使われてきた。しかし，牙以外の動物の歯が装飾品の素材として使われている例はあまり知られていない。本論で珍しい例として"鶴天（かくてん）"と呼ばれる江戸時代の工芸品についての宝石学的，歯科解剖組織学的研究結果について報告する。

鶴天とは，"緒締（おじめ）"の一種で，径1～1.5 cm程度の球形に整形され，朱色と白色，あるいは黒と白，茶と白の不規則な縞模様を示す小型の工芸品である。緒締とは，印篭と根付の間を結ぶ紐を締める役割を果たす球形，方形などの小型工芸品の総称で，印篭，根付ととも

〒271-8587　松戸市栄町西2-870-1（平成13年11月10日受付，平成14年5月10日受理）

に世界中に愛好家，収集家がおり，研究会が組織されている[1-2]。また，根付，緒締の専門書が出版され[1-3]，欧米各国の美術館には専門とする展示ブースがある。代表的な例としてロンドンのBritish Museumおよび Victoria and Albert Museumをあげておく。根付，緒締に関してはいくつかの専門書と研究会の刊行物が知られている[1-3]。根付，緒締がこのように広い関心を呼んだのは，主として江戸職人の示した高い芸術性に依るのであろう。モチーフの珍しさに加えて表現の繊細さが欧米人の心を揺さぶったためか，明治の開国とともに多くの逸品が海外に流出してしまった。根付，緒締を日本のmagical jewelsと見なしていたようである。

根付，緒締ともに種々の材料が使われている。根付の方はサイズが大きいため，緒締よりも材料に制限があったが，それでも，象牙，イッカク鯨や鹿の角，琥珀，柘植，紫檀，黒檀などの生物起源の材料，瑪瑙，孔雀石などの鉱物，銀，赤銅，白銅，洋白，真鍮などの金属が使われている。緒締の材料はもっと多種類にわたり，珊瑚，牛の枝角，象牙，柘植，琥珀，漆，貴金属，陶器，ガラス，宝石鉱物などが使われている。その中でも白と朱色の不規則な縞模様を持つ球形の緒締は鶴天と呼ばれ，鶴の頭頂部の鶏冠と信じられ格別の関心が寄せられ，蒐集家の間では特に高く評価されてきた。根付研究の古典にあたる装剣奇賞[4]では，同じ意味で鳳天という名が使われている。装飾品素材として使われている象牙質材料などをまとめたEspinoza and Mannの書[5]には，後述の冠犀鳥の冠の別名として“ho-ting”および“golden jade（金色翡翠）”の名称があげられているところを見ると，鶴天はもともと冠犀鳥の冠で鳳天と呼ばれていた物と考えられる。

このように生物起源の宝飾品について未解明の点が多く残されており，近代的な分析法を用いたより深い理解が必要であるという共通認識で，著者の一人（木村）が所有する鶴天について研究することとなった。パリ郊外の獣医科大学のMusee Fragonard d'Alfort, Ecole Nationale Verinaire d'Alfortに動物の器官中に出来た結石類，およびそれより作られた装飾品のコレクションがあり，その試料を研究したJean Poirotに本標本について問い合わせをしたが，該当する材料につき納得できる回答を得られなかった。そこで，組織観察および顕微FT－IR（微小部フーリエ変換赤外吸収分光法）を利用して検索した結果，鶴天の素材は草食性動物の歯であり，それを球形に整形し染色したものであることが判明した。動物の歯を装飾品の材料として使った例は極めて珍しく，歯科解剖学にとっても興味があると考え，ここに報告する。

材料および方法

鶴天試料は，径1.7 cmの球形で中心に貫通する孔が穿たれている。朱色と白色の不規則な縞模様を示す。Fig. 1に2方向から撮影した試料のマクロ写真を示す。この試料について，比重，屈折率（スポット法による測定），蛍光反応，チェルシーフィルター下での反応など通常の宝石学的検査を行った。構成成分の分析に顕微フーリエ変換赤外分光分析計（micro FT-IR，FT-530，ホリバ㈱，京都）を用いた。試料は無処理で，測定条件を以下に記す。測定モード：反射測定，測定領域：50×50 μm，カセグレン：×16，検出器：MCT（液体窒素冷却），測定波長領域：4000～750 cm^{-1}，分解能：2 cm^{-1}，測定時間：100 sec，反射－透過データ変換：K-K（Kramers-Krönig）変換。K-K変換は反射法で測定した吸収データを擬似的に透過法スペクトルに変換する方法である[6]。したがって吸収スペクトルの正確なバンド位置と強度は得られないが，分子の同定には充分であるといわれている。今回は非破壊で含まれている分子の種類の分析を目的としたためこの方法を採用した。

結果および考察

1．マクロ所見

今回の鶴天試料について通常の宝石学的肉眼鑑定では生物起源の材料を用いたものであることが示唆されたが，物質同定には至らなかった。得られた諸データは，象牙を含む宝石素材の既知の宝石学的データのいずれとも一致しなかった。

2．比重，屈折率，蛍光反応

比重測定，屈折率測定，蛍光反応の結果をTable 1にまとめる。Table 2に象牙質素材について報告されている比重，屈折率の値をまとめて示した[7]。今回の鶴天試料は，象牙，その他の動物の牙，角，骨など可能性のある生物起源の宝石素材の既知のデータと一致せず，報告されている鉱物起源の宝石素材のデータとも一致しない。鶴天の名前から想像できるように，鳥類の作る象牙質が可能性のある素材として想定できるが，その種の唯一の

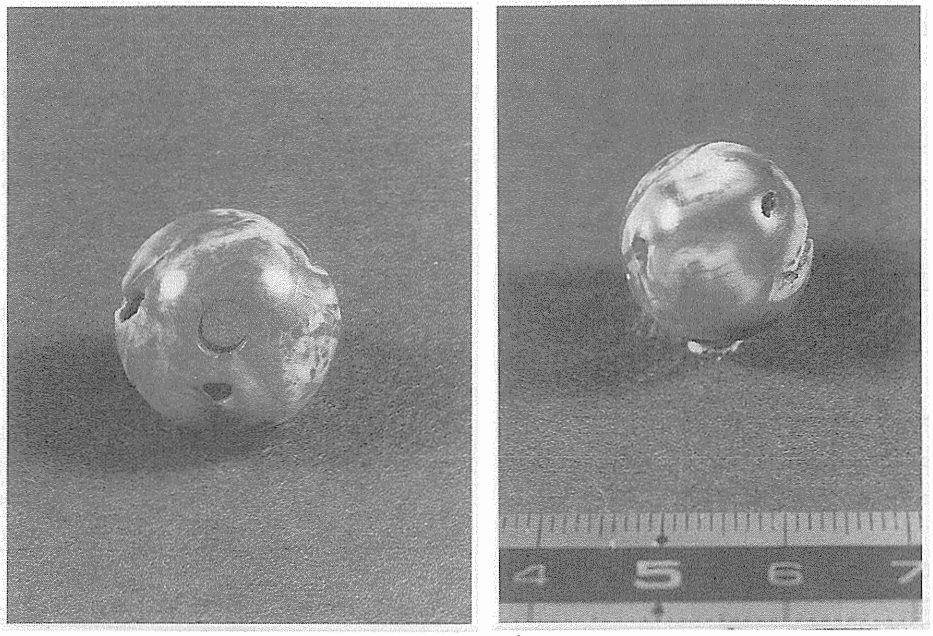

a　　b

Fig. 1　Macroscopic view of the "Kakuten" sample.

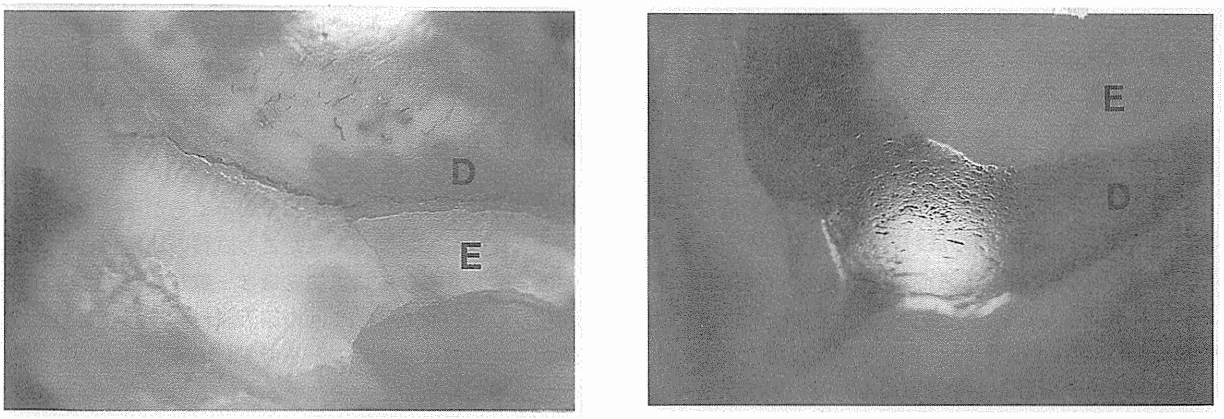

a)　　b)

Fig. 2　Differential interference microscopic images of a) the white part, and b) the vermilion color part of the "Kakuten". After the FT-IR analysis, the part "E" is shown to be enamel and "D" to be dentin.

ものとして考えられる冠犀鳥（Helmeted　Hornbill, *Rhinoplax vigil*；ボルネオにかって生息した犀鳥の1種で絶滅種とされている。その頭頂部に象牙質の冠があり，装飾品材料として使われたことがある）の冠のデータとも一致しない[5]。

この試料が染色されていたことは注目に値する。蒸留水中での比重測定後に使った脱脂綿に朱色が残った事実，および朱肉を使った象牙の印鑑の示す紫外線下の蛍光反応と同じ蛍光反応をこの試料が示したことから，染色されていると結論することができる。染色は朱肉による可能性が高い。

3．組織学的特徴

鶴天の示す複雑な縞模様は白色部と朱色に染まった2種類の異なった組織に由来する。装飾品であるため，破壊検査が許されず，薄片を作って組織を詳しく調べるこ

Table 1　鶴天試料の宝石学的性質

屈折率	黒褐色部	1.57
	赤褐色部	1.58
	白色部	1.60
	平均	1.58
比重		2.176
UV（L）	白色部のみ青白濁蛍光	
UV（S）	白色部のみ黄白濁蛍光	
分光	特有の吸収性なし	
カラーフィルター	赤褐色部の減少が見られる	
特記事項	比重測定中に蒸留水に朱色の染料がわずかに溶出 カラーフィルターで見られた現象は朱肉に染まった象牙の部分でも認められる	

とが出来なかったが，球形試料のままで，高倍率で観察することによって，2種類の組織の違いの大要を知ることが出来た。Fig. 2 a，b に微分干渉反射顕微鏡写真を示す。この観察では，染色されていない白色部は緻密で組織構造が特に認められないが，光沢などからエナメル質に近いと推測された。一方，朱色に染まった部分は多孔質に観察された。多孔質部分は哺乳動物の歯の象牙質部分に一般的にみられる象牙質細管の存在によるものと推測された。エナメル質部と象牙質部の境界はシャープであるが不規則な形状である。この組織の違いは，歯のもつエナメル質と象牙質の組織の差によるものとみなせる。

4．FT－IR 分光分析

顕微 FT－IR 法を適用してそれぞれの部分を選び，微小領域（50×50 μm）内の反射赤外吸収スペクトルをえた。得られた反射 FT－IR スペクトルを K－K 転換し，透過測定に擬似化したスペクトルを Fig. 3 a，b に示す。比較のために，同じ装置を用い KBr 粉末法で得たヒトの永久歯のエナメル質および象牙質の FT－IR スペクトルを Fig. 3 c，d に示した。これらのスペクトルは LeGeros[8]の報告しているヒトのエナメル質と象牙質のデータとよく一致している。

今回の鶴天試料の FT-IR データは反射法で測定して K-K 変換したものなので，吸収バンドの位置と強度は詳細には比較できないが，アパタイトの P-O，アパタイト結晶中の C-O，O-H，そして象牙質中の有機質の吸収バンドが同定できた。Fig. 3 c，d に，アパタイト，蛋白質，炭酸塩鉱物，OH 基の吸収ピークの位置を示してある。ハイドロキシアパタイト結晶中の OH 基を置換した CO_3 基，いわゆる A-site carbonate の吸収（1545，1450 cm^{-1}）[9]は今回の試料では確認できなかった。LeGeros[8]によれば生物起源のアパタイト中には PO_4 基を置換する CO_3 基，いわゆる B-site carbonate（1465，1412 cm^{-1}）のみしか存在しないということであり，確認できなくて当然かもしれない。Fig. 3 の a，b と c，d の対比から，鶴天の白色部は人間の歯のエナメル質部，朱色に染色された部は象牙質部に対応しており，鶴天は晴乳類動物の歯を整形，研磨，染色した物と結論できる。

Table 2　象牙質素材及び成人の歯の屈折率，比重[7]

	屈折率	比　重
象	1.535	1.70～1.90
河馬	1.545	1.90～1.95
セイウチ	1.560	1.95～2.00
イッカク鯨	1.560	1.95
マッコウ鯨	1.560	1.95
骨	1.54	2.60
植物象牙		
コロゾナッツ	1.54	1.40～1.43
エジプトナッツ		1.38～1.40
鶴天	1.57～1.60	2.176
成人の歯（平均）＊		
（乾燥後，全体）	1.60	2.12
エナメル質		2.92
象牙質		2.26
セメント質		2.11

今回の鶴天試料が動物の歯であることが確認できた。象牙と比較して疑問であったこの試料の比重値は，人間の歯で得られている比重値とほぼ一致し，納得できる範囲にはいる（Table 2）。今回の鶴天試料が球形なために構造がより複雑に見えることを考慮しても，白色部と朱色部が複雑に分布していることから，この動物の歯のエナメル質，象牙質の構成，即ち歯の組織は人間の歯のように単純ではなく，複雑であったと考えられる。草食性の動物の歯，特に臼歯はエナメル質が褶曲して複雑な形態をとることがおおいため，今回の歯も草食動物のものであったろうと推定できる[10]。動物の種を同定するためには，薄片を作ってエナメル質，象牙質の分布，形，厚さなどの詳細を調べ，対比照合することが必要になるが，これは非破壊検査のみに制限された今回は実現できなかった。今後 micro-CT などを活用して研究する余地があると思われる。

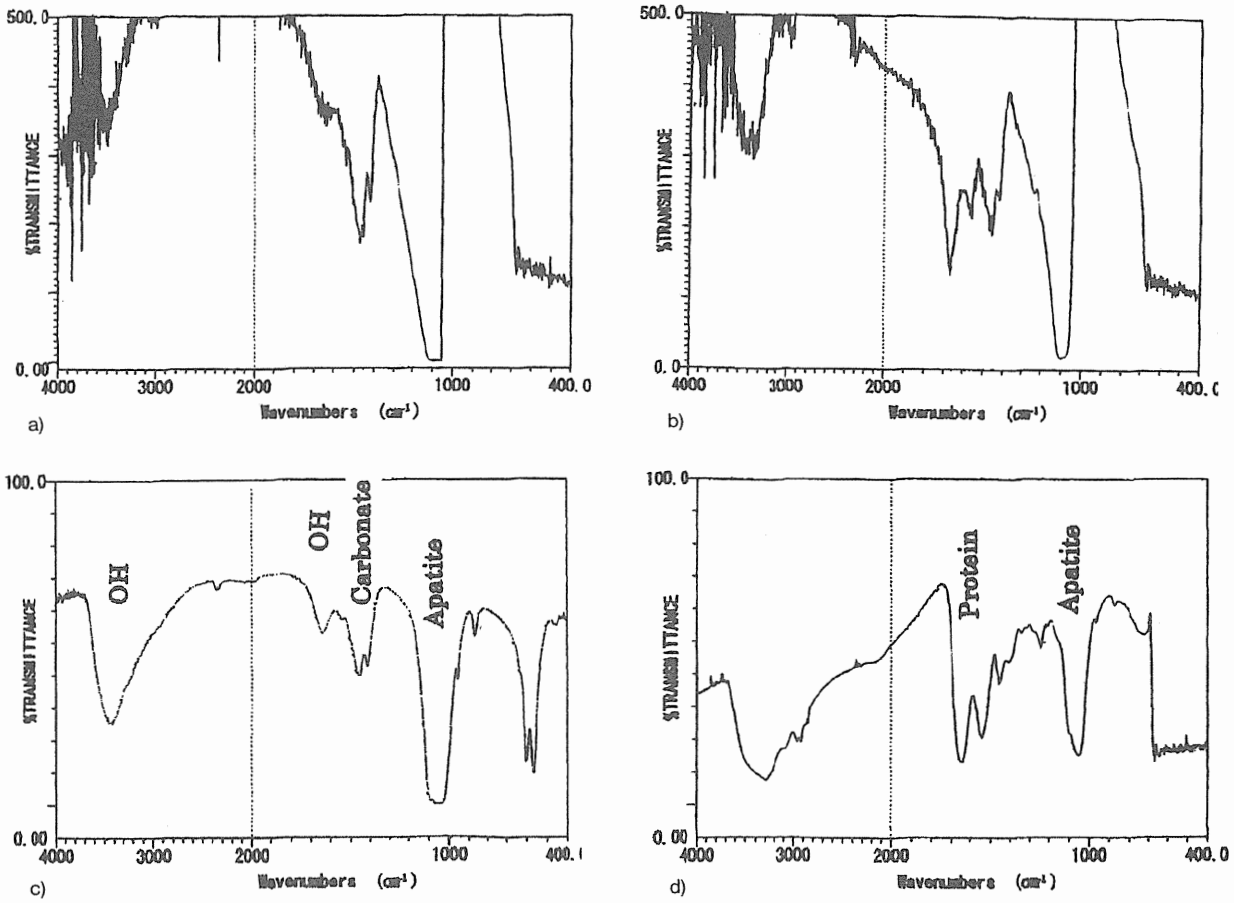

Fig. 3　Micro FT-IR spectra using the reflection mode for a) the white part, and b) the vermilion color part of the "Kakuten". FT-IR spectra for human enamel (c) and dentin (d) using the KBr method is shown together. OH : assigned as water in apatite, Carbonate : caronate ions in apatite, Apatite : phosphate ions in apatite, and Protein : organic matrices in tooth dentin.

よく知られているように，歯の象牙質部は50％のアパタイトと50％の蛋白質で構成され，一方エナメル質部では98％がアパタイト，2％が蛋白質である。象牙質部とエナメル質部での無機物対蛋白質比は動物の種類によって大幅に変わることはない[7]。アパタイトの結晶のサイズ，形，完全性は象牙質とエナメル質で大幅に異なり，それに由来する組織の差が象牙質，エナメル質の機能の差を生んでいる[7]。象牙質部だけが染色されているのは，おもに組織の差，有機質量の差による。生命活動の結果生まれる無機物の結晶は，蛋白質との共同作業で成長する。蛋白質のつくる膜が袋の役割をして，無機物の結晶のサイズや形を制御しているのか，それともエピタキシヤル成長における基盤の役割を蛋白質が担っているのか，生鉱物学にとって今後の課題である。

ま と め

鶴天と呼ばれる江戸時代の工芸品（根付と印篭を結ぶ紐を締める役割をもつ緒締の1種）の素材について宝石学的検査，組織の観察および顕微FT－IR分光法により調べた結果，草食動物の歯を球形に整形，研磨後，染色した物であることが明らかになった。長い間信じられていたような鶴の頭頂にある鶏冠でも，冠犀鳥の冠でもなかった。最初は恐らく冠犀鳥の冠を素材としていたのであろうが，素材の枯渇にともなって，歯を使うようになったのであろう。動物の歯を工芸品あるいは装飾品の素材として使った例は極めて珍しいことである。

参考文献

1) 日本根付研究会二十周年記念出版：根付，江戸細密工芸の華，日本根付研究会，1995.

2) 日本根付研究会二十五周年記念出版：根付の雫，日本根付研究会刊，2000.

3) Kinsey RO: Ojime, Magical Jewels of Japan, H.N. Abrams Inc, New York. 1991.

4) 稲葉通龍：装剣奇賞，第6巻，第7巻，1781.

5) Espinoza EO, Mann M-J: Identification Guide for Ivory and Ivory Substitutes, World Wildfield Fund, 1992.

6) 錦田晃一，西尾悦雄：チャートで見るFT－IR，講談社サイエンティフィック，pp.210，1990.

7) 須賀昭一，田熊庄三郎，佐々木哲：歯の研究法－構造と組成－，医歯薬出版，pp.857，1983.

8) LeGeros RZ: Calcium Phosphates in Oral Biology and Medicine, Karger, Basel, pp.201, 1991.

9) Elliott JC: Structure and Chemistry of the Apatites and Other Calcium Phosphates, Elsevier, Amsterdam, pp.389, 1994.

10) Hilton S: Teeth, Cambridge Manuals in Archeology, Cambridge University Press, UK, 1986.

謝辞：フランスの研究情報についてご教示頂いたJ. Poirot氏，象牙質材料についてご教示頂いた全国宝石学協会福島秀明氏に感謝いたします。研究経費の一部は科学研究費補助金（寒河江，基盤(C)，11671817）によっている。

Journal of Oral Rehabilitation 2004 **31**; 67–73

Calcium phosphate formation on the phosphorylated dental bonding agent in electrolyte solution

T. HAYAKAWA*, M. YOSHINARI†, T. SAKAE‡ & K. NEMOTO* *Department of Dental Materials, Research Institute of Oral Science, Nihon University School of Dentistry at Matsudo, †Department of Dental Materials Science and Oral Health Science Center, Tokyo Dental College, Mihamaku and ‡Department of Anatomy, Research Institute of Oral Science, Nihon University School of Dentistry at Matsudo, Matsudo, Japan

SUMMARY **The aim of the present study was to study the mineral formation on a phosphorylated dental bonding agent using a mineralization inductive solution. Clearfil Photobond, which contained phosphate monomer, was cured by photo-irradiation and heat treated, and was then immersed in Hanks' balanced salt solution (HBSS) with pH = 7·4 for 1, 3, 5, 7, 14, and 28 days at 37 °C. The white substances were deposited on the phosphorylated polymer, i.e. cured Photobond disk, after the immersion in HBSS. The white substances become visible after 3 days immersion. After 7 days immersion, surface of the phosphorylated polymer disk was almost covered with white substance layers. The measurement of white substances by means of X-ray diffraction, Fourier-transform infrared and electron probe microanalysis revealed that their main component was carbonate-containing hydroxyapatite. Scanning electron microscopy pictures showed that a large number of globules of hydroxyapatite were fused together, and that each globule was composed of a group of numerous thin-film form flakes uniting and/or clustering together. The results obtained in this study concluded that the presence of phosphonic acid and phosphate group of phosphorylated dental bonding agent enhanced the nucleation and growth of hydroxyapatite crystals on its surface.**

KEYWORDS: **calcium phosphate, electrolyte solution, phosphorylated dental bonding agent, methacryloxydecyl hydrogen phosphate, carbonate apatite, remineralization**

Introduction

Adhesive dental resins are widely used in dental clinics. They showed superior adhesiveness to tooth, metals and porcelains, etc. Most dental bonding agents contain carboxylic acid or phosphoric acid ester monomers for improving their adhesiveness to tooth substrate (1, 2).

The polymers with phosphate (P) groups are expected to bind calcium (Ca) ions under physiological conditions. It has been reported that the apatite is deposited on polyethylene and polyethyleneterephthalate films when they have been grafted with a P-containing polymer and soaked in a solution saturated with Ca and P ions (3–5). The polymer surface grafted with methacrylate phosphate monomer could induce hydroxyapatite (HA) deposition under a physiological condition to produce a thin HA layer onto the substrate. An organophosphate polymer becomes chemically bound onto a polymer film by surface graft polymerization of P-containing monomer, because the P group is one of the building blocks of HA and, in addition, should have a high affinity toward Ca ions. Mucaro *et al.* (6), Yokogawa *et al.* (7) and Varma *et al.* (8) reported that cotton, chitin fibres or chitosan film form calcium phosphate on their surface in solutions with ion concentrations 1·5 times those of simulated body fluid when they have been phosphorylated and subsequently soaked in saturated calcium hydroxide solution. The P groups of phosphoric ester monomers in dental bonding agents will be exposed on the surface after the curing of dental bonding agents.

© 2004 Blackwell Publishing Ltd

On the basis of the above reports, it is expected that dental bonding agents containing phosphoric acid ester will induce a calcium phosphate layer on the cured bonding agents by the immersion in a simulated physiological solution. If dental polymers with P groups form a calcium phosphate layer on the materials *in vivo*, they could be useful as remineralization induction materials in dental clinics, for example, new types of direct pulp capping materials, or hyper-desensitizer reagents.

To our knowledge, there has been no previous reports on the calcium phosphate induction on the phosphorylated dental resins after the immersion in a electrolyte solution.

In the present study, we selected a commercially available dental bonding agent which contained phosphoric acid ester monomer as a phosphorylated polymer, and studied mineral induction behaviour using a mineralization inductive solution on this materials *in vitro* as a first series of immersion experiments. The composition and properties of deposited calcium phosphate on the dental bonding agent were investigated after immersion in electrolyte solution.

Materials and methods

As a phosphorylated dental bonding agent, Clearfil Photobond®* was used. Clearfil Photobond contains Bis-GMA, triethyleneglycol dimethacrylate, and methacryloxydecyl hydrogen phosphate (MDP) (9). The structure of MDP is shown in Fig. 1. Methacryloxydecyl hydrogen phosphate has a phosphonic acid moiety, P-OH, P=O and phosphate moiety, P-O-C. A tape with a hole measuring 80 mm in diameter and 1 mm thickness was placed on the Teflon mould. After mixing the universal and catalyst liquid of Clearfil Photobond, the mixture was applied inside the hole of the adhered tape. The bonding agent was cured by 60 s photo-irradiation using α-Light II† and heat-cured at 50 °C for 2 h, then at 100 °C for 30 min. The surface of cured bonding agent was polished using no. 1500-water proof paper under running water in order to remove the residual monomers on the surface of bonding agent. The cured Photobond disk was used as a phosphorylated polymer disk.

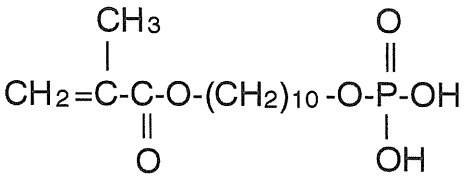

Fig. 1. Structure of methacryloxydecyl hydrogen phosphate (MDP).

Table 1. Ion concentrations in a Hank's balanced salt solution without organic species

Ion	Concentration (mmol L^{-1})
Na^+	142
K^+	5·81
Mg^{2+}	0·811
Ca^{2+}	1·26
Cl^-	145
HPo_4^{2-}	0·778
So_4^{2-}	0·811
HCo_3^-	4·17

The cured Photobond disks were then immersed in 30 mL electrolyte solution with pH = 7·4 at 37 °C for 1, 3, 5, 7, 14 and 28 days in sealed polystyrene bottles. The solution with pH 7·4 was Hanks' balanced salt solution (HBSS) without organic species, which was proposed by Hanawa (10) and Hanawa and Ota (11). The ion concentrations of HBSS are summarized in Table 1. The solutions and bottle were exchanged every day to expose the specimens to fresh solutions. Immediately after immersion, the specimens were again washed by deionized water to remove electrolytes that they did not take up. The specimens were then immediately dried in a desiccator.

The crystallographic structure of products of the immersion experiment at 7 days was analysed by means of thin-film X-ray diffraction‡ (XRD, thin-film attachment) utilizing CuKα-radiation, 50 kV, 250 mA. The surface of cured Photobond disk before immersion were also analysed by Fourier-transform infrared (FT-IR)§ spectrometer in reflection method. The immersion products at 7 days were removed from polymer disk, and their FT-IR spectrum was measured in KBr method. Preliminary experiments showed that it was very difficult to distinguish the peaks derived from

*Kuraray Co. Ltd, Osaka, Japan.
†J.Morita, Tokyo, Japan.
‡Rigaku, RINT 2000, Tokyo.
§Horiba, FT-210, Tokyo.

MDP and calcium phosphate when the immersed samples were measured by reflection method. Analyses were carried out at a constant resolution of 4 cm^{-1}.

The components and Ca and P contents of immersion products were analysed by electron probe microanalysis (EPMA)[¶] at an accelerating voltage of 25 kV. The specimens were coated by carbon before the EPMA measurement. The measured area was 50 × 50 μm. The intensities of Ca-Kα and P-Kα were measured at 1, 3, 5, 7, 14 and 28 days immersion. The Ca/P ratio was obtained from the calculated value of Ca and P with ZAF (Z: Atomic Number Effect, A: Absorption Effect, F: Flourescence Excitation Effect) quantitative correction. The morphology of the reaction products was observed by Field-emission scanning electron microscope (FE-SEM)** at an accelerating voltage of 5 kV. The specimens were coated with platinum before FE-SEM observation.

Results

The formation of white precipitates was observed on the phosphorylated polymer disk, i.e. cured Photobond disk, although no precipitation was observed in test solutions or on the wall of the bottle used for immersion during the experiments. The white precipitates on the cured phosphorylated polymer disk become visible after 3 days immersion in HBSS. After 7 days immersion, surface of the phosphorylated polymer disk was almost covered with white substance layers.

Figure 2 shows the XRD spectrum of white precipitates on the phosphorylated polymer disk after 7 days immersion. Major peaks in the spectrum could be assigned as 002, 210, 211, 112, 202, 310, 113, 222, 213 and 004 of peaks of hydroxyapatite as shown in Fig. 1. X-ray diffraction revealed that hydroxyapatite deposited on the phosphorylated polymer disk.

The FT-IR spectrum of exposed surface of phosphorylated polymer disk is shown in Fig. 3. The peaks between 1000 and 1300 cm^{-1} could be assigned as P=O and P-O-C stretching modes, and the peak around 2700 cm^{-1} could be assigned as P-OH stretching mode of organic phosphonic compounds. The broad peak around 3500 cm^{-1} was attributed as OH of P-OH.

Figure 4 shows the FT-IR spectrum of white precipitates on the phosphorylated polymer disk after 7 days

[¶]Hitachi, X-8010, Tokyo.

**JEOL, JSM-6340F, Tokyo.

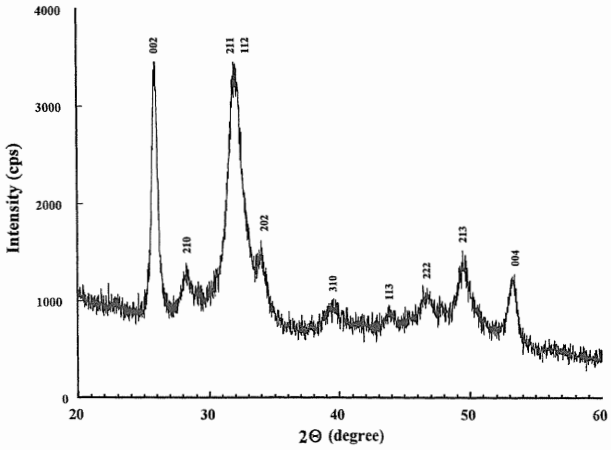

Fig. 2. X-ray diffraction (XRD) spectrum of white substance formed on a cured phosphorylated polymer disk after 7 days immersion in Hanks' balanced solution (HBSS).

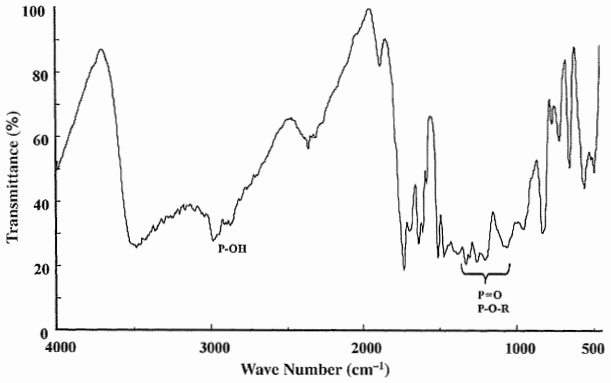

Fig. 3. Fourier-transform infrared (FT-IR) spectrum of the surface of cured phosphorylated polymer disk before immersion in Hanks' balanced solution (HBSS).

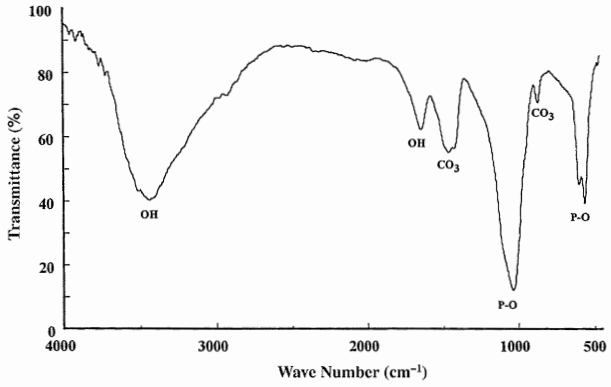

Fig. 4. Fourier-transform infrared (FT-IR) spectrum of white substances formed on a cured phosphorylated polymer disk after 7 days immersion in Hanks' balanced solution (HBSS).

	Immersion periods (day)					
	1	3	5	7	14	28
Calcium (Ca) (cps)	33 (4)	371 (115)	682 (13)	723 (19)	892 (101)	927 (41)
Phosphate (P) (cps)	57 (9)	195 (48)	316 (3)	342 (11)	379 (19)	372 (11)
Ca/P	0·37 (0·01)	1·41 (0·02)	1·43 (0·05)	1·37 (0·03)	1·90 (0·09)	1·82 (0·08)

Values expressed in parenthesis are standard deviation.

Table 2. Results of electron probe microanalysis (EPMA) analysis of the white substances after immersion in Hanks' balanced salt solution (HBSS)

immersion in HBSS. There are two clusters of peaks at 570 and 600 cm^{-1}, and at 1040 cm^{-1}. The former cluster was assigned as P-O bending modes, and the latter was assigned as P-O stretching mode. These are attributed to the P-O bonds of inorganic calcium phosphate materials. The peaks around 1635 and 3450 cm^{-1} were assigned as hydroxyl group of a hydroxyapatite. The peaks derived from carbonate groups were also observed around 870 and 1420 cm^{-1}, indicating that this carbonate groups were incorporated in the apatite structure.

The component of white precipitates was analysed by EPMA. Electron probe microanalysis revealed that the components of white precipitates were Ca, P and O. The intensities of Ca and P and Ca/P ratio of white precipitates were listed in Table 2. The amounts of Ca and P were increased according to the length of immersion periods. After 3 days immersion, the amounts of Ca and P remarkably increased as shown in Table 2. The slight increase of the amounts of Ca and P was observed after 5, 7, 14 and 28 days immersion.

The Ca/P ratio of white substance was about 1·4 at 3, 5, 7 days immersion periods. After 14 and 28 days immersion, the Ca/P ratio was raised to 1·90 and 1·82, respectively.

Figure 5 showed FE-SEM pictures of the surface of the phosphorylated polymer disk after the immersion in HBSS. Scanning electron microscopic observation revealed that there was no precipitate formation on the Photobond polymer surface after 1 day immersion. After 3 days immersion, the formation of precipitated globules was observed. The globules were scattered on the polymer surface. The number of globules was increased at 5 days immersion, but the polymer surface was not completely covered with the globules. After 7 days immersion, the polymer surface was completely covered with calcium phosphate globules. A large number of globules was fused together, and smaller globules were present on the top of fused globules. After 14 and 28 days, new globules were piled up on the precipitated globules. There were no distinct differences in the appearances between 14 and 28 days immersion.

Higher magnification FE-SEM observation of white precipitates (Fig. 6) revealed that each globule was composed of a group of numerous thin-film form flakes uniting and/or clustering together on the phosphorylated polymer disk. The size of flakes was between 100 and 200 nm after both 7 and 28 days immersion. This type of crystal agglomeration was referred as card-house structure.

Discussion

This study revealed that carbonate-containing hydroxyapatite was formed on the phosphorylated polymer disk, i.e. cured Photobond disk, after the immersion of HBSS.

The phosphoric ester monomer, MDP, was incorporated in phosphorylated polymer (9). Fourier-transform infrared spectrum revealed that P-OH group of MDP was existed on the exposed polymer surface after curing. It is presumed that P-OH of MDP dissociates into $P\text{-}O^-$ and H^+ in HBSS and that some dissociated phosphate groups, $P\text{-}O^-$, interact with Ca ions of HBSS. It is also possible that Ca ions interact with partly negative charged oxygen P=O and P-O-C of MDP. Subsequently, Ca ions were adsorbed onto the phosphorylated polymer disk. Afterwards, P ions of HBSS interact with pre-adsorbed Ca ions and then are adsorbed on the Ca pre-adsorbed surface. The P-OH group, P=O and P-O-C of MDP served as a template of a spatial cage for nucleation and growth of calcium phosphate. The calcium phosphate layer is probably formed by repetition of this process.

The carbonate ions were incorporated into the hydroxyapatite and thus carbonate-containing hydroxyapatite formed on the phosphorylated polymer because of the rich amount of carbonate ions in HBSS. Hanawa (10) and Hanawa and Ohta (11)

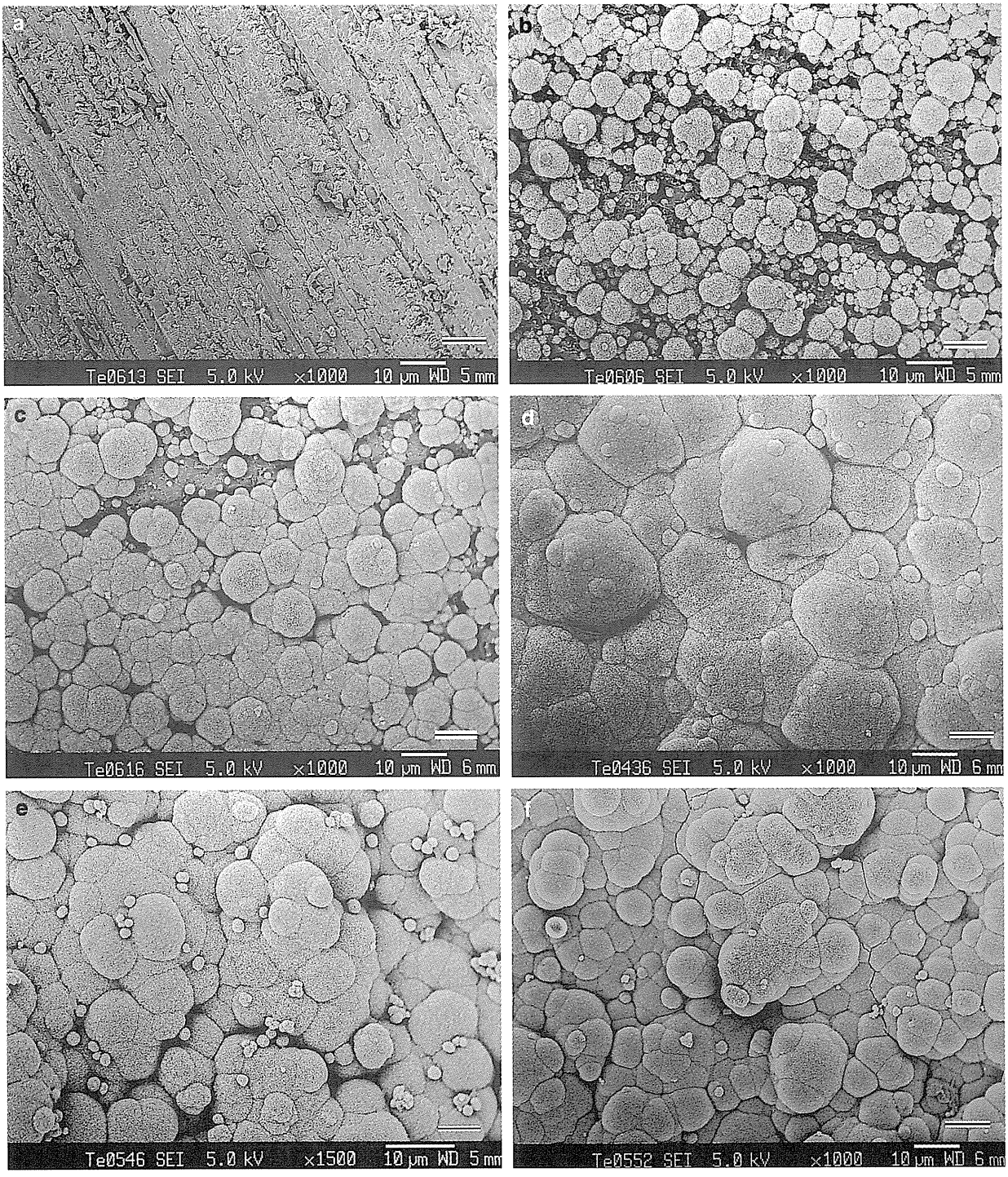

Fig. 5. Field-emission scanning electron microscope (FE-SEM) pictures of the surface of phosphorylated polymer disk after the immersion in Hanks' balanced salt solution (HBSS). (a) 1 day immersion in HBSS. Polished surface of the polymer was observed. There was no precipitation (bar = 10 μm). (b) 3 days immersion in HBSS. The formation of precipitated globules was observed. The globules are scattered on the phosphorylated polymer surface (bar = 10 μm). (c) 5 days immersion in HBSS. The number of globules were increased, but the phosphorylated polymer surface was not completely covered with calcium phosphate globules (bar = 10 μm). (d) 7 days immersion in HBSS. The phosphorylated polymer surface was completely covered with calcium phosphate globules (bar = 10 μm). (e) 14 days immersion in HBSS. The new globules were plied up on the precipitated globules (bar = 10 μm). (f) 28 days in immersion in HBSS. The appearances were almost same as those of 14 days immersion sample (bar = 10 μm).

© 2004 Blackwell Publishing Ltd,

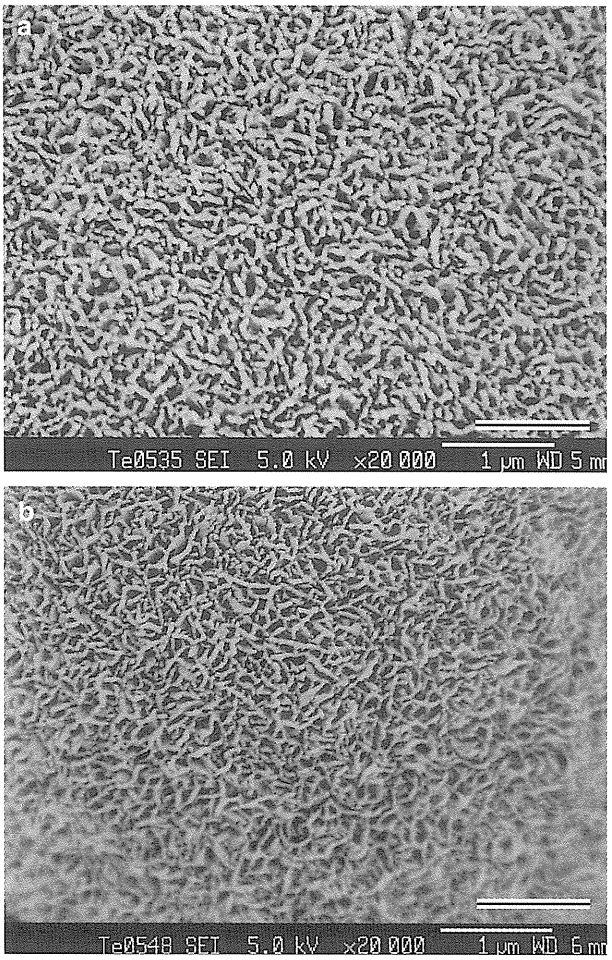

Fig. 6. Higher magnification field-emission scanning electron microscope (FE-SEM) pictures of white precipitates on the phosphorylated polymer disk after the immersion in Hanks' balanced solution (HBSS) at 7 days (a) and at 28 days (b). Each globule was composed of numerous thin-film form flakes uniting and/or clustering together. The size of flakes was between 100 and 200 nm (bar = 1 μm).

found that calcium phosphate deposited on titanium after the immersion in HBSS, and reported that the calcium phosphate was carbonate-containing hydroxyapatite. Their results corresponded with our results. However, they reported that carbonate-containing hydroxyapatite was obtained on titanium surface after 60 days immersion. Serro *et al.* (12) also reported there was no calcium phosphate precipitation on titanium after 7 days of immersion in HBSS. In this study, we observed hydroxyapatite formation on cured Photobond disk after 3 days HBSS immersion macro- and microscopically. This was due to the difference of the surface chemistry of titanium and phosphorylated polymer, namely with or without of phosphonic acid and P group. The present study revealed that the presence of phosphonic acid and P group was favourable for the precipitation of hydroxyapatite.

The Ca/P ratio of deposited hydroxyapatite did not correspond with the theoretical value of hydroxyapatite. The Ca/P ration was less than 1.67 until 7 days immersion, and that was greater than 1.67 after 14 days immersion. Electron probe microanalysis was performed at 25 kV and the depth of detection at this condition was predicted about 2.5 μm. The reduced Ca/P ratio was due to the detection of the phosphorus of phosphorylated polymer disk besides the phosphorous of deposited apatite. The reason for the greater Ca/P ratio after 14 days immersion was not clear. The deposition of calcium phosphate besides hydroxyapatite, for example, tetracalcium phosphate, was a possibility. The detailed mechanism for the deposition of calcium phosphate should be further investigated.

It is widely known that a phosphorylated bonding agent such as Photobond shows good adhesiveness to tooth substrate (13–15). Phosphorylated bonding agent is also used as a direct pulp capping material, and it is reported that there were no severe pulpal reactions after direct pulp capping with a phosphorylated bonding agent (16–19).

In the present study, we found a new function of Photobond which is a phosphorylated bonding agent. Phosphorylated bonding agent can induce the formation of calcium phosphate on its surface after the immersion of HBSS. The main component of induced calcium phosphate was carbonate-containing hydroxyapatite. The results obtained in this study suggested that other phosphorylated bonding agents besides Photobond have a possibility to induce calcium phosphate formation *in vitro*. Tsuneda *et al.* (20) observed the formation of secondary dentin on the exposed pulp of rat after the direct pulp capping with phosphorylated bonding agent. It is presumed that the remineralization induction ability of phosphorylated bonding agent such as Photobond participate in secondary dentin formation when used as direct pulp capping material. The formation of calcium phosphate *in vitro* should be further investigated.

Acknowledgments

This study was supported in part by a grant from the Ministry of Education, Culture, Sports, Science and

Technology to multidisciplinary research projects and to promote 2001-Multidisciplinary Research Projects (in 2001–2005), grants-in-aid for Research for the Frontier Science from the Ministry of Education, Culture, Sports, Science and Technology of Japan, and grants-in-aid for Scientific Research (C)(2)(nos 11671817, 12671904) from Japan Society for the Promotion of Science. This study was also supported in part by Oral Health Science Center grant 992C01 from Tokyo Dental College.

References

1. Erickson RL. Surface interactions of dentin adhesive materials. Oper Dent. 1992;Suppl. 5:81.
2. Perdigao J, Lopes M. Dentin bonding – state of the art 1999. Compend Contin Educ Dent. 1999;20:1151.
3. Tretinnikov ON, Kato K, Ikada Y. *In vitro* hydroxyapatite deposition onto a film surface-grafted with organophosphate polymer. J Biomed Mater Res. 1994;28:1365.
4. Kato K, Eika Y, Ikada Y. Deposition of a hydroxyapatite thin layer onto a polymer surface carrying grafted phosphate polymer chains. J Biomed Mater Res. 1996;32:687.
5. Kamei S, Naohide T, Tamai S, Kato K, Ikada Y. Histological and mechanical evaluation for bone bonding of polymer surfaces grafted with a phosphate-containing polymer. J Biomed Mater Res. 1997;37:384.
6. Mucaro MR, Yokogawa Y, Toriyama M, Suzuki T, Kawmoto Y, Nagata F et al. Growth of calcium phosphate on surface-modified cotton. J Mater Sci Mater Med. 1995;6: 597.
7. Yokogawa Y, Reyes JP, Mucalo MR, Toriyama M, Kawamoto Y, Suzuki T et al. Growth of calcium phosphate on phosphorylated chitin fibres. J Mater Sci Mater Med. 1997;8:407.
8. Varma HK, Yokogawa Y, Espinosa FF, Kawamoto Y, Nishizawa K, Nagata F et al. Porous calcium phosphate coating over phosphorylated chitosan film by a biomimetic method. Biomater. 1999;20:879.
9. Fujisawa S, Kadoma Y, Komoda Y. HPLC separation of methacryloyloxydecyl dihydrogen phosphate from dental bonding agent. J Jpn Soc Dent Mater Devices. 1991;10:30.
10. Hanawa T. Titanium and its oxide film: a substrate for formation of apatite. In: Davies JE, ed. The Bone–Biomaterial Interface. Toronto: University Tronto Press, 1991: 49.
11. Hanawa T, Ota M. Calcium phosphate naturally formed on titanium in electrolyte solution. Biomater. 1991;12:767.
12. Serro AP, Fernandes AC, Saramago B, Lima J, Barbosa MA. Apatite deposition on titanium surfaces – the role of albumin adsorption. Biomater. 1997;18:963.
13. Hirasawa K, Fujitani M, Hosoda H. Studies of newly designed tooth surface treatments for adhesive composite restoration. Bull Tokyo Med Dent Univ. 1992;39:19.
14. Fortin D, Swift EJ Jr, Denehy GE, Reinhardt JW. Bond strength and microleakage of current dentin adhesives. Dent Mater. 1994;10:253.
15. Tyas MJ. Clinical evaluation of five adhesive systems. Am J Dent. 1994;7:77.
16. Kashiwada T, Takagi M. New restoration and direct pulp capping systems using adhesive composite resin. Bull Tokyo Med Dent Univ. 1991;38:45.
17. Onoe N. Study on adhesive bonding systems as a direct pulp capping agent. Jpn J Conserv Dent. 1994;37:429.
18. Kato Y, Kimura T, Inaba T. Clinicopathological study on pulp-irritation of adhesive resinous materials. Jpn J Conserv Dent. 1997;40:153.
19. Akimoto N, Monoi Y, Kohno K, Suzuki S, Otsuki M, Suzuki S et al. Biocompatibility of Clearfil Liner Bond 2 and Clearfi AP-X system on nonexposed and exposed primate teeth. Quintessence Inter. 1998;29:177.
20. Tsuneda Y, Hayakawa T, Yamamoto H, Ikemi T, Nemoto K. A histopathological study of direct pulp capping with adhesive resins. Oper Dent. 1995;20:223.

Correspondence: Dr Tohru Hayakawa, Department of Dental Materials, Nihon University School of Dentistry at Matsudo, 2-870-1, Sakaecho-nishi, Matsudo, Chiba 271-8587, Japan.
E-mail: hayakawa@mascat.nihon-u.ac.jp

原著論文

エナメル質結晶形成に関する研究

Enamel crystal development

[1]日本大学松戸歯学部第2解剖学講座
[2]日本大学歯学部矯正学教室
[3]（社）日本歯科先端技術研究所

小澤 幸重[1], 大久保 厚司[1,3], 老沼 博一[1], 千坂 英輝[1], 本田 知久[1,2], 横田 ルミ[1], 岩佐 由香[1], 鈴木 久仁博[1], 山本 仁[1], 寒河江 登志朗[1]

Yukishige KOZAWA[1], Atsushi OOKUBO[1,3], Hirokazu OINUMA[1], Hideki CHISAKA[1], Tomohisa HONDA[1,2], Rumi YOKOTA[1], Yuka IWASA[1], Kunihiro SUZUKI[1], Hitoshi YAMAMOTO[1], Toshiro SAKAE[1]

[1]Department of Anatomy II, Nihon University School of Dentistry at Matsudo
[2]Department of Orthodontics, Nihon University School of Dentistry
[3]Japan Institute for Advanced Dentistry

高分解能電顕でエナメル質初期結晶形成を観察した. gultalaldehyde 固定によると, 径20-50nm の粒子状構造, 芯をもつ細管状構造, amorphous な物質がトームスの突起間や分泌面に観察される. tannic acid 固定では gultalaldehyde 固定と同大の粒子状構造が細胞膜から数百 nm の範囲に認められ, 同時に中心に芯のある細管状構造が観察された. 芯は1nm以下の大きさの撚糸状構造であり, apatite結晶の構成原子と同大である. これは最初に形成されるエナメル質結晶と推定される. amorphous な粒子状構造は, エナメルタンパクであり, apatite 結晶の構成原子を捕捉する enamelin の疎水部を含む一部と考えられる. これが互いに癒合して細管状構造となり, 内部に原子が集積し, 不規則配列する撚糸状構造をつくる. これが有機基質に富む amorphous な最初の結晶の先駆的構造である. 故に, この構造は酸に不溶であり, 酢酸ウラン-鉛によって染色される.

結晶のC軸は細管状構造の配向により決まる. 細管状構造の enamelin のC末端はトームスの突起の分泌面細胞膜と接着し, N末端は sheathlin に付くと考えられる. このようにして細管の配向が決まり, 結果としておおよその結晶配向が決定する. 細管状構造の内部で, ある程度原子が集積すると amorphous な先駆的エナメル質結晶は結晶核となり, 原子の熱エネルギーが最小の安定な平衡状態へ移行し, 突然数層の原子配列をもつ結晶へ変わると考えられる. これがリボン状結晶である. ついでエピタキシアル成長等により, 結晶上に次々と原子が集積し, 結晶の幅が増し, 板状となり, ついで六角柱状結晶となる. この結晶表面では, 次々に結晶核ができ結晶形成され癒合する。このようにして多角柱状結晶が形成される。結晶の成長は amelogenin の溶解によってできた間隙で起こるため, その大きさが結晶の形と大きさを決める要因となるものと推定できる.

キーワード:エナメル質, 結晶形成, 結晶先駆体, 石灰化, 生体鉱物化

緒 言

ヒトが属する哺乳類の生体中には種々の石灰化物質が存在する. 歯や骨はもとより松果体にある脳砂, 毛や爪, 舌の糸状乳頭が石灰化することもある. 石灰化は文字通り, 体内に無機質の結晶が沈着することであるが, どのようにして最初の結晶が形成され成長するか, また成長が制御され歯や骨の形態が形成されるかについては様々な説があり一定しない. 人体中の結晶はhydroxyapatite, 即ち水酸化リン酸カルシウムがほとんどであるが, リン酸を含まない炭酸カルシウムや修酸カルシウムも含まれるし, 鉄が沈着する場合もある. 広く生物界を見渡せば, Mg(マグネシウム)やMn(マンガン)などが生体石灰化物となることもある[10].

生体内に沈着したこれらの石灰化物の形態や性質を捉えることは, 電子顕微鏡やX線回折法等々によって多く行われてきた[6, 9]. その結果, 結晶は有機基質, 即ちエナメル質ならばエナメルタンパク, 結合組織ならば基質小胞やコラーゲン原線維等々の基質の影響下に形成されることは Frank(1961)[3]と Pautard(1961)[13]以来の研究によってほぼコンセンサスが一致している[1, 2, 5, 6, 7, 14, 15, 18, 19, 21]. しかし, 最初の結晶がどのようにして形成され, 成長し, 配列して成熟した結晶になるかについては, 観察法や研究法の違いによって様々な考えがあり, 一致しないというのが現状である[2, 7].

我々は, 最も基本的な要求として, 最初の結晶形成を形態的に捉えたい, 観察したいと考えている. その結果, エナメル質形成における最初の結晶核形成と結晶の成長について形態学的観察結果によるひとつのモデルを示してきたが[8], その後更に観察を加えて, 今回はより発展させた結晶形成の検討を行った. 更に結晶の成長過程と成熟した結晶も高分解能電子顕微鏡で観察した結果による結晶成長に関する知見を紹介する.

材料と方法

試料は当教室で飼育繁殖している胎生1週齢のジャコウネズミ(*Suncus murinus*)の歯胚を中心に, これまで扱ってきた胎生約8週齢のブタ(*Sus scrofa*), 生後すぐのイヌ(*Canis familiaris*), ネコ(*Felis catus*), オポッサム(*Monodelphis domestica*)及びウシ(*Bos taurus*)を用いた. 各動物は, 頭部から歯胚を摘出し, 2% tannic acid + 4% paraformaldehyde + 2% gultalaldehyde (pH 6.8, 0.1M cacodylate buffer)または 2% gultalaldehyde (pH 6.8, 0.1M cacodylate buffer)で 10−12 時間, 4℃で前固定し, 2% OsO_4(同 buffer)で 30 分間後固定を行った.

試料は固定後, アルコール系列によって脱水, エポキシ樹脂包埋後, ウルトラミクロトームで非脱灰のまま電顕用の超薄切片を作製し, 無染色ないし, 酢酸ウラン一鉛の二重染色を施して観察した. 結晶の観察は上記の動物に加えてナウマンゾウ(*Palaeoloxodon naumanni*)やデスモチルス(*Desmostylus* sp.)やアフリカゾウ(*Loxodonta africana*)のエナメル質や象牙質を, 非脱灰のまま超薄切片を作成し観察した.

結 果

1. エナメル質の沈着

歯胚が鐘状期(Fig. 1)に達し, 象牙質の石灰化がある程度進むと, エナメル芽細胞の分泌面の細胞膜は波状となる(Fig. 2). 象牙質表面とエナメル芽細胞の分泌面はやや離れ, そこに分断された基底膜や細いコラーゲンが不規則に分布する. これ等の間隙にエナメル芽細胞から分泌された amorphous material 又は stippled material と呼ばれる粒子が塊状または散在性に分布する. 最初のエナメル質結晶と考えられる構造は, 石灰化が進んだ象牙質表面の amorphous material やコラーゲンの間にフィラメント状に沈着する(Fig. 3). gultalaldehyde 固定をして, OsO_4 後固定, 酢酸ウラン-鉛の二重染色を施した切片では, 電子密度の高い無方向性の長さ数十 nm の湾曲したフィラメント状構造が一本ないし十数本の集塊となる.

エナメル質形成が進むとフィラメント状構造は多くなり, 象牙質表面に塊状ないし, 島状のエナメル結晶集団を形成する(Fig. 4). 象牙質表面に薄いエナメル質の層が形成されると, エナメル芽細胞の分泌端にトームスの突起が分化し, エナメル小柱の構造が形成される(Fig. 5).

2. 結晶核の形成

盛んにエナメル質形成を行う基質形成期エナメル芽細胞のトームスの突起分泌面近くでエナメル質の結晶形成を観察すると次のようになる. gultalaldehyde 固定による場合, 径 20-50nm 粒子がエナメル芽細胞のトームスの突起間や分泌面の近くに数百 nm の幅に分布する(Fig. 6 Gul TP と分泌顆粒). この粒子はエナメル質の有機基質と言われ, stippled material 又は, coarse ないし fine textured material, amorphous material などと呼ばれる [8, 12]. 同時にこの領域では, エナメル質の結晶が細胞膜にほぼ垂直に配列する.

タンパク質を強く凝集する tannic acid 固定[4]の場合, *Suncus murinus* のトームスの突起先端, 即ちエナメル質基質の分泌面では, 細胞膜外に gultalaldehyde 固定と同様に径 20-50nm の電子密度の高い粒子が認めら

Fig. 1 Bell stage tooth germ. The dentin deposition started. (*Monodelphis*)

Fig. 2 Functional end of ameloblast. The dentin calcification started and the apical cytoplasmic membrane formed irregular wavy. The amorphous materials were observed between the ameloblast and calcified dentin. (*Sus*)

Fig. 3 Initial enamel crystal. Ribbon like fine initial enamel crystals appeared on the calcified dentin. Collagen fibers, absorbing by the ameloblast, and amorphous materials were observed around crystals. (*Canis*)

Fig. 4 When enamel crystal deposition progressed, enamel thickness increased and enamel crystal masses appeared. Collagen fibers, absorbing by ameloblast, and stippled materials were observed between ameloblasts and developing enamel surface. (*Sus*)

Fig. 5 Matrix formation stage of tall ameloblasts developed the Tomes process. (*Felis*)

Fig. 6 Tomes process(t) and secreting stippled materials(s) fixed by gultalaldehyde. Early enamel crystals were observed on the cell membrane among stippled materials. (*Canis*)

Fig. 7 Midair granules were observed by tannic acid fixation. These structures were same size of stippled materials. (t: Tomes process) (*Sus*)

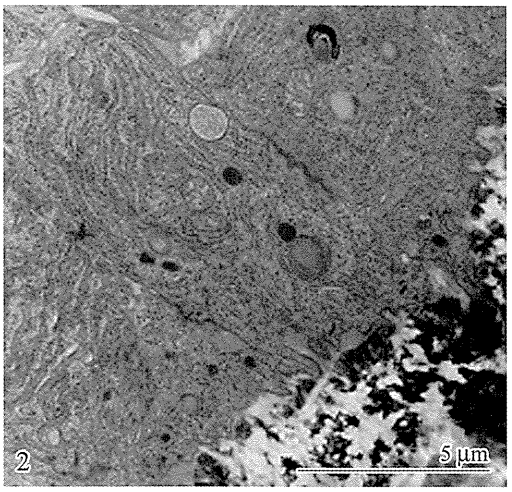
5 μm

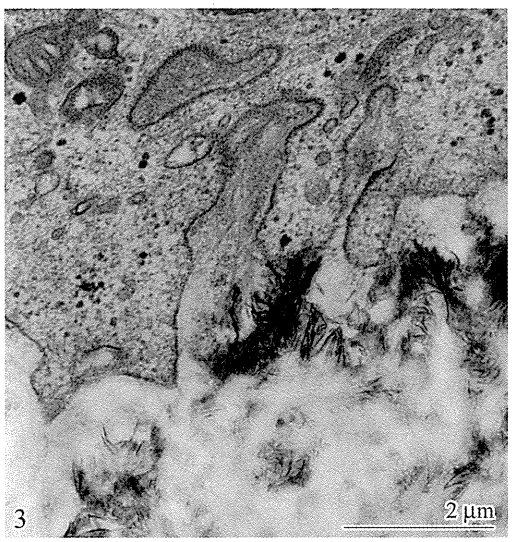
2 μm

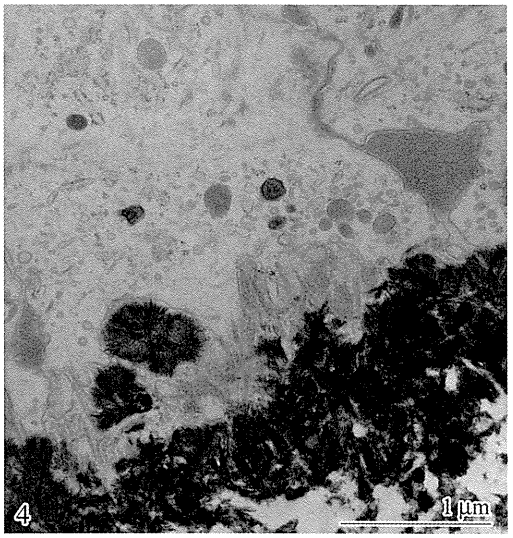
1 μm

5 μm

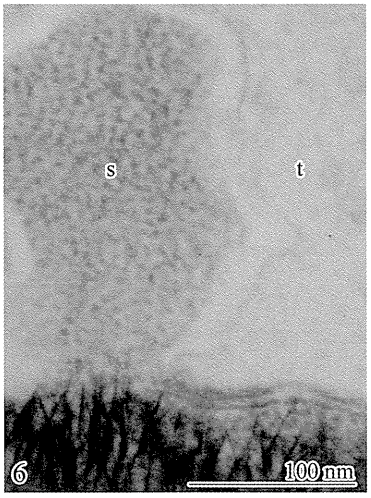
s
t
100 nm

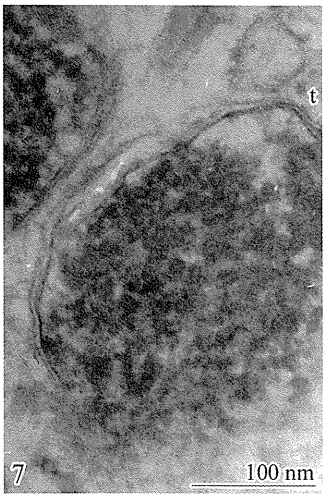
t
100 nm

れる. 粒子は正円ではなく, より細かな粒子が集合した様相を示し, 中空状に認められる(Fig. 7, 8). この粒子は隣接エナメル芽細胞のトームスの突起間にも認められ, 細胞膜から 1-2nm 以内の領域では, 芯構造を持って連続する(Fig. 8).

エナメル芽細胞の分泌面の細胞膜から 1-2 μ m 距離をおいた領域になると, 粒子とともに細管状構造も認められる(Fig. 10). エナメル芽細胞の分泌面の細胞膜に近い粒子は, 中心に電子密度の高い線維状の芯をもつ電子密度の低い幅 20-50nm の細管状構造として認められる. あたかも'綿アメと串'ないし'串団子'のような形態を呈する(Fig. 9). 細管状構造は, 約 20-50nm 間隔で節状に膨隆し, あたかも中空の粒子状構造が連続するような形態を示す(Figs. 11a, b). また, 細管状構造は電子密度の高い幅 0.5nm 以下の線維状の芯を持つ(Fig. 11c). 芯となっている線維構造は, 一本の連続する線維ではなく数珠ないし撚糸状の形態を示す(Fig. 11).

3. エナメル芽細胞分泌面での結晶成長

エナメル芽細胞の分泌面から 200-500nm 離れると湾曲するリボン状結晶が観察される(Fig. 12). リボン状結晶は螺旋状に湾曲して, 時には一本ないし二, 三本が合流ないし分枝する(Figs. 13, 14, 15). 高分解能電顕によると, 結晶格子が湾曲しているのが認められる(Fig. 16). 結晶がさらに成長すると板状の形態をとる(Fig. 17).

4. 成熟した結晶形態

成熟エナメル質結晶は, 教科書では長六角形とかかれているが [17], 六角形は比較少なく(Figs. 18, 19), 多くの場合二ないし三個

Fig. 8 Enamel crystals arranged almost perpendicular to the cytoplasmic membrane of functional end of ameloblast. Tannic acid fixation. (*Sus*)

Fig. 9 The initial enamel crystals had high density core in the center as surrounded by cotton. (*Sus*)

Fig. 10 Tubular structures were observed within about 200nm distance area from the ameloblast with midair granules. The central line (arrows) was recognized in the tubular structures. (*Sus*)

Fig. 11 The high density central core formed a strand structure and the tubular structure shaped band-like segment structures continued midair granules(a, b): High resolution electron micrograph. The strand is continued by granules (arrow) about 0.5 nm in diameter(c). It was presumed that this tubular structure was the organic rich amorphous precursor of enamel crystal. (*Sus*)

Fig. 12 Filament like enamel crystals. These were also amorphous precursor of crystals, because it did not soluble against acetic acid. Some crystals fused (arrows). (*Canis*)

Fig. 13 Filament like enamel crystals. Some crystals fused (arrow) to each others. (*Canis*)

Fig. 14 Filament or ribbon like enamel crystals bended spirally and fused (arrow) to each others. (*Canis*)

Fig. 15 Ribbon like enamel crystals fused(arrows) to each others. (*Canis*)

Fig. 16 Atomic lattices carved at the bending point of a ribbon like crystals by high resolution electron microscopy. (*Bos*)

Fig. 17 Plate like enamel crystals (*Canis*)

Fig. 18 Hexagonal enamel crystal. (*Loxodonta*)

Fig. 19 Hexagonal enamel crystal (*Palaeoloxodon*)

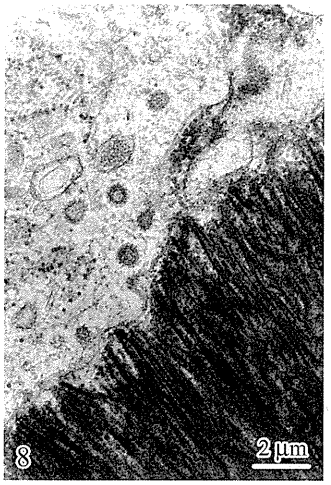
8
2 μm

9
1 μm

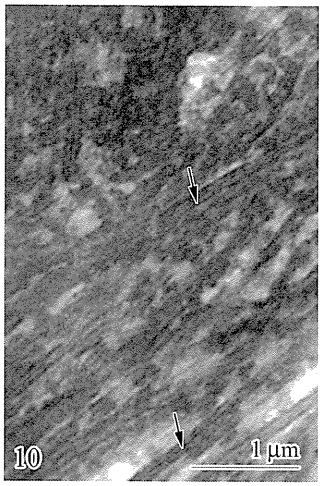
10
1 μm

11a
100 nm

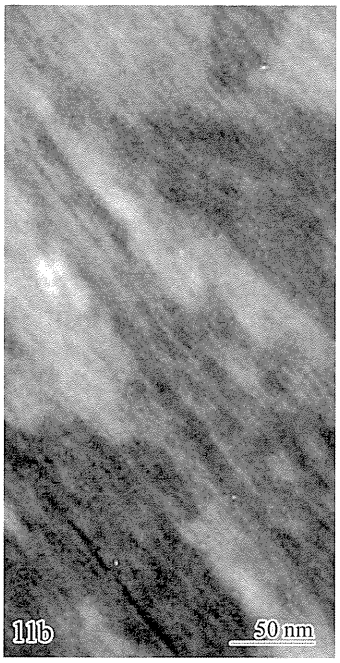
11b
50 nm

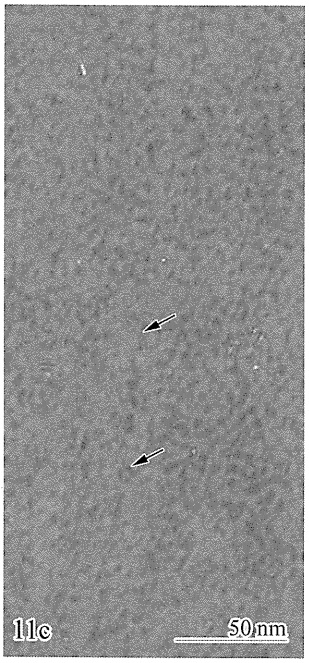
11c
50 nm

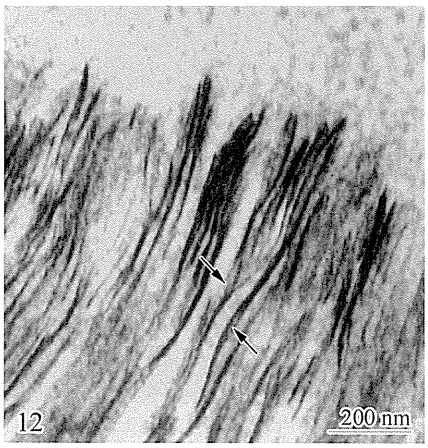
12
200 nm

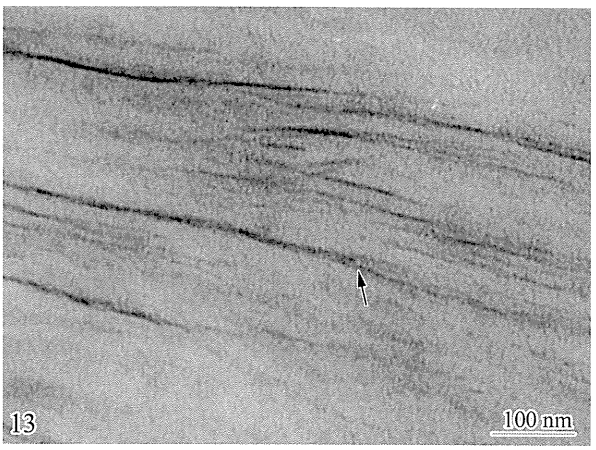
13
100 nm

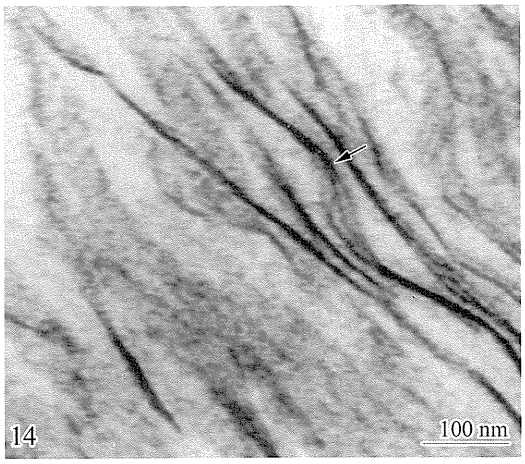
14
100 nm

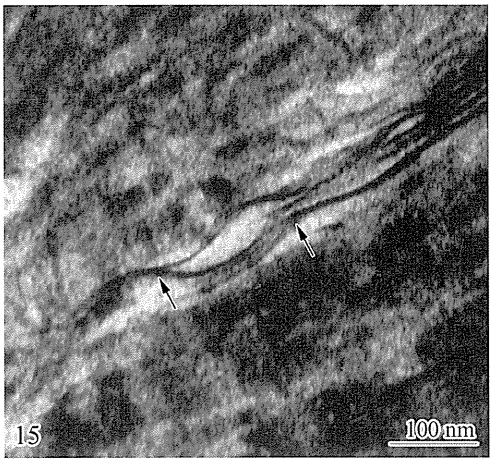
15
100 nm

16
1 nm

17
100 nm

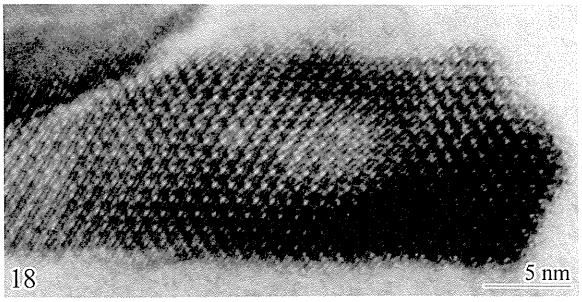
18
5 nm

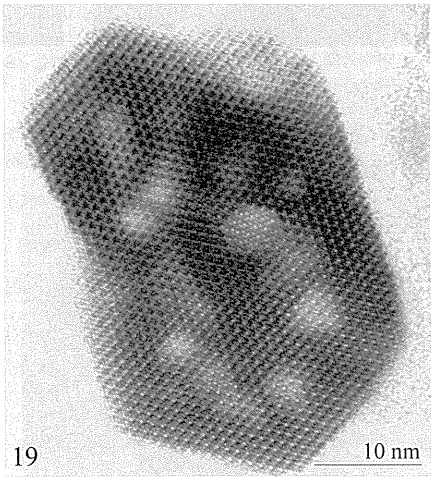
19
10 nm

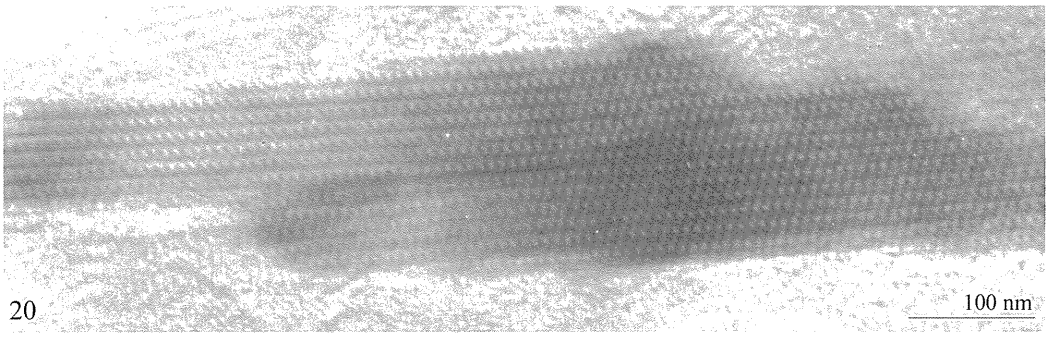
20
100 nm

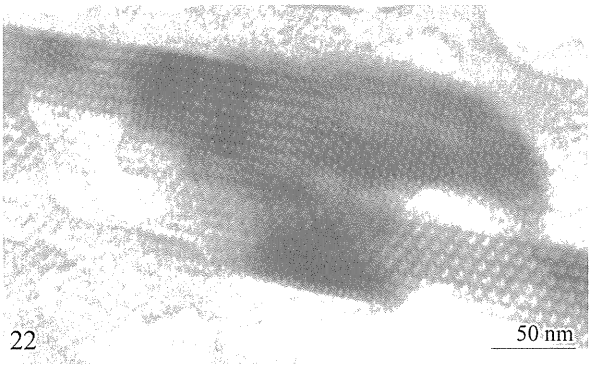
22
50 nm

21
50 nm

23
100 nm

の結晶が接着した多角形状となって観察される(Figs. 20, 21, 22). 高分解能電顕による接着した不規則な多角形結晶の原子配列の観察によると, 原子配列が連続している(Fig. 23). これ等の不規則形結晶の原子配列を詳しく観察すると, 原子間隔が違う原子配列は連続せず, 一部の原子配列のみ連続している結晶がある. つまり別の方向に配向している結晶が一つの結晶を作っていることを示す.

考 察

観察結果から結晶の形成と成長, 完成までの過程を推定してみると次のようになる.
生体内の結晶形成に有機基質が関与する形態学的根拠としては, 骨芽細胞や象牙芽細胞の出芽による基質小胞中での結晶沈着, コラーゲン線維の中への結晶沈着[7]などが挙げられる. 基質小胞は細胞膜に囲まれた細胞内の石灰化であり基質小胞は細胞膜のチャンネルによるカルシウムやリン酸の細胞膜内への濃縮, 同時にアルカリフォスファターゼにより石灰化阻害するピロリン酸の分解, そして第一リン酸カルシウム形成と, より熱力学的に安定した hydroxyapatite 結晶核形成と結晶への成長と説明される. コラーゲンの場合には, コラーゲン原線維中の holezone や gap と呼ばれる分子的な空隙にカルシウムやリンなどが集積する環境がつくられて, 最初の結晶核が形成される. エナメル質ではエナメル芽細胞の遠心端のエナメル質領域の結晶成長部位に有機基質のエナメルタンパクが局在し, これが結晶核形成に関与する[23].

これは, エナメル質も骨や象牙質などと同様に, 有機基質が関与して最初の結晶核形成が起こることを示す. しかし, 有機基質の存在は認められても, 有機基質とイオンがどのような機構で結晶化をするのか説明されてない. そこでエナメル質の結晶形成の過程をたどりながら考察する.

1. エナメル質の結晶核形成と結晶成長

エナメル質結晶形成は大きく次の三つの時期に区分される;1)象牙質形成環境の強い最初の結晶沈着の時期, 2)エナメル芽細胞の分泌の盛んな時期, 3)エナメル芽細胞の吸収が盛んな時期である. 1)はエナメル芽細胞の分化期, 2)は主に基質形成期, 3)は成熟期のエナメル芽細胞に対応する. こ

Fig. 20 Two or more crystals fused, but the atomics arranged straight line. (*Paleoloxodon*)

Fig. 21 Three or more crystals fused and showed irregular form. The atomic lines and lattices arranged straight. (*Palaeoloxdon*)

Fig. 22 Three or more enamel crystals fused. Atomic images arranged straight. (*Palaeoloxodon*)

Fig. 23 Irregular shaped mature enamel crystals. Some variable hexagonal crystals fused to form irregular crystals, because atomic images arranges straight. (*Desmostylus*)

れらの結晶形成の環境は必ずしも同じではないと考えられる.

1)における最初の結晶形成はエナメル芽細胞が分化した直後に石灰化した象牙質表面上に起こる. エナメル芽細胞の分泌端の細胞膜は波状となり, エナメル質有機基質の分泌, イオン等の象牙質表面への輸送と共に, コラーゲン線維や基底膜の分解と吸収機能を行う. 石灰化がある程度進んだ象牙質表面は未石灰化のままで, 象牙質基質に相当するコラーゲンやプロテオグリカン等々が存在する. エナメル芽細胞から分泌されるエナメルタンパクは, amelogenin や enamelin, sheath protein, エナメルタンパクを分解する enamelysin などである[23]. そこには, 基底膜やコラーゲンを分解・吸収する酵素も分泌される.

これらのタンパク質と共に, エナメル質結晶の組成要素である Ca, OH, PO_4, CO_2 などのイオンも次々とエナメル芽細胞から輸送され供給される. 象牙質表面はこのような物質が混然としているゲルの状態であると推定できる. 即ち, 結晶形成イオンが飽和状態となっている複雑なゲルの相で, 融液中において最初のエナメル質結晶核が形成される. いわば豆腐の中に結晶が析出する様な状態と考えられる.

ある程度エナメル質形成が進む2)の分泌期ないし基質形成期には, もはやコラーゲンや基底膜などは無くエナメル芽細胞はエナメル質基質形成のみを行う. この時期のエナメル質形成環境は, エナメル芽細胞がエナメルタンパク各種を分泌し, 次々と輸送され供給されたイオンが飽和状態になっていると推定される. 無論, これらの物質はエナメル芽細胞近くとエナメル質深部では濃度が違うと考えられる. 基本的には, ゲル状のエナメルタンパク中には enamelin, amelogenin, sheath protein, enamelysin があり, そのうちのほとんどを amelogenin が占め, さらに水分と結晶構成要素の原子や分子イオンが飽和している. つまり, 豆腐の中身はエナメル質形成に必要なものだけとなっている. 後述するが, 豆腐の一部が溶解され吸収され, 空隙ができ, そこに結晶核が析出し, 空隙が広くなると結晶化が進む.

3)の成熟期には, 主にエナメル質基質中のエナメルタンパクが分解し, 脱却され, エナメル質結晶成長が進みエナメル質の石灰化が高くなる. エナメル芽細胞は主に enamelysin などの分解酵素と, 水を含む結晶構成の各種イオンを分泌輸送し, エナメルタンパクや水を分解・吸収する. 有機基質の豆腐はぼろぼろになり, その空隙にはイオンが飽和しているため多くの成熟しつつある結晶が析出する. 有機基質は多孔性のゲルとなり, 高野豆腐のような状態であると考えられる.

以上の如く, エナメル質の結晶形成は, 体温下で, エナメルタンパクがゲル状となった中で進行する. これを, 結晶成長学的に考えれば, エナメルタンパクは複雑な構成をしたゲル状と推定され, 液相中で結晶が形成成長する「不均質核形成および結晶の成長」[16]に相当すると考えられる. しかし, エナメル質の有機基質には様々なものが含まれ非常に複雑な環境における結晶形成であり, 無機的な不均質核形成だけでは説明できない複雑な系となっているようである.

2. 結晶成長の段階

初期結晶はこれまでフィラメント状やリボン状結晶と言われてきた. しかし, 今回の観察は, 形態的な面と結晶形成の環境を併せ, 初期結晶形成にはより先駆的な過程があることを示している.

即ち, 結晶形成過程は 1)エナメル芽細胞からやや距離がある象牙質表面に於ける最初の結晶核形成(ここではフィラメント状結晶と呼ぶ), 2)少量のエナメル質が形成されたエナメル芽細胞の分泌面近くに於けるより方向性のある配列をしている撚糸状又はコヨリ状の結晶形成段階, 3)リボン状結晶といわれる原子配列の縞構造が認められる段階, 4)板状結晶の段階, 5)六角柱状の段階, 6)不正多角柱状の完成あるいは成熟エナメル質の段階, に大きく区分できる(Figs. 18, 19).

1)と 2)の時期は形成領域と結晶の方向性(配向性)の違いによるものであり基本的に同様である. 3)は結晶が薄膜状でねじれがある. 電子染色を施すと crystal ghost となって中空に観察される [19]. 4-6)は従来の記載の通りである [9].

3. 初期結晶と有機基質の役割

まず, 生体内の結晶形成には, 有機基質が関与すると広く考えられているのは前に記述したとおりである [1, 5, 6, 7, 14, 15, 18, 19, 21]. 即ち, 豆腐様の構造の中でエナメル質の結晶が形成される. エナメル質形成は, 有機基質の中に結晶が沈着するというエピタキシー結晶形成の考え [5, 14, 21]は早くから示され, 結晶の形成に先立って, tubular 状か tubular compartment ができることが報告されている [1]. 未成熟な結晶周囲に螺旋状の構造があるとの報告もエナメル質の結晶形成と有機基質の関与を推定している [18]. しかし, 考察の最初に記した如く, エナメル質結晶を形成するイオンが有機基質とどのような関係を作り結晶化するのかについて明確な説明はなく, 形態学的根拠も明確ではない.

エナメル質に関与する有機質の4種類, amelogenin, enamelin , sheath protein や enamelysin は遺伝子の DNA の塩基配列がほぼ確定し, amelogenin や enamelin の研究はタンパク質の機能解析まで行われている [22]. amelogenin は 20-50kD の大きさを持つと言われエナメルタンパクの 90%を占めエナメル質の容積を確保するとされる [23], 結晶形成に直接関与すると考えられる enamelin は当初 156kD という大きな分子量のタンパクであるが急速に分解をうける. sheathlin あるいは sheath protein は 13 から 17kD のおおきさのタンパク質でエナメル小柱の小柱鞘や横紋に局在する [23].

直接的な hydroxyapatite 結晶との関係では, 免疫細胞化学的に初期結晶上に amelogenin[20]や enamelin[22]が局在すると言う報告がある. Thoda ら(1997)[20]はエナメル芽細胞の遠心端のごく初期の結晶を観察し, 同時に amelogenin が局在することを免疫細胞化学的に示した. 一方, Uchida ら(2003)[23]は象牙質表面上において最初に認められる結晶の上に amelogenin の局在はなく enamelin が局在することを検証し, enamelin と amelogenin の局在が違うこと, amelogenin がエナメルタンパクのほとんどを占めることから, enamelin は初期結晶形成に関与し, amelogenin はエナメル質の容積を作る, とし

ている.

光学顕微鏡的に有機基質が多い形成中のエナメル質にシュレーゲル条などのエナメル質構造が観察されることは, 豆腐状の構造, 即ち amelogenin はエナメル質の容積のみではなく基本的なエナメル質の構造を形成していて, 全体に硬く石灰化する. エナメル質の基本的構造としては, エナメル小柱, シュレーゲル条, 成長線などであり, Uchida ら(1998)[22]の Fig. 3, 4 にもこれが示されている. つまり, amelogenin はエナメル質の基本構造をつくる豆腐であり, その中で結晶形成と成長が起こる. 換言するなら豆腐状の有機基質でできた構造が結晶に置き換わると推定される.

有機基質の形態

エナメル質の結晶形成に関与する有機基質の形態学的根拠としては, エナメル芽細胞の細胞質内や細胞間隙の分泌顆粒や分泌面に電子顕微鏡によって認められる amorphous material, 又は stippled material と呼ばれる粒子がある. これは石灰化しつつある象牙質中にも認められ, 大きさも多様であるため coarse textured material や fine textured material と呼ばれた[8, 12]. この粒子は, 主に gultalaldehyde による固定で得られた電子顕微鏡像によるものである.

一方, 強くタンパク質を凝集する tannic acid による固定[4]では, エナメル芽細胞から分泌された径20-50nmの中空の粒子が観察され, エナメル芽細胞の分泌面から100-500nm の範囲には芯をもつ数珠ないし撚糸状の細管状構造が認められる(Fig. 11). 細管状構造の直径は 20-50nm であり, 中空の粒子状構造の直径と一致する. それゆえに中空の粒子状構造はつながって細管状構造となる[8]. この細管状構造の中に出現する撚糸状の物質は apatite 結晶の central dark line に相当すると推定された[11]が central dark line である何の証拠もない. 堀篭ら(1997)[8]は, tannic acid で固定されたこの構造が, 酢酸ウラン-鉛で染色されることから, 純粋な無機結晶ではなく有機基質に富んだ最初に現れるエナメル質の結晶, 即ち結晶核と推定している.

これは, エナメル質結晶形成の場に存在する有機基質, 即ちエナメルタンパクが結晶形成に積極的に関与していることを示している. 最初に出現する結晶状の構造が電子染色されることは, 有機基質と硬く結びつき, 有機基質に覆われていることを示している. この状態は, 有機基質に富む amorphous 状先駆的結晶と考えることができよう.

他方, AFM(原子間力顕微鏡)を用いた観察によると, amelogenin は 30-70nm の径をもつ粒子[2, 25]でこれが結晶形成に関与すると推定されているが, 理論的にも形態学的にも結晶形成への関与する根拠は示されていない. AFM による amelogenin の形, 大きさの場合と gultalaldehyde 固定による amorphous material ないし tannic acid 固定による中空の粒子, 細管状構造の直径は近い値を示している. そのため, これらの大きさの異なるタンパク質が電顕的な stippled material, amorphous material ないし coarse や fine textured material と考えて間違いないものと言える.

4. 先駆的結晶形成とその成長(Fig. 24a, b)

ここでは, 象牙質表面ないし, エナメル芽細胞の分泌面に於いて形成される最初の結晶形成について述べる. 高分解能電子顕微鏡による観察では, 有機基質の細管が節状に認められ, 粒子状構造が連続して粗な細管状構造となることを示していた(Figs. 8, 9, 10, 11). 細管状構造の芯も細粒子が数珠ないし撚糸状となり, その細粒子は 1nm 以下で約 0.5 nm の直径である. この形態学的事実によると, 細粒子は原子, 分子レベルの大きさである. 綿アメ状構造は, 有機基質の細管状構造の中で Ca, PO_4, OH, CO_2 などの原子, 分子が不規則配列して撚糸状構造となり, 全体として amorphous 状となっていると推定される. この撚糸状構造は, Höhling ら(1969)[6]によって, 電顕的に dot-like structure として報告された最初の結晶構造と類似する.

中空の粒子は Uchida らの考え(2003)[23]に基づいて推定すると enamelin の疎水部が Ca, PO_4, OH, CO_2 などの apatite 結晶の構成原子, 分子を捉えた形態と考えられる. enamelin 粒子の疎水部はこれ等のイオンを捉え enamelysin によって急激に分解されながらエナメル芽細胞に吸収される. 吸収された跡の空隙には, 次々とイオンがエナメル芽細胞から輸送され, 過飽和に近い状態となる. 急激な分解されない一部の enamelin はイオンを捉えたまま, 集積し細管状の様相を示す. つまり, enamelin の上ではイオンが集積し小型の臨界核(最初の結晶核)形成が進行する. このようにして enamelin 残存部は径 20-50nm の細管状となる. enamelin に捕捉されたイオンは enamelin と共に集積し長く連鎖状となって小型の臨界核(最初の結晶核)が形成される. この状態が, 形成されつつある amorphous の前駆的結晶である. フィラメント状ないし撚糸状構造は原子や分子が有機基質のゲル状の中に配列しているために電子染色によって, 細管状構造内部のフィラメント状ないし撚糸状として観察される先駆的結晶である. 撚糸状構造をつくる小粒子は 1nm 以下であり, 十分に小さい臨界核と考えられる. 繰り返すが, 細管状構造と芯, つまり撚糸状構造は, 有機基質に厚く保護されたため酸に溶けず, 有機基質が染色されたため amorphous 状となった有機基質に富むエナメル質結晶の先駆的結晶と考えることができる(Fig. 24). 一方, 有機基質の大半を占める amelogenin は, 水溶液中の酸素イオンを捕捉するとも考えられ, エナメル質の基本構造を形成するのみではなく, 結晶形成への酸素イオンの供給という形で石灰化に関することも考えられる.

以上の結晶核形成は, 飽和状態の融液に於ける臨界核形成に近いモデルと考えることができる[16]. 即ち, enamelin に捉えられた原子は, 体温条件下で, よりエネルギーを少なく安定した熱平衡状態に移ろうとして, apatite に近い線状の配列をなすと考えられる[16]. 論を進めるなら, 有機基質の吸収は盛んに行われ, 結晶成長の空隙が広がる. その空隙にはイオンは輸送されてくるため, 過飽和の状態にあり, 更に結晶形成が進行するのである.

結晶の配向(Fig. 24a, b)

結晶形成の初期は, enamelin の粒子状構造であり, 中の疎水部に Ca や OH, PO_4, CO_2

を捕捉し, この構造が連鎖して 50-100nm の長さの細管状となるとともに, 内部に不規則な撚糸状配列の amorphous 状先駆的結晶が形成され, これが成長し, 無機基質のみのフィラメント状からリボン状結晶へ成長すると推定される. エナメル芽細胞の分泌面近くでは, 撚糸状先駆的結晶はある程度の規則性をもち, 細胞膜に対して垂直方向に配列・配向する. これは細管状構造の長軸方向に長く連鎖することによる. 即ち, 先駆的結晶の配向・配列の決定は enamelin の細管の配列方向によると考えられる.

Enamelin の C 末端はトームスの突起の細胞膜と親和性があり, 分泌端の細胞膜に付く[23], N 末端は sheathlin と親和性があり, エナメル小柱の横紋やトームスの突起の吸収面に向かうことから enamelin のおおまかな方向性が決まると考えられる. このようにして enamelin の細管の方向・配向が決まり, その内部で形成された臨界核が成長し, 最終的に apatite の C 軸が決定される. このようにしてほぼトームスの突起の細胞膜に垂直に配列する結晶配向[24]が決定されるのであろう.

一方, 象牙質の表面に於いては, コラーゲンなど間葉性有機基質とエナメル芽細胞から分泌されるエナメルタンパクによって満たされた複雑な溶媒がゲル状態にあり, 輸送されてくる apatite 構成のイオンが飽和状態になっている. 象牙質表面の最初のエナメル質結晶形成では, エナメル芽細胞の分化が不規則な状態で分泌吸収が進む. それ故, enamelin の連続的集積も方向性が不十分となり, 結果として, 不規則なフィラメント状結晶の配列を示すのである.

分化が進むと, これ等のフィラメント状構造は酸に溶解し, crystal ghost となり, 中身が溶失するため, 成長した結晶構造であると考えられる.

リボン状結晶から板状結晶への成長(Fig. 24b)

生体内における最初の apatite 形成の形態学的提案は, Höhling ら(1969)[6]による dot-like structure が最初であり, 今回の結果はこれを裏付けている. しかし, 撚糸状ないしフィラメント状先駆的結晶構造からリボン状結晶への移行は明確に捉えられていない. 最初に捉えられる結晶がリボン状であり, よじれた膜状の結晶で, 電子染色で溶失する. リボン状結晶は高分解能電顕では, 数層の原子配列による格子構造が認められる最も幼若な結晶であった. しかし, Tohda ら(1997)[20]はほんの 3-4 層の初期原子配列を報告し, より初期の結晶像を捉えた. 撚糸状ないしフィラメント状構造から結晶格子形成はどのような過程で起こるのか検討する.

初期結晶形成は, 前記の如く細管状構造となった有機基質中で Ca, PO_4, OH, CO_2 などの分子が不規則配列する amorphous 状先駆的結晶である. ある程度原子が集積し臨界核を形成すると急激に原子配列が規則的となり, 二次元的結晶形成が進む. エナメルタンパクが分解・吸収を受け, 各種イオンが次々と分泌され過飽和状態にあるため, 臨界点を超すと急激に原子間エネルギーが最小の熱力学的に安定な平衡状態となり, 原子が数列の整然とした結晶の原子配列へと変化し, リボン状結晶となるためと考えられる. 撚糸状構造から結晶格子形成は急激な変化によるものであるため, また電子顕微鏡の

限界もあるため捉えにくい構造と考えられる. しかし, 象牙質表面やエナメル芽細胞のトームスの突起分泌面近くの先駆的結晶は, 酸溶失しにくいため観察が比較的容易である. その結晶癒合, 分枝やねじれの観察像から, フィラメント状結晶が癒合や分枝をしつつ成長していると考えられる. フィラメント状先駆的結晶やリボン状結晶は薄膜状をなし, 周囲に有機基質に富むことや(whitorocite)[11]であるなどのために, 水や有機基質が脱却されると湾曲状態を示す可能性があり, 結果として曲走したリボン状結晶として観察される[19].

六角柱状結晶から不正多角柱結晶への成長(Fig. 24b, c)

基質形成期から成熟期エナメル芽細胞に於ける結晶成長は多数報告されている. そのほとんどは, 結晶がエピタキシーによって成長するとの考えである. しかし, リボン状結晶や板状結晶でも, a, b 軸, つまり横の面, 幅や厚みの面は明瞭な面を呈し, いわゆる sharp な面に原子が次々と付着し結晶成長する. ここでは amelogenin がイオンを捕捉すると共に enamelysin によってどんどん分解され, 小柱鞘を通って脱却される. 一方, エナメルタンパクや水と共にイオンは次々と送られてきて, 結晶成長し, 板状から六角柱状へと成長する. このような環境で sharp な a, b 軸の界面にエピタキシー成長が進む.

一方, エナメル芽細胞の細胞膜面では必ずしも結晶は sharp な面を呈していない. これはエナメル芽細胞の細胞膜面は複雑な物質の移動があることにより, 依然として enamelin による不均質結晶核形成が進行し, これが成長しつつある結晶に融合すると考えられる.

結晶の間, 側面では, sharp 面での成長だけではなく, 不均質核形成も進み, これが結晶へ付着癒合することは, 六角柱状の結晶が必ずしも一定の大きさでないことが示している. 成長しつつある結晶は小型の結晶を含めて相互に融合し, 新しい結晶が付着癒合し, 結晶の間隙を埋めて不正多角柱状

Fig. 24 Schema of enamel crystal development.
A hydrophobic end of a part of enamelin catches atoms and molecules in the center to form the crystal precursor (a-1-3, b-1-3). It forms the organic rich tubular structure. Atoms and molecules continue and accumulate in it, and arrange irregularly, showing strand structures in the center (a-3, 4, b-2, 3). It is the precursor of enamel crystal as organic rich amorphous phase. The C-terminal of enamelin attach to the ameloblast cytoplasmic membrane, as the result it forms the c-axes of hydroxyapatite crystals (a-4). When atoms and molecules over saturate, the crystal structure having lattices suddenly appears by the atomic balance of energy (b-3). These initial enamel crystals grow to ribbon, plate and hexagonal columnar with the absorption of enamel proteins (b-4, 5, 6, c). The crystals fused together along the development (b-6). The digested enamel protein by the enamelsin is absorbed by the ameloblast (a-5).
Amelogenin forms the enamel volume and fundamental enamel structures (b). Small spaces appear in the amelogenin because it is digested by the ameloblast (c). The initial crystal precursors arise in this small space and grow up to hexagonal along with the spaces increase by the enamel protein absorption(b).
The crystal growth is classified into, 1) catch ions(c-1), 2) crystal precursors(c-2), 3) initial crystals as amorphous phase and crystal nucleation(c-3), 4) ribbon like crystals, 5)plate like crystals (c-5), 6)hexagonal crystals(c-6), 7)mature polygonal crystal(c-7).

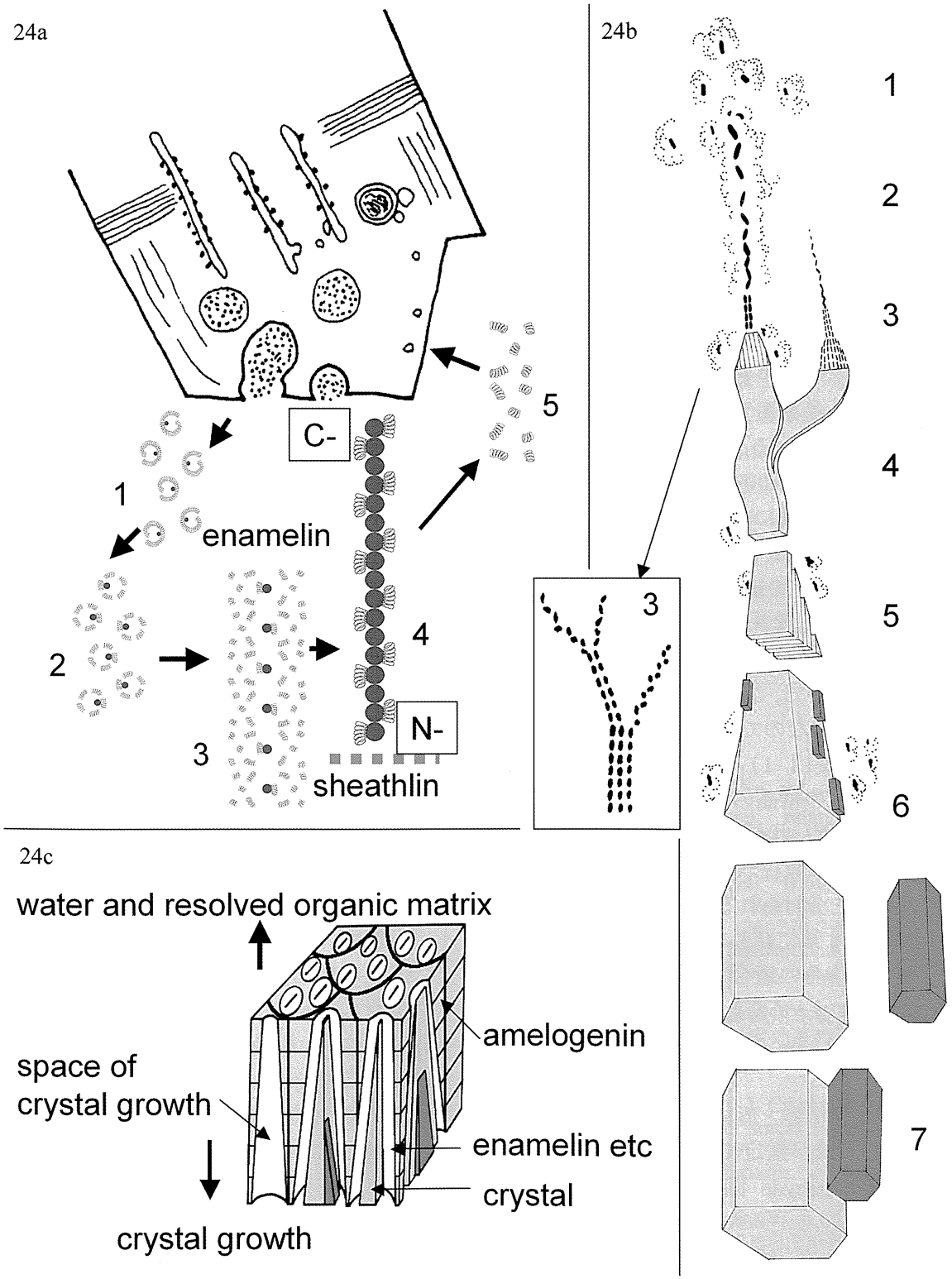
24a
C-
N-
1
enamelin
2
3
4
5
sheathlin
24b
1
2
3
4
5
6
7
24c
water and resolved organic matrix
amelogenin
space of
crystal growth
enamelin etc
crystal
crystal growth

の成熟したエナメル質結晶になる.

以上の如く, 先駆的結晶形成からリボン状, 板状結晶を経て六角柱状, そして不正多角柱状結晶へと成長して, 成熟エナメル質結晶となる. ラットのエナメル質で六角柱状の結晶が多く, エナメル質結晶の形として教科書 [17]にも載せられているが, これは熟成していない結晶の段階であると考えられる. 研究には多くの場合ラットの切歯が用いられるが, このエナメル質は六角柱状をなしていて, ヒトの結晶のように成熟する以前の段階のものと考えられる. エナメル質の石灰化機構は, 当初エナメルタンパクによる不均質核形成と融液成長に相当するが, 次第にエピタキシー, 面成長が主体となる複合的複雑なもので, 種々の結晶形成が同時進行するものである. エナメル質を例に挙げても, 生体の石灰化は多くの結晶化機構が複雑に進行するもので, この複雑性が生体石灰化に特有のものなのである.

結晶成長は 1)イオン捕捉の段階, 2) amorphous の結晶の段階, 3)結晶核形成の段階, 4)リボン状結晶の段階, 5)板状結晶の段階, 6)六角柱状結晶の段階, 7)結晶癒合の段階と分けられる. 但し, エナメル質形成過程では常に結晶核形成が行われ, どの段階でも結晶の癒合が行われている. 以上を総合的にまとめたものが図 24 である.

結 論

エナメル芽細胞と形成中のエナメル質を観察し, 次の点が推定できた.

1. gultalaldehyde 固定をすると, エナメル芽細胞のトームスの突起のエナメル質の形成面に於いて, エナメル芽細胞の分泌物である径 20-50nm の粒子状構造と, 中心に電子密度の高い芯のある径 20-50nm の綿アメ状の初期結晶推定される構造が観察された.
2. tannic acid 固定した場合, エナメル芽細胞から分泌された物質は中空の 20-50nm の粒子として観察された. トームスの突起の形成面から数百 nm の範囲では, 電子密度の高い芯をもつ中空の細管状構造の先駆的結晶と推定できる構造が観察された.
3. 高分解能電顕による観察では, 細管状構造の直径は 20-50nm であり, 節状の構造を呈し, 芯は電子密度の高い線維は撚糸状ないし数珠状の構造をしていた. 粒子の直径は 1nm 以下で約 0.5nm であり, apatite を構成する原子や分子と同じ大きさであった.
4. これをまとめると, エナメル芽細胞から分泌された有機基質のうち, エナメル質結晶の形成に関与するといわれる enamelin の一部は粒子状となり, 疎水部に apatite 結晶構成成分を捉える. 粒子が集合し, 内部に apatite 結晶の先駆的結晶を形成する. 原子はこの状態では不規則に配列し撚糸状となり, 有機基質に富んだ amorphous 状の先駆的結晶となって結晶核に成長する. それ故, 酸に溶解せず, 染色される. amorphous の有機基質の enamelin の C 末端はエナメル芽細胞の膜と親和性を示して関与し, N 末端は sheathlin と関与する, これによって結晶成長の C 軸が決まる.
5. イオンがある程度集積すると, 突然, 結晶核は熱力学的に安定になり規則的原

子配列が形成される. これが数層の原子配列の格子の観察される初期のリボン状結晶であり, 2-3 層の結晶が観察できにくい原因と考えられる.

6. 次いで次々と原子が集積し, 結晶の幅, 更に厚みが増して六角柱状となる. この成長は, エナメル質の容積を確保している amelogenin が溶解し, その間隙が拡大するにつれて結晶成長をする, と推定される. 結晶はある程度成長すると, 面成長やエピタキシーによる結晶形成が進行する. この過程で結晶核から次々と結晶成長が起こると共に, 結晶は配向性に関係なく成長過程で癒合や融合がおき, 最終的に不規則な多角柱状結晶が形成される.
7. 結晶の大きさは amelogenin が分解された空隙と結晶成長の速度によって決まるものと考えられる.
8. 結晶形成段階は1)イオン捕捉段階, 2)イオンの集積する先駆的結晶段階, 3) amorphous の結晶核(臨界核)形成段階, 4)リボン状結晶段階, 5)板状結晶段階, 6)六角柱状結晶段階, 7)成熟結晶段階に区分される.

謝 辞

本研究の一部は文部科学省平成 13 年度学術フロンティア推進事業, 文部科学省平成 15 年度学術フロンティア推進事業(継続分), 平成 15 年度日本大学学術研究助成金(一般研究(共同)課題番号 03-016), 平成 16 年度日本大学学術研究助成金(総合研究(新規)課題番号 総 04-019, 一般研究(個人)課題番号 04-124), 日本大学松戸歯学部鈴木研究費(一般研究 課題番号 03-1002, 奨励研究 課題番号 03-2001), 日本学術振興科学研究費助成金(基盤研究(C)(2)No. 16591840, 若手研究 B No. 16791115)により行われた.

本論は 2004 年のエナメル質比較発生学懇話会, 2002 年度第11回硬組織生物学会年会で発表し検討をいただいた. 本論の趣旨はエナメル質比較発生談話会, 2003年選定学術フロンティア推進事業(日本大学松戸歯学部)のまとめの会で検討いただいた。なお本研究の結晶形成の検討及び, 関連文献について飯島まゆみ先生(朝日大学歯学部), 有機基質については山越康雄先生(元鶴見大学歯学部), 結晶模式図については寒河江登志朗先生にご教示いただいた事に心から御礼申し上げます。

文 献

1) Decker, J. D. Fixation effects on the fine structure of enamel relationships. J. Ultrastructure research 1973; 44: 58-74.
2) Fincham, A. G., Moradian-Oldak, J., Simmer, J. P. The Structural Biology of the Developing Dental Enamel Matrix. J. Structural Biol 1999; 126: 270-299.
3) Frank, R. M. Conceptions nouvelles concernant l'enamil et sa genese. Arch. Oral Biol 1961; 4: 29-33.
4) 二重作 豊. 電子顕微鏡用生物試料作成のためのtannic acidの固定効果の研究. I.固定の機構に関する研究. お茶ノ水医学雑誌 1972; 20(2): 13-34.
5) Gustavsen, F., Silness, J. Crystal shape in the prism sheath region of sound human enamel. Acta Odonto. Scand 1969; 27: 617-629.
6) Höhling, H. J., Pfefferkorn, G., Radicke, J., Speichelsteine, J. V. Elektoronenmikroskopische Untersuchungen zur organischen Matrix und Kristallbildung in menschlichen Speichelsteinen. I. Mitteilung.

DZZ 1969; 24(7): 663-670.
7) Höhling, H. J., Arnold, S., Hohling, J. M., Plate, U., Wiesmann, H. P. Corrlation between the Distribution of Nanometer Sized Apatitic Paracrystalline Particles and the Acidic Sites of Phosphoproteins as Apatitic Nucleators in Developing Hard tissuew. Materialwissenschaft und Werkstofftechnik 2001; 32: 149-153.
8) 堀篭 公彦, 岩佐 由香. エナメル質結晶の形成開始に関する形態学的研究. 日大口腔科学 1997; 23(4): 365-370.
9) 一條 尚. 歯と骨の結晶構造-1,000 万倍の世界-(一條 尚編). 東京, 医歯薬出版株式会社 1995. p.1-127.
10) Lowenstam, H. A. Minerals formed by Organisms. Science 1981; 211(13): 1126-1131.
11) 森脇 豊. う蝕とその予防の結晶化学. 科学と実験 1980; 5: 56-61.
12) 小澤 英浩. エナメル芽細胞の微細構造学的特徴と機能. エナメル質, その形成, 構造, 組成と進化. (須賀昭一 編), 東京, クインテッセンス出版, 1987. p.50-75.
13) Pautard, F. G. E. An X-ray diffraction pattern from human enamel matrix. Arch. Oral Biol 1961; 3: 217-220.
14) Rönnholm, E. III. The Structure of the Organic Stroma of Human Enamel During Amelogenesis. J. Ultrastructure Resaerch 1962; 3: 368-389.
15) Robinson, C., Brookes, S. J., Kirkham, J. The developing enamel matrix: nature and function. Eur. J. Oral Sci 1998; 106: 282-291.
16) 齋藤 幸夫. エピタキシャル成長. 結晶成長(原 康夫編). 東京, 裳華房, 2002. p.1-170.
17) Scott, J. H., Symons, N. B. B. Enamel. Introduction to Dental Anatomy 9th. New york, Charchill Living Stone, 1982. p.179-215.
18) Smales, F. C. Structural subunit in prisms of immature rat enamel. Nature 1975; 258: 772-774.
19) Suzuki, K., Sakae, T., Kozawa, Y. Helix Structure of Ribbon-like Crystals in Bovine Enamel. Connective Tissue Research 1998; 38: 113-117.
20) Tohda, H., Yamada, M., Yamaguchi, Y., Yanagisawa T. High-resolution electron microscopical observations of initial enamel crystals. J. Electron Microscopy 1997; 1: 97-101.
21) Travis, D. F., Gli,cher, M. J. The structure and organization of and the relationship between the organic matrix and the inorganic crystals of embryonic bovine enamel. J. Cell Biol 1963; 18: 109-123.
22) Uchida, T., Karukaya, E., Hiyama, S., Satoda, T., Hayashida, K. Expression and Functional Significance of Enamel Proteins in Amelogenesis. Archives of Comparative Biology of tooth Enamel 2003; 8: 13-15.
23) Uchida, T., Murakami, C., Wakida, K., Dohi, N., Iwai, Y., Simmer, J. P., Fukae, M., Satoda, T., Takahashi, O. Sheath proteins: synthesis, secretion, degradation and fate in forming enamel. Eur. J. Oral Sci 1998; 106: 308-314.
24) 脇田 稔, 塩井 考, 小林 茂夫. エナメル質の微細構造とトームス突起-エナメル質形成における三次元的相関. エナメル質, その形成, 構造, 組成と進化(須賀昭一編). 東京, クインテッセンス出版株式会社, 1987. p.76-91.
25) Wen, B. H., Moradian-Oldak, J., Leung, W., Bringas Jr., P., Ficham, A. G. Microstructures of an Amelogenin Gel Matrix. J. Structural Biol. 1999; 126: 42-51.

(Received: November 30 / Accepted: December 27)

連絡先
小澤 幸重
日本大学松戸歯学部第2解剖学講座
〒271-8587 葉県松戸市栄町西 2-870-1
E-mail, kozawa@mascat.nihon-u.ac.jp
Tel & Fax:047-360-9323

Enamel crystal development

Yukishige KOZAWA[1], Atsushi OOKUBO[1,3], Hirokazu OINUMA[1], Hideki CHISAKA[1], Tomohisa HONDA[1,2], Rumi YOKOTA[1], Yuka IWASA[1], Kunihiro SUZUKI[1], Hitoshi YAMAMOTO[1], Toshiro SAKAE[1]

[1]Department of Anatomy II, Nihon University School of Dentistry at Matsudo
[2]Department of Orthodontics, Nihon University School of Dentistry
[3]Japan Institute for Advanced Dentistry

The initial calcification of enamel was observed by the high resolution electron microscope. With gultalaldehyde fixation, the granular or amorphous structure at 20-50 nm in diameter and rod like structure of 20-50 nm in width having high density fibers in the center, were observed near the Tomes process of the ameloblasts. The grainy materials at 20-50 nm in diameter secreted by the ameloblasts were observed, when the animals were fixed with tannic acid.

The hollow structures located to a distance of the several 100 nm from the cell membrane. And also the tubular structures had high density fibrils in the center. The diameter of these two structures was same as about 20-50 nm. The central fibers formed as twisted threads, strands or beads were less than 1 nm in diameter, were similar size of the atoms composed of apatite crystal.

These phenomena showed the pattern of initial enamel crystals. The amorphous stippled materials fused and formed the tubular structures, which were enamel protein secreted by ameloblast. The hydrophobic small part of the enamelin captured the molecules or atoms of apatite crystal elements. Atoms and molecules accumulated in the tubule and arranged irregularly to form the strand structure in the center. As the result, the initial precursor of crystal formed in the tubular structures. It is to say the precursor hardly packed by the amorphous organic materials of enamel protein.

It is the reason that the structure was insoluble by the acid attack and stained with lead-acetate. It is concluded that this amorphous structure is the precursor of initial enamel crystal.

The c-axis of the crystal growth is decided by the arrangement of these tubular structures of enamelin, which was the crystal developing in the place. The tubules arranged almost perpendicular to the cell membrane of Tomes process, because the C-terminal of the enamelin had an affinity at the cell membrane of the secreting face of Tomes process, the N-terminal attached to the sheathlin in the cross striation of enamel prism.

When atoms accumulated and saturated in the tubular structures, the amorphous precursor crystal, so called as strands or crystal nuclei, changed suddenly to the apatite crystal, having several lattices of atomic images, by the thermal energy potential. This initial crystal was recognized ribbon-shaped crystal of enamel. Next, the atoms adhered on the side of these crystals and grew to the plate forms. These plate-crystals increase the thickness, and finally changed to a hexagonal cylinder shape with the epitaxial growth. New crystallization of the precursor of crystals always occurs between crystals, and new crystals fused matured hexagonal crystals. Finally these crystals formed the irregular polygonal crystals. These processes take place in the spaces of dissolved amelogenin.

In other words, the crystal size and form were depended on the shape and size of the space of the amelogenin, because the spaces appeared by the dissolve of amelogenin.

Keyword: enamel, crystal formation, crystal precursor, calcification, biomineralization

Key Engineering Materials Vols. 192-195 (2001) pp. 347-350
Proceedings of the 13th Int. Symp. on Ceramics in Medicine, Bologna, Italy, 22-26 Nov. (2000) pp. 347-350
© 2001 Trans Tech Publications, Switzerland

In Vitro Interactions of Bone Marrow Cells with Carbonate and Fluoride Containing Apatites

T. Sakae[1], K. Hoshino[1], Y. Fujimori[1], Y. Kozawa[1] and R.Z. LeGeros[2]

[1] Department of Anatomy, Nihon University School of Dentistry at Matsudo, Chiba 271-8587, Japan

[2] Department of Biomaterials, New York University College of Dentistry, USA

Keywords: Carbonate, Fluoride, Hydroxyapatite HA, Osteoclast-Like Cells

ABSTRACT

The purpose of this study was to investigate the *in vitro* interactions between osteoclast-like cells and synthetic apatites. Carbonate-free (HAP), carbonate substituted (CHA), and carbonate- and fluoride-substituted (CFA) apatites were prepared by precipitation method and characterized using X-ray diffraction, infrared spectroscopy, scanning electron microscopy with energy dispersive system and thermo gravimetric analyses. Cells from the bone marrow of one-day old rabbit were seeded on the apatite substrates. After three days in cell culture, all the apatite substrates showed TRAP positive reaction. The intensity of the reaction of TRAP positive cells decreased in the order: CHA>HAP>CFA. SEM observation showed that the morphology of cells on the CFA and/or HAP discs resembled the phagocytes such as monocytes, rather than the osteoclast. These results indicate that carbonate ions in the apatite lattice encourage the cell activity while the fluoride ions inhibit phagocyte cell activity.

INTRODUCTION

Biological apatites in the mineral phases of enamel, dentin and bone are characterized by its nanocrystal size and the presence of carbonate (CO_3) or carbonate and fluoride (F) ions substituted in the apatite lattice [1,2]. Bone and dentin apatite crystallites are much smaller and contain more CO_3 compared to the enamel apatite [2,3]. The bone and dentin apatite crystallites were more soluble than those of enamel and this difference in dissolution properties was partially attributed to the difference in carbonate content: the higher the carbonate content (e.g., in dentin or bone apatite compared to enamel apatite) the higher the solubility [1]. A critical stage in bone remodeling is the resorption of the bone mineral by osteoclasts. Fujimori et al [4] showed that osteoclast-like cells appeared on the surfaces of sintered calcium hydroxyapatite (HA) ceramic disks but resorption of the HA substrates was not observed. Redey et al [5,6] reported that osteoclasts on carbonated hydroxyapatite did not resorb the substrate and that human osteoblast's

collagen production activity was lower on the type A (i.e., CO_3 for OH) carbonate apatite than the stoichiometric hydroxyapatite (HA).

The purpose of this study was to investigate the interaction of bone marrow cells with synthetic apatites which are carbonate-free or contained carbonate with and without the simultaneous presence of F ions.

MATERIALS AND METHODS

Unsubstituted (HAP) and apatites with carbonate substitution (CHA) or carbonate and fluoride substitutions (CFA) were precipitated at 95°C [2,7]. The apatites were characterized using x-ray diffraction (XRD), infrared spectroscopy (FT-IR,), scanning electron microscopy (SEM) with energy dispersive system (EDS) and thermogravimetry (TG-DTA). Disks or pellets were prepared from the apatite powder using 300kgp. Bone marrow cells were derived from one-day-old rabbit femur and cultured on the discs for 3 days under routine conditions. After fixing with 2.5% glutaraldehyde with buffer and critical point drying, the TRAPase reactions were observed under the microscope and with SEM.

RESULTS

XRD analyses confirmed the apatite structure of the unsubstituted (HAP), carbonate- (CHA) and carbonate- and F- (CFA) substituted apatites; with unit cell (*a*- and *c*-axes) dimensions: a=9.379 and c=6.910 A for CHA; a=9.338 and c=6.899 for CFA and a=9.440 and c=6.879 for HAP. These dimensions reflect the incorporations or substitutions of CO_3 (for PO_4) or CO_3 + F (for OH) in the apatite lattice [1,7]. FTIR analyses demonstrated the presence of CO_3 in the CHA and CFA samples by the C-O absorption bands at around 1400 and 1500 cm^{-1} and at around 870 cm^{-1} (Fig. 1). TRAP positive ostoclast-like cells were observed on the surfaces of all apatites. The numbers of TRAP positive cells decreased in the order: CHA>HAP>CFA (Fig 2). The abundance of fibroblastic cells were also observed to decrease in the order: HAP>CHA>CFA. SEM observations showed that TRAP positive cells on CFA surfaces (Fig 4.) were not large as those on the CHA and/or HAP surfaces (Fig 5). Furthermore, the morphology of the cells on the CFA surfaces resembled phagocyte cells such as monocytes rather than osteoclasts. The cells on CHA substrate formed resorption lacunae (Fig. 6).

DISCUSSION

Whether the carbonate ions in bone apatite promote or suppress osteoblastic and/or osteoclastic activities is still unclear. It is known that protons in the media stimulate osteoclasts in the absence of CO_2 and HCO_3^-. But it has also been reported that cell-mediated Ca^{2+} release from bone organ culture is increased only when media are acidified by the reduction of HCO_3^- ion concentration and not by increasing PCO_2. In this study, we found that the number of pits and osteoclast-like cells, as well as fibroblast-like cells on carbonate-containing apatite (CHA)

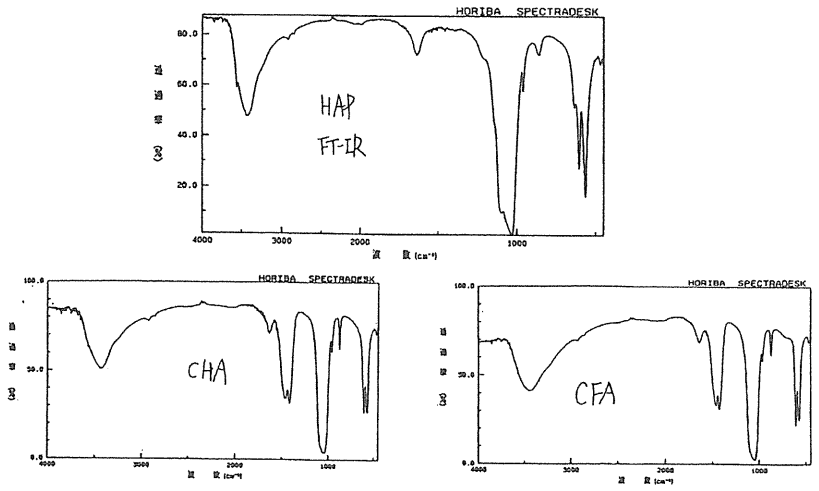

Fig. 1

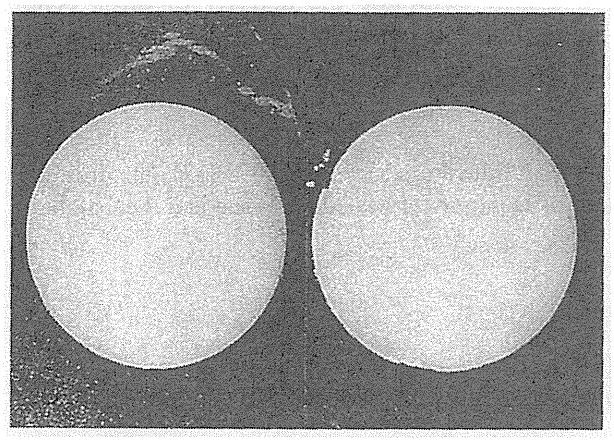

Fig. 2

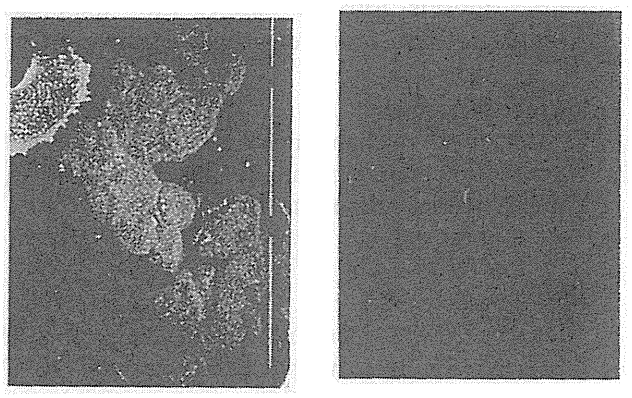

Fig. 3

Fig. 1: FTIR spectra of carbonate-free apatite, HAP (A), carbonate-containing apatite, CHA (B) and carbonate and fluoride-containing apatite, CFA (C).

Fig. 2: TRAP-positive cells (red dots) were more numerous on the surface of CHA disks (left) compared to those on the surface of CFA disks (right).

Fig. 3:Osteoclast-like cells formed many resorption lacunae on CHA surfaces (left) while no resorption lacunae were observed on CFA surfaces (right).

were larger than those on carbonate-free apatite (HAP). Our observation that cells resorbed the carbonate apatite used in this study is not in agreement with the observations of Redey et al [5,6]. This may be due to the fact that carbonate apatite used in this study was type B (CO_3-for-PO_4 substitution) and prepared at about 95°C. The carbonate apatite in Redey's experiments was type A (CO_3-for-OH). Type A carbonate apatite, like stoichiometric HA are prepared at temperatures above 1000°C [8]. Thus, while both Type A and Type B carbonate apatite contain carbonate in the lattice the difference in cell interaction may be related to the difference in dissolution properties caused by difference in preparation temperature (95°C for type B vs. 1000°C for type A) and not to the carbonate content.

It was also observed in this study that the number of pits and cells were much smaller on the fluoride-containing carbonateapatite (CFA) compared to fluoride-free carbonate apatite (CHA). This observation is similar to that in an earlier *in vitro* studies, which demonstrated that F-treated bone, compared to untreated controls, had less number of resorption pits. when exposed to osteoclasts [9]. If resorption is associated with the dissolution properties of apatite, the fluoride effect may be explained by the difference in dissolution properties between carbonate-containing and carbonate and fluoride-containing apatites [7,10].

Results of our study suggest that bone marrow cell interaction depended on the composition of the apatite: that carbonate ions in apatite stimulate the activity of these cells while fluoride ions in apatite may suppress maturation of osteoclast and proliferation of fibroblast. Further studies are needed to confirm this hypothesis.

Acknowledgements
This study was supported by a Grant-in-Aids, Ministry of Education, Japan (11671817); the frontier Science Promotion Program at Nihon University School of Dentistry at Matsudo, Japan and the Calcium Phosphate Research funds.

References

1.LeGeros RZ. Prog Crystal Growth Charact 4: 1-45 (1981).
2.LeGeros RZ. In: .*Hydroxyapatite and Related Compounds*. Brown P, Constanz B (eds). CRC Press, Boca Raton, pp. 3-28; (1994)
3.LeGeros RZ, Sakae T, Bautista , Retino M, LeGeros JP. *Adv Dent Res* 10: 225-231 (1996).
4. Fujimori Y, Mishima H, Sugaya K, Sakae T, LeGeros RZ, Kozawa Y, Nagura H. *Bioceramics 11*, 335-338 (1998).
5. Redey SA, Razzouk S, Rey C, Bernache-Assollant D, Leroy G, Nardin M, Cournot G, *J Biomed Mater Res 45*, 140-147 (1999).
6. Redey SA, Nardin M, Bernache-Assolant D, Rey C, Delannoy P, Sedel I, Marie PJ J Biomed Mater *Res 50* 353-364 (2000)
7. LeGeros RZ. *Calcium Phosphates in Oral Biology and Medicine.* Monographs in Oral Science. Vol. 15. Karger, Basel (1991)
8. Elliott JC. PhD Thesis. University of London (1964).
9. Winter J, Kleckner A, LeGeros RZ, Vernillo A, Rifkin B. *J Dent Res 68*:353, 1989.
10. LeGeros RZ, Tung MS. *Caries Res 17:*419-429 (1983).

日大口腔科学　27：297～303，2001

《原　著》

軟化象牙質の熱分析的研究

田川　元　寒河江　登志朗
日本大学松戸歯学部　第2解剖学教室
（指導：小澤　幸重教授）

キーワード：齲蝕，軟化象牙質，有機質，コラーゲン，変性

要旨：象牙質齲蝕におけるコラーゲンの状態を熱分析の手法を用いて検索した。材料は抜去された齲蝕歯を用い，ホルムアルデヒド溶液で1昼夜固定後洗浄し，Bhuler low speed diamond sawで1 mm厚の切片をつくり，さらに齲蝕部の軟化象牙質と健全部の象牙質をそれぞれ約1 mm角に切りだした。この試料を熱重量・示差熱分析装置を用い，熱的性質の解析を行った。健全部象牙質は従来の象牙質の熱分析実験の報告と同様の発熱反応と重量減少反応を示した。すなわち，約320 °Cに強い発熱・減量反応が出現し，約400 °Cにショルダーが認められた。健全部象牙質では200 °Cから520 °Cの温度範囲で約20mass %の重量減少が認められた。これらの熱反応は象牙質中の有機質の燃焼によるものである。一方，軟化象牙質は健全部象牙質とは異なり，約320 °Cと約440 °Cの2個所に強い発熱・減量反応のピークが存在した。軟化象牙質で顕著となった約440 °Cの発熱・減量反応は，健全部象牙質の有機質の一部がより高温度に耐えられる性質へと変性した結果と考えられる。軟化象牙質の熱反応パターンはPlank-Rychlo溶液で人工的に脱灰した象牙質の発熱・減量パターンと一致した。すなわち，軟化象牙質は緩衝溶液中の弱酸環境と類似した齲蝕進行機構により脱灰されていることが熱分析的に確認できた。軟化象牙質の200 °Cから520 °Cの重量減少は44mass %から62mass %まで試料ごとに異なった値を示した。この結果は軟化象牙質の脱灰の程度の差，すなわち齲蝕進行の程度の差，を表しているものと考えられる。象牙質コラーゲンは脱灰の状態あるいは脱灰処理法で線維間あるいは線維内の結合状態が変化すると考えられていることから，今回得た軟化象牙質の脱灰の状態は，軟化象牙質の新しい治療法の開発研究に重要な情報を与える。

Thermal Analysis of Carious Softened Human Dentin

Hajime Tagawa, Toshiro Sakae
Department of Anatomy
Nihon University School of Dentistry at Matsudo
Matsudo, Chiba 271-8587, Japan
(Director : Prof. Yukishige Kozawa)

Key words : caries, softened human dentin, organic matrix, collagen, degeneration

Abstract : Thermal behaviors of collagen in the carious human dentin

〒271-8587　松戸市栄町西2-870-1（平成13年6月7日受付，平成13年10月12日受理）

were analyzed using thermal analytical technique. Extracted molars were used in this study. These teeth were fixed with a 10 % neutral formaldehyde solution for overnight, rinsed with water, and sectioned into about 1mm thick using a Buehler low speed diamond saw. Then, portions of softened dentin were scraped off using a dental scraper. DTA, TG and DTG curves of the normal and softened dentin were obtained using a thermogravimetric - differential thermal analyzer. The DTA, TG and DTG curves of the normal dentin were the same to the reported data for human dentin. They showed a common pattern ; a strong exothermic reaction at about 320 °C with weak shoulder at about 400 °C. The weight loss between 200 °C and 520 °C was about 20mass %. These reactions were due to combustion of the organic component in the human dentin. The softened dentin showed the different thermal behaviors from those of normal dentin. There were two strong exothermic reactions at about 320 °C and about 440 °C. The latter reaction suggested that part of the organic components degenerated into high-temperature registrant form from the low-temperature registrant form. The thermal behaviors of the softened dentin were close to those of the artificially demineralized dentin using Plank-Rychlo solution. These results indicated that the softened dentin was formed under the buffered weak acidic condition. The weight loss values for the softened dentin samples varied from 44mass % to 62mass %, suggesting that these softened dentin suffered from varied demineralization attack. The softened dentin collagen might be changed their cross-linking types and/or numbers, it should supply important information to develop a new clinical treatment of dental caries.

Nihon Univ. J. Oral Sci. 27 : 297～303, 2001

緒　　言

象牙質の齲蝕は，象牙細管に沿って進行するが有機質が豊富なため脱灰された後にいわゆる“軟化象牙質”が残る。歯冠部象牙質の齲蝕は象牙質齲蝕円錐を形成し，非脱灰標本の顕微鏡観察では，1) 崩壊層，2) 着色層，3) 混濁層，4) 透明層（硬化層），5) 生活反応層（不透明層），に分けることができる[7,22]。これらの中で1)から3)が“軟化象牙質”に相当する部分である。

齲蝕象牙質は程度の差はあるとしても脱灰されている。脱灰の程度を調べるにはコンタクトマイクロラジログラフィ法[23]あるいは定量的元素分析法を用いれば可能であり，実際に行われている[1-3,5,8,25]。齲蝕による脱灰作用が象牙質の無機質成分にもたらした変化についての研究も行われてきている[4,10,16,17,19]。

齲蝕進行に伴って象牙質の有機質に変化が生じることも報告されている[11]。林[18]は乳酸，酢酸およびEDTAによる人工的な脱灰作用で象牙質中のコラーゲン，非コラーゲン性タンパク質，そしてフォスフォフォリンに選択的溶脱が生じることを明らかにした。Klontら[12]はウシ切歯を用いた人工的な脱灰実験で象牙質に含まれるタンパク質の選択的な溶脱が起きていることを示した。Kubokiら[14]は，0.5％塩基性フクシン－プロピレングリコール染色法を用い，染色態度で2分された齲蝕象牙質について，コラーゲンの線維内架橋に違いを認めた。すなわち，健全部象牙質と比較して不染性の齲蝕第2層は架橋が減少し，コラーゲンのプレカーサーが増加していた。可染性の齲蝕第1層では架橋もプレカーサーもともに減少していたと報告している。

コラーゲンの石灰化に相関してコラーゲンの熱的挙動が異なることは，Sakaeら[21]が，そして象牙質の脱灰処理による象牙質有機基質の熱的挙動の変化は谷中ら[24]が報告している。これらのことから，齲蝕象牙質における有機質の状態変化が推測され，特に齲蝕象牙質は健全部象牙質と異なったコラーゲンの状態にあると考えられる。本研究では，このような齲蝕象牙質の有機質の状態変化を熱的挙動変化としてとらえたので報告する。

材料と方法

象牙質の咬合面齲蝕部分を，1) 崩壊層，2) 着色層，3) 混濁層，4) 透明層（硬化層），5) 生活反応層（不透明層），の層別に純粋に分け取る操作は現実には不可能である。ここでは，上記の1)層から3)層に相当する部分で齲蝕象牙質からエキスカベータで容易に切り出せるいわゆる“軟化象牙質”の部分と，そして異常の見られない健全部象牙質の2部に大別した。試料調整は，咬合面に象牙質に達する齲蝕のある第2および第3大臼歯を用い，1昼夜10％ホルマリン溶液で固定，流水で洗浄後，low speed diamond saw（ISOMET®, Buehler Ltd, Illinois, USA）により1mm厚の縦断切片を切り出し，歯冠部の軟化象牙質をエキスカベータで削り出し，残りの部分からlow speed diamond sawを用いて健全部象牙質を約1mm角のブロックに切り出した。これらの試料細片は蒸留水で洗浄後，空気中で乾燥した。実験に使用した歯10本の中で，次の熱分析実験の結果が軟化象牙質と対照健全部象牙質とも安定した成績を示したもの5本について今回の成績とした。

熱分析実験は，熱重量分析・示差熱分析（TG-DTA）同時測定装置（TAS-100，㈱リガク，東京）を用いて，試料量：数mg～十数mg，昇温速度：5℃/min，測定温度範囲：室温～700℃，熱電対：Pt-PtRh，重量測定感度：0.01mg，測定雰囲気：空気，基準物質：コランダムの条件下で行った。微分熱重量（DTG）分析曲線の計算はTAS-100装置付属ソフトウエアによって行った。

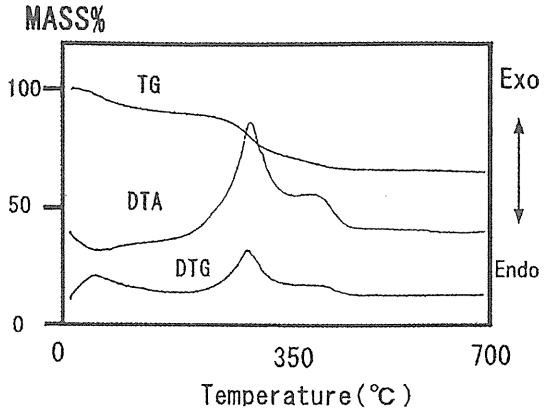

Fig. 1 The representative DTA, TG and DTG patterns for the normal human dentin (HD4).

結　果

5本の大臼歯歯冠部から得た健全部象牙質の熱反応パターンはどれもほぼ一様であった。Fig. 1（HD4）に健全部象牙質の典型的な熱重量（TG）分析曲線，微分熱重量（DTG）分析曲線と示差熱分析（DTA）分析曲線を示した。DTA分析曲線からは，315℃にピークをもつ強い発熱反応が現れ，この発熱反応は400℃にショルダーをもっていた。すなわち，約400℃に弱い発熱反応が付随していることを示した。TG分析曲線では，200℃までの第1段階の重量減少が，その後200℃から520℃にかけ

Table 1 The thermal analysis data of the normal and caries human dentin

Sample		HD1	HD2	HD3	HD4	HD5	Data range
Normal dentin							
	1st exotherm	310	310	315	315	310	310-315
	2nd exotherm	400b sh	400b sh	400b sh	400b sh	400b sh	400b sh
	water cont.	10.9	10.6	13.8	10.8	10.5	10.5-13.8
	Mass loss (%) 200-520	19.1	20.5	20.1	21.4	20.0	19.1-21.4
Carious dentin (softened dentin)							
	1st exotherm	320	320	325	315	310	310-325
	2nd exotherm	445	440	450	435	435	435-450
	water cont.	12.3	13.1	21.3	11.9	16.4	12.3-21.3
	Mass loss (%) 200-520	61.8	48.1	47.9	46.9	44.3	44.3-61.8
	200-360	34.9	30.1	27.8	31.8	29.4	27.8-34.9
	360-520	26.9	18.0	20.1	15.1	14.9	14.9-26.9

て第2段階の重量減少が認められた。5試料とも共通して第1段階の重量減少量は約10mass％で，第2段階の重量減少量は約20mass％であった（Table 1）。DTG分析曲線の解析から，第2段階の重量減少の極大は300℃にあることが求められた。重量減少反応は500℃を超えるところまでゆるやかに引き続いた。DTA分析曲線に現れた発熱反応のショルダーに対応して，DTG分析曲線にもほぼ同じ温度に減量反応のショルダーが認められた。このことは重量減少反応が発熱反応に伴われていることを示唆した。DTG分析曲線の解析によっても200℃から520℃までの連続した第2段階の重量減少反応を正確に2分することはできなかった．DTG分析曲線がDTA分析曲線と同じパターンを示したことから約360℃が2つの反応の中間であると見なし，第2段階の前半部分と後半部分の減量反応の比率として約4：1を得た。

軟化象牙質の熱分析曲線は試料毎に異なった様相を示した。Fig. 2からFig. 6に5試料の軟化象牙質の熱分析曲線を示した。Fig. 2に示した試料番号HD1の軟化象牙質のDTA分析曲線は320℃に第1の，そして445℃に第2の強い発熱反応のピークが存在した。この2つの発熱反応のピーク形状は，320℃の反応の方が鋭かった。この他に260℃にショルダーが認められた。これらの2つの強い発熱ピークとショルダーは，5個の試料に共通して認められた（Figs. 2-6）。

しかし，320℃と445℃の近傍に出現する2つの発熱ピークの強弱と，ピークの鋭さは試料毎に異なっていた。試料HD2の軟化象牙質では第2のピークとほぼ同じ程度に第1のピークは緩やかとなっていた。試料HD3の軟化象牙質では第1と第2の発熱ピークの強さがほぼ等しくなっていた。試料HD4の軟化象牙質では，試料HD1と

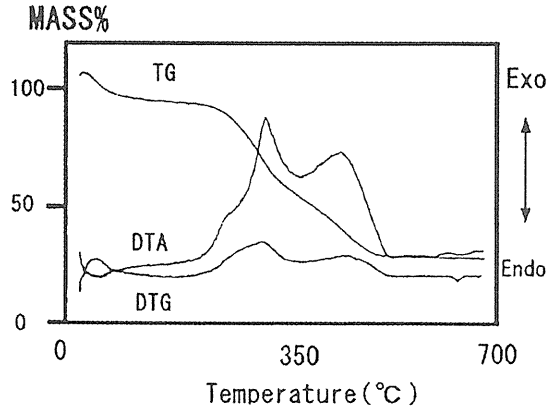

Fig. 2　The DTA, TG and DTG curves for the caries lesion part of the human dentin (HD1).

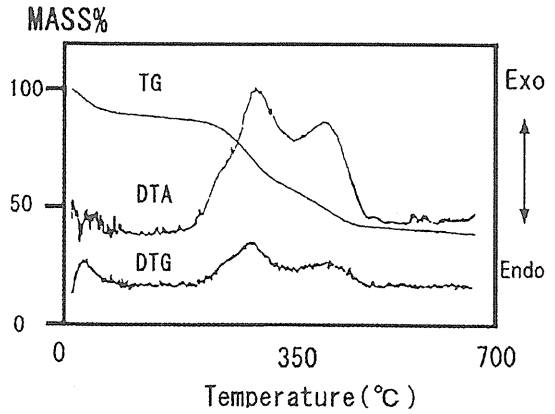

Fig. 3　The DTA, TG and DTG curves for the caries lesion part of the human dentin (HD2).

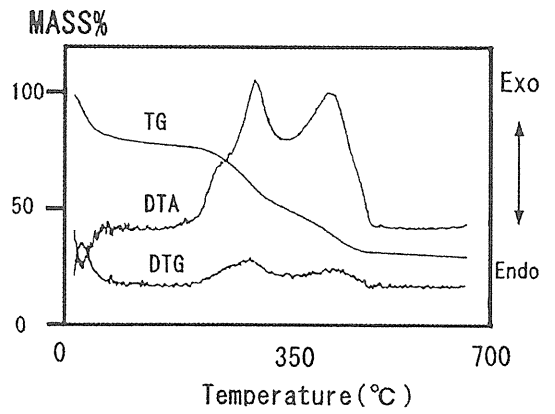

Fig. 4　The DTA, TG and DTG curves for the caries lesion part of the human dentin (HD3).

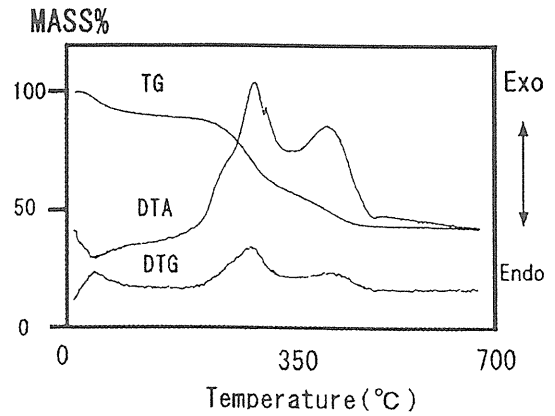

Fig. 5　The DTA, TG and DTG curves for the caries lesion part of the human dentin (HD4).

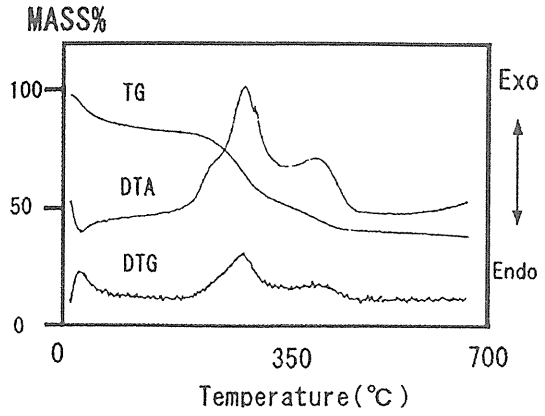

Fig. 6 The DTA, TG and DTG curves for the caries lesion part of the human dentin (HD5).

似たパターンであった。試料 HD5 の軟化象牙質の DTA 分析曲線は第 2 の発熱ピークが 5 試料の中でもっとも弱く，健全部象牙質の DTA パターンに類似した。

軟化象牙質の TG 分析曲線では，200 °C以下の第 1 段階の重量減少と，200 °C以上の第 2 段階の重量減少に分けることが出来た。200 °Cから 520 °Cの第 2 段階の重量減少はさらに TG 分析曲線の傾きから 200 °Cから約 360 °Cの急な反応の領域と約 360 °Cから 520 °Cの緩やかな反応の領域との 2 つに分かれると考えられた。DTG 分析曲線の解析から，試料毎に重量減少反応の 2 つのピークが認められた(Figs. 2-6)。これら 2 つの反応は連続したため厳密な分離は出来ないが，便宜的に中間の 360 °C で分けて数値で表すと約 2：1 の割合となる (Table 1)。5 試料とも軟化象牙質の重量減少量は第 2 段階の前半が大きいことがわかる。DTG 分析曲線に示された 2 つの極大は，それぞれの試料の DTA 分析曲線で現れた 2 つの発熱ピークに対応した。この結果は発熱反応が常に重量減少反応を伴っていることを示唆した。

考　　察

健全部象牙質の熱分析の結果は，5 試料とも同じように，吸着水の離脱に由来する 200 °Cまでの第 1 段階の減量反応と約 20mass %の第 2 段階の重量減少反応を示した。第 2 段階の重量減少は約 310 °Cに出現する発熱ピークに伴っていた。この結果は従来報告された象牙質の熱分析の結果[9,13,15,20,21,24]とよく一致しており，健全部象牙質試料として適切なものであったと考えられる。第 2 段階の発熱・減量反応は有機質の燃焼によるものであることは従来の報告[24]から明らかである。

齲蝕象牙質である軟化象牙質の熱分析の結果は，DTA 分析曲線，TG 分析曲線，DTG 分析曲線のいずれにおいても健全部象牙質のそれとは異なるパターンを示した。その一方で，軟化象牙質試料間の比較では，ピーク温度，ピーク形状と強さなどに若干の違いは認められるが，共通したパターンでまとめることが出来た。齲蝕による軟化象牙質の状態は，人工的に脱灰した象牙質と類似すると推測された。谷中ら[24]は次のように報告した。ギ酸—クエン酸溶液，Plank-Rychlo 溶液，EDTA 溶液を使って人工的に象牙質を脱灰処理したところ，これらの脱灰溶液が象牙質の有機質に異なる影響を及ぼし，象牙質有機質の熱反応はそれぞれ異なった様相を示した。これら 3 者の中で，Plank-Rychlo 溶液で脱灰処理した象牙質の示差走査熱量分析曲線では，260 °Cにショルダー状のそして，340 °Cと 480 °Cに強い発熱反応が認められている。示差走査熱量分析は示差熱分析と基本的には同じ原理で，定量性を向上させたものであるから，結果は同等に比較できる。したがって，今回の軟化象牙質の熱分析パターンは Plank-Rychlo 脱灰した象牙質の熱分析パターンと一致する。このことは，象牙質の齲蝕進行機構は，弱酸で唾液の緩衝作用の存在するような環境下で脱灰作用が進行した事を推測させる。今後，この方面のさらなる研究が必要であろう。

軟化象牙質では約 320 °Cと約 440 °Cの 2 つの強い発熱反応とそれに伴う減量反応が認められた。健全部象牙質でも約 320 °Cに強い発熱・減量反応が観察されたが，約 400 °Cでは弱い発熱･減量反応しか認められなかった。象牙質が脱灰作用を受けると無機質は脱却されるが，有機質はほとんどそのまま残る[6]。したがって，軟化象牙質で約 440 °Cの発熱・減量反応が著しく強く現れたことは，健全部象牙質の約 320 °Cで燃焼する筈の有機質の一部が齲蝕による脱灰作用で，より高温度にならないと燃焼しないような性質に変化したと考えられる。ここではこの性質の変化を“低温型”から“高温型”への変性と呼ぶことにする。

健全な象牙質に含まれる有機質の中で，どの種類のどの程度の量の有機質が齲蝕部の軟化象牙質で“高温型”に変化したかという定量的な問題は今回の研究では明らかにできない。しかし，象牙質の有機質の大部分を占めるコラーゲンが主体であることは容易に推測される。コラーゲンの熱的性質については未解明の問題が残されて

はいるが，Sakae ら[21]および谷中ら[24]は，コラーゲンが石灰化した状態から脱灰された状態へ移ると，燃焼パターンが変化し，400 ℃から 500 ℃の温度領域に強い発熱・減量反応を提示することを報告した。彼らはこの変化をコラーゲンの架橋の変化と結びつけて議論している。Kuboki ら[14]は，0.5 %塩基性フクシン―プロピレングリコール染色法を用いて齲蝕象牙質を可染性と不染性に 2 分し，コラーゲンの生化学的分析を行った。その結果，健全部象牙質と比較して不染性の齲蝕第 2 層はコラーゲンの架橋が減少し，プレカーサーは増加したのに対して，可染性の齲蝕第 1 層では架橋もプレカーサーもともに減少した，と報告した。彼らは生化学的方法で齲蝕進行に伴い象牙質のコラーゲンの架橋に変化が生じることを証明した。

今回の熱分析実験の結果は，健全部象牙質と軟化象牙質の熱的性質に顕著な差を認めた。軟化象牙質では，酸による人工的な脱灰象牙質試料と類似したパターンを示した．以上の結果は，齲蝕による軟化象牙質の有機質は脱灰作用によって熱的により安定な“高温型”へ変性したことを裏付けるものである。この有機質の主体はコラーゲンであり，したがって酸の作用によるコラーゲンの架橋の変化と同様であろうと推測した。このような象牙質有機質の変性の問題は，臨床的な治療を考える上で重要な情報であり，新しい治療法の開発研究に寄与できるものと考える。

結　　論

熱分析により，齲蝕部の軟化象牙質が健全部象牙質と異なる熱反応を示すことを明らかに出来た。健全部象牙質の有機質は約 320 ℃の発熱反応でほぼ 8 割以上燃焼するが，軟化象牙質の有機質は約 320 ℃の発熱反応では有機質の 6 割程度しか燃焼しておらず，より高温側の約 440 ℃の発熱反応で燃焼が完了した。この変化は，象牙質の有機質が齲蝕による脱灰作用の影響を受けて変性したと考えた。軟化象牙質の発熱・減量反応は，象牙質を Plank-Rychlo 液で人工的に脱灰した時の反応パターンと一致した。

以上のことから，齲蝕象牙質は口腔内環境において Plank-Rychlo 溶液脱灰作用と類似した作用を受けたことが確かめられた。さらに，齲蝕象牙質のコラーゲンは石灰化象牙質のコラーゲンの状態とはまったく異なる状態にあることが明らかになった。このことは，今後の臨床治療研究に重要な情報を提供したと考える。

謝辞：本研究をすすめるにあたり，材料を提供して頂き実験の補助をして頂いた佐藤由紀江博士に深く感謝致します。研究のさまざまな段階で御支援，御討論頂いた日本大学松戸歯学部第 2 解剖学教室　小澤幸重教授をはじめ教室員の方々に心より感謝致します。本研究経費の一部は，平成 13 年度日本学術振興会科学研究費補助金（基盤(C)(2)，課題番号 11671817），および平成 10 年度日本大学松戸歯学部学術フロンティア事業（文部科学省），材料研究グループ（4―②―(1)）によった。

文　　献

1) Anderson P, Elliott JC, Bose U, Jones SJ : A Comparison of the Mineral Content of Enamel and Dentine in Human Premolars and Enamel Pearls Measured by X-ray Microtomography, Arch Oral Biol, 41 : 281－290, 1996.

2) Bergman G, Anneroth G : A Semiquantitative Microradiographic Study of the Distribution of Organic Mass in Human Carious Dentine, Arch Oral Biol, 17 : 201－209, 1972.

3) Colbert C, Israel H, Garn SM : Absolute Radiographic Densities of Dentin and Enamel, J Dent Res, 45 : 1826, 1966.

4) Derise NL, Ritchey SJ : Mineral Composition of Normal Human Enamel and Dentin and the Relation of Composition to Dental Caries. II. Microminerals, J Dent Res, 53 : 853－858, 1974.

5) Dowker SE, Davis GR, Elliott JC, Wong FS : X-ray Microtomography : 3-Dimensional Imaging of Teeth for Computer-Assisted Learning, Eur J Dent Educ, 1 : 61－65, 1997.

6) Eastoe JE : Chemical Organization of the Organic Matrix of Dentin, in : Structural and Chemical Organization of Teeth (Miles AEW ed), vol. II, 279-316, Academic Press, New York, 1967.

7) Frank RM : Structural Events in the Caries Process in Enamel, Cementum and Dentin, J Dent Res, 69, Spec : 559－566, 634－636, 1990.

8) Hall AF, Buchanan CA, Millett DT, Creanor SL, Strang R, Foye RH : The Effect of Saliva on Enamel and Dentine Erosion, J Dent, 27 : 333－339, 1999.

9) Holager J : Thermogravimetric Examination of Enamel and Dentin, J Dent Res, 49 : 546－548, 1970.

10) Ingram GS : Chemical Events during Tooth Dissolution, J Dent Res, 69, Spec : 581-586 and 634－636, 1990.

11) Johansen E : Electron Microscopic and Chemical Studies of Carious Lesions with Reference to the Organic Phase of Affected Tissues, Ann NY Acad Sci, 30 : 776-785, 1965.

12) Klont B, ten Cate JM: Release of Organic Matrix Components from Bovine Incisor Roots during in vitro Lesion Formation, J Dent Res, 69: 896－900, 1990.

13) Komrska J: Derivatographic Analysis of Dentin, J Dent Res, 51: 148－151, 1972.

14) Kuboki Y, Ohgushi K, Fusayama T: Collagen Biochemistry of the Two Layers of Carious Dentin, J Dent Res, 56: 1233－1237, 1977.

15) Larmas MA, Häyrynen H, Lajunen LHJ: Thermogravimetric Studies on Sound and Carious Human Enamel and Dentin as well as Hydroxyapatite, Scand J Dent Res, 101: 185－191, 1993.

16) LeGeros RZ: Chemical and Crystallographic Events in the Caries Process, J Dent Res, 69: 567－574, 1990.

17) Levine RS: The Differential Inorganic Composition of Dentine within Active and Arrested Carious Lesions, Caries Res, 7: 245－260, 1973.

18) 林　玉海：齲蝕過程における象牙質基質の変化に関する研究，鶴見歯学，1：249－266，1989.

19) Rowles SL, Levine RS: The Inorganic Composition of Arrested Carious Dentine, Caries Res, 7: 360－367, 1973.

20) Sakae T, Mishima H, Kozawa Y: Changes in Bovine Dentin Mineral with Sodium Hypochlorite Treatment, J Dent Res, 67: 1227－1234, 1988.

21) Sakae T, Mishima H, Kozawa Y, LeGeros RZ: Thermal Stability of Mineralized and Demineralized Dentin: A Differential Scanning Calorimetric Study, Connect Tissue Res, 33: 193－196, 1995.

22) 下野正基：象牙質齲蝕；口腔の病理，南山堂，197－200，1993.

23) 須賀昭一：歯の microradiography；顕微 X 線法（須賀昭一，星野孝編），102－127，医学書院，東京，1970.

24) 谷中眞一，星野和正，寒河江登志朗：脱灰処理が象牙質有機基質特にコラーゲンへ及ぼす影響についての検討―熱重量・示差走査熱量分析法による解析―，日大口腔科学，25：457－464，1999.

25) Zuidgeest TG, Herkstroter FM, Arends J: Mineral Density and Mineral Loss after Demineralization at Various Locations in Human Root Dentine. A Longitudinal Microradiographic Study, Caries Res, 24: 159－163, 1990.

日大口腔科学　27：73～79，2001

《原　著》

ヒトのエナメル質比重分画によるアパタイト結晶中の炭酸イオン分配比率と含有水比率の推定

野崎泰夫　寒河江登志朗
日本大学松戸歯学部 第2解剖学教室
（指導：小澤　幸重教授）

キーワード：歯のエナメル質，重液分離，Aサイト，Bサイト，OHの吸収バンド

要旨：ヒトのエナメル質を比重により分画し，各分画のアパタイト結晶中でA-siteとB-siteを占める炭酸イオンの比率ならびに含有水の変化をフーリエ変換赤外吸収（FT-IR）を利用して調べた。材料はヒト第3大臼歯10本から得たエナメル質粉末をブロモホルムを主体とする重液により比重2.74から3.00まで0.02間隔で比重分画したものを用いた。炭酸イオンと含有水の水酸イオンの同定ならびに測定はKBrペレット法によるフーリエ変換赤外吸収スペクトルを用いた。アパタイト結晶中の炭酸イオンの比率はA-siteとB-siteの炭酸イオンによる吸収バンドの相対比率（A/B）として，含有水の比率はA-siteとB-siteの炭酸イオンの吸収バンドに対する相対比率（W/AおよびW/B）として求めた。観測されたA/B値，W/A値ならびにW/B値は，ともに比重2.80を境として2つの傾向を示した。比重が2.80より高い分画ではA/B値はほぼ一定の約1.2であり，W/A値およびW/B値は1.0より低い値を示した。比重が2.80以下の分画ではA/B値はほぼ一定の約1.1を示したのに対し，W/A値およびW/B値は比重が低下すると伴にそれらの値が1.0より上昇した。W/A値およびW/B値に関しては，比重が2.74より低い分画でみかけ上は比重2.76－2.78分画より低い値を得たが，これは吸収バンドのピーク値を採用した為であり，吸収バンドがブロードになっていることから実際はより多くの含有水を保持しているものと推測された。比重は組成と密接に関連していることから，比重の低い分画のエナメル質結晶は比重の高い分画よりも組成，特に炭酸イオンと水の変動が大きいことが示唆された。これらの結果は，エナメル質を構成するアパタイト結晶が決して一様な組成・構造をもつものではないこと，すなわち生体アパタイトの特徴の一つである多様な組成変動がエナメル質においても現れていることを示したものである。比重の低い分画に相当するエナメル質は組成変動が大きいことから結晶構造の乱れの大きいことが推定され，したがって，齲蝕に対して弱点となる。今後は比重の低い分画の結晶のエナメル質内での分布を検討する必要がある。

Estimation of the Site Occupancy Ratio of Carbonate Ions in the Apatite Lattice and the Water Content Ratio among the Density Fractions of Human Tooth Enamel

Yasuo Nozaki, Toshiro Sakae
Department of Anatomy
Nihon University School of Dentistry at Matsudo
Matsudo, Chiba 271-8587, Japan
(Director：Prof. Yukishige Kozawa)

〒271-8587 松戸市栄町西2-870-1（平成12年11月9日受付，平成13年1月12日受理）

日大口腔科学　27：73～79，2001

Key words: dental enamel, gravity separation, A-site, B-site, OH absorption

Abstract: Density fractions of the human tooth enamel were analyzed by means of Fourie transform infrared absorption technique to reveal the site occupancy ratios among the A-site and B-site of carbonate ions and the water content ratios. The enamel powder obtained from ten human permanent third molars was separated by a series of gravity solutions from 2.74 to 3.00 at the 0.02 intervals prepared using bromoform, tetra-bromoethane and di-iodomethane. FT-IR spectra of these density fractions were obtained using KBr method to identify and analyze carbonate ions and water molecules. The indicators were the A/B ratio, where A was the absorption due to A-site carbonate and B was due to B-site carbonate, and the W/B ratio, where W was the absorption due to the water molecules appearing at about 1650 cm-1. The A/B, W/A and W/B values showed the different tendencies before and after the intercept point at the specific gravity of 2.80. At the heavier density side above 2.80, the A/B values were around 1.2 whereas the lighter density side these values were around 1.1. Almost the all W/A and W/B values were less than 1.0 at the heavier density side above 2.80, whereas the lighter density fractions below 2.80 the W/A and W/B values increased up to 1.88 with decreasing the density. The fraction lower than 2.74 showed the broaden absorption band of water indicating the total water content being much more than the fractions heavier than this. As density relates with its component directly, the lower density fractions may contain much ionic substitutions, especially carbonate and water components, than the heavier fractions. These results indicated that abundant ionic substitutions, which were characterizing biological apatite, also occurred in tooth enamel apatite. The lower density fractions of tooth enamel having the large amount of ionic substitution may have the large amount of lattice distortions, and then these should be the weak points for caries attack. It is needed to clarify the distribution of these lower density fractions in tooth enamel.

Nihon Univ. J. Oral Sci. 27: 73 ～ 79, 2001

緒　　言

エナメル質の分析結果が不定比組成を示すことは古く1900年代初頭から知られていた[1]。しかし，組成分析で検出される多量の炭酸イオンがエナメル質をはじめとする生体アパタイトの結晶格子中にイオン置換して存在する可能性については，近代的な分析方法が発達する以前は否定的であった[2]。不定比組成の原因が，いわゆる生体アパタイトの特徴である多種多様なイオン置換にあると突き止められたのはX線回折法が導入されてからのことであった[3]。LeGeros ら[4]は，アパタイト結晶中の炭酸イオンの存在，およびそのイオン置換の場所，現在では A-site と B-site と呼ばれるそれぞれ水酸イオンの位置とリン酸イオンの位置，における炭酸イオンの置換が実際に起こりうるという先駆的な研究を行った。

その後，生体アパタイトの中でも特に結晶性の高いエナメル質で結晶中の炭酸イオン置換が A-site か B-site のどちらに生じるか，あるいは同時に両者に生じているのか，について多数の研究者によって X 線回折法，フーリエ変換赤外吸収（FT-IR）法，NMR（核磁気共鳴）法などの近代的分析法を用いた研究が行われた[5]。その結果，エナメル質をはじめ生体アパタイト結晶では両者において炭酸イオン置換が生じていることが確かめられた[6]。

Holcomb ら[7]は比重 2.94 以上のエナメル質アパタイト結晶中の炭酸イオンが加熱により脱却される過程を追求し，炭酸イオンは加熱による脱却過程で A-site と B-site の間を移動すると結論づけた。Elliott ら[8]は 1545 cm^{-1}, 1450 cm^{-1}, 880 cm^{-1} に特徴づけられる A-site の炭酸イオ

ンに注目し，比重2.94以上のヒトエナメル質アパタイト結晶中におけるA-siteでリン酸イオンに対する置換の割合が約11%あると報告した。しかし，LeGeros[9]は特に1415 cm^{-1}で特徴づけられるB-siteにおける炭酸イオン置換が，その量的な割合からも生体アパタイトを特徴づけるものであると述べている。Reyら[10]も炭酸イオンのほとんどはB-siteにあると述べている。一方で，Sonju Clasenら[11]は，エナメル質中の炭酸イオンのA-siteとB-siteへの割合を乳歯と永久歯で比較した。その結果は，炭酸イオンの量としては乳歯エナメル質のほうが多く含まれ，乳歯エナメル質ではA-siteの炭酸イオンが顕著に多いと報告している。このように生体アパタイト結晶中の炭酸イオンの存在場所，分配については未だに検討の余地が残されている。

Weatherellら[12]，Sakae[13]，ならびにLeGerosら[14]は，エナメル質結晶の組成がエナメル質内で決して一様ではなく，部位的な違いあるいは層別の違いを示すことを明らかにしている。また，赤石ら[15]およびSakaeら[16]は，エナメル質を比重分画して熱分析法あるいはX線回折法によって詳細に検討した結果，それぞれの比重分画は結晶学的な性質に一部違いが認められることを明らかにした。

これらの結果は，エナメル質の結晶が一定不変ではないことを示している。したがって，生体アパタイトを特徴づける炭酸イオンの分配についても，その変動に興味がもたれる。そこで，本研究では，エナメル質の比重分画を用いてフーリエ変換赤外吸収法による分析を行い，その結果，エナメル質結晶の炭酸イオン置換について新しい知見を得たので報告する。

材料と方法

実験材料：

試料は，Sakaeら[16]で述べられた方法により比重分画されたエナメル質粉末試料である。当教室に保存されていた萌出後の齲蝕のない上下顎第3大臼歯から，歯科用エンジンを用いエナメル質部分を水中で削り取り，メンブレンフィルター（45 μm）で漉しとった。この方法で抜去歯10本を用いてエナメル質切削片を回収し，蒸留水にて洗浄後，空気中で乾燥し，めのう乳鉢で粉末とした。10本から得たエナメル質粉末を合し，200 mesh篩を通過したものをエナメル質粉末試料とした。

エナメル質粉末試料は，di-iodomethane(Kanto Chemicals Co. Ltd., S.G. 3.325)，tetra-bromoethane(Kanto Chemicals Co. Ltd., S.G. 2.964)，bromoform (4-0212, Sigma Co. Ltd., S.G. 2.89) を混合し，エチルアルコールで調整した重液により，比重2.74から3.00まで0.02間隔で比重分画に分けた。調整した重液の比重はガラス瓶型浮遊比重計により確かめた。回収した比重分画はエチルアルコールで洗浄後，空気中で乾燥した。これ以降それぞれの比重分画をその中間値を用いて，例えば比重2.98-3.00の分画は比重2.99分画のように，呼ぶことにする。なお，比重3.00以上の分画は＞3.00分画，また，比重2.74以下の分画は＜2.74分画と呼ぶ。

フーリエ変換赤外吸収実験：

比重分画されたエナメル質粉末試料は，ホリバ製FT-210フーリエ変換赤外吸収光度計を用い，KBrペレット法によるフーリエ変換赤外吸収データ収集と解析がなされた。実験条件は次の通りである：scan range：4000-400 cm^{-1}, resolution：2 cm^{-1}, scan：30 times, gain：4, function：H-G, 対照補正：ホリバ sample shuttle 方式。データ収集後，ノイズ除去の目的でフーリエ変換赤外吸収パターンをスムージング処理した。比重2.74-2.76の分画については，試料量が試料全体の2%以下と極端に少なくそのためノイズの多いフーリエ変換赤外吸収パターンのため，今回はデータとして採用しなかった。

炭酸イオンのA-siteとB-siteを占有する比率（A/B）と含有水比率（W/AおよびW/B）の測定：

アパタイト結晶構造中の炭酸イオンがA-siteとB-siteを占める比率は，フーリエ変換赤外吸収スペクトルでそれぞれ1450 cm^{-1}ならびに1415 cm^{-1}に出現する吸収バンドを用いた。含有水比率は1650 cm^{-1}に出現する水酸イオンの振動吸収バンドを用いた。近傍における最適化ベースラインを引いた後，それぞれの吸収バンドの強度を相対強度として読み取り，それらの比をA/B値，W/A値およびW/B値とした。

結　果

Fig.1に今回の実験の代表的な3つのフーリエ変換赤外吸収パターンとして，エナメル質比重分画＞3.00，2.81および＜2.74のフーリエ変換赤外吸収スペクトルを示した。今回実験したエナメル質分画のフーリエ変換赤外吸収スペクトルは基本的にすべて同じ吸収パターンを示し

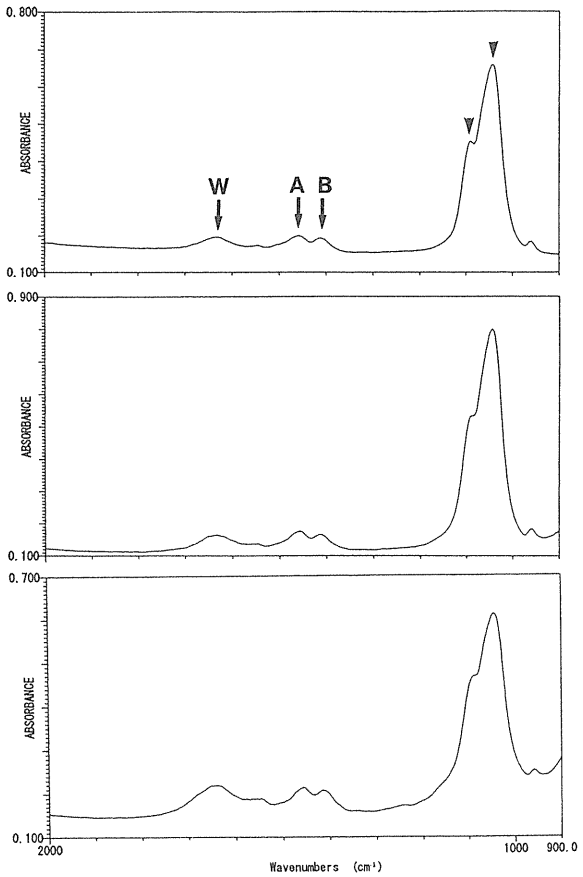

Fig. 1　Fourier transform infra-red (FT-IR) absorption spectrum for the human enamel density fractions of ＞ 3.00 (Top), 2.81 (Middle) and ＜ 2.74 (Bottom). A: A-site carbonate absorption. B: B-site cabonate absorption. W: O-H absorption. Arrow heads: P-O absorption.

ており，生体アパタイトのリン酸イオンによる吸収バンドが 1000-1100 cm^{-1}に強い吸収として現れ，A-site および B-siteの炭酸イオンによる吸収バンドがそれぞれ約 1450 cm^{-1}および 1415 cm^{-1}に弱い吸収として出現した。また，これらの炭酸イオンによる吸収のほかに 1650 cm^{-1}付近に含有水による水酸イオンの吸収バンドが弱い吸収として出現した。

各エナメル質比重分画の炭酸イオンおよび含有水による吸収バンド出現領域のフーリエ変換赤外吸収スペクトルを Fig. 2 に示した。これらのスペクトルの比較から，約 1450 cm^{-1}の A-site および約 1415 cm^{-1}の B-site のそれぞれの炭酸イオンによる吸収バンドの強さは，比重 2.80 を境として相対強度が異なることが読み取れた。また，約 1650 cm^{-1}の含有水による水酸イオンの吸収バンドの強さも同じように比重 2.80 を境として変化していることが読み取れた。

Table 1 に約 1450 cm^{-1}の A-site および約 1415 cm^{-1}の B-siteのそれぞれの炭酸イオンによる吸収バンドの強さの比 A/B 値，および約 1650 cm^{-1}の含有水による水酸イオンの吸収バンドの強さと約 1450 cm^{-1}の A-site および約 1415 cm^{-1}の B-siteの炭酸イオンによる吸収バンドの強さの比，W/A 値および W/B 値，を示した。Fig. 3に A/B 値，W/A 値および W/B 値をプロットしたグラフを示した。

Fig. 3 のグラフから明らかなように，A/B 値は比重 2.80 より比重の高い分画では 1.18 から 1.27 の間の値であり平均で約 1.2 を示したが，比重 2.80 より低い分画では 1.10 から 1.13 の間の値で，約 1.1 であった。

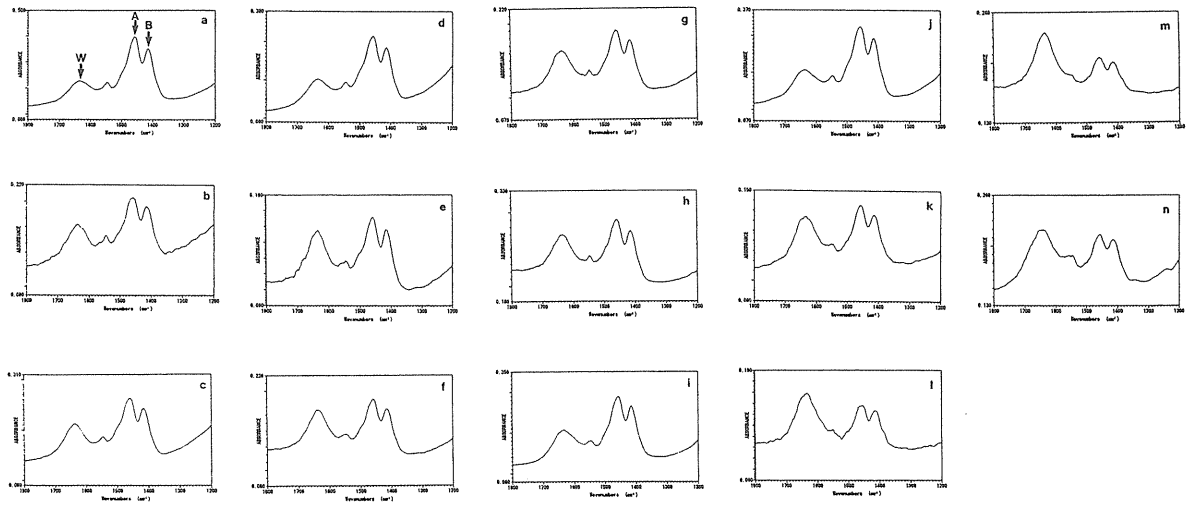

Fig. 2　FT-IR spectra of the 1200 to 1800 cm^{-1} region for the density fractions of a) ＞ 3.00, b) 2.99, c)2.97, d) 2.95, e) 2.93, f) 2.91, g) 2.89, h) 2.87, i) 2.85, j) 2.83, k) 2.81, l) 2.79, m) 2.77, n) ＜ 2.74. A: A-site carbonate absorption. B: B-site cabonate absorption. W: O-H absorption.

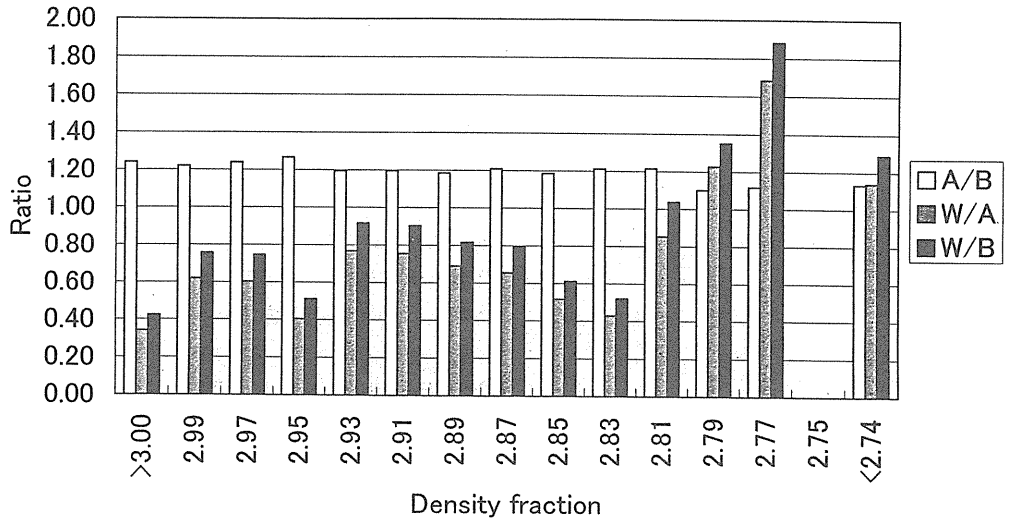

Fig. 3 Plots of the A/B, W/A and W/B values for the human density fractions. Fraction 2.75 was not determined.

Table 1 FT-IR data for the density fractions of the human tooth enamel.

Density Fraction	Density Range	Absorbance W (OH^-) 1650 cm^{-1}	Absorbance A ($A\text{-}CO_3^{2-}$) 1450 cm^{-1}	Absorbance B ($B\text{-}CO_3^{2-}$) 1415 cm^{-1}	Ratio W/A	Ratio W/B	Ratio A/B
> 3.00	> 3.00	30	88	71	0.34	0.42	1.24
2.99	2.98 − 3.00	31	50	41	0.62	0.76	1.22
2.97	2.96 − 2.98	50	83	67	0.60	0.75	1.24
2.95	2.94 − 2.96	25	62	49	0.40	0.51	1.27
2.93	2.92 − 2.94	33	43	36	0.77	0.92	1.19
2.91	2.90 − 2.92	37	49	41	0.76	0.90	1.20
2.89	2.88 − 2.90	40	58	49	0.69	0.82	1.18
2.87	2.86 − 2.88	38	58	48	0.66	0.79	1.21
2.85	2.84 − 2.86	33	64	54	0.52	0.61	1.19
2.83	2.82 − 2.84	27	63	52	0.43	0.52	1.21
2.81	2.80 − 2.82	29	34	28	0.85	1.04	1.21
2.79	2.78 − 2.80	27	22	20	1.23	1.35	1.10
2.77	2.76 − 2.78	64	38	34	1.68	1.88	1.12
2.75	2.74 − 2.76	n.d.	n.d.	n.d.	n.d.	n.d.	n.d.
< 2.74	< 2.74	49B	43	38	1.14	1.29	1.13

n.d.: not determined. B: Broaden band.

W/A 値および W/B 値については比重 2.80 を境としてそれより高い比重分画と低い比重分画で異なった傾向を示した。比重が 2.80 より高い分画では，W/A 値は 0.34 から 0.85 の値を示した。W/B 値は同じ比重分画範囲で 0.42 から 1.04 の値であった。W/A 値および W/B 値はともに比重が 2.80 より低い分画で 1.0 より大きな値を取るようになり，比重分画 2.77 ではそれぞれ 1.68 および 1.88 であった。もっとも低い分画＜ 2.74 の W/A 値および W/B 値は比重分画 2.77 より小さい値となった。しかし，Fig. 2 に示した比重分画＜ 2.74 のフーリエ変換赤外吸収スペクトルから，比重分画＜ 2.74 では水酸イオンの吸収バンドがほかの分画の場合よりも幅広く広がっている様子が読み取れた。

考　　察

エナメル質の比重に関しては，Manly ら[17]の報告に始

まり，Berghash ら[18]，Stack[19]，Coklica ら[20]，Weatherell ら[21]，Brudevold ら[22]，赤石ら[15]，Sakae ら[16]らが研究を行ってきている。それらの研究の結果，エナメル質結晶の比重は2.74以下から3.00以上までの幅広い分布をしていることが明らかである。しかし，エナメル質結晶の比重がなぜこのように幅広い分布を示すかという問題については，未だに解明されていない。

Elliott[23]はエナメル質の理想的な比重として3.0 g cm^{-3}を想定して，エナメル質における結晶の占有体積を見積もっているが，この比重値の仮定が妥当でないことは，今回の研究のみならず従来の比重分析の結果からも明らかである。

比重の低い方の分画には有機質が多いという予測がなされるが，実際にエナメル質比重分画を TG-DTA（熱重量－示差熱分析）法で解析した実験結果は，比重 2.84 から 2.98 までの範囲で有機質量の差が認められなかった(赤石ら[15])。今回と同じ手順で比重分画されたエナメル質の X 線結晶学的性質について Sakae ら[16]は結晶性の変化が認められると報告した。したがって，分画の示す比重値は無機質に起因していることがほぼ確かである。本研究では，エナメル質結晶の比重は組成と密接な関連があると考えられるので，フーリエ変換赤外吸収スペクトルによる組成分析を行った。

エナメル質の比重分画試料のフーリエ変換赤外吸収スペクトルから求めた A-site および B-site の炭酸イオンによる吸収バンドの強さの比 A/B 値は，比重 2.80 より比重の高い分画ではほぼ一定の値，約 1.2，を示したが，比重 2.80 より低い分画ではより低い値の約 1.1 であった。すなわち，エナメル質結晶中の炭酸イオンの A-site および B-site への分配比率は比重階級によって一定ではないことが明らかとなった。

A/B 値は定量的な分析値ではないが，エナメル質の比重分画の大部分にわたって 1.2程度の低い値であり，さらに比重が 2.80 より低い比重分画においては約 1.1 であった。この結果は，エナメル質結晶中の炭酸イオンの分配について Elliott ら[8]が報告した比重2.94以上のヒトエナメル質アパタイト結晶中における A-site でリン酸イオンに対する置換の割合が約 11 %あるという結果，ならびに，Sonju Clasen ら[11]の乳歯エナメル質では A-site の炭酸イオンが顕著に多いという報告，について再検討の必要性を示唆している。

一方で，今回の A/B 値の結果は，LeGeros [9]の報告のように B-site における炭酸イオン置換がその量的な割合からも生体アパタイトを特徴づけるものであるという主張，ならびに，Rey ら[10]のブタのエナメル質では炭酸イオンのほとんどは B-site にあるという報告と一致している。

今回の研究で，エナメル質結晶には比重分布があり，比重の高低によって結晶の組成が異なる可能性を指摘した。組成の変化は結晶構造に乱れなどを生じる原因となり，そのため比重と組成・構造との密接な関連が示唆された。したがって，今回の研究結果は比重 2.94 以上に限定して実験を行った Holcomb ら[7]の炭酸イオンの加熱による分配比率の変化，ならびに，同様に比重 2.94 以上に限定して実験を行った Elliott ら[8]のヒトエナメル質アパタイト結晶中における A-site の炭酸イオンの割合が約 11 %あるという結果がエナメル質全体を代表するものではないことを示した。

エナメル質の比重分画の含有水の比率を表す W/A 値および W/B 値は，比重 2.80 を境にして，比重が高い分画と比較して比重が低い分画で含有水比率が高くなる傾向を示した。比重分画＜ 2.74 のフーリエ変換赤外吸収スペクトルから，比重分画＜ 2.74 では水酸イオンの吸収バンドがほかの分画の場合よりも幅広く広がっている様子が読み取れた。したがって，比重分画＜ 2.74 における含有水は量的には減少しているのではなく，かえって増加していると推定できる。含有水の性質は今回の実験では明らかにできないが，想定される種類として結晶表面の“吸着水”，結晶表面でゆるく結合した“表面結合水”，構造の一部に組み込まれしかも脱着が容易に生じる“沸石水”(LeGeros ら[24])，あるいはエナメル質に固有の有機質に結合する水，などが候補にあげられる。赤石ら[15]は，ヒトの第 3 大臼歯エナメル質で比重が低い分画に有機質が多いこと，および水分量も多いことを報告している。今回のフーリエ変換赤外吸収スペクトルによる方法で得た含有水比率の結果は同じ傾向を示した。

吸着水および表面結合水の量は粒子の表面積と結晶の性質に相関する。今回のエナメル質粉末は 200 mesh 篩を通過したものを用い，これが最大粒径を規制しているが，試料の粒度分布については検討していない。今後は粒径および有機質との関連を考慮に入れた含有水分析を行う予定である。

結　　論

ヒトのエナメル質を比重により分画して，アパタイト

結晶中の A-site および B-site の炭酸イオンの比率，A/B 値，ならびに含有水の比率 W/A 値および W/B 値，をフーリエ変換赤外吸収スペクトルで検討した。その結果，比重 2.80 を境として A/B 値の傾向に違いが認められ，比重が 2.80 より高い分画では A/B 値は約 1.2 であるが，低い分画では約 1.1 であった。W/A 値および W/B 値についても比重 2.80 を境として 2 つに分かれる傾向が認められた。これらの結果は，エナメル質を構成するアパタイト結晶が決して一様な組成・構造をもつものでないこと，すなわち生体アパタイトの特徴の一つである多様な組成変動がエナメル質においても現れていることを示したものである。比重の低い分画に相当するエナメル質の組成変動が大きいことから，結晶構造の乱れの大きいことが推定された。したがって齲蝕に対して弱点となるため，比重の低い値をもつ結晶のエナメル質内での分布を検討する必要がある。

謝辞：本研究を進めるにあたり当教室小澤幸重教授をはじめ教室員の方々に様々な段階でご支援・ご協力を頂いたことをここに記して感謝致します。本研究の経費の一部は日本学術振興会科学研究費助成金：基盤(C)（2)「アモルファスリン酸カルシウム－コラーゲン複合体の生体親和性と結晶化学的性質」（寒河江)，日本大学原子力研究所電子線利用研究施設学術フロンティア推進事業（文部省）「可変長高輝度単色光源の高度利用に関する研究」（研究分担寒河江）による。

文　献

1) McConnell D：Apatite, 22 － 32, Springer-Verlag, Wien, 1973.

2) Sakae T, Suzuki K, Kozawa Y：A Short Review of Studies on Chemical and Physical Properties of Enamel Crystallites ; *in* Tooth Enamel Microstructure (v. Koenigswald W, Sander PM eds), A.A. Balkema, Rotterdam, 31 － 40, 1997.

3) McConnell D：Apatite, 68 － 80, Springer-Verlag, Wien, 1973.

4) LeGeros RZ, LeGeros JP, Trautz OR, Klein E：Spectral Properties of Carbonate in Carbonate-containing Apatites, Dev Appl Spec, 7：139 － 142, 1965.

5) Young RA：Implications of Atomic Substitutions and Other Structural Details in Apatite, J Dent Res, 53：193 － 203, 1974.

6) LeGeros RZ, Trautz OR, Klein E, LeGeros JP：Two Types of Carbonate Substitution in the Apatite Structure, Experientia, 25：5 － 7, 1969.

7) Holcomb DW, Young RA：Thermal Decomposition of Human Tooth Enamel, Calcif Tisuue Int, 31：189—201, 1980.

8) Elliott JC, Holcomb DW, Young RA：Infrared Determination of the Degree of Substitution of Hydroxyl by Carbonate Ions in Human Denatl Enamel, Calcif Tissue Int, 37：372 － 375, 1985.

9) LeGeros RZ：Calcium Phosphates in Oral Biology and Medicine, 108 － 129, Karger, Basel, 1991.

10) Rey C, Renugopalakrishnan V, Shimizu M, Collins B, Glimcher MJ：A Resolution-enhanced Fourier Transform Infrared Spectroscopic Study of the Environment of the CO_3^{2-} Ion in the Mineral Phase of Enamel during Its Formation and Maturation, Calcif Tissue Int, 49：259 － 268, 1991.

11) Sønju Clasen AB, Ruyter IE：Quantitative Determination of Type A and Type B Carbonate in Human Deciduous and Permanent Enamel by Means of Fourier Transform Infrared Spectroscopy, Adv Dent Res, 11：523 － 527, 1997.

12) Weatherell JA, Robinson C, Hallsworth AS：Variations in the Chemical Composition of Human Enamel, J Dent Res, 53：180 － 192, 1974.

13) Sakae T：X-ray Diffraction and Thermal Studies of Crystals from the Outer and Inner Layers of Human Dental Enamel, Arch Oral Biol, 33：707 － 713, 1988.

14) LeGeros RZ, Sakae T, Bautista C, Ritino M, LeGeros JP：Magnesium and Carbonate in Enamel and Synthetic Apatites, Adv Dent Res, 10：225 － 231, 1996.

15) 赤石茂，寒河江登志朗：歯のエナメル質粉末の比重構成，日大口腔科学，14：147 － 162，1988.

16) Sakae T, Hirai G, LeGeros RZ：Specific Gravity Distribution of Powdered Human Enamel and Its Characterization ; *in* Tooth Enamel V (Fearnhead RW ed), 403 － 409, Florence Pub, Tokyo, 1989.

17) Manly RS, Hodge HC, Ange LE：Density and Refractive Index Studies of Dental Hard Tissues. II. Density Distribution Curves, J Dent Res, 18：203 － 211, 1939.

18) Berghash SR, Hodge HC：Density and Refractive Index Studies of Denatl Hard Tisuues. III. Density Distribution of Decidous Enamel and Dentin, J Dent Res, 19：487 － 495, 1940.

19) Stack MV：Mineral and Protein Levels in Enamel from Human, Monkey, and Rat Molars, Odont Rev, 8：89 － 93, 1957.

20) Coklica V, Brudevold F：Density Fractions in Human Enamel, Arch Oral Biol, 11：1261 － 1268, 1966.

21) Weatherell JA, Widmann SM, Hamm SM：Sampling of Enamel Particles by Means of Strong Acids for Density Measurements, Arch Oral Biol, 11：107 － 111, 1966.

22) Brudevold F, Bakhos Y, Srinivasan BN：Separation of Human Enamel Structures by Density Fractionation, Arch Oral Biol, 21：113 － 119, 1976.

23) Elliott JC：Structure, Crystal Chemistry and Density of Enamel Apatites, Ciba Found Symp, 205：54 － 72, 1997.

24) LeGeros RZ, Bonel G, Legros R：Types of "H_2O" in Human Enamel and in Precipitated Apatites, Calcif Tissue Res, 26：111 － 118, 1978.

日大口腔科学　27：80～84，2001

《原　著》

動脈硬化症にみられた興味ある結晶構造物に関する一知見

松村　恵美子　宇都宮　忠彦*　寒河江　登志朗**
R.Z. LeGeros***　山本　浩嗣*
日本大学大学院松戸歯学研究科　口腔病理学専攻
*日本大学松戸歯学部　病理学教室　**第2解剖学教室
***ニューヨーク大学歯学部　リン酸カルシウム研究所

キーワード：動脈硬化症，結晶構造，病理組織学，生体鉱物学

要旨：動脈硬化症は病理組織学的に脂質沈着を伴って，粥腫形成，潰瘍および石灰化からなる，主に内膜性硬化として出現する。動脈硬化症の発生機序に関しては，これまで比較的多彩な研究が報告されているが，その石灰化に継発する結晶体はいまだ十分な検索がなされているとはいえない。今回我々は病理解剖検体に得られた動脈硬化症における結晶構造物を病理組織学的および生体鉱物学的に検討した。

病理解剖学的に自験例の主病変は肺蛋白症，副病変が両側気管支肺炎，日本住血吸虫症，カタール性胃・腸炎であった。病理組織学的に，動脈の内膜は線維性に肥厚し，空胞状の脂質沈着やコレステリン裂隙からなる粥腫形成がみられ，その一部にヘマトキシリンに染まる顆粒状ないし塊状，びまん性の石灰沈着が観察された。偏光顕微鏡にて，粥腫内およびその周囲の内膜において光輝性の針状結晶を束ねた高い複屈折性を示す黄色～青色調の結晶構造物が散在性に認められ，ロゼット状，扇状，松葉状あるいはそれらが互いに連結したような形態を示した。またこれら結晶構造物はvon Kossa染色で陰性を示す部と，黒褐色に染色された部が混在していた。顕微FT-IR解析および走査型電子顕微鏡的観察結果において，これら結晶構造物はリン酸カルシウムあるいはシュウ酸カルシウム結晶と考えられた。

以上の結果から，本結晶構造物は異種の結晶が混在する可能性を有し，寄生虫感染あるいは消化管疾患を背景とした成因が推察された。

A Study of Characteristic Crystal in Arteriosclerosis

Emiko Matsumura, Tadahiko Utsunomiya*, Toshiro Sakae**,
R.Z. LeGeros***, Hirotsugu Yamamoto*
Nihon University Graduate School of Dentistry at Matsudo, Oral Pathology
Departments of *Pathology and **Anatomy, Nihon University
School of Dentistry at Matsudo, ***New York University College of
Dentistry Calcium Phosphate Research Laboratory
Matsudo, Chiba 271-8587, Japan

Key words: arteriosclerosis, crystal, histopathology, biomineralogy

〒271-8587 松戸市栄町西2-870-1（平成12年11月10日受付，平成13年2月9日受理）

Abstract: Arteriosclerosis, which consisted of lipid pigmentation, atheroma, and calcification, is mainly occurred in the tunica intima. Although many studies concerning about pathogenesis of the lesion have been reported, the study of crystal formation has not been done, extensively and conclusively, as yet. The purpose of the study was to investigate the morphological feature of the crystal in the arteriosclerosis from histopathological and biomineralogical viewpoints, and following results were obtained:

1. From the results of autopsy, pulmonary proteinosis was indicated as chief findings, whereas bronchopneumonia of the both lungs, schistosomiasis, catarrhal gastritis and enteritis were observed as accessory findings.
2. Histopathologically, the arteriosclerosis was composed of fibrous hypertrophy of the tunica intima with formation of atheroma, ulcer and calcification.
3. From the findings using a polarization microscopy, several pieces of crystal structure, which showed with high birefringence, were scattered in the area of arteriosclerosis. The morphological features indicated a bundle, rosette, or fused appearance of the crystals. In addition, the crystals were negative or dyed black with von Kossa staining.
4. From the analysis using Fourier transform infrared spectroscopy and scanning electron microscopy, the component of the crystal was thought to be calcium phosphate and/or calcium oxalate.

In conclusion, the results suggest that the both crystals, which are consisted of calcium phosphate or calcium oxalate, are co-localized in the arteriosclerosis. Furthermore, the pathogenesis may have a relationship of oxalosis due to infection of major parasite or intestinal disorders.

Nihon Univ. J. Oral Sci. 27 : 80 ～ 84, 2001

緒　　言

動脈硬化症は病理学的に脂質沈着を基礎として，粥腫形成，潰瘍および石灰化を伴い，主に内膜性硬化（粥状硬化）として出現し，形態学的あるいは分子生物学的手法を用いて比較的多彩な研究がなされている[1)]。しかし，動脈硬化症と継発する結晶については余り検索されておらず，その詳細が明確にされているとはいえない。

今回我々は動脈硬化症においてやや特異な結晶様構造物を見出し，その形態学的特徴や組成を生体鉱物学的な見地から検索して若干の興味ある知見を得たので報告する。

材料および方法

材料は80歳の男性で，主病変が肺蛋白症，副病変が，両側気管支肺炎，日本住血吸虫症，カタール性胃・腸炎の，病理解剖症例にて採取された10％ホルマリン液中にて浸漬固定中の肉眼的に粥腫形成や潰瘍，石灰化を呈する腹部大動脈を用いた。

光学顕微鏡および偏光顕微鏡的観察用には，切り出した検体を通法に従ってパラフィン包埋ブロックを作成した。必要に応じて厚さ約4 μm に切片標本を薄切製作し，更にヘマトキシリン・エオジン重染色(H・E)，von Kossa染色を施行した。

顕微フーリエ変換赤外分光分析(顕微FT-IR解析)法(ホリバ社製，FT530）を行うにあたって，検体試料の調整は，顕微鏡観察に用いた切片標本の一部をFT-IR用ステンレス製（2センチ四方）のプレートに薄切切片を載せ，乾燥後，脱パラフィンを施行した。測定法は，はじめに，試料の結晶部以外の組織部をバックグラウンドとし，FT-530に付属の顕微鏡により任意の部位，分析領域で試料のスペクトルを検出した（測定条件分解能；4 cm^{-1}，スキャン回数；30回，検出器；MCT)。

走査型電子顕微鏡（SEM）的観察については，光学顕微鏡に用いた切片標本の一部をのせ乾燥した後，通法に従い脱パラフィンし，カーボン蒸着を行った（TB-500, Emscope, England)。走査型電子顕微鏡（JSM-200，日本電子）を用い，加圧電子25 kvにて2次電子像を観察した。

結　　果

1．光学顕微鏡および偏光顕微鏡的所見

自験例の病理組織像における動脈の内膜は線維性に肥厚し，内膜表層から中膜との境界部にかけて，空胞状の脂質沈着やコレステリン裂隙からなる高度の粥腫形成がみられた（Fig. 1）。その一部にヘマトキシリンに濃染し，von Kossa染色にて黒褐色に染まる顆粒状塊状，びまん性の石灰沈着が認められた（Figs. 1, 2）。偏光顕微鏡を用いた観察では，これらの粥腫内およびその周囲の内膜に光輝性の針状結晶を束ねたような，いわゆる多針状で，黄色～青色調の多色性を示す，高い複屈折性結晶構造が散在していた。結晶の形態は，ロゼット状，扇状，松葉状または，それらが互いに連結しているような状態を呈し，大きさが大小様々であった（Fig. 3）。

2．顕微 FT-IR 解析

スペクトルは，1640，1540，1250 cm^{-1}付近でのピークがみられた。これは主にアミドⅠ（1650，1550 cm^{-1}）に指定された。現在この他に，1500～1000 cm^{-1}領域にいくつかの吸収バンドがみられた（Fig. 4）。

3．SEM 所見

EDSの分析ポイントをFig. 5に示す。表面性状が粗顆粒状～球状にみられる結晶であった。定性解析を行った結果，カルシウム（以下 Ca）が検出された。

考　　察

自験例における動脈硬化症の光学顕微鏡による病理組織像は内膜～中膜付近にかけて脂質沈着，コレステリン裂隙，浮腫，潰瘍形成や石灰化を随所に伴った粥腫形成しており，他の報告とほぼ同様の所見が得られた[2]。更に自験例では偏光顕微鏡的観察において，粥腫内，とくに中膜内に多針状色調は黄色～青色の高い複屈折性を呈する光輝性結晶がみられた。これらの結晶構造物は脱パラフィン過程においてアルコール処理を行って消失しない結晶即ち，非脂質系のものと推察された[3,4]。また，von Kossa法で石灰化物の多くの部は陰性であり，リン酸基を含有していないが，一部で陽性の部分があり，リン酸基を含有する部も混在していると考えられる[5]。

顕微 FT-IR 解析の吸収スペクトルから，シュウ酸 Ca，リン酸 Ca，炭酸 Ca の存在が考えられるが[6]，赤外吸収のみでは特定できなかった。一方 SEM では，表面性状が凹凸な球状の構造物が観察され，定性解析においてはCaを検出したが，リンの検出はみられなかった。

以上の所見を総括すると，多針状の結晶構造物はReyesら[7]が結核時の肺において，また，原ら[8]が肺アスペルギルスにおいて報告したシュウ酸Ca結晶と構造が類似しており，且つ，von Kossa染色では陰性を呈したことから，シュウ酸 Ca と考えたい。しかし，von Kossa 染色陽性部も存在するので，リン酸 Ca 結晶の存在も否定できず，前述の結晶と混在しているものと推察される。自験例の動脈硬化症と同様に，尿管でみられる Ca 結石は，シュウ酸 Ca と，リン酸 Ca の混合結石として検出される。最近の研究では，動脈硬化の石灰化は尿路結石の発生機序との類似性も指摘され[9,10]，その有機成分としては，オステオポンチンとカルルプロテクチンが挙げられており[11]，マクロファージが関与して形成するとの報告もある[12]。なお，シュウ酸は異常なアミノ酸代謝，殊に特殊な結合組織，グリシンあるいは食物中の 'かぶ' や 'ほうれんそう' 等に由来するといわれている[13]。

また，シュウ酸結晶は水分を含有する不安定な weddelite と水分を含有しない安定した whewellite とに分類され[14]，動脈硬化症においてはリン酸Ca結晶を検出した報告があるが，シュウ酸 Ca 結晶の報告は比較的少ない[15]。しかし，自験例の如く動脈や，その他，心，脳，骨，甲状腺，精巣，前立腺，肝，骨格筋，唾液腺等において腎不全やシュウ酸症に随伴して出現したとする報告もある[16,17]。生体内では異常なアミノ酸代謝により，シュウ酸症それに継発するシュウ酸尿症を引き起こすが，それは①原因不明の原発性のものと②糖尿病，腎不全，肝硬変，心不全，サルコイドーシス，寄生虫疾患および，小腸疾患に随伴する２次性のものとがある[18]。自験例は，日本住血吸虫症とカタール性腸炎があり，それら疾患に基づいて，シュウ酸症を惹起していた可能性が高く，そのことが，シュウ酸結晶様構造物の生成に何らかの関与をしていたと考えられる。

今後，動脈硬化のメカニズムの解明に寄与できるよう検索を重ねて結晶の特定を行っていく予定である。

結　　論

病理解剖検体にみられた動脈硬化症における結晶構造物を病理組織学的および生体鉱物学的に検討し，以下の結論を得た。

1

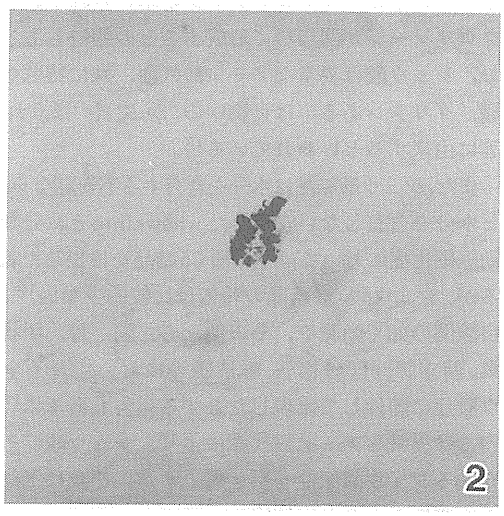
2

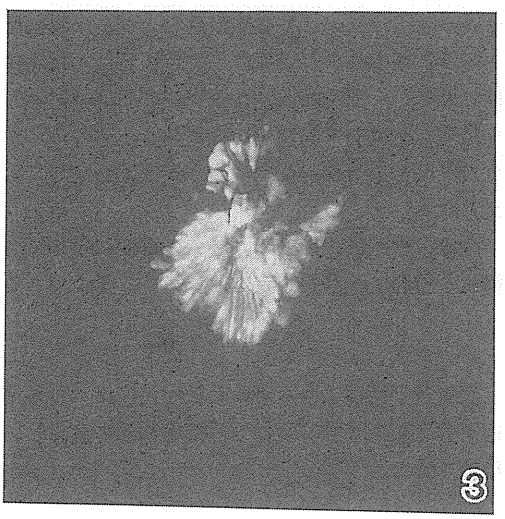
3

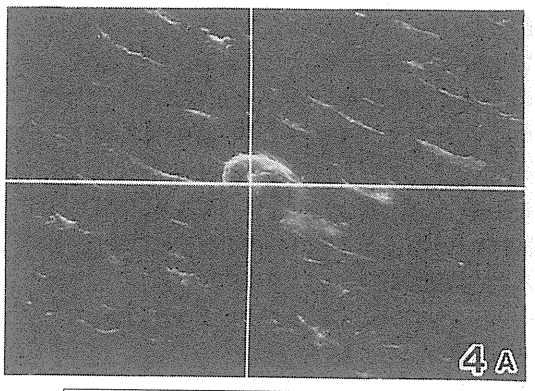
4A

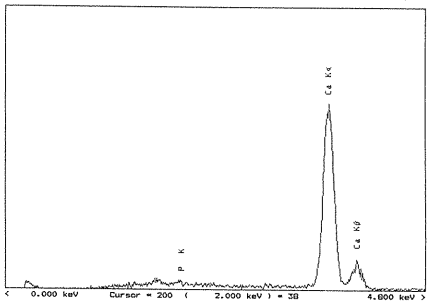
Ca Kα
Ca Kβ
P K
0.000 keV
Cursor = 200 (2.000 keV) = 38
4.000 keV

4B

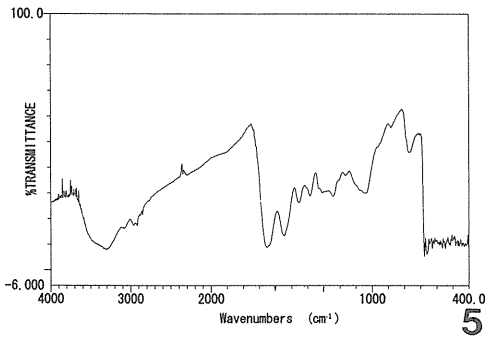
100.0
%TRANSMITTANCE
-6.000
4000
3000
2000
1000
400.0
Wavenumbers (cm-1)

5

1. 理解剖学的に自験例の主病変は肺蛋白症，副病変が両側気管支肺炎，日本住血吸虫症，カタール性胃・腸炎であった。

2. 病理組織学的に，動脈の内膜は線維性に肥厚し，空胞状の脂質沈着やコレステリン裂隙からなる粥腫形成がみられ，その一部にヘマトキシリンに染まる顆粒状ないし塊状，びまん性の石灰沈着が観察された。

3. 偏光顕微鏡にて，粥腫内およびその周囲の内膜において光輝性の針状結晶を束ねた高い複屈折性を示す黄色～青色調の結晶構造物が散在性に認められ，ロゼット状，扇状，松葉状あるいはそれらが互いに連結したような形態を示した。またこれら結晶構造物はvon Kossa染色で陰性を示す部と黒褐色に染色された部が混在していた。

4. 顕微FT-IR解析および走査型電子顕微鏡的観察結果において，これら結晶構造物はリン酸Caあるいはシュウ酸Ca結晶と考えられた。

以上の結果から，本結晶構造物は異種の結晶が混在する可能性を有し，寄生虫感染あるいは消化管疾患を背景とした成因が推察された。

謝辞：本研究遂行にあたり，貴重な病理解剖検体を供与いただきました愛知県県立病院臨床検査部　鈴木春実博士に深謝いたします。また，標本作製にあたり多大なアドバイスをいただいた松本敬技師（本学付属歯科病院検査科）に感謝致します。

尚本研究は科学研究費補助金（基盤研究(c)(2)課題番号10671718，奨励研究(A)課題番号1177124）及び学術フロンティア推進事業により実施された。

文　献

1) 都島基夫：カルシウムと動脈硬化研究　最近の進歩－石灰化の成因と臨床意義，Clin Cal, 10:144－148, 2000.

2) 柿内裕明，生沼利倫，山田　勉：高齢者剖検例における動脈硬化退縮の検討(2)潰瘍性病変と中心に陥没を有する動脈硬化性病変との関連，日老医誌，32:503－510, 2000.

3) 飯島宗一監修：組織病理アトラス，第4版，xvi-xvii，文光堂，東京，1999.

4) Kato Atsuhiko *et al.*：イヌ大動脈口の石灰化病変の組織病理学的特徴，J Toxicol Pathol, 12, 53—58, 1999.

5) 小川浩美：組織内無機物の染色，Medical Technology 別冊　染色法のすべて，医歯薬出版，東京，94－95，1992.

6) 錦田晃一，西尾悦雄：チャートで見るFT-IR，講談社サイエンティフィック，東京，150－151, 1993.

7) Reyes CV, Kathuria S, MacGlashan A：Diagnostic Value of Calcium Oxalate Crystals in Respiratory and Pleural Fluid Cytology, A Case Report, Acta Cytol, 23:65－68, 1979.

8) 原　喜与一，吉岡高広，桂　栄孝，里中和廣：気管支擦過細胞診標本中の蓚酸カルシウム結晶が真菌発見の契機となった肺アスペルギルス症の1例，日臨細胞誌，38:431－435, 1999.

9) 瀬山義幸：血管壁石灰化の機序，Clin Cal, 6:342—345, 1996.

10) 郡　健次郎：遺伝子発現からみた尿路結石と動脈硬化の石灰化の類似性，Prog Med, 16:1139－1145, 1996.

11) 竹本　稔，多田　恵，中塚勝彦，森山剛栄，数井英雄，横手幸太郎，松本太郎，齋藤　康，森聖二郎：加齢ならびに高コレステロール血症の血中オステオポンチン濃度に及ぼす影響，日老医誌，36:799－802, 1999.

12) 田中　清：動脈硬化病変の進展におけるカルシウムの役割，Clin Cal, 9:202－207, 1996.

13) 柴田　進：病態生化学，金芳堂，京都，140－141, 1967.

14) Joint Committee on Powder Diffaraction Standards: Power Diffraction File, Pennsylvania: JCPDS, Card No. 9－432 and Card No. 17－541, 1976.

15) Le Meur Y, Moesch C, Rince M, Aldigier JC, Leroux-Robert C: Potential Nephrotoxicity of Intravenous Infusion of Naftidrofuryl Oxalate, Nephrol Dial Transplant, 10:1751－1755, 1995.

16) Yamamoto H, Sakae T, Takagi M, Otake S, Hirai G: Weddellite in Submandibular Gland Calculus, J Dent Res, 62:16－19, 1983.

17) Jahn H, Frank. RM, Voegel, JC, Schohn, D: Scanning Elecctron Microscopy and X-ray Diffraction Studies of Bone Oxalosis, Calcif Tissue Int, 30:109－119, 1980.

18) 今村一男，岸本　孝，高橋悦司，和久正良，大島博幸編：エッセンシャル泌尿器科学，第5版，医歯薬出版，東京，127－130, 1989.

Fig. 1　Low-power view of arteriosclerosis showing the tunica intimal fibrous hyperplasia with atheroma, ulcer and calcification (H・E original magnification × 40).

Fig. 2　The crystal dyed black with von Kossa staining (original magnification × 400).

Fig. 3　Polarization microscopic feature of the crystal showing rosette-like appearance (original magnification × 400).

Fig. 4　A. Scanning microscopic feature (× 750) B. EDS analysis.

Fig. 5　FT-IR pattern of the crystal.

Jpn. J. Oral Biol., 44 : 1-6, 2002.

ORIGINAL

Genotyping of Heterogenous Osteopetrotic Mice Using Microsatellite Markers

Yoshinobu Asada, Yukie Sato*, Takehiko Shimizu**, Toshiro Sakae***
Hirotsugu Yamamoto* and Takahide Maeda**

Department of Pediatric Dentistry, Tsurumi University School of Dental Medicine
**Department of Pathology, Nihon University School of Dentistry at Matsudo*
***Department of Pediatric Dentistry, Nihon University School of Dentistry at Matsudo*
****Department of Anatomy, Nihon University School of Dentistry at Matsudo*
2-1-3 Tsurumi, Tsurumi-ku, Yokohama 230-8501, Japan
,,*** 2-870-1 Sakaecho-Nishi, Matsudo 271-8587, Japan*
〔Received on July 30, 2001 ; Accepted on October 19, 2001〕

Key words : osteopetrosis／op mouse／microsatellite marker

Abstract : The aim of this study was to elucidate the three genotypes (*op*/*op*, *op*/+ and +/+) of heterogenous osteopetrotic mice using microsatellite markers. The genotyping analysis was performed on genetic crosses using B6C3Fe-*op*/+ and A/WySnJ mice. In this study, we used five MIT markers, D3Mit11, 75, 101, 102 and 189 that are closely linked to the *op* locus and which segregate polymorphic variants in mating between B6C3Fe-*op*/+ and A/WySnJ mice, and the homozygous *op*/*op* F3 mice were obtained by F2 mice mating. From the results of F3 genotyping, it was possible to determine the genotype of the *op* gene without a complicated molecular process. Histopathological studies revealed that the F3-*op*/*op* mice showed similar femur bone structures to those of B6C3Fe-*op*/*op* mice. Based on these findings, it is suggested that genotyping of heterogenous osteopetrotic mice using microsatellite markers is a powerful technique for investigating the mechanism of osteoclast development and genetic studies of osteopetrosis.

抄録：大理石骨病交雑系モデルマウスを用い，マイクロサテライトマーカーによる遺伝子型を検出することで *op* 遺伝子の3つの遺伝子型（*op*/*op*，*op*/+，+/+）を判定できるか否かを目的とし本実験を行った。B6C3Fe-*op*/+マウスとA/WySnJマウスとの交配より得られたすべてのF2マウスの遺伝子型をマイクロサテライトマーカーにて判定したところ，すべてのマウスで表現型（切歯の萌出の有無）と一致していた。さらに，肉眼的には+/+と判別困難なヘテロ型（*op*/+）マウスをマイクロサテライトマーカーより判定し，選抜したF2ヘテロ型マウス雌雄を交配したところ，F3マウスにおいて *op*/*op* マウスを作成することができた。また，組織学的所見より従来の *op* マウスとF3-*op*/*op* マウスでは大腿骨における形態学的特徴が類似していた。以上の結果より，大理石骨病交雑系モデルマウスはマイクロサテライトマーカーを用いることで簡便に遺伝子型を判定できることが明らかとなり，破骨細胞の分化に対するメカニズム解明ならびに大理石骨病の遺伝学的研究に有用であることが示唆された。

Introduction

Osteopetrosis is well known as an autosomal recessive disease in several species, including man[1,2]. In mice, the osteopetrosis (*op*) occurred spontaneously in the C57BL/6J-*dw* (dwarf, recessive gene) stock. The osteopetrotic (*op*/*op*) mutant mouse is characterized by reduced numbers of osteoclasts, macrophages and monocytes[3]. The *op* mouse is an important animal model for investigating the histopathology of the interactions between the alveolar bone and impacted

dental germs. In fact, the mutant *op/op* mouse can be recognized clearly at 10 days of age by failure of tooth eruption and separated from the wild type control (+/+, *op*/+) at weaning. However, it has not been possible to differentiate between *op*/+ and +/+ as heterozygous and homozygous because of the recessive mutation of the *op* gene. Recent studies showed that the changing of structure and composition of bone in osteopetrotic mice were associated with their genotype[4,5]. To detect the genotype of the *op* gene, a new strain of osteopetrotic mouse was produced by mating B6C3Fe-*op*/+ mice and A/WySnJ mice. It has been demonstrated that this heterogenous osteopetrotic mouse is useful for investigating the histopathological study of osteopetrosis[6]. Recently, some informative microsatellite markers were found as the flanking markers for the *op* gene[7]. The aim of this study was to elucidate the three genotypes (*op/op*, *op*/+ and +/+) of heterogenous osteopetrotic mice using the microsatellite markers.

Materials and Methods

1. Experimental design

B6C3Fe-*op*/+ mice were purchased from CLEA Japan Inc. (Tokyo, Japan). A/WySnJ were obtained from the National Institute of Genetics (Shizuoka, Japan). (B6C3Fe-*op*/+ female × A/WySnJ male) F1, the F2 intercross (F1 female × F1 male) and the F3 intercross (F2 female × F2 male) were obtained by mating the mice in our laboratory. The F1 mice were mated randomly and half of the normal offspring are expected to be op^{op}/A^{+} and half op^{+}/A^{+}, the two classes being indistinguishable. Homozygous osteopetrotic op^{op}/op^{op} mice can be clearly distinguished from their normal siblings by the absence of incisors. If we find the affected (non-eruption of incisors) mice in the F2 line, their parent F1 mice are heterozygotes (op^{op}/A^{+}) for *op* mutant alleles. The homozygous op^{op}/op^{op} F3 mice were produced by the F2 mice, which are hypothesis heterozygotes (op^{op}/A^{+}). All mice were maintained in a conventional environment in the Nihon University School of Dentistry at Matsudo Dental Center Animal Facility according to the guidelines of the Animal Use and Care Committee.

2. DNA

DNA samples were prepared from the spleen of parents (B6C3Fe-*op*/+ and A/WySnJ), F1 hybrids, and F3 intercross mice. A DNA sample of F2 intercross mice was prepared from the orbital sinuses because of hypothesis genetic mating. DNA extraction was carried out as described by Nomura, *et al.*[8].

3. Polymerase chain reaction conditions

A thermalcycler 480 (TaKaRa, Tokyo, Japan) was used for polymerase chain reaction (PCR). The reagents and PCR conditions were performed as described by Asada, *et al.*[9]. PCR products were electrophoresed in 8% polyacrylamide gels (running buffer : 1 × TBE) at 100 V for 1.5 h. The gels were stained with ethidium bromide for 8 min. PCR products were examined in ultraviolet light and photographed.

4. Simple sequence-length polymorphism markers

The microsatellite marker used in this study is one of the most useful SSLP markers in genetic research[10-12]. MIT primers for microsatellite loci were purchased from Research Genetics Inc. (Boston, MA). MIT markers, D3Mit11, 75, 101, 102 and 189, used in this study have been determined as informative markers, being polymorphisms between C57BL/6J and A/WySnJ. Also, these markers have been mapped near the osteopetrosis (*op*) gene[7,12].

5. Detection of the hypothesis genotype

SSLP typing of F2 and F3 mice was performed using informative markers on the mouse chromosome 3 in order to detect the hypothesis genotype against the *op* gene. Illustration of the link between the *op* locus and MIT marker is shown in Fig. 1. Since the five MIT markers used in this study were closely linked to the *op* gene, the probability of interchromosomal recombination occurring between the two loci would be very low. Hence it allows that the hypothesis genotype of F2 and F3 mice is evaluated by SSLP typing.

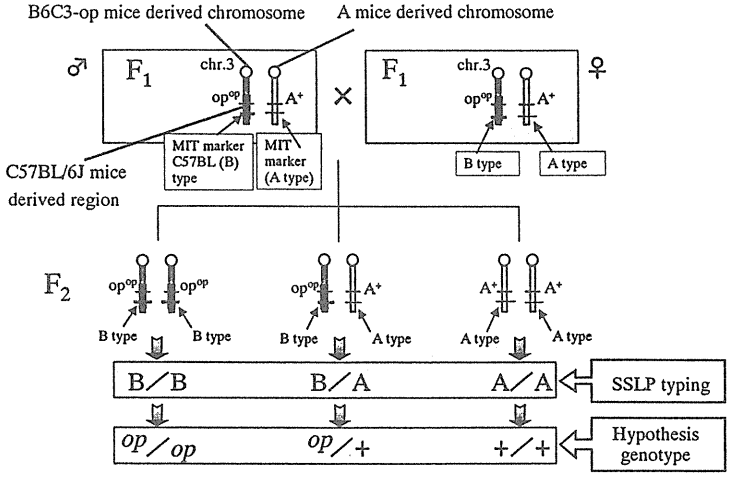

Fig. 1 Illustration of the link between *op* locus and MIT marker.

6. Estimate of incisor eruption

Homozygous osteopetrotic mice were evaluated by the absence of incisors eruption, according to the previous study[6].

7. Histology

In our experiment, the determination of the genotype of the F3-*op/op* was evaluated by the absence of incisor eruption. Osteopetrotic (*op/op*) mice were obtained from B6C3Fe-*op*/+ breeding pairs and were used as histological controls. The F3-*op/op* mice and *op/op* mice were killed 24 days after birth. Femurs were removed and fixed with 10% neutral buffered formalin in 0.1 M phosphate buffer (pH 7.4) for 4 days. They were demineralized in 10% sodium format-citrate for 2 weeks at 4°C. For hematoxylin-eosin (H. E.) staining, the femurs were embedded in paraffin by the usual method, and frontal sections of 4 μm thick were made and stained with H. E. F 3-*op/op* and *op/op* mice were evaluated by the morphological changes of cartilage continued to the trabecular bone in the femurs[6,13].

Results

1. Individual genotyping

The F2 (No. 1) mouse and F3 mice (Nos. 7, 8 and 10) had no incisor eruption and their genotypes were evaluated by a complete phenotype (Fig. 2).

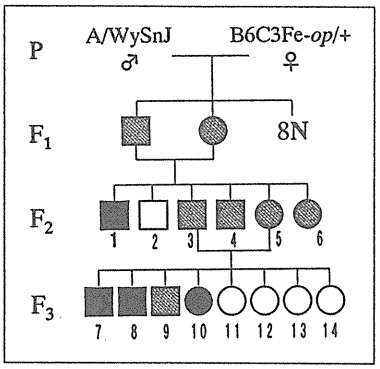

Fig. 2 Pedigrees of families with a new strain of osteopetrotic mice.
■ : Heterozygous male mouse (op^{op}/A^+).
● : Heterozygous female mouse (op^{op}/A^+).
■ : Homozygous male mouse (op^{op}/op^{op}).
● : Homozygous female mouse (op^{op}/op^{op}).
□ : Homozygous male mouse (A^+/A^+).
○ : Homozygous female mouse (A^+/A^+).
The designations in brackets are individual recognition.
N : Incisor erupted normal littermate mouse (op^{op}/A^+ or op^+/A^+).

Individual genotyping of 6 F2 mice (Nos. 1—6) and 8 F3 mice (Nos. 7—14) was performed using SSLP analysis. The SSLP typing at D3Mit11 and D3Mit101 is shown in Fig. 3. As shown in Table 1, the hypothesis genotyping of F2 and F3 mice was performed by SSLP typing with MIT markers and compared with their phenotype. No genotype was in conflict with its

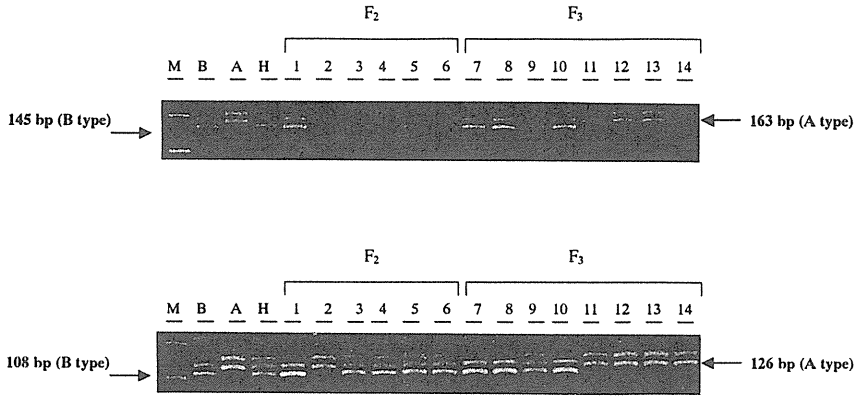

Fig. 3 SSLP typing of F2 and F3 mice using MIT primers (Top ; D3Mit11, bottom ; D3Mit101). PCR products were electrophoresed in 8% polyacrylamide gels. Odd lanes indicate expected PCR products (A ; A/WySnJ mice, B ; C57BL/6J mice, H ; 1 : 1 mix controls). The sample number corresponds to the pedigree chart. M : molecular size marker (100 bp DNA ladder).

Table 1 Detection of the hypothesis genotype using MIT markers

Strain	Sex	SSLP typing with MIT marker					Hypothesis genotype	Eruption of incisors
		11	75	101	102	189		
F_2 (No. 1)	M	*B	B	B	B	B	*op/op*	non-eruption
F_2 (No. 2)	M	**A	A	A	A	A	+/+	normal
F_2 (No. 3)	M	***H	H	H	H	H	*op*/+	normal
F_2 (No. 4)	M	H	H	H	H	H	*op*/+	normal
F_2 (No. 5)	F	H	H	H	H	H	*op*/+	normal
F_2 (No. 6)	F	H	H	H	H	H	*op*/+	normal
F_3 (No. 7)	M	B	B	B	B	B	*op/op*	non-eruption
F_3 (No. 8)	M	B	B	B	B	B	*op/op*	non-eruption
F_3 (No. 9)	M	H	H	H	H	H	*op*/+	normal
F_3 (No. 10)	F	B	B	B	B	B	*op/op*	non-eruption
F_3 (No. 11)	F	A	A	A	A	A	+/+	normal
F_3 (No. 12)	F	A	A	A	A	A	+/+	normal
F_3 (No. 13)	F	A	A	A	A	A	+/+	normal
F_3 (No. 14)	F	A	A	A	A	A	+/+	normal

* B : C57BL/6J homozygote, ** A : A/WySnJ homozygote, *** H : A/C57BL heterozygote

phenotype.

2. Histology

As shown in Fig. 4 a—d, the femur of the F3-*op/op* mice and B6C3Fe-*op/op* mice had thin cortical bone, and reticular bone existed along the long axis. The development of the cortical bone and medullary cavity was immature, appearing as woven bone as seen in the immature stage (Fig. 4 c, d). From the epiphysis to the center of the diaphysis, cartilage existed around the trabecular bone and its appearance exhibited an unusual bi-concave or hourglass shape (Fig. 4 a, b).

Discussion

Notable features in the *op/op* mutant mouse such as skull deformation and tooth eruption failure are considered to be a result of defective bone resorption and remodeling[14-16]. This is the result of the CSF-1 gene mutation, and *op/op* mice are cured by CSF-1 injec-

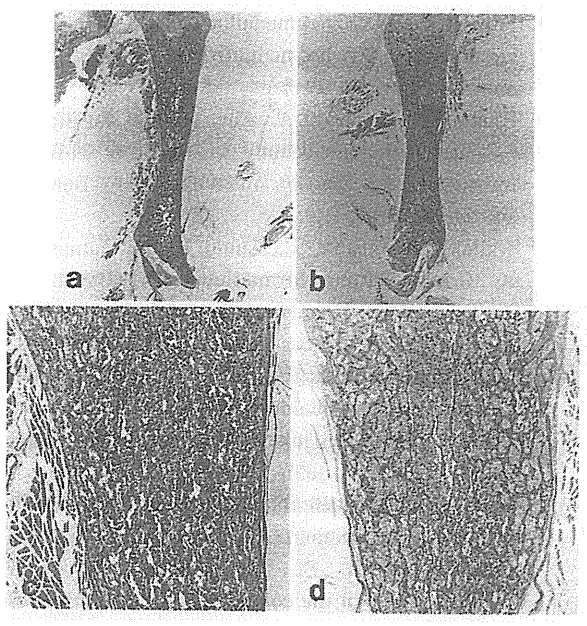

Fig. 4 Micrograph of the femur of both F3-*op*/*op* and B6C3Fe-*op*/*op* mice stained by H. E.
a : The femur of the F3-*op*/*op* mouse. (original magnification : ×2.5)
b : The femur of the B6C3Fe-*op*/*op* mouse. (original magnification : ×2.5)
c : High magnification of the metaphysis in Fig. 4 a. (original magnification : ×20)
d : High magnification of the metaphysis in Fig. 4 b. (original magnification : ×20)

tion[3,17,18]. Begg, *et al.*[19] reported that a hematopoietic system has the capacity to use alternative mechanisms to compensate for the absence of CSF-1 in *op*/*op* mice. A recent study revealed that two growth factors, vascular endothelial growth factor (VEGF) and placenta growth factor (PIGF), induce the osteoclasts in the *op*/*op* mice, suggesting that osteoclast differentiation in the op mice is not mediated by the CSF-1 receptor[20]. It is considered that the mechanism of osteoclast development is more complicated in op mice. In order to study the effects of osteoclast deficiency on the ankylosis process of tooth eruption in op mice, detecting the genotype at stages prior to the first appearance of the morphological abnormalities will be required. Since an enormous amount of murine genetic information is available, the genotype of a target mutation gene can easily be detected using MIT markers[21,22]. In this study, genotyping of the heterogenous osteopetrotic mice was performed using five MIT markers, D3Mit11, 75, 101, 102 and 189 that are closely linked to the *op* locus (Table 1). As shown in Fig. 3, polymorphism can easily be detected using PCR for D3Mit11 and D3Mit101. Based on the SSLP typing data using PCR, the hypothesis genotypes of F2 and F3 mice were compared with their phenotype. Although it does not enable visual differentiation between *op*/+ and +/+ genotypes, we could make a clear distinction between the two genotypes using the five MIT markers. Indeed, the homozygous *op*/*op* F3 mice were obtained by the hypothesis mating of F2 mice (Fig. 2). These findings suggest that it is possible to detect the three genotypes of the *op* gene without a complicated molecular process.

Our histological study was carried out to compare the histopathological changes in the femur in F3-*op*/*op* mice with B6C3Fe-*op*/*op* mice. The major skeletal metabolic changes in B6C3Fe-*op*/*op* mice are an increase in bone matrix formation and cytological evidence for a reduction in remodeling. Histopathological studies revealed that the F3-*op*/*op* mice showed similar femur bone structures to those of B6C3Fe-*op*/*op* mice.

In conclusion, this study suggests that genotyping of the heterogenous osteopetrotic mice using microsatellite markers is a powerful technique for investigating the mechanism of osteoclast development and genetic studies of osteopetrosis.

Acknowledgements

We are grateful to Dr. Norihisa Inuzuka (Department of Anatomy, the University of Tokyo) and Dr. Hiroyuki Okada (Department of Pathology, Nihon University School of Dentistry at Matsudo) for their valuable advice on this study. This work was supported by a grant from research for the Frontier Science (The Ministry of Education, Science, Sports and Culture of Japan).

References

1) Marks, S. C., Jr. and Lane, P. W. : Osteopetrosis, a

new recessive skeletal mutation on chromosome 12 of the mouse. J. Hered. **67** : 11—18, 1976.

2) Marks, S. C., Jr. : Morphological evidence of reduced bone resorption in osteopetrotic (op) mice. Am. J. Anat. **163** : 157—167, 1982.

3) Felix, R., Cecchini, M. G., Hofstetter, W., Elford, P. R., Stutzer, A. and Fleisch, H. : Impairment of macrophage colony-stimulating factor production and lack of resident bone marrow macrophages in the osteopetrotic op/op mouse. J. Bone Miner. Res. **5** : 781—789, 1990.

4) Sato, Y., Okada, H., Sakae, T. and Yamamoto, H. : Bone structure in op/op mice as revealed by backscatter imaging. J. Dent. Res. **74** : 567, 1995.

5) Sato, Y., Okada, H., Sakae, T. and Yamamoto, H. : Structure and composition of bone in osteopetrotic (op/op) mice. J. Dent. Res. **76** : 1183, 1997.

6) Sato, Y. : Construction and histopathological study of a new osteopetrotic mouse strain. Jpn. J. Oral. Biol. **40** : 108—119, 1998.

7) Asada, Y., Takamori, K., Yamamoto, H. and Maeda, T. : Detection of the flanking MIT markers for the *op* gene on mouse chromosome 3. Ped. Dent. J. **10** : 29—32, 2000.

8) Nomura, R., Nakamura, H., Matsune, K., Shimizu, T., Asada, Y. and Maeda, T. : Detection of informative SSLP markers for searching a causative gene(s) of absence of the third molars in EL mice. Ped. Dent. J. **10** : 75—79, 2000.

9) Asada, Y., Varnum, D. S., Frankel, W. N. and Nadeau, J. H. : A mutation in the Ter gene causing increased susceptibility to testicular teratomas maps to mouse chromosome 18. Nature Genet. **6** : 363—368, 1994.

10) Dietrich, W. F., Miller, J. C., Steen, R. G., Merchant, M., Damron, D., Nahf, R., Gross, A., Joyce, D. C., Wessel, M., Dredge, R. D., Marquis, A., Stein, L. D., Goodman, N., Page, D. C. and Lander, E. S. : A genetic map of the mouse with 4,006 simple sequence length polymorphisms. Nature Genet. **7** : 220—245, 1994.

11) Matin, A., Collin, G. B., Asada, Y., Varnum, D., Martone, D. L. and Nadeau, J. H. : Simple sequence length polymorphisms (SSLPs) that distinguish MOLF/Ei and 129/Sv inbred strains of laboratory mice. Mamm. Genome **9** : 668—670, 1998.

12) Eppig, J. T., Blake, J. A., Davisson, M. T. and Richardson, J. E. : Informatics for mouse genetics and genome mapping. Methods **14** : 179—190, 1998.

13) Fawcett, D. W. : The amedullary bones of the Florida manatee (Trichechus Latirostris). Am. J. Anatomy **71** : 271—309, 1942.

14) Kanno, E., Yamasaki, A., Abe, M. and Morikawa, S. : Histopathological study on impaired dentition in osteopetrotic (*op/op*) mice. Ohu Univ. Dent. J. **20** : 24—30, 1993.

15) Niida, S., Wakisaka, H., Kanno, E. and Yamasaki, A. : Cranial flat bone formation in the osteopetrotic (op/op) mouse. Biomedical Res. **15** : 37—44, 1994.

16) Kawata, T., Niida, S., Kawasoko, S., Kaku, M., Fujita, T., Sugiyama, H. and Tanne, K. : Morphology of the mandibular condyle in "toothless" osteopetrotic (op/op) mice. J. Craniofac. Genet. Dev. Biol. **17** : 198—203, 1997.

17) Yoshida, H., Hayashi, S., Kunisada, T., Ogawa, M., Nishikawa, S., Okamura, H., Sudo, T., Shultz, L. D. and Nishikawa, S. : The murine mutation osteopetrosis is in the coding region of the macrophage colony stimulating factor gene. Nature **345** : 442—444, 1990.

18) Felix, R., Cecchini, M. G. and Fleisch, H. : Macrophage colony stimulating factor restores in vivo bone resorption in the op/op osteopetrotic mouse. Endocrinology **127** : 2592—2594, 1990.

19) Begg, S. K., Radley, J. M., Pollard, J. W., Chisholm, O. T., Stanley, E. R. and Bertoncello, I. : Delayed hematopoietic development in osteopetrotic (op/op) mice. J. Exp. Med. **177** : 237—242, 1993.

20) Niida, S., Kaku, M., Amano, H., Yoshida, H., Kataoka, H., Nishikawa, S., Tanne, K., Maeda, N., Nishikawa, S. and Kodama, H. : Vascular endothelial growth factor can substitute for macrophage colony-stimulating factor in the support of osteoclastic bone resorption. J. Exp. Med. **19** : 293—298, 1999.

21) Copp, A. J., Checiu, I. and Henson, J. N. : Developmental basis of severe neural tube defects in the loop-tail (Lp) mutant mouse : use of microsatellite DNA markers to identify embryonic genotype. Dev. Biol. **165** : 20—29, 1994.

22) Dietrich, W. F., Miller, J., Steen, R., Merchant, M. A., Damron-Boles, D., Husain, Z., Dredge, R., Daly, M. J., Ingalls, K. A., O'Connor, T. J., Evans, C.A., DeAngelis, M.M., Levinson, D.M., Kruglyak, L., Goodman, N., Copeland, N.G., Jenkins, N.A., Hawkins, T.L., Stein, L., Page, D.C. and Lander, E.S. : A comprehensive genetic map of the mouse genome. Nature **380** : 149—152, 1996.

Key Engineering Materials Vols. 240-242 (2003) pp. 395-398
© 2003 Trans Tech Publications, Switzerland

Bone Formation Induced by Several Carbonate- and Fluoride-Containing Apatite Implanted in Dog Mandible

T. Sakae,[1] A. Ookubo,[2] R.Z LeGeros[3]
R. Shimogoryou,[2] Y. Sato,[1]
S. Lin[3], H. Yamamoto,[1] Y. Kozawa [1]
[1] Nihon University, School of Dentistry at Matsudo, Chiba, 271-8587, Japan.
[2] Japan Institute for Advanced Dentistry, Nagasaki, Japan.
[3] New York University, College of Dentistry, NY, USA.
sakae@mascat.nihon-u.ac.jp

Keywords: Carbonate, Fluoride, Apatite, Implant, Dog Mandible, Bone graft, Histology, Animal Studies

Abstract Synthetic hydroxyapatite (HAP), carbonate-apatite (CHA) and carbonate-fluoride-apatite (CFA) were implanted into dog mandible bone for 2, 3, 4, 5 and 6 weeks. The chemical composition and crystallographic properties of the synthetic apatites were examined using FT-IR, TG-DTA, AAS and X-ray diffraction. The comparative resorption in vivo for the experimental period was in the order: CHA >> CFA > HAP. CHA formed new bone comparable with the sham-control, and CFA induced fast bone-remodeling and newly formed Haversian system. The results confirmed that CHA are potential bone-grafting materials and also showed that CFA, compared to CHA or HAP materials, accelerate bone formation.

Introduction

Carbonate- and/or fluoride-containing calcium hydroxyapatite are considered as possible bone graft materials [1-3]. *In vitro* and *in* vivo studies showed that fluoride present in synthetic or bone apatite enhances osteoblastic activity [3, 4]. *In vitro* studies also showed that fluoride-containing apatite inhbited osteoclastic activity [5].The aim of this study was to compare the biocompatibility and bio-degradation carbonate- and fluoride-containing apatites implanted in dog mandible bone.

Materials and Methods

Carbonate hydroxyapatite (CHA), carbonate- and fluoride-containing apatite (CFA) and carbonate- and fluoride-free apatite (HAP) were synthesized according to methods previously described [6, 7]. Their chemical and crystallographic properties were determined using X-ray diffraction (XRD), FT-IR, thermogravimetry (TG-DTA), and AAS. The materials were powdered, sieved with 200-mesh, sterilized and implanted in surgically created holes (3mm diameter) in the mandible of Beagle dogs. The implanted materials were covered with biodegradable membranes to prevent material loss during the experiment. After 2, 3, 4, 5, and 6 weeks, the dogs were sacrificed under anesthesia. Histological stained sections of the mandible bones were observed using a microscope.

Results

XRD analysis confirmed the substitution of carbonate (CO_3) and fluoride (F) in the apatite structure based on shifts in diffraction peaks reflecting lattice parameter changes due to CO_3-for-PO_4 and F-for-OH substitutions in calcium hydroxyapatite, $Ca_{10}(PO_4)_6(OH)_2$. Carbonate substitution in CHA and in CFA was demonstrated as the absorbance bands at about 1400 to 1560 and at about 770 to 800 cm-1 in the FT-IR spectra[7] and the weight losses above 400°C in TG-DTA.
Histological sections of these materials showed a clear difference in the extent of resorption or dissolution of the implanted apatites and in the pattern and type of bone formation. HAP remained even after 6 weeks, CHA disappeared after 2 weeks, and CFA disappeared after about 4 weeks (Table 1). After 6 weeks, although the bone formation or induction started earlier, all the implants

formed bone. The new bone formed associated with the materials gave the following characteristics: HAP-induced bone showed characteristics of immature bone in the very early stage; CHA-induced bone was in a more advanced stage but remodeling had not occurred; and CFA-induced bone was the most advanced and showed Haversian system indicating that bone remodeling had started.

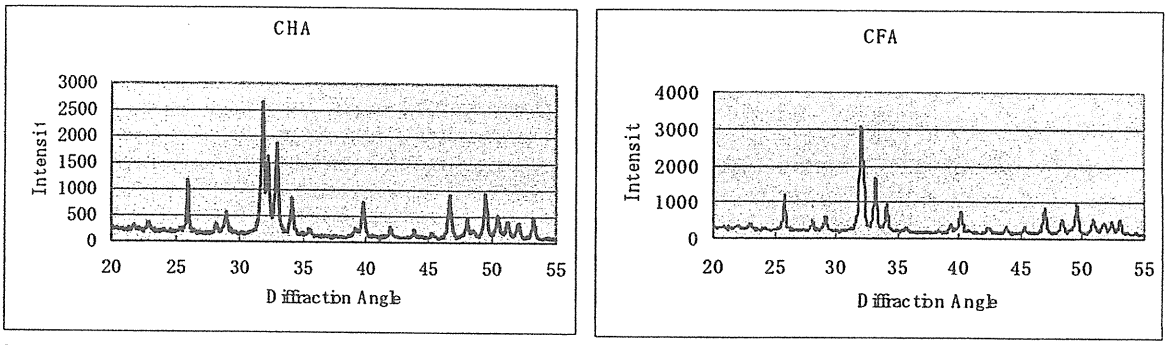

Fig. 1. XRD pattern of the CHA (Left) and the CFA (Right), showing the peak-shift between them indicating the ionic-substitution.

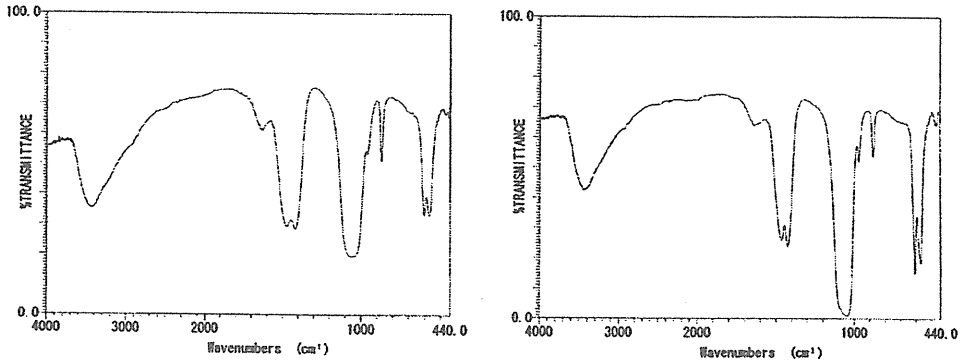

Fig. 2. FT-IR pattern of the CHA (Left), and the CFA (Right), indicating that the CHA containing the more carbonate content than the CFA.

Table 1. Comparison of bone formation pattern for HAP, CHA, CFA implanted in dog mandible.

Type	After 2 weeks	After 6 weeks
HAP	remain	remain
CHA	dissolved	Immature bone
CFA	remain	Haversian

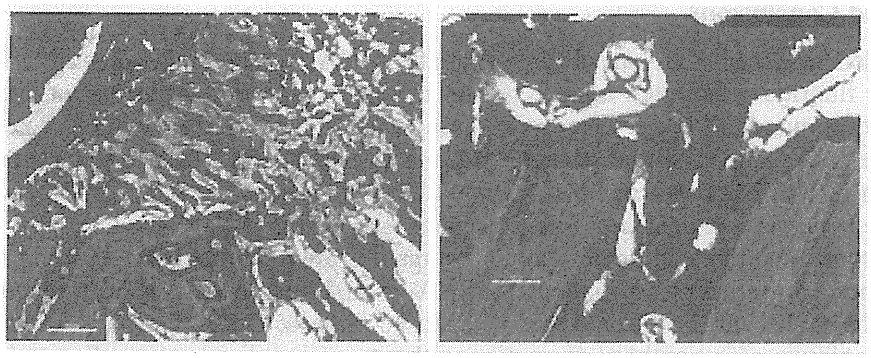

Fig. 3. Bone formation after 2w in the control (Left, x2), and high power view (Right, x10).

Fig. 4. HAP implanted after 2w (Left, x2), and high power view (Right, x10).

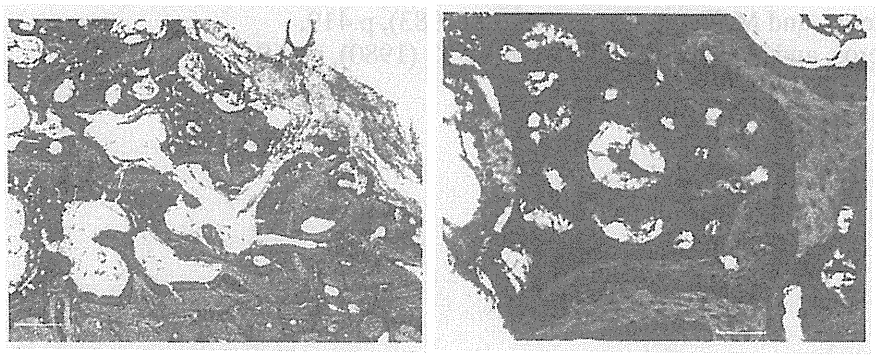

Fig.5. CHA implanted after 4w (Left, x2) and high power view (Right, x10)

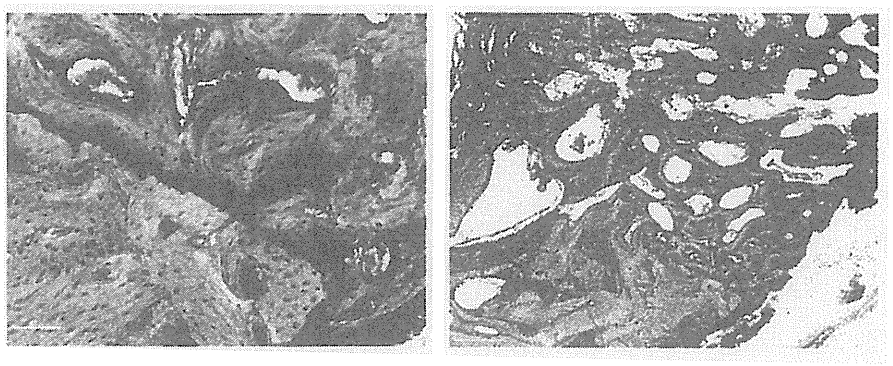

Fig. 6. CFA implanted after 4w (Left, x2), and high power view (Right, x10).

Discussion and Conclusions

This study demonstrated that unsubtituted apatite (HAP), carbonate-substituted (CHA) and carbonate and fluoride-substituted apatite (CFA) materials all formed bone after six weeks when implanted in dog mandible bone. However, these materials differed in extent of resorption with CHA being the fastest and HAP the slowest. These materials also differed in the pattern and type of new bone formed: CFA demonstrated accelerated Haversian bone formation; CHA was associated with immature bone but a later stage of development than HAP.
These results confirmed that carbonate-containing apatites are potential bone-grafting materials. The results also showed that CFA, compared to CHA or HAP materials, accelerate bone formation attributed to the F content. Further studies need to be done to determine the critical amount of F required for maximum effect on bone formation without causing disease (e.g., fluorosis).

Acknowledgements

This study was supported by research grants from the Frontier Science Project from the MECSST, Japan (T.S.), the National Institute for Dental and Cranio-facial Research of NIH (RZL) and the L. Linkow Professorship in Implant Dentistry (RZL). The authors thank to Prof. I. Sato at LEBRA (Laboratory for Electron Beam Research and Application), Institute of Quantum Science, Nihon University for the use of his facilities.

References

[1] C. Frondoza, *et al.*: Bioceramics 11 (1998), p.289.
[2] A. M. Gatti, *et al.*: Bioceramics 11 (1998), p.399.
[3] M. Okazaki, *et al.*: Bioceramics 12 (1999), p.337.
[4] J. Kazimiroff, *et al.*: Bioceramics 9 (1997), p.169.
[5] T. Sakae, *et al.*: Key Engineering Materilas 192-195 (2001), p.347.
[6] R. Z. LeGeros, and M. Tung: Caries Res 17 (1983), p.419.
[7] R.Z. LeGeros, and S. Suga: Calcif Tissue Int 32 (1980), p.169.

Journal of Hard Tissue Biology 12[1] (2003) p1-p5
© 2003 The Society of Hard Tissue Biology
Printed in Japan, All rights reserved.
CODEN-JHTBFF, ISSN 1341-7649

ORIGINAL

Microbeam X-ray Diffraction Analysis of Human Tooth Enamel from EDJ to Enamel Surface

Toshiro SAKAE [1], Yoshiho CHIGONO [2] and Noriyuki NAGAI [3]

[1] *Department of Anatomy, Nihon University School of Dentistry at Matsudo, Chiba, 271-8587, Japan*
[2] *Department of Oral Surgery, Teikyo University Medical School, Itabashi, Tokyo, 173-8605, Japan*
[3] *Department of Oral Pathology, Okayama University Dental School, Okayama, 700, Japan*
(Accepted for publication :February 6, 2003)

Abstract: Crystals in tooth enamel were analyzed by X-ray diffraction, XRD, using a 100 μm in diameter microbeam. A polished section of human tooth enamel was made, and the microbeam XRD patterns were obtained at six positions from the enamel-dentin junction region to the surface region. Although the apatite unit cell dimensions of the six positions were almost the same, the orientation of crystallites changed abruptly at the surface layer. It was noted that the crystallites aligned not only in their c-axis but also in their a-axis.

Key words: Micro XRD, Micro FT-IR, Tooth Enamel, Crystal

Introduction

Orientation of crystallites in enamel can be studied using a polarized light microscope[1,2], scanning and transmission electron microscope[3,4], and micro-Raman spectroscopy[5]. However, three-dimensional crystallite orientation analysis is complicated and troublesome using such techniques. X-ray diffraction (XRD) provides a quick and reliable result for such purpose. Using XRD, Hirota[6] showed the enamel prism arrangement. In this study, a microbeam XRD technique was introduced to study the enamel crystallites layer by layer.

Materials and Methods

A polished section of tooth enamel was prepared from a human molar, which was extracted for clinical reason, and fixed by neutral formaldehyde solution. XRD pattern was obtained using a RINT-RAPID machine (Rigaku Co. Ltd., Tokyo) under the following conditions: X-ray tube accelerating voltage; 50 kV, accelerating current; 30 mA, X-ray type; monochromatized CuKα (1.5418Å), X-ray beam collimater; 100 μm in diameter, incident angle to sample; 20 degree, efficient beam area on sample plane; 100x290 μm in ellipse form, and exposure time; 60 min.

The polished section was set on a sample holder to maintain the short axis of the efficient beam ellipse normal to the enamel surface, in such a manner that the six analytical positions covered the whole thickness of the enamel from the enamel-dentin junction to the surface (Fig. 1).

The XRD patterns were recorded with a semicircular cylinder-type Imaging-Plate system (IP, Fuji Film Co. Ltd., Tokyo), attached to the RINT-RAPID. The IP system covered a diffraction pattern from -15 degree to 160 degree (2 θ) in the horizontal axis and -40 degree to 40 degree in the vertical axis. The XRD pattern analysis was carried out using RINT software, (Rigaku Co. Ltd., Japan) and JADE software (Materials Data Inc, California, USA).

Results

Two typical microbeam X-ray diffraction images of the human tooth enamel are shown in Fig. 2, together with the three-dimensional representations of crystallite orientation. The diffraction intensity was represented in color scale mode. In the three-dimensional representations, change of crystallites orientation was clearly shown.

Figure 3 shows the XRD results of the six positions from the innermost enamel-dentin junctional region, #280-625, to the surface region, #280-675; the regions correspond to those shown in Fig. 1. In Figs. 2 and 3 the selected areas of diffraction images are shown.

As shown in Fig. 3, crystallite orientation was almost the same

Correspondence to T. Sakae : Nihon University School of Dentistry at Matsudo, Chiba, 271-8587, Japan, Phone: 047-360-9323, FAX 047-360-9324, e-mail:sakae@mascat.nihon-u.ac.jp

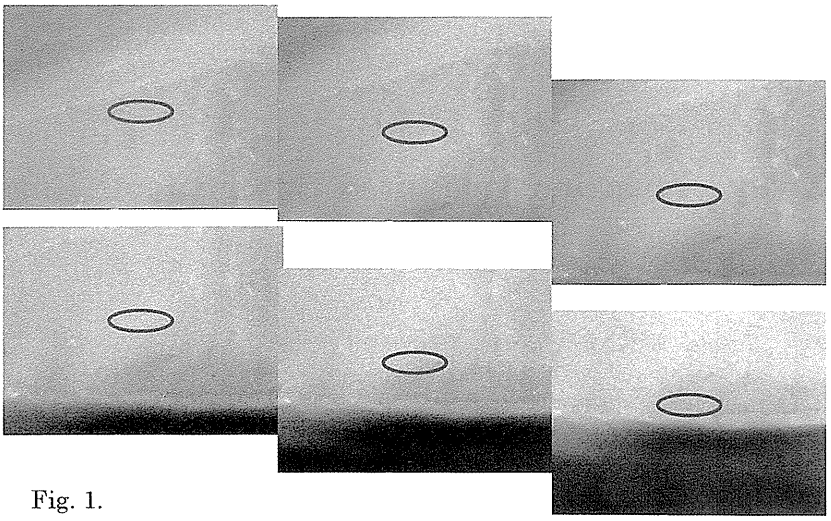

Fig. 1.

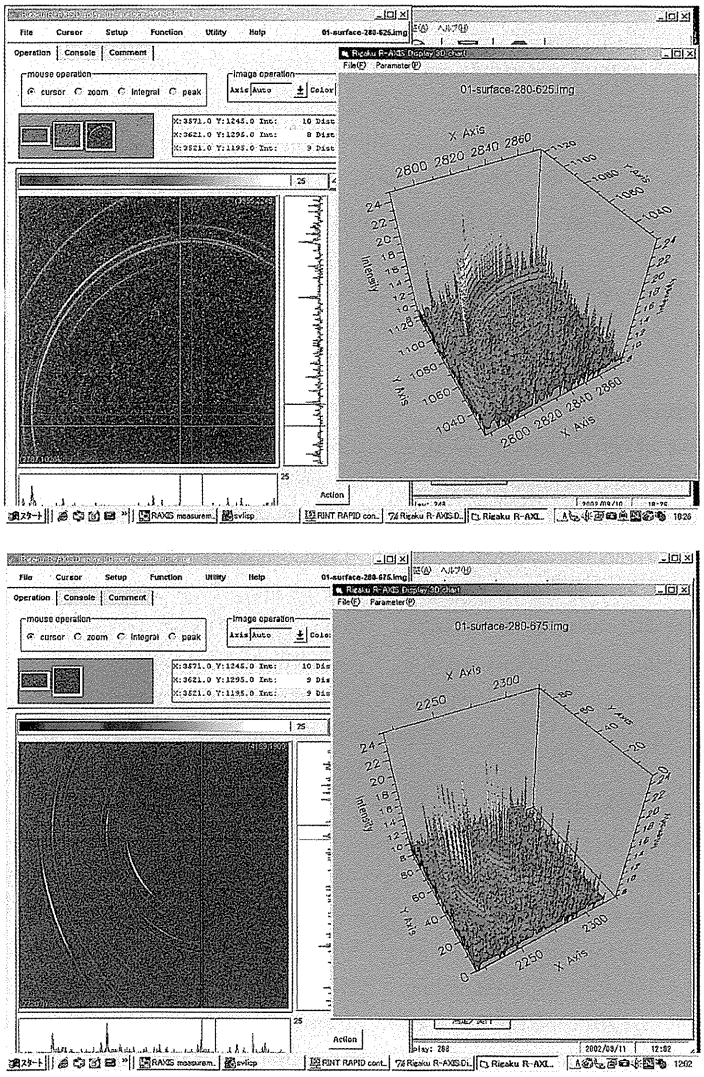

Fig. 2

Fig. 1. The selected regions in the human tooth enamel from the enamel-dentin junction to the enamel surface.Each ellipse represents the efficient X-ray beam area of a microbeam 100 μm in diameter.

FFig. 2. Two typical micro X-ray diffraction patterns of the selected regions in the human tooth enamel. Top: #280-625; the innermost EDJ region. Bottom: #280-675; the outermost surface region. The left panels are the micro diffraction patterns and the right panels are three-dimensional representation of the crystal orientation.

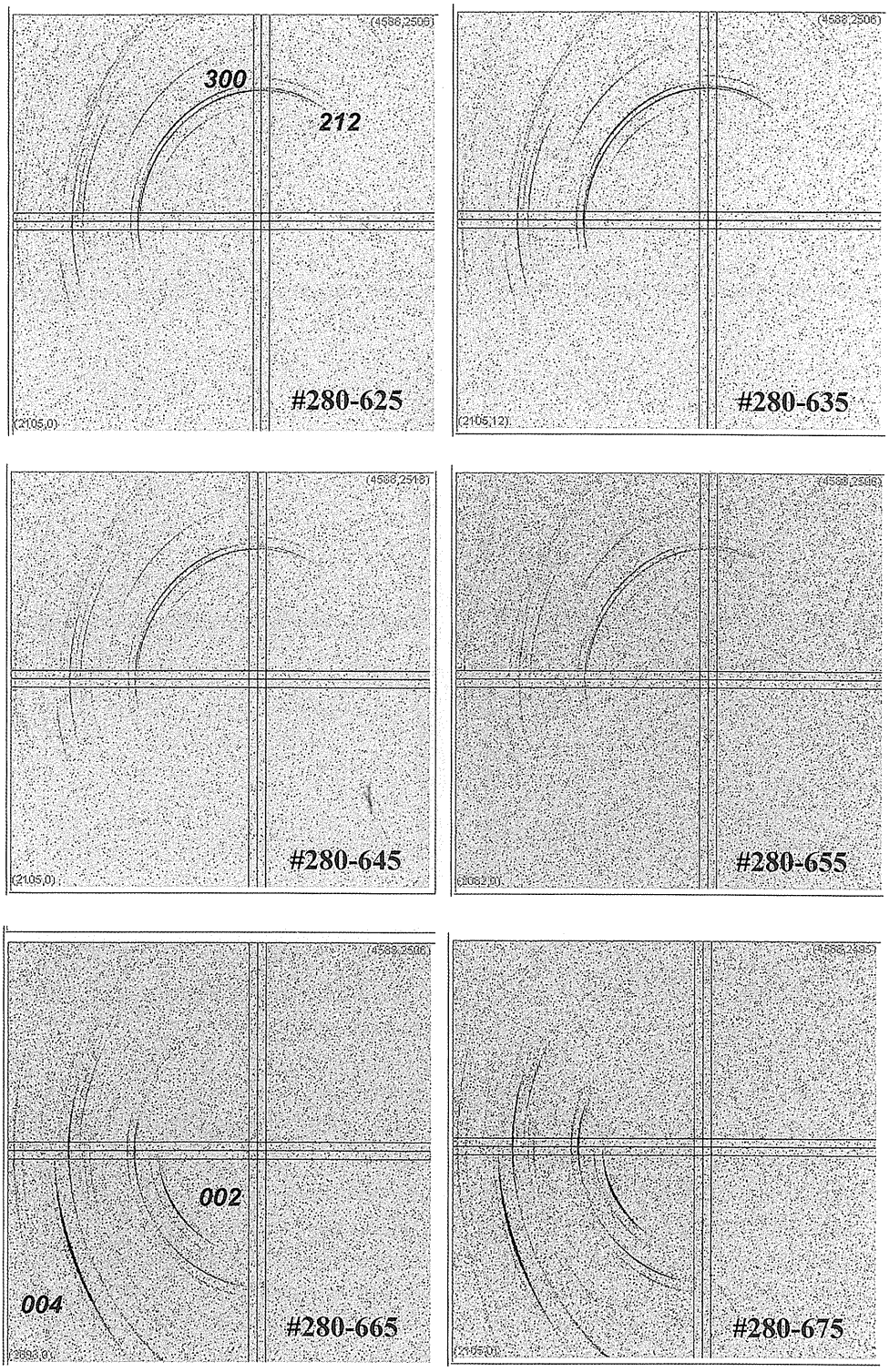

Fig. 3. The micro X-ray diffraction patterns of the selected regions in the human tooth enamel. Figures in the charts are Miller indices (hkl) for the reflection plane.

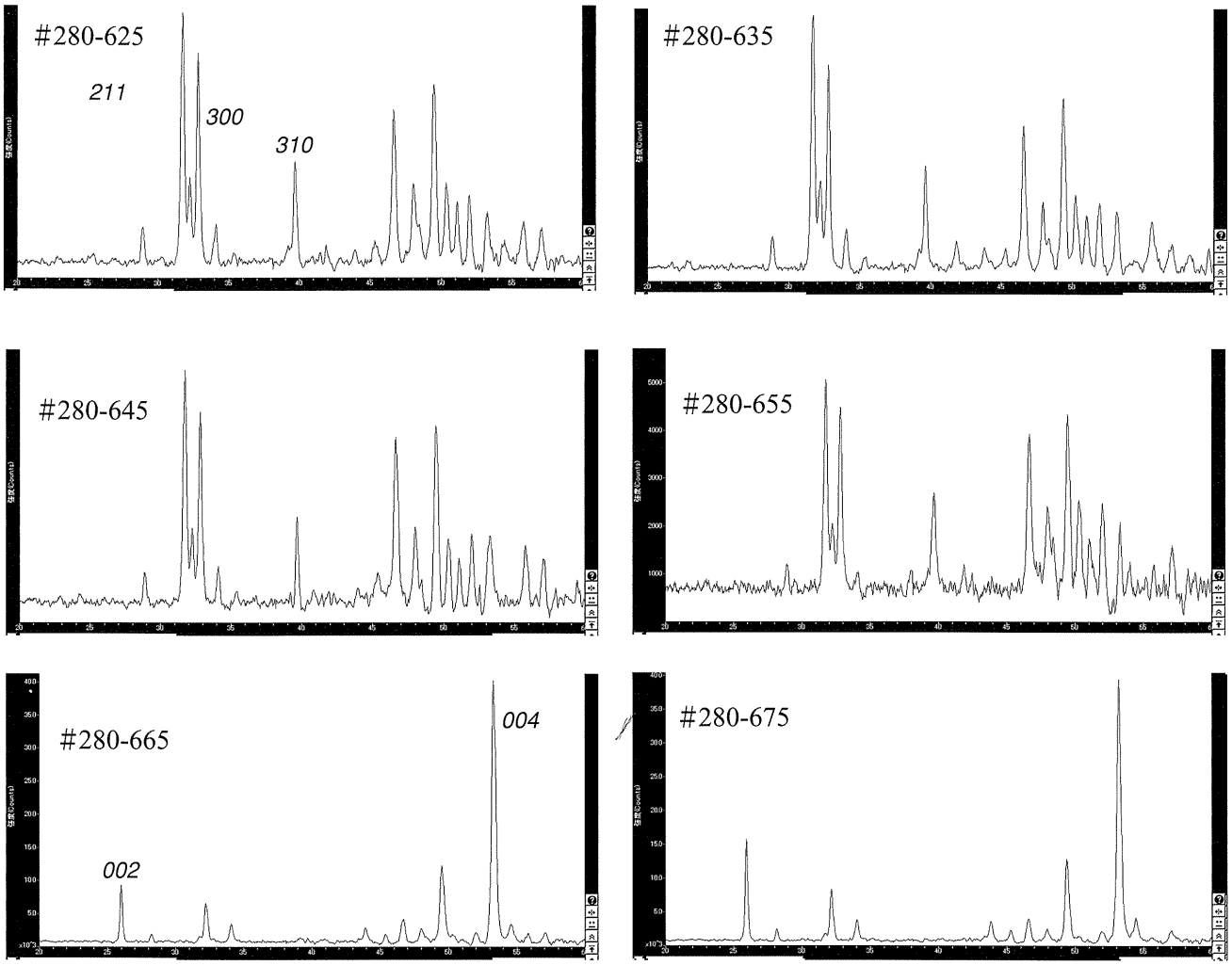

Fig. 4. Normal diffraction chart style representations of the micro X-ray diffraction patterns of the selected regions in human enamel. The horizontal axis is diffraction angle from 20 to 60 degree (2θ). The vertical axis is diffraction intensity in arbitrary scale. Figures in the charts are Miller indices (hkl) for the reflection plane.

for the four inner enamel regions (position numbers from #280-625 to #280-655), but the orientation changes abruptly in the enamel surface regions (position number #280-665 and #280-675).

In Fig. 3, the upper four diffraction images showed intense apatite 300 reflection, indicating that the apatite crystallites were arranged along the a-axis almost normal to the X-ray beam. The four diffraction images showed no apatite 002 or 004 reflection, indicating that the c-axis direction of the crystallites was not in the position normal to the X-ray beam. These results indicated that the crystallites in these positions aligned well and orientated almost in the same direction.

On the contrary, the lower two diffraction images in Fig. 3 showed intense apatite 002 and 004 reflections, indicating that the crystallites aligned well along the c-axis and were directed normal to the X-ray beam. In the lower two diffraction images, the apatite 300 and 211 reflections were too weak to observe. These results strongly indicated that the crystallites in one-third of the enamel thickness from the surface were aligned not only in the crystallite c-axis but also in the a-axis.

Figure 4 shows the usual XRD chart style conversions of the XRD images. In Fig. 4, it was clearly shown that the apatite 300 reflection together with 211 and 112 reflections were intense in the sample positions from #280-625 to #280-655. On the contrary, the apatite 002 and 004 reflections were intensified in the XRD charts of sample positions #280-665 and #280-675.

The unit cell dimensions of the measured enamel regions were calculated and listed in Table 1. The values for a-axis length were from 9.431 to 9.453 and the values for c-axis length were from 6.863 to 6.880. These values were in the range of the reported human tooth enamel[7,8,9].

Discussion

It is a well-known fact that at Hunter-Schreger bands enamel prisms of dia-zone and para-zone crossed at an angle. Hirota[10] showed that this enamel prism crossing resulted in the two-direction fiber axis patterns of enamel on XRD. However, in this

Table 1. Unit cell dimensions for the six selected regions (100 μm in diameter) of the human enamel

Point location	a-axis length	esd	c-axis length	esd
280-625	9.431	0.003	6.872	0.002
280-635	9.453	0.002	6.880	0.002
280-645	9.440	0.003	6.864	0.001
280-655	9.444	0.003	6.865	0.001
280-665	9.446	0.002	6.876	0.001
280-675	9.435	0.002	6.863	0.001

Esd: estimated standard diviation.

study there was no such two-direction orientation of enamel crystallites. In this study, the efficient beam area was 100x290 μm in ellipse form on the enamel sample plane, and should cover a sufficient area for the two zones of Hunter-Schreger bands. Therefore, a detailed study of the crystallite orientation in enamel prism is needed.

This study showed an interesting result that the orientation of apatite crystallites in the tooth enamel changed at one-third of the thickness from the surface, and the enamel apatite crystallites aligned very well not only on the c-axis but also on the a-axis. In many reports on the crystallite orientation of tooth enamel, the enamel apatite crystallites aligned in the crystallite c-axis but not in the a-axis. This study indicates that, at least in some cases, the apatite crystallites in tooth enamel align in particular directions on the crystallographic axis.

Acknowledgements

The X-ray diffraction experiments were carried out at LEBRA, Laboratory for Electron Beam Research and Application, Nihon University. The authors thank to Prof. Isamu Sato at LEBRA for providing opportunity to use the XRD instruments. A part of expense of this study was defrayed by a Frontier Science Project Grant from MEXT, Japan.

References

1) Bres EF, Voegel JC, Frank RM.: High-resolution electron microscopy of human enamel crystals. J Microsc, 160 (Pt 2):183-201, 1990

2) Hanaizumi Y., Maeda T., Takano Y.: Three-dimensional arrangement of enamel prisms and their relation to the formation of Hunter-Schreger bands in dog tooth. Cell Tissue Res, 286(1):103-14, 1996

3) Hirota F.: Prism arrangement in human cusp enamel deduced by X-ray diffraction. Arch Oral Biol, 27(11):931-7, 1982

4) Hirota F.: An explanation for the "two fiber axes" problem in human enamel by x-ray diffraction. J Dent Res, 65(7):978-81, 1986

5) LeGeros R.Z., Sakae T., Bautista C., Retino M., LeGeros JP. : Magnesium and carbonate in enamel and synthetic apatites. Adv Dent Res, 10(2):225-31, 1996

6) Okuda A, Okada K, Sakae T, Hirai G.: Lattice parameters of human enamel apatites. Nichidai Koko Kagaku, 13(3):317-23, 1987

7) Osborn J.W., Hillman J.: Enamel structure in some therapsids and mesozoic mammals. Calcif Tissue Int, 29(1):47-61, 1979

8) Sakae T.: X-ray diffraction and thermal studies of crystals from the outer and inner layers of human dental enamel. Arch Oral Biol 1988;33(10):707-13, 1988

9) Schmidt W.J. and Keil A.: Polarizing Microscopy of Dental Tissues. Pergamon Press, Oxford, 1971

10) Tsuda H, Arends J.: Orientational micro-Raman spectroscopy on hydroxyapatite single crystals and human enamel crystallites. J Dent Res, 73(11):1703-10, 1994

Journal of Hard Tissue Biology 12[1] (2003) p25-28
© 2003 The Society of Hard Tissue Biology
Printed in Japan, All rights reserved.
CODEN-JHTBFF, ISSN 1341-7649

ORIGINAL

Intermittent Crystal Growth of Unusually Long Submandibular Sialolith Revealed by Micro-Focus- and Selected-Area- X-Ray Diffraction.

Toshiro SAKAE[1], Yoshiaki AKIMOTO[2], Takashi KANEDA[3], Akira FUJII[4], Tadahiko UTSUNOMIYA[5], Hirotsugu YAMAMOTO[5], Takaatsu HARADA[2], Kazuo HIGUCHI[2], Seiichi. SATO[2] and Racquel.Z. LeGeros[6]

[1]*Department of Oral Histology, Nihon University School of Dentistry at Matsudo, Chiba, 271-8587, Japan,*
[2]*Department of Oral Surgery, Nihon University School of Dentistry at Matsudo, Chiba, 271-8587, Japan,*
[3]*Department of Radiology, Nihon University School of Dentistry at Matsudo, Chiba, 271-8587, Japan,*
[4]*Department of Pharmacology, Nihon University School of Dentistry at Matsudo, Chiba, 271-8587, Japan,*
[5]*Department of Oral Pathology, Nihon University School of Dentistry at Matsudo, Chiba, 271-8587, Japan,*
[6]*Department of Biomaterials and Biomimetics, New York University College of Dentistry, New York, New York, USA*
(Accepted for publication : May 30, 2003)

Abstract: BACKGROUND: Sialolith is a pathological calcification found inside salivary glands, composed principally of apatite crystals. The purpose of this study was to investigate detailed structural properties to gain insight into the formation of sialolith. METHODS: A 45 mm long sialolith from a human submandibular gland was studied using micro-FTIR and three types of X-ray diffraction (XRD) techniques: i) conventional, ii) micro-focus, and iii) "selected-area XRD" (SA-XRD). RESULTS: The longitudinal section of the sialolith showed a stratified structure perpendicular to the long axis. XRD and FTIR showed that the bulk of the sialolith was composed of carbonate hydroxyapatite. Micro-XRD revealed that crystal orientation was slightly different in each incremental zone. "SA-XRD" showed that the average unit cell dimensions of apatite crystals were different for each zone. CONCLUSION: These results suggest that the stratified structure in the sialolith was a result of intermittent and incremental additional growth reflecting compositional changes in the microenvironment.

Key words: Salivary Gland Calculi, Carbonate apatite, FTIR, X-Ray Diffraction

Introduction

Sialoliths are pathological calcifications sometimes occurring in the salivary glands. In our previous paper, we reported a 45 mm long sialolith from a submandibular Wharton's duct showing a stratified (banded) structure[1] similar to those observed in sialolith from other salivary glands[2,3]. In general, banded textures in hard tissues indicate that the calcification process occurred by intermittent growth. The banded structure observed in some sialoliths suggest intermittent mineralization [4]. Sialoliths consist of mostly a mineral phase. Like human dental calculus, the mineral phase of sialoliths is usually composed of different calcium phosphates (apatite, whitlockite, octacalcium phosphate), with apatite showing the greatest abundance and occurring in greatest frequency [5, 6, 7]. There is a clinical need for treatment and prevention of sialolithiasis. The purpose of this study is to investigate detailed structural properties of sialolith to gain insight into its formation. For this study, three X-ray diffraction (XRD) analytical techniques, in addition to FTIR, were used to reveal the crystallographic characteristics of the unusually long sialolith: conventional XRD for bulk analysis, micro XRD for point analysis and crystal orientation analysis, and a new technique, "selected-area XRD" for analysis of specific selected areas, having the potential of the data accuracy same to conventional XRD and the spatial resolution of point-analysis similar to that of micro XRD.

Correspondence to Toshiro. Sakae : Nihon University School of Dentistry at Matsudo, Chiba, 271-8587, Japan.Phone: 047-360-9323, FAX 047-360-9324, e-mail:sakae@mascat.nihon-u.ac.jp

Materials and methods

Salivary calculus used in this study was the unusually long sialolith from the submandibular Wharton's duct described in[1]. It is yellowish-white in color, a slightly bent and wedge-shaped cylindrical form with rounded end, 45 mm x 7 mm in size and 1.34 g in weight. The sialolith was cut longitudinally into halves for X-ray diffraction analysis. The sectioned plane showed a stratified texture normal to the long axis under a binocular scope. The histological and microscopic examination indicated that this sialolith was composed of intermittent layers of calcified materials. To investigate the crystallographic character of the sialolith, three kinds of X-ray diffraction analysis were carried out using the following conditions.

Conventional X-ray Diffraction (XRD)

For this powder-type of XRD analysis, data was collected using a RIGAKU RINT 2000, powder-type X-ray diffractometer, RIGAKU Co. Ltd. Tokyo, under the following conditions; X-ray generation: Cu rotary target, accelerating voltage: 50 kV, accelerating current: 200 mA, monochrometer: graphite plate crystal, X-ray wavelength: 1.5418 Angstrom (CuKα), detector: scintillation counter, scan speed: 1 degree (2θ/min), scan range: 3-120 degree (2θ). X-ray data analysis was carried out using JADE (Material Data Inc.), using conventional slit-system. The X-ray radiation area on the sample was 10mm x 20mm at the low angle region.

Micro X-ray Diffraction (Micro-XRD)

Micro-focus X-ray diffraction (micro-XRD) data of the sialolith from a point 100 μm in diameter was collected using a RIGAKU RINT RAPID with IP (imaging plate) system, RIGAKU Co. Ltd. Tokyo. The image data was digitally recorded and directly transferred to a computer. The experimental conditions were as follows; X-ray tube target: Cu, tube voltage: 50 kV, tube current: 30 mA, monochrometer: graphite plate crystal, X-ray wavelength: 1.5418 Angstrom (CuKα), collimator: 100 μm in diameter, Imaging Plate®(IP, Fuji Film Co. Ltd., Tokyo) recording system with IP size: 466 mm x 256 mm, camera radius: 127.4mm, pixel size: 100 μm x 100 μm, sample setting: reflection-mode, exposure time: 20 min. X-ray diffraction IP imaging analysis system: RIGAKU R-AXIS display software.

Selected-Area X-ray Diffraction (SA-XRD)

In this study, another type of micro-XRD analysis was applied. The auto-slit-width-arrange-system, equipped on the RIGAKU RINT 2000, allows a fixed X-ray exposed area on a sample plane at any given scanning angle by controlling the X-ray incident beam width. In this study, the X-ray exposed width was fixed at 1 mm on the sample plane, and then the radiation window area was 1mm width x 10mm length. The other experimental conditions were similar to the conventional XRD measurement. This method that we refer to as "Selected-Area X-ray diffraction" (SA-XRD), has not been used in the investigation of pathological materials. This method has some advantages in data-collection time, accuracy of data and data compatibility with conventional powder XRD method compared with the micro-focus XRD. Applying this method to the specimen, the window area of 1 mm in width was set perpendicular to the longitudinal axis of the sialolith. The unit cell dimensions were calculated using the JADE program.

Micro Fourier Transform Infrared Analysis (Micro FT-IR)

Carbonate and phosphate composition was analyzed using a micro FT-IR, HORIBA FT-530, under the following conditions; measurement mode: reflection, analyzing area: 20x100 μm, detector: MCT (cooling by LN_2), Cassegrain mirror: x4, measurement cycle: 60, resolution: 4cm^{-1}, measurement range: 750-4000 cm^{-1}. The measurements were carried out at the positions where the XRD studies were carried out. The observed raw data was transformed to a pseudo-transmitting absorption spectrum by the Kramers-Krönig analysis.

Results

The long sialolith was divided into three portions namely as the thin head-portion, the body-portion at the middle and the thick tail-portion, for placing the sample in the sample holder (Fig. 1). The sialolith showed a stratified texture on the sectioned plane with a loose concentric pattern. These bands consisted of alternating narrow and wide bands. The wide bands were relatively glossy and transparent, suggesting that relatively large crystals are arranged in an organized manner in contrast with the crystals located in the narrow slightly brownish bands.

The conventional-type XRD patterns of the three portions showed apatite structure (Fig. 2). The conventional XRD patterns showed the diffraction peak broadening which was usually observed in biologic apatites. No other crystalline phase was detected in these patterns.

Micro-XRD IP images of thirty points on the sections of the three portions were obtained. An example of a micro-XRD pattern is shown in Fig. 3. The two-dimensional micro-XRD image clearly showed preferred crystal orientation as the strong 002 circular arc. A series of micro-XRD images of the sialolith showed that there were slight differences in the preferred crystal orientation among the neighboring points. The converted powder pattern of this micro-XRD data (Fig. 4) identified the crystals as apatite.

All the sixty SA-XRD patterns of the sialolith were identified as apatite (Fig. 5). There were small differences in the peak positions among the analyzed areas, indicating possible differences in composition of the apatite. The unit cell dimensions of the apatite crystals are summarized in Table 1. These values were slightly, but significantly, different from each other. The variations in the unit cell dimensions indicated that the crystals in incremental bands slightly differed in chemical composition resulting from changes in the type and amount of substituting ions in the apatite crystal

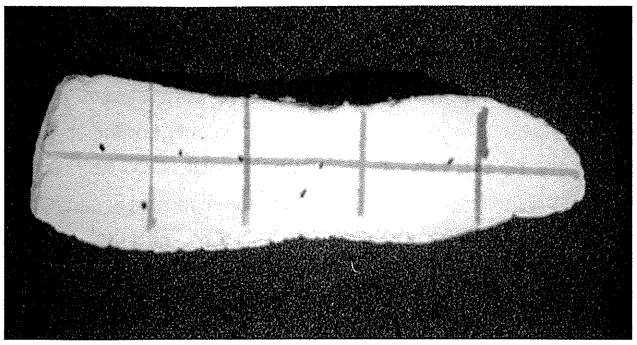

Fig. 1. Photograph of the head-portion section plane of the unusually long sialolith, showing the selected area analysis points at the cross-points of the lines. The tangential axis line also indicated the line of points for the micro XRD analysis.

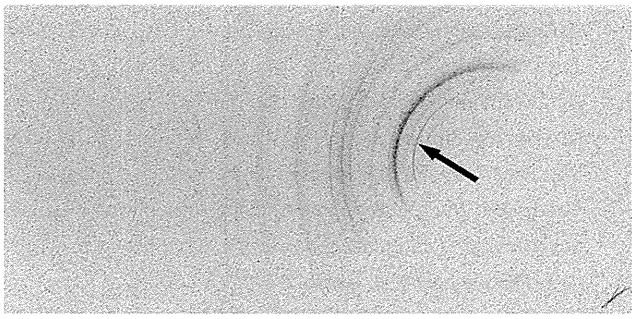

Fig. 3. Micro-XRD IP image from a 100 μm in diameter point on the section of the sialolith. The right portion of the image was hidden by sample holder. The 002 reflection (arrow) showed arcs in stead of the complete diffraction ring, indicating preferred crystal orientation.

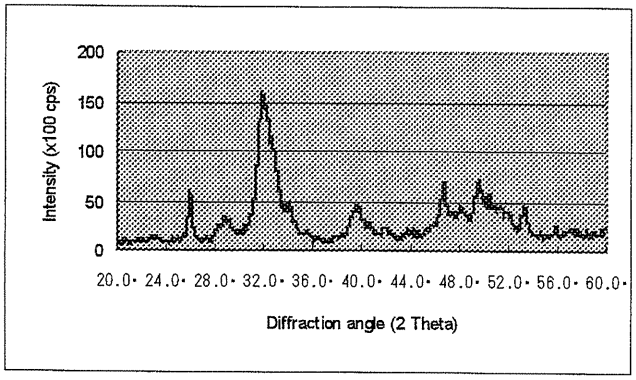

Fig. 5. SA-XRD pattern of the sialolith showing apatite diffraction peaks.

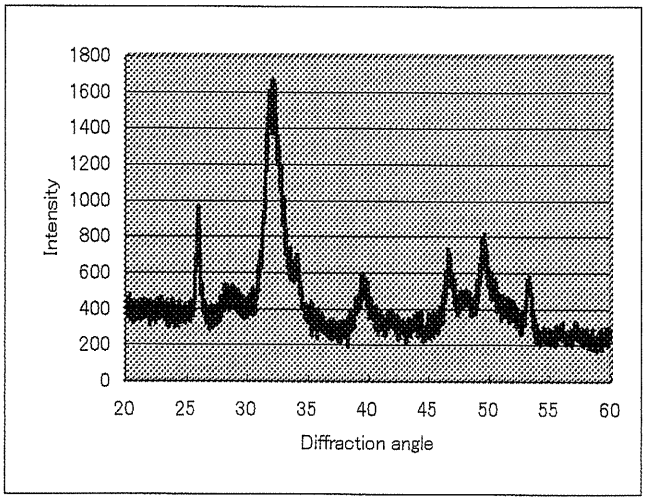

Fig. 2. Conventional XRD pattern of the head-portion section, showing an apatitic diffraction pattern.

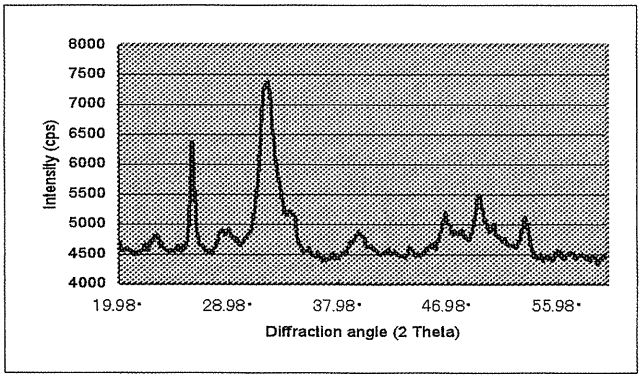

Fig. 4. Converted XRD pattern of the micro-XRD image (Fig. 3) showing the apatite diffraction peaks.

lattice.

The micro FT-IR analysis revealed the main constituent of the sialolith was carbonate apatite, carbonate absorption bands appearing at about 1400 cm^{-1} and 1600 cm^{-1} (Fig. 6).

Discussion

In this study, three types of XRD were applied to reveal the crystallographic characters of the sialolith. The conventional XRD

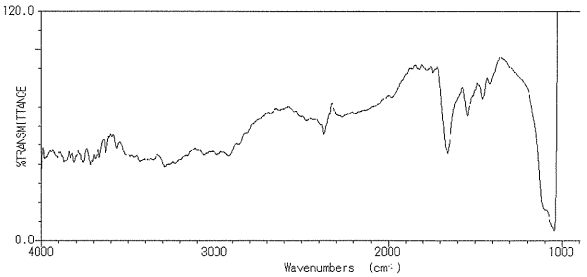

Fig. 6. Micro FT-IR spectrum of the sialolith showing the absorption bands of phosphate ions at about 1050 cm^{-1} and the bands of carbonate ions at about 1450 cm^{-1} and 1550 cm^{-1}.

Table 1. Crystallographic values (unit cell dimenstions) of apatite crystals from different areas of the sialolith analyzed using selected-area XRD.

position No.	a-axis length* (Angstrom)	b-axis length* (Angstrom)
Head 01-1	9.412(11)	6.893(12)
Head 02-1	9.433(16)	6.888(18)
Head 03-1	9.426(25)	6.889(21)
Tail 01-1	9.405(23)	6.903(26)
Tail 01-2	9.430(15)	6.900(12)
Tail 01-3	9.440(22)	6.871(19)
Tail 02-1	9.421(14)	6.886(11)
Tail 03-1	9.431(18)	6.880(13)
Tail 04-1	9.423(10)	6.874(08)

*: The estimated standard deviations were represented in parenthesis.

showed the sialolith being composed of apatite. The micro-XRD showed the preferred crystal orientation in the sialolith. SA-XRD analysis, used for the first time in the analysis of pathological calcifications revealed inhomogeneity in the chemical composition of apatite from layer to layer. The intermittent growth of the apatite crystals was confirmed by crystal orientation analysis.

X-ray diffraction analysis provided information on the crystalline phases present in the sialolith[7, 8]. However, in the present study, the diffraction peaks of the apatite crystals in the sialolith were too broad to allow accurate analysis. Variations in the unit cell dimensions strongly suggested changes in apatite composition, reflecting changes in the environmental condition and composition[7].

Information on the crystalline phase, composition and orientation, could lead to a better understanding of the formation mechanism of sialolith and may provide insights on the appropriate treatment regimen for lithotrypsy[9, 10]

Acknowledgements

The authors thank Professor Isamu Sato, Director of LEBRA (Laboratory for Electron Beam Research and Application), Institute of Quantum Science of the Nihon University, for the opportunity to use the RIGAKU RINT-RAPID and RIGAKU RINT- 2000 X-ray diffraction instruments This study was supported in part by the Frontier Science Project granted from the MECSST, Japan.

References

1. Akimoto Y, Kaneda T, Fujii A, et al. A long submandibular sialolith lying in the Wharton's duct. In: Fuchihata H, ed., Oral and Maxillofacial Radiology Today, Elsevier, 2000; 615-7.
2. Yamamoto H, Sakae T, Takagi M, Otake S. Scanning electron microscopic and X-ray microdiffractometeric studies on sialolith-crystals in human submandibular glands. Acta Pathol Jpn 1984; 34: 47-53.
3. Tohda H, Yamakura K, Yanagisawa T. High-resolution electron microscopic study of salivary calculus. J Electron Microsc (Tokyo) 1995; 44: 399-404.
4. Brady JM, McKinney L, Stanback JS. Scanning electron microscopy of submandibular sialoliths: a preliminary report. Dentomaxillofac Radiol 1989; 18: 42-4.
5. Sakae T, Yamamoto H, Hirai G. Mode of occurrence of brushite and whitlockite in a sialolith. J Dent Res 1981; 60: 842-4.
6. Boskey AL, Burstein LS, Mandel ID. Phospholipids associated with human parotid gland sialoliths. Arch Oral Biol 1983; 28: 655-7.
7. LeGeros RZ. Calcium Phosphates in Oral Biology and Medicine. Basel: Karger, 1991: 130-153.
8. McCONNEL D. Apatite. New York: Springer-Verlag, 1973:111.
9. Iro H, Nitsche N, Meier J et al. Piezoelectric shock wave lithotripsy of salivary gland stones: an in vitro feasibility study. J Lithotr Stone Dis 1991; 3: 211-6.
10. Korago AA, Matina VN, Veroman VIu et al. The composition and structure of salivary calculi (sialoliths) Stomatologiia (Mosk) 1993; 72: 7-12.

グローバル
エンドドンティクス

第3部

PRPの臨床的確認と歯根端切徐術への応用

大久保厚司*1~3／下御領良二*1／山根　進*1／寒河江登士郎*2／小澤幸重*2

*1社団法人日本歯科先端技術研究所
*2日本大学松戸歯学部第２解剖学教室
*3大谷同行会
連絡先：〒857-1151 長崎県佐世保市日宇町695-6 大久保第２ビル２F 日宇歯科・矯正歯科

The Clinical Evaluation of Platelet-Rich Plasma and Application of Apectomy Method to the Origin of Endodontic Lesion

Atsushi Ookubo, Ryouji Shimogoryo, Susumu Yamane, Toshiro Sakae, Yukishige Kozawa

はじめに

歯内由来の根尖病変へのアプローチは，根管の無菌操作と洗浄，緊密充塡を行い，感染源を経年的に遮断することにある．しかし，適格な歯内療法を行っても病変が消失せずに再発する症例にまれに遭遇する．

再発の原因として，根管に由来する管外側枝，歯根亀裂(ヒビ)，セメント質剝離[1]，ならびに根尖部の歯石沈着[2]があげられる．また，細菌や生体に由来する陳旧的に細菌と歯周組織の共生関係が成り立っている場合[3]，および異物由来の抗原に対するT細胞を活性化する抗原提示細胞(樹状細胞)などにより補体系が出現[4]する自己免疫異常がある．

これらはX線像では確定診断は難しく，細菌感染由来であれば，的確な歯内療法や歯根端切除や掻爬などの外科処置を施行すれば，治癒率は高くなるが，自己免疫異常の症例は外科処置を行っても，治癒する可能性は低い．

そこで，本稿では，生体由来による自己免疫異常の可能性があると診断した根尖病変アレルギーⅠ型に対して，より感染がなく，安全で外科臨床で広く行われている多血小板血漿(Platelet-Rich Plasma：以下，PRP)[5~10]を局所埋入する方法と，適正なPRP量の臨床的確認を行う方法について述べる．

1. PRPとは

PRPとは，高濃度の血小板を含んだ自己由来の血漿で，骨髄巨核球の細胞質に由来し，1つの巨核球から2,000～5,000個の血小板が産生される．血小板は，無核で直径１～４μm程度で，その細胞質中に数10個存在するα顆粒から，骨形成に関与するTGF-β(Transforming Growth Factor-β)，間葉系細胞に対し遊走・増殖刺激活性するPDGF(Platelet-Derived Growth Factor)，成長ホルモン依存性に骨発育させるソマトメジンCであるIGF(Insulin Growth Factor)を放出する．PRPは，他にEGF(Epidermal Growth Factor／生理作用が多用因子)，FGF(Fibroblast Growth Factor Family／ヘパリンと親和性があり線維芽細胞や血管新生の増殖促進因子)，PDEGF(Platelet-Derived Endothelial Growth Factor／上皮の成長因子)，セロトニン，ADP，トロンボキサンA_2，止血に関与するフィブリノゲンを放出する．

骨形成に関与するTGF-βスーパーファミリーに属するペプチドには，いずれも約200～400個のアミノ酸からなる前駆体としてつくられた後，C末端側

の110～140個のアミノ酸からなる部分が切断される．この部分は7個のシステイン残基がほとんど共通してみられる活性をもつペプチドとなる．このペプチドは，多くの細胞に強力な増殖抑制因子として作用し，細胞外マトリックスの産生を促進するTGF-β1～3，細胞分化に関与するアクチビンとインヒビン，骨や軟骨の形成を促進するBMP2～4，BMP5～8，GDF5～7（BMP2，6は骨化，BMP12，13は軟骨化），ミュラー管抑制因子やミオスタチンを含む[11]．

TGF-βとPDGFは，インターロイキン1，6，8と同様に炎症性サイトカインにも分類されているので，正常組織に応用すれば骨形成に進む．ところが，炎症組織では，拡炎する可能性があるので，不良肉芽は完全に除去し，健康骨を露出させて埋入する必要性がある．

骨および軟組織で治癒を促進するためには，PRP量を1,000,000/5mLとしている．それより高い濃度では骨造成が進み，以下の濃度では治癒促進が遅れるとしている[8]．しかし，十分なPRP量を凝集する方法がなく，臨床応用の際にPRP量が確認されていなかったために，骨造成率にはばらつきがある．

PRPの利点としては，
①術式が簡便，②自己組織応用のため安全，③フィブリンによる付着力・弾力に富む，④歯根表面への生物学的適応性が高い，⑤成長因子を含む，⑥血管新生作用がある，⑦骨伝導能がある，⑧止血作用がある，⑨白血球が高濃度に含まれるため抗感染作用がある，⑩創傷治癒効果が得られる，
ことなどである．

PRPの効果をMarx REらは，6か月の単独での海面骨移植より，併用のほうが骨形成量が20%増加し，骨形成の早さが2倍になる[8]と報告している．血小板の寿命は7～14日であること，抽出したPRPは約7～10日でその発現を終え，手術部にさらなるPRPが流出する要因が少ないことなどから，初期のジャンプスタートとしての役割をもつと考えられる．われわれの動物実験では，5週間で約13%の造成率をみたが，それ以上の長期観察は行っていない．しかし，初期の感染や免疫応答に関与する抗原提示細胞が分化して，B，T，NK細胞や好中球，マクロファージなどの出現をPRPで制御する可能性があるので，創傷治癒の初期段階のはたらきは行えるものと考える．

2．PRPの精製抽出法

PRP抽出には種々の機器が販売されており，3～5倍の濃縮が可能である．市販されているPRP抽出キットの問題点は，シリコン類のシリンジ，フィルター，チューブが数多く使われること，わずかではあるが体内に戻す際に，内分泌撹乱[12]の可能性が拭いきれないこと，操作が複雑であること，機器やキット価格が高いことなどがあげられる．

われわれは，操作をより簡便化し，価格も数百円と安価で，無菌ガラス製品2個とフィルターを使うだけの以下の方法で抽出している．

1）PRPの抽出方法（*図1a*）

①②：あらかじめ抗凝固剤として，3.8%クエン酸ナトリウム0.5mL（東亜薬品工業株式会社，診断用クエン酸ナトリウム液）を注入したシリコンコーティングをしていない滅菌真空ガラス採血管10mL用（VACUTAINER Brand Tube for Determinations Requiring serum10m Draw：テクノ鈴田社製）に8mL静脈血を採血する．
③：遠心器CN-1040（回転数0～4,000rpm，最大遠心力1,880G，井内盛栄堂社製）を用いて1,200rpm（160G）で10分間遠心分離する．
④：血球層との境界より2mL残存させた状態で，採血管上部のクエン酸ナトリウムとPPP（Platelet-Poor Plasma）を，テルモシリンジγ線滅菌済ラテックスフリー2.5mLに，γ線滅菌済みニプロカテラン針18G×70RBのシリンジで，取り除いた．
⑤：さらに1,600rpmで5分間遠心分離して血球境界上方のPRPを1.2mL採取する．PRP抽出に際して遠心力110～160Gは，PRPの形態変化を行わない最適な遠心力である．この遠心力は，$G=11.18\times10^{-6}\times r\times n^2\times G$（r：回転半径，n：回転数）の式[13]で求めることができる．

健常者の血小板数は150,000～350,000/mLである．骨形成に有効な濃縮量をMarksらは，それから約3倍多い1,000,000/5mL[8]としているが，臨床では患者の体調や血液比重などによりPRP量が不確定に抽

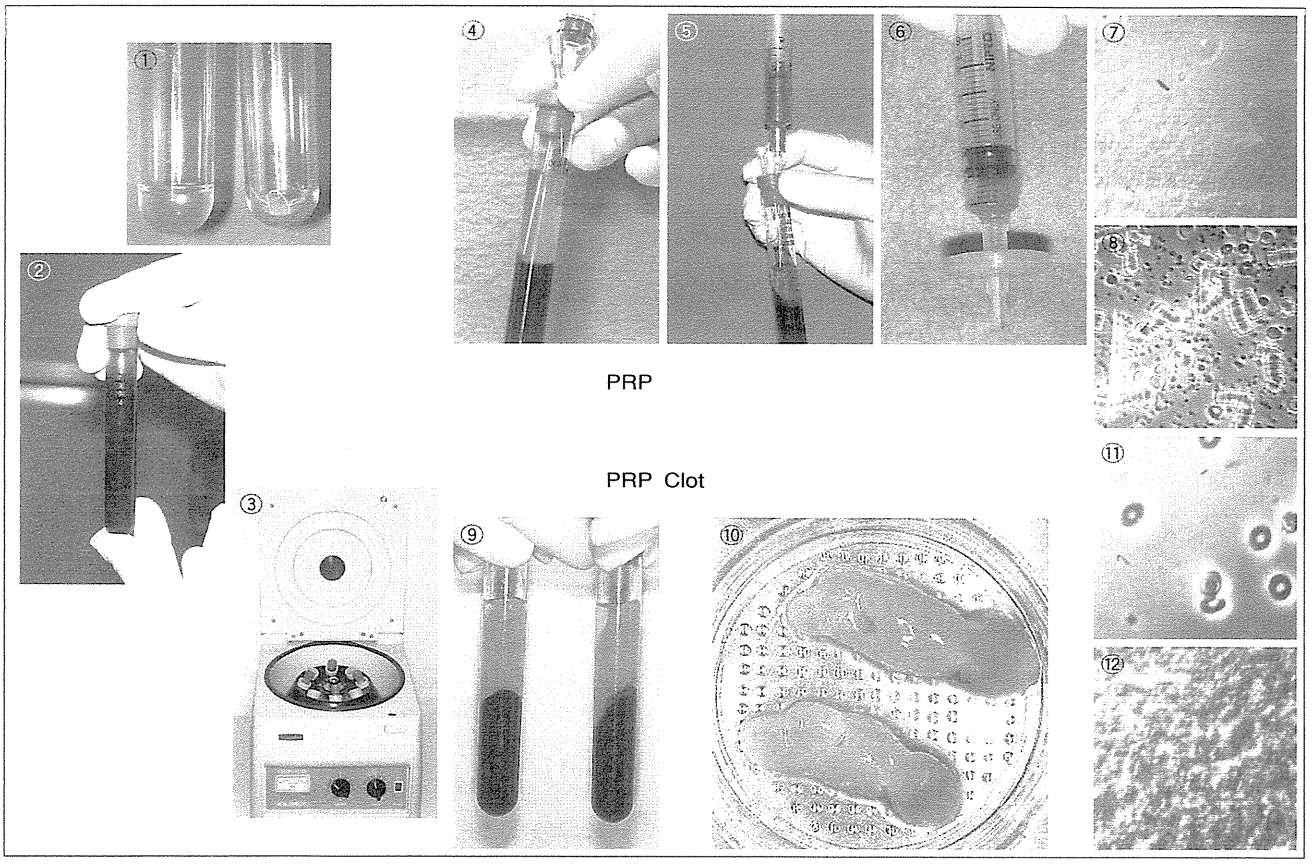

図1a PRPとPRP Clotの抽出法．①3.8%クエン酸ナトリウム0.5cc．②採血．③CN-1040．④1,200rpm/10min．⑤1,600rpm/ 5 min．⑥抽出PRP溶液をさらにフィルターで凝集．⑦PPP．⑧塩化カリウムの代わりにCHA注入．1,200,000/μL．⑨1,600rpm/10min．⑩PRP Clot．⑪PPP．⑫PRP Clot．*PRPの器材についての問合先：テクノ鈴田(0956-28-4305)

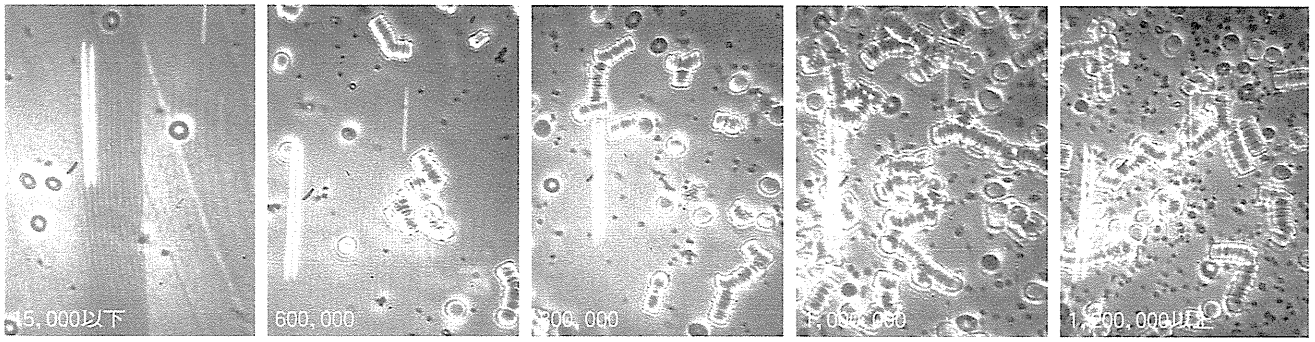

図1b 位相差顕微鏡によるPRP量の確認(検査PRP量＝23G注射針１滴)．他項目自動血球係数装置K-2000(Sysmex社)を用いて，電気抵抗法で測定したPRP溶液を位相差顕微鏡で比較観察し，PRP量を視認的に臨床応用の目安にする．PRP量が少なければ，骨造成率は期待できず，ゲル化しない．100万を超えるPRP量が得られれば，トロンビンを加えなくともゲル化することができ，骨造成率は13～20%増加すると考える．

出されるために，骨造成率に議論があったと考える．

PRP量測定の確実な方法は目視法を用いるが，他に他項目自動血球係数装置K-4500(Sysmex社)を用いて電気抵抗法で測定することもある(*図1b*)．しかし，遠心操作によるマイクロパーティクルの出現，血小板数の直線性範囲外であること，また，高回転の遠心力やEDTA以外の抗凝固剤による血小板サイズの変化に留意する必要がある．手術中に早急を要する場合は，抽出したPRP１滴を位相差顕微鏡でカウントして全体像としてとらえ，有効なPRPの濃縮が十分なされていることを視認的に確認することが重要である．

⑥⑦：抽出したPRP溶液の濃縮が不十分な場合や骨造成材を併用する場合に必要量のPRPを濃縮するために0.45μmメッシュ状のフィルター(東洋濾紙，DISMIC 03CPO45AS)もしくは0.2μmメッシュ状の

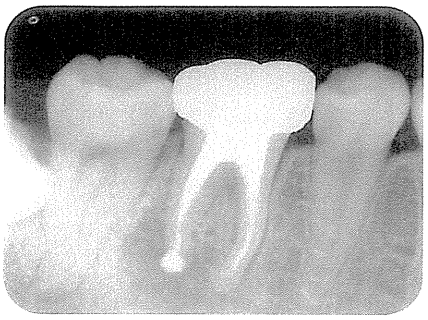

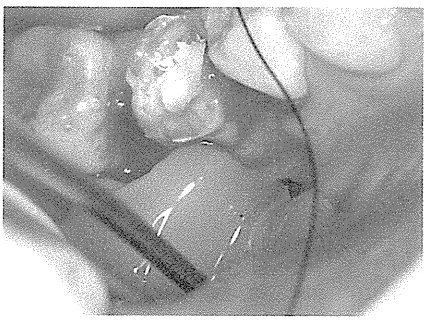

図2 | 図3
図4 | 図5

図2　右側顎下リンパ節の腫脹を伴う急性歯槽膿瘍にて来院．近心根，遠心根周囲骨の透過像を認める．問診では根充後８年経過．遠心根尖からガッタパーチャの溢出部の吸収もなく，根尖部に補体系が出現していると考える．
図3～5　根尖から約２㎜を歯根端切除術．ならびに根尖部膿胞摘出手術を行う．この時PRPを顎骨内に，PRP Clotを頬側開窓部に自己由来の生体膜として埋入する．

フィルター（東洋濾紙，DISMIC 13CPO20AS）でPPPを排出し，さらに残留した溶液からPRPの濃縮を行う．

⑧：手術移植部に埋入する際に，ゲル化させるには，塩化カルシウムを混入し，中和させる．トロンビンは牛由来であるために使用せず，血中の自己トロンビンにて凝固させる．

また，PRP溶液１mLに対して中和を目的として塩化カルシウムの代わりに，われわれが研究してきたカーボネイトアパタイト[11]を0.2g/mL量入れ，10分ほど経過させると，トロンビンを混入させることなく，ゲル化をする．骨置換材料であるカーボネイトアパタイトは，飛躍的に骨造性率を高くする．

２）PRP Clotの抽出法

⑨：PRP Clotの作製にはテクノ鈴田社製10mLガラス試験管で８cc静脈血を採取し，1,600rpm（170G）で10分間遠心分離する．

⑩：血小板は空気に触れると，フィブリンにより線維性結合反応を起こし，内部は血漿も多く含まれた状態でゲル化する．このなかには生体維持に必要なタンパクも混在していること，PRP Clotはゲル状で時間経過とともに内容物の血漿が浸透する．

⑪⑫：PRP Clotは生体膜やスペースメイキングとして使用することが可能であり，自己生体由来であるので露出しても感染の心配はなく，手術による侵襲は最小で抑えられて治癒創傷が得られる．

3．臨床応用

以下に，歯根端切除術症例に埋入したPRPならびにPRP Clotの経過を報告する．

１）初診時

患者：24歳，女性．
初診：2001年11月12日．
主訴：6|の疼痛を伴う右下頬部の腫脹にて来院．
一般歴：アレルギー性鼻炎，じんましん，鉄欠乏性貧血．
現病歴：1988年と1993年に根管治療の既往．
現症：6|遠心根尖からオブチュレーションの溢出と周囲組織にX線透過像を認め，近心根尖部もX線透過像を認めた．自発痛（＋＋），咬合痛（＋＋），誘発痛（＋＋＋），歯肉の発赤（＋），腫脹（＋＋＋），リンパ節の軽度の腫脹（＋＋），動揺度（M２）．

歯周情報として6|のプロービングデプスは２mmと健康な歯周付着を保ち，歯周ポケット部に歯石やセメント質の剝離は認められなかった．
当医院における臨床診断名：急性根尖性歯周膿瘍．根尖病変のアレルギーⅠ型．

図6 術後5か月．X線所見では通常の歯根端切除術後の根尖部の骨改造現象による不透過性に比べて早く骨造成しているように思える．

図7 術後10か月のX線所見．歯槽白線の再現を認める．

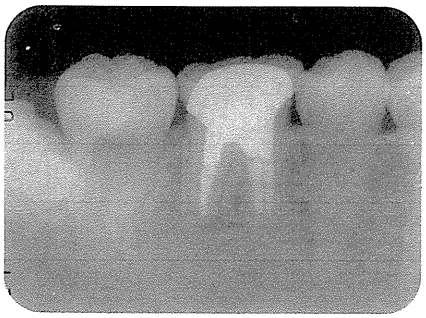

図8 術後24か月のX線所見．根尖周囲および嚢胞の存在した部分は骨梁の改造現象様の所見を認める．

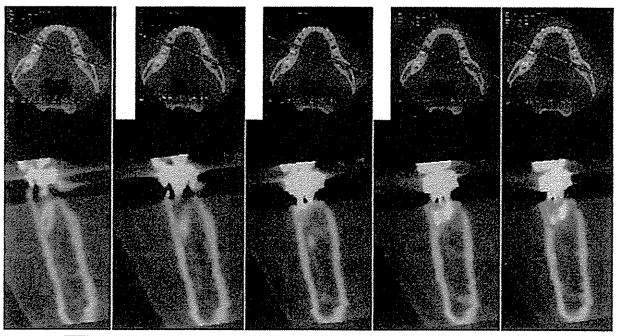

図9 $\overline{6}$の近心根から分岐部にかけてのマイクロCT(sagittal)．近心根から根分岐部までのサジタル方向のマイクロCT像では根尖部から根分岐部まで外側皮質骨に覆われており，根尖病変が存在した部分は，骨改造現象がすすみ海面骨が形成され，根尖病変の消失と歯根をとりまく緻密骨の形成を認める．

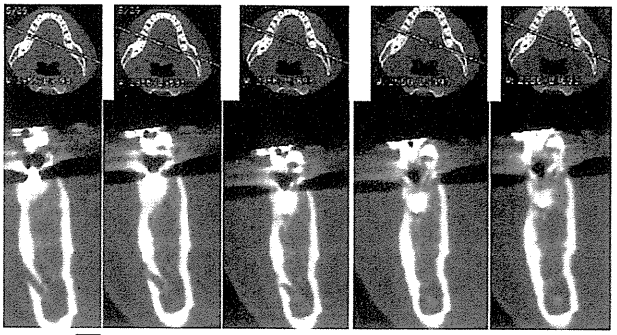

図10 $\overline{6}$の分岐部から遠心根にかけてのマイクロCT(sagittal)．根分岐部から遠心根尖にかけてサジタル方向のマイクロCTでは根尖病変の消失と歯根を取り巻く外皮質骨の形成を認める．分岐部は外側皮質骨で覆われているが，遠心根の根尖部にわずかに海綿様骨を認める．術後24か月経過するが，根尖病変が存在した部分は，骨改造現象が進み，海綿骨が形成され，臨床症状はなく順調な予後を得る．

通常，根尖より溢出したオブチュレーションガッタ(以下OG)は，X線透過像が収縮した後に，吸収機構に入るが，当患者は，根尖孔より溢出したOGは根管充填後約8年経過しても吸収していないこと，また，アレルギー性鼻炎，一部のじんましんなどの現症はアナフィラキシー型のⅠ型アレルギーであり，根尖部にも樹状細胞により分化したT細胞，β細胞，マクロファージ，好中球，肥満細胞が存在し，IgEの免疫グロブリンの上昇による継続する補体系の発現[15,16]が示唆され，根尖部病変は外科処置なくしては拡大すると考える(*図2*)．

2)治療経過

● 1回目

2001年11月12日，$\overline{6}$の根管治療開始．クラウンとメタルコアを除去．ガッタパーチャ除去後に根管治療を行う．根尖部にファイルで到達すると，根管内より出血と排膿を認めた．抗生物質(ケフレックス250mg×3回／日，4日分)と消炎鎮痛剤(ボルタレン25mg・疼痛時服用)の投与．

● 2回目

2001年11月21日，$\overline{6}$の根管治療．動揺度(M1)と他の臨床症状は消失．ラバーダム防湿．H_2O_2と滅菌水で根管洗浄，根管形成，綿球にてFC貼薬，ZOE仮封．

● 3回目

2001年11月29日，$\overline{6}$の臨床症状なし．開封後に滅菌水で根管洗浄，エンドサクションで乾燥後，OGを加熱軟化させT. L. C. Brasselerにて根管充填[15]，仮封．歯根端切除術と根尖病変の摘出，根尖周囲掻爬ならびに硬組織の一層除去して健康骨面を露出させた．さらに根尖部骨欠損部にPRP Clot，ならびにPRPの注入(PRPの精製には前述した方法を用いた*図3～5*)．

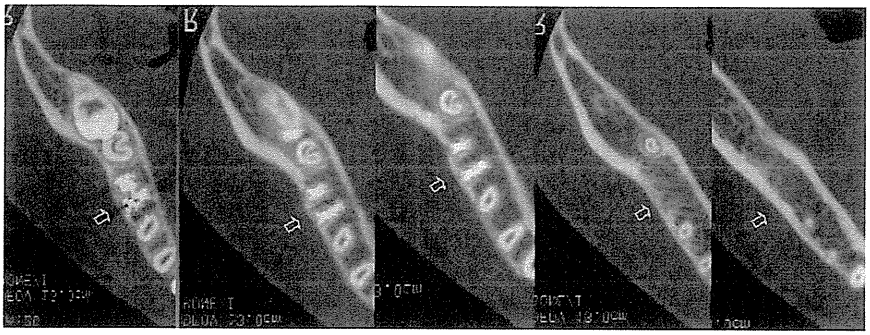

図11　6|の歯頸部から根尖にかけてのマイクロCT(horizontal)．ホリゾンタル方向のマイクロCTによる根尖病変の消失と歯根をとりまく緻密骨の形成を認める．膿胞の存在した根尖部，根分岐部および根尖側下方の下顎骨はすべて海面骨の再生を認める．

3)予後

●2002年１月17日，術後約２か月特記すべき臨床症状なし．根尖周囲組織のX線透過像のわずかな縮小を認める．

●1996年11月１日，特記すべき臨床症状なし．メタルクラウン装着．

●2002年４月18日，術後約５か月．根尖周囲組織のX線透過像の縮小を認める(*図6*)．

●2003年11月28日，術後約24か月(*図8*)．特記すべき臨床症状なし．根尖周囲組織のX線透過像の消失とCTにて根尖部の正常な骨の改造現象像を認める(*図9～11*)．

4．まとめ

根尖病変のⅠ型アレルギー反応に対して，歯根端掻爬や歯根端切除術を試行する場合に，自己採血であるPRP Clotや凝集したPRPは，免疫学的，組織工学的に安全である．その発現が初期の７～10日までは有効に補体系の産生を阻止し，同時にスペースメイキングや微少血管系の新生が可能で，継続する骨改造現象をスムーズに行わせて，骨造成率を増加させる可能性がある．根尖病変のⅠ型やⅡ型アレルギーに対して外科処置を行う場合は，PRPやPRP Clotを埋入することも１つの方法であると考えられる．

参考文献

1．横浜歯科臨床座談会分科会，丸森英史他：セメント質剝離の臨床像と考察，歯周病の一因として．歯界展望，97(６)：1173-1198，2001.

2．戸村二郎，小林千尋，須田英明：根尖歯石の話．日歯内療誌，18(１)：52-56，1997.

3．小林千尋：歯外療法のすすめ．日歯内療誌，18(１)：６-11，1997.

4．庄司茂：歯周疾患，外傷性咬合はどのように関与するのか？．日歯内療誌，16(１)：131-134，1995.

5．Jakse N, Tangl S, Gilli R, Berghold A, Lorenzoni M, Eskici A, Haas R, Pertl C:Influence of PRP on autogenous sinus grafts. An experimental study on sheep. Clin Oral Implants Res, 14(５)：578-583，2003.

6．Della Valle A, Sammartino G, Marenzi G, Tia M, Espedito di Lauro A, Ferrari F, Lo Muzio L：Prevention of postoperative bleeding in anticoagulated patients undergoing oral surgery：use of platelet-rich plasma gel. Oral Maxillofac Surg, 61(11)：1275-1278，2003.

7．Sanchez AR, Sheridan PJ, Kupp LI：Is platelet-rich plasma the perfect enhancement factor? A current review. Int J Oral Maxillofac Implants, 18(１)：93-103，2003.

8．Marx RE：Platelet-rich plasma(PRP)，what is PRP and what is not PRP?. Implant Dent, 10(４)：225-228，2001.

9．Marx RE, Garg AK:A novel aid to elevation of the sinus membrane for the sinus lift procedure. Implant Dent, 11(３)：268-271，2002.

10．山根進，小田亮，樋口勝規，下御領良二，田中悟，松江正芳，上野徹，中根高信：多血小板血漿(PRP)の精製法についての検討．日口腔インプラント誌，16(１)：77-83，2003.

11．宮園浩平，管村和夫編：サイトカイン・増殖因子．第３章増殖因子，第４章TGF-βスーパーファミリィ．羊土社：80-163，2000.

12．実験医学別冊：クローズアップ実験法，総集編．羊土社，2002.

13．日本生化学会編：続生化学実験講座８血液(下)．830-839，1987.

14．Sakae T, Ookubo A, Racquel Z, LeGeros：Shimogoryou R, Sato Y, Lin S, Yamamoto H, Kozawa Y：Bone Formation Induced by Several Carbonate-and Fluoride-Containing Apatite Implanted in Dog Mandible. Bioceramics, 15：395-398，2003.

15．大久保堯司，辻本恭久，三島弘幸：糖尿病により口腔インプラント長期経過に伴い撤去に至った一症例―全身疾患の発症と増悪を予知するための血液検査の必要性．日歯先技研会誌，８(２)：64-69，2002.

16．大久保堯司，三島弘幸，小澤幸重：管理された糖尿病患者の上顎インプラントの長期経過観察．日歯先技研会誌，８(４)：173-180，2002.

17．大久保堯司，辻本恭久，鈴木久仁博：下顎大臼歯の歯内，歯周病変Ⅰ型の根管治療．日歯内療誌，23(１)：61-68，2002.

Int J Oral-Med Sci 2(1):50-53, 2004

Case Report

An Unusually Large Submandibular Salivary Calculus: Case Report and Structural Analysis

Yoshiaki Akimoto,[1] Toshiro Sakae,[2] Chie Toyoda,[1] Makiko Ono,[1] Kazuhiro Hasegawa,[1] Shigeo Tanaka,[1] Jun Shibutani,[1] Takashi Kaneda,[3] Takeshi Maeda,[4] Teruyasu Hirayama,[4] Akira Fujii,[5] Hirotsugu Yamamoto,[6] and Racquel Z LeGeros[7]

Departments of [1]Oral Surgery, [2]Anatomy, [3]Radiology, [4]Neurological Surgery, [5]Pharmacology, and [6]Pathology, Nihon University School of Dentistry at Matsudo, Matsudo, Chiba 271-8587, Japan
[7]Department of Biomaterials and Biomimetics, New York University College of Dentistry, New York, NY, USA

Correspondence to: Yoshiaki Akimoto
E-mail: yoshi@mascat.nihon-u.ac.jp

Key words:
large calculus, submandibular duct, structural properties, X-ray diffraction

Abstract

We present a case involving an unusually large calculus of Wharton's duct. To gain insight into the formation of this calculus, detailed structural properties were investigated using an X-ray diffraction technique. A 70-year old man, brought a calculus to a dental consultation, by himself, when it perforated the floor of the mouth. The calculus was unusually long, measuring 4.5 cm in length. X-ray diffraction and micro-FT-IR analyses were employed to investigate structural properties of the calculus, which suggested that its stratified structure, reflecting compositional changes in the microenvironment, was a result of intermittent and incremental growth.

Introduction

Sialolithiasis accounts for more than 50% of diseases of the major salivary glands and is thus the most common cause of acute and chronic infections at these sites. More than 80% of calculi occur in the submandibular gland or its duct, 6% in the parotid gland and 2% in the sublingual gland or minor salivary glands (1). Sialolithiasis in the submandibular gland or its duct can cause symptoms, consisting of pain or discomfort before or during meals, or can be asymptomatic. Associated recurrent submandibular swelling is often described. Clinically, calculi are round or ovoid, rough or smooth, and are of a yellowish color, varying in size from a few millimeters up to several centimeters, although such large calculi are rare (2,3). The calculus described in the present report is of interest owing to its size and shape, particularly as it was removed by the patient himself. In order to gain insight into the formation of this sialolith, detailed structural properties were determined using X-ray diffraction analysis and micro fourier transform infrared analysis (Micro FT-IR).

Case Report

A 70-year-old man visited a dental practitioner requesting new dentures, and gave a history of intermittent swelling and pain in the right submandibular region during meals for the previous 5 years. Oral examination showed a swelling of the right sublingual region. Bimanual palpation of the oral floor indicated the swelling to be a mass that was hard, smooth and painless, and measured approximately 3 cm in length. The overlying mucosa was normal in color. Panoramic radiography revealed a single, well-defined, homogenous radiopaque mass in the floor of the mouth, extending from the mandibular canine area to the mandibular angle (Fig. 1). A diagnosis of submandibular sialolithiasis was made and the dentist recommended examination by an oral surgeon. However, three weeks after the dental consultation, before the patient had attended the referral appointment, the tip of calculus perforated through the floor of the mouth. The patient removed the calculus by himself and brought it to the dentist and to our hospital. The calculus was long and tapered in shape, yellowish white in color, 4.5 x 0.7 cm in length and width, and 1.34 g in dry weight (Fig.

Fig.1. Panoramic radiograph showing a long radiopacity superimposed over the right mandibular cuspid area and the mandibular angle region.

2). Panoramic radiography at this point revealed that the calculus had been removed in its entirety (Fig. 3). Compared to that of the other side, the affected submandibular gland was noted to smaller and harder after calculus removal because of atrophy and fibrosis; however, salivary secretion was unimpeded and the patient had no complaints. Subsequent follow-up over three years was uneventful.

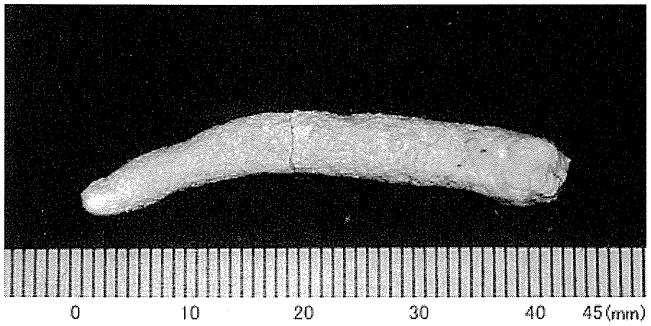

Fig. 2. A 4.5-cm long calculus shown to scale. The right side of the calculus was exposed within the oral floor.

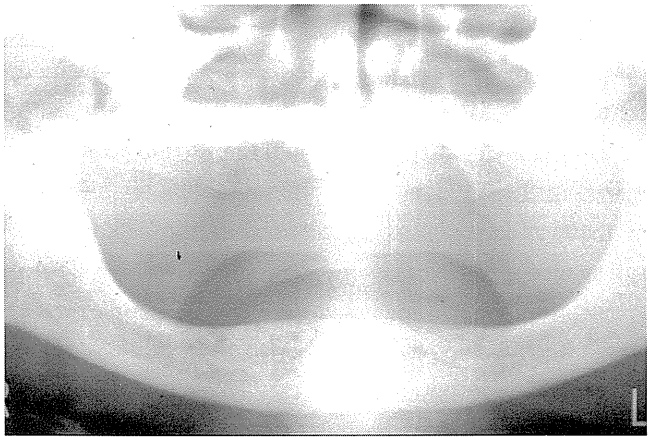

Fig. 3. Panoramic radiograph after removal of calculus by the patient showing no radiopacity.

Analysis of the Calculus

In order to gain insight into the formation of this calculus, its detailed structural properties were investigated. Three X-ray diffraction (XRD) analytical techniques were employed to reveal the crystallographic characteristics of the calculus: conventional XRD for bulk analysis, micro-XRD for point analysis and crystal orientation analysis, and selected-area XRD (SA-XRD) for analysis of specific selected regions. This combination of modalities, has the potential to achieve the data accuracy of conventional XRD and a spatial resolution for point-analysis similar to that of micro XRD(4). Micro fourier transform infrared analysis (Micro FT-IR) was also used to reveal carbonate and phosphate composition.

Conventional XRD patterns demonstrated the structure and diffraction peak broadening usually observed in biologic apatite (Fig. 4). No other crystalline phase was detected in this analysis.

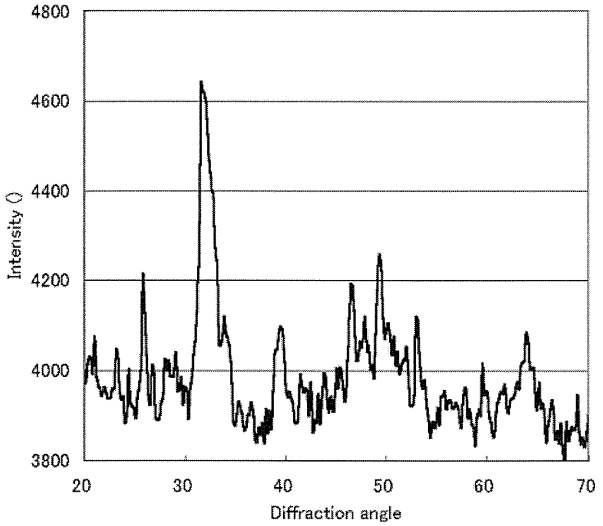

Fig. 4. Conventional XRD pattern showing a diffraction pattern consistent with apatite.

A series of micro-XRD images of the calculus revealed slight differences in the preferred crystal orientation among neighboring points and conversion of this micro-XRD data to determine powder pattern identified the crystals as apatite (Fig. 5a, b).

All 60 SA-XRD patterns of the calculus were consistent with apatite (Fig. 6); however, small differences in peak

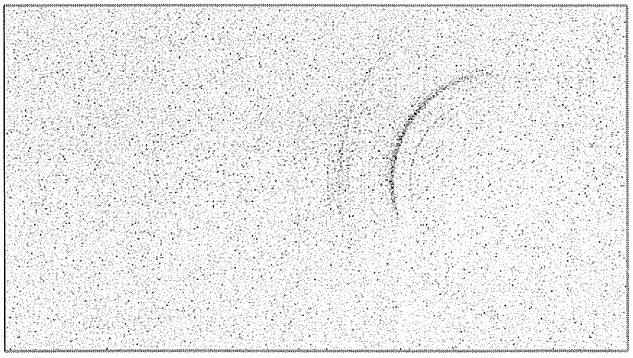

Fig. 5a. The micro-diffractogram recorded on an imaging plate.

positions were noted within the analyzed area, indicating possible differences in composition of the apatite.

Micro-FT-IR analysis revealed the main constituent of the calculus to be carbonate hydroxyapatite, with carbonate absorption bands appearing at around 1,400 cm^{-1} and 1,600 cm^{-1} (Fig. 7).

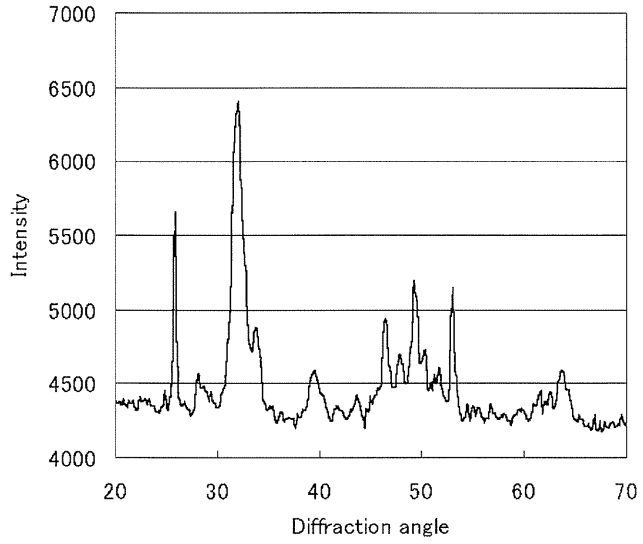

Fig. 5b. The diffraction pattern converted from Figure 5a.

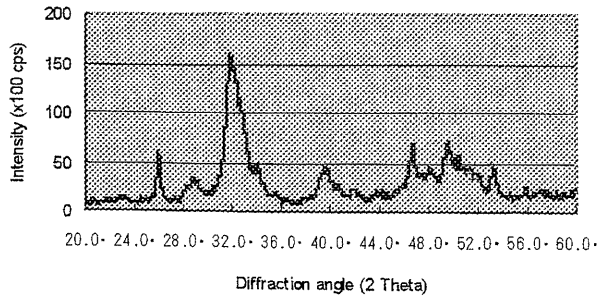

Fig. 6. SA-XRD pattern of the calculus showing apatite diffraction peaks.

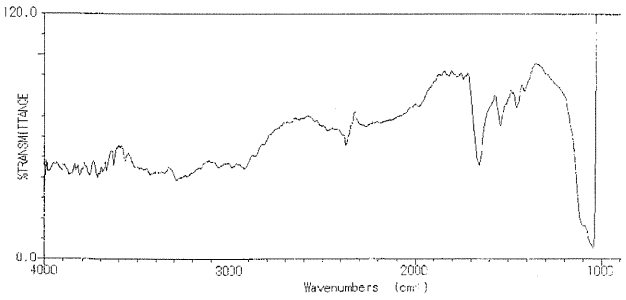

Fig. 7. Micro FT-IR spectrum of the sialolith showing the absorption bands of phosphate ions at about 1050 cm^{-1} and the bands of carbonate ions at about 1450 cm^{-1} and 1550 cm^{-1}.

Table 1. Review of literature reports of calculus measuring 4 cm or more in the submandibular gland or duct

Author	Age	Sex	Size (cm)	Weight (g)[1]
Martin (5)	60	M	6 x 1.5	-
Mustard(6)	42	M	5.6	-
Raksin (7)	52	M	5.5 x 2	9.5
Hubar (8)	65	M	5.2	17.5
Eiraku[2]	56	M	5.1 x 1.1	3.5
Koshal (9)	40	M	5.0 x 2.8	-
Meyers (10)	50	M	5 x 3.0	2.8
Tinsley (11)	48	M	5	23.56
Present case	70	M	4.5 x 0.7	1.34

[1] Dry or wet weight.
[2] Abstract of 53rd Annual Meeting of Japanese Stomatological Society, Eiraku D et al.: A case of large intraductal sialolith, No. 1-F-53, 1999.

Discussion

Reports of large calculi (measuring 4 cm or more in length) within the submandibular gland or its duct are summarized in Table 1. In all cases, patients were males aged over 40 (5-11). Martin *et al.* (5) reported the largest calculus (length, 6 cm), with the present case (4.5 cm) ranking 9th in size. Calculus shape was cylindrical except in the cases reported by Koshal *et al.* and Tinsley, in which oval calculi were identified (6,11). The present case represents the only report in which the calculus was not surgically extracted. Since the calculus was long and extremely narrow in shape and its tip happened to perforate the anterior part of the floor of the mouth, the patient could easily pull it out. Although a perforation of the floor of the mouth is more likely occur in cases of anterior ductal calculus than in those involving the posterior duct (12-14), it is very rare for patients to remove calculi by themselves.

Three types of XRD were employed to reveal the crystallographic characteristics of the calculus. Conventional XRD, showed the sialolith to be composed of apatite, micro-XRD demonstrated the preferred crystal orientation, and SA-XRD revealed inhomogeneity in the chemical composition from layer to layer. Intermittent growth of the apatite crystals was confirmed by crystal orientation analysis.

X-ray diffraction analysis provided information on the crystal-line phases present in the sialolith (15,16). However, diffraction peaks of the apatite crystals in the calculus were

too broad to allow accurate analysis. Variations in unit cell dimensions strongly suggested changes in apatite composition, reflecting alterations in micro environmental conditions and composition of the calculus (16).

Detailed investigations of crystalline structure are not generally performed when patients with sialolithiasis; however, we believe that analysis of crystalline phase, composition, and orientation could lead to a better understanding of the formation mechanism of calculus.

References

1. Zenk J, Benzel W, Iro H: New modalities in the management of human Sialolithiasis. Minimal Invasive Therap, 3:275-284, 1994.
2. Waal I, Kwast WAM. Oral Pathology. In: Salivary gland diseases, Sialolithiasis, 1st ed, 1988, Quintessence Pub, Chicago, USA p. 254-255.
3. Fuchihata H. Oral and Maxillofacial Radiology Today. In: Akimoto Y, Sakae T, Kaneda T et al., A long submandibular sialolith lying in the Wharton's duct, Elservier, Amsterdam, Netherlands, 2000. p. 615-617.
4. Sakae T, Akimoto Y, Kaneda T et al.: Intermittent crystal growth of unusually long submandibular sialolith revealed by micro-focus- and selected-area- X-ray Diffraction. J Hard Tissue Biol, 12:25-28, 2003.
5. Martin PA, Alonso T JL, Wscapa GJ, Capa F: Giant calculus of the submaxillary gland. Acta Otorrinolaringo Esp, 41:265-267, 1990.
6. Mustard TA: Calculus of unusual size in Wharton's duct.. Br Dent J, 79:129, 1945.
7. Raksin SZ, Could ST, Williams AC: Submandibular duct sialolith of unusual size and shape. J Oral Surg, 33:142-145, 1975.
8. Hubar JS, Guggenheimer J, Evan M: Megalith. Oral Surg Oral Med Oral Pathol, 70: 245,1990.
9. Koshal KD, Naik RS: Giant submaxillary sialolith. J Ind Med Assoc, 77:14-15, 1981.
10. Meyers H: Large salivary calculus in submaxillary gland. Dent Dig, 48:420-421, 1942.
11. Tinsley G: An extraordinarily large asymptomatic submandibular salivary calculus. Br Dent J, 166:199, 1989.
12 El Deeb M, Holte N, Gorlin RJ: Submandibular salivary gland sialoliths perforated through the oral floor. Oral Surg, 51:134-139, 1981.
13. Paul D, Chauhan SR: Salivary megalith with a sialo-cutaneous and sialo-oral fistula: a case report. J Laryngol Otol, 109:767-769, 1995.
14. Sutay S, Erdag TK, Ikiz AO, Guneri EA: Large submandibular gland calculus with perforation of the floor of the mouth: Otolaryngol Head Neck Surg, 128:587-588, 2003.
15. Boskey AL, Burstein LS, Mandel ID: Phospholipids associated with human parotid gland sialoliths. Arch Oral Biol, 28:655-657, 1983.
16. LeGeros RZ: Oral Biology and Medicine, Calcium phosphates, 1991. Karger, Basel, Switzerland

<原　著>

Enhanced Gene Expression by Low-Level Laser Irradiation in Osteoblast

——Identification of Annexin III Gene by Subtractive Gene Cloning——

Masahisa Yamamoto[1], Mitsuaki Kawahara[1] and Yoshimitsu Abiko[1,2]

低出力レーザー照射による骨芽細胞の遺伝子発現の変動

——その1　遺伝子差分化法によるAnnexin III 遺伝子の同定——

山本　雅久[1]　河原　三明[1]　安孫子宜光[1,2]

The recent advent of improved low-level laser irradiation (LLLI) therapy has promoted interest in clinical implantology. It has been reported that LLLI on bony implant sites might have positive effects on the integration of implants. The biostimulatory effect of cell proliferation and bone formation by LLLI has been investigated, but little is known about the molecular basis of biostimulatory mechanisms. Since LLLI will be useful to support implant therapy, it is important to elucidate the mechanism of the biostimulatory effect of LLLI on bone formation.

We previously constructed the cDNA library of mouse osteoblastic cells (MC 3 T 3-E 1), which enhanced gene expression by LLLI using a subtracted gene cloning technology. In the present study, we further analyzed the DNA nucleotide sequence of gene clones, and focused on a gene clone designated MCL-174. The nucleotide sequence of MCL-174 insert was determined and assessed in the standard nucleotide-nucleotide BLAST (blastn) homology-search using NCBI DNA databases. DNA nucleotide sequences of clone MCL-174 inserted DNA exhibited 99% homology with *Mus musculus* annexin III gene. Reverse-transcription PCR analysis showed that the mRNA level was enhanced by LLLI. These findings suggest that LLLI may enhance mRNA transcription and play a role in stimulating proliferation of osteoblasts through the enhancement of annexin III gene expression. Annexin III was detected in secretory ameloblasts and odontoblasts, and it was thought to be involved in the regulation of cell calcium. These findings suggest that the biostimulatory effect of LLLI on bone formation may relate through gene expression of annexin III.

Key words : *osteoblast, low-level laser, nucleotide sequence, annexin III, gene expression*

[1] 日本大学松戸歯学部生化学教室（主任：安孫子宜光教授）
[2] 日本大学松戸歯学部口腔科学研究所（所長：笹原廣重教授）
[1] Department of Biochemistry, Nihon University School of Dentistry at Matsudo (Chief : Prof. Yoshimitsu Abiko)
[2] Research Institute of Oral Science, Nihon University School of Dentistry at Matsudo (Chief : Prof. Hiroshige Sasahara)
平成14年3月4日受付

Introduction

Various biostimulatory effects of low-energy laser irradiation (LLLI) have been reported that included wound healing[1], cell proliferation of fibroblasts[2] and chondrocytes[3], collagen synthesis[4], and nerve regeneration[5]. Of particular interest for implant research, the acceleration of bone regeneration by laser treatment has been investigated[6~9]. The recent advent of improved laser delivery systems promoted interest in the application of lasers in implantology[10]. DÖRTBUDAK et al.[11] reported that LLLI on bony implant sites, after drilling and implant insertion in baboons, stimulated osteocyte viability, and suggested a positive effect on the integration of implants. Since LLLI will be useful to support implant therapy, it is important to elucidate the mechanism of the biostimulatory effect of LLLI on bone formation.

We studied the effects of LLLI at various cell culture stages of osteoblast cells, and found that cellular proliferation, bone nodule formation, alkaline phosphatase activity, and osteocalcin gene expression were only enhanced at the early stage[12]. These findings suggest that laser irradiation may principally play two roles in cell proliferation of bone nodule-forming cells of osteoblast lineage, and stimulation of cellular differentiation. However, the molecular bases of mechanisms leading to these findings are not elucidated.

To accomplish this, we previously constructed the cDNA library of MC 3 T 3-E 1, a clonal osteoblastic cell line, which enhanced gene expression by LLLI using a subtracted gene cloning procedure[13]. Among subtractive genes, we found a gene clone, exhibited a high homology nucleotide sequence with DNA replication licensing factors MCM 3[14] and MCM 5[15] genes, and ATP biosynthesis involving mitochondrial enzyme FOA 1-ATPase gene[16].

In the present study, we further characterized the gene library by the DNA nucleotide sequence of gene clones, and focused on a gene clone encoding a high homology nucleotide sequence with *Mus musculus* annexin III gene.

Materials and Methods

1. Cell culture and laser irradiation

MC 3 T 3-E 1 cells, established from newborn mouse calvaria by KODAMA et al.[17], were cultured in minimal essential medium (α-MEM ; Gibco BRL, USA) containing 10% fetal calf serum, 100 μg/ml of penicillin G (Sigma Chemical Co., USA), and 50 μg/ml of gentamicin sulfate (Sigma). The cultures were kept at 37°C in a humidified incubator (Forma CO_2 incubator MIP-3326, Sanyo Electric Medica System Co., Tokyo, Japan) in the presence of 95% air and 5% CO_2.

The LLLI was carried out according to a previous report[12]. Briefly, a Ga-Al-As diode laser device (Model Panalas® 1000 ; Matsushima Industrial Equipment Inc., Osaka, Japan) was used. Laser irradiation was performed so that the axis of the three beams met at right angles to the cell monolayer. The specification of this laser device was wavelength 830 nm and output power 100～700 mW variable. Laser irradiation was performed at a distance of 550 mm (area of spot size : 78.5 cm^2) from the probe to the cell layer. Continuous wave, at 500 mW output power for 20 min (power density : 7.64 J/cm^2), was used.

2. Restriction endonuclease analysis

Plasmid DNA from subtracted gene clones was isolated and digested with *Mlu* I and *Not* I. DNA fragments were run on 1% agarose gel-electrophoresis. The gel was stained with ethidium bromide under UV irradiation.

3. DNA nucleotide sequencing homology search

Dideoxy-chain termination sequencing[18] was performed with fluorescent dye-labeled T 7 universal primers (Aloka, Japan) and Sequi Therm™ Long-Read™ cycle sequencing kits for Li-Cor® Sequencing (Epicentre Technologies, USA). The reaction products were analyzed by a 4000 LS Long

ReadIR™ DNA sequencing system (LI-Cor, USA). Representative clones were randomly selected from a subtracted cDNA library, and a 5′-portion of each insert was nucleotide-sequenced.

The homology-search of the DNA sequence of cloned DNA was carried out by the standard nucleotide-nucleotide BLAST (blastn) homology-search, using NCBI DNA databases.

4. Reverse transcription polymerase chain reaction

Total cellular RNA was extracted from MC 3 T 3-E 1 cells with or without LLLI by acid guanidium thiocyanate-phenol-choloroform extraction[19]. cDNA synthesis and amplification by reverse transcription-polymerase chain reaction (RT-PCR) were carried out, using a GeneAmp RNA PCR kit (Perkin-Elmer, Norwalk, CT, USA). The PCR DNA primers were as follows : 5′-TCT ATC TGG GTT GGA CCT CGA GGA-3′ (the forward primer for mouse annexin III) ; 5′-CTT CTA CCA TCT GCC AGA GTC AGC-3′ (the reverse primer for mouse annexin III) ; 5′-ATC ACC ATC TTC CAG GAG-3′ (the forward primer for mouse GAPDH) ; 5′-ATG GAC TGT GGT CAT GAG-3′ (the reverse primer for mouse GAPDH) PCR products were electrophoresed on 1.5% agarose gel and subsequently stained with ethidium bromide.

Results

Figure 1 shows the agarose electrophoresis pattern for the screening of DNA insert size from subtracted gene clones. Plasmid DNAs with different sizes of inserts were selected and nucleotide sequenced.

The endonuclease digestion pattern of plasmid DNA from MCL-174 is shown in Fig. 2. The result suggests that MCL-174 clone has a 1.5 kb-size insert.

Then, nucleotide sequence homology of MCL-174 insert was examined. A blastin search showed many blast hits on the query sequence, with a variety of homology, as shown in Fig. 3.

Among hit genes, MCL-174 DNA exhibited with annexin III genes of *Mus musculus* (99%), *Rattus norvegicus* (89%), and *Homo sapiens* (85%), as shown in Table 1. Figure 4 showed the identification of nucleotide sequences between MCL-174 and *Mus musculus* annexin III gene.

To confirm the enhanced mRNA level of annexin III gene in LLLI cells, RT-PCR analysis was carried out. Figure 5 showed higher levels of annexin III mRNA level in LLLI MC 3 T 3-E 1 cells compared with non-LLLI, while mRNA levels of GAPDH, as a house keeping control, were the same between with or without LLLI cells.

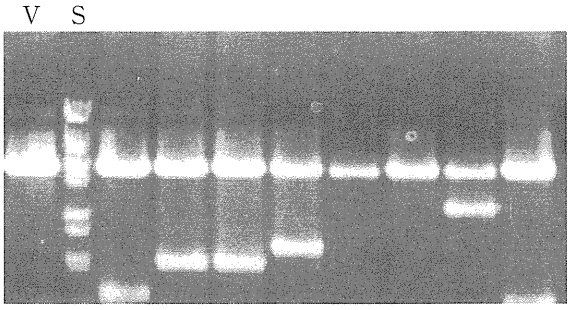

Fig. 1 Agarose gel electrophoresis pattern for the screening of DNA insert size from a subtracted gene library
V, Vector plasmid pAP 3 neo DNA ; S, Size marker of λ DNA *Hind* III digestion ; other lanes, subtracted gene clone plasmid DNA

Fig. 2 The endonuclease digestion pattern of plasmid DNA from MCL-174
S, Size marker λ *Hind* III digestion ; 1, Vector plasmid pAP 3 neo ; 2, plasmid DNA from MCL-174

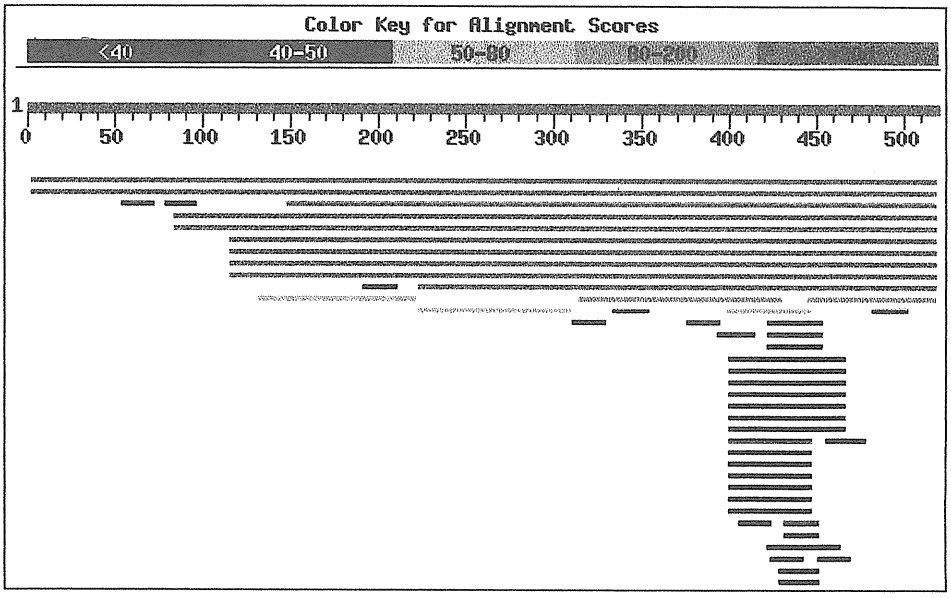

Fig. 3 Distribution of Blastin search hits on the Query sequence
Number showed nucleotide bp. Lines showed the identical DNA sequences region.

Discussion

In this study, we found the annexin III gene in a subtractive gene library, which enhanced its gene expression by LLLI. The nucleotide sequence of DNA insert of MCL-174 had high homology with mouse annexin III. Further, RT-PCR analysis results confirmed an elevated mRMA level in LLLI cells. These findings suggested that LLLI enhanced the transcription of annexin III in the osteoblastic cell line MC 3 T 3-E 1.

Mouse annexin III cDNA was first characterized as expressed sequence tag clones by molecular sequencing, chromosomal mapping, and systematic analysis. cDNA sequences extended the location of intron 7, with respect to the human gene, and mapped to the middle of mouse chromosome 5[20]. Our gene clone MCL-174 has a high nucleotide sequence homology with mouse annexin III reported in this literature.

Annexins are soluble proteins capable of binding to phospholipid membranes in a calcium-dependent manner in neutrophils[21]. By immunofluorescence microscopy observation, annexin III was more likely to be associated with specific granules in neutrophils, suggesting annexins could be implicated in processes of granule fusion.

Study of the annexin protein family on hard tissues, immunoblot analyses, and ultrastructural immunogold experiments have been conducted on secretory ameloblasts and odontoblasts of rat incisor. GOLDBERG et al.[22] found that annexins I and II were seen in soluble and particulate fractions of enamel-related portion, but not in dentin-related portion, and annexins III, IV and V were detected in both soluble and particulate fractions of enamel- and dentin-related portions. They speculated that annexins are implied in the regulation of cell calcium. These findings suggest that the mechanism of the biostimulatory effect by LLLI on bone formation may relate through annexin III gene expression in osteoblasts.

While laser treatment has been utilized in oral surgery for many years, the recent advent of improved laser delivery systems has promoted interest in the application of lasers in implantology. WALSH[10] reviewed the use of lasers in laboratory and clinical techniques used in implantology, and provided useful information with particular refer-

ence to carbon dioxide, Nd : YAG, argon, and erbium : YAG lasers. It is of interest to determine whether screws were able to osseointegrate in a laser-prepared bone defect, and to compare the pattern of bone healing around these screws. Osseointegration of titanium screws can be achieved using an erbium : YAG laser to prepare the implant

Table 1 Result of Blastin search

Homologous gene	Species	Gene ID	Similarity (%)	Identity (bp)
Annexin III	mouse	NM 013470	99	514/518
Annexin III	mouse	AJ 001633	99	514/518
Annexin III	rat	NM 012823	89	394/440
Annexin III	human	BC 000871	85	345/405

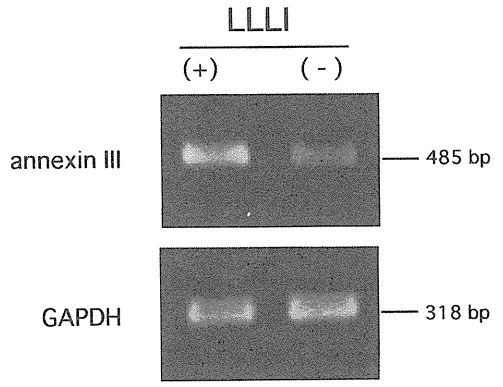

Fig. 5 RT-PCR analysis of the annexin III mRNA level Ethidium bromide staining pattern of amplified PCR products on agarose gel electrophoresis. RT-PCR method and DNA primers used were described in Materials and Methods.

```
Score =  979 bits (494), Expect = 0.0
Identities = 514/518 (99%), Gaps = 2/518 (0%)
Strand = Plus / Plus

Query: 3   gggagctacggccggccgaggctgatctttcaccttcgctgagcttctgcctgggcttcg 62
           ||||||||||||||||||||||||||||||||||||||||||||||||||||||||||||
Sbjct: 87  gggagctacggccggccgaggctgatctttcaccttcgctgagcttctgcctgggcttcg 146

Query: 63  cctccgcggccccaaggattgctgtgatctcggcttgagagaaaggtggactgtcatggc 122
           | ||||||||||||||||||||||||||||||||||||||||||||||||||||||||||
Sbjct: 147 c-tccgcggccccaaggattgctgtgatctcggcttgagagaaaggtggactgtcatggc 205

Query: 123 ctctatctgggttggacctcgaggaaccataaaagattatccaggctttagccccgtcgg 182
           ||||||||||||||||||||||||||||||||||||||||||||||||||| |||||
Sbjct: 206 ctctatctgggttggacctcgaggaaccataaaagattatccaggctttagccc-gtcgg 264

Query: 183 tggatgccgaagctatccggaaagcgatcagaggacttgggactgacgagaaaacccctca 242
           ||||||||||||||||||||||||||||||||||||||||||||||||||||||||||||
Sbjct: 265 tggatgccgaagctatccggaaagcgatcagaggacttgggactgacgagaaaacccctca 324

Query: 243 tcaacattctgacggagcggtcgaacgcgcagcgacagctgattgtcaagcagtaccaag 302
           ||||||||||||||||||||||||||||||||||||||||||||||||||||||||||||
Sbjct: 325 tcaacattctgacggagcggtcgaacgcgcagcgacagctgattgtcaagcagtaccaag 384

Query: 303 cagcgtatgaacaggagctgaaagatgacttgaagggtgatctctctggccacttcgagc 362
           ||||||||||||||||||||||||||||||||||||||||||||||||||||||||||||
Sbjct: 385 cagcgtatgaacaggagctgaaagatgacttgaagggtgatctctctggccacttcgagc 444

Query: 363 acgtcatggtggctcttgttactgcaccagccctgtttgatgcgaagcaactgaagaaat 422
           |||||||||||||||||||||||||||||||||||||||||||||||  ||||||||||||
Sbjct: 445 acgtcatggtggctcttgttactgcaccagccctgtttgatgcgaacgaactgaagaaat 504

Query: 423 ccatgaagggaactggcacagatgaagatgccctgattgaaatcctaacaaccaggtcaa 482
           ||||||||||||||||||||||||||||||||||||||||||||||||||||||||||||
Sbjct: 505 ccatgaagggaactggcacagatgaagatgccctgattgaaatcctaacaaccaggtcaa 564

Query: 483 gcaggcagatgaaggaaatctcgcaggcctattataca 520
           ||||||||||||||||||||||||||||||||||||
Sbjct: 565 gcaggcagatgaaggaaatctcgcaggcctattataca 602
```

Fig. 4 Identification of nucleotide sequences between MCL-174 and mouse annexin III genes
Query, MCL-174 ; Sbjct, mouse annexin III

bed[23].

Among the many physiological effects of low-energy laser irradiation, anti-inflammatory functions have also been reported. HONMURA et al.[24] reported the therapeutic effect of Ga-Al-As laser irradiation on experimental carrageenin-induced inflammation. We previously reported that Ga-Al-As diode LLLI caused inhibition of prostaglandin E 2 (PGE 2) and IL-1 β[25], as well as plasminogen activator production[26] in mechanically stressed human periodontal ligament cells.

Osteogenesis and the bone healing process following implant therapy are very important to lead successful result. Thus, the most important biostimulatory effect of LLLI for implant therapy should be the acceleration of bone formation. DÖRTBUDAK et al.[11] examined the effects of LLLI on osteocytes and bone resorption at bony implant sites in iliac crest of baboon. Holes for accommodating implants were drilled and irradiated with LLLI, then immediately inserted implants. Histochemical studies showed that osteocyte viability was significantly higher in LLLI subjects. In contrast, the bone resorption rate was not affected by LLLI. These findings suggest that more vital bone tissue is present in the LLLI area compared with control sites. Tissue engineering can be defined as one of the most challenging fields in medicine. Bone tissue engineering, using bone marrow derived mesenchymal cells, has been heralded as an alternative strategy to regenerate bone. It has been reported that LLLI stimulated bone matrix formation in osteoblasts derived from bone marrow cells[27].

Taken together of these investigations, the biological effects of bone formation and anti-inflammation, the utilizing of LLLI can be expected to reduce healing times and speed up osseointegration of implants.

The lack of knowledge of the biological mechanism about LLLI may bring a delay in clinical use of laser therapy, including clinical implantology. The findings presented here clearly provide evidence that LLLI alters the transcription level in osteoblasts. Further studies for another candidate genes, which involve bone formation, are progress in our laboratory.

The authors are grateful to Mr. Akira Kaneda, senior engineer of Matsushita Industrial Equipment Company Limited, for providing the laser therapy apparatus, and to Dr. Kazutoshi Tamura for helping in the construction of a subtractive gene library. This research was supported in part by a Grant from the Ministry of Education, Culture, Sports, Science, and Technology of Japan, to promote 2001-Multidisciplinary Research Projects, and a Suzuki Memorial Grant from Nihon University School of Dentistry at Matsudo.

References

1) MESTER, E., MESTER, A.F. and MESTER, A. : The biomedical effects of laser application ; Lasers Surg. Med., 5, *31～39,* 1985.
2) BOULTON, M. and MARSHALL, J. : He-Ne laser stimulation of human fibroblast proliferation and attachment in vitro ; Lasers Life Sci., 1, *125～134,* 1986.
3) SCHULTZ, R.J., KRISHNAMURTHY, S., THELMO, W., RODRIGUEZ, J. and HARVEY, G. : Effects of varying intensities of laser energy on articular cartilage ; Lasers Surg. Med., 5, *557～588,* 1985.
4) LAM, T.S., ABERGEL, R.P., MEEKER, C.A., CASTEL, J. C., DWYER, R.M. and UITTO, J. : Laser stimulation of collagen synthesis in human skin fibroblasts cultures ; Lasers Life Sci., 1, *61～77,* 1986.
5) ANDERS, J.J., BORKE, R.C., WOOLERY, S.K. and MERWE, W.P. : Low power laser irradiation alters the rate of regeneration of the rat facial nerve ; Lasers Surg. Med., 13, *72～82,* 1993.
6) CHEN, J.W. and ZHOU, Y.C. : Effect of low level carbon dioxide laser radiation on biochemical metabolism of rabbit mandibular bone callus ; Laser Therapy, 1, *83～87,* 1989.
7) NAGASAWA, A., KATO, K. and NEGISHI, A. : Bone regeneration effect of low level lasers including argon laser ; Laser Therapy, 3, *59～62,* 1991.
8) TANG, X.M. and CHAI, B.P. : Effect of CO_2 laser irradiation on experimental fracture healing : A transmission electron microscopic study ; Lasers Surg. Med., 6, *346～352,* 1986.
9) TRELLES, M.A. and MAYAYO, E. : Bone fracture consolidates faster with low-power laser ; Lasers Surg. Med., 7, *36～45,* 1987.

10) WALSH, L.J. : The use of lasers in implantology : an overview ; J. Oral Implantol., 18, *335～340,* 1992.
11) DÖRTBUDAK, O., HAAS, R. and MAILATH-POKORNY, G. : Effect of low-power laser irradiation on bony implant sites ; Clin. Oral Implants Res., 13, *288～292,* 2002.
12) OZAWA, Y., SHIMIZU, N., KARIYA, G. and ABIKO, Y. : Low-energy laser irradiation stimulates bone nodule formation at early stages of cell culture in rat calvarial cells ; Bone, 22, *347～354,* 1998.
13) TAMURA, K., HOSOYA, S., NOMURA, K. and ABIKO, Y. : Construction of subtracted osteoblast cDNA library with laser-irradiation-enhanced transcription ; Laser Therapy, 9, *107～114,* 1997.
14) YAMAMOTO, M., TAMURA, K., HIRATSUKA, K. and ABIKO, Y. : Stimulation of MCM 3 gene expression in osteoblast by low level laser irradiation ; Lasers Med. Sci., 16, *213～217,* 2001.
15) TAMURA, K., HOSOYA, S. and HIRATSUKA, K. : Enhancement of mouse CDC 46 gene expression in the osteoblast by laser irradiation ; Laser Therapy, 10, *25～32,* 1988.
16) TAMURA, K., HOSOYA, S., TAKEMA, T., SAKURA, Y., FUJII, T. and ABIKO, Y. : Low level laser irradiation enhances expression of FoF 1-ATPase subunit-b gene in osteoblastic cells ; Laser Therapy, 10, *107～116,* 1998.
17) KODAMA, H., AMAGI, Y., SUDO, H., KASAI, S. and YAMAMOTO, S. : Establishment of clonal osteogenic osteoblastic cell line from newborn mouse calvaria ; Jpn. J. Oral Biol., 23, *899～901,* 1981.
18) SANGER, F., NICKLEN, S. and COULSON, A.R. : DNA sequencing with chain-terminating inhibitors ; Proc. Natl. Acad Sci. USA, 74, *5463～5467,* 1977.
19) CHOMCZYNSKI, P. and SACCHI, N. : Single-step method of RNA isolation by acid guanidinium thiocyanate-phenol-chloroform extraction ; Anal. Biochem., 162, *156～159,* 1987.
20) FERNANDEZ, M.P., COPELAND, N.G., GILBERT, D.J., JENKINS, N.A. and MORGAN, R.O. : Mouse annexin III cDNA, genetic mapping and evolution ; Gene, 207, *43～51,* 1998.
21) LE CABEC, V. and MARIDONNEAU-PARINI, I. : Annexin 3 is associated with cytoplasmic granules in neutrophils and monocytes and translocates to the plasma membrane in activated cells ; Biochem J., 15, *481～487,* 1994.
22) GOLDBERG, M., FEINBERG, J., RAINTEAU, D., LECOLLE, S., KAETZEL, M.A., DEDMAN, J.R. and WEINMAN, S. : Annexins I-VI in secretory ameloblasts and odontoblasts of rat incisor ; J. Biol. Buccale., 18, *289～298,* 1990.
23) EL-MONTASER, M., DEVLIN, H., DICKINSON, M.R., SLOAN, P. and LLOYD, R.E. : Osseointegration of titanium metal implants in erbium-YAG laser-prepared bone ; Implant Dent., 8, *79～85,* 1999.
24) HONMURA, A., YANASE, M., OBATA, J. and HARUKI, E. : Therapeutic effect of Ga-Al-As diode laser irradiation on experimentally induced inflammation in rats ; Lasers Surg. Med., 12, *441～449,* 1992.
25) SHIMIZU, N., YAMAGUCHI, M., GOSEKI, T., SHIBATA, Y., TAKIGUCHI, H., IWASAWA, T. and ABIKO, Y. : Inhibition of prostaglandin E 2 and interleukin 1 β production by low-power laser irradiation in stretched human periodontal ligament cells ; J. Dent. Res., 74, *1382～1388,* 1995.
26) OZAWA, Y., SHIMIZU, N. and ABIKO, Y. : Low-energy diode laser irradiation reduced plasminogen activator activity in human periodontal ligament cells ; Lasers Surg. Med., 21, *456～463,* 1997.
27) DÖRTBUDAK, O., HAAS, R. and MAILATH-POKORNY, G. : Biostimulation of bone marrow cells with a diode soft laser ; Clin. Oral Implants Res., 11, *540～545,* 2000.

日レ歯誌 J. Jpn. Soc. Laser Dent. 13 : 79-88, 2002

原　著

差分化遺伝子クローニングによる骨芽細胞への低出力レーザー照射の生物学的効果の機序解明

安孫子宜光

日本大学松戸歯学部生化学講座
（主任：安孫子宜光教授）

（受理：平成14年7月15日）

Elucidation of Mechanisms for the Biostimulatory Effect of Low Level Laser Irradiation on Osteoblasts by Subtractive Gene Cloning

Yoshimitsu ABIKO

Department of Biochemistry and Oral Science Research Institute,
Nihon University School of Dentistry at Matsudo
(Chief : Prof. Yoshimitsu ABIKO)

(Accepted for Publication : July 15, 2002)

Abstract : Various biostimulatory effects of low-energy laser irradiation (LLLI) have been reported that involve the acceleration of bone regeneration. We reported that LLLI stimulated cellular proliferation, bone nodule formation, alkaline phosphatase activity, and osteocalcin expression. However, the molecular basis of the mechanisms leading to these findings has not been elucidated. To accomplish this, we constructed the cDNA library of MC3T3-E1, a clonal osteoblastic cell line, which enhanced gene expressions by LLLI using a subtracted gene cloning procedure. In the present study, we further characterized gene library by DNA nucleotide sequence and homology-search with a DNA database. Among 88 subtractive genes, several clones exhibited high homology with mitochondrial protein genes, signal transduction-related genes, and EST genes. These findings may help to elucidate the molecular-based mechanisms for the biostimulatory effect of LLLI on osteoblasts.

(J. Jpn. Soc. Laser Dent. 13 : 79~88, 2002 Reprint requests to Dr. ABIKO)

Key words=Low-energy laser irradiation, Osteoblast, Gene expression

キーワード=低出力レーザー，骨芽細胞，遺伝子発現

緒　言

低出力レーザー照射が創傷や難治性潰瘍に治癒効果があると言及されて以来，炎症抑制，疼痛減少，骨折治癒促進など広範な臨床効果が報告されている[1,2]。しかしながら，低出力レーザー照射による生物学的効果の作用機序は不明な点が多い。とくに分子レベルでの実証科学的な解明は遅れている。

歯科医学領域にも積極的な応用が期待されているなかで，レーザー医療をさらに推進，発展させるためには，有用性

〒271-8587 千葉県松戸市栄町西2-870-1 TEL 047-360-9332, FAX 047-360-9329
2-870-1 Sakaecho-nishi, Matsudo City, Chiba 271-8587, Japan TEL +81-47-360-9332, FAX +81-47-360-9329

の高いレーザー照射の機種，照射法を開発するとともに，生物学的効果を実証科学的に解明していく必要があると思われる。

従来の分子レベルでの研究アプローチは，生理活性物質の発見→精製→遺伝子クローニング→機能解析→タンパク質一次構造の解析が行われてきた。しかし，これらの研究方法では，すでによく知られている生理活性物質あるいは同定，精製に成功した分子しか捉えることはできない。当然ながら，目的とする生命現象に関わる未知の遺伝子については研究することは不可能である。

近年，ゲノムサイエンス研究の飛躍的な進展に伴い，ヒトを含む種々の生物のゲノム計画が進められている[3]。ゲノムデータベースの充実に伴って，細胞内で変動する遺伝子のトランスクリプトーム解析は，生命現象を理解することに多くの情報を与え得ると期待されている。

遺伝子発現の変動を捉える方法として，遺伝子バンクを作成し，対照のmRNAで差し引きするサブトラクション遺伝子クローニング法が開発されている[4]。レーザー照射した細胞からmRNAを分離してcDNA遺伝子バンクを調製し，非レーザー照射細胞のmRNAを用いて同一の遺伝子を差し引いた（差分化）残りの遺伝子群は，レーザー照射によって遺伝子発現が増大した遺伝子ということになる。この差分化遺伝子ライブラリーを作成し，得られた遺伝子クローンの塩基配列を解読してゲノムデータベースの遺伝子配列とホモロジー検索することによって関与する遺伝子を同定し，その遺伝子の遺伝子産物の機能を明らかにすることが可能となる。

本研究では，骨芽細胞に低出力レーザー照射して差分化遺伝子ライブラリーを構築して新たに得た88遺伝子クローンについて塩基配列を解読し，低出力レーザー照射の生物学的効果の作用機序の解明を試みた。

実験方法

1. 細胞培養

骨芽細胞として，マウス新生仔の頭蓋骨から樹立され，骨結節形成能を有するMC3T3-E1[5]を用いた。細胞は，10% 牛胎児血清，100μg/mlペニシリンG，50μg/mlゲンタマイシン硫酸を添加したα-MEM培地で，95% air-5 % CO_2，37℃の条件化，CO_2インキュベーターで培養した。培養ディシュ（75cm²）に培養液10mlの培養液を加えて培養を行った。

2. レーザー装置

低出力レーザー照射装置は，Ga-Al-As半導体レーザー装置（モデルPanalas-1000，波長 830nm，最大出力500 mW；松下電器）を用いた。細胞表面から5 cmの距離に照射部を設定し，500mWで培養ディシュ75cm²に対して20分間照射した。この照射条件で，エネルギー密度は7.6 J/cm²になる。培養液の存在下および非存在化でレーザー照射を行って調べたところ，両条件でのエネルギー量に差は認められなかった。このことから培養液中の赤色物質による吸収は軽微と考えられ，照射時に培養液を取り除かず実験を行った。また，この照射条件で培養液の温度の変化に有意差は認められない。

3. cDNA ライブラリーの作成

本実験では，細胞増殖への影響も調べるために，MC3T3-E1細胞をセミコンフルエントまで培養し，レーザー照射後，1，6，12，24時間後に細胞から総RNAを回収した。総RNAを混合して，mRNAを精製し，cDNAライブラリーを作成した。5 μgのポリA-RNAをテンプレートにして，1.6 μg *Not* Iサイトをもつoligo dTをプライマーに，メチル化デオキシヌクレオチドを用いて逆転写酵素（Superscript Ⅱ）反応によってcDNAを合成した。合成試料からRNAをRNase Hを用いて取り除いた後，*Bgl*Ⅱ-*Sma*Iアダプターを付加してベクタープラスミドに一方向で挿入できるようにした。300bp以下の短いDNAフラグメントをスピンカラムで除き，ベクタープラスミドpAPneoに挿入し，T4リガーゼでキメラプラスミドを作成した[6]（図1）。

4. 差分化遺伝子クローニング

キメラプラスミドを宿主細胞 *Escherichia coli* DH5αF 7IQにエレクトロポーレーション法で形質転換し，R408ファージを感染させて一本鎖化して回収した。次いで，レーザー非照射MC3T3-E1から回収，精製したmRNAをビオチン標識し，一本鎖化キメラプラスミド ライブラリーとハイブリダイズさせ，さらにストレプトアビジンを結合させた。共通するmRNA結合キメラプラスミドをフェノール法で除去し，残ったキメラプラスミド，すなわちレーザー照射でmRNA レベルが上昇した遺伝子を含むキメラプラスミドを回収した。この操作を二度繰り返した。差分化キメラプラスミドにBcaBEST DNA ポリメラーゼを用いて二本鎖DNAプラスミドにした後，*E. coli* MC1061Aに形質転換して差分化遺伝子クローン ライブラリーを作成した[6]（図2）。

5. 塩基配列の解読

単一コロニーの*E. coli*遺伝子クローンをランダムに回収後，自動プラスミド精製装置（Kurabo，PI-100）でプラスミドを回収，精製した。各キメラプラスミドの挿入DNA断片の塩基配列の解読は，dideoxy chain termination法[7]で行った。塩基配列の解読は蛍光自動DNAシーケンサー（LiCor，Epicenter Technolgy社），蛍光標識

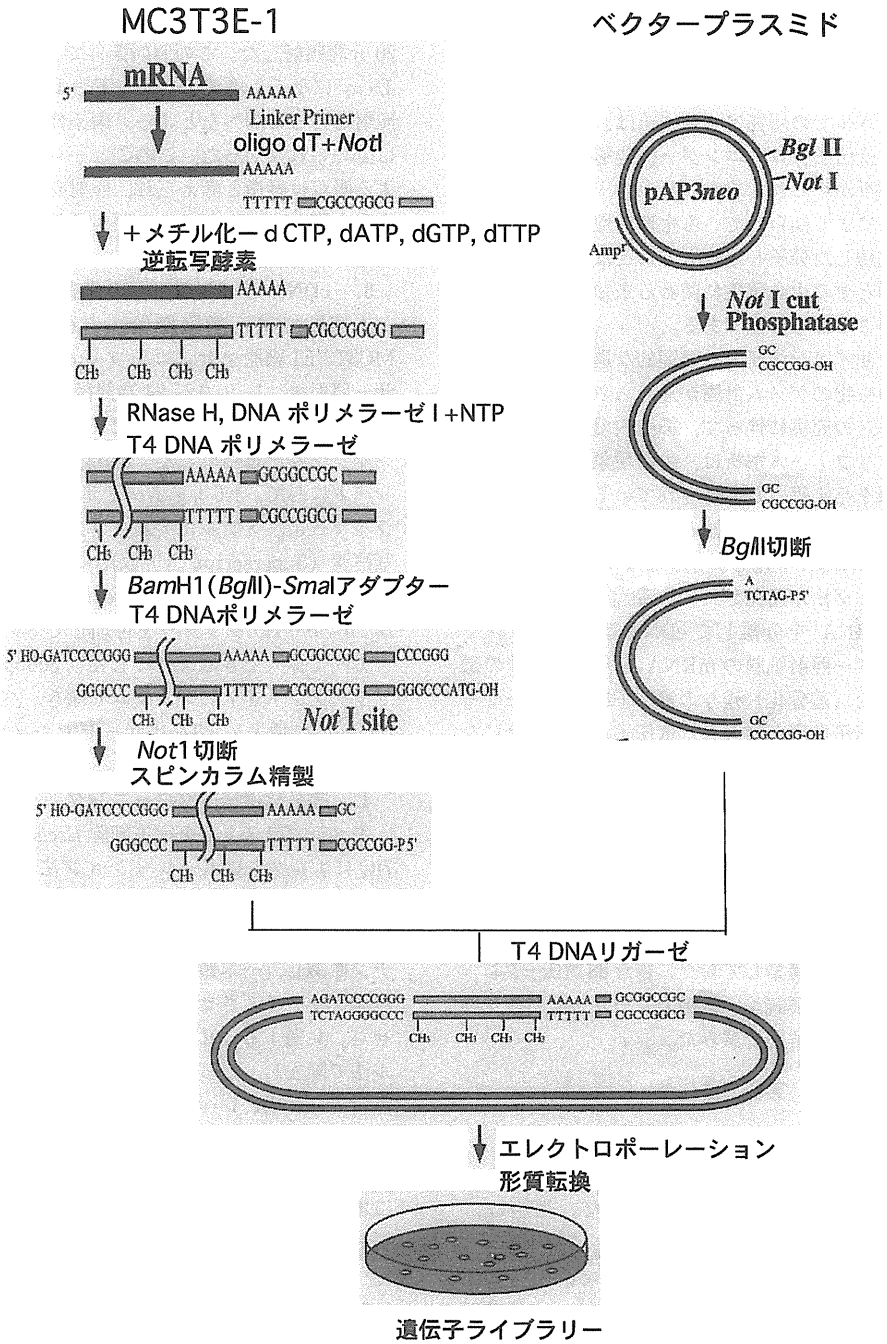

図 1　非レーザー照射細胞遺伝子バンク作成の概略
制限酵素リンカー付加の工夫によって cDNA 断片の挿入方向は一定となり，差分化する際の非レーザー照射細胞 mRNA に対するアンチセンス鎖がプラスミド DNA の一本鎖として残る。

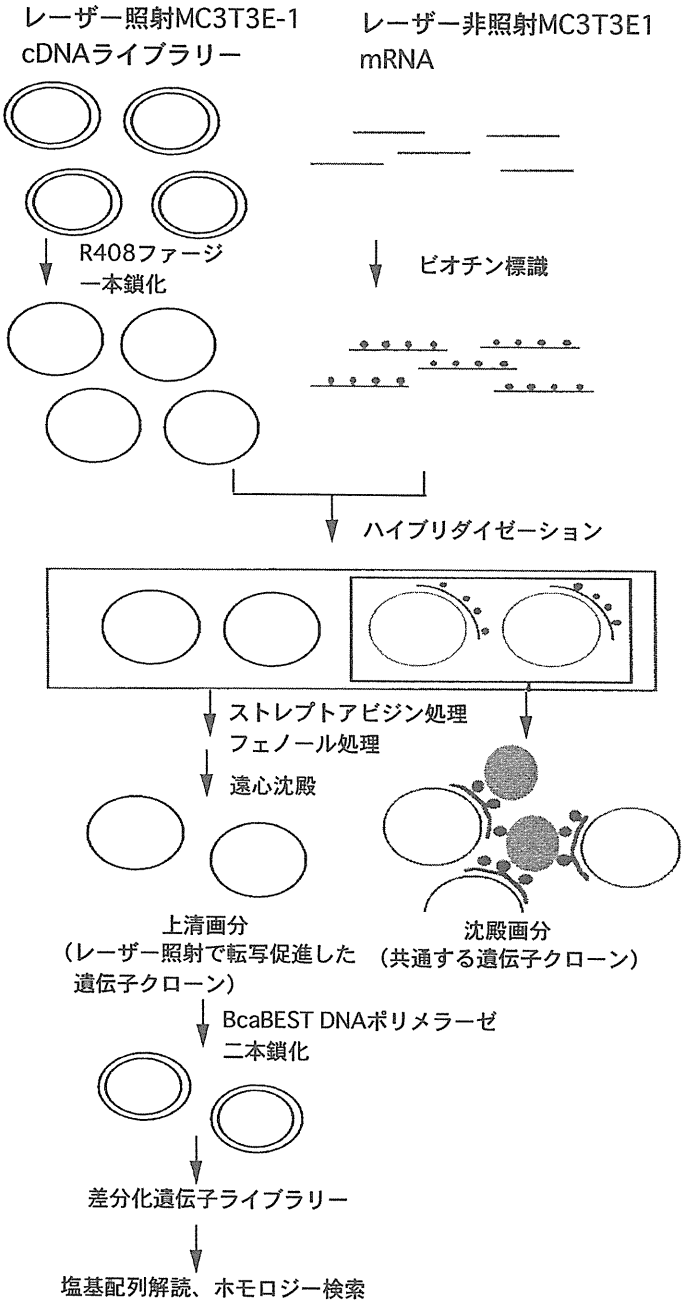

図 2　差分化遺伝子ライブラリー作成の概略
プラスミド遺伝子バンクの一本鎖化された DNA にビオチン標識した非レーザー照射細胞 mRNA が結合する。ビオチンにストレプトアビジンが結合したプラスミドはフェノール処理で取り除かれる。上清画分に残ったプラスミド DNA を二本鎖に戻して大腸菌宿主に形質転換して差分化遺伝子ライブラリーを得る。

DNA プライマー，Sequi therm Long-Read cycle sequencing kit（LiCor, Epicenter Technolgy 社）を用いて行った。

6. データベース検索

National Center for Biotechnology Information（NCBI）の BLAST（Basic Local Alignment Search Tool）を利用して，塩基配列のホモロジー検索（Nucleotide BLAST；blastn）を行った。約 520bp の塩基配列のホモロジー検索の結果で既知遺伝子と一部の相同性が見られたものを Known gene クローン，アノテーションがない EST（Expression Sequence Tag）gene とのホモロジーが見られたものを EST クローン，30bp 以上相同性が見られないのを Unknown gene クローンとした。

結　果

差分化遺伝子ライブラリーからプラスミド DNA を抽出，精製し制限酵素で切断してアガロースゲル電気泳動を行い，挿入断片を調べた。図 3 にその一部を示す。

300bp 以上の挿入断片をもち，かつ制限酵素消化パターンが異なる 88 遺伝子クローンを選び，プラスミド DNA を精製し，それぞれの挿入 DNA 断片の塩基配列について 520bp 解読した。得られた塩基配列情報を NCBI の BLAST プログラムで塩基配列のホモロジー検索を行った。図 4 は，No. 1-178 クローンを一例として示したもので，図 4A が塩基配列，図 4B が DNA データベースとのホモロジー検索で相同性のあった遺伝子とのアライメントスコアー，図 4C がホモロジー検索で相同性の極めて高いトップ 4 遺伝子のアノーテーション情報である。そして，図 4D は，No. 1-178 の塩基配列（Query）と NM02553.1 遺伝子（Sbjct）の DNA 塩期配列ホモロジー検索結果である。相同性の高かった 4 遺伝子のアノーテーションは，いずれもマウスのミトコンドリアのリボゾームタンパク質 L11 であった。

88 遺伝子クローンについてのホモロジー検索の結果を表1にまとめた。22 クローンが Known 遺伝子，38 クローンが EST クローン，30 クローンが Unknown 遺伝子であった。また，表 2 に 22 クローンの既知遺伝子についてのアノテーション情報を示した。

考　察

低出力レーザー照射の生物学的効果として，炎症抑制，疼痛減少，創傷治癒促進，骨折治癒促進などが報告されている。しかしながら，一方ではレーザー照射の効果について心理的なプラセボー効果が大きいとする懐疑的な見方や単なる温度上昇効果によるものであるとする意見もある。

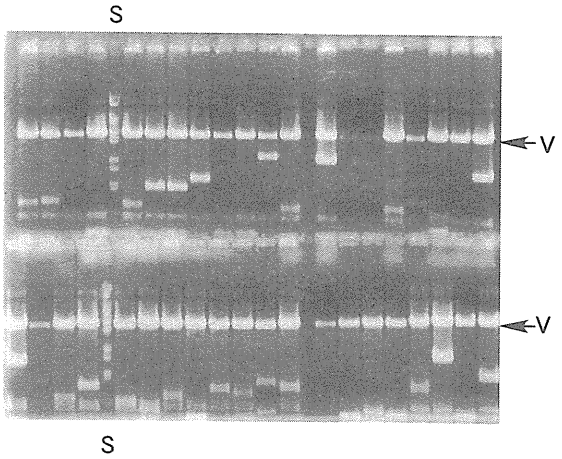

図 3　差分化遺伝子クローンのスクリーニング
差分化遺伝子ライブラリーの大腸菌クローンを培養し，集菌後，プラスミド DNA を分離する。制限酵素 *Not* I, *Bgl* II で切断し，アガロース電気泳動を行う。300bp 以上の挿入 DNA をもつクローンを選択する。S, サイズスタンダード DNA；V, ベクタープラスミド DNA 断片

このような背景のなかで，歯科領域への低出力レーザーの積極的な応用をさらに推進，発展させるためには実証科学的な方法で作用メカニズムを解明する基礎研究が必要であると考えられる。

われわれは，レーザー照射の骨形成促進メカニズムを解明するために in vitro 実験系を設定し検討を行っている。ラット胎仔の頭蓋骨から採取した骨芽細胞に低出力レーザー照射を行い，骨結節数が照射量に比例して増大し，アルカリホスファターゼ活性，コラーゲン産生が促進されることを見いだしている[8]。さらに，培養早期のレーザー照射がより強い骨形成促進効果を有することを報告している[9]。この結果は，レーザー照射が未分化間葉系細胞の増殖と骨芽細胞への分化を促進することを示唆する。

近年，ゲノム科学を基盤とする研究技術が進展し，ゲノム情報をすべて解読するゲノムプロジェクトの進展とその応用によって先進的な研究が行われている。細胞・組織から mRNA を抽出して，ランダムプライマーを用いて mRNA の遺伝子増幅を行って遺伝子発現レベルの差を同定するデファレンシャル ディスプレイ法や遺伝子バンクを作成して対照の mRNA で差し引くサブトラクション遺伝子クローニング法などが開発されている。そして，得られた遺伝子の塩基配列情報をゲノムデータベースと照合することで，その生命現象に関与する遺伝子発現を未知遺伝子も含めて同定することが可能である。

A 塩基配列

TACATCATGTCCAAGCTAAGCCGGGCCACTCGGACCCTCAAGAAGCCCGAGGCCGGCGGCGTGATCCGGTCCATCG
TGCGAGCAGGCCAAGCTATTCCTGGGCCTCCACTAGGTCCCATCTTGGGTCAGCGAGGTGTCTCTATCAACCAGTT
CTGCAAAGAGTTCAACGAGAAGACAAAGGACATCAAAGAAGGCATTCCCCTGCCTACAAAAATTTTTATAAAGCCC
GACAGGACATTTGAGCTCAAGATTGGGCAGCCCACTGTTTCTTACTTTTTGAAGGCAGCTGCTGGGATCGAGAAGG
GGGCCCGGCATACAGGGAAAGAGGTGGCAGGCCTGGTGAGTTTGAAGCACGTATATGAGATTGCCTGTGTCAAAGC
TAAGGATGATGCTTTTACCATGCAAGATGTGCCCCTGTCTTCTGTGGTCCGTTCCATCATTGGCTCTGCCCGTTCC
CTGGGCATTCGAGTGGTGAAGGACCTCAGTGCAGAAGAACTGGAGGCTTTCCAGAAGGAACGAG

B ホモロジー検索でヒットした遺伝子

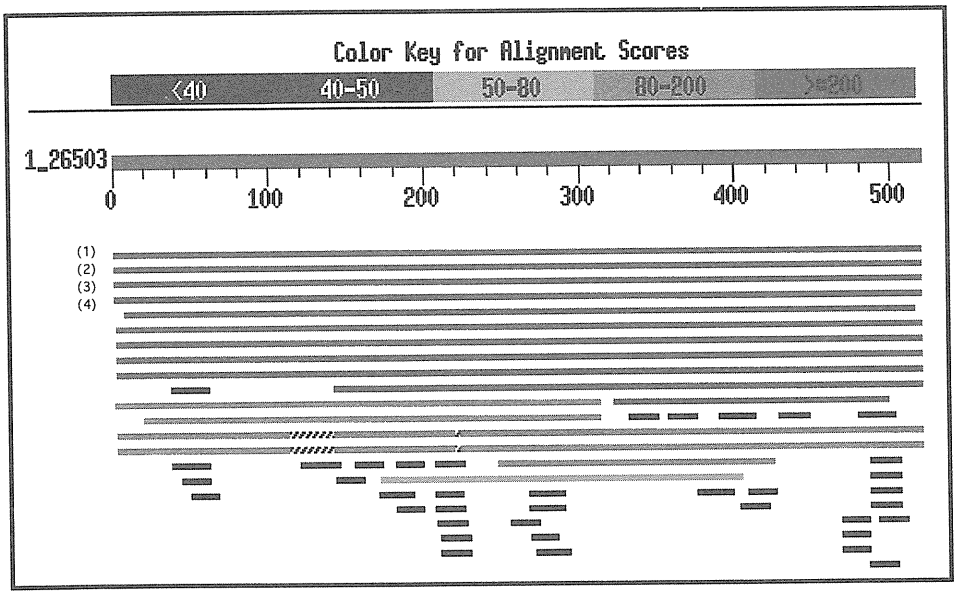

C ホモロジーの高い４遺伝子のアノテーション

(1) gi|13384979|ref|NM_025553.1|
Mus musculus mitochondrial ribosomal protein L11　Identities = 519/520 (99%)

(2) gi|12845690|dbj|AK010329.1|AK010329
Mus musculus ES cells, mitochondrial ribosomal protein L11　Identities = 519/520 (99%)

(3) gi|12833044|dbj|AK002797.1|AK002797
Mus musculus kidney, mitochondrial ribosomalprotein L11　Identities = 519/520 (99%)

(4) gi|13559368|dbj|AB049639.1|AB049639
Mus musculus MRPL11, mitochondrial ribosomal protein L11　Identities = 519/520 (99%)

D 塩基配列のホモロジー

```
(1) gi|13384979|ref|NM_025553.1
Query:   1 tacatcatgtccaagctaagccgggccactcggaccctcaagaagcccgaggccggcggc 60
           ||||||||||||||||||||||||||||||||||||||||||||||||||||||||||||
Sbjct:  74 tacatcatgtccaagctaagccgggccactcggaccctcaagaagcccgaggccggcggc 133

Query:  61 gtgatccggtccatcgtgcgagcaggccaagctattcctgggcctccactaggtcccatc 120
           ||||||||||||||||||||||||||||||||||||||||||||||||||||||||||||
Sbjct: 134 gtgatccggtccatcgtgcgagcaggccaagctattcctgggcctccactaggtcccatc 193

Query: 121 ttgggtcagcgaggtgtctctatcaaccagttctgcaaagagttcaacgagaagacaaag 180
           ||||||||||||||||||||||||||||||||||||||||||||||||||||||||||||
Sbjct: 194 ttgggtcagcgaggtgtctctatcaaccagttctgcaaagagttcaacgagaagacaaag 253

Query: 181 gacatcaaagaaggcattcccctgcctacaaaaatttttataaagcccgacaggacattt 240
           ||||||||||||||||||||||||||||||||||||||||||||||||||||||||||||
Sbjct: 254 gacatcaaagaaggcattcccctgcctacaaaaatttttataaagcccgacaggacattt 313

Query: 241 gagctcaagattgggcagcccactgtttcttacttttgaaggcagctgctgggatcgag 300
           ||||||||||||||||||||||||||||||||||||||||||||||||||||||||||||
Sbjct: 314 gagctcaagattgggcagcccactgtttcttacttttgaaggcagctgctgggatcgag 373

Query: 301 aaggggggcccggcatacagggaaagaggtggcaggcctggtgagtttgaagcacgtatat 360
           ||||||||||||||||||||||||||||||||||||||||||||||||||||||||||||
Sbjct: 374 aaggggggcccggcatacagggaaagaggtggcaggcctggtgagtttgaagcacgtatat 433

Query: 361 gagattgcctgtgtcaaagctaaggatgatgcttttaccatgcaagatgtgcccctgtct 420
           |||||||||||||||||||||||||||||||||| ||||||||||||||||||||||||
Sbjct: 434 gagattgcctgtgtcaaagctaaggatgatgcttttgccatgcaagatgtgcccctgtct 493

Query: 421 tctgtggtccgttccatcattggctctgcccgttccctgggcattcgagtggtgaaggac 480
           ||||||||||||||||||||||||||||||||||||||||||||||||||||||||||||
Sbjct: 494 tctgtggtccgttccatcattggctctgcccgttccctgggcattcgagtggtgaaggac 553

Query: 481 ctcagtgcagaagaactggaggctttccagaaggaacgag 520
           ||||||||||||||||||||||||||||||||||||||||
Sbjct: 554 ctcagtgcagaagaactggaggctttccagaaggaacgag 593
```

図 4　差分化遺伝子クローンのホモロジー検索の一例
1-178 と名付けた差分化遺伝子クローンの塩基配列を NCBI の BLAST サーチを行った結果，マウスのミトコンドリアのリボゾームタンパク質 L11 遺伝子と高い相同性が得られた。A，No. 1-178 クローンの塩基配列解読結果：B，BLAST 解析した結果のホモロジーをもつ遺伝子のアライメント結果：C，相同性の極めて高いトップ 4 遺伝子のアノーテーション情報 D，塩基性配列のホモロジー情報

表 1　88 遺伝子クローンのホモロジー検索結果

Unknown	EST		Known
1-87	1-79	332/332 (100%)	1-81 /32kDa
1-93	1-83	129/130 (99%)	1-84 /Thirod reductase
1-97	1-102	35/37 (94%)	1-85 /Myosin
1-100	1-112	291/306 (95%)	1-95 /TF
1-109	1-114	30/31 (96%)	1-104 /ESNRA
1-113	1-116	71/76 (93%)	1-122 /Msx Zn finger
1-121	1-125	239/254 (94%)	1-126 /sn RNA
1-143	1-127	54/54 (100%)	1-133 /galactin
1-149	1-128	297/300 (99%)	1-155 /c-jun
1-152	1-131	509/512 (99%)	1-164 /hydrolase
1-160	1-132	431/442 (97%)	1-167 /Centromere
1-163	1-136	199/218 (91%)	1-174 /Annexin Ⅲ
1-165	1-147	233/251 (92%)	1-178 /Mt rRNA protein
1-168	1-150	237/240 (98%)	1-191 /hydrolase
1-169	1-151	494/516 (95%)	1-198 /EST／MHC
1-171	1-157	181/192 (94%)	1-199 /G protein
1-172	1-161	507/521 (97%)	2p-12 /phosphatase
1-173	1-162	156/171 (91%)	2p-16 /GDP／disof.
1-180	1-176	518/518 (100%)	2b-59 /Tyr-phosphatase
1-182	1-177	487/494 (98%)	2b-46 /silence Med-EST
1-183	1-194	519/520 (99%)	
1-187	1-195	473/473 (100%)	
1-192	1-197	413/420 (98%)	
2b-45	2b-51	82/82 (100%)	
2b-47	2b-52	418/466 (89%)	
2b-50	2b-54	520/520 (100%)	
2b-55	2b-56	83/85 (97%)	
2b-57	2b-58	410/453 (90%)	
2b-58	2p-1	516/518 (99%)	
2p-20	2p-2	517/517 (100%)	
	2p-6	517/518 (99%)	
	2p-7	182/191 (95%)	
	2p-8	516/517 (99%)	
	2p-10	127/134 (94%)	
	2p-11	509/516 (98%)	
	2p-13	418/425 (98%)	
	2p-18	301/304 (99%)	
	2p-19	515/515 (100%)	
30 clones	38 clones		20 clones

表 2　22-Known クローンの既知遺伝子のアノテーション情報

Gene ID No.	Description	Identities
AB049639	Mus musculus MRPL 11 mRNA for mitochondrial ribosomal protein L11	515/516 (99%)
AA285552	Mus musculus GDP-dissociation inhibitor	513/518 (99%)
AJ001633	Mus musculus mRNA for annexin Ⅲ	513/517 (99%)
AI006497	Human protein phosphatase PP2A, 65kD regulatory subunit	511/518 (98%)
AF039567	Mus musculus Msx-interacting-zinc finger protein 1 (Miz 1)	492/494 (99%)
AF112439	Mus musculus Fanconi anemia group G protein	465/472 (98%)
AA856395	Mus musculus Hypotical 32.8kD pritein in PDE1-CSE1 interigenic region	363/375 (96%)
BF714528	Mus musculus SnRNA activating protein 50kD subunit	352/408 (86%)
AF116187	Mus musculus inner centromere protein	278/296 (93%)
AF218069	Mus musculus galectin-8	267/270 (98%)
BE334277	Mus musculus c-jun protein oncogene	259/263 (98%)
AF230356	Mus musculus U2 small nuclear ribonucleoprotein A	240/258 (93%)
U28807	Mus musculus lymphoid-specific transcription factor NFATc3	239/244 (97%)
AF110520	Mus musculus major histocompatibility complex NG27, 28, RPS28	190/194 (97%)
BF730197	Human Ubiquitin carboxyl-terminal hydrolase 16	158/170 (92%)
AF013490	Mus musculus protein-tyrosine phosphatase	128/133 (96%)
BC006075	Mus musculus Myosin, heavy polypeptide 9	121/134 (90%)
AA166294	Mus musculus Silencing mediator of retinoid & thyroid action	71/ 72 (98%)
AA611370	Mus musculus Bleomycin hydrolase	60/ 61 (98%)
AW743450	Mus musculus Thioredoxin-dependent peroxide reductase	46/ 49 (93%)

われわれはすでに，低出力レーザー照射したマウス骨芽細胞様細胞から遺伝子バンクを作成し，レーザー非照射細胞から回収した mRNA を結合させて取り除き，レーザー照射によって発現促進した約 50 遺伝子クローンを単離している。DNA ホモロジー検索の結果から，細胞周期のライセンス因子[10]や ATP 合成酵素の F0F1-ATPase[11]などの遺伝子を同定することに成功している。

本研究では，新たにレーザー照射 MC3T3E-1 の差分化 88 遺伝子クローンについて塩基配列を解読した。その結果，特にホモロジーが高かった既知遺伝子として，mitochondria ribosomal protein L11, GDP-dissociation inhibitor, annexin Ⅲ, protein phosphatase, MSX-interacting-zinc finger protein, Fraconi anemia group G protein などが同定された。また，ホモロジーが極めて高い EST クローンが数個同定された。

ribosomal protein L11 は，EF-G の機能に関与することが報告されており，タンパク質合成過程で重要な働きをすると考えられている[12]。GDP-dissociation inhibitor, protein phosphatase, G protein はいずれも情報伝達系において重要な役割を果たしている。Annxin Ⅲは，エナメル芽細胞や象牙芽細胞に見いだされており[13]，細胞カルシウムの調節に関与するといわれている[14]。MSX-2 は，顎顔面の発育に関与することが知られているが[15]，MSX-interacting-zinc finger protein は，MSX-2 の応答性エレメント DNA への結合に関与すると示唆されている[16]。今後，RT-PCR 法やノーザンブロット法によって mRNA レベルが上昇しているかを確認し，これら遺伝子の転写の促進が，どのように骨芽細胞の増殖，分化に関与するかの研究を進める必要がある。

また，EST クローンのなかには，ホモロジーが極めて高い EST 遺伝子が多く同定されている。マウスのゲノムプロジェクトが進展しており，新規に同定され機能が判明する遺伝子の情報がデータベースに蓄積されていくことから，ホモロジー検索を続けることによって新規遺伝子の発見が期待できる。

結　論

骨芽細胞 MC3T3E-1 に Ga-Al-As 半導体レーザー（モデル Panalas-1000，波長 830nm）照射し，非照射細胞の mRNA を用いて差分化遺伝子ライブラリーを作成した。新たに 88 遺伝子クローンの塩基配列を解読し，DNA データベースとホモロジー検索を行った。その結果，情報伝達系，タンパク合成系などに関与する遺伝子が同定された。これらの結果から，低出力レーザー照射は，これら遺伝子の転写促進により，骨芽細胞の増殖，分化に関与している可能性が示唆された。

謝　辞

本研究の一部は，文部科学省の科学研究費補助金基盤研究（A-1, 13357059）および学術フロティアー研究推進事業の補助を受けた。レーザー装置の使用について松下産業機器社の御協力に感謝致します。

文　献

1) Mester, E., Mester, A.F. and Mester, A.: The biomedical effects of laser application. Lasers Surg. Med., **5**, 31-39, 1985.
2) Ohshiro, T. and Calderhead, R.G.: Development of low reactive-level laser therapy and its present status. J. Clin. Laser Med. Surg., **9**: 267-275, 1991.
3) Vukmirovic, O.G. and Tilghman, S.M.: Exploring genome space. Nature, **405**: 820-822, 2000.
4) Tanaka, H., Yoshimura, Y., Nishina, Y., Nozaki, M., Nojima, H. and Nishimune, Y.: Isolation and characterization of cDNA clones specifically expressed in testicular germ cells. FEBS Lett., **355**: 4-10, 1994.
5) Kodama, H., Amagi, Y., Sudo, H., Kasai, S. and Yamamoto, S.: Establishment of clonal osteogenic osteoblastic cell line from newborn mouse calvaria. Jpn. J. Oral Biol., **23**: 899-901, 1981.
6) Hosoya, S., Tamura, K., Nomura, K., Abiko, Y.: Construction of subtracted osteoblast cDNA library with laser-irradiation-enhanced transcription. Laser Therapy, **9**: 107-114, 1997.
7) Sanger, F., Nicklen, S. and Coulson, A.R.: DNA sequencing with chain-terminating inhibitors. Pro. Natl. Acad. Sci. USA, **74**: 5463-5467, 1977.
8) Ozawa, Y., Shimizu, N., Mishima, H., Kariya, G., Yamaguchi, M., Takiguchi, H., Iwasawa, T. and Abiko, Y.: Stimulatory effects of low-power laser irradiation on bone formation in vitro. Advanced Laser Dentistry, International Conference, p 281-288, 1995.
9) Ozawa, Y., Shimizu, N., Kariya, G. and Abiko, Y.: Low-energy laser irradiation stimulated bone nodule formation at early stages of cell culture in rat calvarial cells. Bone, **22**: 347-354, 1998.
10) Yamamoto, M., Tamura. K., Hiratsuka, K. and Abiko, Y.: Stimulation of MCM3 gene expression in osteoblast by low level laser irradiation. Lasers Med. Sci., **16**: 213-217, 2001.
11) Tamura, K., Hosoya, S., Takema, T., Sakurai, Y., Fujii, T. and Abiko, Y.: Low level laser irradiation enhances expression of F0F1-ATPase subunit-b gene in osteoblastic cells. Laser Therapy, **10**: 107-116, 1998.
12) Agrawal, R.K., Linde, J., Sengupta, J., Nierhaus, K.H. and Frank, J.: Localization of L11 protein on the ribosome and elucidation of its involvement in EF-G-dependent translocation. J. Mol. Biol., **311**: 777-787, 2001.
13) Le Cabec, V. and Maridonneau-Parini, I.: Annexin 3 is associated with cytoplasmic granules in neutrophils and monocytes and translocates to the plasma membrane in activated cells. Biochem. J., **15**: 481-487, 1994.
14) Goldberg, M., Feinberg, J., Rainteau, D., Lecolle, S., Kaetzel, M.A., Dedman, J.R. and Weinman, S.: Annexins I - VI in secretory ameloblasts and odontoblasts of rat incisor. J. Biol. Buccale., **18**: 289-298, 1990.
15) Foerst-Potts, L. and Sadler, T.W.: Disruption of Msx-1 and Msx-2 reveals roles for these genes in craniofacial, eye, and axial development. Dev. Dyn., **209**: 70-84, 1997.
16) Wu, L., Wu, H., Ma, L., Sangiorgi, F., Wu, N., Bell, J.R., Lyons, G.E. and Maxson, R.: Mizl, a novel zinc finger transcription factor that interacts with Msx2 and enhances its affinity for DNA. Mech. Dev., **65**: 3-17, 1997.

原　著

歯科材料・器械 Vol. 24 No. 1　39－46（2005）

分子プレカーサー法で形成されたアパタイト薄膜の性質

—擬似体液中でのアパタイト薄膜上へのリン酸カルシウム生成—

髙橋健一[1]　早川　徹[1]　原　広樹[2]
吉成正雄[3]　望月千尋[2]　佐藤光史[2]
根本君也[1]

Properties of Hydroxyapatite Thin Film Prepared by Molecular Precursor Method

—Calcium Phosphate Formation on Apatite Thin Film in Simulated Body Fluid—

Kenichi TAKAHASHI[1], Tohru HAYAKAWA[1], Hiroki HARA[2],
Masao YOSHINARI[3], Chihiro MOCHIZUKI[2], Mitsunobu SATO[2]
and Kimiya NEMOTO[1]

Keyword：Titanium, Hydroxyapatite, Dental implant, Crystal growth, Surface modification

In the present study, the formation of calcium phosphate crystals was investigated in order to apply the thin film produced by the molecular precursor method as dental implant material. After the application of the precursor solution firing at 600℃ formed a crystalline carbonate-containing hydroxyapatite film on the titanium substrate.

The greater amount of formation of calcium phosphate crystals was observed on the titanium coated with carbonate-containing hydroxyapatite thin film compared with non-coated titanium after 1 day immersion in Hanks' balanced salt solution. After 7 days and 14 days immersion, the phosphate was carbonate-containing hydroxyapatite, which was aligned in C axis in thin film X-ray diffraction and Fourier transform infrared spectrum.

In conclusion, it is expected that the carbonate-containing hydroxyapatite thin film, produced by molecular precursor methods, will have excellent bone compatibility.

キーワード：チタン，ハイドロキシアパタイト，人工歯根，結晶成長，表面改質

本研究では，分子プレカーサー法を用いた薄膜形成法を歯科用インプラント材料に応用するための基礎実験として，擬似体液中でのリン酸カルシウム結晶の形成挙動について検討した．

プレカーサー溶液塗付後，600℃ で加熱焼成を行うことにより炭酸含有アパタイト薄膜をチタン基板に形成することができた．

炭酸含有アパタイト薄膜コーティングチタンはハンクス溶液浸漬１日後でコーティング処理を施していないチタン表面に比べて多数のリン酸カルシウム結晶が生成し，浸漬期間が７日，14日と長くなると，析出する結晶の量が増加した．結晶の薄膜Ｘ線回折測定およびフーリエ変換赤外分光測定の結果から，析出物はＣ軸に配向した炭酸含有アパタイトであることが分かった．

以上の結果から，分子プレカーサー法を用いて形成した炭酸含有アパタイト薄膜は良好な骨適合性が期待でき，歯科用インプラントとして臨床応用できる可能性のあることが示唆された．

原稿受付　2004年10月4日，受理　2004年12月13日

[1]日本大学松戸歯学部歯科理工学教室，口腔科学研究所（〒271－8587　松戸市栄町西2－870－1）
[2]工学院大学工学部配位工学研究室（〒192－0015　八王子市中野町2665－1）
[3]東京歯科大学歯科理工学講座，口腔科学研究センター（〒261－8502　千葉市美浜区真砂1－2－2）
[1]Department of Dental Materials Research Institute of Oral Science, Nihon University School of Dentistry at Matsudo（870－1, Sakaecho, Nishi 2, Matsudo, Chiba 271－8587）
[2]Coordination Engineering Laboratory, Faculty of Engineering, Kogakuin University（2665－1, Nakano, Hachioji, Tokyo 192－0015）
[3]Department of Dental Materials, Science and Oral Health Science Center, Tokyo Dental College（1－2－2, Masago, Mihama-ku, Chiba 261－8502）

緒　　言

アパタイトコーティングインプラントはチタンインプラントと比較して，骨形成速度や骨への結合力が勝っているなどの利点を有している[1~3]．しかしながら，現在歯科臨床で最も普及しているプラズマスプレー法によるアパタイトコーティングインプラントでは，アパタイト粉末をガラス状態に溶融してチタン基板に吹きつけて作製しているために，コーティング層の組成が不均一で，厚みが約50～100 μmと比較的厚くなってしまうなどの欠点がある．さらに，コーティング層とチタンとの密着性が不十分なために，長期間の臨床応用によってコーティング層の剥離や，コーティング層内での破壊が起こるなどの問題点が指摘されている[4,5]．

これらの問題点を改善するために，密着性に優れ，かつ均一な組成を有した数ミクロン以下の薄膜コーティング法が検討されている[6~10]．今までに，イオンプレーティング法[6]，マグネトロンスパッタリング法[7,8]，イオンビームダイナミックミキシング法[9,10]などの物理気相蒸着（PVD）法が導入されている．これらのPVD法で作製したアパタイトコーティング薄膜はチタン表面との密着性に優れ，組成も比較的均一である．PVD法を用いて作製したアパタイト薄膜コーティングインプラントの骨適合性について，細胞培養実験や動物実験などでその有効性が報告されている[11,12]．このようにPVD法はプラズマスプレー法の欠点を克服できる利点を有しているが，真空中で操作を行うために特別な器械を必要とする．また，複雑な形状を有する物体に均一にコーティングすることは困難である．そこで，ウェットプロセスによるアパタイト薄膜コーティング法も検討されている[13]．

Kimら[13]は，硝酸カルシウム，トリエチルフォスフェートなどを出発原料とするゾル-ゲル法について報告している．チタン基板を原料溶液に浸漬し，80℃で12時間乾燥させた後，500℃で1時間加熱焼成を行うことにより，チタン基板上にアパタイト薄膜およびフルオロアパタイト薄膜を形成した．細胞培養試験では，アパタイト薄膜およびフルオロアパタイト薄膜コーティングチタン基板は純チタンに比べて高いアルカリフォスファターゼ活性を示すことを報告している．

一方，Satoら[14~17]はセラミックスや金属材料上に金属酸化物被膜を形成する新たな手法である分子プレカーサー法を考案した．この分子プレカーサー法は，水溶性のEDTA-金属錯体を有機溶媒中でアルキルアミンと反応させることでエタノールなどの揮発性有機溶媒に可溶化させ，それをプレカーサーコーティング溶液として使用するものである．このプレカーサーコーティング溶液を基板上に塗布し，その後，至適温度で加熱処理を行うという簡便な工程で均一かつ高純度の薄膜を形成することができる画期的な手法である．ゾル-ゲル法では原料のポリマー化が製膜原理であるので溶液の保存性に問題があるが，この分子プレカーサー法ではEDTA-金属錯体が単独で存在するため，プレカーサー溶液の安定性が高く長期保存ができる，目的とする薄膜の成分比率は原料のプレカーサー溶液の組成比率で制御することができる，熱処理前では水洗によりプレカーサー膜を洗浄して基板を再生できるなどの優れた特徴がある[17]．

Satoらは，EDTA-金属錯体としてEDTA-Ca錯体を含有するプレカーサー溶液を用いると，チタン基板上にアパタイト薄膜が形成できることを見出した[18,19]．筆者らは，プレカーサー溶液塗布後の加熱焼成温度や薄膜の密着性などについて検討したところ，600℃で2時間，加熱焼成を行うことによりチタン基板上に密着性に優れた炭酸含有アパタイト薄膜を形成できることが判明し，歯科用インプラント材料の新規なアパタイト薄膜コーティング法としての有効性が示唆された[20,21]．

そこで本研究では，この分子プレカーサー法を用いた薄膜形成法を歯科用インプラント材料に応用するための基礎実験として，擬似体液中でのリン酸カルシウム形成挙動について検討を行った．

材料と方法

1. アパタイト膜形成用プレカーサー溶液の調製

アパタイト膜形成用プレカーサー溶液は既報に従い[20,21]，EDTA-Ca錯体とジブチルアミン（$(C_4H_9)_2NH$）のエタノール溶液とメタリン酸ジブチルアンモニウム塩（$((C_4H_9)_2NH_2)_2P_2O_6 \cdot 2H_2O$）を用いて調製した．

900mlの純水中に0.46 gのEDTA（関東化学）を加えた懸濁溶液に12.38 gの酢酸カルシウム一水和物（$Ca(CH_3COO)_2 \cdot H_2O$，関東化学）を加えて75℃で1時間加熱撹拌し反応させた．その後室温まで冷却し，さらに一晩放置後に，CaH_2（edta）$\cdot 2H_2O$の白色結晶を得た．この白色結晶を濾過した後，水とエタノールにて洗浄し，乾燥した．次に，4.00 gのCaH_2（edta）$\cdot 2H_2O$と3.26 gの$(C_4H_9)_2NH$（関東化学）とを43 gのエタノール中での還流下にて反応させてEDTA-Caエタノール溶液を得た．

$((C_4H_9)_2NH_2)_2P_2O_6 \cdot 2H_2O$は以下の方法で合成した．5.8 gの85%$H_3PO_4$（関東化学）を10 gのエタノール溶液に溶解し，その溶液を19.4 gの$(C_4H_9)_2NH$（関東化学）を含む10 gのエタノール溶液に加えた．5分間加熱還流して反応させ，冷却後，白色結晶（$(((C_4H_9)_2NH_2)_2P_2O_6 \cdot 2H_2O$）を減圧下で回収した．エタノールを用いて再結晶を行った．

$((C_4H_9)_2NH_2)_2P_2O_6 \cdot 2H_2O$をEDTA-Caエタノール溶液にCa/P比が1.67となるように加えてアパタイト膜形成用プレカーサー溶液を調製した．

2. アパタイト薄膜コーティング

基板には機械研磨（メーカー出荷時）した純チタン（直径15 mm，厚さ1.0 mm，99.9mass%，フルウチ化学）を使用した．チタン基板をエタノールで洗浄後，上記の方法で調製したアパタイト膜形成用プレカーサー溶液20 μl をチタン基板上に塗布した．その後，卓上型高速昇温電気炉（MSFT－1520－P，ニッカトー）を用いて，60℃ で20分間，予備乾燥を行いエタノールを揮発させ，その後600℃ で2時間，加熱焼成を行った．

チタン基板上に形成された薄膜について，薄膜X線回折法（XRD，MXP18AHF22，マックサイエンス）を用いて，電圧45kV，電流300mA，CuKα 線にて入射角度1° の条件で分析した．また，フーリエ変換赤外分光高感度反射法（FT－IR－RAS，FT－IR－210，ホリバ）による分析も併せて行った．

3. 擬似体液浸漬実験

アパタイトコーティングチタン基板をpH 7.4に調製した30ml の擬似体液中に浸漬した．擬似体液にはハンクス溶液[22,23]を用いた．Table 1にハンクス溶液の組成を示す．ハンクス溶液とポリスチレン容器は毎日交換した．1日，7日および14日間ハンクス溶液に浸漬後，サンプルを取り出し，蒸留水で洗浄後，デシケーター内で乾燥した．比較としてアパタイトコーティング処理を施していないチタン基板を用い，同様にして浸漬実験を行った．

チタン基板およびアパタイトコーティングチタン基板の表面に析出した結晶の形態を電界放射走査電子顕微鏡（FE－SEM，JSM－6340F，日本電子）を用いて加速電圧5kVで観察した．なお，結晶は乾燥後，イオンコータ（JFC－1600，日本電子）を用いて白金蒸着を施した．

また，析出した結晶の断面観察するために，ハンクス浸漬7日後のサンプルをMMA（1.25ml dibuthylphthalate，0.025 g pekadox，20ml MMA）溶液を用いて包埋した．MMA重合後，マイクロ・カッティング・マシン（BS－300CP，盟和商事）を用いてサンプルを切断し，#1000の耐水ペーパーと6 μm，1 μm，0.25 μm のダイヤモンドペースト（straeus）を順次用いて鏡面研磨を行った後，超音波洗浄を行い，同様にしてFE－SEMを用いて断面観察した．

結晶の構造解析は，薄膜XRDを用いて，電圧45kV，電流300mA，CuKα 線にて入射角度1° の条件で行った．また，フーリエ変換赤外分光KBr法（FT－IR－KBr，FT－IR－210，ホリバ）による分析も併せて行った．

Table 1 Composition of Hanks' balanced salt solution without organic species

Composition	Weight (g)
NaCl	8.00
KCl	0.40
$Na_2HPO_4 \cdot 12H_2O$	0.12
KH_2PO_4	0.06
$MgSO_4 \cdot 7H_2O$	0.20
$NaHCO_3$	0.35
$CaCl_2$	0.35

Each inorganic salt was dissolved in 1L of double distilled water

結　果

調製したアパタイト膜形成用プレカーサー溶液は無色透明で，チタン基板上へ容易に塗付することができた．アパタイト膜形成用プレカーサー溶液をチタン基板に塗付後，600℃ で焼成した試料の薄膜XRDの測定結果をFig. 1に示す．図に示すように，2θ =31.8° (211)，33.0° (300)，46.8° (222)，49.5° (213) のピークはアパタイトのピークとほぼ一致していた．その他に基板由来のチタン，ルチル，アナターゼのピークが観察された．この結果から，薄膜の主成分はアパタイトであることが判明した．

FT－IR－RASの測定結果をFig. 2に示す．550～600 cm^{-1} 付近と900～1200 cm^{-1} 付近にアパタイトのリン

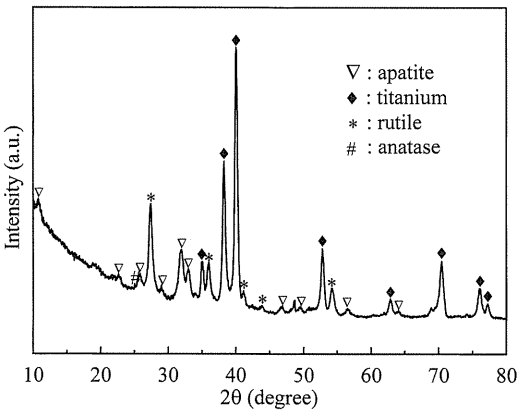

Fig. 1 X-ray diffraction patterns of carbonate apatite coatings with firing temperature at 600℃

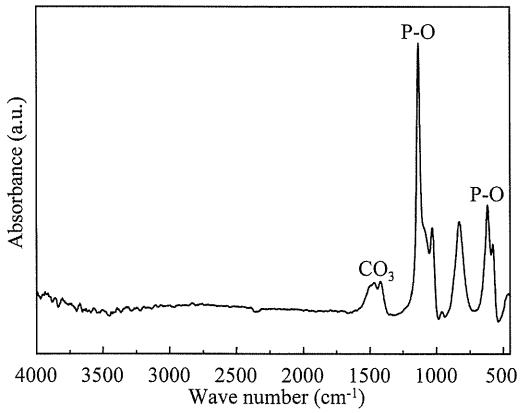

Fig. 2 FT-IR spectrum of carbonate apatite coatings with firing temperature at 600℃

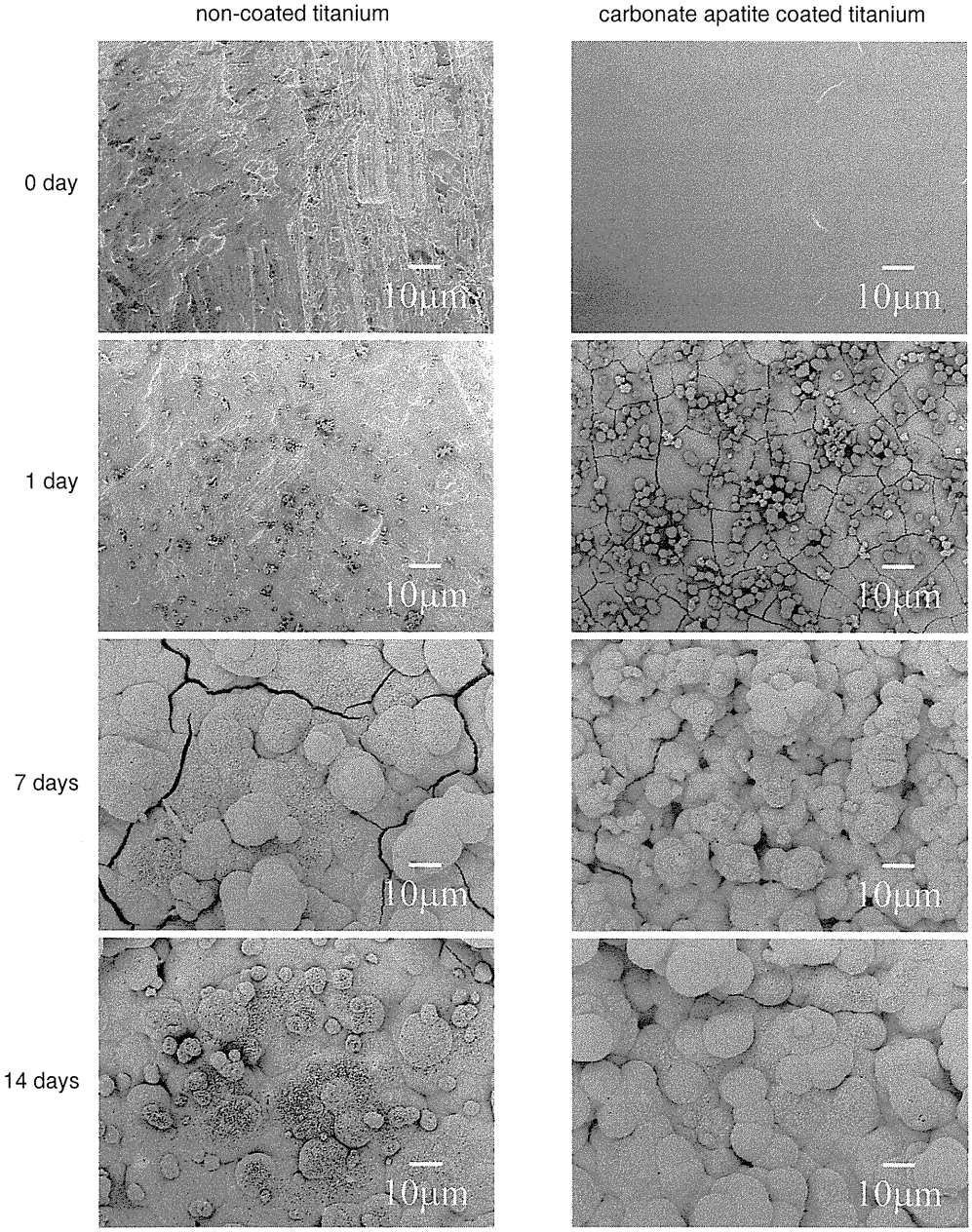

Fig. 3 FE-SEM pictures of surface appearances of carbonate apatite coated titanium and non-coated titanium after the immersion in Hanks' balanced salt solution

酸基のP-O結合に由来するピークが観察された．また，1300～1600 cm^{-1}付近に炭酸基に由来するピークが観察されたことから，形成した薄膜は炭酸含有アパタイトであることが判明し，以前の報告と一致していた[18~21]．

Fig. 3にハンクス溶液浸漬前および浸漬後のチタン基板とアパタイトコーティングチタン基板表面のFE-SEM像を示す．浸漬1日後では，チタン基板表面にはわずかに結晶が析出しているのが観察された．一方，アパタイトコーティングチタン基板表面にはチタン基板表面よりも多数の球状結晶が生成している様子が観察された．浸漬7日後と14日後では，チタン基板とアパタイトコーティングチタン基板ともに，表面全体が球状の結晶で覆われており，肉眼的にも白色結晶の析出が確認できた．

Fig. 4に浸漬7日後に生成した結晶断面のFE-SEM像を示す．基板表面から結晶が剥離していたが，これは包埋もしくは観察時のアーチファクトによるものだと考えられる．それぞれの基板上に析出した結晶を観察すると，アパタイトコーティングチタン基板上では約20 μm，チタン基板上では約10 μmの厚みで結晶が生成しており，アパタイトコーティングチタン基板上でより多くの結晶が生成していることが確認できた．

浸漬7日後と14日後に析出した白色結晶のFE-SEMによる強拡大像をFig. 5に示す．14日後では結晶が緻密

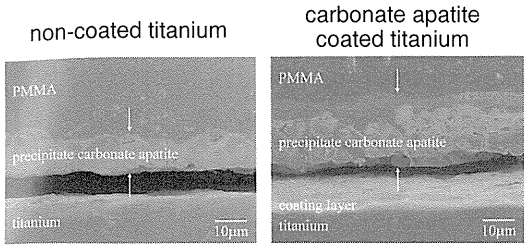

Fig. 4 FE－SEM pictures of cross-section view of carbonate apatite coated titanium and non-coated titanium after 7 days immersion in Hanks' balanced salt solution

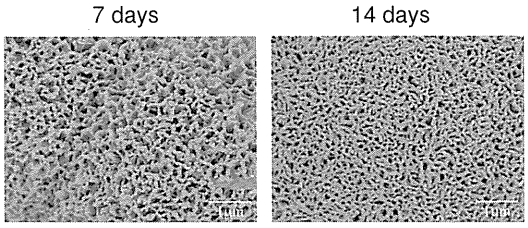

Fig. 5 Higher magnification FE－SEM pictures of the surface of carbonate apatite coated titanium after the immersion in Hanks' balanced salt solution at 7 days and at 14 days

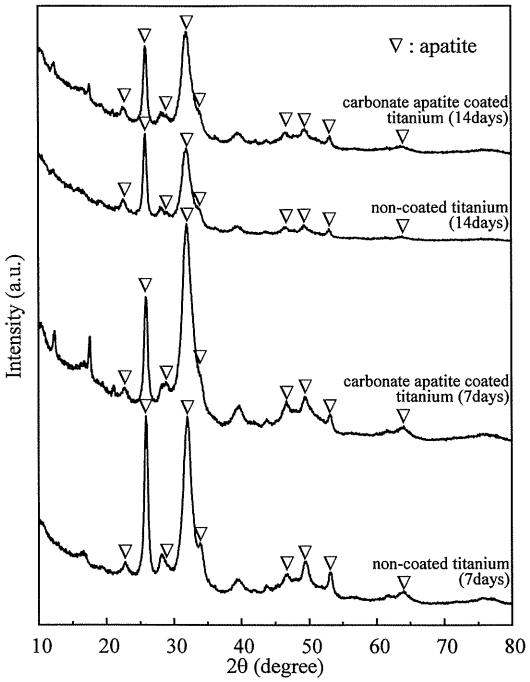

Fig. 6 X－ray diffraction patterns of white substance formed on carbonate apatite coated titanium and non-coated titanium after 7 days and 14 days immersion in Hanks' balanced salt solution

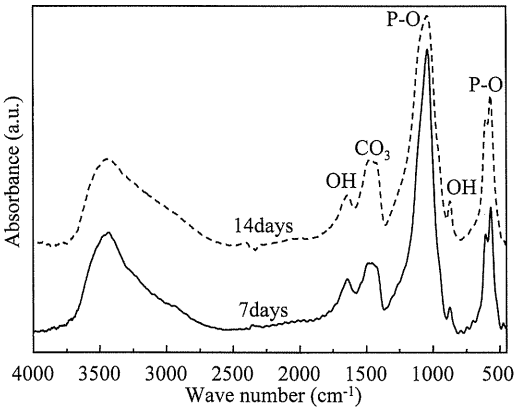

Fig. 7 FT－IR spectra of white substance formed on calcium phosphate coated titanium after 7 days and 14 days immersion in Hanks' balanced salt solution

になっている様子が確認できる．一つの結晶塊の大きさは約5～10μmであった．

ハンクス溶液浸漬7日後と14日後にチタンおよびアパタイトコーティングチタン基板表面に析出した結晶の薄膜XRDの測定結果をFig. 6に示す．2θ=31.9° (211)，25.8° (002)，49.5° (213)，46.7° (222) のピークはアパタイトのピークとほぼ一致しており，析出物の主成分はアパタイトであることが判明した．一方，ハンクス溶液浸漬前に観察されたチタン，ルチルならびにアナターゼのピークはほぼ消失した．また，チタンおよびアパタイトコーティングチタン基板表面に析出した結晶のXRDの結果に違いは認められなかった．

ハンクス溶液浸漬7日後，14日後それぞれの (002) 面ピークは浸漬前のサンプルのピークより大きいことから，ハンクス溶液浸漬により析出するアパタイト結晶は，分子プレカーサー法によって基板にコーティングされたアパタイトと結晶構造が異なるC軸配向性を持つことが確認された．さらに，2θ=25.8° (002) に観察されるピークの強度比を比較した結果，チタンおよびアパタイトコーティングチタン基板表面ともに，7日後に比べ14日後のほうが強度比が増大しており，六方晶アパタイトがC軸方向に配向して成長析出していることを示している．

ハンクス溶液浸漬7日後と14日後にアパタイトコーティングチタン基板表面に析出した結晶のFT－IRの測定結果をFig. 7に示す．FT－IR－RAS法では，結晶のピークがアパタイトコーティング膜のピークと重なってしまい測定が困難であったので，析出した結晶を基板からかきとりKBr法にて測定した．Fig. 7に示すように，550～600 cm^{-1}付近と900～1200 cm^{-1}付近にP－O結合に由来するピークが観察された．このピークはアパタイトのリン酸基に由来するものと考えられる．1300～1600 cm^{-1}付近に炭酸基に由来するピークが観察されたことから，析出物は炭酸含有アパタイトであることが分かった．Fig. 2と異なり，アパタイトの水酸基のピーク

が明瞭に観察されたが，これは測定方法の違いに起因するものと思われる．また，7日後と14日後ではFT－IRスペクトルにほとんど違いは見られなかった．

考　　察

本研究では，分子プレカーサー法を用いた炭酸含有アパタイト薄膜形成法を歯科用インプラント材料に応用するための基礎実験として，擬似体液中でのリン酸カルシウム結晶の形成挙動について検討を行った．

分子プレカーサー法はEDTA－金属錯体のアルコール溶液を基板上に塗布し，その後，至適温度で加熱焼成を行うという簡便な工程で基板表面に密着性の良い均一な金属薄膜を得る手法である[17]．この分子プレカーサー法の利点として，溶液の濃度や塗布回数により膜厚のコントロールが容易であり，また，あらゆる形状の物体やポーラス体などへの薄膜コーティングが可能であることが挙げられる．Satoらはこれまでに分子プレカーサー法を用いた製膜法でTiO_2，Co_3O_4，$SrTiO_3$などの薄膜形成に成功してきた[14~16]．

本研究においても，EDTA－Caエタノール溶液に$((C_4H_9)_2NH_2)_2P_2O_6 \cdot 2H_2O$を添加して合成したアパタイト膜形成用プレカーサー溶液[20,21]は，容易にチタン基板に塗布することができ，また塗布後，加熱処理のみの簡便な工程でチタン基板状にクラックや剥離のない密着性の良い炭酸含有アパタイト薄膜を形成することができた．

FT－IR－RASの測定結果から，形成した薄膜は炭酸含有アパタイトであることが判明した．これは，原料に用いたEDTAの酢酸残基の一部が焼成時にCO_3となってアパタイト膜中に残存し，リン酸カルシウム中の水酸基と置換して，炭酸含有アパタイトになったものと考えられる．

通常，マグネトロンスパッタリング法やイオンビームダイナミックミキシング法のようなPVD法を用いてチタン基板上に形成されたアパタイト薄膜はアモルファス状態であり，薄膜を結晶化させるためには何らかの熱処理が必要となる．しかしながら，電気炉を用いた熱処理法では熱膨張係数の違いから薄膜がチタン基板から剥離したり，クラックが発生することなどが問題となっている[24,25]．Yoshinariら[26]は赤外線急速加熱処理法を用いると，チタン基板上に形成されたアモルファスなアパタイト薄膜がチタン基板から剥離することなく，また薄膜にクラックが生じることなく結晶化できることを見出した．今回用いた分子プレカーサー法は，プレカーサー溶液塗布後の600℃加熱焼成処理で，炭酸含有アパタイト薄膜の形成と同時に，形成された炭酸含有アパタイト薄膜の結晶化も同時に行えるという利点を有していることが分かった．

チタンの生体適合性を検討するための予備実験の一つとして，擬似体液浸漬実験が報告されている．Hanawaら[22,23]は，チタン基板をハンクス溶液に浸漬すると，基板表面に炭酸含有アパタイトが析出することを見出した．また，Takadamaら[27]とZhangら[28]はチタンをNaOHやKOHなどのアルカリ処理後，加熱処理を施してヒトの体液（血清）とほぼ等しい無機イオン濃度を有する擬似体液に浸漬すると，チタン表面に骨類似のアパタイト層が形成することを明らかにした．

本研究では，擬似体液としてHanawaらと同様の組成をもつハンクス溶液[22,23]を用いてチタンおよび炭酸含有アパタイトコーティングチタン基板表面でのリン酸カルシウム結晶の析出状態を調べた．その結果，浸漬1日後においてチタン基板ではほとんど結晶が観察されなかったが，炭酸含有アパタイトコーティングチタン基板では，直径3~5μmの球状をした炭酸含有アパタイトの生成が観察できた．この結果から，炭酸含有アパタイトコーティングチタン基板は，コーティング処理を施していないチタン基板に比較して早期に炭酸含有アパタイトの生成を促進することが分かった．

Strnadら[30]は，ブラスト処理のみのチタンインプラントを擬似体液に浸漬したところ50日浸漬でもリン酸カルシウムの結晶形成が認められなかったが，プラズマスプレー法によって作製したアパタイトコーティングインプラントの場合にはその表面に骨様アパタイトが早期に形成することを報告しており，本研究の結果と同様の傾向を示している．

分子プレカーサー法で形成された炭酸含有アパタイト薄膜表面はアパタイト中のOH^-とPO_4^{3-}によってマイナスに帯電していることが予想される．したがって，ハンクス溶液中で，まず溶液中のCa^{2+}が薄膜表面に吸着する．その結果，今度は表面がプラスに帯電して溶液中のPO_4^{3-}が付着する．この工程を繰り返すことで，アパタイト薄膜表面に炭酸含有アパタイトが形成するものと思われる[31]．また，炭酸含有アパタイト中のCa^{2+}が一部溶解して，ハンクス溶液中のCa^{2+}濃度を上昇させ，結晶性成長を促進させている可能性も考えられる[32,33]．詳細なメカニズムは今後の検討課題である．

薄膜XRDの測定結果から，ハンクス溶液浸漬により析出する炭酸含有アパタイトは，基板にコーティングされた炭酸含有アパタイトとは結晶構造が異なるC軸配向性を持つことが確認された．Ueshimaら[34]は，分極化させたアパタイトを擬似体液中に浸漬することで，析出するアパタイト結晶の配向性を制御することに成功している．また，Asadaら[35]，Yenら[36]の報告によると，ハンクス溶液中で析出するアパタイトは（002）面配向する傾向があり，本研究においても同様の結果が得られた．

一方，ハンクス溶液浸漬前のチタン，ルチルならびにアナターゼのピークがほぼ消失したが，これは析出した結晶が基板表面を覆い，チタン基板やコーティング膜のピークが現れなかったためだと考えられる．

また，ハンクス溶液浸漬7日後および14日後の薄膜XRDの測定結果では，14日後のサンプルのピーク強度が7日後のサンプルのピークと比較して小さくなっていた．これは，14日浸漬サンプルのほうがより多くのアパタイトが析出して表面が粗くなり，X線が散乱して，その結果ピーク強度が小さくなったためかと考えられる．

一般に生体活性といわれているアパタイトや生体ガラスなどが擬似体液中で骨様アパタイト，すなわち炭酸含有アパタイトを形成することはよく知られており[37,38]，擬似体液中でのアパタイト形成能が骨適合性の指標の一つとして用いられている．したがって，本研究の結果から分子プレカーサー法によって形成された炭酸含有アパタイト薄膜は良好な組織適合性が期待できるものと考えられ，歯科用インプラントとして臨床応用できる可能性のあることが示唆された．

結　　論

分子プレカーサー法を用いることにより，チタン基板上に溶液を塗布し焼成を行うという簡便な工程で結晶化した炭酸含有アパタイト薄膜を得ることができた．分子プレカーサー法でコーティングしたチタン基板を擬似体液中に浸漬すると，コーティング処理を施していないチタン基板よりも早期に基板表面に炭酸含有アパタイトが析出することが分かった．また，析出した炭酸含有アパタイトはチタン基板にコーティングした炭酸含有アパタイトと結晶構造が異なるC軸配向性を持つことが分かった．

以上の結果から，分子プレカーサー法を用いて形成した炭酸含有アパタイト薄膜は良好な組織適合性が期待できることが分かった．

謝　　辞

本研究の一部は，日本学術振興会平成15年度科学研究費補助金（基盤C2：15592073）および文部科学省平成13年度学術フロンティア推進事業によって行った．

文　　献

1) Mohammadi S, Esposito M, Hall J, Emanuelsson L, Krozer A, Thomsen P. Short-term bone response to titanium implants coated with thin radiofrequent magnetron-sputtered hydroxyapatite in rabbits. Clin Implant Dent Relat Res 2003；5：241－253.
2) Yang Y, Bumgardner JD, Cavin R, Carnes DL, Ong JL. Osteoblast precursor cell attachment on heat-treated calcium phosphate coatings. J Dent Res 2003；82：449－453.
3) Son WW, Zhu X, Shin HI, Ong JL, Kim KH. In vivo histological response to anodized and anodized/hydrothermally treated titanium implants. J Biomed Mater Res 2003；15：520－525.
4) Cheang P, Khor KA. Addressing processing problems associated with plasma spraying of hydroxyapatite coatings. Biomaterials 1996；17：537－544.
5) Jansen JA, van der Waerden, JPCM, Wolke JCG. Histologic investigation of the biological behavior of different hydroxyapatite plasma-sprayed coatings in rabbits. J Biomed Mater Res 1993a；27：603－610.
6) Yoshinari M, Ozeki K, Sumii T. Properties of hydroxyapatite-coated Ti－6Al－4V alloy produced by the ion-plating method. Bull Tokyo Dent Coll 1991；32：147－156.
7) Jansen JA, Wolke JGC, Swann S, van der Waerden JPCM, de Groot K. Application of magnetron sputtering for producing ceramic coatings on implant materials. Clin Oral Impl Res 1993；4：28－34.
8) Wolke JCG, de Groot K, Jansen JA. In vivo dissolution behavior of various RF magnetron sputtered Ca－P coatings. J Biomed Mater Res 1998；39：524－530.
9) Yoshinari M, Ohtsuka Y, Derand T. Thin hydroxyapatite coating produced by the ion beam dynamic mixing method. Biomaterials 1994；15：529－535.
10) Yoshinari M, Klinge B, Derand T. The biocompatibility (cell culture and histologic study) of hydroxy-apatite-coated implants created by ion beam dynamic mixing. Clin Oral Implants Res 1996；7：96－100.
11) Hulshoff JEG, Hayakawa T, van Dijk K, Leijdekkers-Govers AFM, van der Waerden JPCM, Jansen JA. Mechanical and histologic evaluation of Ca－P plasma-spray and magnetron sputter-coated implants in trabecular bone of the goat. J Biomed Mater Res 1997；36：75－83.
12) Hayakawa T, Yoshinari M, Nemoto K, Wolke JGC, Jansen JA. Effect of surface roughness and calcium phosphate coating on the implant/bone response. Clin Oral Implants Res 2000；11：296－304.
13) Kim HW, Kim HE, Knowles JC. Fluor-hydroxyapatite sol-gel coating on titanium substrate for hard tissue implants. Biomaterials 2004；25：3351－3358.
14) Sato M, Hara H, Nishide T, Sawada Y. A water-resistant precursor in a wet process for TiO_2 thin film formation. J Mater Chem 1996；6：1767－1770.
15) Sato M, Hara H, Kuritani H, Nishide T. Novel route to Co_3O_4 thin films on glass substrates via *N*-alkyl substituted amine salt of Co（Ⅲ）－EDTA complex. Sol Energy Mater Sol Cells 1997；45：43－49.
16) Sato M, Tanji T, Hara H, Nishide T, Sakashita Y. $SrTiO_3$ film fabrication and powder synthesis from a non-polymerized precursor system of a stable Ti（Ⅳ）complex and Sr（Ⅱ）salt of etda. J Mater Chem 1999；9：1539－1542.
17) 佐藤光史．分子プレカーサー法の新展開―欠陥のない金属酸化物薄膜を作る―．未来材料 2002；2, 12－17.
18) Sato M, Mochizuki C. Hydroxyapatite film fabrication by molecular precursor method (2). Proceeding of International Symposium on Advanced Technology 2002；p. 76.
19) Sato M, Hara H, Tomikoshi H, Mochizuki C. Film fabrication of monolithic hydroxyapatite by an application of molecular precursor method. International Symposium on Advance Technology, ISAT－2nd. Nanotechnology&Its Related Sciences. p. 892.
20) 高橋健一，早川　徹，原　広樹，吉成正雄，佐藤光史，根本君也．分子プレカーサー法を用いたチタン基板上へのアパタイト薄膜形成　その1 ―焼成温度による影響―．歯材器 2004；（抄録集）23：124.
21) 高橋健一，早川　徹，原　広樹，吉成正雄，佐藤光史，根

本君也．分子プレカーサー法を用いたチタン基板上へのアパタイト薄膜形成　その2　—薄膜の密着性—．歯材器 2004；(抄録集) 23：405.

22) Hanawa T. Titanium and its oxide film：a substrate for formation of apatite. Davies 編．The Bone-Biomaterials Interface. University of Toronto Press. 1991. p. 49－61.

23) Hanawa T, Ota M. Calcium phosphate naturally formed on titanium in electrolyte solution. Biomaterials 1991；12：767－774.

24) Ong JL, Lucas LC, Lacefield WR, Rigney ED. Structure, solubility and bond strength of thin calcium phosphate coatings produced by ion beam sputter deposition. Biomaterials 1992；13：249－254.

25) Ohtsuka Y, Matsuura M, Chida N, Yoshinari M, Sumii T, Derand T. Formation of hydroxyapatite coating on pure titanium substrates by ion beam dynamic mixing. Surf CoatTech 1994；65：224－230.

26) Yoshinari M, Hayakawa T, Wolke JGC, Nemoto K, JA Jansen. Influence of rapid heating with infrared radiation on RF magnetron-sputtered calcium phosphate coatings. J Biomed Mater Res 1997；37：60－67.

27) Takadama H, Kim HM, Kokubo T, Nakamura T. An X-ray photoelectron spectroscopy study of the process of apatite formation on bioactive titanium metal. J Biomed Mater Res 2001；55：185－193.

28) 張　栩，宮路史明，八尾　健，小久保正，大槻主税．チタン金属への生体活性の付与．粉体および粉末冶金 1994；41：664－997.

29) Yang BC, Weng J, Li XD, Zhang XD, The order of calcium and phosphate ion deposition on chemically treated titanium surfaces soaked in aqueous solution. J Biomed Mater Res 1999；47：213－219.

30) Strnad Z, Strnad J, Povysil C, Urban K, Effect of plasma-sprayed hydroxyapatite coating on the osteoconductivity of commercially pure titanium implants. Oral Maxillofac Implants 2000；15：483－490.

31) Kim HM, Himeno T, Kawashita M, Kokubo T, Nakamura T. The mechanism of biomineralization of bone-like apatite on synthetic hydroxyapatite：an in vitro assessment. JR Soc Lond Interface 2004；1：1－6.

32) Khor KA, Li H, Cheang P. Characterization of the bone－like apatite precipitated on high velocity oxy-fuel (HVOF) sprayed calcium phosphate deposits. Biomate-rials 2003；24：769－775.

33) Gu YW, Khor KA, Cheang P. In vitro studies of plasma-sprayed hydrxyapatite/Ti－6Al－4V composite coatings in simulated body fluid (SBF). Biomaterials 2003, 24. 1603－1611.

34) Ueshima M, Nakamura S, Ohgaki M, Yamashita K. Electrovectorial effect of polarized hydroxyapatite on quasi-epitaxial growth at nano-interfaces. Solid State Ionics 2002；151：29－34.

35) Asada M, Miura Y, Osaka. A hydroxyapatite crystal growth on calcium hydroxyapatite ceramics. J Mater Sci 1988；23：3202－3205.

36) Yen SK, Lin CM. Characterization of electrolytic Al_2O_3/CaP composite coatings on pure titanium. J Electrochem Soc 2002；149：79－87.

37) Kokubo T, Ito S, Huang ZT, Hayashi T, Sakka S. Ca, P-rich layer formed on high-strength bioactive glass-ceramic A-W. J Biomed Mater Res 1990；24：331－343.

38) 小久保正．骨になじむセラミックス．第5回「大学と科学」公開シンポジウム組織委員会．医療のための新しい材料生体機能性材料の新展開：1991；p. 35－49.

Available online at www.sciencedirect.com
SCIENCE DIRECT®
Thin Solid Films 484 (2005) 1–9
thin solid films
www.elsevier.com/locate/tsf

Molecular precursor method for thin calcium phosphate coating on titanium

Kenichi Takahashi[a,*], Tohru Hayakawa[b], Masao Yoshinari[c], Hiroki Hara[d], Chihiro Mochizuki[d], Mitsunobu Sato[d], Kimiya Nemoto[b]

[a]*Department of Dental Materials, Nihon University Graduate School of Dentistry at Matsudo, 2-870-1, Sakaecho-nishi, Matsudo, Chiba 271-8587, Japan*
[b]*Department of Dental Materials, Research Institute or Oral Science, Nihon University School of Dentistry at Matsudo, 2-870-1, Sakaecho-nishi, Matsudo, Chiba 271-8587, Japan*
[c]*Department of Dental Materials, Science and Oral Health Science Center, Tokyo Dental College, 1-2-2 Masago, Mihamaku, Chiba 261-8502, Japan*
[d]*Coordination Engineering Laboratory, Faculty of Engineering, Kogakuin University, 2665-1, Nakano, Hachioji, Tokyo 192-0015, Japan*

Received 2 August 2004; accepted in revised form 22 December 2004
Available online 21 January 2005

Abstract

Carbonate-containing hydroxyapatite was deposited onto titanium using a molecular precursor method, which is a novel technique for coating metal oxide film. The molecular precursor solution was prepared by the addition of dibutylammonium metaphosphate salt to an ethanol solution of Ca-ethylenediamine-*N*,*N*,*N*′,*N*′-tetraacetic acid/amine complex. The molecular precursor solution was applied to titanium and fired at different temperatures from 300 to 700 °C for 2 h using a furnace under ordinary atmospheric conditions. A firing temperature below 400 °C did not produce an apatite film on the titanium. Firing at 600 or 700 °C formed a crystalline carbonate-containing hydroxyapatite film on the titanium substrate. Thermal analysis confirmed that a firing temperature above 500 °C is necessary to form calcium phosphate films on titanium substrates. The coating thickness and Ca/P ratio determined by electron probe microanalysis were about 0.44±0.01 μm and 1.56±0.04, respectively. After immersion of coated specimens in phosphate buffered saline (PBS) solution for periods of 1 week and 1 month, the formation of slight cracks in the coated films was observed. The tensile bond strength measurement and scratch test showed an excellent degree of adhesion of the coated film on the titanium after the PBS immersion. Finally, we concluded that a firing temperature of 600 °C is suitable for producing an adherent carbonate-containing apatite film on titanium.
© 2005 Elsevier B.V. All rights reserved.

PACS: 36; 73; 91; 492
Keywords: Biomaterials; Coatings; Deposition process; Titanium

1. Introduction

In the last decade, physical vapor deposition (PVD) techniques such as ion plating [1], magnetron sputtering [2], and ion beam dynamic mixing [3] have been introduced to deposit thin calcium phosphate coatings on medical implants, especially oral implants. The PVD methods can avoid some intrinsic shortcomings of plasma-sprayed calcium phosphate coatings [4–6]. For example, PVD deposited calcium phosphate coatings are more adherent to the underlying titanium surface and less prone to form cracks than are plasma-sprayed coatings [2,3]. Frequently, these coatings initially appear to be amorphous, which can easily be improved by rapid heat treatment with infrared radiation [7]. The main component of the crystalline structure of these heat-treated films is hydroxyapatite. Previous cell cultures and animal experiments have indicated the biological feasibility of this type of coating [8–11].

The deposition of carbonate apatite film on a titanium substrate is interesting because of its chemical resemblance to bone mineral. Recently, Leeuwenburgh et al. [12,13] reported a new coating technology referred to as electrostatic spray deposition (ESD), which was originally

* Corresponding author. Tel.: +81 47360 9349; fax: +81 47360 9350.
E-mail address: hashiken@mascat.nihon-u.ac.jp (K. Takahashi).

0040-6090/$ - see front matter © 2005 Elsevier B.V. All rights reserved.
doi:10.1016/j.tsf.2004.12.052

developed to synthesize thick ceramic films for solid electrolytes [14]. They found that crystalline carbonate apatite coatings were formed after heat treatment of as-deposited ESD coating. Siebers et al. [15] assayed the cell proliferation, alkaline phosphatase activity, and osteocalcin concentration of osteoblast-like cells on such calcium phosphate coatings deposited by ESD.

A disadvantage of the ESD technique is that it is a line-of-sight technique, which makes it difficult to apply uniform coatings on complex implant surface geometries or inside porous scaffold materials, such as titanium fiber mesh [16].

Liu et al. [17] deposited a thin hydroxyapatite film on stainless steel using a water-based sol-gel technique. A dense and adhesive apatite coating can be produced through water-based sol-gel technology after short term annealing at around 400 °C in air. Kim et al. [18] used a sol-gel method to coat a fluoro-hydroxyapatite film on a zirconia substrate. The use of the sol-gel technique has the potential for applying uniform coatings to porous substrates.

However, in the conventional sol-gel process alkoxides are employed and the rigorous exclusion of water from the system is essential for the synthesis and conservation of the precursor alkoxides and their solutions since the process is based on partial or complete hydrolysis of such metal alkoxides [19].

Sato et al. [20–22] also developed a novel method for coating ceramics and metal materials with metal oxide film. They called their method the molecular precursor method. The principle of the method is the application of an alcoholic precursor solution of an ethylenediamine-*N*,*N*,*N*′,*N*′-tetraacetic acid (EDTA)–metal complex on the substrate and then firing the material at around 500–700 °C. Film formation can be attained by a combination of anionic species involving metal ions and adequate alkylammonium cations without a polymerization process. Thin films of TiO_2, Co_3O_4, and $SrTiO_3$ were coated onto a glass substrate using a Ti–EDTA or Co–EDTA complex by the molecular precursor method. The molecular precursor method was also used to produce $SrTiO_3$ thin film using a mixture of the Ti–EDTA and Sr–EDTA complex.

Recently, Sato et al. [23] found that hydroxyapatite can be deposited on titanium by using a precursor solution of a Ca–EDTA complex. Two types of precursor solutions, i.e., those with or without water, were evaluated. It was found that the Ca–EDTA precursor solution without water is more stable during storage. Thus, the recommended precursor solution is the ethanol solution reported here. To examine the possibility of applying this method to the dental and orthopedic fields, a detailed analysis of the effects of firing temperatures on titanium and a more comprehensive characterization of the deposited films should be made.

In the present study, we aimed to deposit carbonate-containing hydroxyapatite on titanium using the molecular precursor method. We investigated the influence of firing temperatures on the fabrication of carbonate-containing hydroxyapatite coating on titanium as well as some physical properties of the deposited carbonate–apatite film for implant use.

2. Experimental details

2.1. Preparation of molecular precursor solution

The molecular precursor solution for the carbonate-containing hydroxyapatite coating was obtained by adding metaphosphate salt to a Ca–EDTA/amine ethanol solution. The general procedure for the preparation of the molecular precursor solution is shown in Fig. 1.

2.1.1. Step 1: Ca–EDTA/amine ethanol solution

To a suspended solution of 20.46 g of EDTA (Kanto Chemicals, Tokyo, Japan) in 900 ml deionized water (18MΩcm), 12.38 g of $Ca(CH_3COOH)_2$ was added with stirring at 75 °C for 1 h, and then the reaction mixture was cooled to room temperature. After that the reaction mixture was allowed to stand overnight. $CaH_2(edta)\cdot 2H_2O$ was obtained as a white precipitate. The white precipitate was collected by filtration and rinsed with deionized water and ethanol, then dried in a vacuum. The yield of $CaH_2(edta)\cdot 2H_2O$ was about 67%, and the structure was confirmed by elemental analysis of carbon, hydrogen and nitrogen (Perkin Elmer 2400 Series II CHN-analyzer, Norwalk, CT, USA) and Fourier transform infrared (FT-IR) spectra (FT-210 spectrophotometer, Horiba, Tokyo, Japan).

The Ca–EDTA/amine ethanol solution was prepared from the reaction of 4.00 g of $CaH_2(edta)\cdot 2H_2O$ and 3.26 g of dibutylamine in 43 g ethanol under reflux conditions. A clear Ca–EDTA/amine ethanol solution was obtained.

2.1.2. Step 2: Metaphosphate salt

An ethanol solution of 10 g containing 5.8 g of phosphoric acid (85 mass%, Kanto Chemicals, Tokyo, Japan) was added to 10 g of ethanol solution of 19.4 g of dibutylamine, and the mixed solution was stirred for 5 min

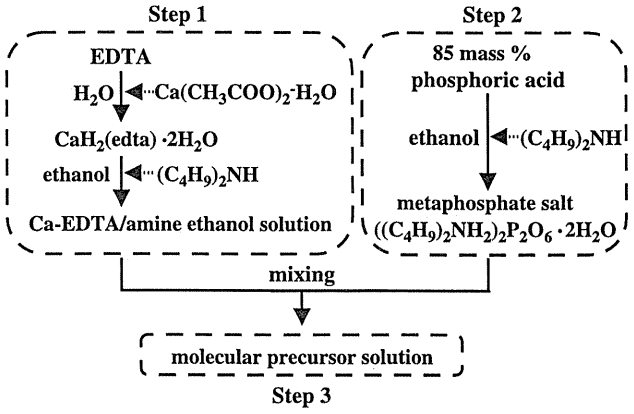

Fig. 1. Schematic presentation of preparation of precursor solution.

under reflux conditions. After cooling, the white precipitate, dibutylammonium metaphosphate salt $((C_4H_9)_2NH_2)_2P_2O_6 \cdot 2H_2O$), was collected under reduced pressure. The recrystallization of the crude product was carried out from the ethanol. The yield of dibutylammonium metaphosphate salt was about 94% and the structure was also confirmed by elemental analysis, Fourier-transform infrared (FT-IR) measurement, and ^1H and ^{13}C nuclear magnetic resonance (NMR) measurements (JNM-EX270, JEOL, Tokyo, Japan) in D_2O using tetramethylsilane in a capillary as an internal reference. The ^{13}C NMR spectrum was measured under RF irradiation in the ^1H resonance region.

2.1.3. Step 3: Molecular precursor solution

Finally, the molecular precursor solution was obtained by adding dibutylammonium metaphosphate salt to the Ca–EDTA/amine ethanol solution by adjusting Ca/P=1.67.

2.2. Calcium phosphate coatings

Machined commercially pure wrought titanium disks (JIS, Japan Industrial Specification H 4600, 99.9 mass% Ti, Furuuchi Chemical, Tokyo, Japan) with a diameter of 12 mm and a thickness of 1.0 mm were used as the substrate material.

The surface roughness (Ra) of the wrought titanium, as measured with Handysurf E-30A (Tokyo Seimitsu, Tokyo Japan) with a scan length of 4 mm and a cut off value of 0.8, was 0.94±0.02 μm. The disks were cleaned in ethanol prior to coating.

A molecular precursor solution of 20 μl was dropped on the titanium surface to cover the entire area of a titanium disk. The precursor films that formed on the disks were dried at 60 °C for 20 min and then fired at 300, 400, 500, 600 or 700 °C for 2 h using a furnace (MSFT-1520-P, Nikkato, Tokyo, Japan) under atmospheric conditions.

2.3. Characterization of coated calcium phosphate films

The surface roughness after coating was measured according to the same method as that used for the wrought titanium substrate.

The crystal structure of the calcium phosphate coatings was characterized by X-ray diffraction (XRD, θ–2θ diffractometer, MXP-18 AHF22, MAC Science, Kanagawa, Japan) with a thin layer attachment (incidence angle θ=0.3°) which had an X-ray source of CuKα, power of 45 kV×300 mA, and FT-IR reflection-absorption spectroscope (FT-IR-RAS, FT-210, Horiba, Kyoto, Japan) at a resolution of 4 cm^{-1}.

The film thickness and Ca/P ratio were determined by electron probe microanalysis (EPMA, X-8010, Hitachi, Tokyo, Japan) at an accelerating voltage of 25 kV by measuring the X-ray intensity of Ca–Kα, P–Kα, and Ti–Kα using energy dispersion spectrometry. The specimens were coated with carbon before EPMA analysis.

X-ray intensity ratio of K was calculated; the film thickness was estimated as follows [7,24].

$$K = I_{HA}/I_{Ti} \tag{1}$$

where I_{HA} is the total intensity of Ca–Kα and P–Kα, and I_{Ti} is the intensity of Ti–Kα.

An electron striking against the specimen will travel into a certain depth. Generally, this penetration depth (x μm) of incident electron to solid substrate, i.e., the analytical depth measured by EPMA, is given as:

$$x = \mathrm{const}\left(V_0^{1.7} - V_k^{1.7}\right)(A/\rho z) \tag{2}$$

where V_0 is the accelerating voltage (kV), V_k is the excitation potential (kV), A is the atomic weight, ρ is the density (g/cm^3), and z is the atomic number.

The penetration depth (x_{HA} μm) of an electron passed into the HA film can be expressed as:

$$x_{HA} = \mathrm{const}_{HA}\left(V_0^{1.7} - V_{xHA}^{1.7}\right)(A_{HA}/\rho_{HA} z_{HA}) \tag{3}$$

where V_k in Eq. (2) was replaced by V_{xHA} as the excitation potential of HA.

Thus, if the electron penetrates into the titanium substrate and stops at a distance of x_{Ti} μm from the HA film–Ti interface, x_{Ti} can be expressed as:

$$x_{Ti} = \mathrm{const}_{Ti}\left(V_{xHA}^{1.7} - V_{Ti}^{1.7}\right)(A_{Ti}/\rho_{Ti} z_{Ti}) \tag{4}$$

where V_{Ti} is an excitation potential of Ti.

In addition, the X-ray intensity ratio K was defined and expressed from the electron-range model of characteristic X-rays.

$$K = I_{HA}/I_{Ti} = \left(x_{HA}^3 \rho_{HA}/x_{Ti}^3 \rho_{Ti}\right) \tag{5}$$

where ρ_{HA}=3.15 g/cm^3, average of (atomic weight /atomic number)=A_{HA}/z_{HA}=$0.4(A/z)_{Ca}$+$0.18(A/z)_P$+$0.41(A/z)_O$=2.0, and V_{Ti}=4.95 kV, A_{Ti}=47.9, ρ_{Ti}=4.51 g/cm^3, z_{Ti}=22 are substituted into Eqs. (3) and (4) and const_{Ti} and (const_{Ti}/const_{HA}) are replaced by C_1 and C_2, respectively. Accordingly, Eq. (5) can be rearranged as:

$$K = I_{HA}/I_{Ti} = 0.70x_{HA}^3/\left\{0.48C_1\left(V_0^{1.7} - 15.2\right) - 0.76C_2 x_{HA}\right\}^3 \tag{6}$$

Constants C_1=0.0046 and C_2=−0.50 were decided by the pre-measured intensity ratios 1.03 and 0.27, which corresponded to film thicknesses of 1.0 and 0.5 μm, respectively. An accelerating voltage of 25 kV was considered to be suitable for estimating the thickness of films because the intensity ratio of (Ca+P)/Ti was almost 1.0 when the film thickness of HA on the Ti substrate was 1.0 μm according to the Monte Carlo simulation. Oxygen intensity was negligible because its intensity was much less than that of Ca or P under the accelerating voltage of 25 kV.

The surface appearance of the coated calcium phosphate films was observed by a field-emission scanning electron

microscope (FE-SEM, JSM-6340F, JEOL) at an accelerating voltage of 5 kV. The specimens were coated with platinum before the FE-SEM observation.

2.4. Thermal analysis of molecular precursor gel

Thermogravimetry (TG) and differential thermal analyses (DTA) were performed using a thermogravimetry differential thermal balance (TG-DTA 2000s, MAC Science, Kanagawa, Japan). The molecular precursor solution was placed in a platinum pan. The sample pan was heated at 70 °C for 15 min and at 100 °C for 10 min to evaporate the ethanol, and then was transferred to the sample holder of the instrument. Al_2O_3 was used as a reference material. The temperature was raised from 25 to 1000 °C at a rate of 10 °C/min. Measurements were performed under an airflow condition at a rate of 100 ml/min.

2.5. Dissolution behavior in buffer solution

The stability of the calcium phosphate film coated on titanium was evaluated by the immersion of calcium phosphate coated specimens in phosphate buffered saline (PBS) solution. The specimens were fired at 600 °C as described above. Then, the calcium phosphate coated titanium disks were immersed in 30 ml of PBS solution with pH=7.4 for 1 day, 1 week, and 4 weeks at 37 °C. The PBS solution was not renewed during the respective immersion period. Immediately at the end of each immersion period, the specimens were washed with double-distilled water and dried with a gentle stream of dry air and stored in a desiccator. The solubility of the coating was evaluated by using EPMA to estimate the film thickness on the titanium substrate. Ca/P ratio of coated film during PBS immersion was also determined using EPMA. Three runs of measurement were performed for each surface.

2.6. Adhesion test of coated film to titanium

The measurement of tensile bond strength and a scratch test were performed to determine the degree of adherence of the coated film onto the titanium.

The gluing surfaces of the titanium were roughened by blasting with 120 μm alumina and cleaned with acetone to avoid the detachment of epoxy glue from titanium surface during adhesion test. The tensile bond strengths of the coated film before PBS immersion and that after PBS immersion for 4 weeks were measured. Coated specimens before or after PBS immersion, and uncoated titanium substrates were glued to stainless rods using a thermal curing epoxy resin (Bond E39, Konishi, Osaka, Japan) according to the reported method [3]. The bonded specimens were cured in a furnace at 150 °C for 30 min. Tensile testing was performed at a cross-head speed of 1 mm/min using a universal joint to ensure axial loading using a universal testing machine (TG-5kN, Techno Graph, Minebea, Tokyo, Japan). Eight samples were selected for each surface condition.

A scratch test of the coated film was performed using a scratch tester (CSR-101, Rhesca, Tokyo, Japan) equipped with a Rockwell diamond C stylus of 200 μm radius and friction force measurement. The measurements were made at progressive loads from 0 to 10 N. The stage speed was 0.40 mm/s and the stylus was pressed on a sample at the rate of 0.26 mm/s. All scratch traces were observed by microscopy. The crucial load at the first appearance of a crack in the coating (Lc) was recorded. Three samples were selected for each condition and tests were performed twice for each sample.

2.7. Statistical analyses

Values of film thickness, tensile bond strengths, and critical load forces were expressed as mean±SD (standard deviation). Differences were statistically evaluated using a one-way analysis of variance and Scheffe's test for multiple comparison among the means at $P=0.05$.

3. Results

3.1. Preparation of molecular precursor solution

Table 1 lists the results of elemental analysis of $CaH_2(edta)\cdot 2H_2O$ and dibutylammonium metaphosphate salts. Values obtained from elemental analyses corresponded to the calculated values.

Fig. 2 shows the FT-IR spectra of $CaH_2(edta)\cdot 2H_2O$ and dibutylammonium metaphosphate salts. The characteristic carbonyl peaks of $CaH_2(edta)\cdot 2H_2O$ can be observed around 1300–1400 cm^{-1} and 1600–1700 cm^{-1} (Fig. 2a). The peaks around 3300–3500 cm^{-1} can be assigned to hydroxyl groups of EDTA and coordinated water. Dibutylammonium metaphosphate salts show peaks around 900–1200 cm^{-1} derived from P–O bonds and peaks around 2800–3000 cm^{-1} derived from NH_2 groups.

^1H and ^{13}C NMR spectra of the dibutylammonium metaphosphate, which were measured in D_2O, indicated that the compound is highly pure. Peak assignment of the

Table 1
Elemental analyses of carbon, hydrogen and nitrogen in $CaH_2(edta)\cdot 2H_2O$ and dibutylammonium metaphosphate salt

	$CaH_2(edta)\cdot 2H_2O$		Dibutylammonium metaphosphate salt	
	Found (wt.%)	Calculated (wt.%)	Found (wt.%)	Calculated (wt.%)
C	32.69	32.78	42.38	42.28
H	5.06	4.95	9.80	9.76
N	7.71	7.65	6.26	6.17

Elemental analyses were performed by quantification of CO_2, H_2O, N_2 after the complete combustion of examined materials.

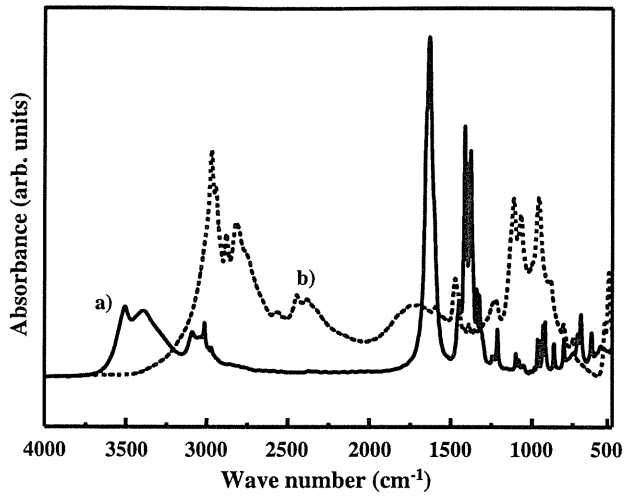

Fig. 2. FT-IR spectra of H_2edta and CaH_2(edta)·$2H_2O$ (a) and dibutylammonium metaphosphate salts (b).

NMR spectra of dibutylammonium metaphosphate salt in D_2O is shown in Table 2. The two triplets in the ^1H NMR spectrum at 0.264 and 2.363 ppm can be assigned to the terminal methyl group and the methylene linked to the nitrogen atom of the butyl groups, respectively. The other two multiplets at 0.724 and 0.989 ppm are caused by the two residual methylene groups of the alkyl groups. In the ^{13}C NMR spectrum, only 4 signals at 12.78, 19.17, 27.3, 47.31 ppm could be observed. Thus, these spectral results were coincident to the proposed components from the results of elemental analysis of the compound.

3.2. Characterization of thin calcium phosphate film

EPMA measurement revealed that only Ca, P, and Ti were present in the coated film. The coating thickness determined by EPMA was about 0.44±0.01 μm, and the Ca/P ratio was 1.56±0.04. The Ra value of the coated film was 0.94±0.02 μm. No distinct difference was seen in the Ra value before and after coating.

Fig. 3 shows the XRD patterns of the surface of calcium phosphate coated titanium at different firing temperatures. No peak was caused by the crystallized calcium phosphate when the precursor films were fired at 300 and 400 °C, although peaks assignable to titanium were observed at 2θ=35.10°, 38.35°, 40.15°, and 53.00°.

Table 2
Peak assignment of NMR spectra of dibutylammonium metaphosphate salt in D_2O

^1H NMR		^{13}C NMR	
ppm	Functional group	ppm	Functional group
0.264	$-CH_2$–N–	12.776	$-CH_2$–N–
0.724, 0.989	$-CH_2$–	19.173, 27.565	$-CH_2$–
2.363	CH_3–	47.313	CH_3–

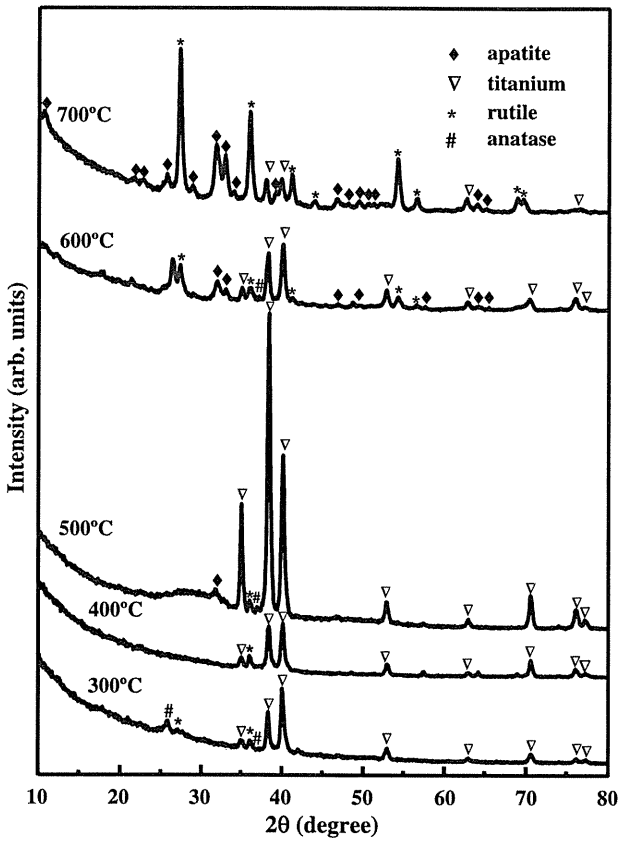

Fig. 3. X-ray diffraction patterns of calcium phosphate coatings. ♦: Carbonate apatite, ∇: titanium, *: rutile TiO_2, #: anatase TiO_2.

In contrast, in the XRD spectrum of the film fired at 500 °C, the broad peak observed between 2θ from about 25° to 34° besides the titanium peaks may be caused by an amorphous calcium phosphate. The films fired at 600 and 700 °C showed a more apatitic crystallized structure of calcium phosphate by reflection peaks at 2θ=31.95° (211), 33.05° (300), 46.90° (222), and 49.50° (213). The greater intensities of the reflection of the rutile or anatase peaks resulted from the heat treatment of the titanium substrate.

Fig. 4 shows the FT-IR spectra of the surface of calcium phosphate coated titanium at different firing temperatures. The specimens fired at 300 and 400 °C showed two P–O peaks derived from the P–O bonds of the dibutylammonium metaphosphate salts at around 550–600 cm^{-1} and around 900–1200 cm^{-1}. The broad peak around 1600–1700 cm^{-1} can be assigned to the carbonyl group of CaH_2(edta)·$2H_2O$. The intensity of the carbonyl peak of the specimen fired at 400 °C decreased and the intensity of the peaks around 1300–1500 cm^{-1} increased.

In the FT-IR spectra of the specimen fired at 500 and 600 °C, the carbonyl peaks at 1600–1700 cm^{-1} diminished, and the peaks derived from carbonate groups appeared around 1300–1500 cm^{-1}, indicating that the carbonate group was incorporated in the apatite structure. Two types of P–O peaks, the stretching mode at 900–1050 cm^{-1} and the

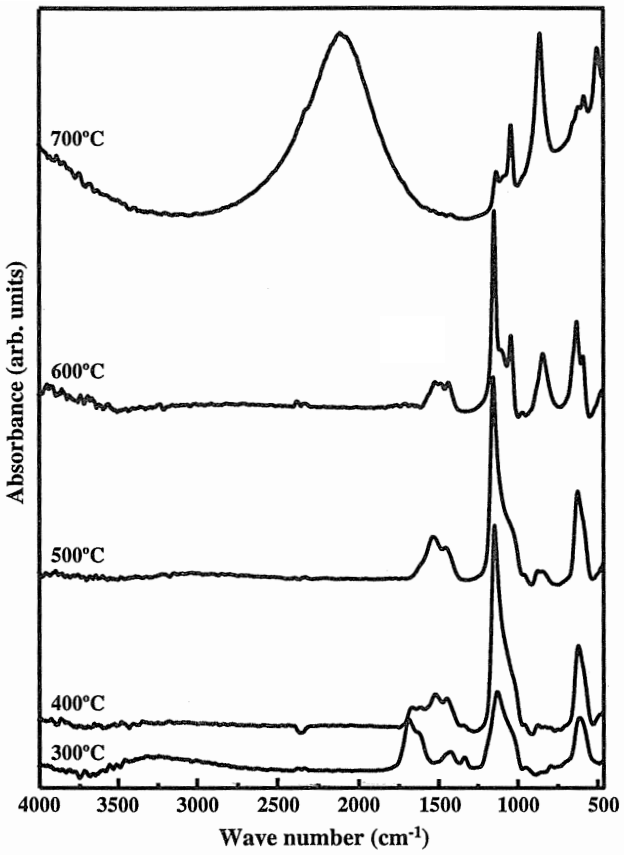

Fig. 4. FT-IR spectra of calcium phosphate coatings.

bending mode at 550–600 cm^{-1}, were observed. In the film formed at 600 °C, these P–O bonds split into more defined peaks, corresponding to the observed increase in crystallinity measured by XRD.

The new peaks appeared around 870 cm^{-1} in the FT-IR spectra of the specimen fired at 600 and 700 °C. At 700 °C, a new broad band appeared around 1750–2500 cm^{-1}. These peaks resulted from the heat treatment of the titanium substrate, corresponding to the observation of XRD patterns of greater intensities of anatase and rutile peaks in the 600 and 700 °C specimens.

3.3. Thermal analysis of molecular precursor gel

Fig. 5 shows the TG and DTA curves of the molecular precursor gel. In the DTA curves, an endothermic peak was observed at 206 °C. It is presumed that this peak is derived from the evaporation of coordinated water and excess amounts of dibutylamine of Ca–EDTA/amine. The exothermic peaks at 270 and 360 °C are attributed to the combustion of organic materials, EDTA and the amine, as verified by the corresponding decrease of mass in the TG curves. The exothermic peak at 555 and 702 °C can be primarily attributed to the crystallization of hydroxyapatite and to the combustion of small amounts of organic materials such as carbon adsorbed onto the hydroxyapatite, respectively.

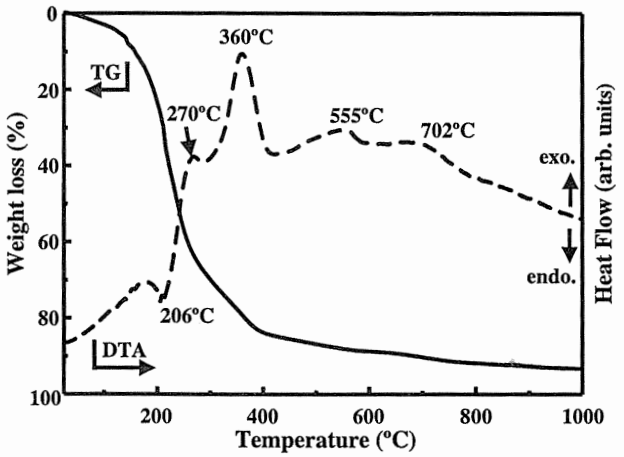

Fig. 5. TG–DTA curves of molecular precursor gel obtained by evaporation of molecular precursor solution.

3.4. Dissolution behavior in buffered solution

Table 3 lists the changes in coating thickness and Ca/P ratio of the calcium phosphate film on the disks after immersion in PBS. There were no significant differences in the coating thickness among the immersion periods tested in the present study. Slight decrease of Ca/P ratio was observed during the immersion in PBS.

The surface appearances of calcium phosphate coatings before and after immersion in PBS observed by FE-SEM are shown in Fig. 6. Before immersion, the surface of the calcium phosphate coating was smooth and there are no apparent cracks. After immersion in PBS, there are no distinct differences in the surface appearances of the coatings. Formation of a slight crack in the coated film was observed after immersion for 1 week and 1 month. No apparent degradation was seen in the coating.

3.5. Adhesion test of coated film to titanium

Table 4 lists the tensile bond strengths of the coated film to titanium. No significant differences of bond strength were recognized among the three specimens, i.e., uncoated titanium, coated film before PBS immersion, and coated film after PBS immersion. Cohesive failures in epoxy glue were primarily observed on the uncoated and coated specimens. A bond strength of approximately 40 MPa is the maximum value in the manufacturer's literature.

The Lc value of coated film before PBS immersion was 2.6±0.4, and that after PBS immersion was 2.9±1.0 kgf.

Table 3
Change in thickness of calcium phosphate coating after immersion in PBS

Immersion period (day)	0	1	7	28
Coating thickness (μm)	0.44±0.01	0.45±0.01	0.43±0.01	0.45±0.04
Ca/P ratio	1.56±0.04	1.40±0.05	1.41±0.04	1.31±0.05

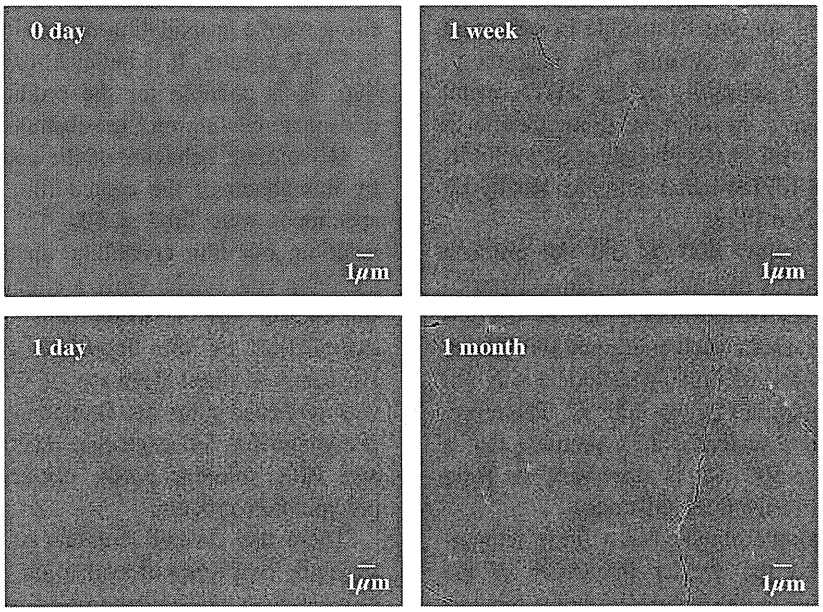

Fig. 6. FE-SEM picture of the surface appearance of calcium phosphate coatings before and after immersion in PBS. The specimens fired at 600 °C were immersed in PBS solution.

There are no significant differences in the Lc value between coated film before and after PBS immersion.

4. Discussion

In the present study, we introduce a novel technology for coating titanium with a calcium phosphate thin film using a molecular precursor method.

Hydroxyapatite or calcium phosphate films for dental and orthopedic implants are generally deposited on pure titanium or titanium alloy such as Ti-6Al-4V. In the present study, we used pure titanium as a substrate because the difference between pure titanium and titanium alloy has no significant influence on the calcium phosphate coating using a molecular precursor method.

The study revealed that thin and adherent carbonate-containing hydroxyapatite film was coated on the titanium using molecular precursor solution containing a Ca–EDTA complex. The surface topography of the coated film was almost the same as uncoated titanium. The advantage of the molecular precursor method is simplicity in preparing adherent thin film coating and that the Ca/P ratio of coated calcium phosphate film is precisely controlled by the ratio of the starting molecular precursor solution. The process is simply casting the solution on the substrate and then firing.

Table 4
Tensile bond strength of coated film to titanium (MPa)

Substrate	Tensile bond strength
Uncoated titanium	42.1±9.4
Coated film before PBS immersion	40.2±5.6
Coated film after PBS immersion	38.6±6.3

Another advantage of the molecular precursor method is the facile control of film thickness by regulating the amount of the application onto the substrate and the concentration of the solution. In addition, it is possible to form thin films on any substrate shape and inside porous materials, and there is no need for heat treatment to obtain a crystalline structure after firing.

A biomimetic process using simulated body fluid for hydroxyapatite coating has been proposed [25,26]. Hydroxyapatite crystals were deposited onto titanium surface in simulated body fluid. This process also enables to deposit hydroxyapatite onto any shapes of substrates. However, in this process titanium should be treated by NaOH and heated before immersion in simulated body fluid and it took at least several days to form hydroxyapatite layer onto titanium. On the contrary, there are no needs for the pretreatment of titanium surface using molecular precursor method and it took only a few hours for hydroxyapatite coating.

A molecular precursor solution for the calcium phosphate coating was easily prepared by the addition of dibutylammonium metaphosphate salt to a Ca–EDTA/amine ethanol solution. Sato et al. [23] first prepared a molecular precursor solution composed of Ca–EDTA/amine ethanol solution and 85 mass% phosphoric acid. However, this type of precursor solution degrades during storage, and it is speculated that a large amount of water in the precursor solution affects the stability of the anionic species involving Ca^{2+} ion, which can result in the oligomerization of Ca^{2+} ions due to hydrolysis. The molecular precursor solution used in the present study was an ethanol solution that contained a negligible amount of water. It is reported that the present molecular precursor solution does not degrade during several months of storage due to this negligible amount of water.

Generally EDTA–metal complex is soluble in water and not in organic solvents such as ethanol. The addition of dibutylamine improves the solubility of the EDTA–metal complex in organic solvents. In addition, dibutylamine in the precursor solution as well as the phosphate salt inhibits the crystal growth of the EDTA–metal complex locally on the titanium substrate before firing.

A firing temperature below 400 °C did not produce calcium phosphate film on the titanium. Thermal analysis of the molecular precursor gel demonstrated that the decomposition of organic materials occurred at around 360 °C and that complete decomposition of organic materials was not achieved at a firing temperature below 400 °C. Therefore, from the results of thermal analysis, it is assumed that a firing temperature above 500 °C is necessary to form calcium phosphate films on titanium substrates.

In XRD patterns, a sample obtained at a firing temperature of 500 °C showed the greater intensities of the titanium peaks. According to the increased firing temperature from 300 to 500 °C, the thickness of the coated precursor gel was decreased because of the combustion and evaporation of organic material. As a result, the intensities of the titanium peaks of the specimen fired at 500 °C increased in comparison with those of the specimens fired at 300 and 400 °C. The intensities of the titanium peaks of the specimens fired at 600 and 700 °C were reduced because the crystalline structure of hydroxyapatite was clearly detected by X-ray irradiation.

The calcium phosphate film was formed at a firing temperature above 500 °C. The crystallinity of the hydroxyapatite coating was influenced by the firing temperature. The calcium phosphate film that formed at a firing temperature of 500 °C had an amorphous structure, but the films formed at firing temperatures of 600 and 700 °C showed a crystalline structure. This result corresponded with the results of thermal analysis. Crystallization of the hydroxyapatite coating was observed at around 555 °C in the TG curves.

The main component of the coated film was carbonate-containing hydroxyapatite. The possible source of the carbonate ions is the EDTA. The organic materials in the precursor film on the titanium substrate disappeared when the firing temperature was around 600–700 °C, but the carbonate group of the EDTA through the deposit coating was not completely evaporated. Thus, the carbonate group was incorporated into the hydroxyapatite during the firing process.

PVD methods provide amorphous coatings of calcium phosphate. Heat treatment procedures such as infrared rapid heat treatment are needed to obtain crystalline apatitic calcium phosphate film after PVD coating [7]. However, firing around 600–700 °C produces not only carbonate-containing hydroxyapatite film, but also a crystalline structure of hydroxyapatite. By using the molecular precursor technique, it is possible to obtain a thin film of a crystalline hydroxyapatite.

Titanium is known to have a structural phase transition point at around 882 °C. At temperatures higher than 700 °C, firing results in oxidation of the titanium surface, as shown in FT-IR spectra. It is believed that a firing temperature of 600 °C is suitable for the production of a thin calcium phosphate coating on the substrate.

Dissolution behavior of the coated films was evaluated by immersion of the coated film into PBS solution. The specimens were fired at 600 °C. After immersion in PBS solution, our thin crystalline apatite film on the titanium substrate was stable. Only a slight crack was formed after immersion for 1 week and 1 month. No distinct degradation of the deposited coatings was observed. However, a slight decrease of Ca/P ratio of coated film was observed after the immersion in PBS solution. It is presumed that ion exchange reaction between coated film and PBS solution partly occurred via the dissolution/precipitation process.

There are several methods to evaluate the interfacial strength. Two types of evaluation, i.e. tensile bond strength measurement and scratch test, were employed in the present study. The tensile bond strength of coated film onto titanium have been reported to be 31.9 MPa with the plasma spraying method [27], 8.02–45.82 MPa with ion beam sputtering deposition [28], 59.0 MPa with ion beam dynamic mixing [3], and 32.50 MPa with plasma spraying coating to titanium plasma-sprayed titanium [29]. The bond strength obtained in the present study was compatible with reported value, although it was impossible to obtain the real interfacial bond strength with this method because cohesive failure in epoxy glue mainly existed.

Wang et al. [30] insisted that a scratch test might be a convenient method for avoiding factitious influences such as glue infiltration. A scratch test is basically a comparison test. In the present study, the Lc values of coated films were compared before and after PBS immersion. The scratch test also revealed the stable attachment of the coated film to titanium, as indicated from SEM observation. It revealed that the coated film on titanium produced by the molecular precursor method showed excellent adhesion to the titanium after PBS immersion. It is assumed that the adhesive characteristic of the coated film poses no problem for clinical applications.

Differences in thermal expansion is one of the factors that affect the bonding between the coating and the underlying titanium substrate. The influence of the difference in the thermal expansion coefficient between hydroxyapatite film and titanium is negligible because of the very thin nature of the deposited hydroxyapatite coating. As a result, a stable bond between the coating and the titanium was achieved. Although the exact bonding mechanism of the coating and the titanium in the molecular precursor method is not clear, it is thought that some intermediate compound is formed between the coated hydroxyapatite film and the titanium. Yoshinari et al. [3] indicated the presence of intermediate compounds such as Ti_3P_4 after the coating of hydroxyapatite film using ion beam dynamic mixing. Further studies related to the observation of the

interface between the coated hydroxyapatite film and the titanium substrate are needed.

Wolke et al. [31] examined the in vivo dissolution behavior of sputter-coated apatite film on titanium and conclude that 1 μm thick heat-treated apatite sputter coating on roughened titanium implants appear to be of sufficient thickness to show bioactive properties. They also insisted that in vivo dissolution behavior of sputter coatings is determined by their degree of crystallinity. Our previous study [11] demonstrated that apatite coating film with a 0.5 μm thickness had a beneficial effect on the bone response during the healing phase. Biological activities of the present carbonate-containing hydroxyapatite film should be elucidated at a next series of our experiment.

5. Conclusion

In conclusion, a thin and strongly adherent carbonate-containing hydroxyapatite film was coated on a commercially pure titanium substrate using a molecular precursor method. The calcium phosphate phase produced in the present study is particularly interesting because of its chemical resemblance to bone mineral. The current study shows the ease of the molecular precursor method for producing thin and adherent calcium phosphate coatings on titanium substrates. Biological activity, such as culture cell growth or tissue response in relation to thin apatite-coated titanium, will be the subject of further investigations.

Acknowledgments

The authors would like to thank Ms. Feng Lan and Mr. Tohru Takahashi of Rhesca for providing the scratch test. This study was supported in part by a grant from the Ministry of Education, Culture, Sports, Science and Technology of Japan to promote 2001-Multidisciplinary Research Projects (in 2001–2005), by Grants-in-Aid for Scientific Research (C)(2)(15592073) and (14207093) from the Japan Society for the Promotion of Science, by Oral Health Science Center Grant 5A10 from Tokyo Dental College, and by the Research Institute of Science and Technology, Kogakuin University.

References

[1] M. Yoshinari, K. Ozeki, T. Sumii, Bull. Tokyo Dent. Coll. 32 (1991) 147.
[2] J.A. Jansen, J.G.C. Wolke, S. Swann, J.P.C.M. van der Waerden, K. de Groot, Clin. Oral Implants Res. 4 (1993) 28.
[3] M. Yoshinari, Y. Ohtsuka, T. Dérand, Biomaterials 15 (1994) 529.
[4] C.P.A.T. Klein, J.G.C. Wolke, J.M.A. de Blieck-Hogervorst, K. de Groot, J. Biomed. Mater. Res. 28 (1994) 909.
[5] P. Cheang, K.A. Khor, Biomaterials 17 (1996) 537.
[6] M. Ogiso, Y. Yamashita, T. Matsumoto, J. Biomed. Mater. Res. 39 (1998) 23.
[7] M. Yoshinari, T. Hayakawa, J.G.C. Wolke, K. Nemoto, J.A. Jansen, J. Biomed. Mater. Res. 37 (1997) 60.
[8] J.E.G. Hulshoff, T. Hayakawa, K. van Dijk, A.F.M. Leijdekkers-Govers, J.P.C.M. van der Waerden, J.A. Jansen, J. Biomed. Mater. Res. 36 (1997) 75.
[9] J.E.G. Hulshoff, K. van Dijk, J.E. de Ruijter, F.J.R. Rietveld, L.A. Ginsel, J.A. Jansen, J. Biomed. Mater. Res. 40 (1998) 464.
[10] T. Hayakawa, M. Yoshinari, K. Nemoto, J.G.C. Wolke, J.A. Jansen, Clin. Oral Implants Res. 11 (2000) 296.
[11] T. Hayakawa, M. Yoshinari, H. Kiba, H. Yamamoto, K. Nemoto, J.A. Jansen, Biomaterials 23 (2002) 1025.
[12] S.C.G. Leeuwenburgh, J.G.C. Wolke, J. Schoonman, J.A. Jansen, J. Biomed. Mater. Res. 66A (2003) 330.
[13] S.C.G. Leeuwenburgh, J.G.C. Wolke, J. Schoonman, J.A. Jansen, Biomaterials 25 (2004) 641.
[14] A.A. van Zomeren, E.M. Kelder, J.C.M. Marijnissen, J. Schoonman, J. Aerosol Sci. 25 (1994) 1229.
[15] M.C. Siebers, X.F. Walboomers, S.C.G. Leeuwenburgh, J.G.C. Wolke, J.A. Jansen, Biomaterials 25 (2004) 2019.
[16] J.W.M. Vehof, J. van den Dolder, J.E. de Ruijter, P.H.M. Spauwen, J.A. Jansen, J. Biomed. Mater. Res. 64A (2003) 417.
[17] D.M. Liu, Q. Yang, T. Troczynski, Biomaterials 23 (2002) 691.
[18] H.W. Kim, Y.M. Kong, C.J. Bae, Y.J. Noh, H.E. Kim, Biomaterials 25 (2004) 2919.
[19] D.W. Bruce, D. O'Hare (Eds.), Inorganic Materials, John Wiley & Sons, Wet Sussex, 1993, p. 519.
[20] M. Sato, H. Hara, T. Nishide, Y. Sawada, J. Mater. Chem. 6 (1996) 1767.
[21] M. Sato, H. Hara, H. Kuritani, T. Nishide, Sol. Energy Mater. Sol. Cells 45 (1997) 43.
[22] M. Sato, T. Tanji, H. Hara, T. Nishide, Y. Sakashita, J. Mater. Chem. 9 (1999) 1539.
[23] M. Sato, C. Mochizuki, K. Yamada, in: Ichiro Okura (Ed.), 6th International Porphyrin-Heme Symposium in Association with 9th International SPACC Symposium, Tokyo, Japan, July 6–7, ISSN: 0918-4368, vol. 11, 2002, p. 97.
[24] M. Yoshinari, Y. Watanabe, Y. Ohtsuka, T. Dérand, J. Dent. Res. 76 (1997) 1486.
[25] H. Takadama, H.M. Kim, T. Kokubo, T. Nakamura, J. Biomed. Mater. Res. 57 (2001) 441.
[26] H.M. Kim, T. Mimeno, M. Kawashita, J.H. Lee, T. Kokubo, T. Nakamura, J. Biomed. Mater. Res. 67A (2003) 1305.
[27] M. Zablotsky, R. Meffert, O. Mills, A. Burgess, D. Lancaster, Clin. Oral Implants Res. 3 (1992) 189.
[28] J.L. Ong, L.C. Lucas, W.R. Lacefield, E.D. Rigney, Biomaterials 13 (1992) 249.
[29] Y. Yang, J.L. Ong, J. Biomed. Mater. Res. 64A (2003) 509.
[30] J. Wang, P. Layrolle, M. Stigter, K. de Groot, Biomaterials 25 (2004) 583.
[31] J.G.C. Wolke, J.P.C.M. van der Waerden, H.G. Schaeken, J.A. Jansen, Biomaterials 24 (2003) 2623.

Molecular and Cellular Biochemistry 238: 11–18, 2002.
© 2002 *Kluwer Academic Publishers. Printed in the Netherlands.*

Tumor necrosis factor α (TNF-α)-induced prostaglandin E_2 release is mediated by the activation of cyclooxygenase-2 (COX-2) transcription via NFκB in human gingival fibroblasts

Sumi Nakao,[1] Yorimasa Ogtata,[2] Emi Shimizu,[3] Muneyoshi Yamazaki,[3] Shunsuke Furuyama[4] and Hiroshi Sugiya[4]

Departments of [1]Pharmacology; [2]Periodontology; [3]Endodontics; [4]Physiology, Research Institute of Oral Science, Nihon University School of Dentistry at Matsudo, Matsudo, Chiba, Japan

Received 17 September 2001; accepted 8 February 2002

Abstract

Nuclear factor kappaB (NFκB) is a transcription factor and plays a key role in the expression of several genes involved in the inflammatory process. Cyclooxygenase (COX) is the key regulatory enzyme of the prostaglandin/eicosanoid synthetic pathway. COX-2 is a highly inducible enzyme by proinflammatory cytokines, of which gene expression is regulated by NFκB. TNF-α is a pro-inflammatory cytokine. In this paper, we investigated the involvement of NFκB on TNF-α-mediated prostaglandin E_2 (PGE_2) release and COX-2 gene expression in human gingival fibroblasts (HGF). TNF-α-induced PGE_2 release and COX-2 mRNA accumulation in a time- and concentration-dependent manner in HGF. The results of transient transfection assays using a chimeric construct of the human COX-2 promoter (nts –1432 ~ +59) ligated to a luciferase reporter gene indicated that TNF-α stimulated the transcriptional activity ~ 1.4-fold. Gel mobility shift assays with a radiolabelled COX-2-NFκB oligonucleotide (nts –223 to –214) revealed an increase in the binding of nuclear proteins from TNF-α-stimulated HGF. The COX-2-NFκB DNA-protein complex disappeared after treatment with pyrrolidine dithiocarbamate (PDTC; an antioxidant) or herbimycin A (a tyrosine kinase inhibitor). PDTC and herbimycin A attenuated TNF-α-stimulated PGE_2 release. These results suggest that NFκB transcription factor is a key regulator of COX-2 expression in TNF-α-induced PGE_2 production, which is mediated through a tyrosine kinase pathway in HGF. (Mol Cell Biochem 238: 11–18, 2002)

Key words: TNF-α, COX-2, gene regulation, NFκB, PGE_2, human gingival fibroblasts

Introduction

TNF-α is a pleiotropic cytokine primarily produced by activated macrophages and T lymphocytes and contributes to the pathogens of a variety of conditions, including rheumatoid arthritis, periodontitis and many types of infection [1–3].

Arachidonic acid is converted to prostaglandins by cyclooxygenase (COX). There are two distinct COX isozymes encoded by separate genes: constitutive COX-1 and inducible COX-2 [4–6]. COX-2 is selectively expressed in response to various inflammatory stimuli and its induction is suppressed by dexamethasone [7, 8]. Therefore, COX-2 expression is considered to play a pivotal role in the production of prostanoids,

Address for offprints: H. Sugiya, Department of Physiology, Nihon University School of Dentistry at Matsudo, Matsudo, Chiba 271-8587, Japan (E-mail: sugiya@mascat.nihon-u.ac.jp)

especially in inflammatory response, and to be regulated at transcriptional and/or posttranscriptional levels.

NFκB is an essential transcription factor in the expression of vital genes, as well as a number of genes involved in immune, inflammatory, and growth responses [9, 10]. NFκB is present in the cytosol in an inactive form, as a heterodimer of p50 and p65 subunits, bound to one of the IκB inhibitory proteins. Proinflammatory and mitogenic agents rapidly phosphorylate IκB-α, resulting in its ubiquitination and proteolytic degradation. The NFκB complex subsequently translocates into the nucleus, where it activates gene transcription [11]. Sequencing of the human COX-2 promoter region has revealed the presence of NFκB consensus sites, which are important in the induction of the COX-2 gene expression [12].

Human gingival fibroblasts (HGF) play an active role in inflammation by producing various cytokines and eicosanoids [13–17]. While we have previously demonstrated that the activation of NFκB is necessary for IL-1β-induced COX-2 expression and prostaglandin E_2 (PGE_2) production in HGF [15], the regulation of COX-2 expression and PGE_2 production by TNF-α has not been well elucidated. In this report, we demonstrate that TNF-α induces COX-2 gene expression and that NFκB is a critical transcription factor for TNF-α-induced COX-2 expression in HGF.

Materials and methods

Materials

Cell culture media, fetal calf serum (FCS), penicillin, streptomycin, trypsin-EDTA and Superscript One-step RT-PCR with Platinum Taq were obtained from GIBCO BRL Life Technologies (Tokyo, Japan). TNF-α was obtained from Genzyme-Techene (Minneapolis, MN, USA). PGE_2 enzyme immunoassay kit was obtained from Cayman (Ann Arbor, MI, USA). Rneasy was obtained from QIAGEN (Tokyo, Japan). Pyrrolidine dithiocarbamate (PDTC) was obtained from Sigma-Aldrich Japan (Tokyo, Japan). Herbimycin A and all other reagents were obtained from Wako Pure Chemical Industries (Tokyo, Japan).

Cell culture

HGF were obtained from explants of healthy human gingival connective tissue according to the methods of Somerman *et al.* [18]. The cells were maintained in α–minimum essential medium (α-MEM) containing 10% FCS, 100 U/ml penicillin and 100 μg/ml streptomycin at 37°C under 5% CO_2 in air. When the cells surrounding the tissue explants were confluent, they were subcultured with 0.05% trypsin and 0.53 mM EDTA in Hanks's balanced salt solution, and transferred to tissue culture flasks [19].

Measurement of PGE_2

HGF were cultured in 24-well culture plates in α-MEM containing 10% FCS. When the cells were confluent, they were maintained in the medium deprived of serum for 18 h, and then stimulated with various concentrations of TNF-α. Medium was collected at suitable times and the amount of PGE_2 in the medium was determined by the enzyme immunoassay with acetylcholinesterase-labeled PGE_2 as a tracer, using a commercially available kit [16].

RT-PCR

Total RNA was isolated using Rneasy. RT-PCR was performed using SuperScript One-Step RT-PCR with Platinum Taq System. Primers were synthesized on the basis of the reported human cDNA sequence for COX-2 and glyceraldehyde-3-phosphate dehydrogenase (GAPDH) [21, 22]. Sequences of the primers used for PCR were as follow: COX-2 forward, 5′-ATGAGATTGTGGAAAAATTGCT-3′; COX-2 reverse, 5′-GATCATCTCTGCCTGAGTATC-3′; GAPDH forward, 5′-CCACCCATGGCAAATTCCATGGCA-3′; GAPDH reverse, 5′-TCTAGACGGCAGGTCAGGTCCACC-3′. The PCR reactions were performed in a final volume of 50 μl, which contained 25 μl Reaction Mix, 1 μg total RNA, 10 μM each of forward and reverse primers and 1 μl Taq Mix. A two-step cycling program was used and consisted of the following: an initial template melting step at 94°C for 2 min, denaturation at 94°C for 30 sec, annealing at 55°C for 30 sec and extension at 72°C for 30 sec (30 cycles), and a final extension at 72°C for 10 min [20]. After amplification, 10 μl of each reaction mixture was analyzed by 2% agarose gel electrophoresis (0.5 × Tris-borate buffer) and visualized by ethidium bromide staining under UV light. The relative amount of PCR product was normalized to the corresponding amount of GAPDH PCR product. The PCR products for COX-2 and GAPDH were 300 and 598 bps, respectively.

Transient transfection assays

All the transfection assay were performed on exponentially growing ROS 17/2.8 cells. Twenty four hours after plating, cells at 50–70% confluence were transfected using LipofectACE reagent [23]. The transfection mixture included 1 μg of a luciferase construct (phPES2 (–1432/+59) [5] and 2 μg of pSV-β-galactosidase control vector (β-gal; Promega) as an internal control. Two days post-transfection, the cells were

cultured in the medium deprived of serum for 24 h, and 10 ng/ml TNF-α was added for 2 h prior to harvesting. The luciferase assay was carried out according to the supplier's protocol (PicaGene, Tokyo Inki, Japan) using a Luminescence reader BLR20 (Aloka) to measure the luciferase activity [24].

Gel mobility shift assay

Confluent HGF in T-75 flasks incubated for 15, 30, 60, 120 min or 6 h with 10 ng/ml TNF-α in α-MEM without serum were used to prepare nuclear extracts. Nuclear proteins were extracted by the method of Digman *et al.* [25] with the addition of extra proteinase inhibitors (the extraction buffer was 0.42 M NaCl, 1.5 mM $MgCl_2$, 0.2 mM EDTA, 1 mM dithiothreitol (DTT), 0.25% (V/V) glycerol, 0.5 mM phenylmethylsulfonyl fluoride, 2 μg/ml leupeptin, 2 μg/ml pepstatin, 1 μg/ml aprotinin, pH 7.9). Double-stranded oligonucleotides corresponding to the NFκB motif (COX-2-NFκB; –230 to –207) (5′-GAGAGTGGGGACTACCCCCTCTGC) in the human COX-2 gene promoter [5], consensus NFκB sequence (consensus-NFκB) (5′-AGTTGAGGGGACTTTCCCAGGC) and consensus AP-1 (5′-CGCTTGATGAGTCAGCCGGAA) (Promega) were end-labelled with [γ-^{32}P]-ATP using T4 polynucleotide kinase, and the radiolabelled oligonucleotides (0.1 pM) were incubated at 21°C for 20 min in binding buffer (50 mM KCl, 0.5 mM EDTA, 10 mM Tris-HCl (pH 7.9), 1 mM DTT, 0.04% Nonidet P-40, 5% glycerol and 1 μg poly(dI-dC)) with nuclear protein extracts (5 μg). In some assays, a 20-, 40-, or 100-fold molar excess of non-radiolabelled double-stranded oligonucleotide was incubated as a competitor. In each case, the reaction mixtures were analyzed on 5% non-denaturing acrylamide gels followed by evaluation with an imaging analyzer [26].

Statistical analysis

Significant differences were determined using the Student's *t*-test.

Results

We first determined the effect of TNF-α on PGE_2 release in HGF. When the fibroblasts were incubated with 10 ng/ml TNF-α, PGE_2 release was clearly detected 3 h after stimulation, and increased up to 24 h (Fig. 1A). Figure 1B summarizes PGE_2 release induced by various concentrations of TNF-α for 24 h. TNF-α provoked PGE_2 release in a concentration-dependent manner in HGF.

To determine the regulation of COX-2 expression by TNF-α, we performed RT-PCR using total RNA extracted from HGF treated with TNF-α. Figure 2A shows the time course of COX-2 mRNA expression induced by 10 ng/ml TNF-α. TNF-α markedly up-regulated COX-2 mRNA accumulation in HGF treated for 3 h. The COX-2 mRNA reached maximal levels at 6 h and these levels were maintained up to 24 h. When HGF were treated with TNF-α for 24 h, 0.1–100 ng/ml TNF-α increased COX-2 mRNA, with a maximal effect at 1 and 10 ng/ml (Fig. 2B).

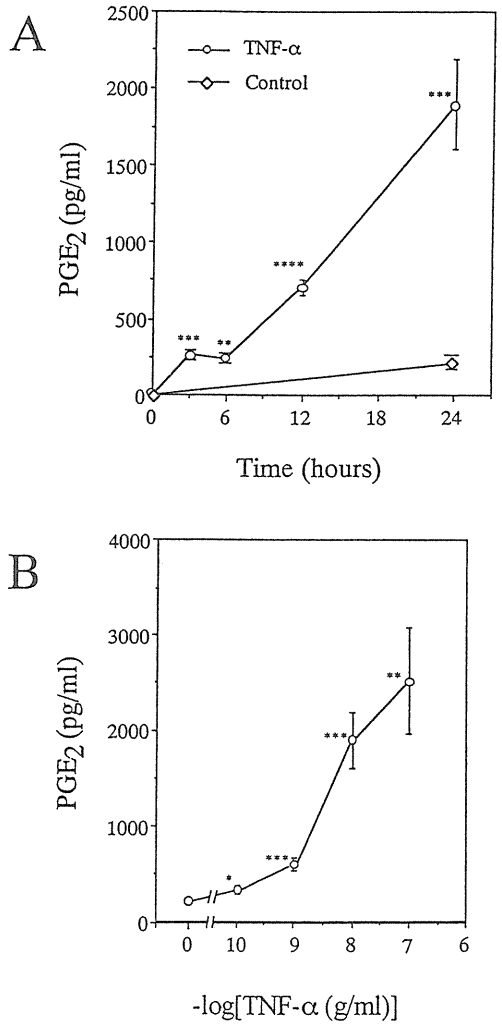

Fig. 1. TNF-α-induced prostaglandin E_2 release in human gingival fibroblasts. (A) time-dependency. Human gingival fibroblasts were incubated with TNF-α (10 ng/ml) for the indicated times. (B) Dose-dependency. Human gingival fibroblasts were incubated with the indicated concentrations of TNF-α for 24 h. At the end of incubation, prostaglandin E_2 levels in the media were measured by an enzyme immunoassay. Values are expressed as means ± S.E. of 4 independent experiments. Significant differences from control: ****$p < 0.01$; ***$p < 0.02$; **$p < 0.05$; *$p < 0.1$.

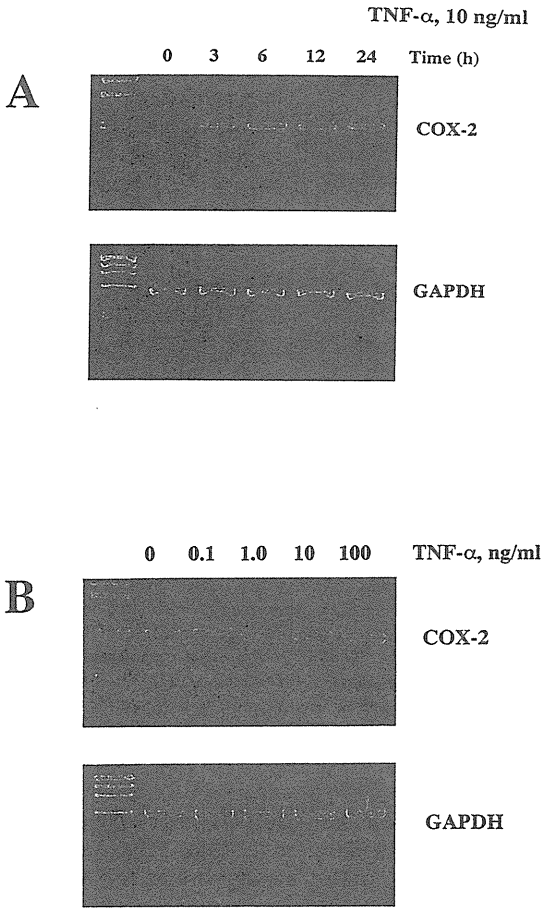

Fig. 2. TNF-α induces an increase in COX-2 mRNA in human gingival fibroblasts. (A) Time-dependency. Human gingival fibroblasts were incubated with TNF-α (10 ng/ml) for the indicated times. (B) Dose-dependency. Human gingival fibroblasts were incubated with indicated concentrations of TNF-α for 24 h. The levels of COX-2 and glyceraldehyde-3-phosphate dehydrogenase (GAPDH) mRNA were assessed by RT-PCR (30 cycles). Molecular size markers (Hae III-digested ϕX-174) are shown in the left lane. COX-2 PCR products run near the 310-bp fragment.

Since the effects of TNF-α are likely to involve transcription factor interaction in the promoter region of the human COX-2 gene, subsequent studies were directed at transcriptional regulation using a chimeric construct prepared from the promoter from the human COX-2 gene. Transient transfection of the chimeric construct of the human COX-2 promoter (nts –1432 ~ +59) ligated to a luciferase reporter gene was performed. The results of the luciferase assays indicated a ~ 1.4-fold TNF-α-induced increase in transcription as shown in Fig. 3.

NFκB is a critical transcription factor and involved in the transcriptional control of COX-2 gene expression [27, 28]. To test the binding of the NFκB sequence to nuclear proteins, COX-2-NFκB oligonucleotide was end-labelled and incubated with aliquots (5 μg) of nuclear proteins extracted from confluent HGF treated with or without 10 ng/ml TNF-α for 15, 60, 120 min or 6 h (Fig. 4). There was no significant binding with the probe alone (Fig. 4, lanes 1 and 7) or in the nuclear extract from the control cultures of HGF (Fig. 4, lanes 2 and 8). After stimulation by TNF-α for 15 min, the formation of COX-2-NFκB DNA-protein complexes increased and reached a maximal at 60 min, then declined up to 6 h (Fig. 4, lanes 3–6). In the subsequent experiment, the cells were incubated with various concentrations of TNF-α for 60 min. The maximal COX-2-NFκB DNA-binding was induced by 10 ng/ml TNF-α (Fig. 4, lane 11). Competition experiments using an excess of COX-2-NFκB and consensus NFκB reduced the amount of complex formed in a dose-dependent manner (20-, 40-, or 100-fold molar excess) (Fig. 5, lanes 4–9), whereas the consensus sequence for AP-1 did not compete with complex formation (Fig. 5, lanes 10–12), indicating that the DNA-protein complex represents a specific interaction.

The effects of an antioxidant and a tyrosine kinase inhibitor on TNF-α-induced NFκB activation and PGE_2 release were investigated. Antioxidants such as PDTC have been shown to be effective inhibitors of NFκB activation, presumably working through the inhibition of IκB degradation [29]. PDTC blocked the formation of the COX-2-NFκB DNA-protein complex after stimulation by TNF-α for 60 min (Fig. 6, lane 4). Since the participation of NFκB on TNF-α-induced

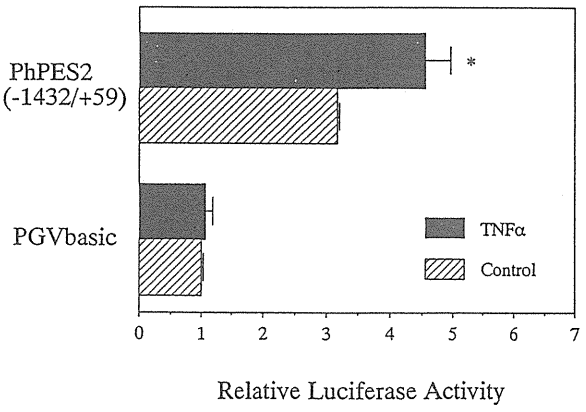

Fig. 3. Transient transfection analysis of human COX-2 promoter constructs in the presence or absence of TNF-α (10 ng/ml) for 2 h. Transcription activity of a chimeric construct that included a human COX-2 promoter ligated to a luciferase reporter gene was analyzed following transient transfection of ROS 17/2.8 cells. The results of transcriptional activity obtained from three separate transfections with constructs; PGVbasic and PhPES2(–1432/+59) have been combined and the values expressed with standard errors. Significant differences from control: *$p < 0.1$.

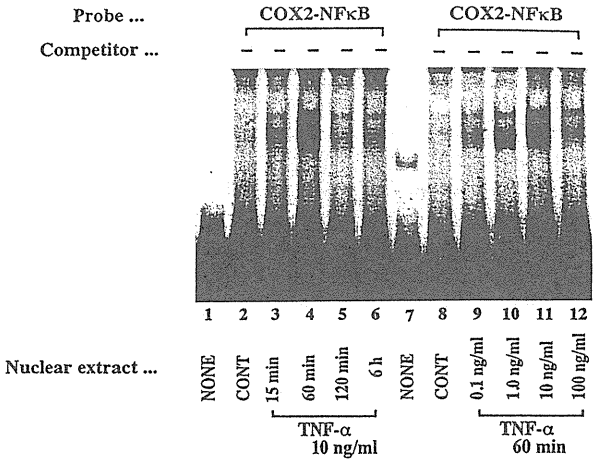

Fig. 4. TNF-α up-regulates a nuclear protein that recognizes the NFκB sequence in a time- and dose-dependent manner. Radiolabelled double-stranded COX-2-NFκB was incubated for 20 min at 21°C with a nuclear protein extract (5 μg) obtained from human gingival fibroblasts incubated with or without TNF-α (10 ng/ml) for 15, 60, 120 min and 6 h or the indicated concentrations of TNF-α for 60 min. DNA-protein complexes were separated on 5% polyacrylamide in low ionic strength Tris borate buffer, dried under vacuum, and exposed to an imaging plate for quantitation using an imaging analyzer. NONE, no nuclear extract added; CONT, nuclear extract from the control confluent cells.

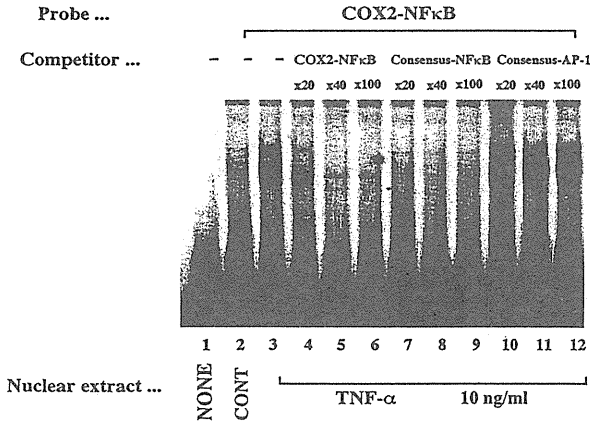

Fig. 5. Specific binding of a nuclear protein to the NFκB. Radiolabelled double-stranded COX-2-NFκB was incubated for 20 min at 21°C with or without the indicated fold excess of nonradiolabelled double-stranded oligonucleotide competitors (COX-2-NFκB, consensus-NFκB and consensus-AP-1). A nuclear protein extract (5 μg) obtained from human gingival fibroblasts incubated with or without TNF-α (10 ng/ml) for 60 min was added and the reaction mixture was incubated for 20 min at 21°C. DNA-protein complexes were separated on 5% polyacrylamide in low ionic strength Tris borate buffer, dried under vacuum, and exposed to an imaging plate for quantitation using an imaging analyzer. NONE, no nuclear extract added; CONT, nuclear extract from the control confluent cells.

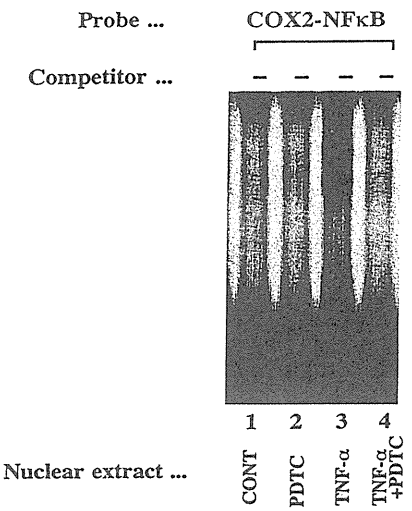

Fig. 6. Inhibition of DNA-protein complex formation induced by TNF-α by antioxidant. Radiolabelled double-stranded COX-2-NFκB was incubated for 20 min at 21°C with a nuclear protein extract (5 μg) obtained from human gingival fibroblasts preincubated with or without PDTC (100 μM) for 30 min, and then incubated with or without TNF-α (10 ng/ml) for 60 min. DNA-protein complexes were separated on 5% polyacrylamide in low ionic strength Tris borate buffer, dried under vacuum, and exposed to an imaging plate for quantitation using an imaging analyzer. CONT, nuclear extract from the control confluent cells.

PGE_2 release was demonstrated, PDTC was evaluated for its ability to inhibit PGE_2 release in HGF. Pretreatment with PDTC for 30 min resulted in a decrease in TNF-α-induced PGE_2 release (Table 1).

Next, we determined whether tyrosine phosphorylation is involved in TNF-α signal transduction. The tyrosine kinase inhibitor herbimycin A completely blocked the formation of the COX-2-NFκB DNA-protein complex after stimulation by TNF-α for 60 min (Fig. 7, lane 4). In the cells pretreated with herbimycin A, TNF-α failed to induce PGE_2 release (Table 1).

Table 1. Effects of tyrosine kinase inhibitor and antioxidant on TNF-α-induced PGE_2 release

Inhibitor	Control	TNF-α
None	166.8 ± 4.91	1684.1 ± 307.9
PDTC	147.1 ± 4.11	158.6 ± 1.15
Herbimycin A	193.7 ± 6.21	189.2 ± 12.5

Confluent human gingival fibroblasts were preincubated with 50 μM PDTC for 30 min or 1 μM herbimycin A for 18 h, and then treated wtih or without TNF-α (10 ng/ml) for 24 h. At the end of the incubation, the PGE_2 level (pg/ml) in the medium was measured by an enzyme immunoassay. Values are mean ± S.E. from 4 independent experiments.

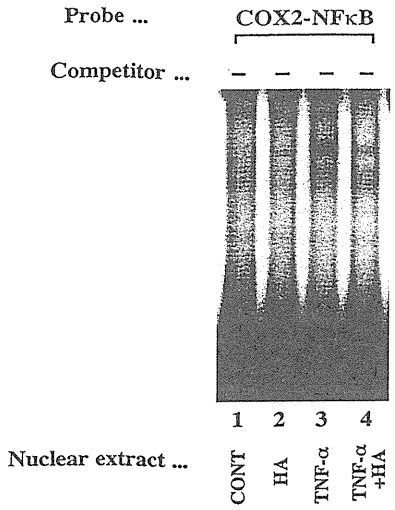

Fig. 7. Inhibition of DNA-protein complex formation induced by TNF-α by tyrosine kinase inhibitor. Radiolabelled double-stranded COX-2-NFκB was incubated for 20 min at 21°C with a nuclear protein extract (5 μg) obtained from human gingival fibroblasts preincubated with or without herbimycin A (1 μM) for 18 h, and then incubated with or without TNF-α (10 ng/ml) for 60 min. DNA-protein complexes were separated on 5% polyacrylamide in low ionic strength Tris borate buffer, dried under vacuum, and exposed to an imaging plate for quantitation using an imaging analyzer. CONT, nuclear extract from the control confluent cells.

Discussion

We demonstrated here that TNF-α increases the expression of the COX-2 gene in HGF through a tyrosine kinase signaling pathway which targets a NFκB element in the gene promoter. TNF-α provoked PGE_2 release, and this effect was inhibited by PDTC antioxidant and tyrosine kinase inhibitor, indicating that the activation of NFκB by TNF-α results in the induction of COX-2 mRNA and then leads to an increase in PGE_2 formation.

While it is well known that the expression of COX-2 is induced by TNF-α, the signaling pathways after stimulation by TNF-α have not been fully clarified in HGF [15, 30]. NFκB transcription factor has been shown to be involved in the regulation of COX-2 transcription in many different cell types including bronchial epithelial cells [27], mouse osteoblast-like cells [31], immortalized human myometrial cells [32] and human rheumatoid synoviocytes [33]. The stimulated expression of COX-2 by TNF-α is evident from an increase in the steady-state level of COX-2 mRNA (Fig. 2A), which occurs after an appropriate lag time after stimulation by TNF-α. At first NFκB translocation was evident within 15 min detected by a gel shift assay (Fig. 4), the COX-2 expression increased at 3 h (Fig. 2A), and the PGE_2 release was detected at 3 h and increased thereafter (Fig. 1A). These results suggest that the enzyme activity of the newly synthesized COX-2 protein might contribute to the PGE_2 production and release in HGF.

The human COX-2 gene contains two NFκB binding sites and high numbers of the 'AUUUA' RNA instability element, which emphasizes the role of COX-2 an immediate-early gene with a short mRNA half-life [2, 12]. In cultured macrophages, LPS-induced COX-2 expression is mediated through NFκB and mitogen-activated protein kinase [34, 35]. A role of NFκB in COX-2 expression in an IL-1β-stimulated human epithelial cell line has also been reported [27]. While LPS strongly upregulates COX-2 expression in rat microglia cells, proinflammatry cytokines such as TNF-α, IL-1β and IL-6 fail to markedly induce COX-2 expression [36]. These reports imply that tissue specific COX-2 induction is present.

NFκB is found to respond to reactive oxygen intermediates, such as hydrogen peroxide or superoxide [37]. In this study, we demonstrated that the free radical scavenger PDTC inhibited the NFκB activation in HGF (Fig. 6), and reduced the PGE_2 release in HGF (Table 1). Therefore, it is most likely that NFκB activation contributes to the TNF-α-induced COX-2 transcription and PGE_2 production. We previously demonstrated that tyrosine phosphorylation is involved in the IL-1β-induced COX-2 expression and PGE_2 release in HGF [15]. TNF-α also induced COX-2 expression and PGE_2 release via a tyrosine kinase pathway in HGF (Fig. 7; Table 1). These results suggest that the NFκB is downstream of tyrosine phosphorylation and that the activation of NFκB is crucial for COX-2 expression in gingival connective tissues.

Understanding the mechanism underlying the increased and sustained COX-2 expression in HGF may help to elucidate the factors responsible for gingivitis and periodontitis. In summary, we have shown that TNF-α induces NFκB translocation and subsequently induces COX-2 expression and PGE_2 production through a tyrosine kinase pathway. The regulation of COX-2 expression might be a critical step to prevent inflammatory diseases such as periodontitis and rheumatoid arthritis.

Acknowledgements

We thank T. Tanabe for the gift of phPES2 human COX-2 promoter luciferase construct. This work was supported in part by grants-in-aid for Scientific Research (No. 07771795, 08771738, 09771650, 11672089, 12671865) from the Ministry of Education, Science, and Culture of Japan, Nihon University Research Grant (Joint Research Grant for 2001, and General Individual Research Grant for 1997 and 2001), and Suzuki Memorial Grant of Nihon University School of Dentistry at Matsudo (Joint Research Grant for 1997 and 2000, and General Individual Research Grant for 1998, 1999

and 2000). Research for the Frontier Science (The Ministry of Education, Science, Sports and Culture). A Grant from the Ministry of Education, Culture, Sports, Science and Technology to promote 2001-Multidisciplinary Research Projects (in 2001–2005).

References

1. Smith CA, Farrah T, Goodwin RG: The TNF receptor superfamily of cellular and viral proteins: Activation, co stimulation, and death. Cell 76 : 959–962, 1994
2. Graves DT, Delima AJ, Assuma R, Amar S, Oates T, Cochran D: Interleukin-1 and tumor necrosis factor antagonists inhibit the progression of inflammatory cell infiltration toward alveolar bone in experimental periodontitis. J Periodontol 69: 1419–1425, 1998
3. Delima AJ, Oates T, Assuma R, Schwartz Z, Cochran D, Amar S, Graves DT: Soluble antagonists to interleukin-1 (IL-1) and tumor necrosis factor (TNF) inhibits loss of tissue attachment in experimental periodontitis. J Clin Periodontol 28: 233–240, 2001
4. Feng L, Sun W, Xia Y, Tang WW, Chanmugam P, Soyoola E, Wilson CB, Hwang D: Cloning two isoforms of rat cyclooxygenase: Differential regulation of their expression. Arch Biochem Biophys 307: 361–368, 1993
5. Inoue H, Nanayama T, Hara S, Yokoyama C, Tanabe T: The cyclic AMP response element plays an essential role in the expression of the human prostaglandin-endoperoxide synthase 2 gene in differentiated U937 monocytic cells. FEBS Lett 350: 51–54, 1994
6. Kosaka T, Miyata A, Ihara H, Hara S, Sugimoto T, Takeda O, Takahashi E, Tanabe T: Characterization of the human gene (PTGS2) encoding prostaglandin-endoperoxide synthase-2. Eur J Biochem 221: 889–897, 1994
7. Inoue H, Umesono K, Nishimori T, Hirata Y, Tanabe T: Glucocorticoid-mediated suppression of the promoter activity of the cyclooxygenase-2 gene is modulated by expression of its receptor in vascular endothelial cells. Biochem Biophys Res Commun 254: 292–298, 1999
8. Lasa M, Brook M, Saklatvala J, Clark AR: Dexamethasone destabilizes cyclooxygenase 2 mRNA by inhibiting mitogen-activated protein kinase p38. Mol Cell Biol 21: 771–780, 2001
9. Barnes PJ, Karin M: Nuclear factor κB: A pivotal transcription factor in chronic inflammatory disease. N Engl J Med 336: 1066–1071, 1997
10. Baeuerle PA, Baltimore D: NFκB: Ten years after. Cell 87: 13–20, 1996
11. Karin M, Ben-Neriah Y: Phosphorylation meets ubiquitination: The control of NFκB activity. Annu Rev Immunol 18: 621–663, 2000
12. Appleby SB, Ristimaki A, Neilson K, Narko K, Hla T: Structure of the human cyclo-oxygenase-2 gene. Biochem J 302: 723–727, 1994
13. Kent LW, Rahemtulla F, Michalek SM: Interleukin (IL-1) and porphyromonas gingivalis lipopolysaccharide stimulation of IL-6 production by fibroblasts derived from healthy or periodontally diseased human gingival tissue. J Periodontol 70: 274–282, 1999
14. Lo YJ, Liu CM, Wong MY, Hou LT, Chang WK: Interleukin 1β-secreting cells in inflamed gingival tissue of adult periodontitis patients. Cytokine 11: 626–633, 1999
15. Nakao S, Ogata Y, Shimizu-Sasaki E, Yamazaki M, Furuyama S, Sugiya H: Activation of NFκB is necessary for IL-1β-induced cyclooxygenase-2 (COX-2) expression in human gingival fibroblasts. Mol Cell Biochem 209: 113–118, 2000
16. Nakao S, Ogata Y, Modeer T, Furuyama S, Sugiya H: Bradykinin potentiates prostaglandin E_2 release in the human gingival fibroblasts pretreated with interleukin-1β via Ca^{2+} mobilization. Eur J Pharmacol 395: 247–253, 2000
17. Nakao S, Ogata Y, Modeer T, Segawa M, Furuyama S, Sugiya H: Bradykinin induced a rapid cyclooxygenase-2 mRNA expression via Ca^{2+} mobilization in human gingival fibroblasts primed with interleukin-1β. Cell Calcium 29: 446–452, 2001
18. Somerman MJ, Archer SY, Imm GR, Foster PA: A comparative study of human periodontal liagament cell and gingival fibroblasts *in vitro*. J Dent Res 67: 66–70, 1988
19. Ogata Y, Niisato N, Sakurai T, Furuyama S, Sugiya H: Comparison of the characteristics of human gingival fibroblasts and periodontal ligament cells. J Periodontol 66: 1025–1031, 1995
20. Beasley D: COX-2 and cytosolic PLA_2 mediate IL-1β-induced cAMP production in human vascular smooth muscle cells. Am J Physiol 276: H1369–H1378, 1999
21. Hla T, Neilson K: Human cyclooxygenase-2 cDNA. Proc Natl Acad Sci USA 89: 7384–7388, 1992
22. Tokunaga K, Nakamura K, Sakata K, Fujimori M, Ohkubo M, Sawada K, Sakiyama S: Enhanced expression of a glyceraldehyde-3-phosphate dehydrogenase gene in human lung cancers. Cancer Res 47: 5616–5619, 1987
23. Rose JK, Buonocore L, Whitt MA: A new cationic liposome reagent mediating nearly quantitative transfection of animal cells. Biotechniques 10: 520–525, 1991
24. Ogata Y, Niisato N, Furuyama S, Cheifetz S, Kim RH, Sugiya H, Sodeck J: Transforming growth factor-β1 regulation of bone sialoprotein gene transcription: Identification of a TGF-β activation element in the rat BSP gene promoter. J Cell Biochem 65: 501–512, 1997
25. Dignam JD, Lebovitz RM, Roeder RG: Accurate transcription initiation by RNA polymerase II in a soluble extract from isolated mammalian nuclei. Nucleic Acids Res 11: 1475–1489, 1983
26. Shimizu-Sasaki E, Yamazaki M, Furuyama S, Sugiya H, Sodek J, Ogata Y: Identification of a novel response element in the rat bone sialoprotein (BSP) gene promoter that mediates constitutive and fibroblast growth factor 2-induced expression of BSP. J Biol Chem 276: 5459–5466, 2001
27. Newton R, Kuitert LM, Bergmann M, Adcock IM, Barnes PJ: Evidence of involvement of NF-κB in the transcriptional control of COX-2 gene expression by IL-1β. Biochem Biophys Res Commun 237: 28–32, 1997
28. Callejas NA, Casado M, Bosca , Martin-Sanz P: Requirement of nuclear factor κB for the constitutive expression of nitric oxide syhthase-2 and cyclooxygenase-2 in rat trophoblasts. J Cell Science 112: 3147–3155, 1999
29. Heitmeier MR, Scarim AL, Corbett JA: Double-stranded RNA-induced inducible nitoric-oxide synthase expression and interleukin-1 release by murine macrophage requires NFκB activation. J Biol Chem 273: 15301–15307, 1998
30. Yucel-Lindberg T, Nilsson S, Modeer T: Signal transduction pathways involved in the synergistic stimulation of prostaglandin production by interleukin-1β and tumor necrosis factor alpha in human gingival fibroblasts. J Dent Res 78: 61–68, 1999
31. Yamamoto K, Arakawa T, Ueda N, Yamamoto S: Transcriptional roles of nuclear factor κB and nuclear factor-interleukin-6 in the tumor necrosis factor α-dependent induction of cyclooxygenase-2 in MC3T3-E1 cells. J Biol Chem 270: 31315–31320, 1995
32. Belt AR, Baldassare JJ, Molnar M, Romero R, Hertelendy F: The nuclear transcription factor NF-kappaB mediates interleukin-1β-induced expression of cyclooxygenase-2 in human myometrial cells. Am J Obstet Gynecol 181: 359–366, 1999

33. Crofford LJ, Tan B, McCarthy CJ, Hla T: Involvement of nuclear factor κB in the regulation of cyclooxygenase-2 expression by interleukin-1 in rheumatoid synoviocytes. Arthritis Rheum 40: 226–236, 1997
34. D'Acquisto F, Iuvine T, Rombola L, Sautebin L, Di Rosa M, Carnuccio R: Involvement of NF-kappaB in the regulation of cyclooxygenase-2 protein expression in LPS-stimulated J774 macrophages. FEBS lett 418: 175–178, 1997
35. Hwang D, Jang BC, Yu G, Boudreau M: Expression of mitogen-inducible cyclooxygenase induced by lipopolysaccharide: Mediation through both mitogen-activated protein kinase and NF-kappaB signaling pathways in macrophages. Biochem Pharmacol 54: 87–96, 1997
36. Bauer MK, Lieb K, Schulze-Osthoff K, Berger M, Gebicke-Haerter PJ, Bauer J, Fiebich BL: Expression and regulation of cyclooxygenase-2 in rat microglia. Eur J Biochem 243: 726–731, 1997
37. Muller JM, Rupec RA, Baeuerle PA: Study of gene regulation by NF-kappa B and AP-1 in response to reactive oxygen intermediates. Methods 11: 301–312, 1997

2002年10月

キーワード
・組織特異性
・骨芽細胞
・転写調節
・骨シアロタンパク質

日歯保存誌 45 (5)：753～761，2002

骨シアロタンパク質遺伝子プロモーター中の骨芽細胞特異的発現調節配列の検索

齋藤綾一朗　佐本　博*　清水映美**
葛西一貴*　山崎宗与　小方頼昌**

日本大学松戸歯学部保存学III講座(歯内療法学)
(主任：山崎宗与教授)
*日本大学松戸歯学部矯正学講座
(主任：葛西一貴教授)
**日本大学松戸歯学部保存学II講座(歯周病学)
(主任：小方頼昌教授)
(受付：平成14年6月28日)

Analysis of Osteoblast-specific *cis*-acting Element in the Bone Sialoprotein Gene Promoter

SAITO Ryoichiro, SAMOTO Hiroshi*, SHIMIZU Emi**,
KASAI Kazutaka*, YAMAZAKI Muneyoshi and OGATA Yorimasa**

Department of Endodontics, Nihon University School of Dentistry at Matsudo
(Chief: Prof. YAMAZAKI Muneyoshi)
870-1, Sakaecho, Nishi-2, Matsudo, Chiba 271-8587, Japan
*Department of Orthodontics, Nihon University School of Dentistry at Matsudo
(Chief: Prof. KASAI Kazutaka)
870-1, Sakaecho, Nishi-2, Matsudo, Chiba 271-8587, Japan
**Department of Periodontology, Nihon University School of Dentistry at Matsudo
(Chief: Prof. OGATA Yorimasa)
870-1, Sakaecho, Nishi-2, Matsudo, Chiba 271-8587, Japan
(Received for Publication: June 28, 2002)

Bone sialoprotein (BSP) is a major noncollagenous protein of mineralized bone extracellular matrix that has been implicated in the nucleation of hydroxyapatite. The mechanisms governing osteoblast-specific gene expression are still unknown. To understand these mechanisms, we analyzed the *cis*-acting elements of rat BSP gene, which is a well-characterized osteoblast-specific gene, by DNA transfection experiments in osteoblastic and nonosteoblastic cell lines, and by gel shift assays. Osteoblast-like rat ROS 17/2.8 and UMR 106 cells expressed BSP mRNA; however, RL 34 rat liver epithelial-like cells, L 6 rat myoblasts, C 3 H 10 T 1/2 mouse fibroblasts, HSY human parotid epithelial cells, and HGF human gingival fibroblasts did not express BSP. 5'-deletion analysis of a BSP promoter-luciferase chimeric gene showed that the region located between −116 and −43 contained the

regulatory elements required for osteoblast-specific expression. In gel shift assays, cAMP element (CRE), located between −75 and −68, bound a factor present only in nuclear extracts of osteoblast-like cells. These studies therefore demonstrate that CRE may be responsible for osteoblast expression of BSP.

(Request original article reprints to Dr. OGATA)

緒　言

骨シアロタンパク質(BSP)は，リン酸化および硫酸化を受けた糖タンパク質で，その配列中にRGD(アルギニン-グリシン-アスパラギン酸)細胞接着配列およびグルタミン酸連続配列を有し，RGD配列で細胞に接着し，グルタミン酸連続配列で，アパタイト結晶に結合することが報告されている[1,2]．BSPは石灰化初期に石灰化組織特異的に発現し，アパタイト結晶形成能を有することから石灰化における役割が注目されているタンパク質である[3]．

石灰化組織特異的に発現するタンパク質は，現在オステオカルシンとBSPが知られている．オステオカルシンは石灰化の後期に発現し，そのノックアウトマウスは大理石病を発症することから，骨吸収および骨の恒常性の維持に関与すると考えられる[4]．一方BSPは，石灰化結合組織特異的に発現し，アパタイト結晶形成能を有すること[3]，乳ガン細胞等で発現し，ガンの骨転移に関与していることが報告されているが[2,5]，ノックアウトマウスに関する報告はない．

BSP遺伝子の上流域(プロモーター領域)には，ホルモンや成長因子に応答する遺伝子配列が存在し，転写の調節を行っていると考えられている．ラットおよびヒトBSPのプロモーター領域の塩基配列は，転写開始点から370塩基対上流までは約75%の相同性を示す[6]．その配列中には逆方向のTATA配列(−20塩基対上流)[7]と重複したビタミンD受容体結合配列(VDRE)[8]，逆方向のCCAAT配列(−50塩基対上流)[9]，cAMP応答配列(CRE；−70塩基対上流)，FGF 2応答配列(FRE；−90塩基対上流)[10]，下垂体特異的転写因子結合配列(Pit 1；−108塩基対上流)[11]，TGF-β応答配列(−500塩基対上流)[12]，グルココルチコイド応答配列(GRE；−930塩基対上流)[13]および同配列に重複したアクチベータープロテイン1(AP 1)結合配列[14]等が存在することが報告されている(Fig. 1)．BSPは石灰化結合組織特異的に発現するタンパク質であることから，その組織特異的発現を調節する遺伝子配列がBSP遺伝子のプロモーターに存在すると考えられる．Bensonらは，ホメオボックス関連転写因子であるDlx 5が，マウスBSP遺伝子プロモーターに存在するホメオドメインに結合することで骨芽細胞特異的発現を調節していると報告した[15]．

今回われわれは，種々の培養細胞を用い，ラットBSP遺伝子プロモーターに存在すると考えられる，石灰化組織特異性を調節する転写因子結合配列を解析することを目的に本実験を行った．

材料および方法

1．材　料

本実験に使用した材料は，Alpha-minimum essential培地(α-MEM)，ペニシリン・ストレプトマイシン，trypsin-EDTA，ウシ胎児血清(FCS)，アクリルアミド，アガロース(Gibco)，細胞培養シャーレーおよびフラスコ(Corning)，ルシフェラーゼアッセイ基質(東洋インキ)，[γ-^{32}P] ATPおよび[α-^{32}P] dCTP(Nen)である．他の試薬はすべて特級品(和光純薬工業)を用いた．

2．細胞培養

骨芽細胞様細胞としてROS 17/2.8細胞[16]およびUMR 106細胞[17]を用い，10%ウシ胎児血清(FCS)を含むα-MEM培地中にて，37°C，CO_2インキュベーター中で培養を行った．またラット肝臓由来上皮様細胞(RL 34)，ラット骨格筋細胞(L 6)，マウス未分化間葉細胞(C 3 H 10 T 1/2)，ヒト唾液腺腺房細胞(HSY)およびヒト歯肉線維芽細胞(HGF)を非石灰化細胞として，10% FCSを含むD-MEM培地中で培養を行った．なお，両培養液は抗生物質(100 units/mlペニシリンと100 μg/mlストレプトマイシン)を含んでいる．

3．ノーザンブロット解析

細胞がコンフルエントになった後，FCSを含まない培地にて12時間培養し，細胞を回収した．グアニジンチオシアネート法にてRNAを抽出後，20 μgの全RNAを1.2%アガロースゲルで電気泳動し，ナイロンメンブレンに転写した．転写後のメンブレンは，紫外線照射しRNAの固定を行った．泳動サンプル溶

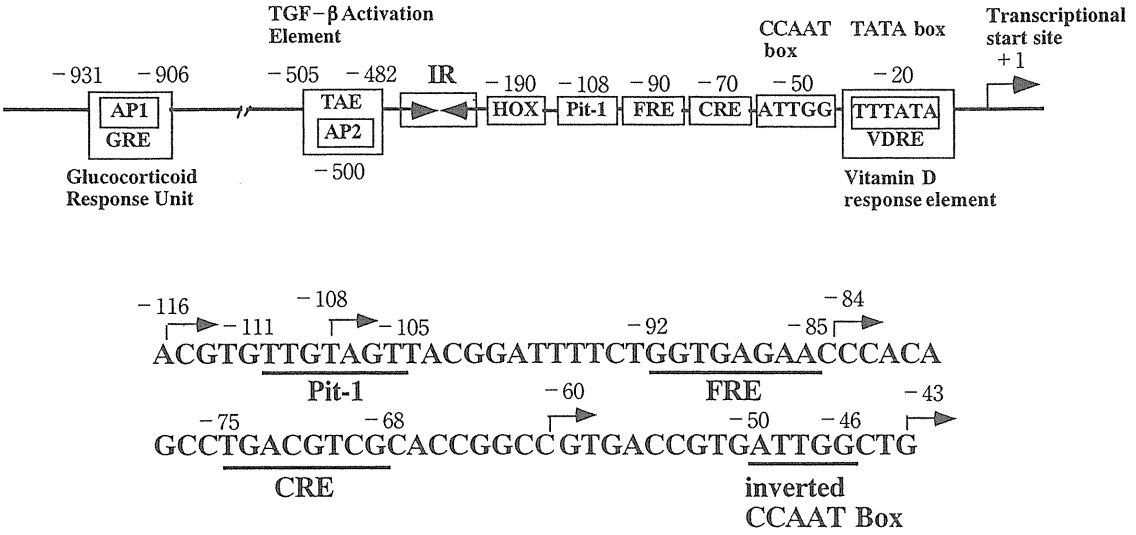

Fig. 1 Regulatory elements in the proximal rat BSP promoter. The inverted TATA and CCAAT boxes, cAMP response element (CRE), FGF response element (FRE), pituitary-specific transcription factor-1 binding site (Pit-1), homeobox-binding site (HOX), inverted repeat (IR), TGF-β activation element (TAE) overlapping with AP 2 and glucocorticoid response elements (GRE) overlapping the AP 1, a vitamin D response element (VDRE) that overlaps the inverted TATA box are present within a proximal promoter are shown. The nucleotide sequences of the rat BSP gene proximal promoter is shown from nts −116 to −43.

液中にエチジウムブロマイドを入れ，泳動後にRNAが同量泳動されていることを確認した．ランブムプライム法を用い，BSPcDNAを［α-^{32}P］dCTPにて標識し，42°Cでハイブリダイゼイションを行った．ハイブリダイゼイション後，メンブレンを0.1% SDSを含む2×SSC(30 mmol/l酢酸ナトリウム，0.3 mol/l塩化ナトリウム，pH 7.0)で25°C，30分間2回洗浄し，さらに55°Cで30分間洗浄した．次に0.1×SSC(0.1% SDSを含む)で55°C，30分間2回洗浄した後，フジBAS 2000イメージングプレートにメンブレンを約12時間コンタクトさせた．ハイブリダイゼイションの結果は，フジBAS 2000イメージングアナライザーにて解析を行った．

4．ルシフェラーゼアッセイ

ホタルの発光酵素であるルシフェラーゼ遺伝子を組み込んだルシフェラーゼプラスミドを，制限酵素Hind IIIおよびSal Iで切断し，種々の長さに調節したラットBSP遺伝子プロモーター配列を挿入した[13]．作成したコンストラクトは，pLUC 2(−43〜+60塩基対)，pLUC 3(−116〜+60塩基対)，pLUC 4(−425〜+60塩基対)，pLUC 5(−801〜+60塩基対)およびpLUC 7(−1149〜+60塩基対)で，pLUCBはBSPプロモーターを含まないルシフェラーゼプラスミドである[13]．プラスミドを細胞に導入する1日前に，各種細胞を35 mmディッシュに播種し，細胞が40〜60%コンフルエントの状態で，ルシフェラーゼプラスミドとコントロールとしてβガラクタシダーゼ(β-Gal)プラスミド(pSV-β-Galactosidase Control Vector，Promega)をリポフェクトエース(Gibco)を用いて細胞に導入した[18]．プラスミドが導入されたROS 17/2.8およびUMR 106細胞は，10% FCSを含むα-MEM培地で2日間培養し，RL 34，L 6，C 3 H 10 T 1/2，HSY，HGF細胞は10% FCSを含むD-MEM培地で2日間培養した．その後無血清培地で12時間培養後，ルシフェラーゼアッセイを行った．細胞はPBSで2回洗浄し，細胞溶解液(125 μl)にて溶解後，12,000×gで1分間遠心し，上清を活性の測定に用いた．20 μlの上清と100 μlのルシフェラーゼ基質を混合し，ルミノメーター(アロカ)にて活性の測定を行った．プラスミドの導入効率を補正する目的で，60 μlの上清と66 μlのβ-Gal基質を混合し，37°Cで12時間インキュベート後，420 nmで吸光度を測定し，活性値の補正に用いた[12]．

5．ゲルシフトアッセイ

ルシフェラーゼアッセイの結果から，pLUC 3に特異的なラットBSPプロモーター(−43〜−116)配列

の中で，転写因子結合配列と考えられるDNA配列を合成した．合成オリゴヌクレオチドは相補鎖同士がそれぞれ終濃度10 pmolになるように調整し，100°Cで5分間煮沸後，室温に放置して2本鎖にするためのハイブリダイズを行った．2本鎖オリゴヌクレオチドは2 pmolに希釈し，T4ポリヌクレオチドキナーゼを用いて，[γ-^{32}P] ATPにて標識を行った．各種細胞を12時間無血清後，核内タンパク質の抽出を行った[19]．核内タンパク質には，緩衝液(10 mmol/l Tris-HCl，50 mmol/l KCl，1 mmol/l DTT，0.04% Nonidet P-40，5% glycerol，0.5 mmol/l EDTA)と1 μg/μl polyd I-dCを加え，アイソトープ標識したオリゴヌクレオチドを添加し，20分間室温でインキュベート後，5%ポリアクリルアミドゲルにて電気泳動を行った．ゲルを乾燥後，イメージングプレートにコンタクトし，約12時間後，フジBAS 2000イメージングアナライザーで解析を行った[12]．

結　果

1. 各種細胞におけるBSPmRNAの発現の変化

使用した各種細胞におけるBSPmRNAの発現の量および有無を検索するために，ROS 17/2.8，UMR 106，RL 34，L 6，C 3 H 10 T 1/2，HSYおよびHGF細胞より全RNAを抽出し，ノーザンブロット法により検索を行った．骨芽細胞様細胞であるROS 17/2.8およびUMR 106細胞では，BSPmRNAの発現が認められたが，ROS 17/2.8細胞ではその発現量は少なく，UMR 106細胞ではROS 17/2.8細胞に比べて約4倍の発現が認められた．一方，RL 34，L 6，C 3 H 10 T 1/2，HSYおよびHGF細胞ではBSPmRNAの発現は認められなかった(結果は示していない)．

2. 各種細胞におけるBSPプロモーターの転写活性の変化

BSP遺伝子プロモーターの長さを変化させたルシフェラーゼプラスミド(pLUC 2，3，4，5および7)を用い，BSPプロモーター中のどの塩基配列が骨芽細胞での組織特異的発現を調節しているかを検索した．転写活性は，ROS 17/2.8細胞に導入したpLUC 2の活性を1として比で表した．ROS 17/2.8細胞に導入したpLUC 3(−116〜+60塩基対)の転写活性はpLUC 2の約4倍であり，それよりも長いルシフェラーゼコンストラクトではその活性は徐々に低下した(Fig. 2)．UMR 106細胞ではpLUC 3で約2.5倍の活性が認められ，それよりも長いコンストラクトにおいても転写活性はあまり低下しなかった(Fig. 3)．肝臓の上皮様細胞であるRL 34細胞を用いてルシフェ

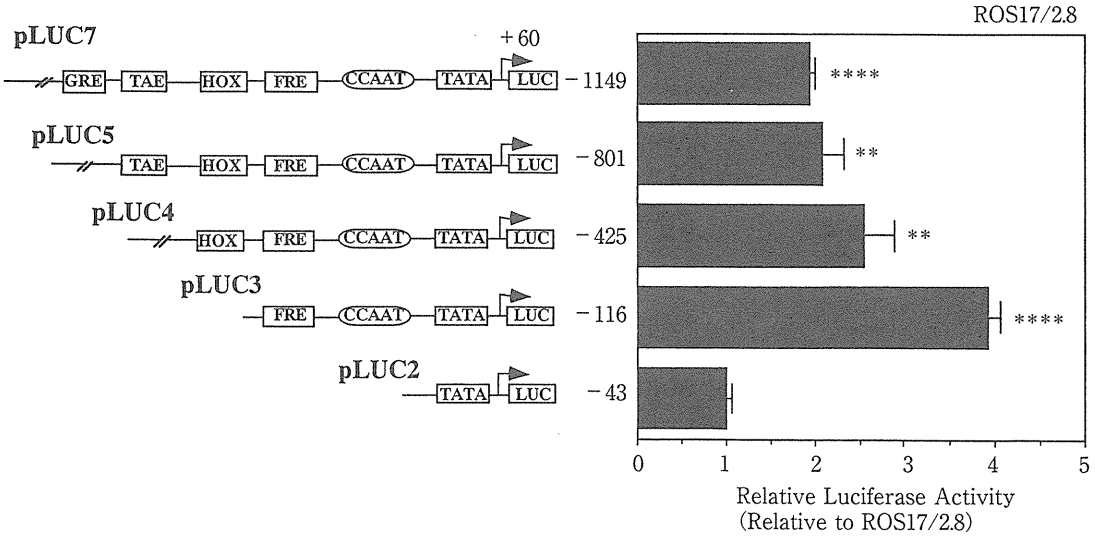

Fig. 2 Transient transfections of ROS 17/2.8 cells were used to determine transcriptional activity of chimeric constructs that included various regions of the rat BSP promoter ligated to a luciferase reporter gene. The results of transcriptional activity obtained from three separate transfections with constructs; pLUC 2, 3, 4, 5 and 7 have been combined and the values (relative to pLUC 2) expressed by with standard errors. Significant differences from control: **($p<0.05$); ****($p<0.01$).

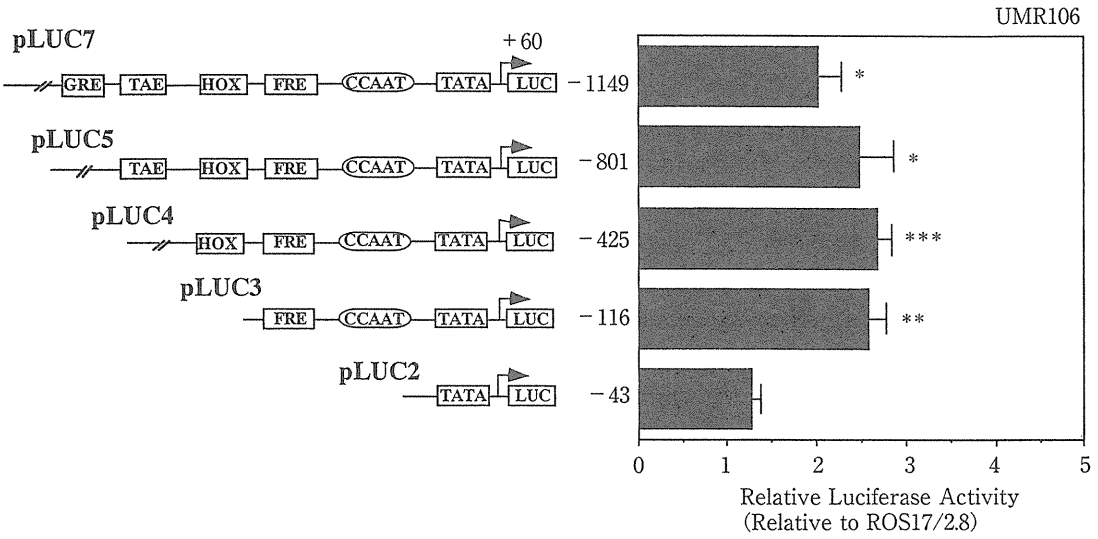

Fig. 3 Transient transfections of UMR 106 cells were used to determine transcriptional activity of chimeric constructs that included various regions of the rat BSP promoter ligated to a luciferase reporter gene. The results of transcriptional activity obtained from three separate transfections with constructs; pLUC 2, 3, 4, 5 and 7 have been combined and the values (relative to pLUC 2 activity in ROS 17/2.8 cells) expressed by with standard errors. Significant differences from control: *($p<0.1$); **($p<0.05$); ***($p<0.02$).

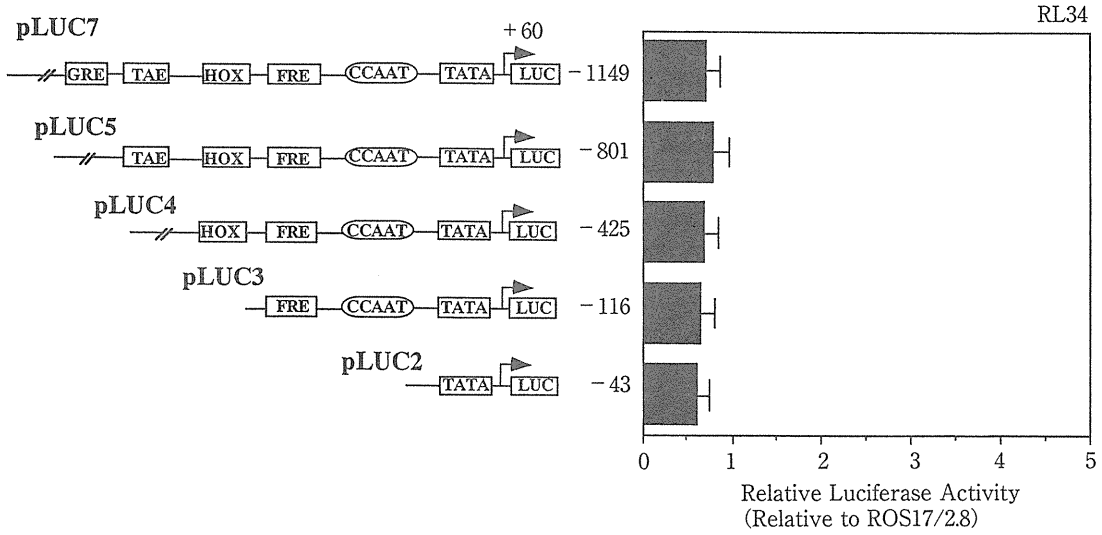

Fig. 4 Transient transfections of RL 34 cells were used to determine transcriptional activity of chimeric constructs that included various regions of the rat BSP promoter ligated to a luciferase reporter gene. The results of transcriptional activity obtained from three separate transfections with constructs; pLUC 2, 3, 4, 5 and 7 have been combined and the values (relative to pLUC 2 activity in ROS 17/2.8 cells) expressed by with standard errors.

ラーゼアッセイを行った結果，ROS 17/2.8細胞と比較してその活性が低く，プロモーター配列の長さを変化させても，同じ程度の低い活性しか認められなかった(Fig. 4)．骨格筋由来筋細胞であるL6細胞および未分化間葉細胞であるC3H10T1/2細胞を用いると，両細胞とも転写活性は低く，どの長さのプロモーター配列を含むコンストラクトでも活性に変化はなかった(Fig. 5, 6)．HSY唾液腺腺房細胞および

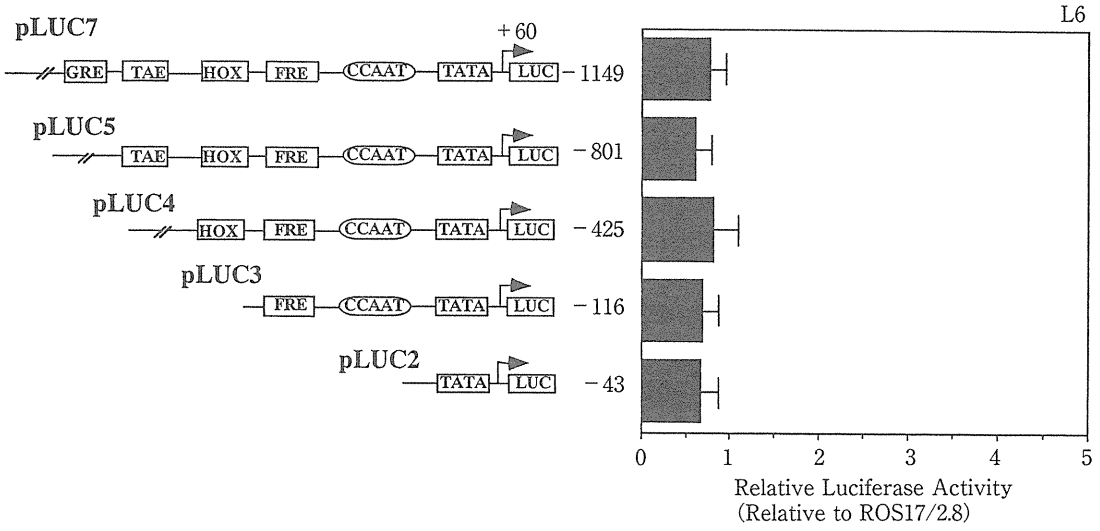

Fig. 5 Transient transfections of L 6 cells were used to determine transcriptional activity of chimeric constructs that included various regions of the rat BSP promoter ligated to a luciferase reporter gene. The results of transcriptional activity obtained from three separate transfections with constructs; pLUC 2, 3, 4, 5 and 7 have been combined and the values (relative to pLUC 2 activity in ROS 17/2.8 cells) expressed by with standard errors.

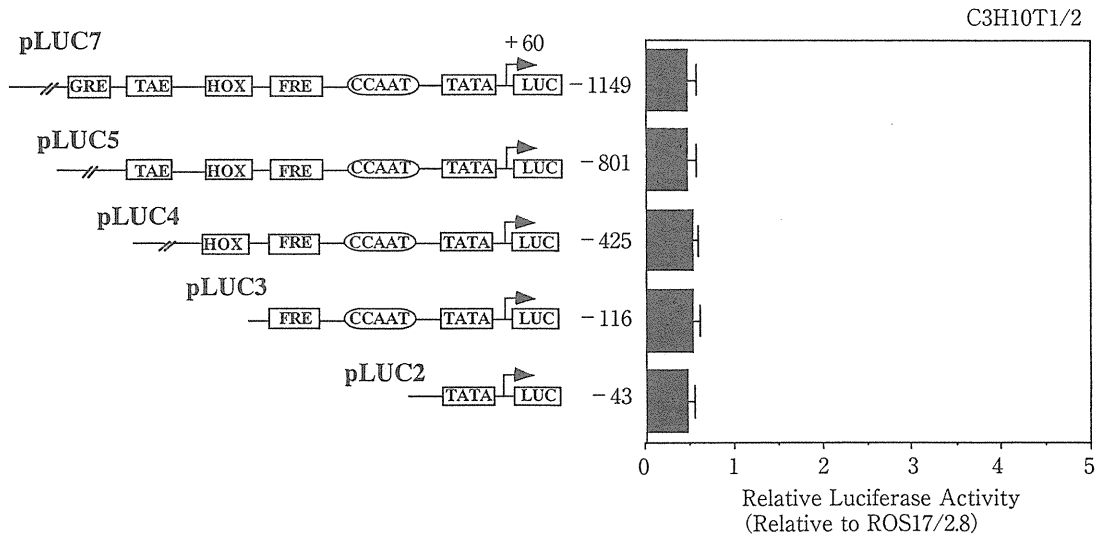

Fig. 6 Transient transfections of C 3 H 10 T 1/2 cells were used to determine transcriptional activity of chimeric constructs that included various regions of the rat BSP promoter ligated to a luciferase reporter gene. The results of transcriptional activity obtained from three separate transfections with constructs; pLUC 2, 3, 4, 5 and 7 have been combined and the values (relative to pLUC 2 activity in ROS 17/2.8 cells) expressed by with standard errors.

HGF 歯肉線維芽細胞のルシフェラーゼアッセイを行った結果，両細胞とも転写活性が低く，プロモーターの長さを変化させてもその活性に変化は認められなかった(Fig. 7, 8)．

3. BSP プロモーター配列に結合する核内タンパク質の結合性

ルシフェラーゼアッセイの結果，転写開始点から−116 塩基対上流までを含む pLUC 3 が，骨芽細胞様細胞で高い転写活性を示すことから，石灰化組織特異

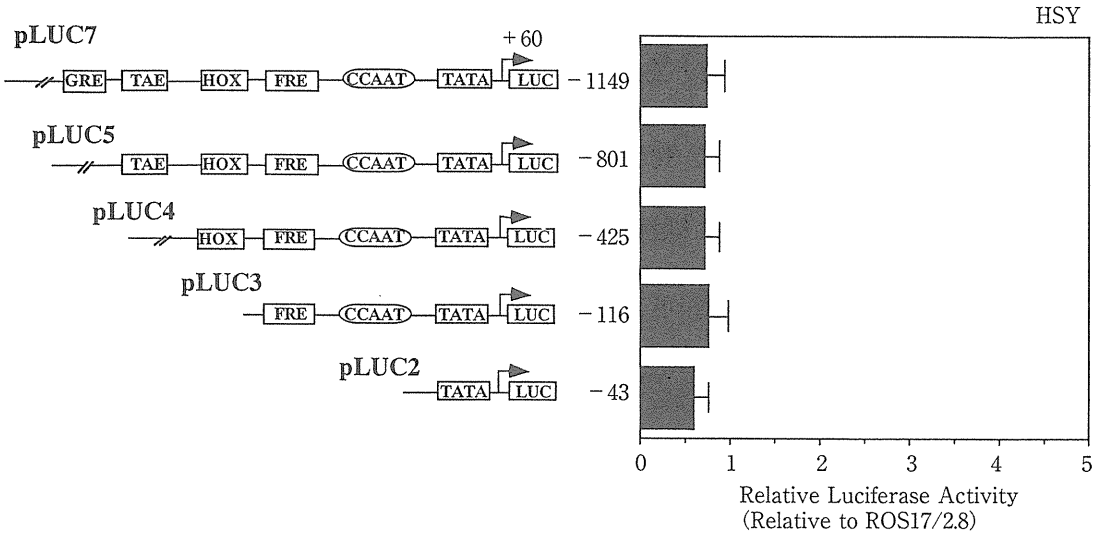

Fig. 7 Transient transfections of HSY cells were used to determine transcriptional activity of chimeric constructs that included various regions of the rat BSP promoter ligated to a luciferase reporter gene. The results of transcriptional activity obtained from three separate transfections with constructs; pLUC 2, 3, 4, 5 and 7 have been combined and the values (relative to pLUC 2 activity in ROS 17/2.8 cells) expressed by with standard errors.

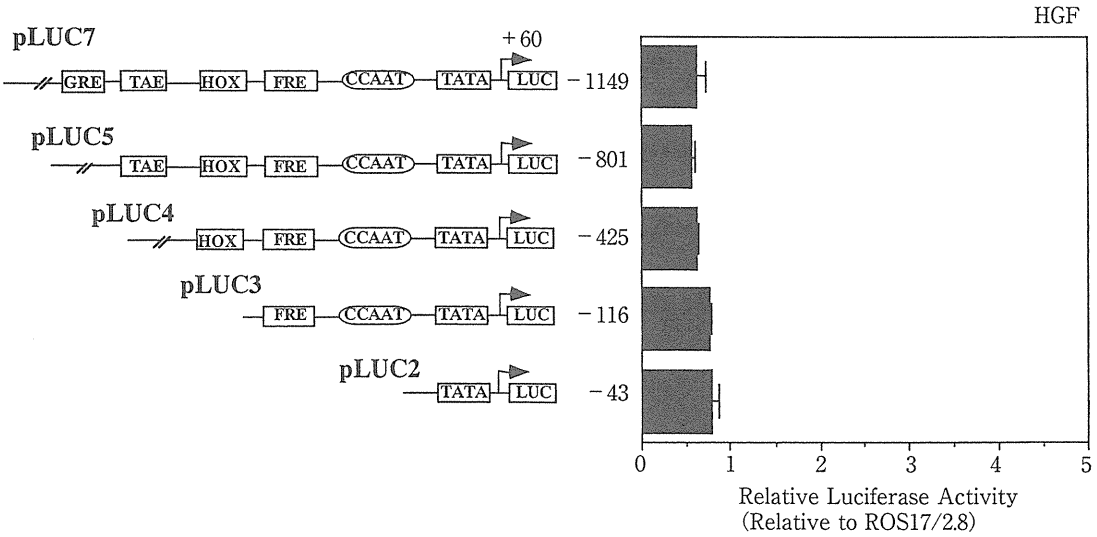

Fig. 8 Transient transfections of HGF were used to determine transcriptional activity of chimeric constructs that included various regions of the rat BSP promoter ligated to a luciferase reporter gene. The results of transcriptional activity obtained from three separate transfections with constructs; pLUC 2, 3, 4, 5 and 7 have been combined and the values (relative to pLUC 2 activity in ROS 17/2.8 cells) expressed by with standard errors.

性を規定するプロモーター配列は，pLUC 3 に特異的な塩基配列中(−43〜−116 塩基対までの間)に存在すると考えられた．この配列中の特異的な転写因子結合配列として，逆方向の CCAAT，CRE，FRE，Pit 1 配列などが存在する(Fig. 1)．これらの配列のどの部位が石灰化組織特異性を規定しているのかを検索する目的でゲルシフトアッセイを行った結果，CRE 配列に結合する核内タンパク質が骨芽細胞様細胞である ROS 17/2.8 および UMR 106 細胞でのみ認められた(結果は示していない)．

考　察

BSPは石灰化結合組織特異的に発現し，初期の石灰化において重要な役割を果たすと考えられることから，BSPの石灰化組織特異的発現を調節する遺伝子配列を検索することは，石灰化機構の解明につながると考えられる．ノーザンブロット解析の結果，骨芽細胞様細胞であるROS 17/2.8とUMR 106細胞においてBSPmRNAの発現が認められたが，それ以外のRL 34，L 6，C 3 H 10 T 1/2，HSYおよびHGF細胞においては認められなかった．ルシフェラーゼアッセイの結果，−116〜+60までのBSPプロモーター遺伝子配列を挿入したpLUC 3ルシフェラーゼコンストラクトは，ROS 17/2.8とUMR 106細胞で高い転写活性を示したが，それ以外の細胞ではほとんど転写活性は認められなかった．以上の結果から，pLUC 3に特異的な−116〜−43までのBSPプロモーター遺伝子配列中に石灰化組織特異的発現に関与する塩基配列が含まれる可能性が示唆された．pLUC 3に特異的なプロモーター配列中には，逆方向のCCAAT，CRE，FRE，Pit 1配列などが存在し，これらのいずれかが組織特異性に関与している可能性が考えられる．さらに，pLUC 3の中に存在する塩基配列を用いたゲルシフトアッセイの結果，CREに結合する核内タンパク質は，ROS 17/2.8とUMR 106細胞には存在するが，他の細胞にはほとんど認められなかったことから，CRE配列(TGACGTCG)に結合する核内転写因子が，BSPの石灰化組織特異性を調節している可能性が考えられた(Fig. 1)．

Ducyらはマウスオステオカルシンプロモーターに骨芽細胞特異的な核内タンパク質が結合する2つの領域(OSE 1およびOSE 2)が存在することを報告した[20]．そのうちのOSE 2(CCAACCAC)に結合する転写因子(Osf 2)は，後にCbfa 1と呼ばれる転写因子であり，Cbfa 1のノックアウトマウスは完全に骨を欠損することが明らかとなった[21]．

Rossertらはマウスpro-α1(I)コラーゲンプロモーター中に骨芽細胞特異的発現を調節する塩基配列があることを報告した[22]．さらに，Kernらはラット，マウス，ヒトα1(I)およびα2(I)コラーゲンプロモーター中に存在するcbfa 1結合配列が骨芽細胞特異的発現を調節していることを報告した[23]．Bensonらはホメオボックス関連転写因子であるDlx 5が，マウスBSP遺伝子プロモーターに存在するホメオドメイン配列(TCAATTAA)に結合し，BSPの石灰化組織特異的発現を調節していることを報告した[15]．しかし，このホメオドメインは転写開始点から約−190塩基対上流に存在し，pLUC 3には含まれないことから，今回のわれわれの結果とは異なる結果であった．以上のことから，今後BSPプロモーター中の石灰化組織特異的発現調節機構のさらなる解析が必要であると考えられた．

結　論

骨芽細胞様細胞であるROS 17/2.8およびUMR 106細胞，ラット肝臓由来上皮様細胞(RL 34)，ラット骨格筋細胞(L 6)，マウス未分化間葉細胞(C 3 H 10 T 1/2)，ヒト唾液腺腺房細胞(HSY)およびヒト歯肉線維芽細胞(HGF)を用いて，BSPの石灰化組織特異的発現を調節するプロモーターを検索した結果，以下の知見を得た．

1．ノーザンブロットの結果，骨芽細胞様細胞であるROS 17/2.8およびUMR 106細胞ではBSPmRNAの発現が認められたが，RL 34，L 6，C 3 H 10 T 1/2，HSYおよびHGF細胞ではBSPmRNAの発現は認められなかった．

2．ルシフェラーゼアッセイの結果，ROS 17/2.8およびUMR 106細胞に導入したpLUC 3(−116〜+60塩基対)の転写活性は高く，RL 34，L 6，C 3 H 10 T 1/2，HSYおよびHGF細胞でのpLUC 3の活性は低かった．

3．ゲルシフトアッセイの結果，CRE配列に結合する核内タンパク質が骨芽細胞様細胞であるROS 17/2.8およびUMR 106細胞でのみ認められた．

4．以上の結果より，石灰化組織特異性を規定するプロモーター配列は，pLUC 3に特異的な塩基配列中(−43〜−116塩基対までの間)に存在すると考えられ，その1つの候補はCRE配列であると考えられた．

本研究は文部省科学研究費(No. 12671865，14571989)，日本大学松戸歯学部鈴木研究費(平成12年度；共同研究，平成12，13，14年度；一般研究)，および日本大学学術研究助成金(平成13年度；一般研究，平成14年度；総合研究)，平成10年度および平成13年度学術フロンティア推進事業(文部科学省)の補助のもとに行われた．

文　献

1) Oldberg Å, Franzèn A, Heinegård D: The primary atructure of a cell-binding bone sialoprotein; J Biol Chem 263, 19430—19432, 1988.
2) Ganss B, Kim RH, Sodek J: Bone Sialoprotein; Crit Revs Oral Biol Med 10, 79—98, 1999.
3) Hunter GK, Goldberg HA: Nucleation of hydroxyapatite by bone sialoprotein; Proc Nathl Acad Sci USA 90, 8562—8565, 1993.
4) Ducy P, Desbois C, Boyce B, Pinero G, Story B, Dunstan C, Smith E, Bonadio J, Goldstein S, Gundberg C, Bradley A, Karsenty G: Increased bone formation in osteocalcin-deficient mice; Nature 382, 448—452, 1996.
5) Bellahcène A, Merville MP, Castronovo V: Expression of bone sialoprotein, a bone matrix protein, in human breast cancer; Cancer Res 54, 2823—2826, 1994.
6) Sodek J, Li JJ, Kim RH, Ogata Y, Yamauchi M: Characterazation of bone sialoprotein (BSP) gene promoter; Connect Tissue Res 35(1—4), 23—31, [77—85], 1996.
7) Li JJ, Kim RH, Sodek J: An inverted TATA box directs downstream transcription; Biochem J 310, 33—40, 1995.
8) Kim RH, Li JJ, Ogata Y, Yamauchi M, Freedman LP, Sodek J: Identification of a vitamin D_3-response element that overlaps a unique inverted TATA box in the rat bone sialoprotein gene; Biochem J 318, 219—226, 1996.
9) Kim RH, Sodek J: Transcription of the bone sialoprotein gene is stimulated by v-Src acting through an inverted CCAAT box; Cancer Res 59, 565—571, 1999.
10) Shimizu-Sasaki E, Yamazaki M, Furuyama S, Sugiya H, Sodek J, Ogata Y: Identification of a novel response element in the rat bone sialoprotein (BSP) gene promoter that mediates constitutive and fibroblast growth factor 2-induced expression of BSP; J Biol Chem 276, 5459—5466, 2001.
11) Ogata Y, Nakao S, Kim RH, Li JJ, Furuyama S, Sugiya H, Sodek J: Parathyroid hormone regulation of bone sialoprotein (BSP) gene transcription is mediated through a pituitary specific transcription factor-1 (Pit-1) motif in the rat BSP gene promoter; Matrix Biol 19, 395—407, 2000.
12) Ogata Y, Niisato N, Furuyama S, Cheifetz S, Kim RH, Sugiya H, Sodek J: Transforming growth factor-β 1 regulation of bone sialoprotein gene transcription: Identification of a TGF-β activation element in the rat BSP gene promoter; J Cell Biochem 65, 501—512, 1997.
13) Ogata Y, Yamauchi M, Kim RH, Li JJ, Freedman LP, Sodek J: Glucocorticoid regulation of bone sialoprotein (BSP) gene expression: Identification of a glucocorticoid response element in the bone sialoprotein gene promoter; Eur J Biochem 230, 183—192. 1995.
14) Yamauchi M, Ogata Y, Kim RH, Li JJ, Freedman LP, Sodek J: AP-1 regulation of the rat bone sialoprotein gene transcription is mediated through a TPA response element within a glucocorticoid response unit in the gene promoter; Matrix Biol 15, 119—130, 1996.
15) Benson MD, Bargeon JL, Xiao G, Thomas PE, Kim A, Cui Y, Franceschi RT: Identification of a homeodomain binding element in the bone siaoloprotein gene promoter that is required for its osteoblast-selective expression; J Biol Chem 275, 13907—13917, 2000.
16) Majeska RJ, Rodan SB, Rodan GA: Parathyroid hormone-responsive clonal cell lines from rat osteosarcoma; Endocrinology 107, 1494—1503, 1980.
17) Partridge NC, Alcorn D, Michelangeli VP, Ryan G, Martin TJ: Morphological and biochemical characterization of four clonal osteogenic sarcoma cell lines of rat origin; Cancer Res 43, 4308—4314, 1983.
18) Rose JK, Buonocore L, White MA: A new cationic liposome reagent mediating neary quantitative transfection of animal cells; Biotechniques 10, 520—525, 1991.
19) Dignam JD, Lebovitz RM, Roeder RG: Accurate transcription initiation by RNA polymerase II in a soluble extract from isolated mammalian nuclei; Nucleic Acids Res 11; 1475—1489, 1983.
20) Ducy P, Karsenty G: Two distinct osteoblast-specific cis-acting element control expression of a mouse osteocalcin gene; Mol Cell Biol 15, 1858—1869, 1995.
21) Komori T, Yagi H, Nomura S, Yamaguchi A, Sasaki K, Deguchi K, Shimizu Y, Bronson RT, Gao YH, Inada M, Sato M, Okamoto R, Kitamura Y, Yoshiki S, Kishimoto T: Targeted disruption of Cbfa 1 results in a complete lack of bone formation owing to maturational arrest of osteoblasts; Cell 89, 755—764, 1997.
22) Rossert JA, Chen SS, Eberspaecher H, Smith CN, de Crombrugghe B: Identification of the mouse pro-α 1(I)collagen promoter that confers high-level osteoblast expression in transgenic mice and that binds a protein selectively present in osteoblasts; Proc Natl Acad Sci USA 93, 1027—1031, 1996.
23) Kern B, Shen J, Starbuck M, Karsenty G: Cbfa 1 Contributes to the osteoblast-specific expression of type I collagen genes; J Biol Chem 276, 7101—7107, 2001.

Original paper

Dental Materials Journal 21(3) : 250−260, 2002

In vitro Study of Collagen Coating of Titanium Implants for Initial Cell Attachment

Megumi NAGAI, Tohru HAYAKAWA[1], Akira FUKATSU, Masafumi YAMAMOTO[2], Masahiko FUKUMOTO, Fumio NAGAHAMA, Hiroyuki MISHIMA[3], Masao YOSHINARI[4], Kimiya NEMOTO[1], and Takao KATO

Department of Comprehensive Clinical Dentistry, Research Institute of Oral Science
[1]Department of Dental Materials, Research Institute of Oral Science
[2]Department of Oral Medicine, Research Institute of Oral Science
[3]Derpartment of Anatomy, Research Institute of Oral Science,
Nihon University School of Dentistry at Matsudo
2-870-1, Sakaecho-nishi, Matsudo, Chiba 271-8587, Japan
[4]Department of Dental Materials Science and Oral Health Science Center, Tokyo Dental College,
1-2-2 Masago, Mihamaku, Chiba 261-8502, Japan

Received April 3, 2002/Accepted June 24, 2002

The aim of this study was to examine the influence of collagen coating on titanium on the initial attachment of human gingival fibroblasts for the development of the implant with peri-implant soft tissue attachment. The morphological changes of cultured human gingival fibroblasts were investigated by scanning electron microcopy (SEM). Four different surfaces, *i.e.* non-coated mirror-polished titanium, collagen-coated titanium, non-coated tissue-culture polystyrene, and collagen-coated polystyrene were examined. Collagen coating of titanium was effective for enhancing the initial cell attachment. It is expected that collagen coating of titanium implants will improve the attachment of the peri-implant soft tissue to titanium at early stages after the implantation. SEM observation revealed the morphological effect of collagen coating on both titanium and polystyrene surfaces. Many lamellipodia and filopodia were recognized on collagen-coated titanium or polystyrene. Collagen coating improved the activity of human gingival fibroblasts.

Key words : Titanium implant, Collagen, Human gingival fibroblast

INTRODUCTION

Presently titanium and titanium alloy implants are widely used as biomaterials for dental implants because of their superior mechanical properties and their direct bone anchorage called osseointegration[1,2]. The direct bone contact of titanium and titanium alloy implants produce suitable stability into the bone tissue. However, implant failures sometimes occur due to inflammatory gingival breakdown around the implant material[3,4]. This is caused by the accumulation of bacterial plaque surround-

ing the implant surface.

There is a basement membrane between human natural teeth and the cell membrane. The cells adhere to this base membrane by means of hemidesmosomes. Jansen *et al.*[5] reported that hemidesmosomal contacts were found only on apatite and polystyrene implants and not on various metals including titanium implants. A recent ultrastructural study revealed that hemidesmosomes were rare and absent in the upper and middle regions of the peri-implant epithelium-implant interface, and existed only in the lower region[6]. These studies supported the poor attachment of peri-epithelium soft tissues to the implant materials. This poor attachment caused the bacteria invasion around the titanium implant.

There have been many studies on the chemical and physical modifications of titanium implant materials to obtain stable and tight contact to bony tissues, for example, calcium phosphate coating[7,8] or greater surface roughness[9,10]. However, few studies related to the improvement of the gingival tissue attachment to the implant materials have been reported. The first biological reaction at the biomaterial-tissue interface is the adsorption of body fluid proteins including extracellular matrix components onto its surface after the implantation of biomaterials into a foreign body[11–13]. It is widely accepted that these adsorbed proteins control the subsequent biological response of the implant-tissue interface[14,15]. Coating of the implant surface with cell-adhesive proteins will improve the cell activity at the implant-tissue interface, and will improve the connection between the implant and peri-implant soft tissue.

Some studies for the coating of the titanium surface with cell-adhesive proteins have been reported. Dean *et al.*[16] investigated the effectiveness of the coating of titanium with fibronectin or laminin on the attachment of human gingival cells or human epithelial cells. They found that fibronectin coating of titanium implants enhanced the gingival fibroblast binding and laminin coating of titanium implants enhanced the gingival epithelial cell binding. Cannas *et al.*[17] reported that the coating of titanium with fibronectin enhanced the adhesive characteristics of baby hamster kidney fibroblasts. Endo[18] evaluated the efficacy of immobilized fibronectin on the human gingival cell culture. It was also reported that the coating of titanium with collagen exhibited favorable effects on the initial adhesion and growth activities of rat calvarial osteoblasts[19,20]. Morikawa *et al.*[21] reported the immobilization of collagen onto the titanium surface using gold deposition and production of a monomolecular layer with cystein.

There have been few studies related to the collagen coating of titanium substrate on human gingival cell activity. In the present, we examined the initial attachment of human gingival cells by the collagen coating on the titanium surface for the development of the implant with peri-implant soft tissue attachment. The morphological influence of human gingival cells by the collagen coating was also evaluated by scanning electron microscopy (SEM).

MATERIALS AND METHODS

Titanium substrate

Commercially pure wrought titanium disks (JIS, Japan industrial Specification H 4600, 99.9 mass% Ti, Furuuchi Chemical Corp., Tokyo) with a diameter of 15 mm were used. They were ground down to 1200 grit, finally polished using colloidal silica with pH 9.8, and then ultrasonically cleaned with acetone. Before use in the cell culture experiments, all polished titanium disks were autoclaved for 30 min at 120℃.

Cell isolation and cultures

Cells used in *in vitro* experiments were from pieces of gingival tissue by the excision during routine periodontal surgical procedures at the Dental Hospitals attached to Nihon University School of Dentistry at Matsudo. The study was explained to the patients and their informed consent was obtained. Small pieces of tissue were washed several times with Dulbecco's Modified Eagle Medium (DMEM, Gibco BRL, Rockville, MD, USA) containing 100 U/ml penicillin G (Gibco BRL, Rockville, MD, USA), 100 μg/ml streptomycin (Gibco BRL, Rockville, MD, USA), 0.2 μg/ml amphotericin B (Gibco BRL, Rockville, MD, USA). The epithelial layer was then mechanically separated from the connective tissue with sterile forceps. Primary cultures were incubated in an atmosphere of 5%CO_2, 95% air at 37℃ in the following medium, DMEM supplemented with 10% fetal calf serum, 100 μg/ml streptomycin, 100 U/ml penicillin G, and 0.2 μg/ml amphotericin B, and routinely passaged using 0.25% trypsin and 0.02% EDTA in Dulbecco's phosphate-buffered saline. The cells were fed twice per week and subcultured using 0.25% trypsin. Cells for use in the experiments described were used between passages 15-20. Phase contrast micrography of primary human gingival fibroblasts are shown in Fig. 1.

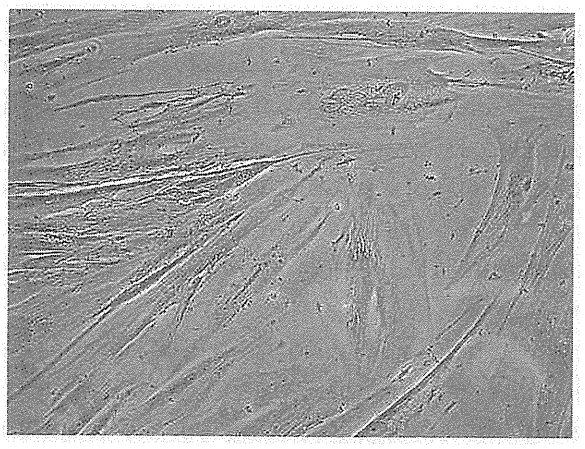

Fig. 1 Phase contrast micrograph of primary cultured human gingival fibroblasts.
(original magnification × 40)

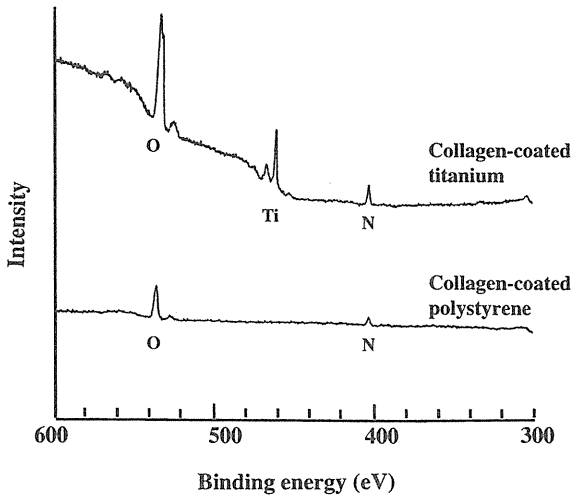

Fig. 2 Spectra of collagen-coated titanium and tissue-culture polystyrene by the measurement of X-ray photoelectron spectroscopy.

Collagen coating

Collagen type I of commercial pig derivation (Nitta Gelatine, Osaka, Japan) (3.0 mg/ml, pH 3.0) was dissolved into distilled water, and was diluted ten times to adjust to 300 μg/ml according to the manufacturer's instruction.

For coating with collagen, titanium disks were placed in a 24-well culture dishes (FALCON, Becton Dicknson Labware, NJ, USA), and were exposed to a 0.5 ml collagen solution at room temperature for 1 h. Then, they were rinsed with phosphate buffer saline (PBS, pH=7.4) solution twice. Tissue-culture polystyrene dishes were also coated with collagen as the same method described above. The presence of coated collagen was identified by X-ray photoelectron spectroscopy (ESCA-750, Shimadzu, Kyoto, Japan) measurement. Before collagen coating, no peak of 1s electron of nitrogen (N1s) was detected on titanium and polystyrene. A N1s peak from coated collagen was observed at about 402 eV of binding energy as shown in Fig. 2.

Thus, we examined four different surfaces, *i.e.* non-coated tissue-culture polystyrene, collagen-coated polystyrene, non-coated mirror-polished titanium, and collagen-coated titanium.

Cell attachment assay

When the outgrown cells became confluent after 15-20 passages, they were treated with a trypsin solution, and resuspended in DMEM. The suspension was plated on the non-coated or collagen-coated titanium disks in 24-well culture dishes at a cell population density of 1×10^5 cells/ml. The cell suspension was also plated in non-coated tissue-culture polystyrene and collagen-coated polystyrene. The cell suspension was allowed to incubate for 1.5 hr under standard culture conditions. Afterwards, cells were washed three times with PBS, and non-adherent cells were

washed away. The adherent cells were removed from the titanium disks or polystyrene by trypsinzation and the number of adherent cells were counted using a Coulter counter (Nikkaki, Tokyo, Japan). The viable cells in a hemocytometer was counted using the trypan blue dye exclusion assay, and the cell viability was determined from the ratio of the number of viable cells towards the number of initial attached cells. Unstained cells were counted as viable cells. Cell attachment experiments were performed in triplicate. The data were analyzed by t-test at $p=0.05$.

Scanning electron microscopy (SEM) observation

After incubation of the test materials as described above, culture wells containing test materials were rinsed three times with PBS. Attached cells were fixed with 1% glutaraldehyde for 15 minutes, rinsed three times with PBS, and then fixed with 2% osmium tetroxide for 15 minutes. Fixed cells were taken in stages of 5 minutes each (50%, 70%, 80%, 90%, 95%, 99.9%) to 100% ethanol, dried using critical drying apparatus and ion-coated with gold and palladium. The morphology of cells was observed with a scanning electron microscope (S-2150, Hitachi, Tokyo, Japan).

RESULTS

Fig. 3 shows the number of adherent cells on non-coated or collagen-coated tissue-culture polystyrene and non-coated or collagen-coated titanium. The number of adherent cells on collagen-coated polystyrene was approximately 570 cells/cm^2 which is identical to that seen in non-coated polystyrene plates. On the other hand, coating of collagen on the titanium surface resulted in a significant increase of adherent cells. The number of adherent cells on non-coated titanium was approximately 450 cells/cm^2, and that on collagen-coated titanium was approximately 930 cells/cm^2. The number of attached cells increased almost two-fold by collagen coating.

The cell viability obtained from trypan blue staining is shown in Fig. 4. The cell

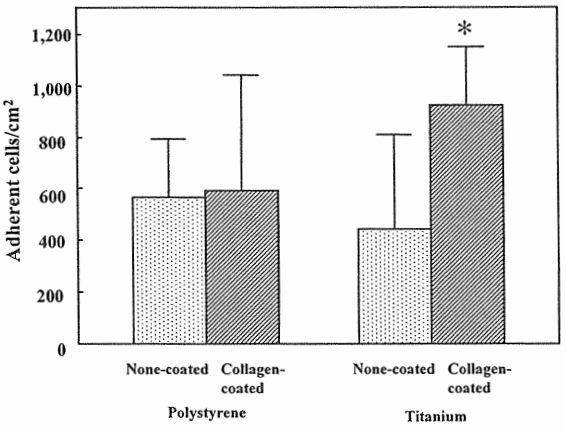

Fig. 3 Number of cells adhered to non-coated or collagen-coated titanium or tissue-culture polystyrene.
*: significant difference ($p<0.05$)

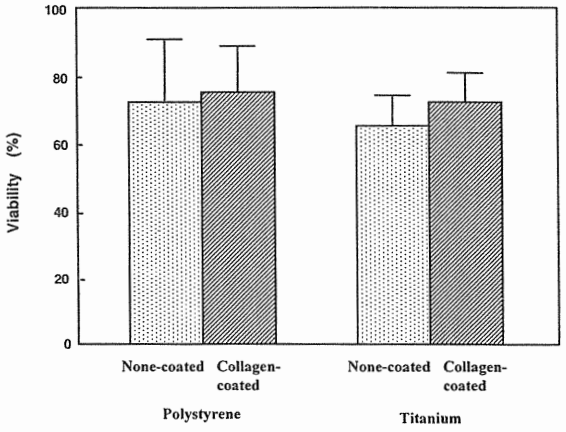

Fig. 4 Cell viability on non-coated or collagen-coated titanium or tissue-culture polystyrene.

viability was approximately 70% on the different surfaces, *i.e.* non-coated or collagen-coated polystyrene and non-coated or collagen-coated titanium surfaces, and there were no significant differences among each surface ($P>0.05$).

SEM pictures of human gingival fibroblasts adhered to different materials are shown in Figs. 5-8. Figs. 5 and 6 show the SEM pictures of attached cells on non-coated and collagen-coated tissue-culture polystyrene, respectively. The SEM pictures revealed the differences in the surface appearances and shapes of attached cells between non-coating and collagen-coated polystyrene, although there was no significant difference among the number of adherent cells. The attached cells on non-coated polystyrene showed a roughened surface appearance, and showed a rounded shape and slight formation of filopodia (thin and stiff protrusions, Fig. 5a, b). The cells attached on collagen-coated polystyrene showed smooth surface appearance and a

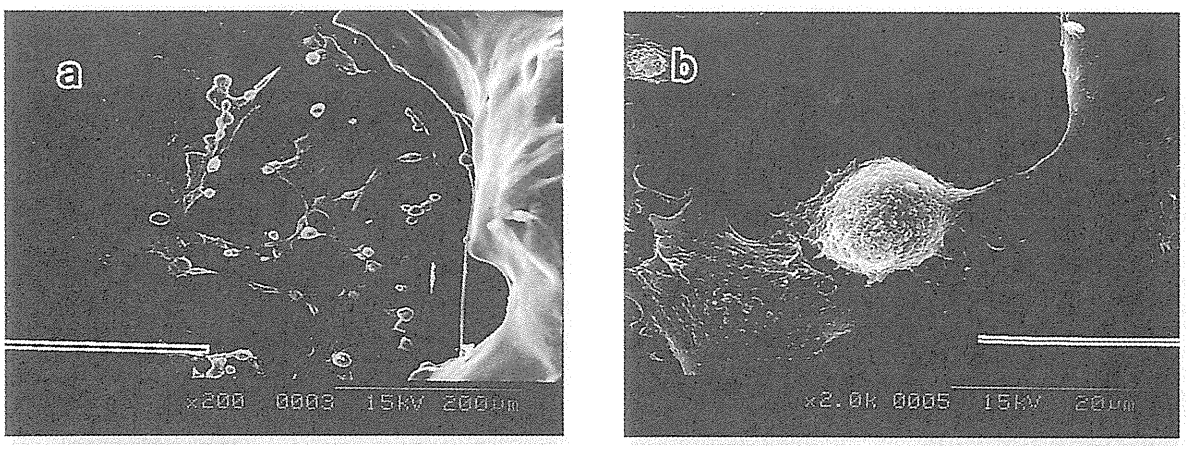

Fig. 5 SEM pictures of human gingival fibroblasts on non-coated tissue-culture polystyrene.
a) lower magnification (bar=200μm), b) higher magnification (bar=20μm)

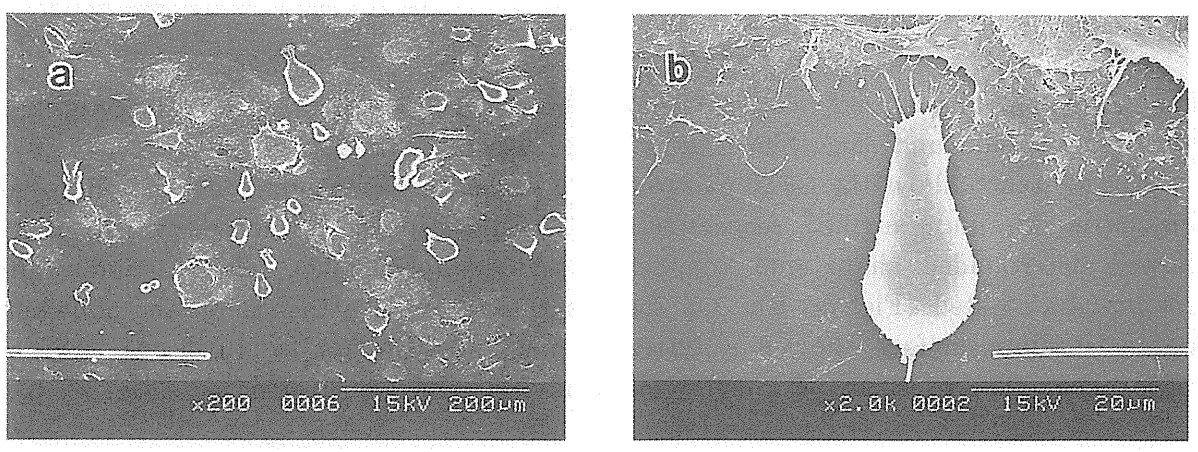

Fig. 6 SEM pictures of human gingival fibroblasts on collagen-coated tissue-culture polystyrene.
a) lower magnification (bar=200μm), b) higher magnification (bar=20μm)

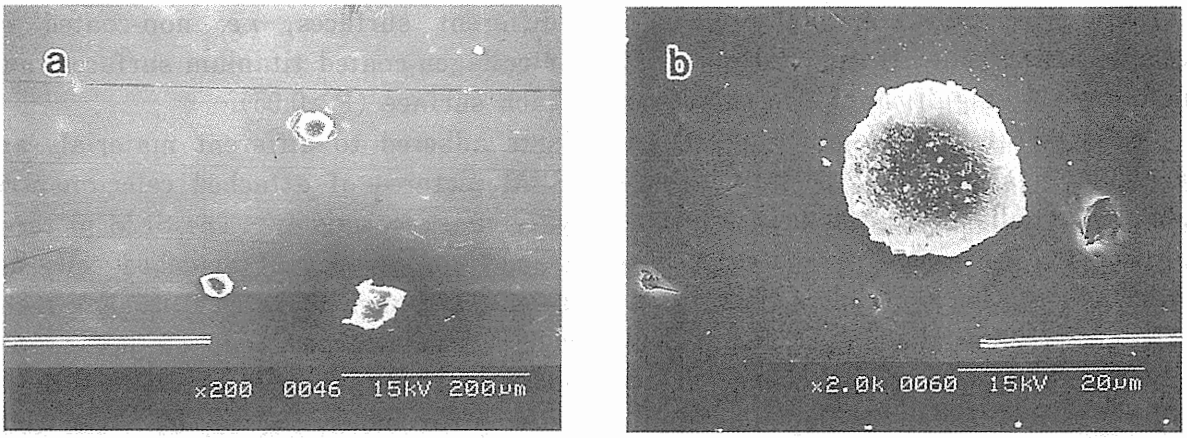

Fig. 7 SEM pictures of human gingival fibroblasts on non-coated titanium
a) lower magnification (bar=200μm), b) higher magnification (bar=20μm)

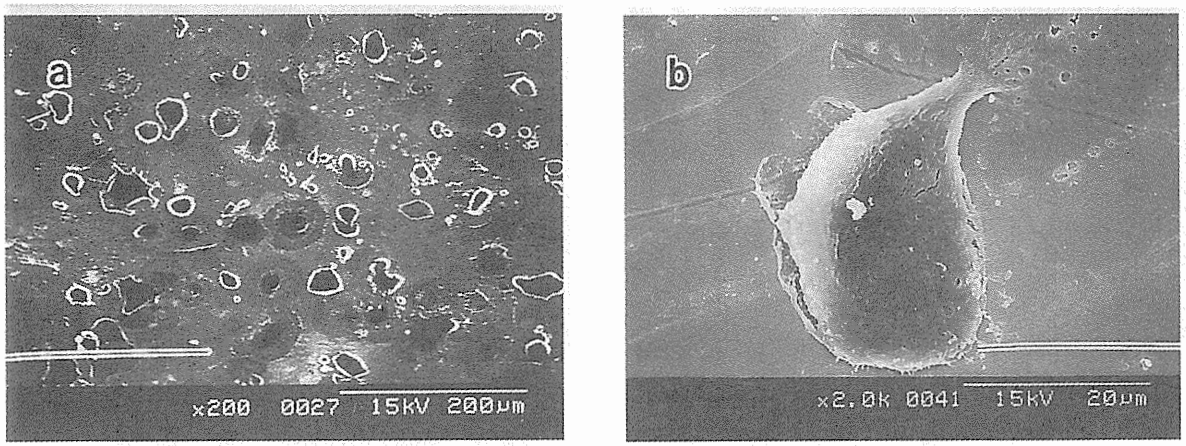

Fig. 8 SEM pictures of human gingival fibroblasts on collagen-coated titanium.
a) lower magnification (bar=200μm), b) higher magnification (bar=20μm)

more flattened and spread shape. They exhibited more spanning of filopodia and lamellipodia (thin and sheet-like leading edge) as shown in Fig. 6a, b.

Figs. 7 and 8 show the SEM pictures of attached cells on non-coating and collagen coating titanium surface, respectively. The cells attached on non-coated titanium showed the rounded shape and roughened surface appearance. No filopodia nor lamellipodia existed (Fig. 7a, b). On the other hand, cells attached on the collagen-coated titanium surface showed a flattened and spread shape, and smooth surface appearance. The presence of lamellipodia and filopodia was confirmed (Fig. 8a, b).

DISCUSSION

In this study, we evaluated the efficacy of collagen coating of titanium or polystyrene on human fibroblast activity.

Collagen is a well known cell-adhesive protein and is effective in promoting cellular adhesion and spreading. Collagen possesses RGD (arginine-glycine-aspartic acid) sequencescm[22–24], which are recognized by integrins such as fibronectin or laminin. It is predicted that the collagen coating of titanium implants will improve the attachment of peri-implant soft tissue to titanium implant materials.

In the present study, human gingival fibroblasts obtained from the primary culture were used to evaluate the effect of collagen coating of titanium on peri-implant soft tissue adhesion. Human gingival fibroblasts actually adhere to the implant surface when the implant is inserted into the tissue. However, there have been few studies related to human gingival fibroblasts assay. It is possible to obtain some useful information for the improvement of the poor attachment of peri-epithelium soft tissues to the implant surface from the results of human gingival fibroblasts assay.

The adhesion of fibroblasts on titanium is a prerequisite for soft tissue integration. In the present study, the number of adherent cells on collagen-coated titanium was significantly greater than that on non-coated titanium. The previous studies[17,18] of osteoblasts reported that collagen coating of titanium accelerated the initial adhesion of osteoblasts. The findings of the present study suggested that collagen coating of titanium was effective not only for osteoblast but also for human gingival fibroblasts in the enhancement of the initial cell attachment.

Cell viability of human gingival cells was also determined. The higher cell viability means less cyotoxicity. The viability of cells on non-coated and collagen-coated titanium or polystyrene was approximately 70%, although the number of adherent cells was different. These results suggested that both titanium and polystyrene possessed equal properties in terms of cytotoxicity with or without collagen coating, and that four different surfaces employed in the present study caused no severe cytotoxicity.

The number of adherend fibroblasts was determined after 90-min cell culture. In the clinical situation, it is better to acquire the strong adhesion of peri-implant soft tissue to implant materials as soon as possible. The present study revealed the collagen coating of titanium enhanced the initial attachment of human gingival fibroblasts within 90 min of cell culture. Thus, it is expected that collagen coating of titanium implants will improve the attachment of the peri-implant soft tissue to titanium at on early stage after the implantation. Further studies related to the time for cell culture are needed to clarify the effect of collagen coating on the time after implantation.

There were no effects on the collagen coating of tissue-culture polystyrene toward the initial cell attachment. It is widely accepted that the cells well attached on the hydrophobic surface. Human gingival fibroblasts attached to tissue-culture polystyrene. Thus, the effect of collagen coating on the number of attached cells was not clearly identified.

However, collagen coating markedly influenced the shape of the attached cells not only on titanium but also on polystyrene. On the collagen coated titanium or the polystyrene surface, a flattened and spread shape of cells was observed and the

presence of lamellipodia and filopodia were clearly recognized. The cells on non-coated titanium or polystyrene showed round shapes, and fewer lamellipodia and filopodia. This suggests that attached cells on collagen-coated titanium or polystyrene exhibited the higher migration ability on non-coated titanium or polystyrene. The improvement in the adherent ability of cells by collagen coating also produce a flattened and spread shape of the attached cells. It revealed that collagen coating was effective for the improvement of the cell activity by SEM observations, although the detailed cell activity such as actin fiber alignment should be investigated by immunostaining techniques.

In the present study, collagen was physically attached to the titanium disk, not chemically attached. The interface between collagen and the substrate, polystyrene or titanium, was not clear. The interface substance has a possibility to influence the results of the cell culture assay. Williams *et al.*[25] investigated the adsorption and desorption behavior of albumin and fibrinogen on 17 different metal surfaces, and found that *in vivo* substantial desorption of preadsorbed proteins occurred within 106 hours for most metals. Hayakawa *et al.*[26] developed a simple immobilization technique of surface-adhesive protein on titanium. The influence of the immobilization of collagen on the titanium surface will be studied in the near future.

Periodontal fibroblasts will also influence the attachment of implants to peri-implant soft tissue. The influence of collagen coating on the periodontal fibroblast cell assay should be further investigated.

Finally, collagen coating of titanium enhanced the initial attachment of human gingival fibroblasts and improved the migration activity. Collagen coating of titanium has a possibility to develop a tight attachment of dental implants to peri-implant soft tissue.

CONCLUSIONS

Human gingival fibroblasts were cultured on four different surfaces, *i.e.* non-coated mirror-polished titanium, collagen-coated titanium, non-coated tissue-culture polystyrene, collagen-coated tissue-culture polystyrene. Collagen coating was effective for enhancing the initial cell attachment on the titanium surface but not on the polystyrene surface by measuring the number of attached cells. The morphological effect by collagen coating was clearly recognized. Many lamellipodia and filopodia were recognized on collagen-coated titanium or polystyrene. It was revealed that collagen coating improved the activity of human gingival fibroblasts.

ACKNOWLEDGMENT

This study was supported by a Grant-in-aid for Research for Frontier Science and a Grant from the Ministry of Education, Culture, Sports, Science and Technology of Japan to promote 2001-Multidisciplinary Research Projects (in 2001-2005).

REFERENCES

1) Brånemark, P. I., Hansson, B. O., Adell, R., Breine, U., Lindström, J., Hallen, O. and Ohman, A.: Osseointegrated implants in the treatment of the edentulous jaw: Experience from a 10-year period, *Scad J Plast Reconstr Surg* **16** : 1-132, 1977.
2) Albrektsson, T., Brånemark, P. I., Hansson, H. A. and Lindström, J.: Osseointegrated titanium implant. Requirements for ensuring a long-lasting, direct bone-to-implant anchorage in man, *Acta Orthop Scand* **52** : 155-170, 1981.
3) Malmstrom, H. S., Fritz, M. E,, Timmis, D. P. and Van Dyke, T. E.: Osseo-integrated implant treatment of a patient with rapidly progressive periodontitis: A case report, *J Periodontol* **61** : 300-304, 1990.
4) Mombellli, A. and Lang, N. P.: The diagnosis and treatment of peri-implantitis, Periodontology **17** : 63-76, 2000.
5) Jansen, J. A., De Wijin, J. R., Wolters-Lutgerhorst, J. M. L. and Van Mullem, P. J.: Ultrastructural study of epithelial cell attachment to implant materials, *J Dent Res* **64**, 891-896, 1985.
6) Ikeda, H., Yamaza, T., Yoshinari, M., Ohsaki, Y., Ayukawa, Y., Kido, M. A., Inoue, T., Shimono, M., Koyono, K. and Tanaka, T.: Ultrasuructural and imminoelectron microscopic studies of the peri-implant epithelium-implant (Ti-6Al-4V) interface of rat maxilla, *J Periodontol* **71**, 961-973, 2000.
7) De Groot, K., Geesink, R., Klein, C. P. A. T. and Serekian, P.: Plasma sprayed coatings of hydroxylapatite, *J Biomed Mater Res* **21** : 1375-1381, 1987.
8) Hayakawa. T., Yoshinari, M., Kiba, H., Yamamoto, H., Nemoto, K. and Jansen, J. A.: Trabecular bone response to surface roughened and calcium phosphate (Ca-P) coated titanium implants, *Biomaterials* **23** : 1025-1031, 2002.
9) Wennerberg, A., Albrektsson, T., Andersson, B. and Krol, J. J.: A histomorphometric and removal torque study of screw-shaped titanium implants with three different surface topographies, *Clin Oral Impl Res* **6** : 24-30, 1995
10) Piattelli, A., Manzon, L., Scarano, A., Paolantonio, M. and Piattelli, M.: Histologic and histomorphometric analysis of the bone response to machined and sandblasted titanium implants: An experimental study in rabbits, *Int J Oral Maxillofac Impl* **13** : 805-810, 1998.
11) Horbett, T. A.: Principles underlying the role of adsorbed plasma proteins in blood interactions with foreign materials, *Cardiovasc Pathol* **2** : 137S-148S, 1993.
12) Wälivaara, B., Aronsson, B. O., Rodahl, M., Lausmaa, J. and Tengvall, P.: Titanium with different oxides: *In vitro* studies of protein adsorption and contact activation, *Biomaterials* **15** : 827-834, 1994.
13) Puleo, D. A. and Nanci, A.: Understanding and controlling the bone-implant interface, *Biomaterials* **20** : 2311-2321, 1999.
14) Chunyan, P., Sadami, T., Kazuaki, M., Naoki, N. and Suong-Hyu, H.: Morphologic study and syntheses of type I collagen and fibronectin of human periodontal ligament cells cultured on poly(ethylene-co-vinyl alcohol)(EVA) with collagen immobilization, *J Biomed Mater Res* **54** : 241-246, 2001.
15) Ahmed, E., Lisa, S. and Jonathan, J.: Laminin-5 coating enhances epithelial cell attachment, spreading, and hemidesmosome assembly on Ti-6Al-4V implant material *in vitro*, *J Biomed Mater Res* **41** : 30-40, 1998.
16) Dean, J. W., Culbertson, K. C. and D'Angelo, A. M.: Fibronectin and laminin enhance gingival cell attachment to dental implant surfaces *in vitro*, *J Oral Maxillofac Implants* **10** : 721-728, 1995
17) Cannas, M., Denicolai, F., Webb, L. X. and Gristina, A. G.: Bioimplant surfaces: Binding of fibronection and fibroblast adhesion, *J Orthop Res* **6** : 58-62, 1998.
18) Endo, K.: Chemical modification of metallic implant surfaces with biofunctional proteins (Part 1) Molecular structure and biological activity of a modified NiTi alloy surface, *Dent Mate J* **14**(2) : 185-198, 1995.

19) Geißler, U., Hempel, U., Wolf, C., Scharnweber, D., Worch, H. and Wenzel, K. W.: Collagen type I -coating of Ti6Al4V promotes adhesion of osteoblasts. *J Biomed Mater Res* **51** : 752-760, 2000.
20) Roehlecke, C., Witt, M., Kasper, M., Schulze, E., Wolf, C., Hofer, A. and Funk, R. H. W.: Synergistic effect of titanium alloy and collagen type I on cell adhesion, proliferation and differentiation of osteoblast-like cells, *Cells tissues Organs* **168** : 178-187, 2001.
21) Morikawa, N., Suzuki, M., Morita, S., Yokoya, S., Miyamoto, M., Fukuoka, S., Ozono, S. and Kinoshita, Y.: Study on improvement of adhesion between gingival tissue and dental implant by collagen immobilization, *J Jpn Soc Biomaterials* **19**(1) : 10-20, 2001. (in Japanese)
22) Ruoslahti, E. and Pierschbacher, M. D.: New perspectives in cell adhesion: RGD and integrins, *Science* **238** : 491-497, 1987.
23) Verrier, S., Bareille, R., Rovira, A., Dard, M. and Amedee, J.: Human osteoprogenitor responses to orthopaedic implant: Mechanisms of cell attachment and cell adhesion, *J Mater Sci Mater Med* **7** : 46-51, 1996.
24) Park, J. C., Kim, H. M.. and Ko, J. S.: Effects of extracellular matrix constituents on the attachment of human oral epithelial cells at the titanium surface, *Int J Oral Maxillofac Implants* **13** : 826-836, 1998.
25) Williams, D. F., Askill, I. N. and Smith, R.: Protein absorption and desorption phenomena on clean metal surfaces, *J Biomed Mater Res* **19** : 313-320, 1985.
26) Hayakawa, T., Yoshinari, M. and Nemoto, K.: Immobilization of cell-adhesive protein onto titanium surface using tresyl chloride, *J J Dent Mater* **21**(Special Issue 39) : 105, 2002. (in Japanese)

Potential Application of High-Resolution Microfocus X-ray Techniques for Observation of Bone Structure and Bone-Implant Interface

Hideo Kiba, PhD[1]/Tohru Hayakawa, PhD[2]/Shigeo Oba, DVM[3]/Masato Kuwabara, PhD[4]/
Isao Habata, DVM[5]/Hirotsugu Yamamoto, DDS, PhD[6]

Purpose: *The aim of the present study was to evaluate the potential application of 2 types of microfocus x-ray units to study the bone structure around dental implants and at the bone-implant interface.* ***Materials and Methods:*** *IMZ titanium implants were placed in the maxilla and mandible of a beagle dog. After implantation periods of 1, 2, and 3 months, the bone-implant interface was evaluated with microfocus x-ray computed tomography (CT) and microfocus x-ray fluoroscopy.* ***Results:*** *Microfocus x-ray CT images of the bone-implant specimen at 3 months after implant placement revealed a clear distinction between the implant and the bone. The implant surface was partially covered with bone, and direct contact between the implant and bone could be clearly seen. Differences in degrees of calcification were identified by the differences in relative black and white intensity. Microfocus x-ray fluoroscopy also showed clear features of the bone and titanium implant. The original drill hole and new bone formation could be recognized. These findings corresponded with traditional histologic observations by light microscopy.* ***Discussion and Conclusion:*** *Microfocus x-ray techniques are non-destructive and require a very short examination time. They are considered useful to observe details of the bone structure and bone-implant interface. Microfocus x-ray fluoroscope and microfocus x-ray CT techniques can provide a clear and distinguishable image of the bone-implant interface because of their high spatial resolution.* (Int J Oral Maxillofac Implants 2003;18:279–285)

Key words: *bone structure, dental implants, dental radiography, microfocus x-ray*

The success of dental implants may be attributed to the osseointegration between the implant material and host bone.[1–4] Conventionally, undecalcified thin sections are an important factor in demonstrating osseointegration. The preparation of thin sections is a very laborious and time-consuming procedure that requires special knowledge and skill. Furthermore, artificial fissures sometimes occur at the bone-implant interface, which may lead to misinterpretation.

Radiography and computed tomography (CT) are expected to be improved techniques for studying bone structure or the bone-implant interface, because they provide sectional images of internal structures without tissue sections and without destroying the specimen. CT is now widely used for the diagnosis of diseases in dental and medical fields. However, it is difficult to observe and analyze fine structures less than a few cubic millimeters in size because of its low spatial resolution, which is more than 100 μm. Conventional radiographic techniques do not provide high enough magnification or spatial resolution for the characterization of bone and the bone-implant interface.

Bonse and coworkers[5] studied absorption-contrast microtomography using synchrotron radiation

[1]Assistant Professor, Department of Oral Pathology, Research Institute of Oral Science, Nihon University School of Dentistry at Matsudo, Chiba, Japan.
[2]Assistant Professor, Department of Dental Materials, Research Institute of Oral Science, Nihon University School of Dentistry at Matsudo, Chiba, Japan.
[3]Assistant Professor, Laboratory of Veterinary Medicine, Department of Veterinary Medicine, College of Bioresource Sciences, Nihon University, Kanagawa, Japan.
[4]Associate Professor, Laboratory of Veterinary Radiology, Department of Veterinary Medicine, College of Bioresource Sciences, Nihon University, Kanagawa, Japan.
[5]Lecturer, Animal Medical Center, College of Bioresource Sciences, Nihon University, Kanagawa, Japan.
[6]Professor, Department of Oral Pathology, Research Institute of Oral Science, Nihon University School of Dentistry at Matsudo, Chiba, Japan.

Reprint requests: Dr Hideo Kiba, Department of Oral Pathology, Research Institute of Oral Science, Nihon University School of Dentistry at Matsudo, 2-870-1, Sakaecho-Nishi, Matsudo, Chiba, 271-8587, Japan. Fax: +81-47-364-6295. E-mail: kiba@mascat.nihon-u.ac.jp

and achieved a spatial resolution of 8 μm for human cancellous bone. Momose and associates[6] observed the soft tissue of cancerous rabbit liver by a modified phase-contrast technique using synchrotron radiation with a spatial resolution of 30 μm. However, the equipment for synchrotron radiation takes up a great deal of space and is expensive to operate.

A new type of microfocus x-ray unit with a spatial resolution less than 10 μm has been developed (Nittetsu Elex, Kanagawa, Japan; Shimadzu, Kyoto, Japan). A magnetic focus-control microfocus x-ray tube was used as an open-vacuum x-ray source, which produces a fine and equal-speed electron beam. Shibata and Nagano[7] applied this type of microfocus x-ray CT to observe the auditory ossicles of a human fetus, the smallest and lightest bones in the skeletal system. The high-resolution microfocus x-ray technique has been used effectively to study trabecular bone structure,[8,9] enamel thickness,[10] and calcification of human teeth,[11] as well as dental root canal morphology.[12,13]

A few studies have examined the bone-implant interface or bone structure around implants using microfocus CT. Sakae and colleagues[13] were able to observe the compact and spongy bone architecture clearly on microfocus tomograms, but noted artificial concentric circles related to the difference in x-ray absorption coefficient between bone and the titanium implant. Van Oosterwyck and coworkers[14] validated the qualitative accuracy of microfocus x-ray CT images by comparing histologic sections with the corresponding CT slices for the same specimen. Their microfocus x-ray tube had a focal spot of 10 μm.

The present study examined a recently developed microfocus x-ray machine that uses an x-ray tube with a focal dimension of 4 μm. The aim was to explore the potential application of 2 types of microfocus x-ray machines—the microfocus x-ray fluoroscope and the microfocus x-ray CT system—to study the bone structure around implants and the bone-implant interface by comparing the images produced by these techniques with stained histologic sections and contact microradiograms.

MATERIALS AND METHODS

Animal Model and Surgical Procedures

The Animal Care and Use Committee of the College of Bioresource Sciences, Nihon University, Japan, approved the protocols and guidelines of this study. A female beagle dog weighing 11 kg was used in the study. The maxillary and mandibular premolars were extracted to create edentulous regions in the jaws. Healing of alveolar bone was achieved approximately 1 year after extraction.

At that time, titanium spray-coated IMZ implants (Friatec AG, Mannheim, Germany) 3.3 mm in diameter and 10 mm in length were placed. The basic IMZ implantation procedure was performed according to the manufacturer's instruction. All surgical procedures for implantation were performed under general anesthesia. Atropine sulfate (Tanabe Seiyaku, Osaka, Japan) 0.04 mg/kg was administered subcutaneously, followed by intravenous sodium thiopental (Tanabe Seiyaku) 17.5 mg/kg. Then 2% isoflurane (Dainippon Pharmaceutical, Osaka, Japan) was given continuously through an 8-mm tracheal tube at an oxygen flow rate of 2 L/min as inhalation anesthesia.

First Implant Surgery. First, 2 implants were placed in the mandible. Crestal incisions were made bilaterally in the mandible, extending from the canine to the first molar. Full-thickness mucoperiosteal flaps were reflected. A small, sharp periosteal elevator was used to separate the periosteum. After exposing the mandible in bilateral premolar regions, pilot holes of 0.6 mm were drilled. The holes were gradually widened with successive drills up to the final diameter (3.3 mm) of the implants. The bone preparation was performed with very gentle surgical techniques using a low drilling speed (500 rpm) and continuous internal cooling with a bone surgery system (Royal, Tokyo, Japan). After press-fit placement of the implants, the soft tissues were closed in separate layers using intracutaneous resorbable Vicryl 3-0 sutures.

Second and Third Implant Surgeries. The second implant placement surgery was performed in the maxilla 1 month after the first implantation. The premolar region of the maxilla was exposed in 1 quadrant, and 1 IMZ implant was placed using the same method as described above. The third implant surgery was performed 1 month after the second. One IMZ implant was placed into the remaining maxillary premolar region with the same surgical procedure.

The dog was fed a soft diet after the implant surgery. To reduce the risk of postoperative infection, prophylactic antibiotic enrofloxacin (Baytril; Bayer AG, Leverkusen, Germany) was administered preoperatively by subcutaneous injection. The position and stability of the placed implants during the healing period was examined by a dental x-ray unit (Max-F1-M, Morita, Kyoto, Japan). All implants demonstrated good primary stability. The health condition of the dog was always checked before and after the surgery, and there were no signs of infection. The weight of the dog remained constant during the experimental period.

Three months after the first implant was placed, the animal was sacrificed by injection of an overdose of pentobarbital sodium (Nembutal; Abbott Laboratories, North Chicago, IL). Three kinds of bone-implant specimens, ie, 1-month (1 implant), 2-month (1 implant), and 3-month (2 implants), were therefore obtained.

Microfocus X-ray Observations

After the animal was sacrificed, the maxilla and mandible were excised. The bone/implant specimens were fixed in 10% buffered formalin, dehydrated through a graded series of ethanols, and embedded in polyester resin (Rigolac; Nisshin EM, Tokyo, Japan).

The mandibular bone/implant specimen obtained 3 months after implantation was examined first, using a microfocus x-ray CT machine (SMX-225CT; Shimadzu, Kyoto, Japan). The microfocus x-ray source of the machine had a focal spot of 4 μm, maximum voltage of 225 kV, and maximum current of 1 mA. The x-ray generator and detectors (image intensifier) were stationary and the sample was rotated on stage. To obtain a cross-sectional image, the CT scanner system accumulated fluoroscopic images from all angles, and a computer reconstructed the inner structural image. The rotational stage moved perpendicularly; thus it was possible to obtain a cross-sectional image of the sample in any position desired. The minimum reconstruction time was 12 seconds for a 512×512 2-dimensional image matrix with an 1,800-angle view using exclusive high-speed computation hardware such as the Digital Signal Processor (NEC Electronics, Kanagawa, Japan). The digitized signals were further transferred to a personal computer equipped with Windows MNT 4.0. Reconstructed images were saved in .bmp or .jpg format.

Buccolingual tomograms parallel to the long axis of the implant were obtained starting from the center of the implant and moving sequentially outward at a slice thickness of 0.1 mm and slice pitch 0.8 mm, with the machine operated at a tube focal length of 4 μm, a tube voltage of 65 kV, and a tube current of 70 μA. The pixel number was 512×512.

Subsequently, the other specimens were studied in a similar way.

Next, 3-mm-thick buccolingual sections including the implant were prepared from the 1-, 2-, and 3-month specimens using a low-speed rotating blade microtome (Isomet; Buehler, Lake Bluff, IL). The bone structures around the implant were observed using a microfocus x-ray fluoroscope (SMX-80; Shimadzu) operating at a tube focal length of 4 μm, an anode voltage of 80 kV, and a tube current of 200 μA. Control of the x-ray source and image tube, positioning of the XY table, and image processing were possible using a personal computer with the Windows system. An AC servo motor was used to activate the XY table. Image-processing software (X-ray Image Viewer; Shimadzu) was incorporated. The fluoroscopic image was inverted and the negative image was used for observations.

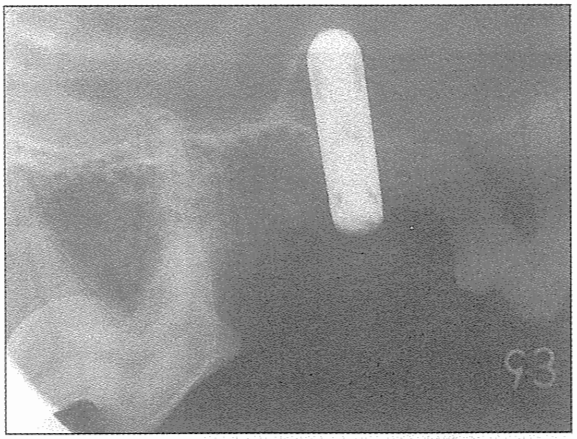

Fig 1 Conventional dental radiograph of the implant and surrounding bone in a specimen obtained 1 month after implant placement. There is no distinct bone resorption at the implant shoulder. Ultra-speed film (DF-55, Eastman Kodak, Rochester, NY); X-ray source: 60 kV and 20 mA.

Histologic Procedures

For comparison with microfocus x-ray observations, undecalcified ground sections were prepared from the 1-, 2-, and 3-month specimens. After fixation, the specimens were dehydrated through a graded series of ethanols and embedded in polyester resin (Rigolac; Nishin EM). After polymerization, 100-μm-thick ground sections were prepared in a direction parallel to the axis of the implant, using a grinding stone. These histologic sections were first studied by a contact microradiographic technique and then stained with methylene blue and basic fuchsin. Contact microradiography was performed in an x-ray cabinet (SRO-M40; Sofron, Soken, Japan) using a high-resolution film (SO-343; Kodak, Rochester, NY) at 30 kV and 3 mA. The implant-bone interface was observed under a light microscope (Eclipse E800M; Nikon, Tokyo, Japan).

RESULTS

All implants were all clinically stable without any mobility. The gingiva around the implants showed no signs of inflammation. In the dental radiograph of a specimen obtained 1 month after implant

Figs 2a to 2c *Microfocus x-ray CT images of a bone/implant specimen obtained 3 months after implant placement.*

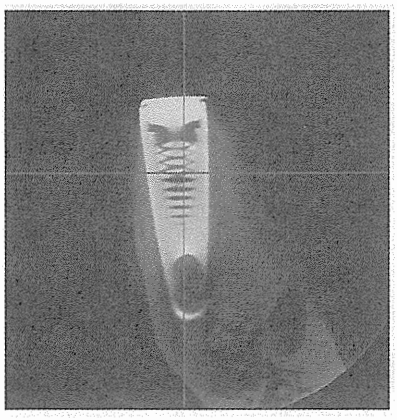

Fig 2a Original longitudinal CT image of a slice at the buccolingual region. The implant is seen as a white object that is clearly distinguishable from the bone, which appears gray. The difference in degree of calcification is identified by the difference in relative black and white intensity. The implant and the bone are in close contact. Slice thickness 100 μm; x-ray source accelerating voltage 65 kV; current 70 μA; geometric magnification ×5.97; spatial resolution 4 μm.

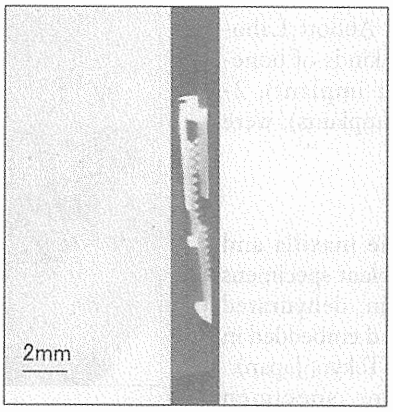

Fig 2b Computer-reconstructed image from the CT image of Fig 2a, on the mesiodistal longitudinal plane along the green line. Slice thickness 100 μm; x-ray source accelerating voltage 65 kV; current 70 μA; geometric magnification ×5.97; spatial resolution 4 μm.

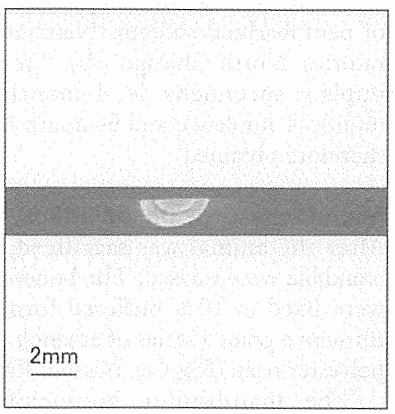

Fig 2c Computer-reconstructed image from the CT image of Fig 2a, on the transverse plane along the red line. Slice thickness 100 μm; x-ray source accelerating voltage 65 kV; current 70 μA; geometric magnification ×5.97; spatial resolution 4 μm.

placement (Fig 1), the bone around the implant showed no significant resorption.

Findings in Microfocus X-ray CT Images

Figure 2a shows a 2-dimensional, buccolingual CT of the 3-month bone/implant specimen. The CT data collection time was less than 60 seconds, and CT image reconstruction time was approximately 10 seconds. There was some evidence of resorption near the top of the alveolar bone on the buccal side, which could not be identified on conventional dental radiographs. The implant and the bone could be clearly distinguished. The implant was white and the bone was gray. The implant surface was partially covered with bone, and direct contact between the implant and bone could be clearly seen. The soft tissues covering the bone could also be clearly distinguished.

Figures 2b and 2c show the reconstructed CT of Fig 2a at the mesiodistal longitudinal plane (along the green line) and transverse plane (red line), respectively. The bone and implant could be seen clearly, even in the longitudinal and transverse reconstructed images, which could be obtained at any level of the implant by reconstruction of the integrated 2-dimensional CT slices.

Findings on Microfocus X-ray Fluoroscopic Images

One Month After Implant Placement. Compact bone could be seen in very close contact with the coronal part of the implant (Fig 3). There was new bone on the buccal side at the base of the implant, but no bone formation was evident on the palatal side.

Two Months After Implant Placement. Denser bone was evident around the implant in the cortical bone area. Fine trabecular bone of 100 μm in diameter could be easily identified. The original drill hole could be recognized (Fig 4, *arrowheads*), and new bone formation was observed between the original bone wall and the titanium implant.

Three Months After Implant Placement. Mature bone was observed around the implant (Fig 5). Direct contact between bone and implant was identified in some areas. An area of calcified material with uniform structure, which was subsequently identified as a remnant of the dental root tip, could be seen at the bottom of the alveolar bone on the lingual side of the implant (Fig 5, *asterisk*). The size of the root remnant was about 0.9×2.5 mm.

Microscopic Findings in Undecalcified Ground Tissue Sections and Contact Microradiograms

Figure 6 shows the light microscopic photograph of an undecalcified ground section at 2 months after

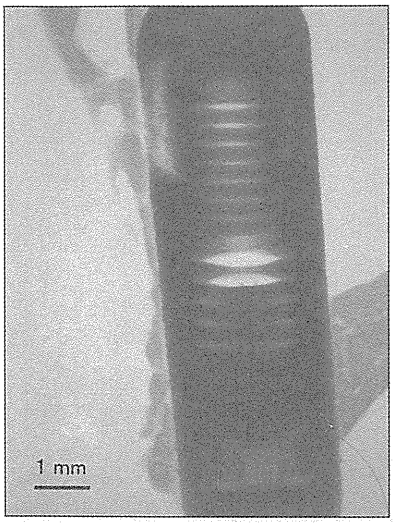

Fig 3 Microfocus x-ray fluoroscopic image of the maxillary premolar area implant 1 month after implant placement. New bone formation can be seen on the buccal side at the coronal part of the implant, but no bone formation is apparent on the palatal side. X-ray source accelerating voltage 80 kV; current 200 μA; geometric magnification ×1.0; spatial resolution 4 μm.

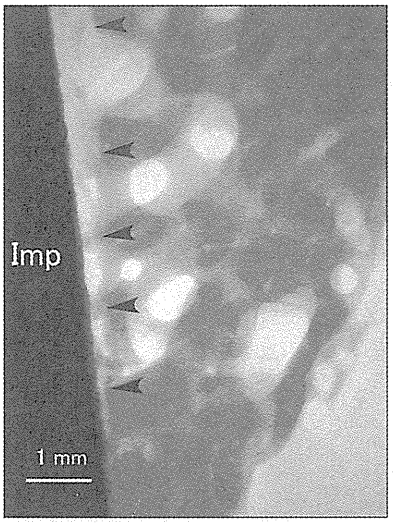

Fig 4 Microfocus x-ray fluoroscopic image of the maxillary premolar area implant at the highest magnification, 2 months after implant placement. New bone formation can be seen between the original bone wall *(arrowheads)* and the titanium implant. X-ray source accelerating voltage 80 kV; current 200 μA; geometric magnification ×1.0; spatial resolution 4 μm.

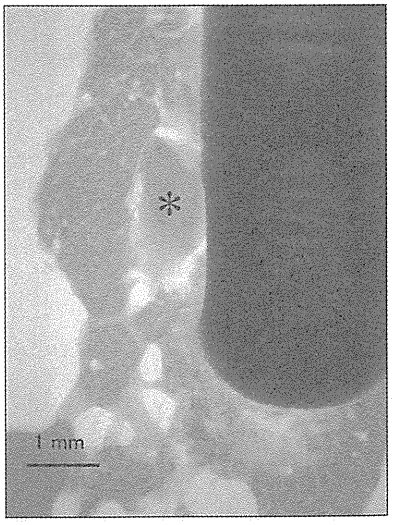

Fig 5 Microfocus x-ray fluoroscopic image of the mandibular premolar area implant 3 months after implant placement. Some direct contact between the bone and the implant can be seen. Calcified material with uniform structure can be seen at the lower part of the alveolar bone on the lingual side of the implant *(asterisk)*. This material was identified as the tip of the dental root. X-ray source accelerating voltage 80 kV; current 200 μA; geometric magnification ×1.0; spatial resolution 4 μm.

implant placement, corresponding with the fluoroscopic image of Fig 4. The implant was shown to have perforated the maxillary sinus at the time of implant placement (Fig 6, *arrowhead*). Mature bone surrounded the implant, and some direct contact between bone and implant could be seen.

Figures 7a and 7b show the light microscopic photograph and the contact microradiogram, respectively, of an undecalcified ground section at 3 months after implant placement. The substance with a uniform structure observed in the fluoroscopic image of Fig 5 was shown to have dental tubules, dental cementum, and dental pulp (Figs 7a and 7b, *asterisks*). Therefore, this appeared to be confirmation of a piece of remnant dental root left over from the time of tooth extraction.

DISCUSSION

In the present study, bone formation and bone-implant contact were seen using the recently developed microfocus x-ray fluoroscopic and microfocus x-ray CT techniques. Light microscopic observations of undecalcified ground sections provided information on the state of bone formation and bone resorption around the implant and changes in soft tissues such as the gingival epithelium and subepithelial connective tissues.

Light microscopy can be an important tool for observing perforations of the maxillary antrum and pathologic changes in soft tissue such as gingivitis and maxillary sinusitis. The extent of calcification and the detailed structure of the hard tissue around the implant can be observed in a contact microradiogram of the ground sections. However, preparation of ground tissue sections is laborious and time consuming, and tissues are sometimes destroyed.

Observation with microfocus radiography is nondestructive and minimizes the risk of artifacts from sample preparation. Moreover, the observation can be completed within a very short time. The traditional dental radiograph identifies the position of the implant, and microfocus x-ray CT can be used to detect dental or medical conditions. However, both conventional techniques do not have high enough resolution to give any information about the detailed structure of the bone and/or bone-implant interface. Recently, microfocus x-ray equipment has been developed using the microfocus x-ray tube as a new generator. The microfocus x-ray tube requires a fine electron beam at constant

Fig 6 Light microscopic observation of an undecalcified ground tissue section 2 months after implantation. The implant perforates the mucosa of the maxillary sinus *(arrowhead)*. Partial detachment between the bone and implant is observed. Mature bone is observed surrounding the implant, and some direct bone-implant contact is observed (methylene blue and basic fuchsin; original magnification ×20).

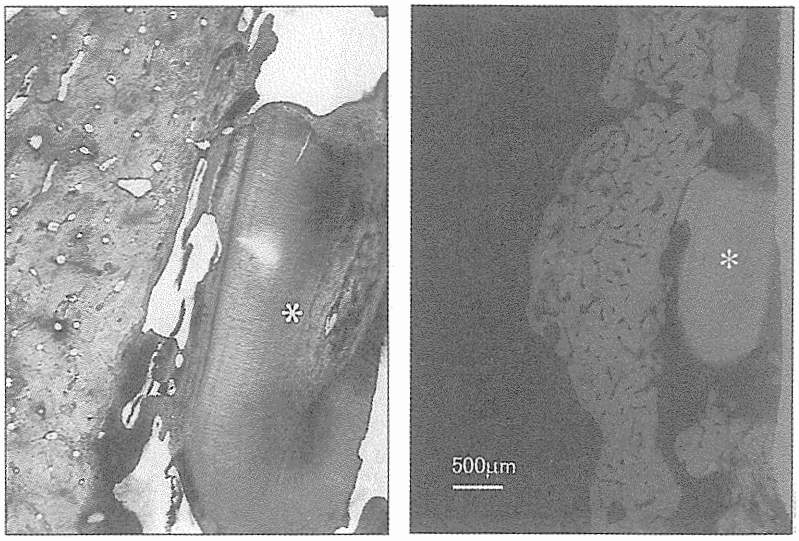

Figs 7a and 7b *(Left)* Light microscopic observation and *(right)* contact microradiogram of undecalcified ground tissue section 3 months after implant placement. The contact microradiograph was obtained using high-resolution film at 30 kV and 3 mA. The material with uniform structure observed in the x-ray fluoroscopic image has dental tubules, dental cementum, and dental pulp *(asterisk)*. Therefore, it is apparently a remnant of dental root left from the time of tooth extraction (*Left:* methylene blue and basic fuchsin; original magnification ×40; *right:* original magnification ×20).

speed. This apparatus allows acquisition of radiographs within a short time and with high resolution. Clear observation of auditory bone structures, detailed trabecular bone structures, and teeth are possible using the newly developed microfocus x-ray technique.[7–13]

In the present study, it was possible to identify some resorption of the bone in microfocus x-ray fluoroscope images but not on conventional dental radiographs. This is the result of improvement of spatial resolution. It was also possible to distinguish the bone and the implant at high contrast in microfocus x-ray images and to identify direct contact between the bone and the implant, the very fine trabecular structure of newly formed bone, and the resorption of alveolar bone. There were no artificial concentric circles, which have been previously reported.[13] This was because of the development of the microfocus x-ray tube and/or image processing technique. The tube used in the present study has a focal dimension of 4 μm.

A piece of remnant dental root close to the implant could also be seen by microfocus x-ray technique, but histology was needed for identification. The time required for CT data collection was less than 60 seconds, and the time for reconstructing CT image was about 10 seconds. Thus, the microfocus x-ray technique can be very effective for making detailed observations of the bone structure around the implant and can save observation time. In the present study, formalin-fixed, resin-embedded samples were observed by microfocus x-ray. Although sample preparation did not cause serious deterioration of the reconstructed images, living tissues, if available, are preferred for observation.

Another advantage of microfocus x-ray technique is the ease of reconstruction of 3-dimensional (3D) images. Wigianto and associates[15] placed implants in rabbit tibiae and made 3D observations of the spongy bone structure around the implant. They embedded the bone containing the implant in resin, ground the sample sequentially from one side, and made observations of serial sections under a light microscope. These images were fed sequentially into a computer through a charge-coupled distributor camera and finally constructed into a 3D image. This method required considerable time and effort for specimen preparation. Van Oosterwyck and coworkers[14] produced 3D reconstruction images of bone/implant systems to create finite element models. They claimed that microfocus x-ray CT would be a powerful tool for the analysis of biomechanics

using the finite element method. Reconstruction of 3D images of bone/implant specimens is now a matter of ongoing research.

Further evaluation of quantitative analysis using the microfocus x-ray technique is needed. The cost of the microfocus x-ray machine is still high for clinical usage. Tuned-aperture CT (TACT) is also a useful method to reconstruct 3D images from multiple 2D projections.[16,17] TACT is an accurate method that facilitates non-destructive assessment of bone or tooth structure, and it is cost-effective. The advantage of microfocus x-ray technique is its high spatial resolution. A comparison of microfocus x-ray technique and TACT for 3D image reconstruction should be performed.

SUMMARY

The results of this investigation indicate that microfocus x-ray techniques such as fluoroscopy and CT, which are non-destructive and involve a very short image acquisition time, can be advantageous tools for observing not only hard tissues such as bone and teeth, but also the interface between bone and titanium implants. Microfocus x-ray techniques can be expected to play an important role in medicine and dentistry because they allow visualization of the fine structures of hard tissues.

ACKNOWLEDGMENTS

This study was supported by a Grant-in-Aid for Research for Frontier Science and a Grant from the Ministry of Education, Culture, Sports, Science and Technology of Japan to promote 2001-Multidisciplinary Research Projects (in 2001–2005) and by a Grant-in-Aid for Scientific Research (C,12671904) from Japan Society for the Promotion of Science.

REFERENCES

1. Brånemark P-I, Hansson BO, Adell R, et al. Osseointegrated implants in the treatment of the edentulous jaw: Experience from a 10-year period. Scand J Plast Reconstr Surg 1977;11 (suppl 16):1–132.
2. Albrektsson T, Brånemark P-I, Hansson HA, Lindstrom J. Osseointegrated titanium implant. Requirements for ensuring a long-lasting, direct bone-to-implant anchorage in man. Acta Orthop Scand 1981;52:155–170.
3. Brånemark P-I. Osseointegration and its experimental background. J Prosthet Dent 1983;50:399–410.
4. Albrektsson T, Eriksson AR, Friberg B, et al. Histologic investigations on 33 retrieved Nobelpharma implants. Clin Mater 1993;12:1–9.
5. Bonse U, Busch F, Günnewig O, et al. 3D computed X-ray tomography of human cancellous bone at 8 μm spatial and 10^{-4} energy resolution. Bone Miner 1994;25:25–38.
6. Momose A, Takeda T, Itai Y, Hirano K. Phase-contrast X-ray computed tomography for observing biological soft tissues. Nature Med 1996;2:473–475.
7. Shibata T, Nagano T. Applying very high-resolution microfocus X-ray CT and 3-D reconstruction to the human auditory apparatus. Nature Med 1996;2:933–935.
8. Ruegsegger P, Koller B, Muller R. A microtomographic system for the nondestructive evaluation of bone architecture. Calcif Tissue Int 1996;58:24–29.
9. Ohta T, Harada Y, Yamada N, Takagi H, Azuma Y, Komoriya K. Three dimensional analysis of bone structure by microfocus X-ray computed tomography (μCT). J Jpn Soc Bone Morphom 1999;9:97–101.
10. Hara T, Hashimoto H, Ide Y. Application of micro-CT to the measurement of enamel thickness. Jpn J Oral Biol 1999;41:303–306.
11. Hayakawa T, Mishima H, Yokota I, Sakae T, Kozawa Y, Nemoto K. Application of high resolution microfocus X-ray CT for the observation of human tooth. Dent Mater J 2000; 19:87–95.
12. Bjørndal L, Carlsen O, Thuesen G, Darvann T, Kreiborg S. External and internal macromorphology in 3D-reconstructed maxillary molars using computerized X-ray microtomography. Int Endod J 1999;32:3–9.
13. Sakae T, Hayakawa T, Ohrigome K, et al. Potential application of micro-CT for study of bone-Ti implant interface. J Hard Tissue Biol 2000;9:15–17.
14. Van Oosterwyck H, Duyck J, Vander Sloten J, et al. The use of microfocus computerized tomography as a new technique for characterizing bond tissue around oral implants. J Oral Implantol 2000;26:5–12.
15. Wigianto R, Ichikawa T, Kanitani H, Kawamoto N, Matsumoto N, Ishizuka H. Three-dimensional bone structure around hydroxyapatite and titanium implants in rabbits. Clin Oral Implants Res 1999;10:219–225.
16. Webber RL, Horton RA, Tyndall DA, Ludlow JB. Tuned-aperture computed tomography (TACT). Theory and application for three-dimensional alveolar imaging. Dentomaxillofac Radiol 1997;26:53–62.
17. Ramesh A, Ludlow JB, Webber RL, Tyndall DA, Paquette D. Evaluation of tuned aperture computer tomography in the detection of simulated periodontal defects. Oral Surg Oral Med Oral Pathol Oral Radiol Endod 2002;93:341–349.

Technical Note

Direct attachment of fibronectin to tresyl chloride-activated titanium

Tohru Hayakawa,[1] Masao Yoshinari,[2] Kimiya Nemoto[1]
[1]*Department of Dental Materials, Research Institute of Oral Science, Nihon University School of Dentistry at Matsudo, 2-870-1, Sakaecho-nishi, Matsudo, Chiba 271-8587, Japan*
[2]*Department of Dental Materials Science and Oral Health Science Center, Tokyo Dental College, 1-2-2 Masago, Mihamaku, Chiba 261-8502, Japan*

Received 3 April 2002; revised 20 February 2003; accepted 2 May 2003
Published online 7 October 2003 in Wiley InterScience (www.interscience.wiley.com). DOI: 10.1002/jbm.a.10143

Abstract: The aim of this study was to bind fibronectin directly to a titanium surface treated with tresyl chloride (2,2,2-trifluoroethanesulfonyl chloride) for the development of a strong connection of a dental implant to subepithelial connective tissues and/or peri-implant epithelia. Basic terminal OH groups of mirror polished titanium were allowed to react with tresyl chloride at 37°C for 2 days. The tresylated titanium disk was then immersed into a fibronectin/phosphate-buffered saline solution for 24 h at 37°C. The activation reaction of the basic OH of titanium with tresyl chloride was confirmed by S2p, F1s, and O1s spectra using X-ray photoelectron spectroscopy and —O—S—O_2— bonds using Fourier transform infrared reflection-absorption spectroscopy. After the reaction of fibronectin with titanium, the X-ray photoelectron spectroscopy revealed the remarkable effect of the activation of terminal OH groups with the tresyl chloride treatment. The N1s peak derived from the attached fibronectin still remained after 60 s of argon-ion sputtering after tresyl chloride treatment. In contrast, the N1s peak of the specimen not treated with tresyl chloride almost disappeared after only 10 s of argon-ion etching. Fibronectin, a well-known cell-adhesive protein, could easily be attached to the titanium surface by use of the tresyl chloride activation technique. © 2003 Wiley Periodicals, Inc. J Biomed Mater Res 67A: 684–688, 2003

Key words: dental implant; titanium; fibronectin; tresyl chloride; X-ray photoelectron spectroscopy

INTRODUCTION

Because of their superior mechanical properties and biocompatibility, titanium and titanium alloys (Ti-6Al-4V) are widely used as biomaterials for dental and orthopedic implants. The higher degree of contact between bone and titanium and titanium alloy implant materials is known as osseointegration, and provides suitable stability into the bone tissue.[1,2] However, poor attachment of subepithelial connective tissues and peri-implant epithelia to titanium enable invasion of the epithelia. Apical migration of the long junctional epithelia leads to development of pockets adjacent to the implants. Such defects cause inflammatory breakdown around dental implants by bacterial invasion, causing peri-implantitis.[3,4]

After the implantation of biomaterials into a foreign body, the first biological reaction at the biomaterial–tissue interface is the adsorption of body fluid proteins including extracellular matrix components onto its surface.[5–7] It is widely accepted that these adsorbed proteins control the subsequent biological responses at the implant–tissue interface.

The modification of implant surfaces for the selective adsorption of beneficial molecules promotes a desirable integration of implants with bodily tissue. It has been reported that precoating the titanium surface with cell-adhesive proteins, such as fibronectin, collagen, and/or laminin, improved cell activity, initial cell attachment, or cell spreading.[8–11]

Some researchers attempted to introduce cell-adhesive proteins onto titanium by forming a covalent bond between cell-adhesive proteins and titanium, using several techniques such as precoating with poly-

Correspondence to: T. Hayakawa; e-mail: hayakawa@masact.nihon-u.ac.jp
Contract grant sponsor: Ministry of Education, Culture, Sports, Science and Technology of Japan to promote 2001-Multidisciplinary Research Projects (in 2001–2005)
Contract grant sponsor: Japan Society for the Promotion of Science (Grant-in-Aid for Scientific Research); contract grant number: C,12671904
Contract grant sponsor: Tokyo Dental College (Oral Health Science Center); contract grant number: 5A10

© 2003 Wiley Periodicals, Inc.

pyrrole or Au and cysteine, pretreatment with silane coupling agents.[12–15] In contrast, Nilsson and Mosbach[16,17] reported the direct and simple immobilization of enzymes to various hydroxyl groups using highly reactive sulfonyl chloride, that is, 2,2,2-trifluoroethanesulfonyl chloride (tresyl chloride). They activated the hydroxyl groups of silica or agarose with the reaction of tresyl chloride, and then coupled an enzyme such as α-chymotrypsin to tresyl-agarose. The advantage of their method is simplicity. Protein can be bound to a substrate without any spacer, for example, the alkyl chain of a silane coupling agent.

The purpose of this study was to bind fibronectin directly to a titanium surface treated with tresyl chloride to develop the necessary tight connection of dental implants to subepithelial connective tissues and peri-implant epithelia.

MATERIALS AND METHODS

Titanium substrate

Commercially pure wrought titanium disks (JIS, Japan industrial Specification H 4600, 99.9 mass % Ti; Furuuchi Chemical Corp., Tokyo, Japan) with a diameter of 6 mm or 15 mm were used. The disks were ground down to 1200 grit, polished using colloidal silica at pH = 9.8, and then ultrasonically cleaned with acetone.

Activation with tresyl chloride and coupling with fibronectin

The surface of the mirror polished titanium disk was completely covered with tresyl chloride (2,2,2-trifluoroethanesulfonyl chloride; Fluka, Buchs, Switzerland) and then stored at 37°C for 2 days. The tresylated titanium disk was washed with water, water–acetone (50:50), and acetone, dried, and stored in a desiccator.

Human plasma fibronectin (Upstate Biotechnology, Lake Placid, NY) was dissolved in phosphate-buffered saline (PBS) solution with pH = 7.4 at a concentration of 0.1 mg/mL. The tresylated titanium disk was immersed into the fibronectin/PBS solution for 24 h at 37°C, then rinsed with double-distilled water. Finally, they were dried with a gentle stream of dry air and stored in a desiccator. For comparison, fibronectin was attached to mirror polished titanium without tresyl chloride activation. This mirror polished titanium was immersed in fibronectin/PBS solution at 37°C. After 24 h, the sample was rinsed with double-distilled water using the same method as described above.

Surface analysis

Surface analyses of the titanium after the reaction with tresyl chloride, and that after the reaction with fibronectin were performed using X-ray photoelectron spectroscopy (XPS) (ESCA-750; Shimadzu, Kyoto, Japan). The coupling reaction with fibronectin was evaluated by the intensity of N1s and O1s spectra. Argon-ion sputtering was performed at 2 kV and 15 mA/cm^2. The binding energies of each of the spectra were calibrated with C1s of 284.6 eV.

The reaction of the titanium surface with tresyl chloride and the presence of the attached fibronectin were also identified by Fourier transform infrared reflection-absorption spectroscopy (FTIR-RAS) (FT-IR-430; Jasco Corp., Tokyo, Japan). The measurement of FTIR-RAS was performed under nitrogen atmosphere.

RESULTS

No elements originating from the tresyl chloride and fibronectin were detected on the mirror polished titanium surface. On the XPS qualitative analysis, the presence of element F and S, derived from the tresyl chloride, was detected on the tresylated titanium. Element N was detected on the fibronectin-attached specimens both with and without the tresyl chloride treatment.

The F1s, S2p, and O1s spectra of the tresylated titanium specimen produced by XPS analysis are shown in Figure 1. There was no evidence of a chloride peak on the titanium surface. A F1s peak, derived from the trifluorocarbon of the tresyl chloride, appeared at 688.6 eV. The intensity of the F1s peak decreased to <20% after 10 s of argon-ion etching. After 20 s of argon-ion etching, there was no distinguishable F1s peak. The S2p peak observed at 168.4 eV was derived from the —O—S—O_2— bonds, which were formed from the reaction of the tresyl chloride and the terminal OH of the titanium surface. After 10 s of argon-ion etching, the S2p peak almost disappeared. Two O1s peaks were also observed at 530.3 and at 532 eV. The O1s peak at 530.3 eV could be attributed to the bulk oxygen in the titanium dioxide.[18] The O1s peak at about 523 eV could be an organic O1s of the Ti—O—S— and —S—O_2—C bond.[19] The O1s peaks at 532 eV decreased after 10 s of argon-ion etching, and almost disappeared after 20 s of argon-ion etching.

Figure 2 shows the N1s and O1s spectra produced by the XPS analysis of the fibronectin-attached titanium after the tresyl chloride treatment. No F1s peaks were detected. An N1s peak at 399.9 eV and an O1s peak at 532 eV were derived from the amide groups of the fibronectin.[20] This derivation was confirmed by the observation of the original fibronectin based on XPS. These peaks still remained on the argon-ion sputtered surface after 60 s. The O1s peak at 530.3 eV derived from TiO_2 was not clearly visible before argon-ion etching. The intensity of the O1s peaks at 532 eV decreased as the argon-ion etching time increased, whereas that of the O1s peaks at 530.3 eV increased as the argon-ion etching time increased.

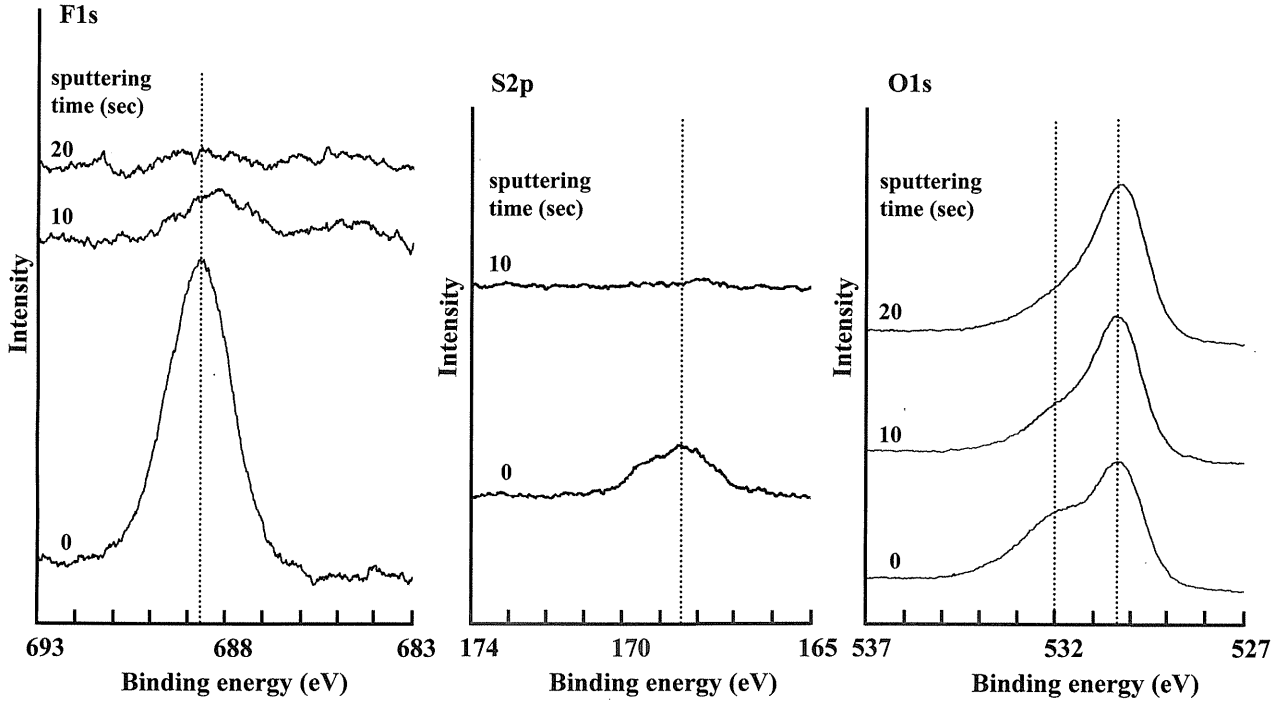

Figure 1. F1s, S2p, and O1s spectra of tresylated titanium specimen by XPS analysis.

The N1s and O1s XPS spectra of the fibronectin-attached titanium without the tresyl chloride treatment are shown in Figure 3. An N1s at 399.9 eV and an O1s at 532 eV derived from the amide groups of fibronectin were also detected. However, these peaks almost disappeared after 10 s of argon-ion sputtering. The ratio of intensity between the O1s at 532 eV and the O1s at 530.3 eV attributed to the oxygen of TiO_2 was almost equal in the outermost layers.

Figure 4 shows the FTIR-RAS spectra of the tresy-

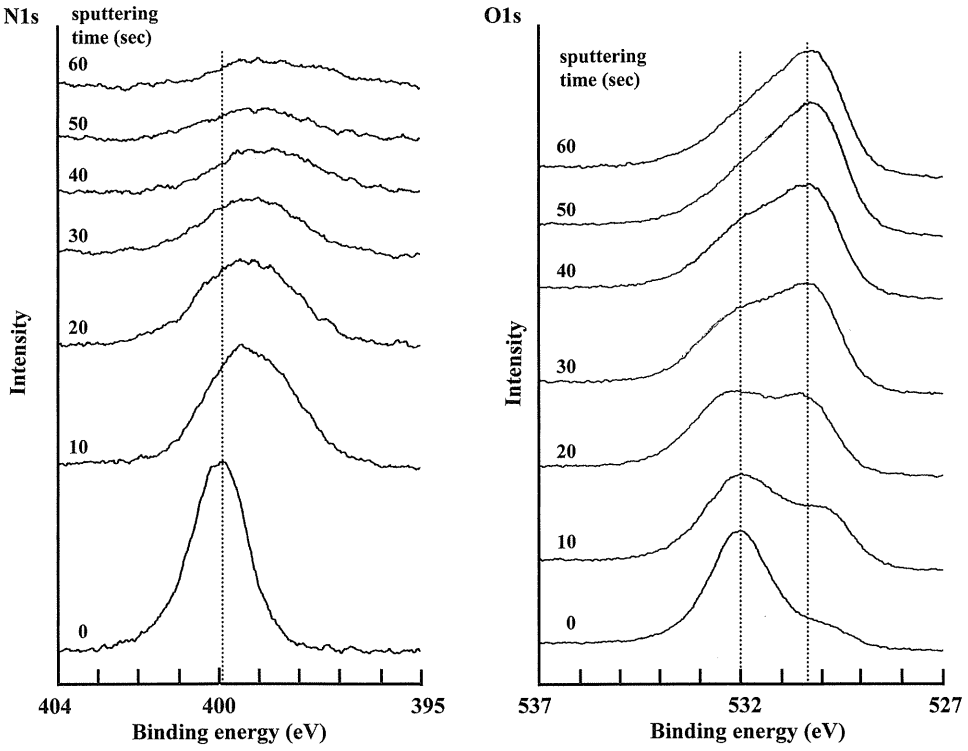

Figure 2. XPS N1s and O1s spectra of fibronectin-attached titanium with tresyl chloride treatment after rinsing.

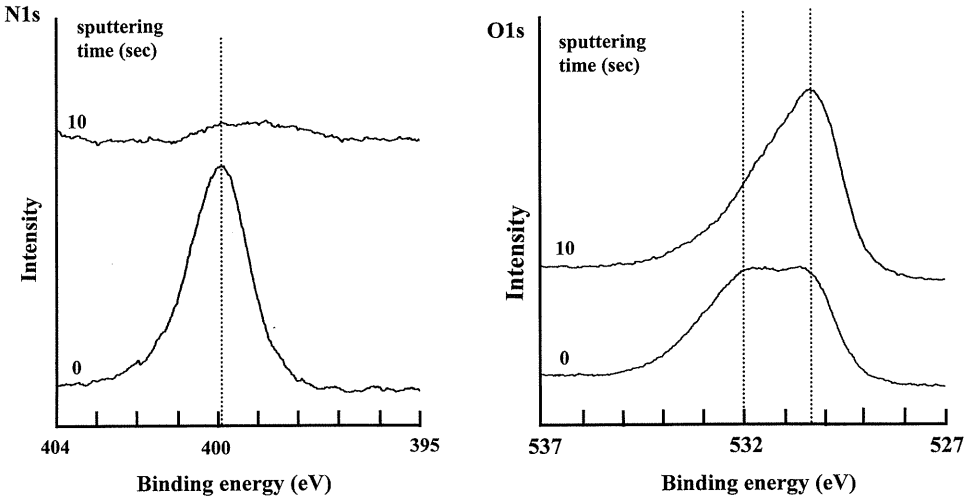

Figure 3. XPS N1s and O1s spectra of fibronectin-attached titanium without tresyl chloride treatment after rinsing.

lated titanium specimen (a) and fibronectin-attached specimens treated with tresyl chloride (b). The peaks at around 1100–1200 cm^{-1} are attributed to the C—F bonds of trifluorocarbon of the tresyl chloride, and peaks at around 1400–1480 cm^{-1} are attributed to the —O—S—O_2— bonds in Figure 4(a). In Figure 4(b), two amide groups at around at 1450–1550 cm^{-1} and 1600–1800 cm^{-1} were identified.

DISCUSSION

Fibronectin is a well-known cell-adhesive protein and is believed to have an important role in governing the interactions of implants with their surrounding matrices.[21–23] Dean et al.[9] and Endo[15] reported the effectiveness of fibronectin precoating or covalent immobilization for binding and growing the gingival fibroblast. It is predicted that the attachment of fibronectin to the titanium biomaterials will improve the connection of dental implant to gingival and/or epithelial tissue.

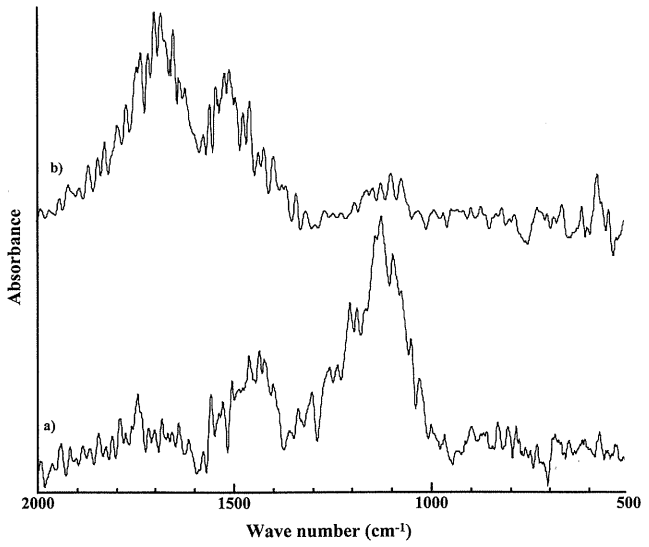

Figure 4. FTIR-RAS spectra of tresylated titanium specimen and fibronectin-attached titanium surface after tresyl chloride treatment.

Nilsson and Mosbach[16,17] developed a skillful method for the activation of a hydroxyl group such as agarose with tresyl chloride and the coupling reaction of proteins and a tresylated hydroxyl group. The advantage of the method using tresyl chloride is simplicity. It is well known that the exposed surface of titanium has two types of OH groups: a basic terminal OH and a bridge OH group.[24] We expected that the basic terminal OH could be activated with tresyl chloride and then coupled with proteins.

In the present study, tresyl chloride reacted directly with titanium without the use of any solvent. Nilsson and Mosbach[16,17] attempted activation reaction of tresyl chloride with agarose in pyridine, which was used as a dehydrochloride reagent. However, a preliminary experiment revealed that tresyl chloride did not react with the OH groups of titanium in pyridine because of an insufficient number of terminal OH groups of titanium. The reaction between tresyl chloride and pyridine was dominant during the activation procedure. To improve the reactivity of tresyl chloride toward the terminal OH groups of titanium, the tresyl chloride was applied directly onto the titanium surface without any dehydrochloride reagent. As a result, F1s and S2p peaks of the tresylated titanium specimen appeared in the XPS spectra. F1s peaks still remained after 10 s of argon-ion etching. The FTIR-RAS spectrum revealed the formation of —O—S—O_2— bonds after the reaction of tresyl chloride and the basic terminal OH of titanium. An O1s peak at 532 eV in the

XPS spectra was still slightly evident after 10 s of argon-ion etching. Thus, we determined that the O1s at 352 eV was an organic oxygen of the —O—S—O_2— bonds. It revealed that the direct application of tresyl chloride on the mirror polished titanium surface is an effective technique for the treatment of the titanium terminal OH.

A comparison of the XPS spectra of the fibronectin-attached specimen with and without the tresyl chloride treatment (Figs. 2 and 3) demonstrated the remarkable effect of the activation of the OH groups with tresyl chloride. N1s peaks derived from attached fibronectin still remained on the surface after 60 s of argon–ion etching if the surface had been treated with tresyl chloride. In comparison, without the tresyl chloride treatment, the N1s peaks of the specimen had almost disappeared after only 10 s of argon-ion etching. The intensity of the O1s at 532 eV in the tresylated specimen was higher than that of the O1s at 530.3 eV before argon-ion etching. In contrast, the intensity ratio of the O1s peak derived from organic oxygen at 532 eV and that from inorganic TiO_2 at 530.3 eV was almost equal at the outermost layer in the XPS spectra of the specimen not treated with tresyl chloride. These results suggested that the reactivity of the activated OH groups of tresylated titanium toward fibronectin was greater than that of the nonactivated OH groups of the titanium surface.

The application of tresylated titanium for the direct attachment of cell adhesive proteins beside fibronectin, such as laminin or collagen, requires further investigation. Moreover, it is not clear whether attached fibronectin molecules may have denatured or may preserve the cell-adhesive activity. Further study is necessary to clarify the biological activity such as cultured cell growth or tissue response of attached cell-adhesive proteins on a tresylated titanium surface during the next stage of our experiments.

In conclusion, fibronectin could easily be attached on a titanium surface using a technique of tresyl chloride activation technique of the basic terminal OH group of titanium.

References

1. Brånemark P-I, Hansson BO, Adell R, Breine U, Lindström J, Hallen O, Ohman A. Osseointegrated implants in the treatment of the edentulous jaw: Experience from a 10-year period. Scand J Plast Reconstr Surg Suppl 1977;16:1–132.
2. Albrektsson T, Brånemark PI, Hansson HA, Lindström J. Osseointegrated titanium implant. Requirements for ensuring a long-lasting, direct bone-to-implant anchorage in man. Acta Orthop Scand 1981;52:155–170.
3. Malmstrom HS, Fritz ME, Timmis DP, van Dyke TE. Osseointegrated implant treatment of a patient with rapidly progressive periodontitis: A case report. J Periodontol 1990;61:300–304.
4. Mombelli A, Lang NP. The diagnosis and treatment of peri-implantitis. Periodontology 2000;17:63–76.
5. Horbett TA. Principles underlying the role of adsorbed plasma proteins in blood interactions with foreign materials. Cardiovasc Pathol 1993;2:137S–148S.
6. Wälivaara B, Aronsson BO, Rodahl M, Lausmaa J, Tengvall P. Titanium with different oxides: *In vitro* studies of protein adsorption and contact activation. Biomaterials 1994;15:827–834.
7. Puleo DA, Nanci A. Understanding and controlling the bone-implant interface. Biomaterials 1999;20:2311–2321.
8. Cannas M, Denicolai F, Webb LX, Gristina AG. Bioimplant surfaces: Binding of fibronectin and fibroblast adhesion. J Orthop Res 1998;6:58–62.
9. Dean JW III, Culbertson KC, D'Angelo AM. Fibronectin and laminin enhance gingival cell attachment to dental implant surfaces *in vitro*. Int J Oral Maxillofac Implants 1995;10:721–728.
10. El-Ghannam A, Starr L, Jones J. Laminin-5 coating enhances epithelial cell attachment, spreading, and hemidesmosome assembly on Ti-6Al-4V implant material *in vitro*. J Biomed Mater Res 1998;41:30–40.
11. Roehlecke C, Witt M, Kasper M, Schulze E, Wolf C, Hofer A, Funk RHW. Synergistic effect of titanium alloy and collagen type I on cell adhesion, proliferation and differentiation of osteoblast-like cells. Cells Tissues Organs 2001;168:178–187.
12. de Giglio E, Sabbatini L, Colucci S, Zambonin G. Synthesis, analytical characterization, and osteoblast adhesion properties on RGD-grafted polypyrrole coatings on titanium substrates. J Biomater Sci Polym Ed 2000;11:1073–1083.
13. Morikawa N, Suzuki M, Morita S, Yokoya S, Miyamoto M, Fukuoka S, Ozono S, Kinoshita Y. Study on improvement of adhesion between gingival tissue and dental implant by collagen immobilization. J Jpn Soc Biomater 2001;19:10–20.
14. Culp LA, Sukenik CN. Cell type-specific modulation of fibronectin adhesion functions on chemically derivatized self-assembled monolayers. J Biomater Sci Polym Ed 1998;9:1161–1176.
15. Endo K. Chemical modification of metallic implant surfaces with biofunctional proteins. I. Molecular structure and biological activity of a modified NiTi alloy surface. Dent Mater J 1995;14:185–198.
16. Nilsson K, Mosbach K. Immobilization of enzymes and affinity ligands to various hydroxyl groups carrying supports using highly reactive sulfonyl chlorides. Biochem Biophys Res Commun 1981;102:449–457.
17. Nilsson K, Mosbach K. Tresyl chloride-activated supports for enzyme immobilization. Methods Enzymol 1987;135:65–78.
18. Healy KE, Ducheyne P. Hydration and preferential molecular adsorption on titanium *in vitro*. Biomaterials 1992;13:553–561.
19. Wagner CD, Riggs WM, Davis LE, Moulder JF, Muilenberg GE. In: Muilenberg GE, editor. Handbook of X-ray photoelectron spectroscopy. Minnesota: PerkinElmer Corporation; 1979. p 42.
20. MacDonald DE, Markovic B, Allen M, Somasundaran P, Boskey AL. Surface analysis of human plasma fibronectin adsorbed to commercially pure titanium materials. J Biomed Mater Res 1998; 41:120–130.
21. Dessau W, Sasse J, Timpl R, Jilek F, von der Mark K. Synthesis and extracellular deposition of fibronectin in chondrocyte cultures. Response to the removal of extracellular cartilage matrix. J Cell Biol 1978;79:342–355.
22. Hassell JR, Pennypacker JP, Kleinman HK, Pratt RM, Yamada KM. Enhanced cellular fibronectin accumulation in chondrocytes treated with vitamin A. Cell 1979;17:821–826.
23. Seitz TL, Noonan KD, Hench LL, Noonan NE. Effect of fibronectin on the adhesion of an established cell line to a surface reactive biomaterial. J Biomed Mater Res 1982;16:195–207.
24. Boehm HP. Acidic and basic properties of hydroxylated metal oxides surface. Faraday Discuss Faraday Soc 1971;52:264–275.

Available online at www.sciencedirect.com
SCIENCE DIRECT®
Biomaterials 25 (2004) 119–127
Biomaterials
www.elsevier.com/locate/biomaterials

Characterization and protein-adsorption behavior of deposited organic thin film onto titanium by plasma polymerization with hexamethyldisiloxane

Tohru Hayakawa[a,*], Masao Yoshinari[b], Kimiya Nemoto[a]

[a] *Department of Dental Materials, Research Institute of Oral Science, Nihon University School of Dentistry at Matsudo, 2-870-1, Sakaecho-nishi, Matsudo, Chiba 271-8587, Japan*

[b] *Department of Dental Materials Science and Oral Health Science Center, Tokyo Dental College, 1-2-2 Masago, Mihama-ku, Chiba 261-8502, Japan*

Received 2 December 2002; accepted 15 June 2003

Abstract

Plasma polymerized hexamethyldisiloxane (HMDSO) thin film was deposited onto titanium using a radio-frequency apparatus for the surface modification of titanium. A titanium disk was first polished using colloidal silica at pH = 9.8. Plasma-polymerized HMDSO films were firmly attached to the titanium by heating the titanium to a temperature of approximately 250°C. The thickness of the deposited film was 0.07–0.35 μm after 10–60 min of plasma polymerization. The contact angle with respect to double distilled water significantly increased after HMDSO coating. X-ray photoelectron spectroscopy revealed that the deposited thin film consisted of Si, C, and O atoms. No Ti peaks were observed on the deposited surface. The deposited HMDSO film was stable during 2-weeks immersion in phosphate buffer saline solution. Fourier transform reflection–absorption spectroscopy showed the formation of Si–H, Si–C, C–H, and C = O bonds in addition to Si–O–Si bonds. Quartz crystal microbalance-dissipation measurement demonstrated that the deposition of HMDSO thin films on titanium has a benefit for fibronectin adsorption at the early stage. In conclusion, plasma polymerization is a promising technique for the surface modification of titanium. HMDSO-coated titanium has potential application as a dental implant material.
© 2003 Elsevier Ltd. All rights reserved.

Keywords: Hexamethyldisiloxane; Plasma polymerization; Titanium; Thin film coating; Protein adsorption; Quartz crystal microbalance-dissipation

1. Introduction

During the past decade, physical vapor deposition (PVD) techniques such as ion plating [1], magnetron sputtering [2], and ion beam dynamic mixing [3] have been introduced for the deposition of a thin calcium phosphate coating on oral and medical implants of titanium or titanium alloys as a means of improving tissue responses. The advantage of PVD is that this method avoids some intrinsic shortcomings of plasma-sprayed Ca-P coatings [4–6]. For example, PVD deposited Ca-P coatings have a stronger adherence to the underlying titanium surface and are less prone to form cracks [2,3].

*Corresponding author. Tel.: +81-47360-9349; fax: +81-47360-9350.

E-mail address: hayakawa@masact.nihon-u.ac.jp (T. Hayakawa).

0142-9612/$ - see front matter © 2003 Elsevier Ltd. All rights reserved.
doi:10.1016/S0142-9612(03)00484-8

However, little attention has been given to the use of chemical vapor deposition techniques other than PVD, such as plasma polymerization for depositing thin films onto titanium for modifying the surfaces of titanium substrates. Films formed by plasma polymerization are generally free of pinholes, have a strong degree of adherence to a wide variety of materials, and have a greater degree of resistance to chemical and physical treatment because of their cross-linked structure [7,8]. Monomers for plasma polymerization need not contain the traditional functional groups, and polymerization of organic compounds can be initiated that will not form polymers under normal polymerization conditions. The polymer films obtained by plasma polymerization are quite different from those derived from polymerized films formed by conventional radical or ion initiation methods. Plasma polymerization of a number of compounds such as hydrocarbons, aliphatic hydrocarbons,

organosilicones, and methacrylates has been reported [9–13].

Among the wide variety of possible monomers for plasma polymerization, considerable attention has been given to the plasma polymerization of organosilicon monomers, particularly hexamethyldisiloxane (HMDSO) [14–19]. These monomers are of interest because of their high deposition rates and the ability to control their structure and properties by varying the deposition conditions. In addition, HMDSO is an easy and safe monomer to handle, especially compared to silane compounds.

In contrast to the extensive literature on the chemistry of HMDSO plasma-deposited films, relatively little attention has been given to the application of these films in the medical or dental fields in respect of their biological properties. A few studies reported the application of plasma polymerization for the immobilization of bioactive molecules on the surfaces of bioinert materials. Miyachi et al. [20] reported the application of plasma-polymerized hexamethyldisiloxane film to immobilize streptavidin on a glass substrate. Puleo et al. [21] found that surface modification of titanium by plasma polymerization of allyl amine is useful for the immobilization of bioactive molecules such as BMP-4.

In this paper, in order to learn more about the efficacy of plasma polymerization as a technique for modifying the surface of titanium, we used plasma polymerization to deposit HMDSO thin films onto titanium and then characterized the chemical properties of the deposited thin films. The chemical properties of the plasma-polymerized thin films were analyzed by measuring the contact angle with respect to distilled water, X-ray photoelectron spectroscopy (XPS) and Fourier transform infrared reflection-absorption spectroscopy (FT-IR-RAS). Recent studies have proven that the quartz crystal microbalance-dissipation (QCM-D) technique is useful for evaluation of surface-related processes in liquids, including protein adsorption [22–24]. The adsorption behavior of protein towards the deposited thin films was also investigated by XPS measurement and by the QCM-D technique.

2. Materials and methods

2.1. Titanium substrate

Commercially pure wrought titanium disks (JIS, Japan industrial Specification H 4600, 99.9 mass% Ti, Furuuchi Chemical Corp., Tokyo) with a diameter of 6 or 15 mm were used. The 6-mm diameter titanium disk was used for the XPS analysis and the 15-mm diameter titanium disk was used for the FT-IR-RAS analysis. The disks were ground progressively finer down to 1200 grit, finely polished using colloidal silica at pH = 9.8, and then ultrasonically cleaned with acetone only in order to avoid affecting the surface conditions of the titanium after mirror polishing.

2.2. Plasma polymerization

Plasma-polymerized thin films were prepared using a commercially available plasma deposition system (High Vapor Deposition System, VEP-1000, ULVAC Inc., Kanagawa, Japan). The titanium substrate was rotated in the stainless steel chamber (300 mm diameter × 500 mm height) at a rotational velocity of 30 rpm and was then heated to a temperature of approximately 250°C. The reservoir (50 mm diameter × 150 mm height) of HMDSO was heated to 40°C and the pipe (15 mm diameter) for introducing the HMDSO was heated to 80°C. The HMDSO gas was then introduced into the equipment chamber through the heated pipe at the HMDSO gas flow rate of 35 sccm. The plasma was generated using a radio-frequency generator operating at 13.56 MHz at a power of 50 W. The pressure of the chamber was maintained at approximately 0.17 MPa throughout the plasma polymerization process. Plasma polymerization was performed for periods of 10, 30, and 60 min. After the plasma was turned off, nitrogen gas was used to purge the chamber, which was then allowed to return to atmospheric pressure. The process resulted in the deposition of plasma-polymerized film on the titanium surface.

2.3. Surface characterization

The thickness of the deposited organic films was determined using a Dektak Stylus Profiler System (Veeco Instrument Inc., Woodbury, NY, USA). The stylus force was 25 mg, and the scanning speed was 200 μm/s. Three measurement runs were performed for each surface.

The contact angle with respect to the double-distilled water was measured using a Contact Angle Meter (CA-D, Kyowa Interface Science Co. Ltd., Tokyo, Japan). Five measurements of 15 s each were made for each surface type, and all analyses were performed at the same temperature and humidity. The data were analyzed by an analysis of variance (ANOVA) and Sheffe's test for the multiple comparisons among the means at $p = 0.05$.

Surface analyses of the plasma-polymerized titanium samples were performed using XPS (ESCA-750, Shimadzu, Kyoto, Japan) by evaluating the intensity of Si2p, C1s, O1s, and Ti2p. Argon-ion sputtering was performed at 2 kV and 15 μA/cm^2. The binding energies of each of the spectra were calibrated with C1s at 284.6 eV.

The stability of deposited HMDSO film was evaluated by the immersion of HMDSO-coated specimen in phosphate-buffered saline (PBS) solution. After a 10-min deposition, the HMDSO plasma-polymerized titanium disk was immersed in PBS solution with pH = 7.4 for 2 weeks. Afterwards, the specimen was rinsed with double-distilled water and the surface was then characterized by XPS as described above. The PBS solution was exchanged every day.

The organic groups in the deposited films were analyzed by Fourier transform infrared reflection-absorption spectroscopy (FT-IR-RAS, FT-IR-430, Jasco Corp., Tokyo, Japan) at 4 cm^{-1} resolution. Two measurements for each surface type were made. The incident angle of the infrared ray to the specimen was 75°. Mirror-polished uncoated titanium was used for the background while calculating the spectrum of the specimen to obtain a spectrum due only to substances formed on the titanium by plasma polymerization.

2.4. Protein adsorption

2.4.1. XPS analysis

Human cell-binding fibronectin (Upsatate Biotechnology, Lake Placid, NY, USA) was dissolved in PBS solution with pH = 7.4 at a concentration of 0.1 mg/ml. The mirror-polished titanium disk and the HMDSO plasma-polymerized titanium disk (30-min coating) were immersed into the fibronectin/PBS solution for 24 h at 37°C, and then rinsed with double-distilled water. Finally, the disks were dried in a gentle stream of dry air and stored in a desiccator. The adsorption of fibronectin onto titanium and HMDSO-polymer coated titanium was confirmed by the N1s peaks of amide bonds of protein. Argon-ion sputtering was performed at 2 kV and 15 μA/cm^2. The binding energies of each of the spectra were calibrated with C1s of 284.6 eV.

2.4.2. QCM-D measurement

The QCM-D technique was used for the evaluation of the adsorption behavior of fibronectin in the presence and absence of HMDSO-polymer coating. The QCM-D instrument (QCM-D, Q-Sense, AB, Göteborg, Sweden) was operated with AT-cut single crystal quartz sensors of 5 MHz resonant frequency. As a sensor, titanium coated QCM-D sensor crystal (14 mm diameter) was used. The HMDSO-coated sensor (30-min HMDSO coating) was prepared according to the method described above. The titanium and HMDSO-coated titanium sensor crystals were cleaned prior to each adsorption measurement in an UV/ozone chamber for 15 min. The crystal resonant frequency (Δf) and the dissipation factor (ΔD) of the oscillator were measured simultaneously at a fundamental resonant frequency (5 MHz) and at a number of overtones, including 35 MHz.

Monitoring the resonance behavior of piezoelectric oscillation allows measurements of the mass being adsorbed at the surface of the oscillation in real time, usually as a function of the decrease in the resonance frequency (f). The frequency shift (Δf) is related to the adsorbed mass (Δm) according to the Sauerbrey relation [25]. At 5 MHz, a frequency shift of 1 Hz corresponds to a mass change of approximately 18 ng/cm^2. This relation is applicable strictly to sufficiently thin, rigid films [26]. A second measurement parameter, dissipation (D), gives qualitative information about the viscoelastic properties of the adsorbed layer.

Fibronectin/PBS solution (20 ppm) was introduced into an axial flow chamber comprising a T-loop in order to thermally equilibrate the sample at 37 ± 0.1°C. The sequence of injections into the QCM cell for an experimental run was as follows: 0.5 ml of distilled water, 0.5 ml of PBS solution, 2 ml of fibronectin/PBS solution.

3. Results

The thickness of the deposited HMDSO films and the contact angles with respect to double-distilled water are listed in Table 1. The film thickness was nearly proportional to the coating time. After a 60-min coating process, the thickness of the deposited film was approximately 0.35 μm. The contact angle with respect to double-distilled water increased after the HMDSO coating, and there were significant differences in the contact angle between un-coated titanium and the HMDSO-coated titanium. After a 30-min coating, the HMDSO-coated surface showed contact angles with respect to double-distilled water of approximately 83°, which were significantly the highest.

The elements detected by the XPS analysis of the mirror polished titanium were Ti, C, and O, and those of the HMDSO-coated titanium were Si, C, and O. No Ti peaks were observed on the surface of the HMDSO-coated titanium. XPS analyses revealed no titanium peaks on an HMDSO-coated surface before argon-ion sputtering, and only Si, O, and C atoms were identified as components of the deposited films.

Table 1
Film thickness and contact angles of plasma-polymerized HMDSO film

Coating time (min)	Thickness (μm)	Contact angle (°)
0	0	33.3 (3.8)[a]
10	0.07 (0.009)	78.4 (1.4)[b]
30	0.18 (0.008)	82.6 (1.9)[c]
60	0.35 (0.02)	74.9 (0.5)[b]

( ) Standard deviation.
Mean values with the same superscripts are not significantly different at $P > 0.05$.

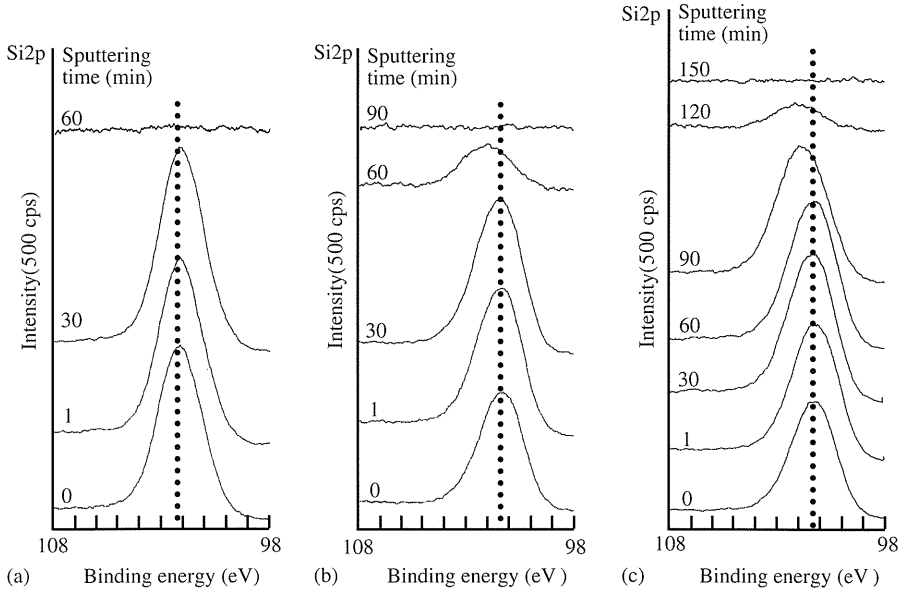

Fig. 1. Si2p spectra of HMDSO film deposited onto titanium by XPS analysis: (a) 10-min coating, (b) 30-min coating, (c) 60-min coating.

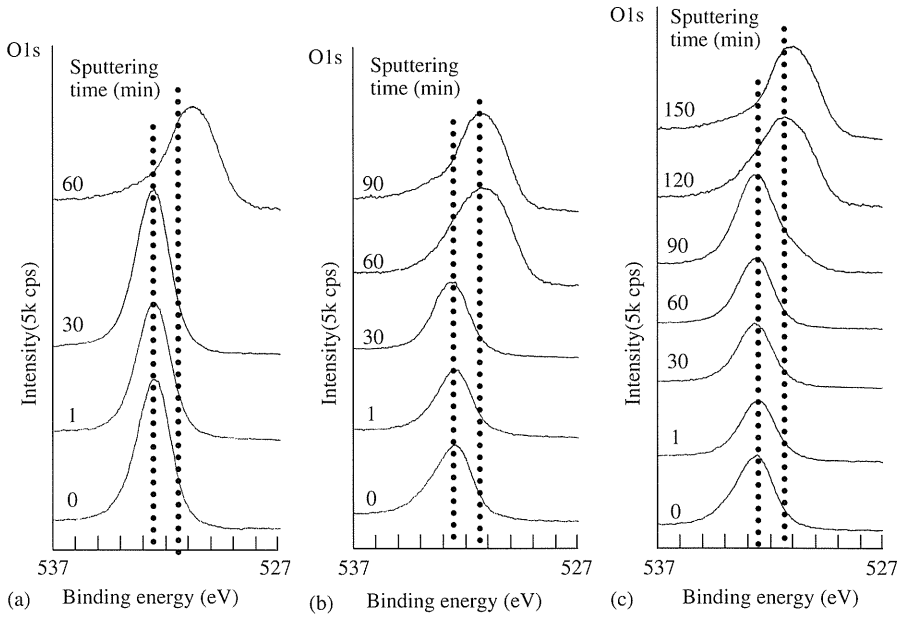

Fig. 2. O1s spectra of HMDSO film deposited onto titanium by XPS analysis: (a) 10-min coating, (b) 30-min coating, (c) 60-min coating.

Fig. 1 shows the Si2p spectra of the HMDSO-coated titanium specimens analyzed by XPS measurement. In the spectra of 10-min coating, the Si2p peak of the HMDSO layer was observed at 102.2 eV before argon-ion sputtering, as indicated by the dotted line in Fig. 1, which shifted approximately 2 eV lower in comparison with the reported energy value [15]. These peaks almost disappeared after 60 min of argon-ion sputtering. In the spectra of the 30-min coating, the Si2p peak of the outermost layer of the HMDSO film appeared at 101.3 eV, as indicated by the dotted line. After 60 min of argon-ion sputtering, the Si2p peak shifted to 102.2 eV, and almost disappeared after 90 min of argon-ion sputtering. The Si2p spectra of the 60-min coating are similar to those of the 30-min coating. The Si2p peak of the outermost layer of HMDSO film was also observed at 101.3 eV, as indicated by the dotted line, and also shifted to 102.2 eV after 90 min of sputtering. The Si2p peaks of 60-min HMDSO deposition almost disappeared after 150 min of argon-ion sputtering.

Fig. 2 shows the O1s spectra of the HMDSO-coated titanium specimens analyzed by XPS measurement. The O1s peaks of the three types of outermost layers of

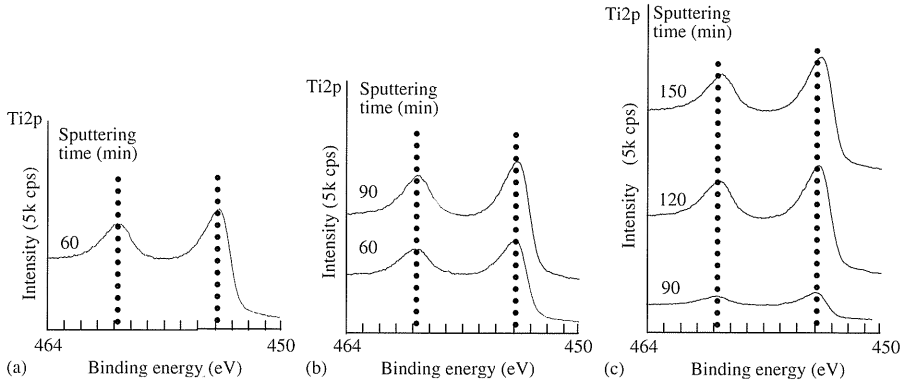

Fig. 3. Ti2p spectra of HMDSO film deposited onto titanium after argon-ion sputtering by XPS analysis: (a) 10-min coating, (b) 30-min coating, (c) 60-min coating.

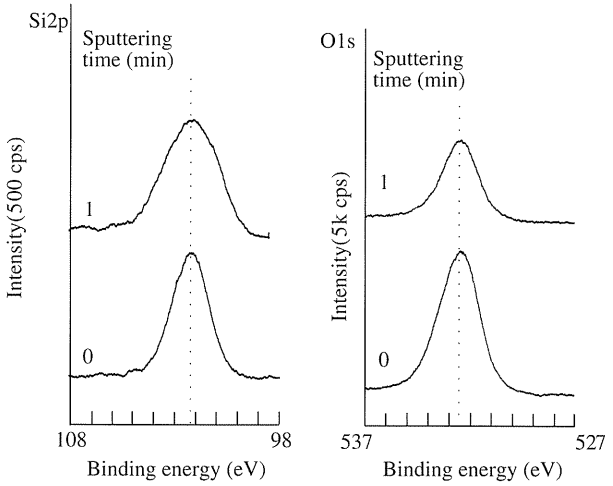

Fig. 4. Si2p and O1s spectra of HMDSO film deposited onto titanium by XSP analysis after immersion for 2 weeks in PBS solution.

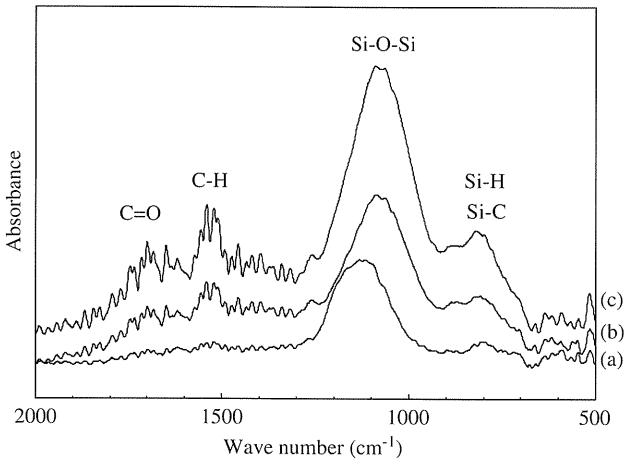

Fig. 5. FT-IR-RAS spectra of HMDSO film deposited titanium: (a) 10-min coating, (b) 30-min coating, (c) 60-min coating.

HMDSO films appeared at 532.6 eV, as indicated by the dotted line, which corresponded with the reported energy value [15]. These peaks also disappeared after long-term argon-ion sputtering. Afterwards, new O1s peaks appeared at 531.4 eV, which corresponds to the bulk oxygen in the titanium dioxide. [27]

Fig. 3 shows the Ti2p spectra of HMDSO-coated titanium specimens analyzed by XPS measurements after argon-ion sputtering. Two Ti2p peaks were observed at 459.8 and 453.9 eV after long-term argon-ion sputtering, as shown in Fig. 3 (dotted line). The $Ti2p_{1/2}$ peak at 459.8 eV and the $Ti2p_{3/2}$ peak at 453.9 eV represented the Ti of metallic titanium [28].

Fig. 4 shows the Si2p and O1s spectra analyzed by XPS measurement of HMDSO-coated specimen after immersion in PBS for 2 weeks. The Si2p and O1s peaks were still observed at 102.2 and at 532.6 eV, respectively.

The FT-IR-RAS spectra of HMDSO-coated specimens are shown in Fig. 5. The peak attributed to Si–O–Si bonds appeared at around 1130 cm^{-1} for the 10-min coated specimen, and at around 1080 cm^{-1} for the 30- and 60-min coated specimens. The peaks around 800 cm^{-1} are attributed to Si–H and Si–C bonds. The two clusters appearing at 1500 and 1700 cm^{-1} in the 30- and 60-min coated specimens are attributed to C–H and C=O bonds, respectively [15–17]. In the 10-min coated specimens, these two peaks are not clearly distinguished.

Fig. 6 shows the XPS spectrum of HMDSO film deposited titanium after the adsorption of fibronectin. N1s peaks were detected at 399.9 eV. These peaks were derived from the amide groups of fibronectin [29]. This derivation was confirmed by XPS observation of the original fibronectin. In addition, Si2p peaks were detected at 101.3 eV.

Fig. 7 compares the N1s spectra produced by the XPS analysis of (a) the fibronectin-attached titanium and (b) the fibronectin-attached HMDSO-coated titanium. Both specimens were rinsed with double-distilled water. N1s peaks of the fibronectin-attached titanium peaks almost disappeared after 10 s of argon-ion etching.

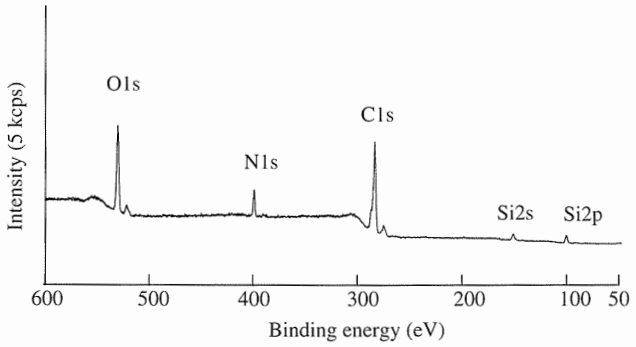

Fig. 6. XPS analysis of fibronectin attached HMDSO coated titanium. The HMDSO plasma polymerization was performed over 30 min.

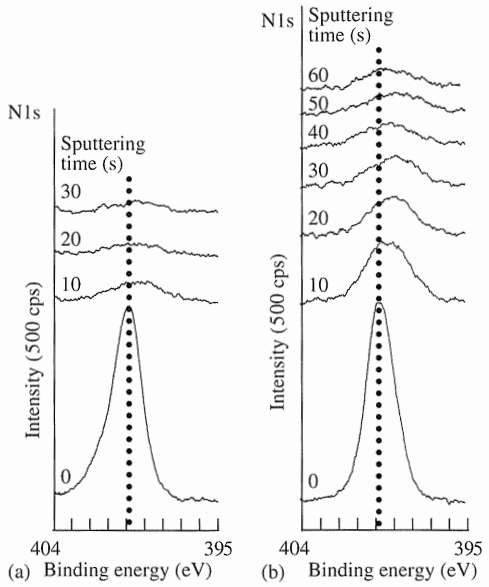

Fig. 7. N1s spectra of fibronectin-attached titanium (a) and fibronectin attached HMDSO coated titanium (b). The HMDSO plasma polymerization was performed over 30 min. The specimens were rinsed with double distilled water after the fibronectin adsorption.

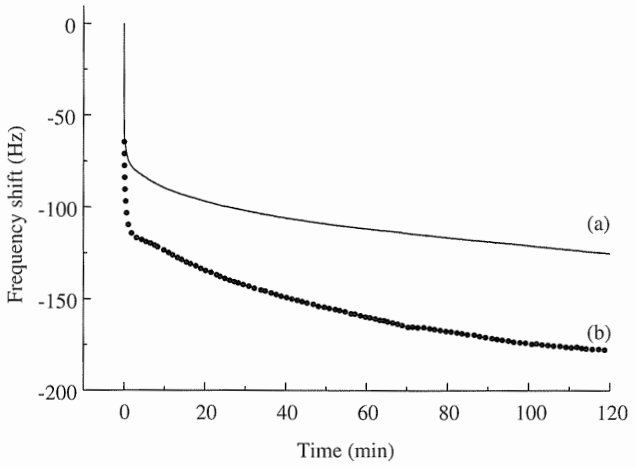

Fig. 8. Frequency shift with respect to time for exposure of a titanium QCM-sensor (a) and HMDSO-coated titanium QCM-sensor (b) to fobronectin.

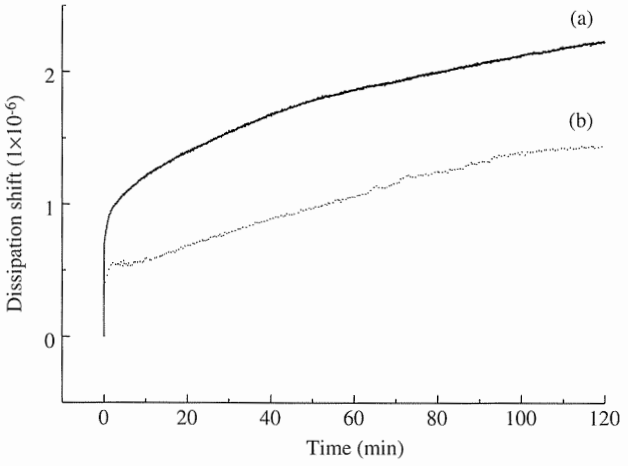

Fig. 9. Dissipation shift with respect to time for exposure of a titanium QCM-sensor (a) and HMDSO-coated titanium QCM-sensor (b) to fobronectin.

However, the N1s peaks of the fibronectin-attached HMDSO-coated titanium remained after argon-ion sputtering for 60 s.

Figs. 8 and 9 show the frequency and dissipation shift obtained via QCM-D measurement. In Fig. 8, the HMDSO-coated specimen revealed a more rapid frequency decrease very quickly and a greater frequency decrease compared to the non-coated titanium surface during 120-min adsorption, which indicates a greater amount of fibronectin adsorbed onto the HMDSO-coated titanium. The dissipation shift differed during 120-min adsorption between the titanium and HMDSO-coated titanium specimens, as shown in Fig. 9. Fibronectin attached to titanium surface showed a greater shift of dissipation than HMDSO-coated titanium.

4. Discussion

The purpose of the present study was to characterize the HMDSO-deposited film on titanium and to examine protein adsorption on the HMDSO plasma-polymerized film.

Compared with PVD techniques such as RF magnetron sputtering, plasma polymerization has the advantages of a high deposition rate and a wide variation of source monomers. Generally, the films deposited by plasma polymerization are free of pinholes and show a strong degree of adhesion to the substrate [7,8]. However, there have been few studies examining plasma polymerization to deposit organic thin films for the surface modification of dental titanium implants. We devised a technique of applying plasma

polymerization for modifying the surface of titanium implant materials.

Investigation via XPS revealed that the titanium surface was completely covered by plasma polymerized HMDSO film. The deposited film was insoluble with organic solvents such as acetone, due to the cross-linking of the deposited film, and firmly adhered to the titanium substrate. According to the procedures given by the Japanese Industrial Standard Committee [30], adhesive tape was applied to deposited film in order to determine the degree of adherence of the film. No organic film deposited under the present procedures was removed from the titanium substrate. XPS measurement after immersion for 2 weeks of HMDSO-coated specimens also confirmed the stability of the deposit film on titanium. No distinct dissolution of deposited films and no swelling were observed during the immersion for 2 weeks.

Two types of Si2p peaks were detected at 102.2 and at 101.3 eV by XPS measurement. Endo et al. [31] analyzed the titanium surface by XPS after the coupling reaction between the silanol end of the silane coupling agent and the surface hydroxyl groups of titanium. They reported that the Si2p peaks of the T–O–Si bond were detected at 102.7 eV. On the other hand, Kalman et al. [32] reported the XPS analysis of silicone rubber in which they detected Si2p peaks of dimethyl silicone rubber near 100 eV. Thus, the Si2p peaks at 102.2 eV could be assigned to Si of the Ti–O–Si bond and the Si2p peaks at 101.3 eV could be assigned to the Si of the siloxane network.

Endo et al. [31] also reported two O1s peaks at 532.0 and 533.1 eV after the same coupling reaction of the silane coupling agent described above. They assigned the O1s peaks at 532.0 eV to the oxygen in the Ti–O–Si bond, and the O1s peaks at 533.1 eV to the oxygen of the cross-linked siloxane network (Si–O–Si). In the present study, O1s peaks other than those for the oxygen derived from TiO_2 were detected at 532.6 eV, which were almost in the middle of 532.0–533.1 eV. It is presumed that the O1s peaks at 532.6 eV could be assigned as the combination of two oxygens derived from the oxygen of Ti–O–Si bonds and Si–O–Si bonds.

FT-IR-RAS measurement showed the difference of Si–O–Si bonds of the siloxane network in the HMDMO deposited film between 10-min coating, and 30 or 60-min coating. The peaks derived from Si–O–Si bonds of deposited HMDSO film in the 30- and 60-min coated specimens appeared around 1080 cm^{-1}, which corresponded to the peaks derived from the Si–O–Si bonds in polydimethyl siloxane [33]. The peaks derived from the Si–O–Si bonds in the 10-min coated specimen appeared at higher wavelengths than those from 30- and 60-min coated specimens. It is presumed that the difference in wavelength of the Si–O–Si bond in 10-min coating is due to the influence of the formation of Ti–O–Si bonds.

It is postulated that the initial step of HMDSO plasma polymerization is the fragmentation of methylsilyl groups and their cleavage off methyl and silyl radicals after the ionization of an HMDSO molecule [17,34]. We suggested that silyl radicals first attach the hydroxyl group of titanium and then formed a metallosiloxiane bond (Ti–O–Si) during the present HMDSO plasma polymerization.

FT-IR-RAS measurement of HMDSO-deposited films showed the presence of new bonds that were absent in the monomer structure, namely, Si–H and C = O bonds in addition to the corresponding monomer bonds: Si–O–Si and Si–C. This resulted from the fragmentation of the Si–C and C–H bonds of the HMDSO monomers and a slight oxidation reaction of the deposited films during the plasma polymerization [18].

The titanium deposited via HMDSO plasma polymerization is more hydrophobic than is mirror-polished titanium, resulting in the high contact angles. It is generally understood that a surface having a greater degree of hydrophobicity results in a greater degree of protein adsorption [35,36]. McDonald et al. [37] reported that hydrophobic preparation of the titanium surface enhanced the fibronectin adsorption as compared to hydrophilic surface preparation.

For a biological examination of HMDSO-deposited films, the adsorption behavior of a protein, fibronectin, onto the HMDSO deposited surface was investigated as a next step of our experiment, including an investigation into the adsorption mechanism of fibronectin. Among the HMDSO plasma-polymerized specimens, the 30-min coating specimen was used because of the significantly higher contact angles, i.e. higher hydrophobicity. XPS analysis revealed that adsorbed fibronectin did not completely cover the surface of the HMDSO-coated specimen. Comparison of N1s spectra between fibronectin-attached titanium and fibronectin-attached HMDSO-coated specimen suggested a difference in the adsorption behavior of fibronectin, for example, a greater amount of the adsorbed fibronectin or tighter binding of adsorbed fibronectin on the HMDSO-coated surface.

QCM-D measurement was performed in order to obtain more detailed information about the protein adsorption. Höök et al. [23] reported the effectiveness of the QCM-D technique for the analysis of adsorption kinetics of three model proteins on titanium oxide surfaces, compared with ellipsometry and optical waveguide lightmode spectroscopy. They also pointed out that the mass calculated from the resonance frequency shift included both protein mass and water that bound or hydrodynamically coupled to the protein adlayer.

In the present study, the amount of fibronectin adsorbed to HMDSO-coated titanium by frequency

shift was greater than that adsorbed to titanium at an early stage of adsorption, i.e. 120 min adsorption. Moreover, there was a difference in dissipation shift between titanium and HMDSO-coated titanium specimens during 120-min adsorption. The difference in dissipation shift suggests that fibronectin adsorbed onto HMDSO-coated titanium has a more rigid structure than that on titanium. The hydrophobic surface of HMDSO-coated titanium will allow a stronger binding with fibronectin, resulting in a more rigid conformation. Further detailed study of the fibronectin adsorption using QCM-D to examine, for example, the influence of different concentrations of fibronectin or the influence of longer adsorption periods or adsorption kinetics, should be conducted in the future.

Fibronectin is a well-known cell-adhesive protein and is believed to play an important role in governing the interactions of biomaterials with their surrounding matrices [38]. It was reported that the precoating of titanium with fibronectin enhanced the adhesive characteristics of cells to titanium [39,40]. The results obtained in this study suggest that an HMDSO-coated titanium surface will easily be covered with protein after implantation into living tissue at an early stage, and will improve the degree of cell activity at the implant–tissue interface.

In conclusion, coating of titanium with organic thin films was shown to be possible via plasma polymerization of HMDSO, and the deposition of HMDSO thin films onto titanium will be beneficial for protein adsorption at the early stage of implantation. It is expected that the application of HMDSO plasma polymerization will become a useful technique for the surface modification of titanium and that HMDSO-coated titanium has potential for application as a dental implant material. Biological activity such as cultured cell growth or tissue response in relation to HMDSO-coated titanium will be the subject of future investigation.

Acknowledgements

This study was supported in part by a Grant from the Ministry of Education, Culture, Sports, Science and Technology of Japan to promote 2001-Multidisciplinary Research Projects (in 2001–2005), and by a Grant-in-Aid for Scientific Research (C)(2)(15592073) from the Japan Society for the Promotion of Science, and by an Oral Health Science Center Grant 5A10 from Tokyo Dental College.

References

[1] Yoshinari M, Ozeki K, Sumii T. Properties of hydroxyapatite-coated Ti–6Al–4V alloy produced by the ion-plating method. Bull Tokyo Dent Coll 1991;32:147–56.

[2] Jansen JA, Wolke JGC, Swann S, van der Waerden JPCM, de Groot K. Application of magnetron sputtering for producing ceramic coatings on implant materials. Clin Oral Impl Res 1993;4:28–34.

[3] Hayakawa T, Yoshinari M, Kiba H, Yamamoto H, Nemoto K, Jansen JA. Trabecular bone response to surface roughened and calcium phosphate (Ca-P) coated titanium implants. Biomaterials 2002;23:1025–31.

[4] Klein CPAT, Wolke JGC, de Blieck-Hogervorst JMA, de Groot KA. Calcium phosphate plasma-sprayed coatings and their stability: an in vivo study. J Biomed Mater Res 1994;28:909–17.

[5] Cheang P, Khor KA. Addressing processing problems associated with plasma spraying of hydroxyapatite coatings. Biomaterials 1996;17:537–44.

[6] Ogiso M, Yamashita Y, Matsumoto T. Microstructural changes in bone of HA-coated implants. J Biomed Mater Res 1998;39: 23–31.

[7] Kurosawa S, Kamo N, Matsui D, Kobatake Y. Gas sorption to plasma-polymerized copper phthalocyanine film formed on a piezo-electric crystal. Anal Chem 1990;62:353–9.

[8] Shi FF. Recent advances in polymer thin film prepared by plasma polymerization: synthesis, structural characterization, properties and applications. Surf Coat Technol 1996;82:1–15.

[9] Fong F-O, Kuo HC, Wolfe JC, Randall JN. Plasma polymerized styrene: a negative resist. J Vac Sci Technol 1988;B6:375–8.

[10] Inagaki N, Nishino K, Katsuura K. Some optical properties of polymer films prepared by glow discharge polymerization from methane, tetrramethylsilane, and tetramethylin. J Poly Sci Polym Ed 1980;18:765–70.

[11] Horn MW, Pang SW, Rothschild M. Plasma-deposited organosilicon thin films as dry resists for deep ultraviolet lithography. J Vac Sci Technol 1990;B8:1493–6.

[12] Wrobel AM, Kowalski J, Grebowicz J, Kryszewski M. Thermal decomposition of plasma-polymerized organosilicon thin film. J Macromol Sci Chem 1982;A17:433–52.

[13] Ward AJ, Short RD. A time-of-flight secondary ion mass spectrometry and X-ray photoelectron spectroscopy investigation of the structure of plasma polymers prepared from the methacrylate series of monomers. Polymer 1993;34:4179–85.

[14] Akovali G. Plasma polymerization of hexamethyldisiloxane in the gas. Phase I. Polymerization studies. Polym Eng Sci 1981;21: 658–61.

[15] Sachdev KG. Characterization of plasma-deposited organosilicon thin films. Thin Solid films 1983;107:245–50.

[16] Kashiwagi K, Yoshida Y, Murayama Y. Hybrid films formed from hexamethyldisiloxane and SiO by plasma process. Jpn J Appl Phys 1991;30:1803–7.

[17] Rau C. Mechanisms of plasma polymerization of various silico-organic monomers. Thin Solid Films 1994;249:28–37.

[18] Lee SH, Lee DC. Preparation and characterization of thin films by plasma polymerization of hexamethyldisiloxane. Thin Solid Films 1998;325:83–6.

[19] Schwarz J, Schmidt M, Ohl A. Synthesis of plasma-polymerized hexamethyldisiloxane (HMDSO) films by microwave discharge. Surf Coat Technol 1998;98:859–64.

[20] Miyachi H, Hiratsuka A, Ikebukuro K, Yano K, Muguruma H, Karube I. Application of polymer-embedded proteins to fabrication of DNA array. Biotechnol Bioeng 2000;69:323–9.

[21] Puleo DA, Kissling RA, Sheu M-S. A technique to immobilize bioactive proteins, including bone morphogenetic protein-4 (BMP-4), on titanium alloy. Biomaterials 2002;23:2079–87.

[22] Rodahl M, Höök F, Kasemo B. QCM operation in liquids: an explanation of measured variations in frequency and Q factor with liquid conductivity. Anal Chem 1996;68:2219–27.

[23] Höök F, Vörös J, Rodahl M, Kurrat R, Böni P, Ramsden JJ, Textor M, Spencer ND, Tengvall P, Gold J, Kasemo B. A

comparative study of protein adsorption on titanium oxide surface using in situ ellipsometry, optical waveguide lightmode spectroscopy, and quartz crystal microbalance/dissipation. Colloids Surf B Biointerfaces 2002;24:155–70.
[24] Andersson A-S, Glasmästar K, Sutherland D, Lidberg Ulf, Kasemo B. Cell adhesion on supported lipid bilayers. J Biomed Mater Res 2003;64A:622–9.
[25] Sauerbrey G. Verwendung non Schwingquarzen zur Wägung dünner Schichten und zur Mikrowägung. Z Phys 1959;155: 206–22.
[26] Rodahl M, Höök F, Fredriksson C, Keller CA, Krozer A, Brzezinski P, Voinova M, Kasemo B. Simultaneous frequency and dissipation factor QCM measurements of biomolecular adsorption and cell adhesion. Faraday Discuss 1997;107:229–46.
[27] Sham TK, Lazarus MS. X-ray photoelectron spectroscopy (XPS) studies of clean and hydrated TiO_2 (rutile) surfaces. Chem Phys Lett 1979;68:426–32.
[28] Wagner CD, Riggs WM, Davis LE, Moulder JF, Muilenberg GE. In: Muilenberg GE, editor. Handbook of X-ray photoelectron spectroscopy. Minnesota: Parkin-Elmer Corporation; 1979. p. 68.
[29] MacDonald DE, Markovic B, Allen M, Somasundaran P, Boskey AL. Surface analysis of human plasma fibronectin adsorbed to commercially pure titanium materials. J Biomed Mater Res 1998; 41:120–30.
[30] Methods of adhesion test for metallic coatings. H8504-1996, Japanese Industrial Standard Committee.
[31] Endo K. Chemical modification of metallic implant surfaces with biofunctional proteins (Part 1) Molecular structure and biological activity of a modified NiTi Alloy surface. Dent Mater J 1995; 14:185–98.
[32] Kalman PG, Ward CA, McKeown NB, McCullough D, Romaschin AD. Improved biocompatibility of silicone rubber by removal of surface entrapped air nuclei. J Biomed Mater Res 1991;25:1990211.
[33] Park JH, Park KD, Bae YH. PMDS-based polyurethanes with MPEG graft: synthesis, characterization and platelet adhesion study. Biomaterials 1999;20:943–53.
[34] Wrobel AM, Kowalski J, Grebowicz J, Kryszewski M. Thermal decomposition of plasma-polymerized organosilicone thin films. J Macromol Sci Chem 1982;A17:433–52.
[35] Haynes CA, Norde W. Globular properties at solid/liquid interfaces. Coll Surfaces B: Biointerfaces 1994;2:517–66.
[36] Absolom DR, Zingg W, Neumann AW. Protein adsorption to polymer particles: role of surface properties. J Biomed Mater Res 1987;21:161–71.
[37] McDonald DE, Deo N, Markovic B, Stranick M, Somasundaran P. Adsorption and dissolution behavior of human plasma fibronectrin on thermally and chemically modified titanium dioxide particles. Biomaterials 2002;23:1269–79.
[38] Seitz TL, Noonan KD, Hench LL, Noonan NE. Effect of fibronectin on the adhesion of an established cell line to a surface reactive biomaterial. J Biomed Mater Res 1982;16: 195–207.
[39] Cannas M, Denicolai F, Webb LX, Gristina AG. Bioimplant surfaces: binding of fibronectin and fibroblast adhesion. J Orthop Res 1998;6:58–62.
[40] Dean JW, Culbertson KC, D'Angelo AM. Fibronectin and laminin enhance gingival cell attachment to dental implant surfaces in vitro. J Oral Maxillofac Implants 1995;10: 721–8.

Int J Oral-Med Sci 3(1):20-24, 2004

Original Article

Frontier Molecular Orbital Study for the Reaction of Tresyl Chloride

Tohru Hayakawa,[1,4] Megumi Nagai,[2] Masafumi Yamamoto,[3,4] Masaharu Makimura,[2,4] and Kimiya Nemoto[1,4]

Departments of [1]Dental Materials, [2]Comprehensive Clinical Dentistry and [3]Oral Medicine, and [4]Research Institute of Oral Science, Nihon University School of Dentistry at Matsudo, Matsudo, Chiba 271-8587, Japan

Correspondence to :
Tohru Hayakawa
E-mail : hayakawa@mascat.nihon-u.ac.jp

Abstract

In the current studies, we used frontier molecular orbital theory to understand the coupling reaction of tresyl chloride ($Cl\text{-}SO_2CH_2CF_3$)-activated titanium and fibronectin. Because titanium contains a large number of basic functions, it is impossible to calculate the molecular orbital of titanium. Therefore, we used methanol as model compound for calculations. Semi-empirical determinations of the highest occupied molecular orbital (HOMO) and lowest unoccupied molecular orbital (LUMO) for methanol, tresyl chloride, tresylated methanol, and methyl amine were obtained using PM3 Hamiltonian calculations. We found that energy difference between the HOMO of methanol and the LUMO of tresyl chloride (9.004 eV) is smaller than that between the LUMO of methanol and the HOMO of tresyl chloride (15.855 eV). This suggests that the reaction of tresyl chloride and methanol is dominated by the interaction of the HOMO of methanol and LUMO of tresyl chloride. In addition, the energy difference between the LUMO of tresylated methanol and HOMO of methyl amine (8.559 eV) is smaller than that between the LUMO of methanol and HOMO of methyl amine (12.909 eV). Therefore, the nucleophilic reaction of methyl amine towards tresylated methanol proceeds more easily than that of the reaction towards methanol. In conclusion, the tresylation of methanol improves its reactivity towards methyl amine by reducing methanol's LUMO energy levels.

Keywords :
semi-empirical molecular orbital calculation, frontier molecular orbital, HOMO, LUMO, tresyl chloride

Introduction

After implantation of a medical device, such as dental implant, the first biological reaction is the adsorption of body fluid proteins, including extracellular matrix components, at the implant-tissue interface (1-3). Modification of the implant surface for the selective adsorption of beneficial molecules promotes a desirable integration with body tissue. For this reason, pre-coating of a titanium implant with cell-adhesive proteins is expected to enhance cellular activity and initial cell attachment around the implanted material.

Nilsson and Mosbach (4, 5) have reported the direct and simple immobilization of enzymes to various hydroxyl groups using highly reactive sulfonyl chlorides, such as 2,2,2-trifluoroethanesulfonyl chloride (tresyl chloride, $CF_3CH_2SO_2Cl$). In these studies, they coupled enzymes, such as α-chymotrypsin, to silica or agarose by activating the hydroxyl groups of silica or agarose withy tresyl chloride.

Similarly, it should be possible to form tresylated titanium by activating basic terminal hydroxyls (6) on the titanium. This should allow an efficient immobilization of proteins to the titanium surface. In fact, in our previous study (7, 8), we succeeded in directly attaching fibronectin to titanium using a tresyl chloride activation technique. X-ray photoelectron spectroscopy (XPS) confirmed that tresyl chloride reacted with a basic hydroxyl group present on the mirror polished titanium surface and that fibronectin could easily attach to the tresylated titanium surface. A quartz-crystal microbalance study

of fiboronecitn adsorption revealed that almost twice as much fibronectin adsorbed onto the tresyl chloride -activated titanium as untreated titanium (9). These findings indicate that tresyl chloride technique is useful for the direct attachment of proteins to titanium.

Despite these studies, the detailed mechanism for the tresyl chloride reaction has not bee determined. The postulated scheme for the tresyl chloride reaction by Nilsson and Mosbach (4, 5) is shown in Fig. 1. However, they did not explain why tresyl chloride treatment is effective for coupling of proteins.

Fukui et al. (10, 11) postulated that the reactivity or selectivity of some organic reactions is controlled by the interactions between highest occupied molecular orbital (HOMO) and lowest unoccupied molecular orbital (LUMO), a concept called a frontier molecular orbital theory. The HOMO energy levels indicate the reactivity towards the electrophile, whereas the LUMO energy levels indicate the reactivity toward the nucleophile. Hayakawa et al. (12, 13) have explained the site- and regio-selectivities in cycloaddition reactions using this frontier molecular orbital theory. In addition, Kawase et al. (14, 15) reported that the dipole moment and energy differences between the HOMO and the LUMO of a substrate influenced the behavior of a hepatocytes culture. HOMO and LUMO energies are calculated from the molecular orbital method, in which bonding in the molecule arises from the overlap of atomic orbitals, and the molecular orbital (Ψ) is formulated with a liner combination of atomic orbitals that have overlapped as follows: (16, 17).

$$\Psi = C_A \Psi_A + C_B \Psi_B$$

The functions of Ψ_A and Ψ_B are those for the atomic orbitals of atoms A and B, respectively, and C_A and C_B represent their weighting factors.

In the present study, we investigated the coupling reaction mechanism of tresyl chloride-activated titanium to fibronectin using frontier molecular orbital theory. Due to the large number of basic functions of titanium, it is impossible to calculate its molecular orbital. Therefore, we used methanol as model compound for the analysis of tresyl chloride reaction.

Activation

$$R\text{-}CH_2\text{-}OH + Cl\text{-}OSO_2CH_2CF_3 \longrightarrow R\text{-}CH_2\text{-}OSO_2CH_2CF_3$$

Coupling

$$R\text{-}CH_2\text{-}OSO_2CH_2CF_3 + H_2N\text{-}R' \longrightarrow R\text{-}CH_2\text{-}HN\text{-}R'$$

Fig. 1. Postulated scheme for the tresyl chloride reaction.

Materials and Methods

Quantum CAChe software (Fujitsu Ltd.,) was used for benchtop molecular design. The chemical structure of methanol, tresyl chloride ($Cl\text{-}SO_2CH_2CF_3$), tresylated methanol ($CH_3\text{-}OSO_2CH_2CF_3$), and methyl amine were drawn using the MOPAC option for molecular orbital calculation, which is based on the PM3 Hamiltonian molecular orbital method developed by Stewart (18, 19). This was used to calculate the geometry of the optimized structure for each compound at the lowest heat of formation. Next, the HOMO and LUMO energy levels and the dipole moment of each compound were obtained by MOPAC calculation. Methanol and methyl amine ($CH_3\text{-}NH_2$) were used as model compounds of titanium and protein, respectively.

Results

The Optimized structure of methanol, tresyl chloride, tresylated methanol ($CH_3\text{-}OSO_2CH_2CF_3$) and methyl amine obtained by MOPAC calculation are shown in Fig. 2, and the HOMO and LUMO energy levels, heat of formation, and dipole moment for these compounds are shown in Table 1. We found that the HOMO and LUMO energies of tresylated methanol are lower than those of methanol. Also, we found that the dipole moment of tresylated methanol was greater than that of methanol.

The energy diagrams of HOMO and LUMO of methanol and tresyl chloride are shown in Fig. 3, and those of methanol, tresylated methanol and methyl amine are shown in Fig. 4. The energy difference between the HOMO of methanol and LUMO of tresyl chloride (9.004 eV) is smaller than that between the

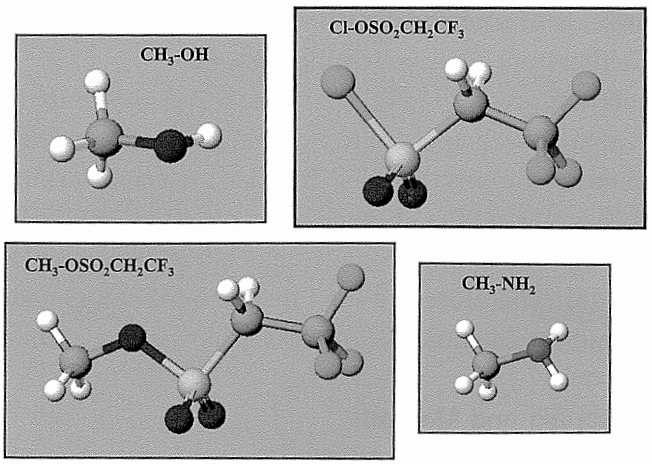

Fig. 2. Optimized structure obtained by MOPAC calculation. Partial charges are also indicated. Dark gray, carbon; red, oxygen; green, fluoride and chloride; gray, hydrogen. Partial charges are indicated.

LUMO of methanol and the HOMO of tresyl chloride (15.855 eV). In addition, the energy difference between the LUMO of tresylated methanol and the HOMO of methyl amine (path a: 8.559 eV) is smaller than that between the LUMO of methanol and HOMO of methyl amine (path b: 12.909 eV).

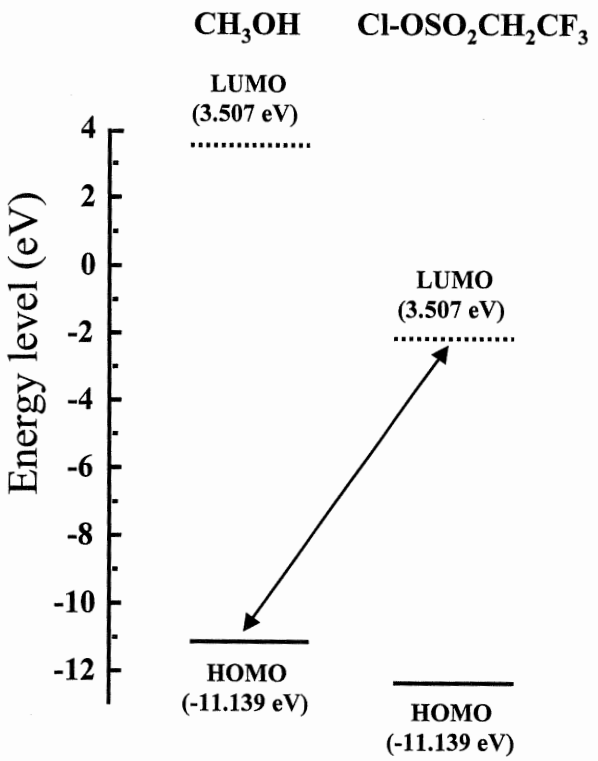

Fig. 3. HOMO and LUMO energy levels for methanol and tresyl chloride (Cl-O-$SO_2CH_2CF_3$).

Discussion

In the present study, we calculated the HOMO and LUMO energies of methanol, tresyl chloride, tresylated methanol and methyl amine to elucidate the mechanism of the tresyl chloride reaction. Three calculation methods, *ab initio*, semi-empirical, and empirical calculations were proposed to solve the Schrödinger equation. *Ab initio* calculations were performed by calculating the base functions of each atomic orbital. Although *ab initio* calculations gave the most accurate results among the three methods, they are computationally intensive and rely on large, ultra high-speed computers. In contrast, Hückel calculations correspond to empirical methods. Empirical methods are very simple, but are not adequate for quantitative analysis. Finally, semi-empirical methods consistently provide more accurate results than empirical methods and are easier and faster than *ab initio* calculations. Some empirical parameters, such as AM1, PM3 or PM5, were used in the semi-empirical calculations to reduce the calculation time (18, 19). MOPAC application in Quantum CAChe can determine both an optimum geometry and electronic

Table 1. HOMO and LUMO energy levels obtained by MOPAC (eV).

	CH_3-OH	Cl-$OSO_2CH_2CF_3$	CH_3-$OSO_2CH_2CH_2CF_3$	CH_3-NH_2
LUMO	3.507	−2.135	−0.843	3.105
HOMO	−11.139	−12.348	−11.947	−9.402
Heat of formation (kcal/mol)	−51.898	−227.621	−270.985	−5.205
Dipole moment (Debye)	1.487	2.333	3.784	1.396

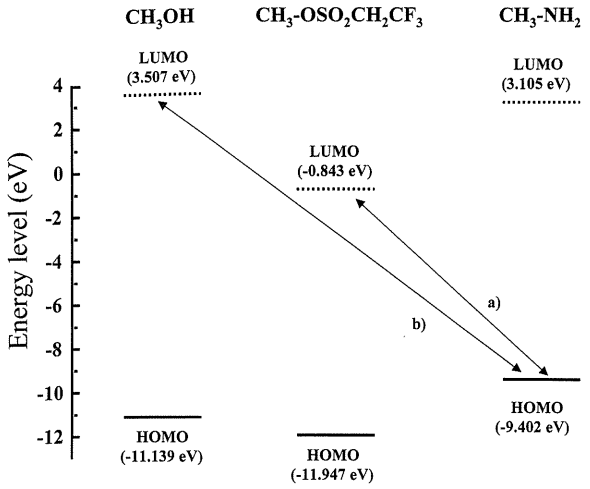

Fig. 4. HOMO and LUMO energy levels for methanol, tresylated methanol (Cl-O-$SO_2CH_2CF_3$), and methyl amine.

properties of molecules by solving the Schrödinger equation using the semi-empirical Hamiltonians developed by Stewart (18, 19). The optimized structure was thereby obtained using the heat of formation calculated for each compound.

According to the frontier molecular orbital theory postulated by Fukui et al. (10, 11), organic reactions are controlled by the interaction of the HOMO and LUMO of reacting molecules. By comparing the energy levels of methanol and tresyl chloride, it is clear that the interaction of the HOMO of methanol and the LUMO of tresyl chloride is dominant for the reaction between tresyl chloride and methanol because the energy differences between HOMO of the methanol and LUMO of the tresyl chloride is smaller than the energy differences obtained from the LUMO of methanol and the HOMO of tresyl chloride. The HOMO energy levels indicate the reactivity towards the electrophile, whereas the LUMO energy levels indicate the reactivity toward the nucleophile. Thus, the reaction between methanol and tresyl chloride was governed by an electrophilic reaction of tresyl chloride towards methanol.

The HOMO and LUMO energy levels of tresylated methanol were lower than that of methanol because of the electron withdrawing property of the sulfonate group. As a result, the energy difference of path a in Fig. 4 is smaller than that of path b. This means that the nucleophilic reaction of methyl amine towards tresylated methanol proceeded easier than that of the reaction towards methanol. Based on these results, we conclude that the tresylation of methanol improves its reactivity towards methyl amine by reducing its LUMO energy levels. In addition, the MOPAC calculation showed that tresylated methanol had a higher polarity than methanol.

Although we used methanol as a model of the titanium surface, the electronic properties of the basic hydroxyl group of titanium are different from those of methanol. In addition, other factors, such as surface electricity of titanium, will influence the reaction of titanium and tresyl chloride and subsequent coupling reaction with protein. For this reason, the influence of these factors is just under investigation. At any event, it is speculated that the tresylated titanium will have a higher reactivity towards fibronectin because of the lower LUMO energy level compared with titanium.

Finally, based on frontier molecular orbital theory, we can understand the effectiveness of tresyl chloride treatment for the coupling reaction of protein with an alkyl hydroxyl group. Tresyl chloride treatment improves the nucleophilic reactivity by reducing the LUMO energy. Finally, our studies suggest that molecular orbital calculations will be useful for investigation of chemical reactions in the dental materials.

Acknowledgments

This study was supported by Nihon University Joint Research Grant for 2003, by a Grant-in Aid for Scientific Research (C2, 15592073) from the Japan Society for the Promotion of Science, and by a Grant from the Ministry of Education, Culture, Sports, Science, and Technology of Japan to promote 2001-Multidisciplinary Research Projects (in 2001-2005).

References

1. Horbett TA : Principles underlying the role of adsorbed plasma proteins in blood interactions with foreign materials. Cardiovasc Pathol, 2 : 137S-148S, 1993.
2. Puleo DA, Nanci A : Understanding and controlling the bone-implant interface. Biomaterials, 20 : 2311-2321, 1999.

3. Wälivaara B, Aronsson BO, Rodahl M, Lausmaa J, Tengvall P : Titanium with different oxides : in vitro studies of protein adsorption and contact activation. Biomaterials, 15 : 827-834, 1994.
4. Nilsson K, Mosbach K : Immobilization of enzymes and affinity ligands to various hydroxyl group carrying supports using highly reactive sulfonyl chlorides. Biochem. Biophys. Res. Commun, 102 : 449-457, 1981.
5. Nilsson K, Mosbach K : Tresyl chloride-activated supports for enzyme immobilization. Methods Enzymol, 135 : 65-78, 1987.
6. Boehm HP : Acidic and basic properties of hydroxylated metal oxides surface. Faraday Discuss. Faraday Soc, 52 : 264-275, 1971.
7. Hayakawa T, Yoshinari M, Nemoto K : Direct attachment of fibronectin to tresyl chloride-activated titanium. J Biomed Mater Res, 67A : 684-688, 2003.
8. Hayakawa T, Yoshinari M, Nemoto K : X-ray photoelectron spectroscopic studies of the reactivity of basic terminal OH of titanium towards tresyl chloride and fibronectin. Biomed Res, 24 : 223-230, 2003.
9. Hayakawa T, Yoshinari M, Nemoto K : Immobilization of cell-adhesive protein onto tresylated titanium. −Analysis using quarts crystal microbalance-dissipation technique−. J J Dent Mater, 22 : 329, 2003.
10. Fukui K, Yonezawa T, Shingu H : A molecular orbital theory of reactivity in aromatic hydrocarbons. J Chem Phys, 20 : 722-725, 1952.
11. Fukui K, Yonezawa T, Nagata C, Shingu H : Molecular orbital theory of orientation in aromatic, heteroaromatic, and other conjugated molecules. J Chem Phys, 22 : 1433-1442, 1954.
12. Hayakawa T, Araki K, Shiraishi S : An account of the site- and regio-selectivity in the reaction of nitrile oxides with substituted *p*-benzoquinones by frontier molecular orbital theory. Bull Chem Soc Jpn, 57 : 1643-1649, 1984.
13. Hayakawa T, Araki K, Shiraishi S : The reactions of nitrile oxides with methoxy p-benzoquinones. Bull Chem Soc Jpn, 57 : 2216-2218, 1984.
14. Kawase M, Takai T, Kurikawa N, Yagi K, Mizoguchi T : Surface characterization of chemically modified glasses and their application for hepatocytes culture. Seitai Zairyou, 16 : 128-132, 1998.
15. Kawase M, Takai T, Kurikawa N, Yagi K, Mizoguchi T : Surface characterization of chemically modified glasses and their application for hepatocytes culture 2 −Significance of hardness−. Seitai Zairyou, 16 : 192-195, 1998.
16. Langford CH, Beebe RA : The development of chemical principles, Addison-Wesley Publishing Co : Boston, 1969. p.291-308.
17. March J : Advance organic chemistry, 2nd ed., McGraw-Hill Kogakusha Ltd : Tokyo, 1977. p.3-14.
18. Stewart JJP : Optimization of parameters for semi-empirical methods. I. Method. J Comput Chem, 10 : 209-220, 1989.
19. Stewart JJP : Optimization of parameters for semi-empirical methods. II. Applications. J Comput Chem, 10 : 221-264, 1989.

J Oral Tissue Engin 2004;1(1):41-49

ORIGINAL ARTICLE

Deposition of Thin Calcium Phosphate Film onto Titanium Using RF Magnetron Sputtering Technique

Tohru HAYAKAWA[1], Masao YOSHINARI[2], Kenichi TAKAHASHI[3] and Kimiya NEMOTO[1]

[1] Department of Dental Materials, Research Institute of Oral Science, Nihon University School of Dentistry at Matsudo, 2-870-1, Sakaecho-nishi, Matsudo, Chiba 271-8587, Japan
[2]Department of Dental Materials, Science and Oral Health Science Center, Tokyo Dental College, 1-2-2 Masago, Mihamaku, Chiba 261-8502, Japan
[3]Department of Dental Materials, Nihon University Graduate School of Dentistry at Matsudo, 2-870-1, Sakaecho-nishi, Matsudo, Chiba 271-8587, Japan
Corresponding author: Dr.Tohru Hayakawa
e-mail: hayakawa@mascat.nihon-u.ac.jp

SYNOPSIS

In the present study, we aimed to deposit thin calcium phosphate film onto titanium substrate using magnetron sputtering method. The hydroxyapatite target and tricalcium phosphate target were prepared by cold isostatic pressing method. When hydroxyapatite target was used, the crack was formed on the target material during the sputtering.

The film thickness was increased according to the increase of the coating time. Heating the titanium substrate around 250°C produced tighter bonding between coated film and titanium, and also increased film thickness compared with no-heating of the titanium. After a 5-hr coating process, the thickness of the deposited film was approximately 0.10 μm when titanium substrate was heated. EPMA and FT-IR-RAS measurement reveled that the main component of coated film was calcium phosphate material.

In conclusions, thin calcium phosphate film was deposited onto titanium using magnetron sputtering method.

***Key words**: calcium phosphate coating, titanium, magnetron sputtering*

INTRODUCTION

It is widely known that calcium phosphate coated titanium implants induce faster bone adaptation and improve integration after installation compared with titanium implants[1)]. Caulier et al.[2,3)] reported on the advantage of calcium phosphate coating for implant integration in bone of low quality or quantity. Currently, plasma-spray technique is the most widely

used method for the deposition of calcium phosphate coatings. However, some short comings of plasma-spraying, such as degradation, fatigue behavior of the coatings and long-term safety in clinical use, have been claimed[4-6].

To overcome these problems, thin film coating technologies using physical vapor deposition (PVD) technique have been introduced for the deposition and adherent calcium phosphate films. Among PVD technique, the efficacy of ion plating[7], radio-frequency magnetron sputtering[8,9], and ion beam dynamic mixing methods[10] have been evaluated as a thin calcium phosphate film coating technique. The frequent initial amorphous nature of these coatings can be easily improved by rapid heat treatment with infrared radiation[11].

Sputtering is the process whereby, in a vacuum chamber, atoms or molecules of a material are ejected from a target by a bombardment of high energy ions. Radio-frequency magnetron sputtering is a high-rate vacuum coating technique for depositing a wide range of materials, including metals, ceramics and plastics[12].

Previous cell cultures and animal experiment have indicated biological feasibility of magnetron sputterd-coatings[13,14]. Hayakawa et al.[15] reported that magnetron sputtered calcium phosphate coatings evoked an enhanced beneficial bone response to implants inserted into trabecular bone, compared to only surface roughened implants.

The properties of the deposited thin calcium phosphate film were influenced of the target materials in the magnetron sputtering method. Jansen et al.[8] prepared the hydroxyapatite target using plasma-spray method. Yamashita et al.[16] prepared the calcium phosphate target with Ca/P ratios of 0.6 to 0.75 by the reaction of $CaCO_3$ and orthophophoric acid at high temperature around 1100°C to 1400°C. They obtained tricalcium and pyrocalcium phosphate thin film. Ding et al.[17] evaluated the hydroxyapatite/titanium composite thin film which was prepared from the hydroxyapatite and titanium composite targets with different composition of hydroxyapatite and titanium.

In the present study, we aimed to deposit thin calcium phosphate coating onto titanium substrate using hydroxyapatite target or tricalcium phosphate target.

MATERIALS AND METHODS

Titanium substrate

Commercially pure wrought titanium disks (JIS, Japan Industrial Specification H 4600, 99.9 mass % Ti, Furuuchi Chemical Corp., Tokyo) with a diameter of 12 mm were used. The disks were ultrasonically cleaned with acetone before sputter-coating.

Magnetron sputtering

The calcium phosphate sputter-coating was performed using a RF magnetron sputter method with a commercially available unit (High Vapor Deposition System, VEP-1000, ULVAC Inc., Kanagawa, Japan). A schematic drawing of the vacuum chamber at which the sputter process takes place is given in Figure 1.

Hydroxyapatite and tricalcium phosphate target was prepared by cold isostatic pressing (CIP) method. Hydroxyapatite and tricalcium powder was pressed at 2000 MPa, and was fired around 950-1000°C. The diameter of target was 52.00 mm, and the thickness was approximately 6.10 mm. Both targets were boded to cupper disc plate.

The titanium substrate was rotated in the stainless chamber (300 mm diameter x 500 mm height) at a rotational velocity of 30 rpm. Two conditions of the heat treatment of titanium substrate were employed. One was without heat treatment of titanium during sputter-coating, and the other was heating substrate around 250°C during sputter-coating.

The flow rate of argon gas was 30 sccm. The magnetron sputtering deposition performed using a radio frequency generator operating at 13.56 MHz at a power of 150 watts. The pressure of the chamber was maintained at approximately 0.3 MPa. The sputtering was preformed for 1, 3 and 5 hours. After sputtering, nitrogen gas was used to purge the cham-

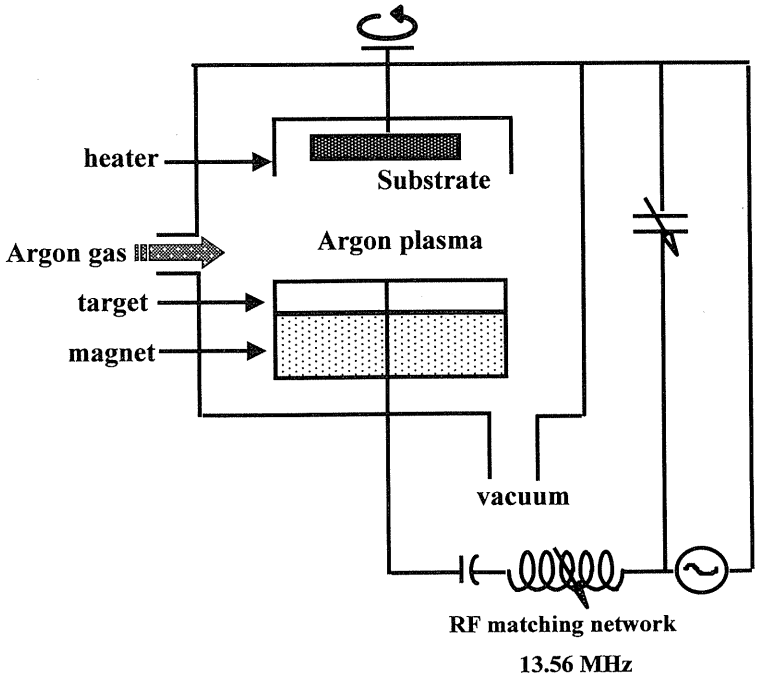

Fig.1 Schematic drawing of the magnetron sputtering process

ber, which was then allowed to return to atmospheric pressure.

Surface characterization

The film thickness was determined using a Dektak Stylus Profiler System (Vecco Instrument Inc., Woodbury, Ny, USA). The stylus force was 25 mg, and the scanning speed was 200 μm/s. Three measurement runs were performed for each surface.

The element on the deposited surface was confirmed by electron probe micro-analysis (EPMA, X-8010, Hitachi, Tokyo, Japan) at an accelerating voltage of 25 kV. Infrared spectra of the coated films on the titanium substrates were obtained by a Fourier transform reflection-absorption spectroscopy (FT-IR-RAS, FT-210, Horiba Ltd., Kyoto, Japan) at 4cm^{-1} resolution.

RESULTS

During the magnetron sputtering, the crack was formed in the hydroxyapatite target as shown in Figure 2. In the present study, it was impossible to deposit calcium phosphate film using hydroxyapatite target. The thin film onto titanium was deposited using tricalcium phosphate target.

The appearance of sputter-coated titanium disk was shown in Figure 3. The surface color of coating was influenced by the coating time and heat treatment of the titanium substrate. After a 1-hr coating without heating the substrate, the appearance was almost same as titanium substrate. On the contrary, when substrate was heated, a 1-hr coated disk was slightly yellowish. Increase in the coating time and heat treatment of titanium substrate produced more yellowish color.

According to the procedures given by the Japanese Industrial Standard Committee[18], adhesive tape was applied to deposited film in order to determine the degree of adherence of the film. When titanium substrate was heated during sputter-coating, no removal of coating from titanium was observed. But when titanium was not heated during sputter-coating, a small part of coating was removed from titanium.

The thickness of the deposited films was shown in Figure 4. The film thickness was increased according to the increase of the coating time, and the heating of the titanium substrate produced thicker film onto titanium. After a 5-hr coating process, the thickness of the deposited film was approximately 0.10 μm when titanium substrate was heated, and was approximately 0.04 μm when titanium substrate was not heated.

Figure 5 shows the result of the EPMA measurement. EPMA measurement revealed that only Ca, P and Ti presented on the coating film.

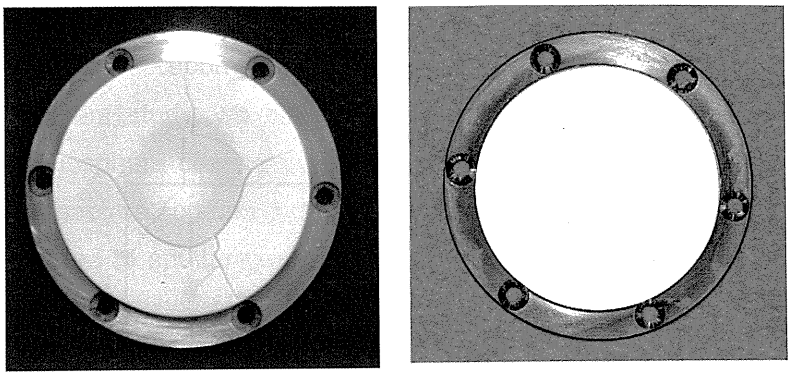

hydroxyapatite target　　tricalcium phosphate target

Fig. 2 Targets used in this study

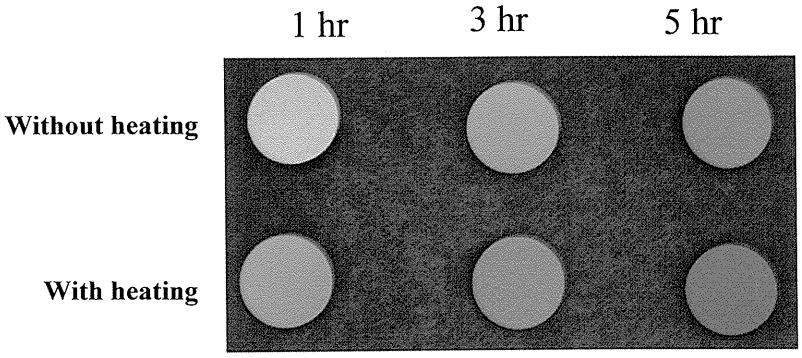

Fig. 3 Surface appearance of the sputter-coated titanium

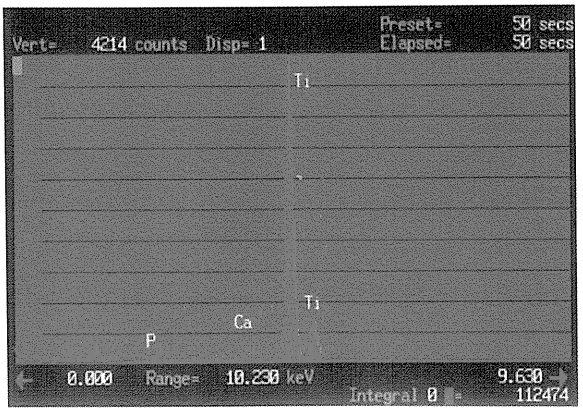

Fig. 5 EPMA analysis of sputter-coated film onto titanium

Figure 6 shows the FT-IR-RAS spectra of deposited film. The specimen was coated for 5 hours. Both samples, i.e. with heat treatment and without heat treatment of titanium substrate, show similar spectra. Two P-O peaks derived from P-O bond of calcium phosphate were observed around 550-600 cm^{-1} and around 1100-1200 cm^{-1}.

The former was derived form P-O bending stretching mode. modes, and latter was derived from P-O

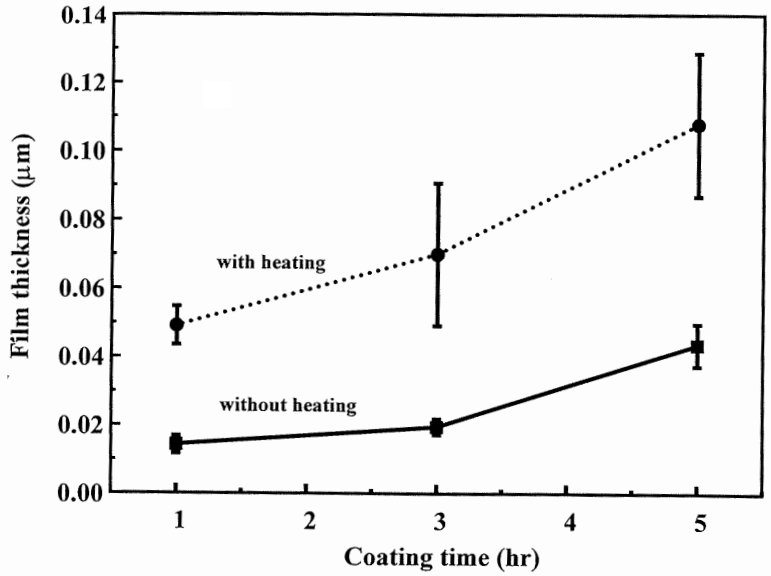

Fig.4 Thickness of sputter-coated film onto titanium

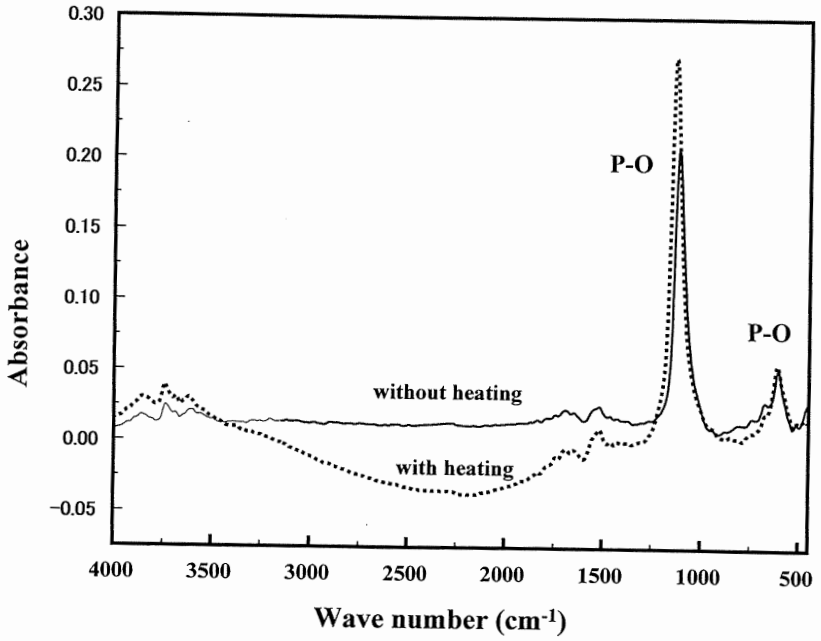

Fig. 6 FT-IR-RAS spectra of sputter -coated film onto titanium

DISCUSSION

In the present study, we performed thin calcium phosphate coating onto titanium using magnetron sputtering method.

First, we tried to sputter-coated onto titanium using hydroxyapatite. Unfortunately, some crack was formed on the hydroxyapatite target (Fig. 2). During the magnetron sputter-coating, the temperature of target was increased by the bombardment of argon plasma. On the other hand, backing cupper plate was cooled by cooling water. As a result, temperature difference was produced between ceramics target and backing cupper plate due to the difference in their thermal conductivities. The temperature difference has a possibility to produce the crack in the ceramic target[19].

In the case of hydroxyapatite target, the dehydration process occurred due to the increase of the temperature of target. It is speculated that the temperature difference between hydroxyapatite target and cupper plate and the dehydration reaction of hydroxyapatite was the reason for crack formation. The process for preparing hydroxyapatite target should be improved to avoid the crack formation. For example, porous and thinner hydroxyapatite target will be applicable.

Heating the titanium substrate influenced the bonding property and thickness of coating film. This was due to the improvement of the reactivity of titanium surface and the improvement of mean free path of plasma molecules, although the detailed study should be further necessary. The present heat temperature around 250°C was determined as a maximum temperature of the sputtering unit in order to elucidate the influence of the heat treatment on the calcium phosphate coating.

EPMA and FT-IR-RAS measurement revealed that main component of deposited film was calcium phosphate materials. To determine the crystallographic structure of coated calcium phosphate coatings, we tried to measure the X-ray diffraction with a thin-layer attachment. But it was impossible to detect the peaks derived from calcium phosphate coating because of too thin film. Only titanium peak was observed in XRD spectrum. It is predicted that the crystallographic structure of coated calcium phosphate coatings will influence the solubility in the body fluid and then will affect the bone formation. Thicker film was needed to analyze the crystallographic structure of coated calcium phosphate coatings. RF magnetron sputtering method can produce thicker film with a uniform thickness by the elongation of coating time.

In conclusions, thin calcium phosphate film was deposited onto titanium using magnetron sputtering method. In

this method, tricalcium phosphate target was used. The heating of the titanium substrate improved the bonding of coated film onto titanium and produced thicker film. Further research will be able to elucidate the crystallographic structure of coated calcium phosphate films. The biological activity such as culture cell growth or tissue response in relation to thin calcium phosphate coated titanium will also be the subject of further investigation.

ACKNOWLEDGEMENT

This study was supported in part by a Grant from the Ministry of Education, Culture, Sports, Science and Technology of Japan to promote 2001- Multidisciplinary Research Projects (in 2001-2005), by a Grant-in-Aid for Scientific Research (C)(2)(15592073) and (14207093) from the Japan Society for the Promotion of Science, and by Oral Health Science Center Grant 5A10 from Tokyo Dental College.

REFERENCES

1) Lacefield WR: Current status of ceramic coatings for dental implants. Implants Dent 7: 315-322, 1998.
2) Caulier H, Vercaigne S, et al: The effect of Ca-P plasma-sprayed coatings on the initial bone healing of oral implants: An experimental study in the goat. J Biomed Mater Res 34: 121-128, 1997.
3) Caulier H, Hayakawa T, et al: An animal study on the bone behaviour of Ca-P-coated implants: influence of implant location. J Mater Sci Materials in Medicine 8: 532-536, 1997.
4) Klein CPAT, Wolke JGC, et al: Calcium phosphate plasma-sprayed coatings and their stability: An *in vivo* study. J Biomed Mater Res 28: 909-917, 1994.
5) Cheang P, Khor KA: Addressing processing problems associated with plasma spraying of hydroxyapatite coatings. Biomaterials 17: 537-544, 1996.
6) Ogiso M, Yamashita Y, et al: Microstructural changes in bone of HA-coated implants. J Biomed Mater Res 39: 23-31, 1998..
7) Yoshinari M, Ozeki K, et al: Properties of hydroxyapatite-coated Ti-6Al-4V alloy produced by the ion-plating method. Bull Tokyo Dent Coll 32: 147-156, 1991.
8) Jansen JA, Wolke JGC, et al: Application of magnetron sputtering for producing ceramic coatings on implant materials. Clin Oral Impl Res 4: 28-34, 1993.
9) van Dijk K, Schaeken HG, et al: Influence of annealing temperature on RF magnetron sputtered calcium phosphate coatings. Biomaterials 17: 405-410, 1996.
10) Yoshinari M, Ohtsuka Y, et al: Thin hydroxyapatite coating produced by the ion beam dynamic mixing method. Biomaterials 15: 529-535, 1994.
11) Yoshinari M, Hayakawa T, et al: Influence of rapid heating with infrared radiation on RF magnetron-sputtered calcium phosphate coatings. J Biomed Mater Res 37: 60-67, 1997.
12) Swann S: Magnetron sputtering. Phys Technol 19: 67-75, 1988.
13) Hulshoff JEG, van Dijk K, et al: Biological evaluation of the effect of magnetron sputtered Ca/P coatings on osteoblast-like cells *in vitro*. J Biomed Mater Res 29: 967-975, 1995.
14) Hulshoff JEG, Hayakawa T, et al: Mechanical and histological evaluation of Ca-P plasma-spray and magnetron sputter-coated implants in trabecular bone of the goats. J Biomed Mater Res 36: 75-83, 1997.
15) Hayakawa T, Yoshinari M: Effect of surface roughness and calcium phosphate coatings on the implant/bone response. Clin Oral Impl Res 11: 296-304, 2000.
16) Yamashita K, Arashi T, et al: Preparation of apatite films through rf-sputtering from calcium phosphate glass. J Am Ceram Soc 77: 2401-2407, 1994.
17) Ding SJ, Ju CP, et al: Characterization of hydroxyapatite and titanium coatings sputtered on Ti-6Al-4V substrate. J Biomed Mater Res 44: 266-279, 1999.
18) Methods of adhesion test for metallic coatings. H8504-1996. Japanese In-

dustrial Standar Committee.
19) Kashimura Y, Miyazaki T, et al: A study of sputtering target. 2002 Japan ANSYS Conference 299-303, 2002.

(Received: February 24 / Accepted: March 5)

Quartz-Crystal Microbalance-Dissipation Technique for the Study of Initial Adsorption of Fibronectin Onto Tresyl Chloride-Activated Titanium

T. Hayakawa,[1] M. Yoshinari,[2] K. Nemoto[1]

[1] Department of Dental Materials, Research Institute of Oral Science, Nihon University School of Dentistry at Matsudo, 2-870-1, Sakaecho-nishi, Matsudo, Chiba 271-8587, Japan

[2] Department of Dental Materials Science and Oral Health Science Center, Tokyo Dental College, 1-2-2 Masago, Mihamaku, Chiba 261-8502, Japan

Received 2 August 2004; revised 7 September 2004; accepted 14 September 2004
Published online 26 January 2005 in Wiley InterScience (www.interscience.wiley.com). DOI: 10.1002/jbm.b.30207

Abstract: The immobilization of cell-adhesive proteins onto titanium implants improves biological response at the implant–tissue interface. Previous studies demonstrated the easy and direct attachment of fibronectin onto titanium with the use of a 2,2,2-trifluoroethanesulfonyl chloride (tresyl chloride) activation technique. The present study investigated the initial adsorption behavior of fibronectin on tresyl chloride-activated titanium by the quartz-crystal microbalance-dissipation (QCM-D) technique. The crystal resonant frequency and the dissipation shift of the oscillator were simultaneously measured by the injection of fibronectin/phosphate-buffered saline solution (pH = 7.4). The tresyl chloride-activated titanium surface showed a faster and greater decrease in frequency than that of untreated titanium, indicating that a greater amount of fibronectin was adsorbed in the former case during a 120-min adsorption. The dissipation-frequency plots revealed that, during the initial stage of adsorption, the bond between fibronectin and tresyl chloride-activated titanium is stronger than that between fibronectin and untreated titanium. The QCM-D technique can provide new insights into the adsorption mechanism of fibronectin. © 2005 Wiley Periodicals, Inc. J Biomed Mater Res Part B: Appl Biomater 73B: 271–276, 2005

Keywords: titanium implants; tresyl chloride-activated titanium; quartz-crystal microbalance-dissipation (QCM-D) technique

INTRODUCTION

Adsorption of body-fluid proteins, including extracellular-matrix components at the implant–tissue interface is the first biological response to the implantation of a biomaterial.[1–3] The modification of implant surfaces for the selective adsorption of beneficial molecules promotes a desirable integration with body tissue.

The most appropriate mode of tissue surrounding titanium dental implant has been regarded as osseointegration, which means a tight connection between the implant and bone tissue.[4,5] However, the degree of attachment of periimplant epithelium and subepithelial connective tissues to titanium is poor, and sometimes bacteria invade, resulting in periimplantitis.[6,7] Thus, tone might hypothesize that the binding of cell-adhesive proteins onto titanium improves the attachment of a dental implant to gingival and/or epithelial tissue. Fibronectin, a cell-adhesive protein, plays an important role in governing the interactions of implants with their surrounding matrices.[8–10] It is predicted that the attachment of fibronectin to titanium biomaterials will improve the connection of dental implants to surrounding tissue elements.

The direct and simple immobilization of enzymes to various hydroxyl groups with the use of highly reactive sulfonyl chlorides such as 2,2,2-trifluoroethanesulfonyl chloride (tresyl chloride, $CF_3CH_2SO_2Cl$) has been reported.[11,12] Hydroxyl groups of silica or agarose were activated by utilizing the reaction of tresyl chloride to couple enzymes such as α-chymotrypsin to tresyl-agarose. Their simple method is highly effective for immobilizing proteins to tresyl chloride-activated materials. Proteins can bind the substrates without any spacers, such as the alkyl chain of a silane coupling agent.

Correspondence to: Tohru Hayakawa (e-mail: hayakawa@masact.nihon-u.ac.jp)
Contract grant sponsor: Ministry of Education, Culture, Sports, Science and Technology of Japan to promote 2001-Multidisciplinary Research Projects (in 2001–2005)
Contract grant sponsor: Japan Society for the Promotion of Science; contract grant number: (C)(2)(15592073)
Contract grant sponsor: Tokyo Dental College Oral Health Science Center; contract grant number: 5A10

© 2005 Wiley Periodicals, Inc.

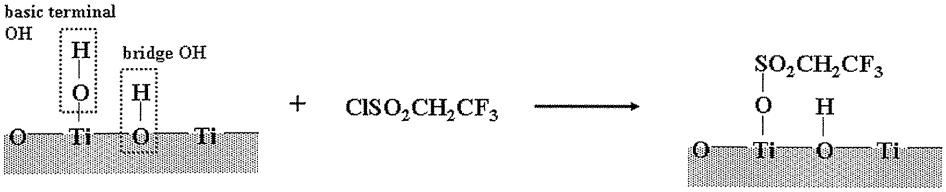

Figure 1. Reaction mechanism between the basic terminal hydroxyl group of the titanium surface and tresyl chloride.

Titanium has two types of hydroxyl groups: a basic terminal hydroxyl and a bridge hydroxyl group.[13] Because tresyl chloride reacts with the basic terminal hydroxyl groups of the titanium surface, tresyl chloride-activated titanium would presumably facilitate the efficient immobilization of proteins. A previous study successfully demonstrated the direct attachment of fibronectin onto titanium by using a tresyl chloride activation technique.[14,15] Tresyl chloride is a liquid. It has been found that tresyl chloride did not react with the basic hydroxyl groups of titanium in a dehydrochloride reagent such as pyridine because of an insufficient number of terminal hydroxyl groups of titanium, and that the reaction between tresyl chloride and titanium directly proceeded without the use of any solvent. X-ray photoelectron spectroscopy (XPS) revealed that tresyl chloride reacted with the basic hydroxyl group of the titanium surface, forming tresyl chloride-activated titanium, that is, Ti-O-$SO_2CH_2CF_3$. Fibronectin could easily attach to the tresyl chloride-activated titanium surface. These findings indicate that the tresyl chloride technique is useful for the direct attachment of proteins onto titanium. However, more detailed information, such as the amount of attached fibronectin, is necessary to assess the effectiveness of the immobilization of fibronectin onto titanium, and the coupling mechanism between fibronectin and tresyl chloride-activated titanium is still unknown.

Recent studies have proven that the quartz-crystal microbalance-dissipation (QCM-D) technique is useful for evaluating surface-related processes in liquids, including protein adsorption and complementary activity on the biomaterials.[16–21] The effectiveness of the QCM-D technique for analyzing the adsorption of three model proteins on titanium oxide surfaces was compared with ellipsometry and optical waveguide light-mode spectroscopy.[22] The authors also pointed out that the mass calculated from the resonance frequency shift included both protein mass and water that was bound or hydrodynamically coupled to the protein adlayer. The amount of proteins adsorbed onto the biomaterials could be estimated by the Sauerbrey equation.[23] However, this estimation assumes that the adsorbed protein is rigid, and neglects its viscoelastic character. QCM-D measurement can be used to evaluate the viscoelastic character of adsorbed protein based on the dissipation (D).

The aim of the present study is to evaluate the effectiveness of the tresyl chloride treatment by estimating the amount of adsorbed fibronectin and to investigate the adsorption mechanism of fibronectin on tresyl chloride-activated titanium by using the QCM-D technique at the initial stage of adsorption.

MATERIALS AND METHODS

The QCM-D instrument (QCM-D300, Q-Sense AB, Göteborg, Sweden) was operated with AT-cut single crystal quartz sensors with a resonant frequency of 5 MHz. Titanium sputter-coated QCM-D crystals (14-mm diameter) were used as sensors. The active side of the titanium sensor crystals were cleaned prior to each adsorption measurement in a UV/ozone chamber for 15 min. Then, the surface of titanium sensor was completely covered with tresyl chloride (Fluka, Lot No. 42216/1 31001, bp 140–141°C, Buchs, Switzerland) without the use of any solvent, and reacted with tresyl chloride at 37°C for 2 days, according the previous method.[21] Preliminary experiments revealed that less than 2 days was not enough for the reaction of tresyl chloride and titanium. The tresyl chloride-activated titanium sensor was washed first with water–acetone (50/50 v/v), then pure acetone, and finally dried. The reaction scheme of titanium's basic hydroxyl group with tresyl chloride is shown in Figure 1. The adsorption behavior of fibronectin to untreated or tresyl chloride-activated titanium sensor was monitored by QCM-D technique. Before the measurement, the resonant frequency of the untreated and tresyl chloride-activated titanium sensors was found and checked.

The crystal resonant frequency (Δf) and the dissipation factor (ΔD) of the oscillator were measured simultaneously at a fundamental resonant frequency (5 MHz) and at a number of overtones, including 35 MHz. Monitoring the resonance behavior of piezoelectric oscillation enables measurements of the mass adsorbing on the surface of the oscillator in real time, usually as a function of the decrease in the resonant frequency (f). The frequency shift (Δf) is related to the adsorbed mass (Δm) according to the Sauerbrey relation.[23] At 5 MHz, a frequency shift of 1 Hz corresponds to a mass change of approximately 18 ng/cm^2. This relationship is strictly applicable to sufficiently thin, rigid films.[23]

A second measurement parameter, dissipation (D), gives qualitative information about the viscoelastic properties of the adsorbed layer. In brief, the dissipation factor D is related to the sum of the energy dissipated by all mechanism in the oscillating system and can be expressed as the following equation:[17]

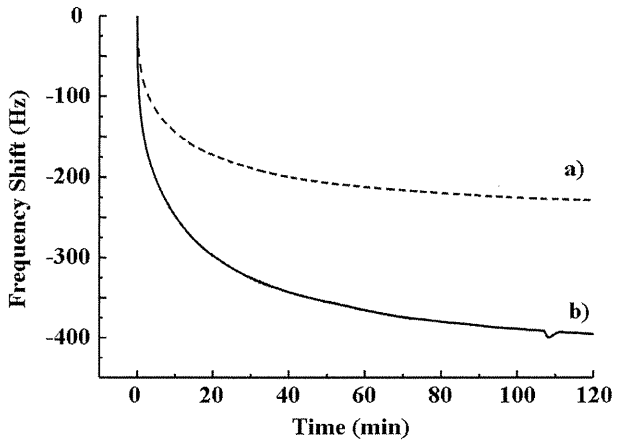

Figure 2. Frequency shift as a function of time for the exposure to fibronectin of (a) an untreated titanium QCM sensor and (b) a tresyl chloride-activated titanium QCM sensor.

$$D = E_{\text{dissipated}}/2\pi E_{\text{stored}}$$

$E_{\text{dissipated}}$ is the energy dissipated during one period of oscillation, and E_{stored} is the energy stored in the oscillating system. The increase in energy dissipation is proportional to the root of the product of viscosity and density. If the adsorbed layer is rigid, low ΔD value will be obtained.

Human cellular fibronectin (270 kDa, Upstate Biotechnology, Lake Placid, NY) was dissolved into PBS solution with pH = 7.4 at a concentration of 20 ppm. To thermally equilibrate the sample at 37 ± 0.05°C, the fibronectin/PBS solution was introduced into an axial flow chamber consisting of a T loop. The injection sequence into the QCM cell for an experimental run was 0.5 mL of distilled water, then 0.5 mL of PBS solution, followed by 2 mL of fibronectin/PBS solution (20 ppm). The pH of the camber was maintained at 7.4. The frequency shift and dissipation changes for the untreated and tresyl chloride-activated titanium sensors during a 120-min adsorption were obtained via QCM-D measurements. The temperature change was monitored during the measurement, and the difference of the temperature was maintained less than ± 0.02°C.

Each sensor, untreated or tresyl chloride-activated titanium sensor, was only used for the single measurement, and was not reused. Three runs of the measurement for untreated and tresyl chloride-activated titanium sensors were performed, respectively.

RESULTS

Figure 2 shows the frequency shift for the untreated and tresyl chloride-activated titanium sensors obtained via QCM-D measurements. The frequency curves in both sensors show a rapid decrease during the early stage of adsorption and, subsequently, a gentle decrease. The tresyl chloride-activated titanium sensor showed a faster and greater decrease in frequency compared to that of the untreated titanium sensor during a 120-min adsorption, indicating that the former had adsorbed a greater amount of fibronectin. Only a slight decrease in the frequency shift around 120-min adsorption means that the initial adsorption of fibronectin onto titanium or tresyl chloride-activated titanium was almost completed. Thus, the fibronectin adsorption at the initial stage was monitored during 120 min.

TABLE I. Estimated Amount of Fibronectin Adsorbate on Titanium

Substrate	Amount of Adsorbate (ng/cm^2)
Titanium	580 (84)
Tresyl chloride–activated titanium	1012 (124)

Note: standard deviation in parentheses.

Table I shows the amount of adsorbed fibronectin estimated by the Sauerbrey equation.[23] The amount of fibronectin adsorbed onto tresyl chloride-activated titanium is almost twice that adsorbed onto untreated titanium; Fisher's PLSD test reveals the significant difference ($p < 0.05$).

Figure 3 shows the dissipation shift obtained for the untreated and tresyl chloride-activated titanium sensors via QCM-D measurements. The dissipation value increased with time; that is, more energy was dissipated as protein adsorption proceeded. Fibronectin adsorbed onto tresyl chloride-activated titanium surface showed a greater shift of dissipation than that adsorbed onto untreated titanium.

Figure 4 shows the relationship between the frequency shift and the dissipation shift. The relationship is independent of time. The *D-f* plot reveals the difference in the adsorption behavior of fibronectin on untreated versus tresyl chloride-activated titanium, especially during the early stage of adsorption ($\Delta f < 120$, i.e., approximately 300 ng/cm^2 of adsorbed fibronectin). The dissipation shift for untreated titanium showed a very rapid increase during the first stage of adsorption, followed by a steady, gradual increase. In con-

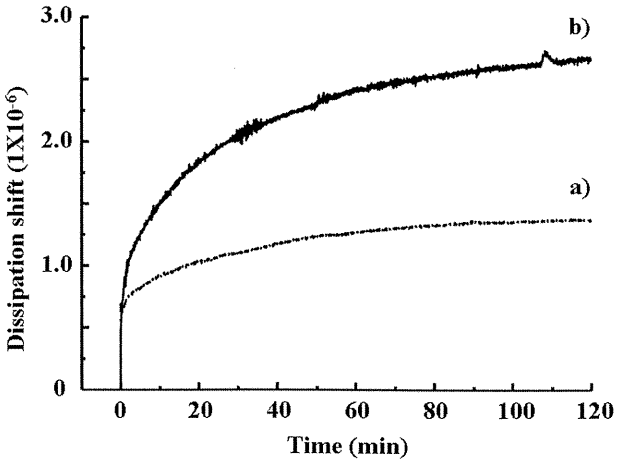

Figure 3. Dissipation shift as a function of time for the exposure to fibronectin of (a) an untreated titanium QCM sensor and (b) a tresyl chloride-activated titanium QCM sensor.

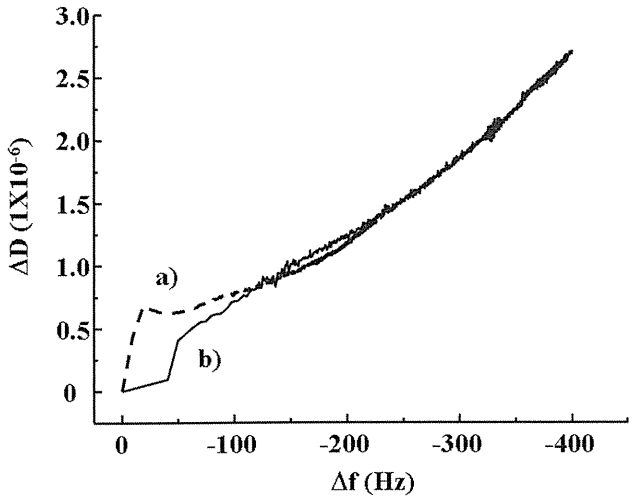

Figure 4. Dissipation shift as a function of frequency for the exposure to fibronectin of (a) an untreated titanium QCM sensor and (b) a tresyl chloride-activated titanium QCM sensor.

trast, the dissipation shift for tresyl chloride-activated titanium exhibited little increase during the first stage of adsorption, followed by a rapid increase, then ending with a gradual increase.

DISCUSSION

In the present study, the initial adsorption behavior of fibronectin on tresyl chloride-activated titanium was monitored by the QCM-D technique. Detailed information such as the amount of attached fibronectin or coupling mechanism between fibronectin and tresyl chloride-activated titanium is necessary to assess the effectiveness of the immobilization of fibronectin onto titanium.

There are several techniques for monitoring interactions between biomolecules, such as protein, and biomaterials. The surface plasmon resonance (SPR) technique, for example, is widely used for the analysis of protein adsorption on biomaterials. In brief, the SPR technique measures changes in the refractive index adjacent to the surface, whereas changes in the frequency of the QCM-D correspond to the changes in the amount of mass coupled to the surface. The application of SPR to the monitoring of the complement activation on titanium surface was reported.[24] The SPR technique is difficult because of the decrease in the light penetration of the modified SPR sensor chip. In contrast, the QCM-D technique can provide quantitative information about protein adsorption on titanium surfaces.

Based on the frequency shift, the amount of fibronectin adsorbed onto tresyl chloride-activated titanium is clearly greater than that adsorbed onto untreated titanium during the first 120 min of adsorption. Tresyl chloride-activated titanium yields approximately twice the amount of adsorbed fibronectin. Thus, tresyl chloride treatment enhances the adsorption of fibronectin onto titanium. However, the Sauerbrey equation employed is strictly applicable to sufficiently thin, rigid films. The QCM-D technique senses both the mass of the adsorbed film and the mass of the liquid coupled to the system.

It was reported that the immobilization of human fibronectin or RGDS (Arg-Gly-Asp-Ser) onto polymer surface enhanced the adhesion of mouse fibroblast with the increasing amount of immobilized fibronectin or RGDS and that the nature of substrate polymers influenced the cell attachment.[25,26] It is predicted that the greater amount of fibronectin adsorption on tresyl chloride-activated titanium will enhance the cell attachment compared with untreated titanium. Further study is necessary to clarify the biological activity such as cultured cell growth or tissue response of attached fibronectin on the tresyl chloride-activated titanium surface during the next series of experiments.

The measurement of dissipation reveals the viscoelastic properties of the adsorbed layer. The dissipation shift of untreated titanium differs from that of tresyl chloride-activated titanium during the 120-min adsorption, as shown in Figure 3. This is due to the difference in the adsorbed mass of fibronectin. The greater the amount of fibronectin adsorbed onto the surface, the higher the elasticity or viscosity of the adsorbed fibronectin and, hence, the higher the dissipation shift.

The relationship between frequency shift and dissipation shift (*D-f* plot) helps clarify the adsorption mechanism. The greater increase in the dissipation shift observed in the case of untreated titanium (Figure 4) indicates that fibronectin forms a softer and more elastic layer on untreated titanium than it does on tresyl chloride-activated titanium. This is attributable to the difference in the binding mechanism: In the first stage of adsorption, fibronectin forms a stronger bond with tresyl chloride-activated titanium than it does with untreated titanium. After this initial stage, that is, once the titanium surfaces are covered with fibronectin, the two types of titanium surfaces exhibit the same adsorption behavior, as evidenced by their overlapping *D-f* plots (Figure 4).

The effective sensor area for detecting frequency shift and dissipation shift was varied by overtone number in the present QCM-D system. For example, effective sensor area is about 41 mm^2 at the overtone number of 1, and about 12 mm^2 at the overtone number of 7, if 90% of signals come from that area. The dissipation shift showed no changes in spite of the change of the overtone number.

The following three coupling mechanisms between fibronectin and the hydroxyl groups of titanium (Figure 5) are postulated: (a) direct bond formation between titanium atoms and the nitrogen of fibronectin, (b) covalent bond formation between the oxygen of titanium's terminal hydroxyl group and the nitrogen of fibronectin, and (c) ionic interaction between the oxygen of titanium's terminal hydroxyl group and the nitrogen of fibronectin.[15] It has been reported that the hydroxyl group of silica or agarose was converted by reaction with tresyl chloride to —C—O—SO_2Cl, and then the tresylated hydroxyl group (—C—O—SO_2Cl) coupled to an enzyme due to a reaction between the tresylated hydroxyl group and the NH_2 group of the enzyme to form —

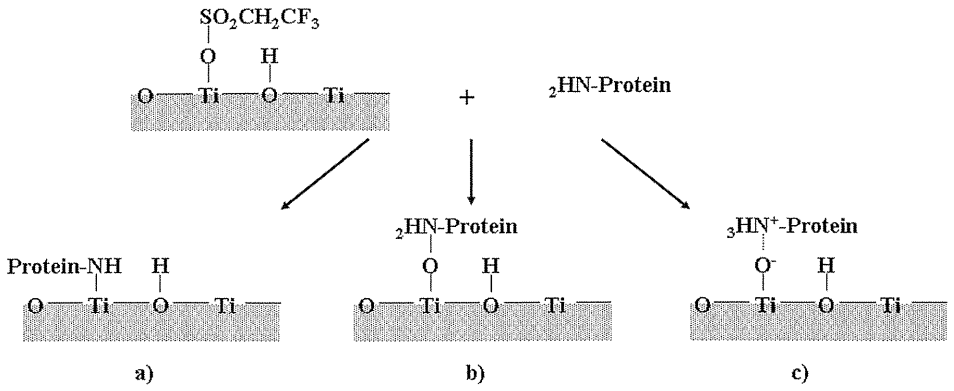

Figure 5. Postulated coupling mechanism between fibronectin and a tresyl chloride-activated titanium surface. (a) Direct bond formation between titanium atom and N of fibronectin. (b) Covalent bond formation between O of the titanium terminal OH and N of fibronectin. (c) Ionic interaction between O of the titanium terminal OH and N of fibronectin.

C—NH—enzyme.[11,12] In the case of Ti—OH, however, mechanisms (a) and (b) are unlikely to occur during the first stage of adsorption. Based on the *D-f* plots (Figure 4), tresyl chloride treatment is presumed to enhance the ionic interaction between the oxygen of the terminal hydroxyl groups of titanium and the nitrogen of fibronectin [mechanism c in Figure 5]. The tresyl chloride treatment presumably increases the ionic characteristics of the oxygen of titanium's terminal hydroxyl group, although further studies would be needed to elucidate its electrical properties.

However, other factors, such as changes of the conformation of fibronectin during adsorption and the different adsorption–desorption behavior between the tresyl chloride-activated titanium sensor and the titanium sensor should be considered for the *D-f* plot. If the conformation of fibronectin changes during adsorption, it would result in a smaller slope in the *D-f* plot. The surface of the tresyl chloride-activated titanium could possibly cause changes in the conformation of the fibronectin through the ionic interaction between the oxygen of the terminal hydroxyl groups of titanium and the nitrogen of fibronectin.

The stability of the fibronectin–titanium bond in an aqueous environment is significant for the performance of dental implants. Previous results confirmed that the fibronectin attached onto the tresyl chloride-activated titanium remained after 60 min of ultrasonic cleaning in a double-distilled water.[15] The influence of pH and/or ionic strength on the adsorption and/or desorption of fibronectin to tresyl-activated titanium and adsorption and/or desorption kinetics will be evaluated.

Monitoring of adsorption behavior besides fibronectin, such as collagen or laminin, should be further investigated. The differences of their reactivity toward tresyl chloride-activated titanium or those of their steric conformation in buffered solution will influence the adsorption behavior, that is dissipation and frequency shift. Moreover, future biochemical analysis of the interaction of the fibronectin and titanium surface should be important.

In conclusion, QCM-D measurements revealed that tresyl chloride treatment enhanced the amount of initial attachment of fibronectin onto titanium and promoted a stronger bond between fibronectin and titanium during the early stage of adsorption. Few report the relationship between the cell activity and the amount of immobilized fibronectin or the different coupling mechanism of fibronectin onto titanium. It is expected that the measurement of the interaction of fibronectin and tresyl chloride-activated titanium is useful for the future biological experiment. The QCM-D technique, which is effective for monitoring interactions between biomaterials and biomolecules such as protein, can shed new light on the adsorption mechanism of fibronectin in addition to providing a quantitative analysis of fibronectin adsorption.

REFERENCES

1. Horbett TA. Principles underlying the role of adsorbed plasma proteins in blood interactions with foreign materials. Cardiovasc Pathol 1993;2:137S–148S
2. Wälivaara B, Aronsson BO, Rodahl M, Lausmaa J, Tengvall P. Titanium with different oxides: *in vitro* studies of protein adsorption and contact activation. Biomaterials 1994;15:827–834.
3. Puleo DA, Nanci A. Understanding and controlling the bone–implant interface. Biomaterials 1999;20:2311–2321.
4. Brånemark PI, Hansson BO, Adell R, Breine U, Lindström J, Hallen O, Ohman A. Osseointegrated implants in the treatment of the edentulous jaw: Experience from a 10-year period. Scad J Plast Reconstr Surg 1977;II(Suppl):16.1–132.
5. Albrektsson T, Brånemark PI, Hansson HA, Lindström J. Osseointegrated titanium implant. Requirements for ensuring a long-lasting, direct bone-to-implant anchorage in man. Acta Orthop Scand 1981;52:155–170.
6. Malmstrom HS, Fritz ME, Timmis DP, van Dyke TE. Osseointegrated implant treatment of a patient with rapidly progressive periodontitis: A case report. J Periodontol 1990;61:300–304.
7. Mombelli A, Lang NP. The diagnosis and treatment of periimplantitis. Periodontology 2000;17:63–76.
8. Dessau W, Sasse J, Timpl R, Jilek F, von der Mark K. Synthesis and extracellular deposition of fibronectin in chondrocyte cultures. Response to the removal of extracellular cartilage matrix. J Cell Biol 1978;79:342–355.
9. Hassell JR, Pennypacker JP, Kleinman HK, Pratt RM, Yamada KM. Enhanced cellular fibronectin accumulation in chondrocytes treated with vitamin A. Cell 1979;17:821–826.

10. Seitz TL, Noonan KD, Hench LL, Noonan NE. Effect of fibronectin on the adhesion of an established cell line to a surface reactive biomaterial. J Biomed Mater Res 1982;16:195–207.
11. Nilsson K, Mosbach K. Immobilization of enzymes and affinity ligands to various hydroxyl group carrying supports using highly reactive sulfonyl chlorides. Biochem Biophys Res Commun 1981;102:449–457.
12. Nilsson K, Mosbach K. Tresyl chloride-activated supports for enzyme immobilization. Meth Enzymol 1987;135:65–78.
13. Boehm HP. Acidic and basic properties of hydroxylated metal oxides surface. Faraday Discuss Faraday Soc 1971;52:264–275.
14. Hayakawa T, Yoshinari M, Nemoto K: Direct attachment of fibronectin to tresyl chloride-activated titanium. J Biomed Mater Res A 2003;67:684–688.
15. Hayakawa T, Yoshinari M, Nagai M, Yamamoto M, Nemoto K. X-ray photoelectron spectroscopic studies of the reactivity of basic terminal OH of titanium towards tresyl chloride and fibronectin. Biomed Res 2003;24:223–230.
16. Rodahl M, Höök F, Fredriksson C, Keller CA, Krozer A, Brzezinski P, Voinova M, Kasemo B. Simultaneous frequency and dissipation factor QCM measurements of biomolecular adsorption and cell adhesion. Faraday Discuss 1997;107:229–246.
17. Vinkinge TP, Hansson KM, Sandström P, Liedberg Bo, Lindahl TL, Lundström I, Tengvall P, Höök F. Comparison of surface plasmon resonance and quartz crystal microbalance in the study of whole blood and plasma coagulation. Biosens Bioelectron 2000;15:605–613.
18. Andersson J, Larsson R, Richter R, Ekdahl KN, Nilsson B. Binding of a model regulator of complement activation (RCA) to a biomaterial surface: surface-bound factor H inhibits complement activation. Biomaterials 2001;22:2435–2443.
19. Glasmäster K, Larsson C, Höök F, Kasemo B. Protein adsorption on supported phospholipid bilayers. J Colloid Interface Sci 2002;246:40–47.
20. Andersson A-S, Glasmästar K, Sutherland D, Lidberg Ulf, Kasemo B. Cell adhesion on supported lipid bilayers. J Biomed Mater Res A 2003;64:622–629.
21. Hayakawa T, Yoshinari M, Nemoto K. Characterization and protein-adsorption behavior of deposited organic thin film onto titanium by plasma polymerization with hexamethyldisiloxane. Biomaterials 2004;25:119–127.
22. Höök F, Vörös J, Rodahl M, Kurrat R, Böni P, Ramsden JJ, Textor M, Spencer ND, Tengvall P, Gold J, Kasemo B. A comparative study of protein adsorption on titanium oxide surfaces using *in situ* ellipsometry, optical waveguide lightmode spectroscopy, and quartz crystal microbalance/dissipation. Colloids Surf B Biointerfaces 2002;24:155–170.
23. Sauerbrey G. Verwendung von Schwingquarzen zur Wägung dünner Schichten und zur Mikrowägung. Z Phys 1959;155: 206–222.
24. Sellborn A, Andersson M, Fran C, Gretzer C, Elwing H. Methods for research on immune complement activation on modified sensor surfaces. Colloids Surf B 2003;27:295–301.
25. Ito Y, Imanishi Y. Attachment and proliferation of fibroblast cells on polyetherurethane urea derivatives. Biomaterials 1987; 8:464–472.
26. Zheng JI, Ito Y, Imanishi Y. Cell growth on insulin/RGDS-coimmobilized poly(methyl methacrylate) films. J Biomater Sci Polymer Ed 1995;7:515–522.

Regulation of Rat Bone Sialoprotein Gene Transcription by Enamel Matrix Derivative

Emi Shimizu,* Yu Nakajima,* Naoko Kato,* Youhei Nakayama,* Ryoichiro Saito,* Hiroshi Samoto,* and Yorimasa Ogata*

Background: Enamel matrix derivative (EMD) has recently been developed for use as a periodontal regenerative treatment. While EMD is believed to induce regeneration of periodontal tissue, the precise mechanism is not known. Bone sialoprotein (BSP), an early phenotypic marker of osteoblast differentiation, has been implicated in the nucleation of hydroxyapatite during bone formation. In this study, we examined the ability of EMD to regulate BSP gene transcription in osteoblast-like cells.

Methods: To determine the molecular basis of the transcriptional regulation of BSP gene transcription by EMD, we conducted Northern hybridization, transient transfection analyses with chimeric constructs of the rat BSP gene promoter linked to a luciferase reporter gene, and gel mobility shift assays.

Results: Using the osteoblastic cell line ROS 17/2.8, we determined that BSP mRNA levels increased ~2.8-fold by EMD. In transient transfection analyses, EMD (50 μg/ml, 12 hours) increased luciferase activities of pLUC4 (nt –425 to +60) and pLUC5 (nt –801 to +60), transfected into ROS 17/2.8 cells. Within the pLUC4 and 5, a homeodomain binding element (HOX) and a transforming growth factor (TGF)-β activation element (TAE) are present. Gel mobility shift assays with radiolabeled HOX and TAE ds-oligonucleotides revealed increased binding of nuclear proteins from EMD stimulated ROS 17/2.8 cells.

Conclusion: These studies have, therefore, identified EMD response elements in the rat BSP gene promoter that may mediates the effects of EMD on BSP gene transcription. *J Periodontol 2004;75:260-267.*

KEY WORDS

Animal studies; enamel matrix derivative; periodontal regeneration; sialoproteins; transcription, genetic.

* Departments of Periodontology, Endodontics, and Research Institute of Oral Science, Nihon University School of Dentistry at Matsudo, Chiba, Japan.

Enamel matrix derivative (EMD),† the acid extracts of porcine cheese-like enamel matrix, has been developed as a clinical treatment to promote periodontal regeneration.[1] Ninety percent of the protein in the EMD is amelogenins and the remaining 10% is non-amelogenin enamel matrix proteins such as enamelins, tuftelin, amelin, and ameloblastin.[2-5] Histological studies of monkeys, dogs, and humans have shown that treatment with EMD results in the formation of a new layer of acellular cementum with inserting collagen fibers and the formation of new alveolar bone.[6-9] The results from a controlled clinical trial and a case series study have also demonstrated that the treatment of intrabony periodontal defects with EMD leads to significant gain of clinical attachment level and bone regeneration as observed on the radiographs.[10,11]

Bone sialoprotein (BSP) is a prominent component of the mineralized bone matrix[12] that has been implicated in tissue mineralization.[13,14] Studies on the developmental expression of BSP have shown BSP mRNA is expressed at high levels by osteoblasts at the onset of bone formation[15] and under steady-state conditions in vitro, BSP nucleates hydroxyapatite crystal formation,[16] indicating a role for this protein in the initial mineralization of bone. Thus, regulation of the BSP gene appears to be important in the differentiation of osteoblasts and for bone matrix

† Emdogain, Biora AB, Malmö, Sweden.

mineralization. BSP is also expressed in several pathologies in which mineralization occurs, including malignant breast cancer where it is associated with the formation of ectopic hydroxyapatite microcrystals.[17,18] Thus, regulation of BSP gene transcription appears to be important in the differentiation of osteoblasts, for bone matrix mineralization, and for pathologic mineralization. To study the transcriptional regulation of BSP gene expression, we and other groups have cloned and sequenced the rat, human, and mouse BSP gene promoters,[19-22] which are highly conserved within a 370 bp proximal region. This region includes an inverted TATA element[23] overlapping a vitamin D response element[24] and an inverted CCAAT box (–50 to –46), which is required for basal transcriptional activity.[25,26] In addition, a cAMP response element (CRE; –75 to –68),[27] a fibroblast growth factor-2 response element (FRE; –92 to –85),[28] a pituitary-specific transcription factor-1 (Pit-1) motif (–111 to –105)[29] which mediates the stimulatory effects of parathyroid hormone and a homeodomain binding element (HOX; –199 to –192),[30] have been characterized. Further upstream in the rat promoter a TGF-β activation element (–499 to –485)[31] and a glucocorticoid response element (–920 to –906),[32] overlapping an AP-1 site (–921 to –915)[33] have also been identified.

Although EMD is used clinically, little is known regarding its effects on bone metabolism. The aim of the present study was to evaluate the ability of EMD to regulate osteoblast specific gene expression such as BSP. In this study we show that EMD regulates BSP expression in osteoblast-like ROS 17/2.8 cells through HOX and TAE elements in the rat BSP promoter.

MATERIALS AND METHODS

Cell Culture

The rat clonal cell line ROS 17/2.8 was used in these studies as an osteoblastic cell line that synthesizes BSP.[28,34] Rat stromal bone marrow cells (SBMC) were kindly provided by Dr. S. Pitaru (Tel Aviv University, Israel).[35] Cells were grown to confluence in 60 mm tissue culture dishes in alpha minimum essential medium (α-MEM)‡ containing 10% (vol/vol) fetal bovine serum (FBS),‡ then cultured in α-MEM without serum and incubated with or without EMD (50 μg/ml) for time periods extending over 3 to 12 hours. RNA was isolated from triplicate cultures at various time intervals and analyzed for the expression of BSP mRNA by Northern hybridization as described below.

Northern Hybridization

Twenty μg aliquots of total RNA were fractionated on 1.2% agarose gel and transferred onto a Hybond-N+ membrane,§ as described previously.[31] Hybridizations were performed at 42°C with either a ^{32}P-labeled rat BSP or a rat glyceraldehyde-3-phosphate dehydrogenase (GAPDH) cDNA probe. Following hybridization, membranes were washed four times for 5 minutes each at 21°C in 300 mM sodium chloride, 30 mM trisodium citrate pH 7.0 containing 0.1% sodium dodecyl sulfate (SDS). This was followed by two 20 minute washes at 55°C in 15 mM sodium chloride, 1.5 mM trisodium citrate pH 7.0, 0.1% SDS. The hybridized bands, representing the two polyadenylated forms (1.6-kb and 2.0-kb) of rat BSP mRNA, were scanned in a bioimaging analyzer‖ and normalized to the expression of glyceraldehyde-3-phosphate dehydrogenase (GAPDH).

Transient Transfection Assays

Exponentially growing ROS 17/2.8 cells were used for transfection assays. Twenty-four hours after plating, cells at 50% to 70% confluence were transfected using a lipofectamine reagent.¶ The transfection mixture included 1 μg of a luciferase (LUC) construct[32] and 2 μg pSV-ß-galactosidase (ß-gal) vector# as an internal control to normalize for individual transfection efficiencies. Two days post-transfection, cells were deprived of serum for 12 hours and each test compound was added and the cells cultured for a further 12 hours prior to harvesting. The luciferase assay** was performed according to the supplier's protocol using a light reader†† to measure the luciferase activity.

Gel Mobility Shift Assays

Confluent ROS 17/2.8 cells in T-75 flasks incubated for 3 and 12 hours with EMD in α-MEM without serum were used to prepare nuclear extracts as described previously.[28,29,31] Double-stranded oligonucleotides encompassing the inverted CCAAT (nts –61 to –37, 5′-CCGTGACCGTG**ATTGG**CTGCTGAGA), homeodomain binding element (HOX; nts –204 to –179, 5′-TCCTCAGCCT**TCAATTAAA**TCCCACA), and TGF-β activation element (TAE; nts –506 to –482, 5′-CAAAGCC**TTGGC**AGCCC**GGCTG**GCT) in the rat BSP promoter were prepared commercially,‡‡ while consensus AP2 (5′-GATCGAACTGACCGCCCGCG-GCCCGT) and consensus NF1 (5′-CCTTTGGCAT-GCTGCCAATAT) were purchased.# For gel shift analysis the double-stranded-oligonucleotides were end-labeled with [γ-^{32}P]ATP and T4 polynucleotide kinase. Nuclear protein extracts (3 μg) were incubated for 20 minutes at room temperature (RT; 21°C) with 0.1 pM radiolabeled double-stranded-oligonucleotide in buffer containing 50 mM KCl, 0.5 mM EDTA, 10

‡ Gibco BRL Life Technologies, Tokyo, Japan.
§ Amersham Biosciences Corp., Piscataway, NJ.
‖ Fuji film, Fuji BAS 2000, Tokyo, Japan.
¶ Invitrogen Corp., Carlsbad, CA.
# Promega Corp., Madison, WI.
** PicaGene, Toyo Inki, Tokyo, Japan.
†† Luminescence BLR201, Aloka, Tokyo, Japan.
‡‡ Bio-Synthesis, Inc., Lewisville, TX.

mM Tris-HCl (pH 7.9), 1 mM DTT, 0.04% Nonidet P-40, 5% glycerol, and 1 μg poly (dI-dC). Following incubation, the protein-DNA complexes were resolved by electrophoresis on 5% non-denaturing acrylamide gels (38:2 acrylamide/bis acrylamide) run at 150 V at RT. Following electrophoresis, the gels were dried and autoradiograms prepared and analyzed using a bioimaging analyzer.‖

Statistical Analysis

Triplicate samples were analyzed for each experiment, and experiments replicated to ensure consistency of the responses to EMD. Significant differences between control and EMD treatment were determined using the Student *t* test.

RESULTS

Stimulation of BSP mRNA Expression in ROS 17/2.8 Cells

To study the regulation of BSP expression by EMD, we performed Northern hybridization analysis of total RNA extracted from osteoblastic ROS 17/2.8 cells. First, a dose-response relation for EMD induction of BSP was established by treating the ROS 17/2.8 cells with different concentrations EMD for 12 hours. EMD increased BSP transcripts at 1 to 200 μg/ml and had a maximal effect between 50 and 200 μg/ml (Fig. 1A). Thus, 50 μg/ml EMD was used to determine the time course of BSP mRNA expression (Fig. 1B). EMD up-regulated BSP mRNA accumulation markedly in ROS 17/2.8 cells. A 2.8-fold stimulation was evident 12 hours after the addition of EMD, whereas no effect on GAPDH mRNA was observed.

Transient Transfection Analysis of Rat BSP Promoter Constructs

Since the effects of EMD likely involve transcription factor interaction in the promoter region of the rat BSP gene, subsequent studies were directed at transcriptional regulation utilizing chimeric constructs prepared from the promoter from the rat BSP gene. Transient transfection of chimeric constructs encompassing different regions of the rat BSP promoter ligated to a luciferase reporter gene (pLUC1 to pLUC5) were performed in ROS 17/2.8 cells. The results of transfection assays (Fig. 2) indicated a ~1.7 (1.7 ± 0.14) -fold increase in transcription with the construct pLUC4 and a ~2.3 (2.3 ± 0.18) -fold increase in pLUC5, encompassing nucleotides –425 to +60 and –801 to +60, after 12 hours treatment with 50 μg/ml EMD. Within the DNA sequence that is unique to pLUC4 and pLUC5, a HOX site (TCAATTAAAT, between nts –194 to –185) and a TGF-β activation element (TAE; CTTGGCAGCCCGGCTGG, between nts –500 to –484) overlapping an AP-2 site are present (Fig. 3).

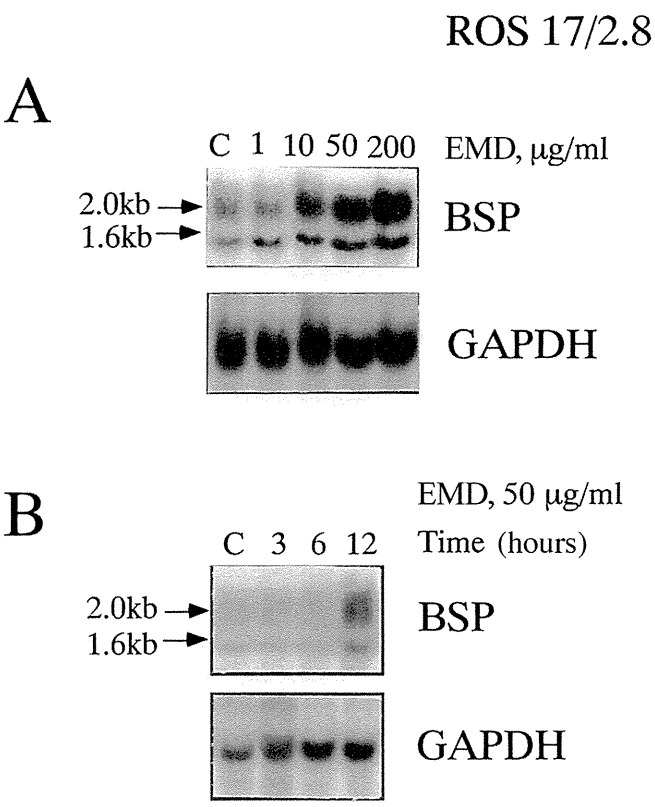

Figure 1.
Northern hybridization analysis of EMD effects on BSP mRNA expression. ***A)*** *Dose-response effect of EMD on BSP mRNA levels in the osteoblastic cell line ROS17/2.8 treated for 12 hours. At 1 to 200 μg/ml, EMD increased BSP mRNA with a maximal effect at 50 μg/ml. This optimal level of EMD was used to determine the time course of BSP mRNA expression.* ***B)*** *Twelve-hour time course revealed an increase in BSP mRNA at 12 hours after the administration of 50 μg/ml EMD to ROS17/2.8 cells. Total RNA was isolated from triplicate cultures harvested after incubation times of 3, 6, and 12 hours, and used for Northern hybridization analysis using a ^{32}P-labeled rat BSP DNA probe and a GAPDH DNA probe.*

Gel Mobility Shift Assays

To identify nuclear proteins that bind to binding elements in pLUC4 and pLUC5, double-stranded oligonucleotides were end-labeled and incubated with nuclear proteins (3 μg) extracted from confluent ROS 17/2.8 cells that were either not treated (control) or treated with 50 μg/ml EMD for 3 and 12 hours (Figs. 4 and 5). With nuclear extracts from confluent control cultures of ROS 17/2.8 cells, a shift of HOX-protein complex was evident (Fig. 4, lane 4). After stimulation by EMD (50 μg/ml) for 3 and 12 hours, DNA binding activity was increased (Fig. 4, lanes 5 and 6). When we used the inverted CCAAT sequence as a probe, the DNA-NF-Y protein complex[25,26] did not change after EMD stimulation (Fig. 4, lanes 1 through 3). That the HOX-protein complex represents specific interac-

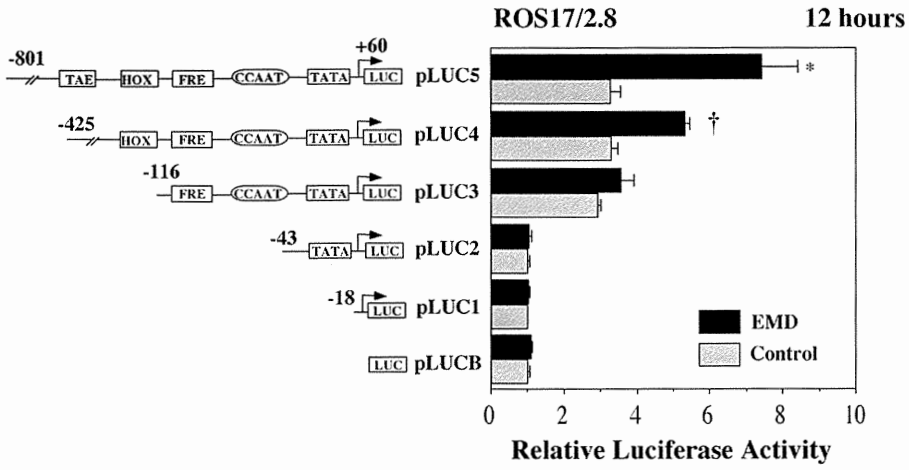

Figure 2.
*EMD up-regulates BSP promoter activity. Transient transfections of ROS 17/2.8 cells, in the presence or absence of EMD (50 μg/ml) for 12 hours, were used to determine transcriptional activity of chimeric constructs that included various regions of the BSP promoter ligated to a luciferase reporter gene. The results of transcriptional activity obtained from three separate transfections with constructs; pLUC basic (pLUCB) and pLUC1 to pLUC5 have been combined and the values expressed with standard errors. Significant differences from control (relative luciferase activity of pLUCB): * P <0.1; † P <0.01.*

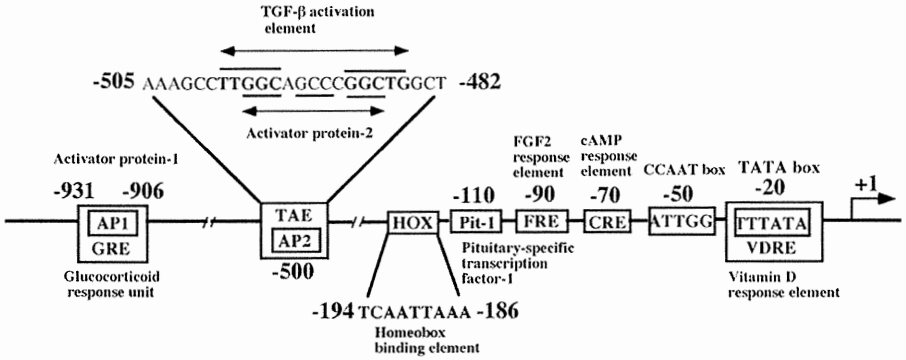

Figure 3.
Sites of the homeodomain binding element (HOX) and TGF-β activation element (TAE) in the rat BSP promoter. A diagrammatic representation of the BSP gene promoter showing the location of the HOX and TAE, which have been expanded, together with the relative positions of the inverted TATA and CCAAT boxes, and a number of putative enhancer elements: vitamin D response element (VDRE) that overlaps the inverted TATA box, cAMP (CRE), FGF2 response element (FRE), and pituitary-specific transcription factor-1 (Pit-1) motif that are present within a highly conserved region (nt +1 to −370) of the promoter. A glucocorticoid response element (GRE) overlapping an AP1 is also shown located further upstream.

tion was indicated by competition experiments in which a 40-fold excess of HOX reduced the amount of complex formation (Fig. 4, lane 7). In contrast, TAE (40-fold) did not compete with complex formation (Fig. 4, lane 8). While 40-fold excess of the inverted CCAAT slightly reduced complex formation (Fig. 4, lane 9), this might have been caused by CCAAT (ATTGG) which resembles the HOX sequence (TCAATTAAAT). TAE was identified as containing the 5′-portion of the NF-1 canonical sequence (TTGGC) overlapping a putative AP-2 site.[31]

When the TAE was incubated with the nuclear extract from control (no treatment) and EMD treatment (3 hours) cultures of ROS 17/2.8 cells, no significant binding was evident (Fig. 5, lanes 1 and 2). After stimulation by EMD (50 μg/ml) for 12 hours, DNA binding activity was increased (Fig. 5, lane 3). The TAE-protein complex representing specific interaction was indicated by competition experiments in which 40-fold excess of TAE reduced the amount of complex formation (Fig. 5, lane 4). In contrast, consensus sequences for NF1 and AP2 (40-fold) did not compete with complex formation (Fig. 4, lanes 5 and 6). When we used the consensus AP2 and consensus NF1 as probes, the DNA-protein complexes did not change after EMD treatment (Fig. 4, lanes 10 through 12; Fig. 5, lanes 7 through 9). While NF1-protein complex competed with 40-fold excess of NF1 (Fig. 5. Lane 11), TAE and AP2 (40-fold excess) did not compete with complex formation (Fig. 5, lanes 10 and 12).

DISCUSSION

Our results show that EMD treatment of ROS 17/2.8 cells increases the steady-state level of BSP mRNA approximately 2.8-fold (Fig. 1). Notably, the magnitude of the EMD effect on the steady-state levels of BSP mRNA was similar to the level of stimulation (pLUC5; ~2.3-fold) of promoter activity by EMD. These results suggest that EMD regulates BSP mRNA expression, at least in part, via transcriptional control. When we used rat stromal bone marrow cells (SBMC)[35] for luciferase assays to see the effect of EMD on BSP transcription, EMD stimulated BSP transcription (unpublished data). Therefore, EMD increases BSP expression not only in transformed ROS 17/2.8 cells, but also in normal osteoprogenitors.

Ninety percent of the protein in EMD is amelogenin, and the remaining 10% is non-amelogenin enamel matrix proteins, serum protein, and growth factors.[1-3,36] Kawase et al. reported that EMD contains TGF-β1 and

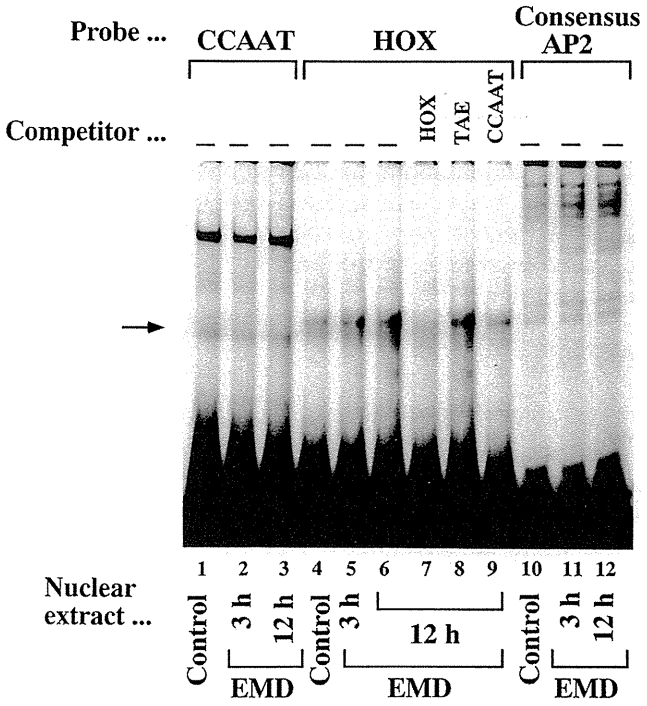

Figure 4.
EMD increases the DNA binding activity recognized by the HOX sequence. Radiolabeled double-stranded inverted CCAAT (−61 CCGTGACCGTGATTGGCTGCTGAGA −37), HOX (−204 TCCTCAGCCTTCAATTAAATCCCACA −179), and consensus AP2 (GATCGAACTGACCGCCCGCGGCCCGT) oligonucleotides were incubated for 20 minutes at 21°C with nuclear protein extracts (3 μg) obtained from ROS 17/2.8 cells incubated without (lanes 1, 4, and 10) or with EMD (50 μg/ml) for 3 hours (lanes 2, 5, and 11) and 12 hours (lanes 3, 6~9, and 12). Competition reactions were performed using a 40-fold molar excess of unlabeled HOX, TAE, and CCAAT. DNA-protein complexes were separated on 5% polyacrylamide gel in low-ionic-strength Tris-borate buffer, dried under vacuum, and exposed to an imaging plate for quantitation using a bioimaging analyzer.

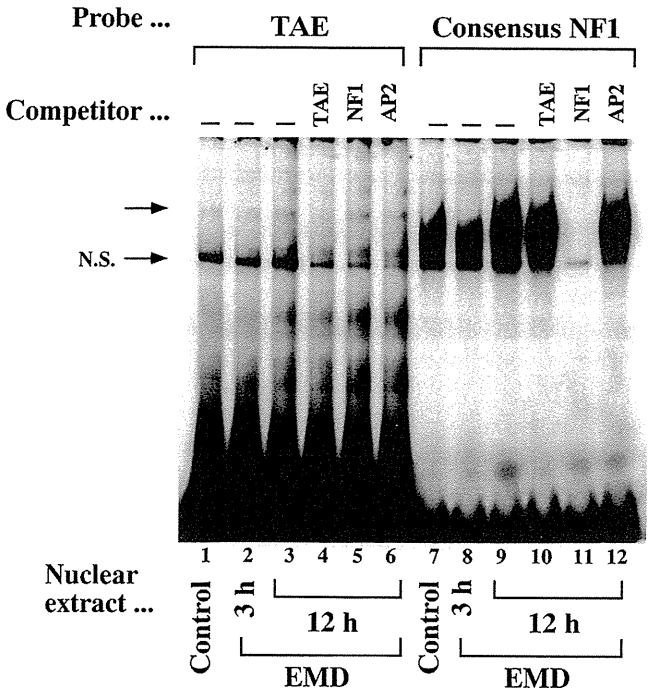

Figure 5.
EMD increases the DNA binding activity recognized by TAE sequence. Radiolabeled double-stranded TAE (−506 CAAAGCCTTGGCAGCCCGGCTGGCT −482) and consensus NF1 (CCTTTGGCATGCTGCCAATAT) oligonucleotides were incubated for 20 minutes at 21°C with nuclear protein extracts (3 μg) obtained from ROS 17/2.8 cells incubated without (lanes 1 and 7) or with EMD (50 μg/ml) for 3 hours (lanes 2 and 8), and 12 hours (lanes 3 through 6 and 9 through 12). Competition reactions were performed using a 40-fold molar excess of unlabeled TAE, consensus NF1 and AP2. DNA-protein complexes were separated on 5% polyacrylamide gel in low-ionic-strength Tris-borate buffer, dried under vacuum, and exposed to an imaging plate for quantitation using a bioimaging analyzer.

stimulates phosphorylation of the mitogen-activated protein (MAP) kinase family and nuclear accumulation of smad2 in both human oral epithelial cells and gingival fibroblasts.[36] EMD inhibited cell proliferation, stimulated alkaline phosphatase activity, and induced osteocalcin production in human osteoblast-like MG63 cells.[37] This suggests that EMD has characteristics similar to bone morphogenetic protein (BMP) and TGF-β. On the other hand, EMD increased cell proliferation and had no effect on alkaline phosphatase activity in pre-osteoblastic cell line 2T9 cells.[37] Therefore, the effect of EMD may be independent of differentiation of immature osteoblastic cells.

EMD increased luciferase activity ~1.7-fold in pLUC4 and ~2.3-fold in pLUC5 constructs. These data suggest that the response element existing in pLUC5 might further enhance pLUC4 promoter activity. The specific sequence in pLUC4 is between −116 and −425, and the identified response element in this region is a HOX.[19,30] Formation of the vertebrate body is controlled in part by homeodomain transcription factors that regulate the temporal appearance of location of preosseous tissues along the vertebral column.[38,39] Two homeobox gene products, the Dlx and Msx family of homeobox proteins, may regulate development of mineralized tissues including bone, cartilage, and tooth.[40] Depending on the anatomical site and stage of development, BMP and TGF-β can initiate osteogenesis. Homeobox-containing gene expressions are transiently found during BMP2-induced ectopic bone formation at the onset of endochondral mineralization.[41] EMD may thus contain BMP activities. We found a protein in nuclear extracts of ROS 17/2.8 cells that selectively bound to the HOX and which was up-regulated by EMD (Fig. 4) in association with increased transcription (Fig. 2). That the protein binds specifically to the HOX was demonstrated by competition gel

mobility shift assays (Fig. 4). Dlx5 gene is selectively up-regulated during development of the osteoblast phenotype and osteocalcin gene expression may be regulated by Dlx5.[39] Benson et al. demonstrated that the Dlx5 homeoprotein binds to the HOX element in the mouse BSP gene promoter which is required for osteoblast-selective expression of BSP.[30] However, recently, two groups showed that tissue-specific expression of BSP gene was not regulated by Dlx5.[42,43] Further study of the transcription factor binding to HOX element in the BSP promoter is required.

The specific sequence in pLUC5 is between –425 and –801, and the identified response element in this region is a TAE.[31] TGF-β1 is a member of the transforming growth factor β (TGF-β) superfamily of cytokines that control growth and differentiation in a wide variety of cell types.[44] Although platelets are the most concentrated source of TGF-β1 in the body,[45] the high yield of TGF-β1 from bone indicates that the greatest amount of TGF-βs are present in skeletal tissues.[46] TGF-β1 released by platelets in fracture sites, or from the bone matrix by osteoclasts during bone remodeling, can stimulate the formation of bone extracellular matrix, but not mineralization, which appears to be suppressed by the downregulation of alkaline phosphatase activity.[47] However, in combination with the related BMPs, which stimulate alkaline phosphatase,[48] TGF-β1 may promote the formation of mineralized bone.[49] We have previously reported that TAE in the rat BSP gene promoter mediates the stimulatory effects of TGF-β1 on BSP transcription.[31] The TAE sequence in the rat BSP promoter is very similar to TGF-β response elements found in the mouse α2(I) collagen promoter between nts –308 and –292,[50] in the rat α1(I) collagen promoter between nts –1643 and –1627,[51,52] and in the human plasminogen activator inhibitor promoter between nts –562 and –546.[53] In studies of the mouse α2(I) collagen promoter, Rossi et al.[50] concluded that an NF-1 binding site was the target of transcriptional activation by TGF-β1, whereas closely associated sites for NF-1 and a USF basic helix-loop-helix transactivator have been implicated as targets for TGF-β1 regulation in the plasminogen activator inhibitor promoter.[53] While there are several NF-1-like binding sequences within the rat BSP promoter, they do not appear to be responsive to TGF-β1. Ritzenthaler et al.[52] reported that TGF-β activates rat α1(I) collagen transcription through a TAE site which has similarities to an NF-1 site but recognizes a nuclear protein that is similar to but distinct from NF-1 protein. Similar to the rat α1(I) collagen promoter, the TAE region in rat BSP promoter comprises an NF-1-like sequence that overlaps a putative AP-2 element. DNA binding and competition studies have shown that the binding of the nuclear proteins to the TAE in ROS 17/2.8 cells was increased following EMD stimulation (Fig. 5) and formation of the DNA-protein complex did not compete by NF-1 and AP2 consensus oligonucleotide (Fig. 5, lanes 5 and 6), suggesting that EMD might contain TGF-β1 and induced TAE binding activities. In addition, the TAE sequence did not compete with NF-1 protein binding to the NF-1 consensus sequence (Fig. 5, lane 10). Thus, the TAE-binding protein is clearly different from the NF-1 binding protein, as observed in studies of the TAE in the rat α1(I) collagen promoter.[51,52]

In this study, we have shown that EMD induced BSP gene expression in osteoblast-like ROS 17/2.8 cells and rat stromal bone marrow cells, and that these effects might be dependent on BMP and TGF-β actions. Our results suggest that EMD can have a positive effect on periodontal regeneration, such as formation of a new connective tissue attachment and new alveolar bone. Continued studies will be targeted at defining the transcription factors in EMD responsible for promoting mineralization.

ACKNOWLEDGMENTS

This work was supported in part by the grants-in-aid for Scientific Research 09771650, 12671865, and 14571989 from the Ministry of Education, Science, and Culture of Japan; Nihon University Research Grant (Interdisciplinary General Joint Research Grant for 2002 and 2003, and General Individual Research Grant for 2001); and Suzuki Memorial Grant of Nihon University School of Dentistry at Matsudo (General Individual Research Grant for 2002 and 2003). Research for the Frontier Science (The Ministry of Education, Science, Sports and Culture), and by a Grant from the Ministry of Education, Culture, Sports, Science and Technology to promote 2001-Multidisciplinary Research Project (in 2001-2005).

REFERENCES

1. Gestrelius S, Andersson C, Johansson A, Persson E, Brodin A, Rydhag L, Hammarström L. Formation of enamel matrix derivative for surface coating; kinetics and cell colonization. *J Clin Periodontol* 1997;24:678-684.
2. Termine JD, Belcourt AB, Christner PJ, Conn KM, Nylen MU. Properties of dissociatively extracted fetal tooth matrix proteins. I. Principle molecular species in developing bovine enamel. *J Biol Chem* 1980;255:9760-9768.
3. Ogata Y, Shimokawa H, Sasaki S. Purification, characterization, and biosynthesis of bovine enamelins. *Calcif Tissue Int* 1988;43:389-399.
4. Cerny R, Slaby I, Hammarström L, Wurtz T. A novel gene expressed in rat ameloblasts codes for proteins with cell binding domains. *J Bone Miner Res* 1995;11:883-891.
5. Krebsbach PH, Lee SK, Matsuki Y, Kozak CA, Yamada KM, Yamada Y. Full-length sequence, localization, and chromosomal mapping of ameloblastin. *J Biol Chem* 1996;271:4431-4435.
6. Hammarström L, Heijl L, Gestrelius S. Periodontal regeneration in a buccal dehiscence model in monkeys after application of enamel matrix proteins. *J Clin Periodon-*

tol 1997;24:669-677.
7. Aroújo MG, Lindhe J. GTR treatment of degree III furcation defects following application of enamel matrix proteins. An experimental study in dogs. *J Clin Periodontol* 1998;25:524-530.
8. Heijl L. Periodontal regeneration with enamel matrix derivative in one human experimental defect. A case report. *J Clin Periodontol* 1997;24:693-696.
9. Mellonig JT. Enamel matrix derivative for periodontal reconstructive surgery: Technique and clinical and histologic case report. *Int J Periodontics Restorative Dent* 1999;19:9-19.
10. Sculean A, Reich E, Chiantella GC, Brecx M. Treatment of intrabony periodontal defects with an enamel matrix protein derivative (Emdogain): A report of 32 cases. *Int J Periodontics Restorative Dent* 1999;19:157-163.
11. Okuda K, Momose M, Miyazaki A, et al. Enamel matrix derivative in the treatment of human intrabony osseous defects. *J Periodontol* 2000;71:1821-1828.
12. Oldberg Å, Franzén A, Heinegård D. The primary structure of a cell-binding bone sialoprotein. *J Biol Chem* 1988;263:19430-19432.
13. Chen J, Shapiro HS, Sodek J. Developmental expression of bone sialoprotein mRNA in rat mineralized connective tissues. *J Bone Miner Res* 1992;7:987-997.
14. Chen J, Shapiro HS, Wrana JL, Reimer S, Heersche JNM, Sodek J. Localization of bone sialoprotein (BSP) expression to sites of mineralized tissue formation in fetal rat tissues by *in situ* hybridization. *Matrix* 1991;11: 133-143.
15. Ganss B, Kim RH, Sodek J. Bone sialoprotein. *Crit Revs Oral Biol Med* 1999;10:79-98.
16. Hunter GK, Goldberg HA. Nucleation of hydroxyapatite by bone sialoprotein. *Proc Natl Acad Sci* (USA) 1993; 90:8562-8565.
17. Waltregny D, Bellahcene A, Leval XD, Florkin B, Weidle U, Castronovo V. Increased expression of bone sialoprotein in bone metastases compared with visceral metastases in human breast and prostate cancers. *J Bone Miner Res* 2000;15:834-843.
18. Ibrahim T, Leong I, Sanchez-Sweatman O, et al. Expression of bone sialoprotein and osteopontin in breast cancer bone metastases. *Clin Exp Metastasis* 2000;18:253-260.
19. Li JJ, Sodek J. Cloning and characterization of the rat bone sialoprotein gene promoter. *Biochem J* 1993;289: 625-629.
20. Kerr JM, Fisher LW, Termine JD, Wang MG, McBride OW, Young MF. The human bone sialoprotein gene (IBSP): Genomic localization and characterization. *Genomics* 1993;17:408-415.
21. Kim RH, Shapiro HS, Li JJ, Wrana JL, Sodek J. Characterization of the human bone sialoprotein (BSP) gene and its promoter sequence. *Matrix Biol* 1994;14:31-40.
22. Benson MD, Aubin JE, Xiao G, Thomas PE, Franceschi RT. Cloning of a 2.5 kb murine bone sialoprotein promoter fragment and functional analysis of putative Osf2 binding sites. *J Bone Miner Res* 1999;14:396-405.
23. Li JJ, Kim RH, Sodek J. An inverted TATA box directs downstream transcription of the bone sialoprotein gene. *Biochem J* 1995;310:33-40.
24. Kim RH, Li JJ, Ogata Y, Yamauchi M, Freedman LP, Sodek J. Identification of a vitamin D3-response element that overlaps a unique inverted TATA box in the rat bone sialoprotein gene. *Biochem J* 1996;318:219-226.
25. Kim RH, Sodek J. Transcription of the bone sialoprotein gene is stimulated by v-Src acting through an inverted CCAAT box. *Cancer Res* 1999;59:565-571.
26. Shimizu E, Ogata Y. Activation of bone sialoprotein gene transcription by flavonoids is mediated through an inverted CCAAT box in ROS 17/2.8 cells. *J Cell Biochem* 2002;86:35-44.
27. Samoto H, Shimizu E, Matsuda-Honjyo Y, et al. TNF-α suppresses bone sialoprotein (BSP) expression in ROS 17/2.8 cells. *J Cell Biochem* 2002;87:313-323.
28. Shimizu-Sasaki E, Yamazaki M, Furuyama S, Sugiya H, Sodek J, Ogata Y. Identification of a novel response element in the rat bone sialoprotein (BSP) gene promoter that mediates constitutive and fibroblast growth factor 2-induced expression of BSP. *J Biol Chem* 2001;276:5459-5466.
29. Ogata Y, Nakao S, Kim RH, et al. Parathyroid hormone regulation of bone sialoprotein (BSP) gene transcription is mediated through a pituitary specific transcription factor-1 (Pit-1) motif in the rat BSP gene promoter. *Matrix Biol* 2000;19:395-407.
30. Benson MD, Bargeon JL, Xiao G, et al. Identification of a homeodomain binding element in the bone sialoprotein gene promoter that is required for its osteoblast-selective expression. *J Biol Chem* 2000;275:13907-13917.
31. Ogata Y, Niisato N, Furuyama S, et al. Transforming growth factor-β1 regulation of bone sialoprotein gene transcription. *J Cell Biochem* 1997;65:501-512.
32. Ogata Y, Yamauchi M, Kim RH, Li JJ, Freedman LP, Sodek J. Glucocorticoid regulation of bone sialoprotein (BSP) gene expression: Identification of a glucocorticoid response element in the bone sialoprotein gene promoter. *Eur J Biochem* 1995;230:183-192.
33. Yamauchi M, Ogata Y, Kim RH, Li JJ, Freedman LP, Sodek J. AP-1 regulation of the rat bone sialoprotein gene transcription is mediated through a TPA response element within a glucocorticoid response unit in the gene promoter. *Matrix Biol* 1996;15:119-130.
34. Majeska RJ, Rodan SB, Rodan GA. Parathyroid hormone-responsive clonal cell lines from rat osteosarcoma. *Endocrinology* 1980;107:1494-1503.
35. Pitaru S, Kotev-Emeth S, Noff D, Kaffuler S, Savion N. Effect of basic fibroblast growth factor on the growth and differentiation of adult stromal bone marrow cells: Enhanced development of mineralized bone-like tissue in culture. *J Bone Miner Res* 1993;8:919-929.
36. Kawase T, Okuda K, Momose M, Kato Y, Yoshie H, Burns DM. Enamel matrix derivative (EMDOGAIN) rapidly stimulates phosphorylation of the MAP kinase family and nuclear accumulation of smad2 in both oral epithelial and fibroblastic human cells. *J Periodont Res* 2001;36:367-376.
37. Schwartz Z, Carnes DL, Pulliam R, et al. Porcine fetal enamel matrix derivative stimulates proliferation but not differentiation of pre-osteoblastic 2T9 cells, inhibits proliferation and stimulates differentiation of osteoblast-like MG63 cells, and increases proliferation and differentiation of normal human osteoblast NHOst cells. *J Periodontol* 2000;71:1287-1296.
38. Tabin C. The initiation of the limb bud: Growth factors, HOX genes, and retinoids. *Cell* 1995;80:671-674.
39. Ryoo HM, Hoffmann HM, Beumer T, et al. Stage-specific expression of Dlx-5 during osteoblast differentiation: Involvement in regulation of osteocalcin gene expression. *Mol Endocrinol* 1997;11:1681-1694.
40. Bidder M, Latifi T, Towler DA. Reciprocal temporospatial patterns of Msx2 and osteocalcin gene expression during murine odontogenesis. *J Bone Miner Res* 1998;13:609-619.
41. Iimura T, Oida S, Takeda K, Maruoka Y, Sasaki S. Changes in homeobox-containing gene expression during ectopic bone formation induced by bone morphogenetic protein. *Biochem Biophys Res Commun* 1994;201:980-987.

42. Kiyoshima T, Yamauchi M, Wong C, Jheon A, Ganss B, Sodek J. An L1 element disrupts human bone sialoprotein promoter: Lack of tissue-specific regulation by distalless (Dlx5) and runt homeodomain protein 2 (Runx2)/core binding factor a1 (Cbfa1) elements. *Gene* 2002;299:205-217.
43. Barnes GL, Della Torre T, Sommer B, Young MF, Gerstenfeld LC. Transcriptional regulation restricting bone sialoprotein gene expression to both hypertrophic chondrocytes and osteoblasts. *J Cell Biochem* 2002;87: 458-469.
44. Massague J. The TGF-β family of growth and differentiation factors. *Cell* 1987;49:437-438.
45. Assoian RK, Komoriya A, Meyers CA, Miller DM, Sporn MB. Transforming growth factor-β in human platelets: Identification of a major storage site, purification, and characterization. *J Biol Chem* 1983;258:7155-7160.
46. Hauschka PV, Maurakos AE, Lafrati MD, Doleman SE, Klagsbrun M. Growth factors in bone matrix: Isolation of multiple types by affinity chromatography on heparin-sepharose. *J Biol Chem* 1986;261:12665-12674.
47. Wrana JL, Maeno M, Hawrylyshyn B, Yao K, Domenicucci C, Sodek J. Differential effects of transforming growth factor-β on the synthesis of extracellular matrix proteins by normal fetal rat calvarial bone cell populations. *J Cell Biol* 1988;106:915-924.
48. Takuwa Y, Ohse C, Wang EA, Wozney JM, Yamashita K. Bone morphogenetic protein-2 stimulates alkaline phosphatase activity and collagen synthesis in cultured osteoblastic cells, MC3T3-E1. *Biochem Biophys Res Commun* 1991;174:96-101.
49. Sodek J, Li IWS, Li H, et al. The role of TGF-β and BMP-7 in regenerating bone and soft tissues. *Mater Sci Eng* 1994;C2:19-26.
50. Rossi P, Karsenty G, Roberts AB, Roche NS, Sporn MB, Crombrugghe B. A nuclear factor 1 binding site mediates the transcriptional activation of a type I collagen promoter by transforming growth factor-β. *Cell* 1988;52: 405-414.
51. Ritzenthaler JD, Goldstein RH, Fine A, Lichtler A, Rowe DW, Smith BD. Transforming growth-factor-β activation elements in the distal promoter regions of the rat α1 type I collagen gene. *Biochem J* 1991;280:157-162.
52. Ritzenthaler JD, Goldstein RH, Fine A, Lichtler A, Smith BD. Regulation of the α1(I) collagen promoter via a transforming growth factor-β activation element. *J Biol Chem* 1993;268:13625-13631.
53. Riccio A, Pedone PV, Lund LR, Olesen T, Olsen HS, Andreasen PA. Transforming growth factor β1-responsive element: Closely associated binding sites for USF and CCAAT-binding transcription factor-nuclear factor I in the type 1 plasminogen activator inhibitor gene. *Mol Cell Biol* 1992;12:1846-1855.

Correspondence: Dr. Yorimasa Ogata, Department of Periodontology, 2-870-1 Sakaecho-nishi, Nihon University School of Dentistry at Matsudo, Chiba, 271-8587, Japan. Fax: 81-47-360-9362; e-mail: ogata@mascat.nihon-u.ac.jp.

Accepted for publication June 27, 2003.

Amelogenin Stimulates Bone Sialoprotein (BSP) Expression Through Fibroblast Growth Factor 2 Response Element and Transforming Growth Factor-β1 Activation Element in the Promoter of the BSP Gene

Emi Shimizu,*† Ryoichiro Saito,* Youhei Nakayama,* Yu Nakajima,* Naoko Kato,* Hideki Takai,* Dong-Soon Kim,* Masato Arai,* James Simmer,‡ and Yorimasa Ogata*†

Background: Amelogenins are a complex mixture of hydrophobic proteins that are the major organic component of developing enamel. The principal function of the amelogenins and their degradation products has been assigned to structural roles in creating the space and milieu for promoting enamel mineralization. Enamel matrix derivative (EMD) has been used clinically for periodontal regeneration and its therapeutic effectiveness has been attributed to amelogenin, non-amelogenin enamel matrix proteins, and growth factors. While EMD is believed to induce periodontal regeneration, the precise mechanism is not known. Bone sialoprotein (BSP), an early phenotypic marker of osteoblast and cementoblast differentiation, has been implicated in the nucleation of hydroxyapatite during bone formation. In this study, we examined the ability of amelogenin to regulate BSP gene transcription in osteoblast like cells.

Methods: We conducted Northern hybridization, transient transfection analyses, and gel mobility shift assays using full-length recombinant amelogenin to determine the molecular basis of the transcriptional regulation of BSP gene by amelogenin.

Results: Recombinant amelogenin (1 μg/ml, 12 hours) increased BSP mRNA levels ~2.4-fold. In transient transfection analyses, amelogenin (1 μg/ml, 12 hours) increased luciferase activity ~1.5-fold in pLUC3 (nucleotides −116 to +60) and further increased pLUC5 (nucleotides −801 to +60) activity ~2.3-fold transfected into ROS 17/2.8 cells. Amelogenin also increased luciferase activities in rat stromal bone marrow cells. The effect of amelogenin was inhibited by the tyrosine kinase inhibitor herbimycin A. Transcriptional stimulation by amelogenin was almost completely abrogated in cells expressing a BSP promoter construct with a mutation in the fibroblast growth factor 2 (FGF2) response element (FRE). Gel mobility shift assays with radiolabeled FRE and transforming growth factor-β1 (TGF-β1) activation element (TAE) ds-oligonucleotides revealed increased binding of nuclear proteins from amelogenin-stimulated ROS 17/2.8 cells.

Conclusion: Amelogenin stimulation alters BSP gene transcription by inducing nuclear proteins that bind to the FRE and TAE in the rat BSP gene promoter. *J Periodontol 2005;76:1482-1489.*

KEY WORDS

Amelogenin; animal studies; bone and bones; dental enamel; enamel matrix derivative; gene transcription; growth factors, FGF2 response element; growth factors, fibroblast; growth factors, transforming; sialoglycoproteins.

* Department of Periodontology, Nihon University School of Dentistry at Matsudo, Chiba, Japan.
† Research Institute of Oral Science, Nihon University School of Dentistry at Matsudo.
‡ Department of Biologic and Materials Sciences, University of Michigan School of Dentistry, Ann Arbor, MI.

Amelogenins constitute 90% of the extracellular matrix secreted by ameloblasts, and the proteins are cleaved in a regulated process during enamel maturation.[1,2] It has been suggested that these proline-rich proteins play a role in the mineralization and structural organization of developing enamel.[3] Amelogenin is a cell adhesion protein,[4] a potential regulator of cementum-associated genes such as bone sialoprotein (BSP) and type I collagen, and specific amelogenin gene splice products may be tissue-specific epithelial mesenchymal signaling molecules.[5] Alternative splicing of the primary transcript as a potential mechanism for generating amelogenin heterogeneity.[6] Amelogenin-deficient mice display an amelogenesis imperfecta phenotype, showed root resportion, and reduced expression of BSP.[7-9] Enamel matrix derivative (EMD), the acid extracts of porcine cheese-like enamel matrix, has been developed as a clinical treatment to promote periodontal regeneration.[10,11] Approximately 90% of the protein in the EMD is amelogenins, and the remaining 10% is comprised of non-amelogenin enamel matrix proteins and growth factors.[12-14]

BSP is a mineralized tissue-specific protein that is glycosylated, phosphorylated, and sulfated.[15,16] BSP nucleates hydroxyapatite crystal formation[17,18] and is expressed in several malignant cancers where it is associated with the formation of ectopic hydroxyapatite microcrystals.[19,20] To study the transcriptional regulation of BSP, rat, human, and mouse BSP gene promoters were cloned and characterized.[21-24] These promoters include an inverted TATA box[25] overlapping a vitamin D response element,[26] an inverted CCAAT box (–50 to –46), which is bound with NF-Y transcription factor.[27,28] A cAMP response element (CRE; –75 to –68),[29,30] a fibroblast growth factor 2 response element (FRE; –92 to –85),[30-32] a pituitary-specific transcription factor-1 (Pit-1) motif (–111 to –105) which mediates the stimulatory effects of parathyroid hormone,[32,33] and a homeodomain binding element (HOX; –199 to –192) have been characterized.[11,34] Further upstream in the rat promoter a transforming growth factor-β (TGF-β activation element (TAE; –499 to –485)[11,35] and a glucocorticoid response element (–920 to –906), overlapping an activator protein (AP)-1 site (–921 to –915) have also been identified.[16,36]

Although EMD is used clinically, little is known about amelogenin effects on bone metabolism. Therefore, we wish to determine the effect of amelogenin on BSP gene expression. The aim of the present study was to evaluate the ability of amelogenin to regulate osteoblast specific gene expression such as BSP. In this study we show that amelogenin regulates BSP expression in osteoblast-like ROS 17/2.8 cells through FRE and TAE in the rat BSP promoter.

MATERIALS AND METHODS

Cell Culture

The rat osteoblast-like ROS 17/2.8 cells[37] and rat stromal bone marrow cells (SBMC)[38] were maintained in alpha minimum essential medium (α-MEM)§ containing 10% fetal calf serum (FCS).§ Cells were grown to confluence in 60 mm tissue culture dishes and then cultured in α-MEM without serum and incubated with or without recombinant amelogenin for time periods extending from 3 to 12 hours. RNA was isolated from triplicate cultures at various time intervals and analyzed for the expression of BSP mRNA by Northern hybridization as described below.

Preparation of Recombinant Porcine Amelogenin

Recombinant porcine amelogenin (rP172) was expressed from the pET11 expression vector in *E. coli* BL21(DE3) cells‖ and purified from *E. coli* extracts by selective precipitation in ammonium sulfate (20% saturation), followed by ion exchange chromatography, followed by separation on a C4 reversed-phase column.[3]

Northern Hybridization

Aliquots (20 μg) of total RNA were fractionated on 1.2% agarose gel and transferred onto a hybond-N+ membrane.¶ Hybridizations were performed at 42°C with either a ^{32}P-labeled rat BSP, osteopontin (OPN), or glyceraldehyde-3-phosphate dehydrogenase (GAPDH) cDNA probe. Following hybridization, membranes were washed four times for 5 minutes each at 21°C in 300 mM sodium chloride and 30 mM trisodium citrate pH 7.0 containing 0.1% sodium dodecyl sulfate. This was followed by two 20 minute washes at 55°C in 15 mM sodium chloride and 1.5 mM trisodium citrate pH 7.0, 0.1% SDS. The hybridized bands were scanned in an imaging analyzer# and normalized to the expression of GAPDH.[31]

Transient Transfection Assays

Exponentially growing cells were used for transfection assays. Twenty-four hours after plating, cells at 50% to 70% confluence were transfected using a lipofectamine reagent.** The transfection mixture included 1 μg of a luciferase (LUC) construct[16] and 2 μg pSV-ß-galactosidase (ß-gal) vector†† as an internal control to normalized for individual transfection efficiencies. Two days post-transfection, cells were deprived of serum for 12 hours and recombinant amelogenin (1 μg/ml) was added and the cells cultured for a further 12 hours prior to harvesting. The luciferase assay was performed according to the

§ GIBCO BRL Life Technologies, Tokyo, Japan.
‖ Stratagene, La Jolla, CA.
¶ Amersham Biosciences, Piscataway, NJ.
# Fuji BAS 2000, Fuji film, Tokyo, Japan.
** Invitrogen Corp., Carlsbad, CA.
†† Promega Corp., Madison, WI.

supplier's protocol[‡‡] using a luminescence reader[§§] to measure the luciferase activity. The protein kinase inhibitor H89 (5 μM) and H7 (5 μM) was used to inhibit protein kinase A and C. Herbimycin A (1 μM) was used for tyrosine kinase inhibition.[30,31] Oligonucleotide-directed mutagenesis by polymerase chain reaction (PCR) was utilized to introduce dinucleotide substitutions using a site-directed mutagenesis kit.[‖] All constructs were sequenced as described previously to verify the fidelity of the mutagenesis.[31]

Gel Mobility Shift Assays

Confluent ROS 17/2.8 cells in T-75 flasks incubated for 3 and 12 hours with amelogenin (1 μg/ml) in α-MEM without serum were used to prepare nuclear extracts as described previously.[33] Double-stranded oligonucleotides encompassing the inverted CCAAT (nucleotides –61 to –37, 5′-CCGTGACCGTG**ATTGG**CTGCT GAGA), FGF2 response element (FRE; nucleotides –98 to –79, 5′-TTTTCT**GGTGAGAA**CCCACA), homeodomain binding element (HOX; nucleotides –204 to –179, 5′-TCCTCAGCCTT**CAATTAAA**TCCCACA) and TGF-β activation element (TAE; nucleotides –506 to –482, 5′-CAAAGCC**TTGGC**AGCCC**GGCTG**GCT) in the rat BSP promoter were prepared commercially,[‖‖] while consensus NF1 (5′-CCTTTGGCATGCTGCCAATAT) were purchased.[††] For gel shift analysis the double-stranded oligonucleotides were end-labeled with [γ-^{32}P] ATP and T4 polynucleotide kinase. Nuclear protein extracts (3 μg) were incubated for 20 minutes at room temperature (RT = 21°C) with 0.1 pM radiolabeled double-stranded-oligonucleotide in buffer containing 50 mM KCl, 0.5 mM EDTA, 10 mM Tris-HCl (pH 7.9), 1 mM DTT, 0.04% nonidet P-40, 5% glycerol, and 1 μg poly (dI-dC). Following incubation, the protein-DNA complexes were resolved by electrophoresis on 5% non-denaturing acrylamide gels (38:2 acrylamide/bis acrylamide) run at 150 V at RT. Following electrophoresis, the gels were dried and autoradiograms prepared and analyzed using an imaging analyzer.

Statistical Analysis

Triplicate samples were analyzed for each experiment and experiments replicated to ensure consistency of the responses to amelogenin. Significant differences between control and amelogenin treatment were determined using the Student *t* test.

RESULTS

Stimulation of BSP mRNA Expression in ROS 17/2.8 Cells

To study the regulation of BSP expression by amelogenin, we performed Northern hybridization analysis of total RNA extracted from osteoblastic ROS 17/2.8 cells. First, a dose-response relation for amelogenin induction of BSP was established by treating the ROS 17/2.8 cells with different concentrations of recombinant amelogenin for 12 hours. Amelogenin increased BSP mRNA levels at 0.01~1 μg/ml and had a maximal effect at 1 μg/ml (~2.4-fold) (Fig. 1A). Thus, 1 μg/ml amelogenin was used to determine the time course of BSP mRNA expression (Fig. 1B). Amelogenin upregulated BSP mRNA accumulation at 12 hours, whereas no effect on OPN and GAPDH mRNA was observed.

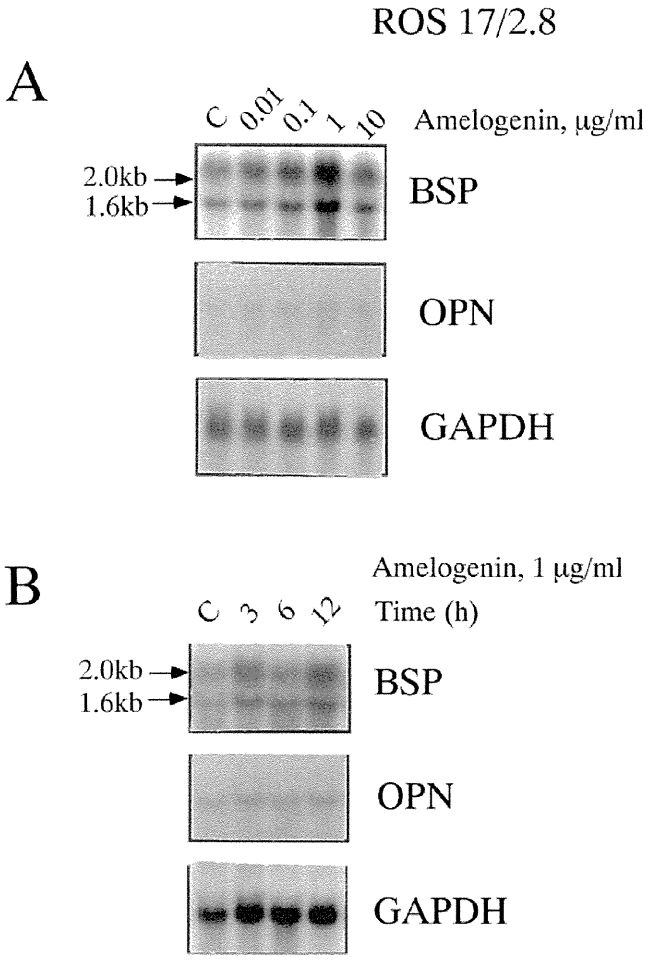

Figure 1.
Northern hybridization analysis of recombinant amelogenin effects on BSP mRNA expression. ***A)*** *Dose-response effect of amelogenin on BSPmRNA levels in the osteoblastic cell line ROS17/2.8 treated for 12 hours. At 0.01 to 10 μg/ml, amelogenin increased BSPmRNA with a maximal effect at 1 μg/ml.* ***B)*** *Twelve-hour time-course revealed an increase in BSP mRNA at 3 and 12 hours after the administration of 1 μg/ml amelogenin to ROS17/2.8 cells. Total RNA was isolated from triplicate cultures harvested after incubation times of 3, 6, and 12 hours and used for Northern hybridization analysis using a ^{32}P-labeled rat BSP DNA probe, an osteopontin DNA probe, and a GAPDH DNA probe.*

‡‡ PicaGene, Toyo Inki, Tokyo, Japan.
§§ Aloka, Tokyo, Japan.
‖‖ Bio-Synthesis, Inc., Lewisville, TX.

Transient Transfection Analysis of Rat BSP Promoter Constructs

Transient transfection of chimeric constructs, encompassing different regions of the rat BSP promoter driving a luciferase reporter gene (pLUC1~pLUC5), were performed in ROS 17/2.8 cells. The results of transfection assays (Fig. 2) indicated a ~1.5-fold (pLUC3; –116 to +60), ~1.5-fold (pLUC4; –425 to +60) and ~2.3-fold (pLUC5; –801 to +60) increase in transcription with the luciferase constructs after 12 hours of treatment with 1 μg/ml amelogenin. In shorter constructs (pLUC1; –18 to +60, pLUC2; –43 to +60), luciferase activities were not increased by amelogenin. When transcriptional activities in response to amelogenin were analyzed in normal rat SBMC, the transcriptional activities of pLUC3 (~1.5-fold), pLUC4 (~1.5-fold) and pLUC5 (~1.7-fold) were increased (Fig. 3). Included within the DNA sequence that is unique to pLUC3 construct (nucleotides –116 to –43) is an inverted CCAAT box (ATTGG; between nucleotides –50 and –46), a CRE (between nucleotides –75 and –68), FRE (between nucleotides –92 and –85), and a Pit-1 motif (between nucleotides –111 and –105) (Fig. 4). There are HOX (TCAATTAAAT, nucleotides –194 to –185) and TGF-β activation elements (TAE; C**TTGGC**AGCCC**GGCTG**G, nucleotides –500 to –484) in the pLUC4 and pLUC5 which were identified as enamel matrix derivative (EMD) response elements in the previous study (Fig. 4).[11] Since protein kinases mediate amelogenin signaling, we also investigated the effects of the protein kinase C inhibitor H7, the protein kinase A inhibitor H89, and the tyrosine kinase inhibitor HA on amelogenin-mediated transcription. Although amelogenin induction of pLUC3 promoter activity was inhibited by HA, no effects were observed for PKC and PKA (Fig. 5), indicating involvement of tyrosine kinase in the signaling pathway. Next we introduced mutations in the possible response elements encoded within nucleotides –116 to –43 of pLUC3 as shown in Figure 6. Whereas mutations in the CRE (M-CRE) and Pit-1 (M-PIT) had no effect on amelogenin stimulation,

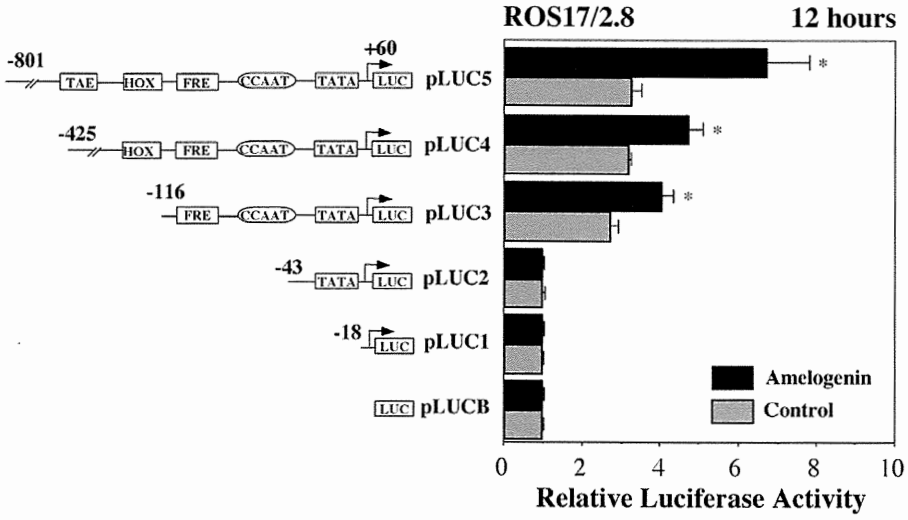

Figure 2.
*Amelogenin upregulates BSP promoter activity. Transient transfections of ROS 17/2.8 cells, in the presence or absence of amelogenin (1 μg/ml) for 12 hours, were used to determine transcriptional activity of chimeric constructs that included various regions of the BSP promoter ligated to a luciferase reporter gene. The results of transcriptional activity obtained from three separate transfections with constructs; pLUC basic (pLUCB) and pLUC1 to pLUC5 have been combined and the values expressed with standard errors. *Significant differences from control (relative luciferase activity of pLUCB), P <0.1.*

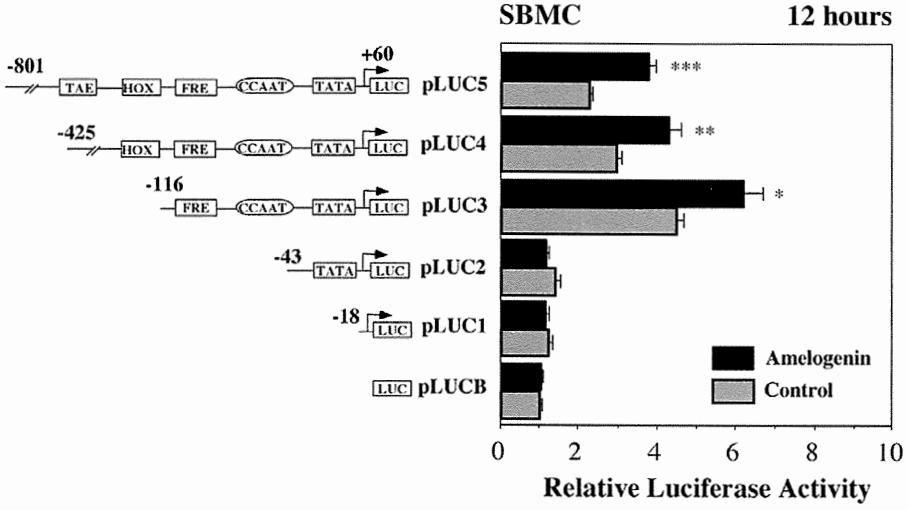

Figure 3.
*Transient transfections of rat stromal bone marrow cells. SBMC cells treated with or without amelogenin (1 μg/ml) for 12 hours were used to determine transcriptional activity of chimeric constructs that included various regions of the BSP promoter ligated to a luciferase reporter gene. The results of transcriptional activity obtained from three separate transfections with constructs; pLUC basic (pLUCB) and pLUC1 to pLUC5 have been combined and the values expressed with standard errors. Significant differences from control (relative luciferase activity of pLUCB): *P <0.1; †P <0.05; ‡P <0.02.*

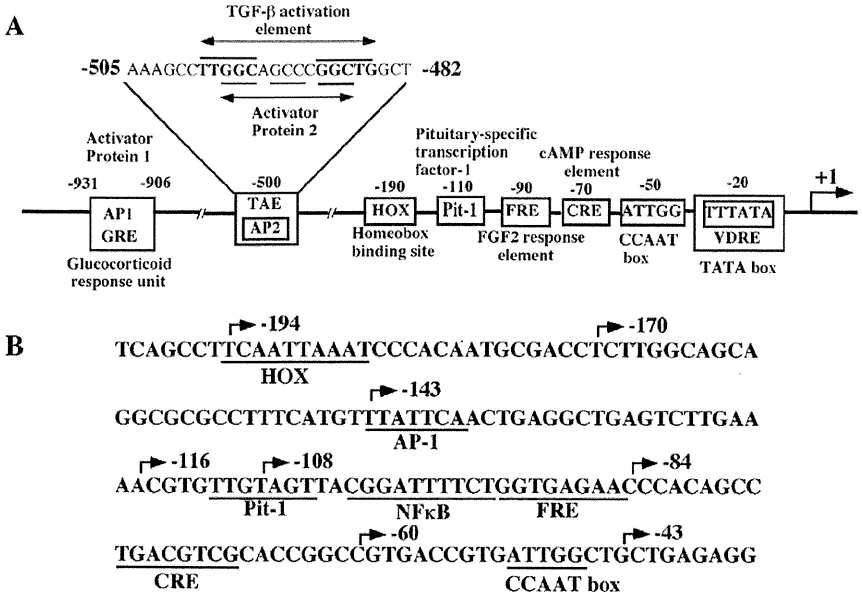

Figure 4.
Regulatory elements in the proximal rat BSP promoter. ***A)*** *The positions of the inverted TATA and CCAAT boxes, a cAMP response element (CRE), an FGF2 response element (FRE), a pituitary-specific transcription factor-1 (Pit-1), a homeobox-binding site (HOX), and a vitamin D response element (VDRE) that overlaps the inverted TATA box are shown in the proximal promoter region of the rat BSP gene, and a TGF-β1 activation element (TAE) overlapping an AP2 element and a glucocorticoid response elements (GRE) overlapping the AP1 in the distal promoter. The numbering of nucleotides is relative to the transcription start site (+1).* ***B)*** *The nucleotide sequence of the rat BSP gene proximal promoter is shown from −201 to −35. Inverted CCAAT box, CRE, FRE, NFκB, Pit-1, AP-1, and HOX are present.*

mutation of the FRE (M-FRE) significantly reduced the amelogenin effect on the transcriptional activity (Fig. 6). These results suggest that the FRE is required as functional *cis*-elements for upregulation of BSP transcription by amelogenin.

Gel Mobility Shift Assays

To identify nuclear proteins that bind to binding elements in pLUC3, pLUC4, and pLUC5, double-stranded oligonucleotides were end-labeled and incubated with nuclear proteins (3 μg) extracted from confluent ROS 17/2.8 cells that were either not treated (control) or treated with 1 μg/ml amelogenin for 3 and 12 hours. With nuclear extracts from confluent control cultures of ROS 17/2.8 cells, shifts of HOX DNA-protein complexes (Fig. 7; lane 1) and a shift of a single FRE DNA-protein complex were evident (Fig. 7, lane 7). While HOX DNA-protein complexes did not change following stimulation by amelogenin (1 μg/ml) for 3 and 12 hours (Fig. 7; lanes 2 and 3), DNA binding activity to FRE was increased (Fig. 7; lanes 8 and 9). That the

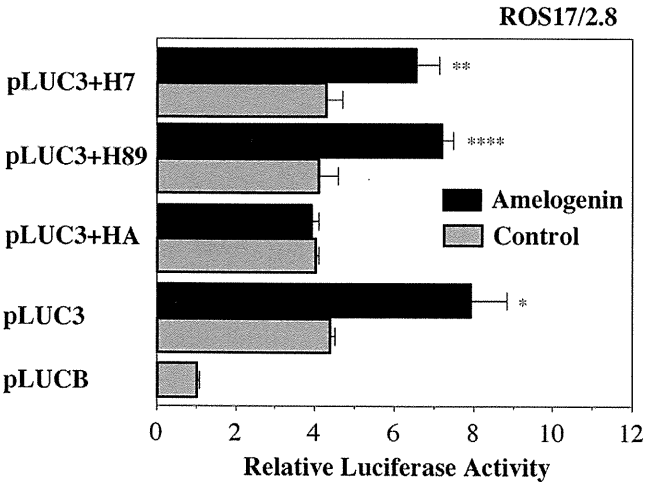

Figure 5.
*Effect of kinase inhibitors on transcriptional activation by amelogenin. Transient transfection analysis of pLUC3 treated with amelogenin (1 μg/ml) for 12 hours in ROS17/2.8 cells is shown together with the effects of the PKC inhibitor (H7, 5 μM), PKA inhibitor (H89, 5 μM), and tyrosine kinase inhibitor (herbimycin A; HA, 1 μM). The results obtained from three separate transfections were combined and the values expressed with standard errors. Significant differences compared to controls are shown at the following probability levels: *P <0.1; †P <0.05; ‡P <0.01.*

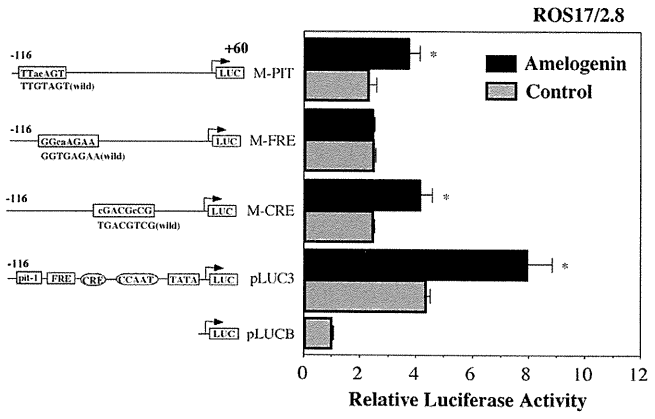

Figure 6.
*Site mutation analysis of luciferase activities. Dinucleotide substitutions were made within context of the homologous -116 to +60 (pLUC3) BSP promoter fragments. M-CRE (**c**GACG**c**CG), M-FRE (GG**ca**AGAA), and M-PIT (TT**ac**AGT) were analyzed for relative promoter activity after transfection into ROS 17/2.8 cells and examined for induction after treatment with amelogenin (1 mg/ml) for 12 hours. The results of transcriptional activity obtained from three separate transfections with constructs were combined and the values expressed with standard errors. Significant differences compared to controls are shown at the following probability levels: *P <0.1.*

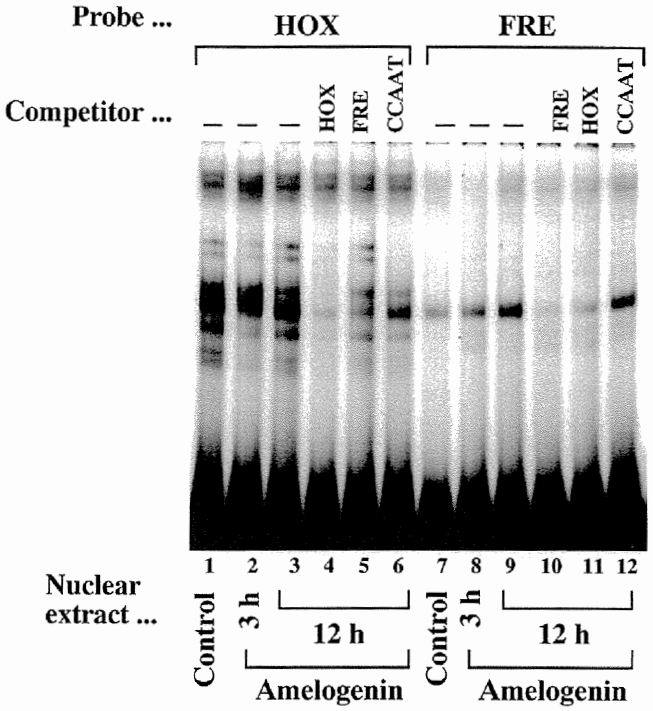

Figure 7.
*Amelogenin increases the DNA binding activity recognized by the FRE sequence. Radiolabeled double-stranded HOX (–204 TCCTCAGCCT **TCAATTAAA**TCCCACA –179; lanes 1 through 6) and FRE (98 TTTT CT**GGTGAGAA**CCCACA 79; lanes 7 through 12) oligonucleotides were incubated for 20 minutes at 21°C with nuclear protein extracts (3 μg) obtained from ROS 17/2.8 cells incubated without (lanes 1 and 7) or with amelogenin (1 μg/ml) for 3 hours (lanes 2 and 8) and 12 hours (lanes 3 through 6 and 9 through 12). Competition reactions were performed using a 40-fold molar excess of unlabeled HOX, FRE, and CCAAT. DNA protein complexes were separated on 5% polyacrylamide gel in low-ionic-strength tris-borate buffer, dried under vacuum and exposed to an imaging plate for quantitation using an imaging analyzer.*

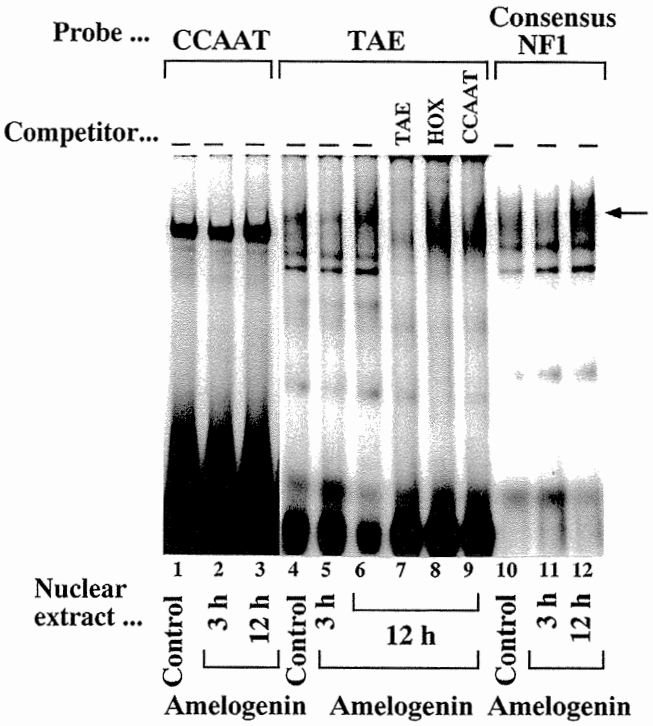

Figure 8.
*Amelogenin increases the DNA binding activity recognized by TAE sequence. Radiolabeled double-stranded inverted CCAAT (–61 CCGTGA CCGTG**ATTGG**CTGCTGAGA –37), TAE (–506 CAAAGCC**TTGGC**A GCCC**GGCTG**GCT –482), and consensus NF1 (CCT**TTGGC**AT GCT**GCCAA**TAT) oligonucleotides were incubated for 20 minutes at 21°C with nuclear protein extracts (3 μg) obtained from ROS 17/2.8 cells incubated without (lanes 1, 4, and 10) or with amelogenin (1 μg/ml) for 3 hours (lanes 2, 5, and 11) and 12 hours (lanes 3, 6 through 9, and 12). DNA protein complexes were separated on 5% polyacrylamide gel in low-ionic-strength tris-borate buffer, dried under vacuum, and exposed to an imaging plate for quantitation using an imaging analyzer.*

DNA protein complexes represent specific interactions were indicated by competition experiments in which a 40-fold excess of HOX and FRE reduced the amount of complex formation (Fig. 7; lanes 4 and 10). In contrast, CCAAT (40-fold) did not compete with complex formation (Fig. 7; lane 6 and 12). While 40-fold excess of the FRE slightly reduced HOX-protein complexes formation (Fig. 7; lane 5) and 40-fold excess of the HOX reduced FRE-protein complex formation (Fig. 7; lane 11). When we used the inverted CCAAT sequence as a probe, the DNA-NF-Y protein complex did not change after stimulation by amelogenin (Fig. 8; lanes 1, 2, and 3).[27,28] TAE was identified as containing the 5'-portion of the NF-1 canonical sequence (TTGGC) overlapping a putative AP-2 site.[35] When the TAE was incubated with the nuclear extract from control (no treatment) and amelogenin treatment (3 hours) cultures of ROS 17/2.8 cells, no significant binding was evident (Fig. 8; lanes 4 and 5). After stimulation by amelogenin (1 μg/ml) for 12 hours, DNA binding activity was increased (Fig. 8; lane 6). The TAE-protein complex representing specific interaction was indicated by competition experiments in which 40-fold excess of TAE reduced the amount of complex formation (Fig. 8; lane 7). In contrast, HOX and CCAAT (40-fold) did not compete with complex formation (Fig. 8; lanes 8 and 9). When we used consensus NF-1 as a probe, NF-1 DNA-protein complex increased after stimulation by amelogenin for 12 hours (Fig. 8; lane 12).

DISCUSSION

These studies have shown that amelogenin increases expression of BSP gene in osteoblastic ROS 17/2.8 cells and SBMC cells. Transduction of the amelogenin signaling is mediated through a tyrosine kinase, which targets nuclear proteins that bind to FRE and TAE elements in the proximal promoter of the BSP gene.

BSP is a unique marker of early osteogenic differentiation that can regulate the formation of mineral crystals.[18] Our results show that amelogenin treatment

of ROS 17/2.8 cells increases the steady-state level of BSP mRNA approximately 2.4-fold (Fig. 1). Amelogenin stimulated BSP promoter activity ~1.5-fold in pLUC3 and pLUC4, and ~2.3 fold in pLUC5 constructs (Fig. 2), which is comparable with the increases in BSP mRNA levels. These results suggest that amelogenin regulates BSP mRNA expression, at least in part, via transcriptional control. When we used SBMC cells for luciferase assays to see the effect of amelogenin on BSP transcription, amelogenin stimulated BSP transcription (Fig. 3). Therefore, amelogenin increases BSP expression not only in transformed ROS 17/2.8 cells but also in normal osteoprogenitors.

From transient transfection assays we initially located the amelogenin responsive region to the proximal promoter (pLUC3; nucleotides –116 to –43) of the BSP gene (Fig. 2), which encompasses an inverted CCAAT box (nucleotides –50 to –46), a cAMP response element (CRE; nucleotides –75 to –68), a FGF2 response element (FRE; nucleotides –92 to –85), and a Pit-1 (nucleotides –111 to –105) motif (Fig. 4). Luciferase activity of pLUC5 further enhanced by amelogenin from 1.5-fold (pLUC3 and pLUC4) to 2.3-fold, suggesting that an amelogenin response region exists not only in pLUC3 but also in pLUC5. Although mutations of the CRE (M-CRE) and Pit-1 (M-PIT) were without effect, the transcriptional stimulation by amelogenin was abrogated in the FRE mutation (M-FRE; Fig. 6). The involvement of the FRE element is further supported by gel shift analyses in which more complexes with the FRE element formed using nuclear extracts from amelogenin stimulated cell (Fig. 7). The nuclear factor binding to the FRE, which is regulated by tyrosine kinase, is the focus of current studies because of its potential role in regulating basal and FGF2-induced transcription of BSP in osteoblast,[31] as well as prostaglandin E_2 effects.[30] In this study the tyrosine kinase inhibitor, herbimycin A inhibited amelogenin-induced promoter activity (Fig. 5), indicating that amelogenin increases expression of the BSP gene through a tyrosine kinase pathway. The nuclear factors binding to the inverted CCAAT box and HOX did not change after stimulation by amelogenin. Very interestingly, HOX oligonucleotides can compete with FRE-protein complex formation (Fig. 7; lane 11), and FRE reduced HOX-protein complexes formation (Fig. 7; lane 5). The results might have been caused by 3'-portion of the FRE (T**GGTGAGAA***CCCACA*GC), which resembles the 3'-portion of the HOX sequence (T**TCAATTAA**AT*CCCACA*AT) (Fig. 4). The specific sequence in pLUC5 is between –425 and –801, and the identified response element in this region is the TAE. TAE was identified as TGF-β1 activation element which containing the 5'-portion of the NF-1 canonical sequence (TTGGC).[35] Results of gel shift assays show that TAE-protein complex and NF-1-protein complex were increased by amelogenin (1 μg/ml) for 12 hours (Fig. 8). These results indicate that amelogenin stimulates BSP expression through FRE and TAE elements in the BSP gene promoter. Further study is necessary to investigate transcription factors that bind to FRE and TAE, and the functional interactions of these elements.

In our previous study, EMD (50 μg/ml, 12 hours) increased luciferase activities of pLUC4 (nucleotides –425 to +60) and pLUC5 (nucleotides –801 to +60). EMD regulates BSP transcription through HOX and TAE elements in the BSP gene promoter.[11] Ninety percent of the protein in the EMD is amelogenin and the remaining 10% is non-amelogenin enamel matrix proteins and growth factors such as TGF-β and bone morphogenetic protein (BMP).[11] Discrepancy between the activities of EMD and amelogenin on BSP transcription might be caused by the complex components of EMD.

In this study, we have shown that amelogenin induced BSP gene expression in osteoblast-like ROS 17/2.8 cells and rat stromal bone marrow cells. Our results suggest that amelogenin can have a positive effect on periodontal regeneration, such as formation of new cementum and alveolar bone. Continued studies necessary to investigate amelogenin effects on periodontal ligament cells, which are crucial cell population for periodontal regeneration and will be aimed at defining the transcription factors that mediate the promotion of mineralization by amelogenin.

ACKNOWLEDGMENTS

This work was supported by the following grants: Grants-in-aid for Scientific Research 14571989 and 16592081 from the Ministry of Education, Science, and Culture of Japan; a Nihon University Research Grant (Multidisciplinary Research Grant for 2002 and 2003, and Assistants and Young Researchers for 2004); Suzuki Memorial Grant of Nihon University School of Dentistry at Matsudo (Research Grant for Assistants for 2003); Research Grant on Priority Areas from Nihon University School of Dentistry at Matsudo; and a Grant from the Ministry of Education, Culture, Sports, Science and Technology to promote 2001-Multidisciplinary Research Project (2001-2005).

REFERENCES

1. Termine JD, Belcourt AB, Christner PJ, Conn KM, Nylen MU. Properties of dissociatively extracted fetal tooth matrix proteins. I. Principle molecular species in developing bovine enamel. *J Biol Chem* 1980;255:9760-9768.
2. Simmer JP, Lau EC, Hu CC, et al. Isolation and characterization of a mouse amelogenin expressed in *Escherichia coli*. *Calcif Tissue Int* 1994;54:312-319.
3. Ryu OH, Hu CC, Simmer JP. Biochemical characterization of recombinant mouse amelogenins: Protein quantitation, proton absorption, and relative affinity for enamel crystals. *Connect Tissue Res* 1998;38:2907-2914.
4. Hoang AM, Klebe RJ, Steffensen B, Ryu OH, Simmer JP, Cochran DL. Amelogenin is a cell adhesion protein. *J Dent Res* 2002;81:497-500.

5. Veis A, Tompkins K, Alvares K, et al. Specific amelogenin gene splice products have signaling effects on cells in culture and in implants in vivo. *J Biol Chem* 2000; 275:41263-41272.
6. Gibson C, Golub E, Herold R, et al. Structure and expression of the bovine amelogenin gene. *Biochemistry* 1991;30:1075-1079.
7. Gibson CW, Yuan Z, Hall B, et al. Amelogenin-deficient mice display an amelogenesis imperfecta phenotype. *J Biol Chem* 2001;276:31871-31875.
8. Hatakeyama J, Sreenath T, Hatakeyama Y, et al. The receptor activator of nuclear factor-kappa B ligand-mediated osteoclastogenic pathway is elevated in amelogenin null mice. *J Biol Chem* 2003;278:35743-35749.
9. Viswanathan HL, Berry JE, Foster BL, et al. Amelogenin: A potential regulator of cementum-associated genes. *J Periodontol* 2003;74:1423-1431.
10. Gestrelius S, Andersson C, Johansson A, et al. Formation of enamel matrix derivative for surface coating; kinetics and cell colonization. *J Clin Periodontol* 1997;24:678-684.
11. Shimizu E, Nakajima Y, Kato N, Nakayama Y, Samoto H, Ogata Y. Regulation of rat bone sialoprotein (BSP) gene transcription by enamel matrix derivative. *J Periodontol* 2004;75:260-267.
12. Ogata Y, Shimokawa H, Sasaki S. Purification, characterization, and biosynthesis of bovine enamelins. *Calcif Tissue Int* 1988;43:389-399.
13. Cerny R, Slaby I, Hammarström L, Wurtz T. A novel gene expressed in rat ameloblasts codes for proteins with cell binding domains. *J Bone Miner Res* 1995;11:883-891.
14. Kawase T, Okuda K, Momose M, Kato Y, Yoshie H, Burns DM. Enamel matrix derivative (EMDOGAIN) rapidly stimulates phosphorylation of the MAP kinase family and nuclear accumulation of smad2 in both oral epithelial and fibroblastic human cells. *J Periodontal Res* 2001;36:367-376.
15. Oldberg Å, Franzén A, Heinegård D. The primary structure of a cell-binding bone sialoprotein. *J Biol Chem* 1988;263:19430-19432.
16. Ogata Y, Yamauchi M, Kim RH, Li JJ, Freedman LP, Sodek J. Glucocorticoid regulation of bone sialoprotein (BSP) gene expression: Identification of a glucocorticoid response element in the bone sialoprotein gene promoter. *Eur J Biochem* 1995;230:183-192.
17. Hunter GK, Goldberg HA. Nucleation of hydroxyapatite by bone sialoprotein. *Proc Natl Acad Sci* (USA) 1993; 90:8562-8565.
18. Ganss B, Kim RH, Sodek J. Bone sialoprotein. *Crit Revs Oral Biol Med* 1999;10:79-98.
19. Waltregny D, Bellahcene A, Leval XD, Florkin B, Weidle U, Castronovo V. Increased expression of bone sialoprotein in bone metastases compared with visceral metastases in human breast and prostate cancers. *J Bone Miner Res* 2005;15:834-843.
20. Ibrahim T, Leong I, Sanchez-Sweatman O, et al. Expression of bone sialoprotein and osteopontin in breast cancer bone metastases. *Clin Exp Metastasis* 2000;18:253-260.
21. Li JJ, Sodek J. Cloning and charaterization of the rat bone sialoprotein gene promoter. *Biochem J* 1993;289:625-629.
22. Kerr JM, Fisher LW, Termine JD, Wang MG, McBride OW, Young MF. The human bone sialoprotein gene (IBSP): Genomic localization and characterization. *Genomics* 1993; 17:408-415.
23. Kim RH, Shapiro HS, Li JJ, Wrana JL, Sodek J. Characterization of the human bone sialoprotein (BSP) gene and its promoter sequence. *Matrix Biol* 1994;14:31-40.
24. Benson MD, Aubin JE, Xiao G, Thomas PE, Franceschi RT. Cloning of a 2.5kb murine bone sialoprotein promoter fragment and functional analysis of putative Osf2 binding sites. *J Bone Miner Res* 1999;14:396-405.
25. Li JJ, Kim RH, Sodek J. An inverted TATA box directs downstream transcription of the bone sialoprotein gene. *Biochem J* 1995;310:33-40.
26. Kim RH, Li JJ, Ogata Y, Yamauchi M, Freedman LP, Sodek J. Identification of a vitamin D3-response element that overlaps a unique inverted TATA box in the rat bone sialoprotein gene. *Biochem J* 1996;318:219-226.
27. Kim RH, Sodek J. Transcription of the bone sialoprotein gene is stimulated by v-Src acting through an inverted CCAAT box. *Cancer Res* 1999;59:565-571.
28. Shimizu E, Ogata Y. Activation of bone sialoprotein gene transcription by flavonoids is mediated through an inverted CCAAT box in ROS 17/2.8 cells. *J Cell Biochem* 2002;86:35-44.
29. Samoto H, Shimizu E, Matsuda-Honjyo Y, et al. TNF-α suppresses bone sialoprotein (BSP) expression in ROS 17/2.8 cells. *J Cell Biochem* 2002;87:313-323.
30. Samoto H, Shimizu E, Matsuda-Honjyo Y, et al. Prostaglandin E_2 stimulates bone sialoprotein (BSP) expression through cAMP and FGF2 response elements in the proximal promoter of the rat BSP gene. *J Biol Chem* 2003;278:28659-28667.
31. Shimizu-Sasaki E, Yamazaki M, Furuyama S, Sugiya H, Sodek J, Ogata Y. Identification of a novel response element in the rat bone sialoprotein (BSP) gene promoter that mediates constitutive and fibroblast growth factor 2-induced expression of BSP. *J Biol Chem* 2001;276: 5459-5466.
32. Shimizu E, Matsuda-Honjyo Y, Samoto H, et al. Static magnetic fields-induced bone sialoprotein (BSP) expression is mediated through FGF2 response element and pituitary-specific transcription factor-1 motif. *J Cell Biochem* 2004;91:1183-1196.
33. Ogata Y, Nakao S, Kim RH, et al. Parathyroid hormone regulation of bone sialoprotein (BSP) gene transcription is mediated through a pituitary specific transcription factor-1 (Pit-1) motif in the rat BSP gene promoter. *Matrix Biol* 2000;19:395-407.
34. Benson MD, Bargeon JL, Xiao G, et al. Identification of a homeodomain binding element in the bone sialoprotein gene promoter that is required for its osteoblast-selective expression. *J Biol Chem* 2000;275:13907-13917.
35. Ogata Y, Niisato N, Furuyama S, et al. Transforming growth factor-β1 regulation of bone sialoprotein gene transcription. *J Cell Biochem* 1997;65:501-512.
36. Yamauchi M, Ogata Y, Kim RH, Li JJ, Freedman LP, Sodek J. AP-1 regulation of the rat bone sialoprotein gene transcription is mediated through a TPA response element within a glucocorticoid response unit in the gene promoter. *Matrix Biol* 1996;15:119-130.
37. Majeska RJ, Rodan SB, Rodan GA. Parathyroid hormone-responsive clonal cell lines from rat osteosarcoma. *Endocrinology* 1980;107:1494-1503.
38. Pitaru S, Kotev-Emeth S, Noff D, Kaffuler S, Savion N. Effect of basic fibroblast growth factor on the growth and differentiation of adult stromal bone marrow cells: Enhanced development of mineralized bone-like tissue in culture. *J Bone Miner Res* 1993;8:919-929.

Correspondence: Dr. Yorimasa Ogata, Department of Periodontology, Nihon University School of Dentistry at Matsudo, Chiba 271-8587, Japan. Fax: 81-47-360-9362; e-mail: ogata@mascat.nihon-u.ac.jp.

Accepted for publication January 29, 2005.

2002年2月

キーワード
・腫瘍壊死因子
・骨シアロタンパク質
・骨芽細胞
・転写調節

日歯保存誌 45 (1)：21～28，2002

骨芽細胞に対する腫瘍壊死因子(TNF-α)の影響

—TNF-α による骨シアロタンパク質の転写の調節—

佐本　博　清水映美*　本城祐子*
斎藤綾一朗*　倉澤俊之*　山崎宗与*
葛西一貴　小方頼昌**

日本大学松戸歯学部矯正学講座
(主任: 葛西一貴教授)
*日本大学松戸歯学部保存学III講座(歯内療法学)
(主任: 山崎宗与教授)
**日本大学松戸歯学部保存学II講座(歯周病学)
(主任：小方頼昌教授)
(受付: 平成13年11月22日)

Effects of Tumor Necrosis Factor-α on Osteoblasts

—Tumor Necrosis Factor-α Regulation of Bone Sialoprotein Gene Transcription—

SAMOTO Hiroshi, SHIMIZU Emi*, MATSUDA-HONJO Yuko*,
SAITO Ryoichiro*, KURASAWA Toshiyuki*, YAMAZAKI Muneyoshi*,
KASAI Kazutaka and OGATA Yorimasa**

Department of Orthodontics, Nihon University School of Dentistry at Matsudo
(Chief: Prof. KASAI Kazutaka)
870-1, Sakaecho, Nishi-2, Matsudo, Chiba 271-8587 Japan
*Department of Endodontics, Nihon University School of Dentistry at Matsudo
(Chief: Prof. YAMAZAKI Muneyoshi)
870-1, Sakaecho, Nishi-2, Matsudo, Chiba 271-8587 Japan
**Department of Periodontology, Nihon University School of Dentistry at Matsudo
(Chief: Prof. OGATA Yorimasa)
870-1, Sakaecho, Nishi-2, Matsudo, Chiba 271-8587 Japan
(Received for Publication: November 22, 2001)

Bone sialoprotein (BSP) is a mineralized tissue-specific protein that appears to function in the initial mineralization of bone. Our previous studies have demonstrated that BSP mRNA expression is essentially restricted to fully-differentiated cells of mineralized connective tissues, and that the expression of BSP is developmentally regulated. Tumor necrosis factor-alpha (TNF-α) is a major mediator of inflammatory responses in many diseases. TNF-α decreases the synthesis of bone matrix proteins, inhibits bone formation, and stimulates bone resorption. To determine the molecular basis

of the transcriptional regulation of BSP gene transcription by TNF-α, we have conducted transient transfection analyses with chimeric constructs of the rat BSP gene promoter linked to a luciferase reporter gene. TNF-α (10 ng/ml) increased transcriptional activity in the construct (pLUC 3; +60 to −116) transfected into ROS 17/2.8 cells for 6 h, as well as in longer constructs (pLUC 4〜7). On the contrary, TNF-α (10 ng/ml) suppressed transcription in these constructs for 24 h. The effects of TNF-α on transcriptional activity were inhibited by a tyrosine kinase inhibitor: herbimycin A. Gel mobility shift assays, using a radiolabeled cyclic AMP response element (CRE) oligonucleotide, revealed increased binding of a nuclear protein from TNF-α stimulated ROS 17/2.8 cells for 6 h. These studies indicate that TNF-α increases BSP gene transcription for 6 h through a tyrosine kinase-dependent pathway that targets the CRE sequence in the BSP gene promoter.

(Request original article reprints to Dr.OGATA)

緒　言

腫瘍壊死因子(TNF-α)は，*in vivo* でマウスに転移した腫瘍に出血性壊死を誘導する因子として発見された，157個のアミノ酸からなる分子量約17 kDのタンパク質である[1]．TNF-αはマクロファージをはじめ多くの細胞で産生され，多様な生物活性を有し，アポトーシス誘導活性のほか，多くの炎症性疾患に関与して，インターロイキン-1(IL-1)と同様に炎症時のサイトカインカスケードにおいて中心的な役割を担っていると考えられる．さらに，骨芽細胞様細胞に作用して，活性型ビタミンD_3により促進されたオステオカルシン遺伝子の発現を抑制し[2]，IL-6およびPGE_2の発現を促進することや[3]，タンパク質分解酵素やIL-8の合成を促進することなどが報告されている[4,5]．また，破骨細胞の分化を促進し，骨吸収を促進するため，慢性関節リウマチや歯周疾患などで認められる炎症性骨吸収の亢進にはTNF-αが関与すると考えられている[6]．

骨シアロタンパク質(BSP)は分子量約33,000のリン酸化および硫酸化を受けた糖タンパク質で，石灰化結合組織特異的に発現することが報告されている[7,8]．そのアミノ酸配列中にはグルタミン酸連続配列およびアルギニン-グリシン-アスパラギン酸細胞接着配列(RGD配列)を有し，グルタミン酸連続配列でハイドロキシアパタイトに結合し，RGD配列で細胞に接着することが知られている[9,10]．また，形態学的報告等から骨，象牙質，セメント質形成初期にBSP遺伝子の発現が上昇することが認められており，初期の石灰化における役割が注目されている[7,8]．BSPの転写はグルココルチコイドやビタミンD_3などのステロイドホルモン[11-14]，トランスフォーミンググロースファクターβ(TGF-β)[15]，副甲状腺ホルモン(PTH)[16]，塩基性線維芽細胞成長因子(FGF 2)[17]などの成長因子により調節を受けていることが報告されている．ほかのホルモン，サイトカインおよび成長因子による転写調節機構や，石灰化組織特異的に発現する機構に関しても研究されているが，完全な解明にはいたっていない．

BSP遺伝子の上流域(プロモーター領域)には，ホルモンや各種成長因子に応答する遺伝子配列が存在し，転写の調節を行っていると考えられている．われわれのグループはすでにラットおよびヒトBSPの遺伝子プロモーター領域のクローニングを行い[12,18,19]，転写開始位置から約3,000塩基上流までの塩基配列の決定を行った．さらに塩基配列の解析の結果，さまざまな転写因子の結合部位が存在することを報告した(Fig. 1)．

ラットおよびヒトBSPのプロモーター領域は非常に相同性が高く，転写開始位置より370塩基対上流までは約75%の相同性を示す[20]．その配列中には逆方向のTATA配列(−20塩基上流)[21]と重複したビタミンD受容体結合配列(VDRE)[13]，逆方向のCAAT配列(−50塩基上流)[22]，FGF 2応答配列(FRE；−90)[17]，サイクリックAMP応答配列(CRE；−70塩基上流)，下垂体特異的転写因子結合配列(Pit-1；−108塩基上流)[16]，TGF-β応答配列(−500塩基上流)[15]，グルココルチコイド応答配列(GRE；−930塩基上流)[12]および同配列に重複したアクチベータープロテイン1(AP 1)結合配列[23]が存在する(Fig. 1)．一般にTATA配列はRNAポリメラーゼIIによる転写の方向を規定する配列であるが，BSPのプロモーターではTATA配列は逆方向であ

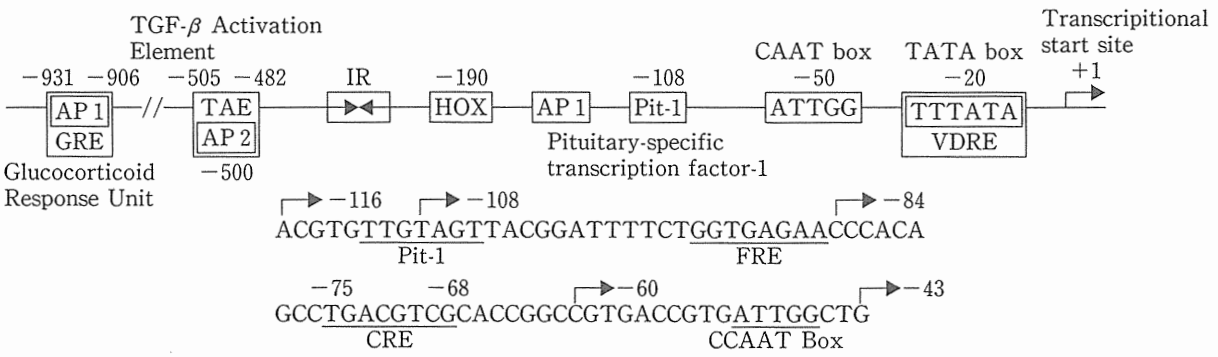

Fig. 1　Regulatory elements in the proximal rat BSP promoter

The inverted TATA and CCAAT boxes, homeobox-binding site (HOX), inverted repeat (IR), TGF-β activation element (TAE) overlapping with AP 2 and glucocorticoid response element (GRE) overlapping the AP 1, a vitamin D response element (VDRE) that overlaps the inverted TATA box, cAMP (CRE; −75 to −68) and Pit-1 (−111 to −105), that are present within a proximal promoter are shown. The numbering of nucleotides is relative to the start site of transcription.

るにもかかわらず，転写は正方向に進むことが報告されている[21]．

そこで今回われわれは，骨芽細胞様細胞であるROS 17/2.8細胞を用い，BSPの発現に対する炎症性サイトカインの1つであるTNF-αの影響，特に転写調節機構を解析することを目的に今回の研究を行った．

材料および方法

1．材料

本実験に使用した材料は，α-minimum essential培地(α-MEM)，ペニシリン，ストレプトマイシン，trypsin-EDTA，ウシ胎児血清(FCS)，アクリルアミド，アガロース(Gibco)，細胞培養シャーレーおよびフラスコ(Corning)，ルシフェラーゼアッセイ基質(東洋インキ)，〔γ-^{32}P〕ATPおよび〔α-^{32}P〕dCTP(NEN)，5,6-dichloro-1-β-D-ribofuranosyl benzimidazole (DRB) (Sigma)，リン酸化阻害剤H 89およびH 7(生化学工業)である．ほかの試薬はすべて特級品(和光純薬工業)を用いた．

2．細胞培養

骨芽細胞様細胞であるROS 17/2.8細胞[24]を用い，細胞培養は37°C，5% CO_2インキュベーター内で行った．培養液は10% FCSおよび抗生物質(100 units/mlペニシリンと100 μg/mlストレプトマイシン)を含むα-MEMを用いた[12]．60 mm培養シャーレ中で，ROS 17/2.8細胞をコンフルエントになるまで培養し，血清を含まないα-MEM中で12時間培養後，TNF-α(10 ng/ml)を作用させ，3，6，12および24時間後に細胞を回収した．BSP mRNAの半減期に対するTNF-αの影響を検索するために，TNF-α(10 ng/ml)で6時間刺激したROS 17/2.8細胞に転写阻害剤であるDRB(60 μmol/l)を作用させ，経時的(3，6，12および24時間)に細胞を回収した．回収した細胞から全RNAを抽出後，以下のようにノーザンブロット解析を行った．

3．ノーザンブロット解析

回収した細胞から，グアニジンチオシアネート法を用いて全RNAを抽出後[15]，20 μgの全RNAを1.2%アガロースゲルで電気泳動し，ナイロンメンブレンに転写した．ランダムプライム法にてBSPおよびコントロールとしてrat glyceraldehyde-3-phosphate dehydrogenase (GAPDH) cDNAを〔α-^{32}P〕dCTPを用いて標識し，ハイブリダイゼーションに用いた．42°Cでハイブリダイゼーション後，メンブレンを0.1% SDSを含む2×SSC(30 mmol/l酢酸ナトリウム，0.3 mol/l塩化ナトリウム，pH 7.0)で25°C，30分間2回洗浄し，さらに55°Cで30分間洗浄した．次に，0.1×SSC(0.1% SDSを含む)で55°C，30分間2回洗浄した後，フジBAS 2000イメージングプレートにメンブレンを約12時間コンタクトさせた．ハイブリダイゼーションの結果は，フジBAS 2000イメージングアナライザーを用いて解析した[15]．

4．ルシフェラーゼアッセイ

ルシフェラーゼプラスミドを制限酵素，*Hind* IIIおよび*Sal* Iで切断し，さまざまな長さに調節したラットBSPプロモーター配列を挿入した．作成した

コンストラクトはpLUC 3(+60～−116塩基対)，pLUC 4(+60～−425塩基対)，pLUC 5(+60～−801塩基対)，pLUC 6(+60～−938塩基対)，pLUC 7(+60～−1149塩基対)で，pLUCBはプロモーター配列を挿入していないルシフェラーゼプラスミドである[12]．プラスミドを細胞に導入する1日前に，ROS 17/2.8細胞を35 mmディッシュに播種し，細胞が40～60%コンフルエントの状態で，ルシフェラーゼプラスミドとコントロールとしてβガラクタシダーゼ(β-Gal)プラスミドをリポフェクトエースを用いて細胞にトランスフェクションした[25]．プラスミドが導入されたROS 17/2.8細胞は，10% FCSを含むα-MEM培地で2日間培養し，次に無血清培地で12時間培養後，TNF-α(10 ng/ml)で6または24時間刺激した．TNF-α刺激後の細胞内情報伝達系を検索する目的で，チロシンキナーゼ阻害剤であるハービマイシンA(1 μmol/l)，プロテインキナーゼA阻害剤であるH 89(5 μmol/l)，プロテインキナーゼC阻害剤であるH 7(5 μmol/l)を用い同様にルシフェラーゼアッセイを行った．刺激した細胞はPBSで2回洗浄し，細胞溶解液(125 μl)にて溶解後，12,000×gで1分間遠心し，上清を活性の測定に用いた．20 μlの上清と100 μlのルシフェラーゼ基質を混合し，ルミノメーター(アロカ)にて活性の測定を行った．プラスミドの導入効率を補正するために，60 μlの上清と66 μlのβ-Gal基質を混合し，37°Cで12時間インキュベート後，595 nmで吸光度を測定し，活性値の補正に用いた[15]．

5．ゲルシフトアッセイ

ルシフェラーゼアッセイの結果から，ラットBSPプロモーター配列中のTNF-αに応答すると考えられるDNA配列の合成を行った．合成オリゴヌクレオチドは相補鎖同士がそれぞれ終濃度10 pmolになるように調整し，100°Cで5分間煮沸後，室温に放置して2本鎖にするためのハイブリダイズを行った．2本鎖オリゴヌクレオチドは2 pmolに希釈し，T_4ポリヌクレオチドキナーゼを用いて，[γ-^{32}P] ATPにて標識を行った．ROS 17/2.8細胞をTNF-α(10 ng/ml)にて経時的に刺激後，核内タンパク質の抽出を行った[26]．核内タンパク質には，緩衝液(10 mmol/l Tris-HCl，50 mmol/l KCl，1 mmol/l DTT，0.04% Nonidet P-40，5% glycerol，0.5 mmol/l EDTA)と1 μg/μl polydI-dCを加え，アイソトープ標識したオリゴヌクレオチドを添加し，20分間室温でインキュベート後，5%ポリアクリルアミドゲルにて電気泳動を行った．ゲルを乾燥後，イメージングプレートにコンタクトし，約12時間後にフジBAS 2000イメージングアナライザーにて解析を行った[15]．

結　果

1．TNF-αによるBSP mRNA発現の変化について

TNF-α(10 ng/ml)にて3，6，12および24時間刺激したROS 17/2.8細胞から全RNAを抽出し，ノーザンブロット解析を行った．TNF-α刺激後のBSP mRNA量はコントロールと比べて6時間後にやや上昇が認められたが，3および12時間後にはほとんど変化はなく，TNF-α刺激24時間後に有意なmRNA量の減少が認められた(結果は示していない)．

2．TNF-αのBSP mRNAの半減期に対する影響

BSP mRNAの分解速度(半減期)に対するTNF-αの影響を検索する目的で，TNF-αにて6時間刺激後に，転写阻害剤であるDRB(60 μmol/l)をROS 17/2.8細胞に添加し，経時的に全RNAを抽出しノーザンハイブリダイゼーションを行った．その結果，コントロールとTNF-α刺激後のBSP mRNAの半減期に変化は認められず，TNF-α(6時間刺激)はBSP mRNAの分解速度に影響を与えないことが判明した(Fig. 2)．

3．TNF-αのBSPの転写活性に対する効果

さまざまな長さに調節したラットBSP遺伝子プロモーター配列を挿入したルシフェラーゼプラスミド(pLUC 3～pLUC 7)を用いてTNF-α(10 ng/ml；6時間刺激)の効果を検索した結果，pLUC 3(+60～−116塩基対)およびそれよりも長いBSPプロモーター配列を含むルシフェラーゼコンストラクト(PLUC 4，5，6および7)でTNF-αによる転写活性の上昇(約2倍)が認められた(Fig. 3)．以上の結果から，ラットBSPプロモーターの−116塩基対上流までの配列中にTNF-α刺激に応答する配列が存在すると考えられた．一方，TNF-α(10 ng/ml)で24時間刺激すると，転写活性の低下(約0.6倍)が認められた(結果は示していない)．

4．TNF-αの作用に対するリン酸化阻害剤の効果

TNF-α(6時間刺激)によるBSPの転写活性の上昇

がどのような情報伝達系を介しているかを検索する目的で，−116塩基対上流までのBSPプロモーター配列を含むpLUC 3コンストラクトを用い，リン酸化阻害剤を用いたルシフェラーゼアッセイを行った．チロシンキナーゼ阻害剤であるハービマイシンAはTNF-α刺激12時間前に，Cキナーゼ阻害剤(H 7)およびAキナーゼ阻害剤(H 89)は刺激30分前に培地に添加し，その後TNF-αと同時に培地に加えて6時間刺激を行った．その結果，チロシンキナーゼ阻害剤であるハービマイシンAによりTNF-αによるBSP

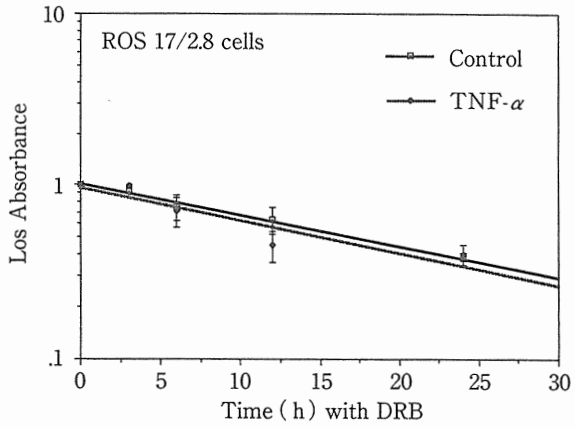

Fig. 2 Analysis of BSP mRNA stability

Confluent cultures of ROS 17/2.8 cells were incubated for 6 h with or without TNF-α (10 ng/ml), prior to the addition of the transcription inhibitor (60 μmol/l, 5, 6-dichloro-1-β-D-ribofuranosyl benzimidazole). Triplicate cultures for each condition were used to prepare total RNA at the times indicated over a 24-h period. The level of BSP mRNA at each time point was analyzed by Northern hybridization and a half-life of～16 h calculated for the mRNA in the ROS 17/2.8 cells.

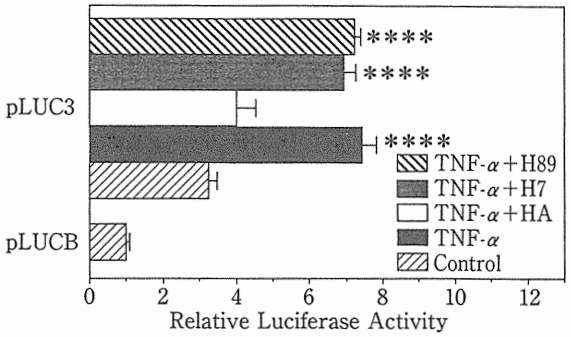

Fig. 4 Role of various kinase inhibitors in the stimulation of BSP gene expression by TNF-α

The effects of the cAMP-dependent protein kinase A inhibitor (H 89), protein kinase C inhibitor (H 7) and tyrosine kinase inhibitor (herbimycin A; HA) were analyzed in transient transfection assays of pLUC 3 in the presence or absence of TNF-α (10 ng/ml) for 6 h in ROS 17/2.8 cells. The relative activities of pLUC 3, determined in three separate transfections, have been combined and the values expressed with standard errors. Significant differences from control. ****$p<0.01$.

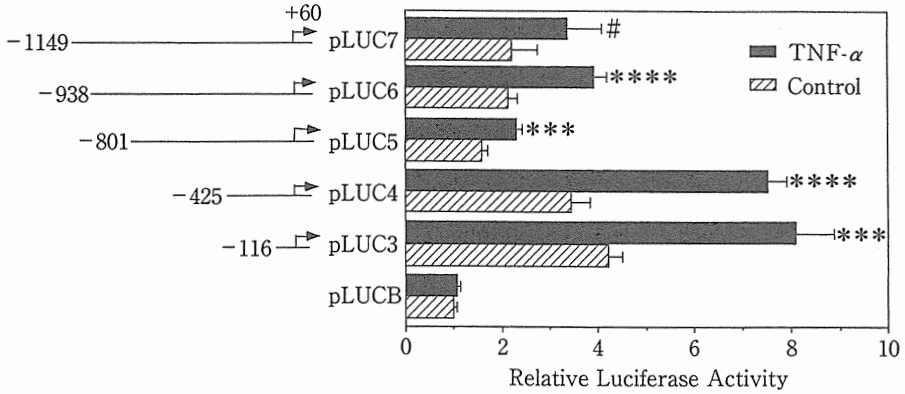

Fig. 3 TNF-α up-regulate BSP promoter activity

Transient transfection of ROS 17/2.8 cells, in the presence or absence of TNF-α (10 ng/ml) for 6 h, were determine transcriptional activity of chimeric constructs that included various regions of the BSP promoter ligated to a luciferase reporter gene. The results obtained from three separate transfections with constructs; pLUC basic (B) and pLUC 3 to pLUC 7 have been combined and the values expressed with standard errors. Significant differences from control. ****$p<0.01$, ***$p<0.02$, #$p<0.2$.

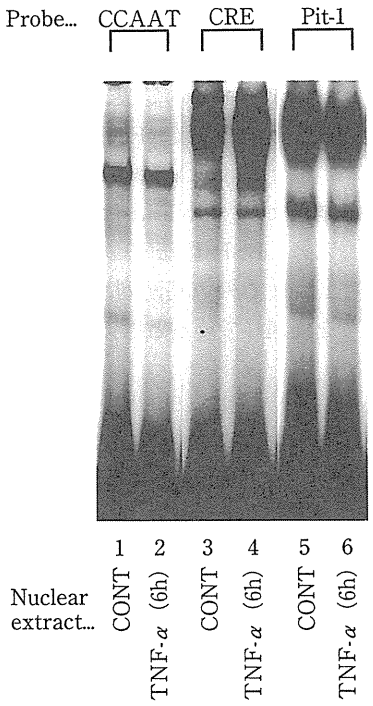

Fig. 5 TNF-α increase DNA binding activity recognizing the cyclic AMP response element (CRE)

Radiolabelled double-stranded inverted CCAAT box, CRE and Pit-1 were incubated for 20 min at 21°C with nuclear protein extract (3 μg) obtained from cells incubated without (Control) or with TNF-α (10 ng/m*l*) for 6 h. DNA-protein complexes were separated on 5% polyacrylamide gel in low ionic strength Tris borate buffer, dried under vacuum, and exposed to imaging plate for quantitation using an imaging analyzer.

の転写活性の上昇が抑制された(Fig. 4).

5. ゲルシフトアッセイの結果

ルシフェラーゼアッセイの結果より，ラットBSPプロモーターの転写開始点から−116塩基対上流までの配列中にTNF-αに応答する配列が存在すると考えられた．この配列中に存在する特徴的な転写因子結合配列は，逆方向のCCAAT配列(−46〜−50)，CRE配列(−68〜−75)，Pit-1(−105〜−111)配列であるため(Fig. 1)，それぞれに相当するオリゴヌクレオチドを合成した．核内タンパク質と各合成DNAとの結合をゲルシフトアッセイにて検索した結果，逆方向のCCAAT配列，Pit-1配列ではコントロールと比べ，TNF-α 6時間刺激後の核内タンパク質とDNAとの結合に変化は認められなかった．一方CRE配列では，TNF-α刺激後の核内タンパク質とDNAとの結合に増加が認められた(Fig. 5).

考　察

BSPは石灰化初期に発現し，初期のアパタイト結晶成長を制御していると考えられている非コラーゲン性タンパク質である．BSPの転写はホルモンや成長因子により調節を受けているが，その機序は完全には明らかにされていない．今回われわれは，炎症性サイトカインの1つであるTNF-αに着目し，TNF-αによるBSPの転写調節機構を検討することを目的に研究を行った．

本研究の結果，TNF-αは骨芽細胞様細胞であるROS 17/2.8細胞において，BSPの転写活性を短時間(6時間)刺激で促進した．そしてその転写調節は，ラットBSPプロモーターの転写開始点から−116塩基対上流までに存在する塩基配列を介すると考えられた．一方，今回の結果には示していないが，TNF-αは24時間刺激では転写活性を抑制した．ラットBSPプロモーターの−116塩基対上流までに存在する転写因子結合配列のなかで，TNF-α 6時間刺激後に核内タンパク質との結合が変化したのはCRE配列だけであった．さらに，TNF-α刺激後の細胞内情報伝達系はチロシンのリン酸化を介すると考えられた．

BSPの転写活性は，TNF-α刺激により6時間後に上昇し，24時間後に低下した．一方，BSP mRNA量は，TNF-α刺激6時間後にわずかに上昇し，24時間後に有意に減少した．TNF-α6時間刺激でBSPの転写活性が約2倍上昇するにもかかわらず，BSP mRNA量がほとんど増加しない原因は不明である．しかし，その1つの要因として，核内で転写された一次転写産物がキャップ形成，ポリアデニル化，もしくはRNAスプライシングの過程でTNF-αによる影響を受け，核外に移行するmRNA量が減少した可能性が考えられる．また，mRNAの合成と分解のバランスがTNF-αによりくずれた可能性も考えられ，現在検索を行っているところである．一方，TNF-α 24時間刺激ではノーザンブロットとルシフェラーゼアッセイの結果は一致し，BSPの転写はTNF-αにより抑制を受けると考えられた．過去の報告の多くは，TNF-αによる骨形成の抑制，および骨吸収の促進効果を示しており[27,28]，本研究におけるTNF-α 6時間刺激後のBSPの転写促進効果は過去の報告とは逆の結果で

ある．しかし，TNF-αは破骨細胞分化因子(Osteoclast differentiation factor；ODF)を介さずに直接破骨細胞の分化を誘導することから[29]，今回行ったような短時間作用では，TNF-αは破骨細胞による骨吸収と，それに続く骨芽細胞による骨形成を活性化し，骨の代謝回転を上昇させる効果を示す可能性がある．また，TNF-αは活性酸素を誘導し，転写因子であるNFκBの発現を誘導することや[30]，NFκBの活性化がTNF-αによるアポトーシスを抑制することなどが報告されており[31]，免疫や炎症反応初期の過程で，細胞質に存在する不活性化されたNFκBが迅速に核内に移行し，BSPまたはサイトカイン，受容体発現等を促進する可能性が考えられる．一方，炎症反応後期には，核内のNFκBは不活性化され，TNF-αによるアポトーシスが誘導されて，BSPの発現を抑制すると考えられる．

骨芽細胞は分化のステージ特異的にさまざまな因子に反応し，分化段階が異なると同じ因子に対して異なった反応を示す場合があるため[32]，分化程度の異なるほかの骨芽細胞様細胞を用いたさらなる検討を行う必要があると考えられた．CRE配列に結合する転写因子は，一般的にはCRE結合タンパク質と呼ばれ，Aキナーゼによりリン酸化を受け活性化される．今回の実験結果から，TNF-α刺激後にチロシンのリン酸化を介してBSPの転写が促進されたことから，CRE結合タンパク質のCREへの結合が，TNF-α刺激後にどのような機序で増加したかは，今後の課題であると考えられた．今後，TNF-α刺激後の核内タンパク質の経時的な発現およびリン酸化，リン酸化阻害剤の影響を検索し，さらには抗酸化剤を用いてTNF-α刺激後の活性酸素の影響等を検討する必要があると考えられた．

結　論

骨芽細胞様細胞であるROS 17/2.8細胞を用いて，TNF-α(10 ng/ml)のBSPの転写に及ぼす影響を検討した結果，以下の知見を得た．

1．ノーザンブロットの結果，TNF-α 6時間刺激後に，BSP mRNA量はわずかに増加した．

2．ルシフェラーゼアッセイの結果，TNF-α(6時間刺激)によりラットBSP遺伝子プロモーターの+60～−116塩基対上流を含むコンストラクトで転写活性の上昇が認められた．

3．TNF-α刺激によるBSPの転写活性の上昇は，チロシンのリン酸化を介することが判明した．

4．ゲルシフトアッセイの結果，TNF-α 6時間刺激後に，核内タンパク質とCRE配列との結合が増加した．

5．以上の結果より，TNF-αはチロシンのリン酸化を介し，ラットBSP遺伝子プロモーター中の−116塩基対上流までの塩基配列，特にCRE配列に応答して転写を促進していると考えられた．

謝　辞

本研究は文部省科学研究費(No. 07771795，08771738，09771650，12671865)，日本大学松戸歯学部鈴木研究費(平成9，12年度；共同研究，平成10～12年度；一般研究)および日本大学学術研究助成金(平成9，13年度；一般研究)，平成10年度および平成13年度学術フロンティア推進事業(文部科学省)の補助のもとに行われた．

文　献

1) Carswell EA, Old LJ, Kassel RL, Green S, Fiore N, Williamson B: An endotoxin induced serum factor that causes necrosis of fumors; Proc Natl Acad Sci USA 72, 3666−3670, 1975.
2) Li Y, Stashenko P: Characterization of a tumor necrosis factor-responsive element which down regulates the human osteocalcin gene; Mol Cell Biol 13, 3714−3721, 1993.
3) Passeri G, Girasole G, Manolagas SC, Jilka RL: Endogenous production of tumor necrosis factor by primary cultures of murine calvarial cells development: Influence on IL-6 production and osteoclast developmet; Bone Miner 24, 109−126, 1994.
4) Panagakos FS, Kumar S: Modulation of proteases and their inhibitors in immortal human osteoblast-like cells by tumor necrosis factor alpha *in vitro*; Inflammation 18, 243−265, 1994.
5) Chaudhary LR, Spelsberg TC, Riggs BL: Production of various cytokines by normal human osteoblast-like cells in responce to interleukin-1 beta and tumor necrosis factor-alpha: Lack of regulation by 17 beta-estradiol; Endocrinology 130, 2528−2534, 1992.
6) Abu-Amer Y, Ross FP, Edwards J, Teitelbaum SL: Lipopolysaccharide-stimulated osteoclastogenesis is mediated by tumor necrosis factor via its P 55 receptor; J Clin Invest 100, 1557−1565, 1997.
7) Chen J, Shapiro, HS, Wrana, JL, Reimers S, Heersche JNM, Sodek J: Localization of bone

sialoprotein (BSP) expression to sites of mineralized tissue formation in fetal rat tissues by *in situ* hybridization; Matrix 11, 133−143, 1991.
8) Chen J, Shapiro HS, Sodek J: Developmental expression of bone sialoprotein mRNA in rat mineralized connective tissues; J Bone Miner Res 7, 987−997, 1992.
9) Ganss B, Kim RH, Sodek J: Bone sialoprotein; Crit Revs Oral Biol & Med; 10, 79−98, 1999.
10) Hunter GK, Goldberg HA: Nucleation of hydroxyapatite by bone sialoprotein; Proc Natl Acad Sci USA 90, 8562−8565, 1993.
11) Oldberg Å, Jirskog-Hed B, Axelsson S, Heinegärd D: Regulation of bone sialoprotein mRNA by steroid hormones; J Cell Biol 109, 3183−3186, 1989.
12) Ogata Y, Yamauchi M, Kim RH, Li JJ, Freedman LP, Sodek J: Glucocorticoid regulation of bone sialoprotein (BSP) gene expression: Identification of a glucocorticoid response element in the bone sialoprotein gene promoter; Eur J Biochem 230, 183—192, 1995.
13) Kim RH, Li JJ, Ogata Y, Yamauchi M, Freedman LP, Sodek J: Identification of a vitamin D_3-response element that overlaps a unique inverted TATA box in the rat bone sialoprotein gene; Biochem J 318, 219—226, 1996.
14) Li JJ, Kim RH, Zhang Q, Ogata Y, Sodek J: Characteristics of vitamin D_3 receptor (VDR) binding to the vitamin D response element (VDRE) in rat bone sialoprotein gene promoter; Eur J Oral Sci 106 (suppl 1), 408—417, 1998.
15) Ogata Y, Niisato N, Furuyama S, Cheifetz S, Kim RH, Sugiya H, Sodek J: Transforming growth factor-β 1 regulation of bone sialoprotein gene transcription: Identification of a TGF-β activation element in the rat BSP gene promoter; J Cell Biochem 65, 501—512, 1997.
16) Ogata Y, Nakao S, Furuyama S, Li JJ, Kim RH, Sugiya H, Sodek J: Parathyroid hormone regulation of bone sialoprotein gene transcription is mediated through a pituitary-specific transcription factor-1 (pit-1) motif in the rat BSP gene promoter; Matrix Biol 19, 395—407, 2000.
17) Shimizu-Sasaki E, Yamazaki M, Furuyama S, Sugiya H, Sodek J, Ogata Y: Identification of a novel response element in the rat bone sialoprotein (BSP) gene promoter that mediates constitutive and fibroblast growth factor 2-induced expression of BSP; J Biol Chem 276, 5459—5466, 2001.
18) Li JJ, Sodek J: Cloning and charaterization of the rat bone sialoprotein gene promoter; Biochem J 289, 625—629, 1993.
19) Kim RH, Shapiro HS, Li JJ, Wrana JL, Sodek J: Characterization of the human bone sialoprotein (BSP) gene and its promoter sequence; Matrix Biol 14, 31—40, 1994.
20) Sodek J, Li JJ, Kim HK, Ogata Y, Yamauchi M: Characterization of bone sialoprotein (BSP) gene promoter; Connect Tissue Res 35 (1—4), 23—31 [77—85], 1996.
21) Li JJ, Kim RH, Sodek J: An inverted TATA box directs downstream transcription of the bone sialoprotein gene; Biochem J 310, 33—40, 1995.
22) Kim RH, Sodek J: Transcription of the bone sialoprotein gene is stimulated by v-Src acting through an inverted CCAAT box; Cancer Res 59, 565—571, 1999.
23) Yamauchi M, Ogata Y, Kim RH, Li JJ, Freedman LP, Sodek J: AP-1 regulation of the rat bone sialoprotein gene transcription is mediated through a TPA response element within a glucocorticoid response unit in the gene promoter; Matrix Biol 15, 119—130, 1996.
24) Majeska RJ, Rodan SB, Rodan GA: Parathyroid hormone-responsive clonal cell lines from rat osteosarcoma; Endocrinology 107, 1494—1503, 1980.
25) Rose JK, Buonocore L, Whitt MA: A new cationic liposome reagent mediating nearly quantitative transfection of animal cells; Biotechniques 10, 520—525, 1991.
26) Dignam JD, Lebovitz RM, Roeder RG: Accurate transcription initiation by RNA polymerase II in a soluble extract from isolated mammalian nuclei; Nucleic Acid Res 11, 1475—1489, 1983.
27) Bertolini DR, Nedwin GE, Bringman TS, Smith DD, Mundy GR: Stimulation of bone resorption and inhibition of bone formation *in vitro* by human tumour necrosis factors; Nature 319, 516—518, 1986.
28) Beutler BA, Cerami A: The biology of cachectin/TNF: A primary mediator of the host response; Annu Rev Immnol 7, 625—655, 1989.
29) Kobayashi K, Takahashi N, Jimi E, Udagawa N, Takami M, Kotake S, Nakagawa N, Kinosaki M, Yamaguchi K, Shima N, Yasuda H, Morinaga T, Higashio K, Martin TJ, Suda T: Tumor necrosis factor alpha stimulates osteoclast differentiation by a mechanism independent of the ODF/RANKL-RANK interaction; J Exp Med 191, 275—286, 2000.
30) Lo YYC, Cruz TF: Involvement of reactive oxygen species in cytokine and growth factor induction of c-fos expression in chondrocytes; J Biol Chem 270, 11727—11730, 1995.
31) Beg AA, Baltimore D: An essential role for NFκB in preventing TNF-α-Induced cell death; Science 274, 782—784, 1996.
32) 小方頼昌：実験動物細胞を用いた骨代謝研究；アニテックス 9, 189—193, 1997.

Journal of Oral Science, Vol. 46, No. 4, 207-213, 2004

Original

Differentiation of the human mesenchymal stem cells derived from bone marrow and enhancement of cell attachment by fibronectin

Naomi Ogura[§,‡], Masaru Kawada[†], Wei-Jen Chang[†], Qi Zhang[*], Sheng-Yang Lee[¶], Toshirou Kondoh[§,‡] and Yoshimitsu Abiko[†,‡]

Departments of [§]Oral Surgery and [†]Biochemistry and [‡]Research Institute of Oral Science, Nihon University School of Dentistry at Matsudo, Chiba, Japan
[*]Wuhan University, School of Stomatology,
[¶]Graduate Institute of Oral Rehabilitation Sciences and School of Dentistry, Taipei Medical University, Taipei, Taiwan

(Received 7 April and accepted 6 September 2004)

Abstract: The ability of human mesenchymal stem cells (hMSC) to differentiate into osteoblasts was examined through the use of osteogenic induction medium (MSCOIM) cultures. hMSC first attached to the dish surface and exhibited fibroblast-like spindle shapes, and after proliferation, formed cuboidal shapes. Calcium assays and the use of von Kossa and alizarin red S staining showed that hMSC were capable of mineralization when cultured in MSCOIM. Gene expressions of Cbfa-1 and BMP-4, which are markers for osteogenic differentiation, were also increased during the hMSC differentiation into osteoblasts. When compared to albumin (Alb)-coated dishes, microscopic observation documented enhanced cell attachment and spreading when hMSC were cultured on fibronectin (FN)-coated dishes. Adherent cell numbers also exhibited a greater increase on the FN-coated dishes during earlier culture stages than that seen for the Alb-coated dishes. These findings suggest that hMSC have the capability to differentiate into osteoblasts and that FN can stimulate the attachment and spreading of the hMSC. (J. Oral Sci. 46, 207-213, 2004)

Correspondence to Dr. Yoshimitsu Abiko, Department of Biochemistry, Nihon University School of Dentistry at Matsudo, 2-870-1 Sakaecho-nishi, Matsudo, Chiba 271-8587, Japan
Tel: +81-47-360-9328,
Fax: +81-47-360-9329.
E-mail: yabiko@mascat.nihon-u.ac.jp

Key words: mesenchymal stem cell; osteoblast; fibronectin.

Introduction

Bone formation comprises a complex set of events that begins with the recruitment and proliferation of osteoprogenitors followed by cell differentiation, osteoid formation, and mineralization. It has been recognized that bone is unique and has a vast potential for regeneration from stem cells (1,2). A number of reports have indicated there is a potential for mesenchymal stem cell (MSC) transplantation from bone marrow for a variety of skeletal disorders (3,4). The development of MSC differentiation from human bone marrow along specific lineages in combination with biomimetic scaffolds provides the possibility of tissue engineering for bone and cartilage (5). The ability of progenitor cells to attach to a scaffold surface during early stages is important in the development of new tissue structures (6,7).

The initial contact of the cells with the implant surface is an important event for adhesion of the bone cells that influence osseointegration. One strategy to improve osseointegration that has been tried involves the precoating of implants with an extracellular matrix protein for use as a scaffold, which enables specific cell-extracellular matrix interactions, along with the use of growth factors to facilitate the differentiation of the osteoblasts (8,9). Extracellular matrices, such as collagen type I and fibronectin (FN), are effective in promoting cellular

adhesion and spreading, and they possess a RGD (arginine-glycine-aspartic acid) sequence, which is recognized by integrins (10-12). Signaling occurs when integrins bind to the extracellular matrix and results in changes in the expression of select genes that control the initial preosteoblast/osteoblast adhesion, proliferation and maturation (10-12).

The aims of the present study were to examine the early stages of cell attachment and the spreading of human mesenchymal stem cells (hMSC) derived from bone marrow on surfaces that were modified by FN.

Materials and Methods

Cell culture

The Poietics^{TM} Human Mesenchymal Stem Cell product (hMSC; Lot No. 9F1938) was obtained from Cambrex Bio Science Walkersville (East Rutherford, NJ, USA). The cells were cultured in MSC growth medium (MSCGM; the cell system components consisted of the MSC basal medium and the SingleQuots® growth supplements MCGS, which contained fetal bovine serum (FBS), L-glutamine and penicillin/streptomycin; Cambrex Bio Science Walkersville) in a humidified incubator (Forma CO_2 incubator MIP-3326; Sanyo Electric Medical System, Japan) in the presence of 95% air and 5% CO_2 at 37°C. In the experiment for osteogenic differentiation, hMSC from the 5th to 7th doubling passages were seeded at 3.1×10^3 cells/cm^2 in MSCGM. After 24 h, the media was changed to MSC osteogenic induction medium (MSCOIM; the cell system components consisted of MSC basal medium and the osteogenic SingleQuots® that contained FBS, L-glutamine, penicillin/streptomycin, dexamethasone, ascorbate, and β-glycerophosphate; Cambrex Bio Science Walkersville,). The media was changed twice a week. The schema for the culture is shown in Fig. 1.

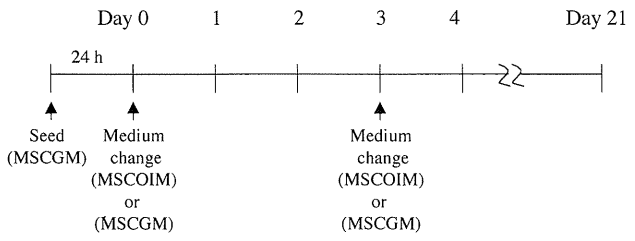

Fig. 1 Schema of hMSC culture. The cells were seeded at 3.1×10^3 cells/cm^2 in MSCGM. After 24 h (day 0), the media was changed to MSCOIM or MSCGM. The media was changed twice a week.

Microscopic observation

Morphology of hMSC was observed by phase-contrast microscopy and pictures were taken of the specimens (DP12, Olympus, Tokyo, Japan).

Histochemical analysis

Mineralization of the cell layer was examined through the use of alizarin red S or von Kossa staining. The cell layers were washed twice with phosphate-buffered saline (PBS) fixed with 10% formalin solution for 30 min, and then washed with pure water two times. For alizarin red S staining, the cells were placed in 1% alizarin red S (Kanto Chemical, Tokyo, Japan) solution for 10 min, washed with pure water three times and then air-dried. The von Kossa staining was performed according to the method of Jaiswal et al. (1). Briefly, the cell layers were placed in a 5% silver nitrate (Kanto Chemical) solution for 10 min, and kept in the dark. After washing with pure water, the cell layers were then exposed to bright light for 15 min.

Calcium assay

Calcium content was measured using a calcium assay kit (Sigma Diagnostics, St. Louis, MO, USA). Briefly, the cell layers were washed twice with PBS. Calcium in the matrix was dissolved with 0.5 M HCl, assay reagent was added, and then the sample was measured at a wavelength of 598 nm.

Alkaline phosphatase assay

The cell lysate was obtained through the use of a solubilizing solution (0.01% NaCl, 0.1% Triton X-100), incubated with *p*-nitrophenyl phosphate solution (Chemicon International, Tenecula, CA, USA) at 37°C, and then 1 M NaOH was added to stop the reaction. The samples were measured at a wavelength of 415 nm. ALP activity was calculated per 10^5 cells, and was determined from a *p*-nitrophenol standard curve with 1 unit representing the release of 1 μmol of *p*-nitrophenol per min at 37°C.

Real-time PCR

Total RNA was extracted using TRIZOL Reagent (Life Technologies, Gaithersburg, MD, USA) and the FastPrep FP120 Instrument (BIO 101, Vista, CA, USA). cDNA was synthesized using a GeneAmp RNA PCR kit (Perkin-Elmer, Norwalk, CT, USA). The real-time PCR was carried out using a DyNAmo SYBR Green qPCR kit (Finnzymes, Espoo, Finland). The PCR mixture, which contained 20 pmol of forward and reverse primers and 2 μl of cDNA, was subjected to amplification with a DNA Engine Opticon 1 (MJ Research, San Francisco, CA, USA). The cycles were set at 95°C for 10 min for preheating, followed by 40

cycles at 94°C for 15 sec, 55°C for 30 sec and 72°C for 30 sec. The amplicons were detected directly by measuring the increase in fluorescence caused by the binding of the SYBR Green I dye to gene-specific, amplified, double-stranded DNA using a DNA Engine Opticon 1. Following the completion of the PCR reaction, the temperature was raised from the annealing temperature to 95°C for a melting curve analysis.

The initial template concentration was derived from the cycle number at which the fluorescent signal crossed a threshold in the exponential phase of the PCR reaction (CT-value). The number of transcripts was determined based on the threshold cycles of Cbfa-1, BMP-4 and GAPDH. ΔCT (CT-Cbfa-1 or BMP-4 minus CT-GAPDH) designated the relative abundance of the Cbfa-1 or BMP-4 transcript. ΔΔCT (ΔCT-osteoinduction minus ΔCT-day 0) represented the relative n-value compared to the control. The 2^{-n} represented the difference in mRNA expressions in osteoinduction cells relative to day 0. The respective primer sequences were 5'-TGA GAG CCG CTT CTC CAA CC-3' (the forward primer for Cbfa-1); 5'-GCG GAA GCA TTC TGG AAG GA-3' (the reverse primer for Cbfa-1); 5'-AAG CGT AGC CCT AAG CAT-3' (the forward primer for BMP-4); 5'-CAT CCA GGT ACA GCA TGG-3' (the reverse primer for BMP-4); 5'-ATC ACC ATC TTC CAG GAG-3' (the forward primer for GAPDH); and 5'-ATC GAC TGT GGT CAT GAG-3' (the reverse primer for GAPDH).

Fibronectin coating

After pouring 500 μl of 6.25 μg/ml fibronectin (human plasma; KOKEN, Japan) or 50 μg/ml albumin (Alb, human; Funakoshi, Japan) in PBS into the wells of a 24-well tissue culture plate (Corning Cell Wells, Corning, NY, USA), the plates were then incubated at 37°C overnight for coating, after which the wells were washed twice with PBS.

Cell adhesion

For adhesion experiments, hMSC were plated at 4.5×10^4 cells/well in a 24-well plate. The cells were cultured in MSC basal medium that was supplied with L-glutamine and penicillin/streptomycin, and serum free in a CO_2 incubator, and then the cells were detached by 0.05% trypsin and 0.02% EDTA. Cell numbers were counted with a coulter counter (Model ZM, Electronics, UK).

Statistics

Multiple samples were collected for each measurement, and the results were expressed as means ± SD. A Student's *t*-test was used for the analysis of the difference.

Results

Differentiation of hMSC

We first examined the ability of hMSC to differentiate into osteoblasts using MSCOIM. Most of the cells that attached to the plastic surface exhibited a fibroblast-like spindle shape. They proliferated to form a uniform confluent cell monolayer and became cuboidal in shape 4 days after changing from MSCGM to the MSCOIM (Fig. 2). The hMSC cultured in MSCOIM stained weakly on day 10, but stained strongly on day 13 or 17 when exposed to alizarin red S, which indicates calcium deposition (Fig. 3). On day 21, formed calcium phosphate deposition was observed after von Kossa staining. In contrast these cells were not found in MSCGM cultures (Fig. 4). Calcium contents of the hMSC cell layers on day 21 were also found to have increased in MSCOIM cultures as compared to controls (MSCGM) (Fig. 5). We then measured ALP activity of hMSC cultured in MSCOIM or MSCGM. As shown in Fig. 6, there was increased ALP activity in the hMSC cultures on day 4, with the increase peaking on day 7. Furthermore, gene expression of Cbfa-1 and BMP-4 were examined by real-time PCR. Both Cbfa-1 and BMP-4 mRNA levels were significantly enhanced on culture day 12 as compared to day 0 (Table 1).

Cell adhesion

The hMSC attachment and spreading were also examined on FN-coated dishes and compared with Alb-coated dishes,

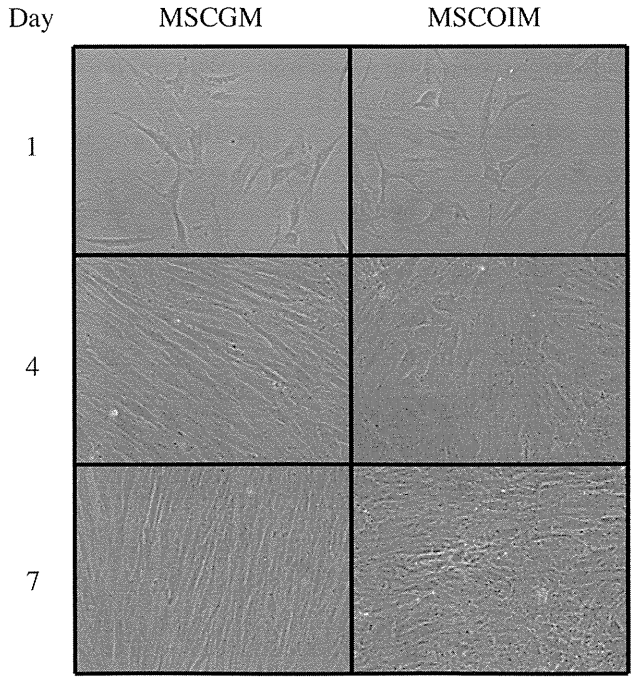

Fig. 2 Morphology of hMSC.

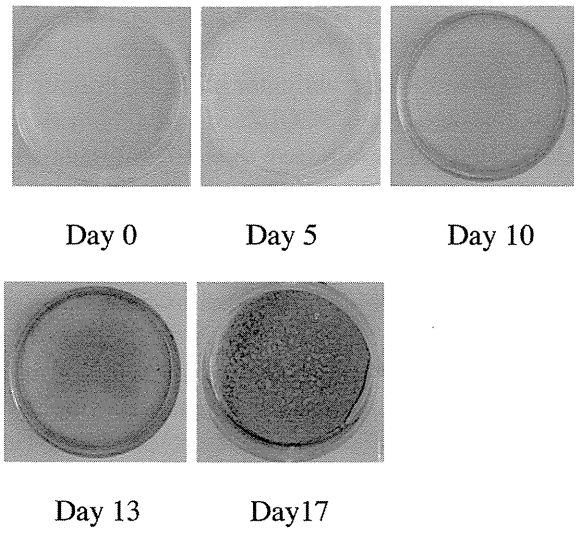

Fig. 3 Alizarin red S staining.

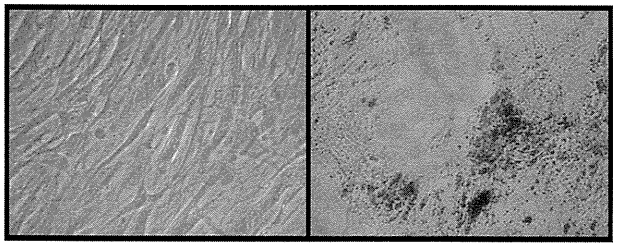

Fig. 4 von Kossa staining on day 21. hMSC were cultured with MSCGM or MSCOIM.

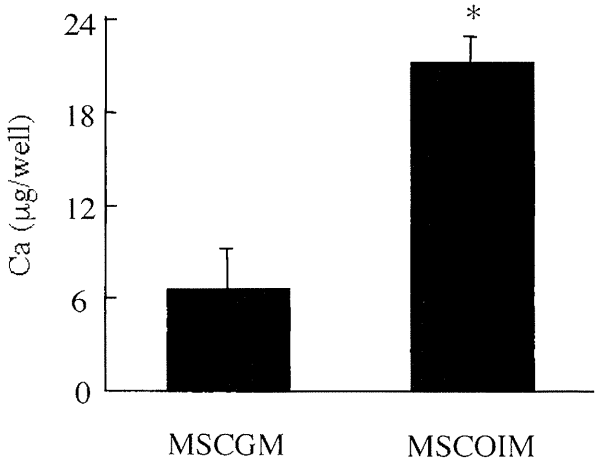

Fig. 5 Level of calcium deposition in the cell layers of hMSC. Values represent the means ± SD of the results from four wells. *, $P < 0.005$ vs. MSCGM.

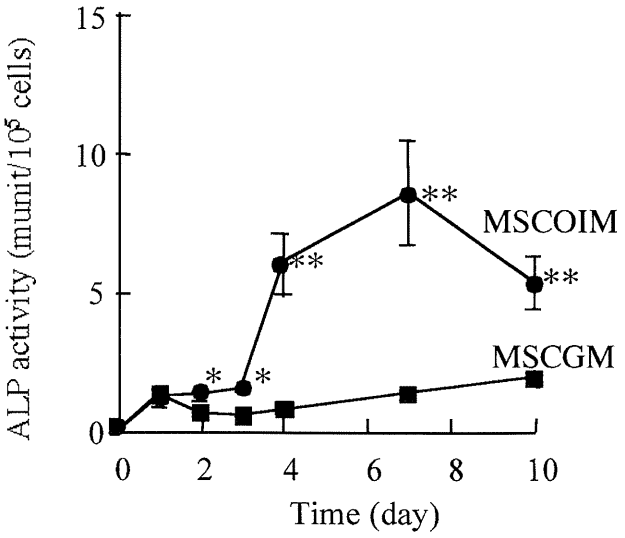

Fig. 6 ALP activity of hMSC. Values represent the means ± SD of the results from four wells. *, $P < 0.01$, **, $P < 0.005$ vs. MSCGM.

Table1 Gene expression of Cbfa-1 and BMP-4 in osteogenic induction of hMSC

	Cbfa-1 (Fold)	BMP-4 (Fold)
Day 0	1.0	1.0
Day 4	2.78	0.87
Day 8	1.44	0.53
Day 12	16.14	3.60

which were used as controls. Enhanced cell attachment and spreading were observed in the FN-coated dishes as compared to the Alb-coated dishes (Fig. 7). To quantitatively confirm the number of adherent cells on the FN-coated and Alb-coated dishes, each were measured and compared. As shown in Fig. 8, hMSC rapidly adhered to the FN-coated dishes in the earlier stages, i.e., up to the 20 minute time point, and higher cell numbers were found in the samples obtained up to the 50 min point as compared to the Alb-coated dishes.

Discussion

Tissue engineering, which includes bed structures for osteogenesis in dental implantations, makes use of the advantage of combining cultured living cells and an implant body that can be used as a scaffold (10-12). Previous attempts to tissue engineer bone or cartilage reconstruction around implants have utilized osteoblasts or chondrocytes encapsulated in various hydrogels, which can survive *in*

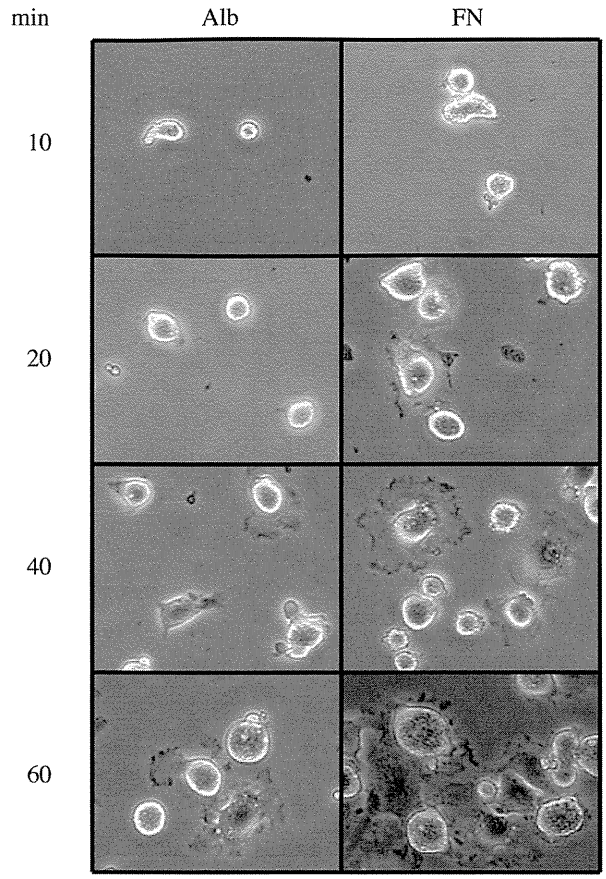

Fig. 7 Morphology of hMSC attachment in Alb- or FN-coated plates.

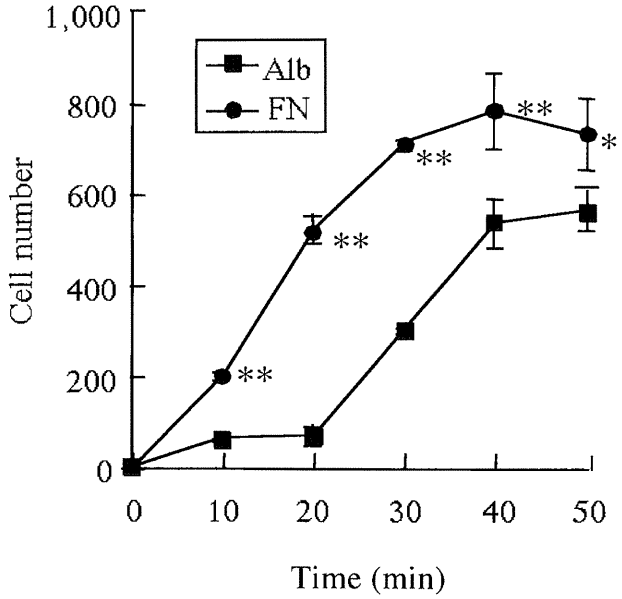

Fig. 8 Cell number attachment for hMSC in Alb- or FN-coated plates. Values represent the means ± SD of the results from four wells. *, $P < 0.01$, **, $P < 0.005$ vs. Alb.

vitro fabrication and be able to synthesize cell-associated scaffold extracellular matrices (13,14). For dental implantation, it is recommended that patients have transplantation of normal osteoblasts or chondrocytes that come from their own bodies. However, this may not always be possible. On the other hand, cultured MSC from bone marrow can be regarded as a bone progenitor/precursor cell population that can be derived from adults (6,7). It has the ability to proliferate extensively, and maintain its ability to differentiate into osteoblastic or chondrocytic cells *in vitro*. The objective of this study was to examine hMSC differentiation into the osteoblastic lineage and study the cell attachment that occurs during early stages when using FN as a scaffold.

In our preliminary experiments, the ability of hMSC to differentiate into osteoblasts was examined. Results obtained from the calcium assay and alizarin red S and von Kossa staining documented that mineralization occurred in the cell layers during osteoblast differentiation of the hMSC in the MSCOIM cultures. ALP activity and gene expression for Cbfa-1and BMP-4, which are markers for osteogenic differentiation, increased for hMSC during cultures with MSCOIM. These findings demonstrate that hMSC maintain the ability to differentiate into osteoblastic cells and thus it seems likely that MSCOIM is necessary in order to be able to induce differentiation and mineralization of hMSC. Therefore our data indicate that the osteogenic potential of hMSC-derived osteogenic precursors may be useful for autologous grafts.

For dental implantation, a stable primary stabilization and a subsequent osseointegration of the endoprotheses are of critical importance with regard to the overall clinical results. In order to accelerate and enhance the bone growth and to strengthen the osseous fixation, implant surfaces have been modified, and in particular, there has been an increased use in surface coatings of functional proteins. Numerous substances, such as growth factors (2,15,16) and extracellular matrices (3-5,16-18), are currently used to coat the surfaces of the biomaterial used in the implants. FN is a major extracellular matrix protein and is found in abundance in blood plasma. This protein is known to be involved in cell adhesion processes and contains the specific amino acid sequence for the RGD motif that is recognized by specific cell membrane receptors such as integrins (19).

In our study, the measurement of cell adhesion during the early stages showed that hMSC had enhanced cell attachment and spreading in FN-coated dishes as compared

to the Alb-coated control dishes. It has also been reported that in non-differentiation, expanded attached hMSC were uniformly positive for SH2, SH3, CD29, CD44, CD71, CD90, CD106, CD120a, and CD124 (7). CD29, which is β1 integrin, has been suggested to be important for cell adhesion in hMSC (20), although there have been no reports on the presence of α integrins (CD49a-f) in hMSC to the best of our knowledge. On the other hand, CD44 is not only hyaluronic acid but also a FN receptor, and it has been implicated in hematopoietic stem cell adhesion, proliferation, and mobilization (21). Enhanced cell attachment and spreading in FN-coated plates may be associated with CD29 and CD44 of the hMSC surface proteins.

The most frequent complication of dental implantation is bone resorption that is initiated by an inflammatory response at the implant site. Recent studies have demonstrated that titanium is the most frequent component of dental implants, and that this material is responsible for inducing apoptosis and suppressing expression of the osteoblastic phenotype in hMSC (22,23). Therefore, it is suggested that precoating dental implants with extracellular matrices such as FN is an important strategy when trying to improve the success rate for tissue regeneration.

The results obtained in this paper are very promising and we propose that the use of culture-expanded osteoprogenitor cells in conjunction with a FN-modified implant body will lead to significant improvements in grafting techniques.

Acknowledgments

We would like to thank Dr. Hideaki Nagura for suggestions with regard to this study.

This study was supported in part by a Grant from the Ministry of Education, Culture, Sports, Science, and Technology to promote 2001-multidisciplinary research projects (in 2001-2005).

References

1. Jaiswal N, Haynesworth SE, Caplan AI, Bruder SP (1997) Osteogenic differentiation of purified, culture-expanded human mesenchymal stem cells *in vitro*. J Cell Biochem 64, 295-312
2. Pittenger MF, Mackay AM, Beck SC, Jaiswal RK, Douglas R, Mosca JD, Moorman MA, Simonetti DW, Craig S, Marshak DR (1999) Multilineage potential of adult human mesenchymal stem cells. Science 284, 143-147
3. Cooper LF, Harris CT, Bruder SP, Kowalski R, Kadiyala S (2001) Incipient analysis of mesenchymal stem-cell-derived osteogenesis. J Dent Res 80, 314-320
4. Young CS, Terada S, Vacanti JP, Honda M, Bartlett JD, Yelick PC (2002) Tissue engineering of complex tooth structures on biodegradable polymer scaffolds. J Dent Res 81, 695-700
5. Alhadlaq A, Mao JJ (2003) Tissue-engineered neogenesis of human-shaped mandibular condyle from rat mesenchymal stem cells. J Dent Res 82, 951-956
6. Howlett CR, Evans MDM, Walsh WR, Johnson G, Steele JG (1994) Mechanism of initial attachment of cells derived from human bone to commonly used prosthetic materials during cell culture. Biomaterials 15, 213-222
7. Grzesiak JJ, Pierschbacher MD, Amodeo MF, Malaney TI, Glass JR (1997) Enhancement of cell interactions with collagen/glycosaminoglycan matrices by RGD derivatization. Biomaterials 18, 1625-1632
8. Yliheikkilä PK, Masuda T, Ambrose WW, Suggs CA, Felton DA, Cooper LF (1996) Preliminary comparison of mineralizing multilayer cultures formed by primary fetal bovine mandibular osteoblasts grown on titanium, hydroxyapatite, and glass substrates. Int J Oral Maxillofac Implants 11, 456-465
9. Shah AK, Lazatin J, Sinha RK, Lennox T, Hickok NJ, Tuan RS (1999) Mechanism of BMP-2 stimulated adhesion of osteoblastic cells to titanium alloy. Biol Cell 91, 131-142
10. Masi L, Franchi A, Santucci M, Danielli D, Arganini L, Giannone V, Formigli L, Benvenuti S, Tanini A, Beghè F, Mian M, Brandi ML (1992) Adhesion, growth, and matrix production by osteoblasts on collagen substrata. Calcif Tissue Int 51, 202-212
11. Cooper LF, Handelman B, McCormack SM, Guckes AD (1993) Binding of murine osteoblastic cells to titanium disks and collagen I gels: implications for alternative interpretations of osseointegration. Int J Oral Maxillofac Implants 8, 264-272
12. Degasne I, Baslé MF, Demais V, Huré G, Lesourd M, Grolleau B, Mercier L, Chappard D (1999) Effects of roughness, fibronectin and vitronectin on attachment, spreading, and proliferation of human osteoblast-like cells (Saos-2) on titanium surfaces. Calcif Tissue Int 64, 499-507
13. Weng Y, Cao Y, Silva CA, Vacanti MP, Vacanti CA (2001) Tissue-engineered composites of bone and cartilage for mandible condylar reconstruction. J Oral Maxillofac Surg 59, 185-190
14. Cassinelli C, Morra M, Bruzzone G, Carpi A, Di Santi G, Giardino R, Fini M (2003) Surface

chemistry effects of topographic modification of titanium dental implant surface: 2. *In vitro* experiments. Int J Oral Maxillofac Implants 18, 46-52
15. Cole BJ, Bostrom MPG, Pritchard TL, Sumner DR, Tomin E, Lane JM, Weiland AJ (1997) Use of bone morphogenetic protein 2 on ectopic porous coated implants in the rat. Clin Orthop 345, 219-228
16. Chaipinyo K, Oakes BW, van Damme M-P I (2002) Effects of growth factors on cell proliferation and matrix synthesis of low-density, primary bovine chondrocytes cultured in collagen I gels. J Orthop Res 20, 1070-1078
17. MacDonald, DE, Markovic B, Allen M, Somasundaran P, Boskey AL (1998) Surface analysis of human plasma fibronectin adsorbed to commercially pure titanium materials. J Biomed Master Res 41, 120-130
18. Geißler U, Hempel U, Wolf C, Scharnweber D, Worch H, Wenzel K-W (2000) Collagen type I-coating of Ti6Al4V promotes adhesion of osteoblasts. J Biomed Master Res 51, 752-760
19. Pierschbacher MD, Ruoslahti E (1984) Variants of the cell recognition site of fibronectin that retain attachment-promoting activity. Proc Natl Acad Sci USA 81, 5985-5988
20. Lee JW, Kim YH, Park KD, Jee KS, Shin JW, Hahn SB (2004) Importance integrin β1-mediated cell adhesion on biodegradable polymers under serum depletion in mesenchymal stem cells and chondrocytes. Biomaterials 25, 1901-1909
21. De Ugarte DA, Alfonso Z, Zuk PA, Elbarbary A, Zhu M, Ashjian P, Benhaim P, Hedrick MH, Fraser JK (2003) Differential expression of stem cell mobilization-associated molecules on muti-lineage cells from adipose tissue and bone marrow. Immunol Lett 89, 267-270
22. Wang ML, Tuli R, Manner PA, Sharkey PF, Hall DJ, Tuan RS (2003) Direct and indirect induction of apoptosis in human mesenchymal stem cells in response to titanium particles. J Orthop Res 21, 697-707
23. Wang ML Nesti LJ, Tuli R, Lazatin J, Danielson KG, Sharkey PF, Tuan RS (2002) Titanium particles suppress expression of osteoblastic phenotype in human mesenchymal stem cells. J Orthop Res 20, 1175-1184

J Oral Tissue Engin 2004;1(1):69-79

ORIGINAL ARTICLE

Immobilization of Fibronectin onto Organic Hexamethyldisiloxane Coatings with Plasma Surface Modification
–Analysis of Fibronectin Adsorption Using Quartz Crystal Microbalance-dissipation Technique–

Masao YOSHINARI [1], Tohru HAYAKAWA [2], Kenichi MATSUZAKA [3], Takashi INOUE [3], Yutaka ODA [1], Masaki SHIMONO [4]

[1]Department of Dental Materials Science and Oral Health Science Center, Tokyo Dental College, 1-2-2 Masago, Mihama-ku, Chiba 261-8502, Japan
[2]Department of Dental Materials, Research Institute of Oral Science, Nihon University School of Dentistry at Matsudo, 2-870-1, Sakaecho-nishi, Matsudo, Chiba 271-8587, Japan
[3]Department of Clinical Pathophysiology, Oral Health Science Center, Tokyo Dental College, 1-2-2 Masago, Mihama-ku, Chiba 261-8502, Japan
[4]Department of Pathology, Oral Health Science Center, Tokyo Dental College, 1-2-2 Masago, Mihama-ku, Chiba 261-8502, Japan
Corresponding author: Dr.Masao Yoshinari
e-mail: yosinari@tdc.ac.jp

SYNOPSIS

The immobilization behavior of fibronectin onto plasma-surface modified titanium was evaluated by using the quartz crystal microbalance-dissipation (QCM-D) technique. The plasma-surface modifications included a thin-film coating of hexamethyldisiloxane (HMDSO) and an O_2-plasma treatment on titanium. The contact angle of HMDSO-coatings against double-distilled water was 100 degrees, and dramatically decreased after the O_2-plasma treatment with less than 5 degrees. XPS analysis indicated the introduction of an O_2-functional group onto the HMDSO surface by the O_2-plasma treatment. The QCM-D technique enabled evaluation the adsorption behavior of fibronectin. The largest amount of fibronectin adsorbed was on both as-coated HMDSO (hydrophobic surfaces) and O_2-plasma treated at 10-min (hydrophilic surfaces) surfaces compared to O_2-plasma treated (24-h) surfaces. These results indicated that two adsorption mechanisms of the fibronectin to substrates were considered, including hydrophobic interaction and ionic bond via OH group and/or O_2-functional group concomitant with hydrophilic surfaces.

Key words: *Surface modification; Plasma polymerization; Adsorption; Fibronectin; Quartz crystal microbalance*

INTRODUCTION

Fibronectin (FN) mediates adhesion of many differentiated cell types to tissue culture and natural collagen substrata. Fibronectin is also believed to play an important role in governing the interactions of biomaterials with their surrounding matrices. It was reported that the precoating of titanium with fibronectin enhanced the adhesive characteristics of cells to titanium[1,2]. Therefore, immobilization of fibronectin onto dental and maxillofacial implants and/or scaffolds is useful for enhancing the various functions such as biological sealing to prevent the invasion of the bacteria and epithelium.

Plasma-surface modification (PSM) including plasma polymerization and plasma surface treatment is an effective and economical surface treatment technique for many materials. The technique is of growing interest in biomedical engineering because it can control the physicochemical properties of biomaterials[1-3].

Films formed by plasma polymerization are generally free of pinholes, have a strong adherence to a wide variety of materials, and have a greater degree of resistance to chemicals and physical treatment because of their of cross-linked structure[4,5]. In particular, plasma polymerization using organosilicon monomers, hexamethyldisiloxane (HMDSO), has come into wide use[6-13]. These monomers are of interest because of their high deposition rates and the ability of varying the deposition conditions to control their structure and properties. In addition, HMDSO is an easy and safe monomer to handle, especially in comparison with silane compounds. Our previous study demonstrated that the deposited HMDSO thin film firmly attached to the titanium and was stable in a phosphate buffer saline solution[14]. At the same time, plasma surface treatments using various gases such as Ar, O_2, N_2, SO_2 have been utilized to modify blood compatibility, to influence cell adhesion and growth, and to control protein adsorption[15-21]. Notably, O_2-plasma treatment was reported able to control hydrophilicity/hydrophobicity and to introduce various functional groups, leading to applications such as humidity sensors, enzyme immobilization, and polymer bonding without the use of adhesive [22-24].

Our previous study revealed that the deposition of HMDSO thin films onto titanium adds the benefit of fibronectin adsorption due to the hydrophobic surfaces of the HMDSO [16]. In the present study, we evaluated the immobilization behavior of fibronectin onto HMDSO-coated and O_2-plasma treated surfaces using the technique of quartz crystal microbalance-dissipation (QCM-D) in order to investigate the adsorption mechanism of

fibronectin in more detail.

MATERIALS AND METHODS

Plasma Polymerization

Plasma-polymerized thin films of HMDSO [$(CH_3)_3SiOSi(CH_3)_3$, Fig.1] were prepared using a commercially available plasma-surface modification apparatus, (VEP-1000, ULVAC Inc., Kanagawa, JAPAN) under the conditions listed in Table 1. Titanium-coated QCM-D sensors (14 mm diameter) were held in a stainless steel chamber at a rotation speed of 3 rpm at room temperature. The reservoir of HMDSO was heated to 70°C and the pipe for introducing the HMDSO was heated to 80°C. The HMDSO gas was then introduced into the equipment chamber through the heated pipe at a gas flow rate of 45 sccm (ml/min). The plasma was generated using a radio-frequency generator operating at 13.56 MHz with the power maintained at 200 W. The chamber pressure was maintained at about 10 Pa throughout the plasma polymerization process. Plasma polymerization was performed for periods of 20 min. After the plasma was turned off, nitrogen gas was used to purge the chamber, which was then allowed to return to ordinary atmospheric pressure. The process resulted in

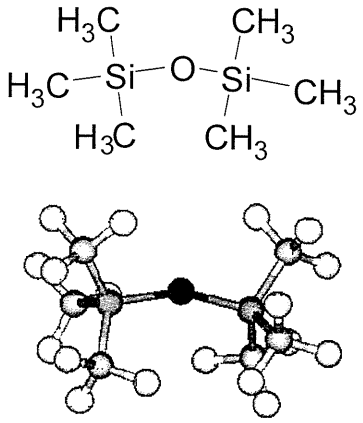

Fig.1 Structural formula of hexamethyldisiloxane [HMDSO, $(CH_3)_3SiOSi(CH_3)_3$].

Table 1 Conditions of plasma polymerization and O_2-plasma treatment

Treatment	Monomer (gas)	Flow rate	Pressure at discharge	Output	Time
		ml/min	Pa	W	min
Plasma polymerization	HMDSO	45	10	200	20
O_2-plasma	O_2	50	1.5	200	10

*Film thickness of HMDSO (as) : approximately 100nm

**O_2-plasma treatments were applied to on HMDSO coated titanium.

the deposition of plasma-polymerized film on the titanium with a film approximately 100 nm thick as determined by a Dektak Stylus Profiler System (Veeco Instruments Inc., Woodbury, NY, USA).

O_2-plasma Treatment

The titanium substrates and HMDSO-coated titanium were then treated with O_2 plasma for 10 min. The same apparatus was used as for the plasma-polymerization under the conditions listed in Table 1. Because surface physicochemical properties change over time, contact angle measurement and a fibronectin-adsorption assay were started 10 min and 24 h after the O_2-plasma treatment.

Surface Characterization

An X-ray photoelectron spectroscopy (XPS) analysis (ESCA-750, Shimadzu, Kyoto, JAPAN) was performed for surface characterization. XPS analysis was carried out with Mg-Kα as an X-ray source at 8 kV and 30 mA to determine the intensity of Si2p, O1s, and C1s. The binding energy of each spectrum was calibrated with C1s of 284.6 eV for charging correction.

The contact angle with respect to double-distilled water was measured using a Contact Angle Meter (CA-P, Kyowa Interface Science Co. Ltd., Tokyo, JAPAN). Five measurements of 15-s each were

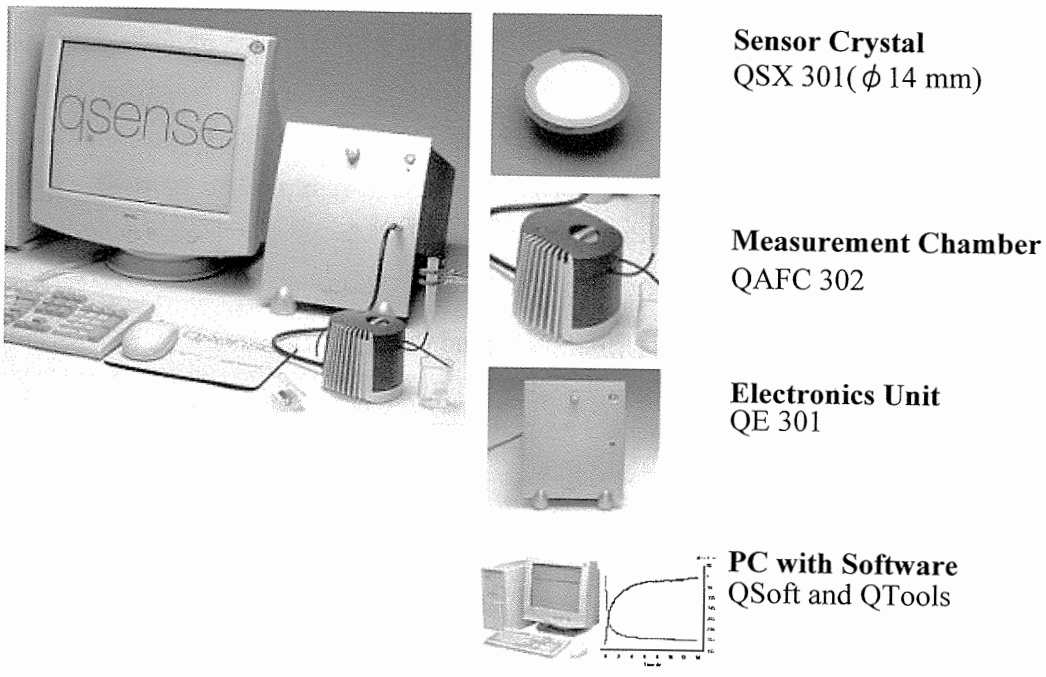

Fig. 2 Quartz crystal microbalance-dissipation (QCM-D) technique for fibronectin- adsorption assay.

made for each surface type; all analyses were performed at the same temperature and humidity.

Fibronectin -adsorption Assay

Human cell-binding fibronectin (270 kDa) (Upsatate Biotechnology, Lake Placid, NY, USA) was dissolved in phosphate-buffered saline (PBS-) solution with pH=7.4 at a concentration of 20ppm.

The QCM-D instrument (QCM-D300, Q-Sense AB, Göteborg, Sweden) was operated with AT-cut single crystal quartz sensors with a resonant frequency of 5 MHz for the adsorption assay (Figs 2 and 3). HMDSO-coated, and O_2-plasma treated QCM-D sensor crystals were used as sensors. The crystal resonant frequency (Df) and the dissipation factor (DD) of the oscillator were measured simultaneously at a fundamental resonant frequency (5 MHz) and at a number of overtones, including 35 MHz. Monitoring the resonance behavior of piezoelectric oscillation enables measurements of the mass adsorption at the surface in real time, usually as a function of the decrease in resonance frequency (f). The frequency shift (Df) is related to the adsorbed mass (Dm). At 35 MHz, a frequency shift of 1 Hz corresponds to a mass change of approximately 2.6 ng/cm^2. This relationship is strictly applicable to sufficiently thin and rigid films. A second measurement parameter, dissipation (D), gives qualitative information about the viscoelastic properties of the adsorbed layer.

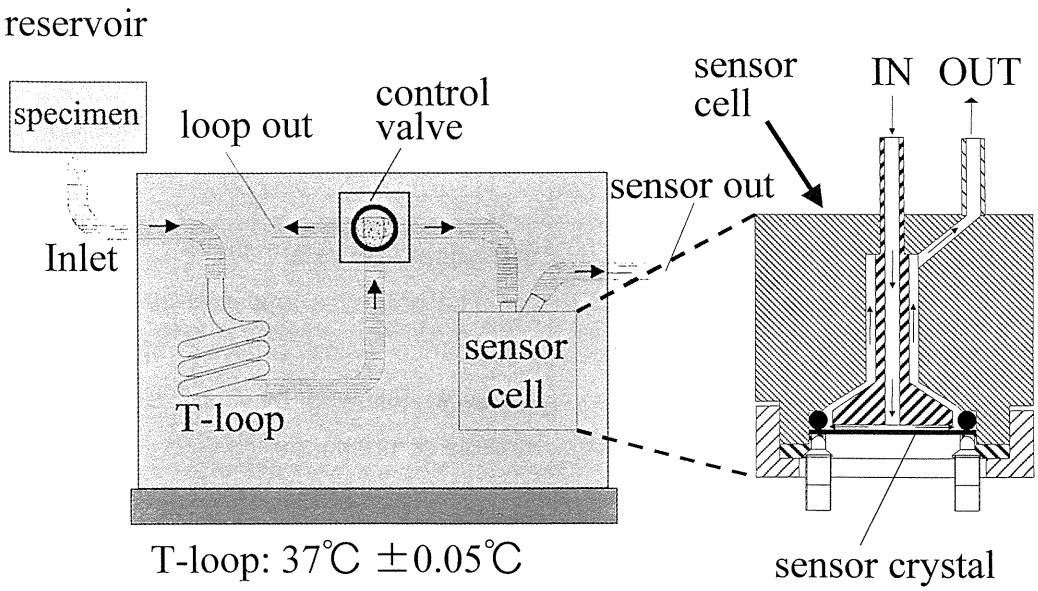

Fig. 3 Schematic illustration of QCM-D apparatus (Q-Sense D300 System).

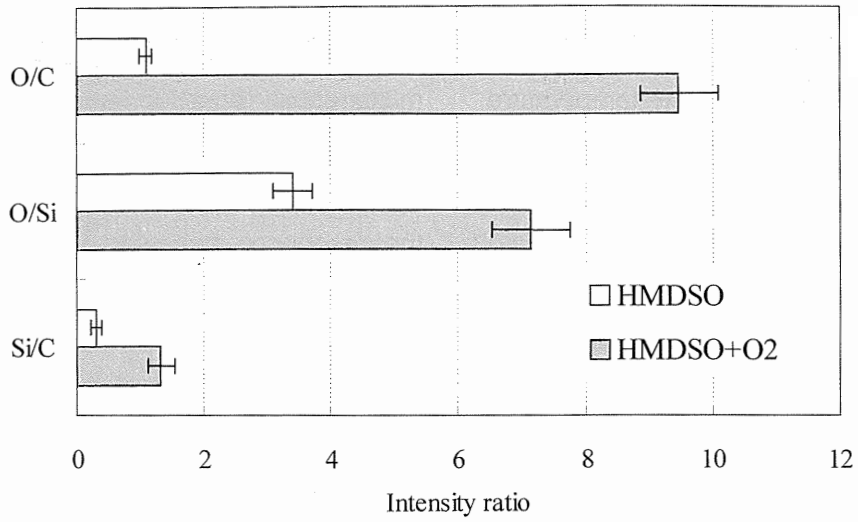

Fig. 4 Intensity ratio of elements on HMDSO and HMDSO + O_2 specimens under XPS analysis

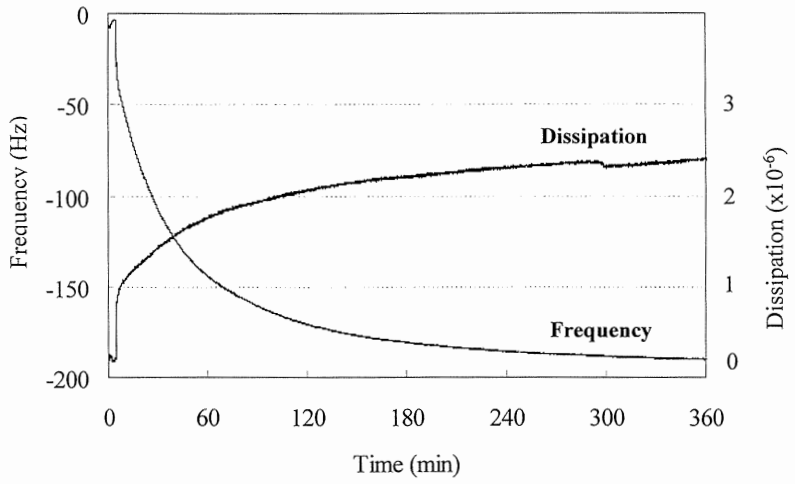

Fig. 5 Typical example of frequency and dissipation shift against time for exposure of a HMDSO + O_2 plasma specimen to fibronectin obtained via QCM-D measurement.

Fibronectin (Fn) /PBS solution (20 ppm) was introduced into an axial flow chamber comprising a T-loop in order to thermally equilibrate the sample at 37±0.05 °C. The sequence of injections into the QCM cell for an experimental run was as follows: 0.5 ml of double-distilled water, 0.5ml of Fn solution, and 0.5 ml of double-distilled water.

Statistical Analysis

The data was analyzed for statistical significance using analysis of variance (ANOVA) followed by Scheffe's test for multiple comparisons.

RESULTS

The intensity ratios of the elements on HMDSO and HMDSO + O_2 (10min) are

shown in Fig. 4. The intensity of O was compared to that of C and Si, and that of Si was compared to that of C increased by the O_2-plasma treatment on the HMDSO coatings ($p<0.01$).

The contact angles against double-distilled water were 100±3 degrees on HMDSO as-coatings. These values dramatically decreased after the O_2-plasma treatment with less than 5 degrees ($p<0.01$). This value gradually increased over time in air atmosphere, and reached 50±2 degrees at 24h (Fig.6).

Fig. 5 plots a typical example of a shift in frequency and dissipation against time for exposure of HMDSO + O_2 to fibronectin (FN) as obtained via QCM-D measurement. The frequency curve shows a decrease over time during the early stage of adsorption until it reached a certain frequency after about 180 min. A small amount of dissipation shift was observed on all specimens. The estimated amounts of Fn adsorption on the QCM sensors are shown in Fig. 6. The amount of FN adsorption was estimated by the Sauerbrey equation[25] 3-h after injection of the FN solution. The largest amount of FN adsorbed was on as-coated HMDSO and O_2-plasma treated (10 min) surfaces compared to O_2-plasma treated (24 h) surfaces ($p<0.01$).

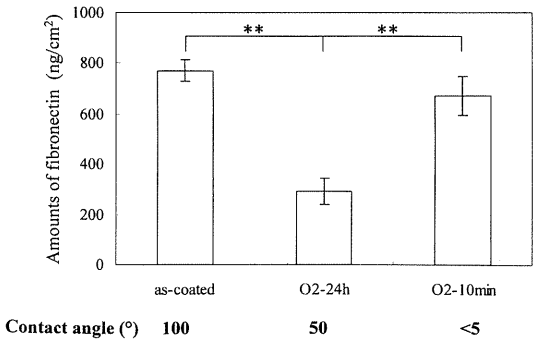

Fig. 6 Amounts of fibronectin adsorbed (3h) and contact angle.

DISCUSSION

The purpose of the present study was to evaluate the immobilization behavior of fibronectin onto plasma surface modified titanium by using the quartz crystal microbalance-dissipation (QCM-D) technique.

Recent studies have confirmed that the quartz crystal microbalance-dissipation (QCM-D) technique is useful for evaluating surface-related processes in liquids, including protein adsorption, complementary activity on biomaterials, and analysis of DNA hybridization[26-30]. Höök et al. reported the effectiveness of the QCM-D technique for analyzing the adsorption kinetics of three model proteins on titanium oxide surfaces compared with ellipsometry and optical waveguide lightmode spectroscopy[31]. QCM-D measurement was performed to obtain more detailed information about the

quantity of protein adsorption. They also pointed out that the mass calculated from the resonance frequency shift included both protein mass and water that was bound or hydrodynamically coupled to the protein adlayer. The results showed a clear difference of frequency shift among the conditions. Consequently, it was shown that the QCM-D technique is able to evaluate the adsorption behavior of proteins such as fibronectin. The present study showed a small amount of change in dissipation (D), suggesting that the fibronectin adsorbed onto the specimens is rigid. Accordingly, the Sauerbrey equation can be used to estimate the amount of FN adsorbed.

The largest amount of FN adsorbed was on both as-coated HMDSO and O_2-plasma treated HMDSO (10 min) surfaces compared to O_2-plasma treated HMDSO (24 h) surfaces. It was shown that the behavior of protein adsorption onto substrates depends largely on surface characteristics, such as wettability (hydrophilicity/hydrophobicity or surface free energy), chemistry, charge, roughness, and dynamics. Wettability is one of the most important parameters in the design of biomaterials and implant devices [31].

It is generally recognized that protein adsorption on more hydrophobic surfaces occurs via hydrophobic interaction. Hydrophobic surfaces support the adsorption of various surfactants and proteins from water because expulsion of solute from solution into the interphase between the bulk solid and solution phases is energetically favorable. Adsorption to hydro-

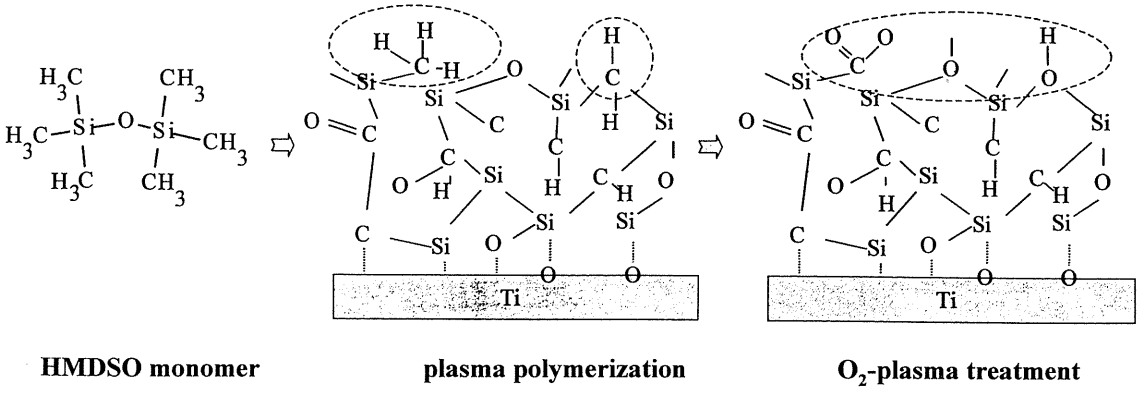

Fig. 7 Possible structure change of HMDSO monomers by plasma polymerization and folowing O_2-plasma treatment.

phobic surfaces is driven by the reduction of interfacial energetics concomitant with the replacement of water molecules at the surface by the adsorbed solute (surface dehydration) [32,33]. In contrast, it was reported that hydrophilic surfaces with a sulfonate group lead to greater adsorption of proteins from plasma [34], and that plasma protein adsorption on a wettability gradient surface increases with an increase in surface wettability. This suggests that more plasma protein adsorption at the hydrophilic positions of the gradient surface reduces platelet adhesion[35]. These reports suggested that the adsorption characteristics of proteins depend on the residual groups of amino acid in proteins.

In this study, the largest amount of FN adsorbed was on both hydrophobic surfaces (as-coated HMDSO) and hydrophilic surfaces (O_2-plasma treated at 10-min) surfaces compared to O_2-plasma treated (24 h) surfaces. Fibronectin has both hydrophobic residual groups of amino acid such as Ile, Leu and Val and hydrophobic residual groups of amino acid with RGD (Arg-Gly-Asp). Two possible adsorption mechanisms are conceivable on HMDSO and O_2-plasma treated HMDSO surfaces: one is due to hydrophobic interaction, and the other is due to ionic bonds by hydrophilic groups. XPS analysis showed that the O_2-plasma treatment increased the intensity of O as compared to that of C and Si, indicating that the treatment introduced an O_2-functional group onto the HMDSO surface. The change of the HMDSO monomer structure caused by plasma polymerization and the O_2-plasma treatment that followed can be presumed to be as illustrated in Fig. 7. That is, the fragmentation of the Si–C and C–H bonds of the HMDSO monomers were caused by plasma polymerization, and changes in the hydrophilic surfaces were concomitant with introduction of an OH group and/or O_2-functional group during O_2-plasma treatment. In conclusion, two mechanisms, including hydrophobic interaction and ionic bond via OH group and/or O_2-functional group with hydrophilic surfaces, are considered to responsible for the adsorption of fibronectin to the substrates.

ACKNOWLEDGMENTS

This study was supported in part by Oral Health Science Center Grant 5A10 from Tokyo Dental College, by a grant from the Ministry of Education, Culture, Sports, Science and Technology of Japan to promote 2001-Multidisciplinary Research Projects (in 2001 2005), and by a Grant-in-Aid for Scientific Research (C)(2)(15592073) and 14207093 from the Japan Society for the Promotion of Science.

REFERENCES

1) Culp LA, Sukenik CN: Cell type-specific modulation of fibronectin adhesion functins on chemically-dereivatized self-assembled monolayers. J Biomater: Sci. Polymer Edn 9: 1161-1176, 1998.
2) Dean JW, Culbertson KC, D'Angelo AM: Fibronectin and laminin enhance gingival cell attachment to dental implant surfaces in vitro. J Oral Maxillofac Implants 10: 721-728, 1995.
3) Chu PK, Chen JY, Wang LP, Huang N: Plasma-surface modification of biomaterials. Materials Science and Engineering R 36: 143–206, 2002.
4) Miyachi H, Hiratsuka A, Ikebukuro K, Yano K, Muguruma H, Karube I: Application of polymer-embedded proteins to fabrication of DNA array. Biotechnol Bioeng 69: 323-329, 2000.
5) Puleo DA, Kissling RA, Sheu M-S: A technique to immobilize bioactive proteins, including bond morphogenetic protein-4 (BMP-4) on titanium alloy. Biomater 23: 2079-2087, 2002.
6) Kurosawa S, Kamo N, Matsui D, Kobatake Y: Gas sorption to plasma-polymerized copper phthalocyanine film formed on a piezo-electric crystal. Anal Chem 62: 353-359, 1990.
7) Shi FF: Recent advances in polymer thin film prepared by plasma polymerization: Synthesis, structural characterization, properties and applications. Surf Coat Technol 82: 1-15, 1996.
8) Akovali G: Plasma polymerization of hexamethyldisiloxane in the gas phase. I. Polymerization studies. Polym Eng Sci 21: 658-661, 1981.
9) Sachdev KG: Characterization of plasma-deposited organosilicon thin films. Thin Solid films 107: 245-250, 1983.
10) Kashiwagi K, Yoshida Y, Murayama Y: Hybrid films formed from hexamethyldisiloxane and SiO by plasma process. Jpn J Appl Phys 30: 1803-1807, 1991.
11) Rau C: Mechanisms of plasma polymerization of various silico-organic monomers. Thin Solid Films 249: 28-37, 1994.
12) Lee SH, Lee DC: Preparation and characterization of thin films by plasma polymerization of hexamethyldisiloxane. Thin Solid Films 325: 83-86, 1998.
13) Schwarz J, Schmidt M, Ohl A: Synthesis of plasma-polymerized hexamethyldisiloxane (HMDSO) films by microwave discharge. Surf Coat Technol 98: 859-864, 1998.
14) Janochaa B, Hegemanna D, Oehra C, Brunner H, Rupp F, Geis-Gerstorfer J: Adsorption of protein on plasma-polysiloxane layers of different surface energies. Surf Coat Technol 142-144: 1051-1055, 2001.
15) Rau C, Kulisch W: Mechanisms of plasma polymerization of various silico-organic monomers. Thin Solid Films 249: 28-37, 1994.
16) Hayakawaa T, Yoshinari M, Nemotoa K: Characterization and protein-adsorption behavior of deposited organic thin film onto titanium by plasma polymerization with hexamethyldisiloxnane. Biomater 25: 119-127, 2004.
17) Steffens GCM, Nothdurft L, Buse G, Thissen H, Hocker H, Klee D: High density binding of proteins and peptides to poly(D,L-lactide) grafted with polyacrylic acid. Biomater 23: 3523-3531, 2002.
18) Bisson I, Kosinski M, Ruault S, Gupta B, Hilborn J, Wurm F, Frey P: Acrylic acid grafting and collagen immobilization on poly(ethylene terephthalate) surfaces for adherence and growth of human bladder smooth muscle cells. Biomater 23: 3149-3158, 2002.
19) Jui-Chea L, Cooper SL: Surface characterization and ex vivo blood compatibility study of plasma-modified small diameter tubing: Effect of sulphur dioxide and hexamethyl-disiloxane plasmas. Biomater 16: 1017-1023, 1995.
20) Shibata Y, Hosaka M, Kawai H, Miyazaki T: Glow discharge plasma treatment of titanium plates enhances adhesion of osteoblast-like cells to the plates through the integrin-mediated mechanism. Int J Oral Maxillofac Impl 2002; 17: 771-777.
21) Ding Z, Chen J, Gao S, Chang J, Zhang J, Kang ET: Immobilization of chitosan onto poly-lactic acid film surface by plasma graft polymerization to control the morphology of fibroblast and liver cells. Biomater 25: 1059-1067, 2004.
22) Ito K, Kondo S, Kuzuya M: A new drug delivery system using plasma-irradiated pharmaceutical aids IX. Chem Pharm Bull 49: 1615-1620, 2001.
23) Suzuki M, Kishida A, Iwata H, Ikada Y: Graft copolymerization of acrylamide onto a polysthylene surface prepared with glow discharge. Macromolecules 19: 184-1808, 1986.
24) Suzuki T, Tanner P, Thiel DV: O2 plasma treated polyimide-based humidity sensors. Analyst 127: 1342-1346, 2002.
25) Ganapathy R, Sarmadi M, Denes F: Immobilization of alpha-chymotrypsin on oxygen RF-plasma functionalized PET

and PP surfaces. J Biomater Sci Polym Ed 9: 389-404, 1998.
26) Wu Z, Xanthopoulos N, Reymond F, Rossier JS, Girault HH: Polymer microchips bonded by O2-plasma activation. Electrophoresis 23: 782-790, 2002.
27) Sauerbrey G: Verwendung non Schwingquarzen zur Wägung dünner Schichten und zur Mikrowägung. Z Phys 155: 206-222, 1959.
28) Miyachi H, Hiratsuka A, Ikebukuro K, Yano K, Muguruma H, Karube I: Application of polymer-embedded proteins to fabrication of DNA array. Biotechnol Bioeng 69: 323-329, 2000.
29) Puleo DA, Kissling RA, Sheu M-S: A technique to immobilize bioactive proteins, including bond morphogenetic protein-4 (BMP-4), on titanium alloy. Biomater 23: 2097-2087, 2002.
30) Rodahl M, Höök F, Kasemo B: QCM operation in liquids: An explanation of measured variations in frequency and Q factor with liquid conductivity. Anal Chem 68: 2219-2227, 1996.
31) Höök F, Vörös J, Rodahl M, Kurrat R, Böni P, Ramsden JJ, Textor M, Spencer ND, Tengvall p, Gold J, Kasemo B: A comparative study of protein adsorption on titanium oxide surface using in situ ellipsometry, optical waveguide light-mode spectroscopy, and quartz crystal micreobalance/dissipation. Colloids Surf B Biointerfaces 24: 155-170, 2002.
32) Andersson A-S, Glasmästar K, Sutherland D, Lidberg Ulf, Kasemo B: Cell adhesion on supported lipid bilayers. J Biomed Mater Res 64A: 622-629, 2003.
33) Vogler EA: Structure and reactivity of water at biomaterial surfaces. Advances in Colloid and Interface Science 74: 69-117, 1998.
34) Martins MC, Ratner BD, Barbosa MA: Protein adsorption on mixtures of hydroxyl- and methyl-terminated alkanethiols self-assembled monolayers. J Biomed Mater Res 67A: 158-171, 2003.
35) Lindblad M, Lestelius M, Johansson A, Tengvall P, Thomsen P: Cell and soft tissue interactions with methyl- and hydroxyl-terminated alkane thiols on gold surfaces, Biomater 18: 1059-108, 1997.
36) Boisson-Vidal C, Jozefonvic J, Brash JL: Interaction of proteins in human plasma with modified polystyrene resins, J Biomed Mater Res 25: 67-84, 1991.
37) Lee JH, Lee HB: Platelet adhesion onto wettability gradient surfaces in the absence and presence of plasma proteins. J Biomed Mater Res 41: 304-311, 1998.

(Received: March 6 / Accepted: March 23)

Geometry of artificial ECM: Three-Dimensional Structure of Titanium-Web (TW) Promotes Differentiation of Human Bone Marrow Mesenchymal Cells into Osteoblasts

Dong Li [1)], Shouhei Iku[2)], Kazuki Nemoto[2)], Yasuo Kokai [1)], Tetsuya Odajima[1)], Ryota Yoshimoto[3)], Tohru Kaku[3)], Hideki Katoh[3)], Hiroyuki Shiota[4)], Yasuo Seki[4)], Naomi Ogura[5)], Yoshimitsu Abiko[5)] Yoshinori Kuboki[1,2,6)]

1) School of Medicine, Sapporo Medical University
2) Koken Bioscience Institute
3) School of Dentistry, Health Sciences University of Hokkaido
4) Medical Device Group, Nippon Cable System Inc.
5) Nihon University School of Dentistry at Matsudo
6) Graduate School of Dental Medicine, Hokkaido University

Abstract: We demonstrate that a new culture system using a titanium web (TW) consisted of titanium fibers (50 μm diameter) can promote differentiation of mesenchymal cells into osteoblasts without conventional application of dexamethasone. Human mesenchymal stem cells (hMSC, Cambrex) and MC3T3-E1 were cultured on titanium web (87% of porosity). ALP/DNA in hMSC at 2weeks was 2 times higher and MC3T3-E1 at 4 weeks was 4 times higher on TW than those on the conventional plastic dishes. Effect of 3D structure of TW is self-evident and the results will open a new age of 3D bone cell biology using TW.

Keywords: three-dimensional culture, scaffold, titanium fibers, bone marrow mesenchymal cells, stem cells

Introduction

There are increasing needs for efficient three-dimensional (3D) scaffold for cell culture systems, since it is becoming clear that there are remarkable differences in cellular behavior between the cells cultured on three-dimensional environment and cells cultured on the conventional flat dishes.[1)] But until recently only a few solid 3D biomaterials with sufficient porosity for cell growth have been provided. We were the first to show that titanium web (TW) consisted of fibers with diameter of 50 μm could provide a suitable environment for bone ingrowth *in vivo*.[2-8)] One of the advantages of TW is its mechanical strength, maintaining a very stable 3D geometry as an artificial extracellular matrix. In this paper, we demonstrate that human bone-derived mesenchymal stem cells (hMSC) differentiate into osteoblasts more rapidly in TW culture than those cultured on plastic dishes.

Materials and Methods

Cell Culture on Titanium Web

Human mesenchymal stem cells (Cambrex Co., USA) were plated at 3.1 x 10^3 cells/ml, grown in the mesenchymal stem cell growth medium (MSCGM, Cambrex Co., USA) supplemented by 10% fetal calf serum, 50 units/ml of Penicillin and 50 ng/ml of Streptomycin. Cultures were maintained until 90% confluent at 37°C in 5% CO^2 in air. To increase cell numbers, subculture was carried out every 3 days by dissociation with 0.05% trypsin and 0.02% EDTA in physiological buffered saline (PBS).

For experiments, cells in the logarithmic growth phase were dissociated, and inoculated at 1 x 10^5 cells/15 mm plastic dish (Falcon). On the bottom of each well, TW (1.5 x 13 mm) was placed. TW is an unwoven sheet consisted of titanium fibers with a diameter of 50 μm, equipped with 87% porosity and average pore size of 200 μm.[2-8)]

Correspondence to Yoshinori Kuboki, Emeritus Professor, Graduate School of Dental Medicine, Hokkaido University, N-13, W-7 Kita-ku, Sapporo 060-8586 Japan. E-mail: kuboki@den.hokudai.ac.jp

For one group of cultures, MSCGM, which was augmented by 0.1 μM dexamethasone, 0.05 mM ascorbic acid-2-phosphate and 10 mM β-glycerophosphate, was used as DEX(+) group. For another group, the same medium except dexamethasone was used as DEX(-) group. Cultures were maintained up to 28 days by feeding every 3 days.

MC3T3-E1 cells, provided by Dr, H. Kodama were grown and cultured in α-modified Eagle's minimal essential medium (α -MEM) supplemented with 10% fetal calf serum as described above. But the medium for MC3T3-E1 cells was not augmented with DEX, β-glycerophosphate, or ascorbic acid-2-phosphate.[9)] In a group of experiment used MC3T3-E1, TW were coated with hydroxyapatite by a modified method reported previously.[6)]

Biochemical Analysis

At the end of culture, insoluble contents of well including TW was washed three times with PBS (-) and extracted in 500 μl of 2M NaCl/0.02M Tris-HCl (pH7.4) for DNA or 500 μl of 0.2% IGEPAL CA-630 (Sigma-Aldrich Co., USA)/10mM/Tris-HCl/1 mM MgCl2 pH 7.4. Alkaline phosphatase activity (ALP) was quantified by the method of Kind and King 3), and DNA content by the method using fluorescent dye (Hoechst 33258). [10)]

Morphological Analysis

At the end of culture, TW with cells and matrix were fixed in 10% neutral formaldehyde, embedded in polyester resin (Rigolac, Oken, Japan), cut and polished into 80 μm section by Maruto Systems (Crystal Cutter Nova MC-415Y and Speed Rap ML-521-d). Sections were stained with Cole's hematoxylin and eosin. In some cases, edge parts of the TW were directly observed by microscopy during culture.

Results and Discussion

Figure 1 shows morphology of the MC3T3-E1 cells cultured on TW for 2 and 4 weeks. They were observed directly by light microscope at their edge of the scaffold (felt side), and by thin (80 μm) section perpendicular to TW disk (right side). From both patterns, it was revealed that the cells were actively developing in the rich networks of collagen fibers, supported three-dimensionally by titanium fibers within TW. The results indicate that TW is a feasible artificial extracellular matrix (ECM) for osteoblasts with its 3D geometry. Development of the osteoblasts within TW was more clearly shown at 6 weeks in Fig. 2 (left side). Interesting finding was that at 8 weeks matrix-like structures were formed on the surface of titanium fibers of TW, on and within which, cells grew. One possibility was that this structure related with hydroxyapatite, since TW used in this group of MC3T3-E1 culture was coated with hydroxyapatite. Precise identification of the matrix-like substances needs further analysis.

Figures 3 and 4 show the effects of TW upon alkaline phosphatase activity per DNA in the hMSC cells cultured with or without DEX. As a strong inducing reagent for osteoblasts differentiation, DEX is widely used in culture medium. Therefore we wanted to know whether the effect of DEX could be replaced by the 3D effect of TW. It was clearly shown that at 2 weeks, ALP of hMSC on TW without DEX was significantly higher than ALP of the cells cultured on plastic dishes, either with or without DEX. Also at 4 weeks, the same was true concerning ALP of hMSC on TW irrespective of presence of DEX. Reason is not clear why ALP in TW culture with DEX was lower than that without DEX at 2 weeks (Fig.3), and ALP in plastic culture without DEX was higher than that with DEX at 4 weeks (Fig.4).

It was clearly demonstrated that the effect of TW on hMSC could replace the effect of DEX both at 2 or 4 weeks. Again, ALP/DNA of MC3T3-E1cells on hydroxyapatite-coated TW was 4 times higher than those on plastic dishes (data not shown).

Mechanism behind the effect of 3D structure on cell differentiation is a central theme of geometry of artificial ECM. [1, 11] This mechanism inevitably involves adhesive proteins, cell surface receptors, and their intracellular signal transduction, for the most of which we need further studies. In this study TW was shown to be a strong tool with its advantages of mechanical stability and controllable pore sizes, compared with previously reported artificial ECM.

References

1) Abbot A. *Nature* 424: 870-872: 2003.
2) Kuboki Y, Takita H, Tsuruga H, Ono M, and Jansen JA. *J Dent Res* 77: Special Issue A, Abstract # 1262: p.263: 1998.
3) Vehof JW, Mahmood J, Takita H, van't Hof MA, Kuboki Y, Spauwen PH, Jansen JA. *Plast Reconstr Surg* 108: 434-443: 2001
4) Vehof JW, Takita H, Kuboki Y, Spauwen PH, Jansen JA. *J Biomed Mater Res* 61:440-449: 2002.
5) Takita H, Vehof JW, Jansen JA, Yamamoto M, Tabata Y, Tamura M, Kuboki Y. *J Biomed Mater Res* 71A: 181-189: 2004.
6) Kuboki Y, Yoshimoto R, Kato H, Li D, Kaku T, Tanaka N, Kaneko M, Yanagisawa Y, Tsuru K, Osaka A, Shiota H, Seki Y, and Takita T. *Archives of Bioceramics Research* 5: 146-149: 2005.
7) Nakade T, Egashira N, Yoshimoto R, Kato H, Shiota H, Seki Y, Kuboki Y *Archives of Bioceramics Research* 5: 277-280: 2005.
8) Jansen JA, Vehof JW, Ruhe PQ, Kroeze-Deutman H, Kuboki Y, Takita H, Hedberg EL, Mikos AG. *J Control Release* 101: 127-136: 2005.
9) Kuboki Y, Kudo A, Mizuno M, Kawamura M. Calcif Tissue Int 50: 473-480: 1992.
10) Labarca C, Paigen K, *Anal Biochem* 102: 344-52: 1980.
11) Kuboki, Jin JQ, Takita H *J Bone Joint Surg* 83-A, S1: 105-115: 2001.

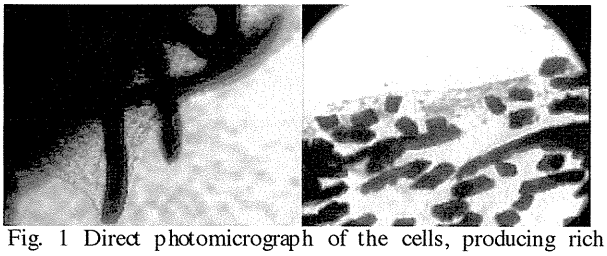

Fig. 1 Direct photomicrograph of the cells, producing rich volume of collagen fibers on TW at 2 weeks (left), and perpendicular section of the cell ingrowth into TW after 4 weeks (right).

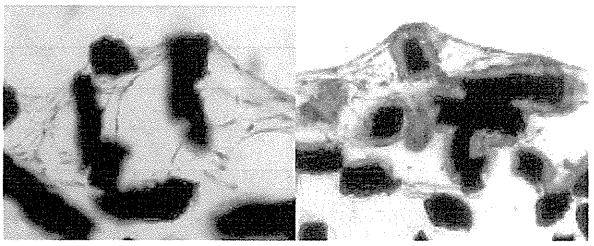

Fig.2 Perpendicular sections of the growth of MC3T3-E1 on TW at 6 weeks (left) and 8 weeks (right). Note the active matrix formation by the cells upon matrix-like layers. Black substances were 50 mm thick Ti fiber in TW.

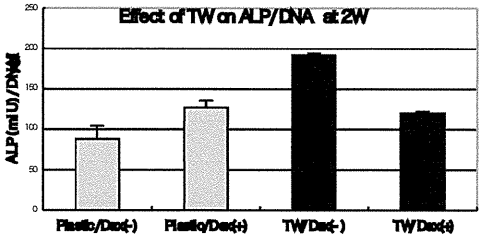

Fig. 3. Alkaline phosphatase activities of human mesenchymal stem cell cultured on titanium web (TW), compared with conventional plastic dishes at 2 week.

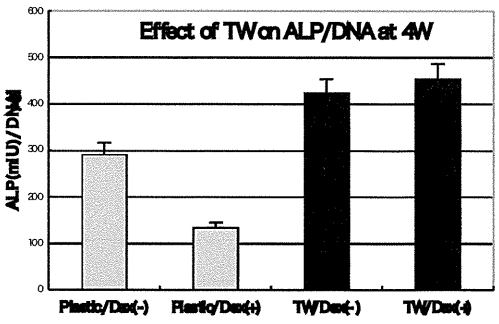

Fig. 4. Alkaline phosphatase activities of human mesenchymal stem cell cultured on titanium web (TW), compared with conventional plastic dishes at 4 week.

小児歯科学雑誌　40(1)：171–176　2002

根尖性歯周炎を惹起した陥入歯に3 DX®を利用し，歯内療法を行った1例

菅野亜里早　清水邦彦　新井嘉則*
篠田宏司*　前田隆秀

要旨：上顎左側側切歯部の自発痛を主訴として来院した10歳10か月の女児において，エックス線写真の所見から上顎左側側切歯の陥入歯を認め，この陥入歯が根尖性歯周炎を惹起したと考えられる1例を経験した。

患児は38.0℃の発熱と左側鼻翼部を中心に顔面腫脹を認めるとともに上顎左側側切歯部の拍動痛を認めた。血液検査より白血球数が$12\times10^3/\mu l$であった。エックス線写真より上顎左側側切歯に陥入歯様の不透過像を認め，さらに根尖部には歯根膜腔の拡大及び骨のびまん性吸収を認めたために上顎左側側切歯部の根尖性歯周炎と診断した。治療に先立ち，複雑な陥入歯の形態を詳細に把握するために3 DX®（モリタ製作所）にて診査を行った結果，陥入歯は上顎左側側切歯の根尖付近まで認められ長さは歯冠頂より19 mm（上顎左側側切歯根長は21 mm）であった。陥入歯の根尖は近心側に向いており側切歯の根尖とは一致していない。3 DX®より得られた情報をもとに陥入歯に歯内療法を行った。その際，陥入歯の根管からは排膿を認めたが，陥入歯周囲に存在する歯髄には生活反応が認められたために，陥入歯のみに根管拡大およびガッタパーチャポイントによる根管充塡を行った。治療後の経過観察において臨床症状は緩解しており，さらに電気歯髄診断によって上顎左側側切歯の生活反応が確認された。

陥入歯の複雑な根管形態の診査が3 DX®により可能になり，治療に有用であった。

Key words：陥入歯，歯内歯，歯内療法，3 DX®

緒　言

陥入歯または歯内歯と呼ばれる奇形歯は歯胚形成時の異常な歯上皮の発育により発生するとされている。陥入歯は1856年にSocratesにより最初に報告されて以来[1]，これまでに数多くの報告が成されているが[2~4]，原因は明らかにされていない。この形態異常歯は歯の中にもう一つの歯が存在するような形態から歯内歯（dens in dente）と呼ばれていたが（2歯胚説），1歯の歯冠部がエナメル質とともに根尖方向に陥入していることが証明されて以来，陥入歯（dens invaginatus）とも呼ばれている（1歯胚説）[5]。陥入は歯の表面の盲孔からエナメル質及び象牙質へ深く進入しており，歯根深部に及ぶこともある。陥入歯は多様な形態を示し，その陥入の深さによって大きく3つに分類されている[6]。1型では，陥入が歯冠内にとどまっているが，2型では陥入がエナメルセメント境よりも根尖方向に進入している。3型では陥入が完全に歯根内部に及んでおり，時に根尖の閉鎖を阻害している状態も観察される。通常，陥入部は歯髄と直接交通していないが，複雑な形態による細菌の停滞と陥入部の石灰化が不十分なために歯髄感染をおこしやすいといわれている[7]。今回我々は，3型の陥入歯が根尖性歯周炎を引き起こしたと考えられる1例を経験した。この陥入歯の形態，根管形態及び，根尖病巣との位置関係について口内法エックス線写真と3 DX®（モリタ製作所）[8]を用い観察し，得られた画像をもとに歯内療法をおこなったので報告する。なお，本症例の報告にあたり，患児および保護者の承諾を得ている。

日本大学松戸歯学部小児歯科学講座
千葉県松戸市栄町西2-870-1
（主任：前田隆秀教授）
*日本大学歯学部歯科放射線学講座
東京都千代田区神田駿河台1-8-13
（主任：篠田宏司教授）
（2001年12月12日受付）
（2002年1月21日受理）

症　例

患児：10歳10か月，女児，1990年1月7日生
主訴：上顎左側側切歯の咀嚼時疼痛，顔面部腫脹
初診：2000年11月16日

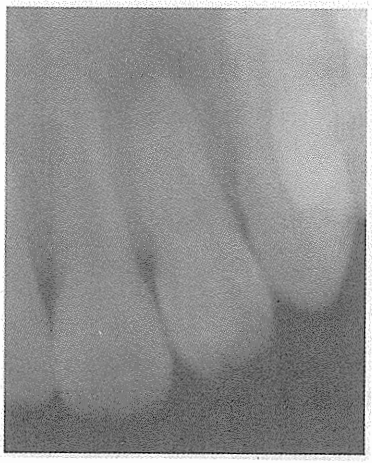

図1　初診時（平成2000年11月16日）のエックス線写真

図2　根管充塡後（2000年12月27日）のエックス線写真

図3　初診より約1年経過後（2001年12月6日）のエックス線写真

現病歴：2000年11月12日に全身倦怠感及び上顎左側側切歯の疼痛を認めるが放置，翌日37.0℃の発熱及び上顎左側側切歯部の拍動痛を訴えたため，母親が患児に小児用バファリン®を服用させたところ疼痛は緩解した。11月14日に左側鼻翼部を中心に顔面の腫脹を認めたため，内科を受診し抗生剤，消炎剤を投薬されたが顔面の腫脹は緩解せず，翌15日には咀嚼時疼痛及び38.0℃の発熱を認めたため11月16日当科を受診した。

医科的既往歴：特記すべき事項なし

家族歴：姉の上顎左側側切歯に陥入歯を認める（図7）。

現症：

1．全身所見

咀嚼時疼痛があったが食事の摂取は可能である。来院時体温は37.8℃であった。

2．顔貌所見

左側鼻翼部を中心にびまん性の腫脹を認める。

3．血液検査

WBCが12.0×10³/μlでありneutが78.3%，lymphが15.8%であった。またCRPは1.5 mg/dlであった。その他の検査値は正常範囲内であった。

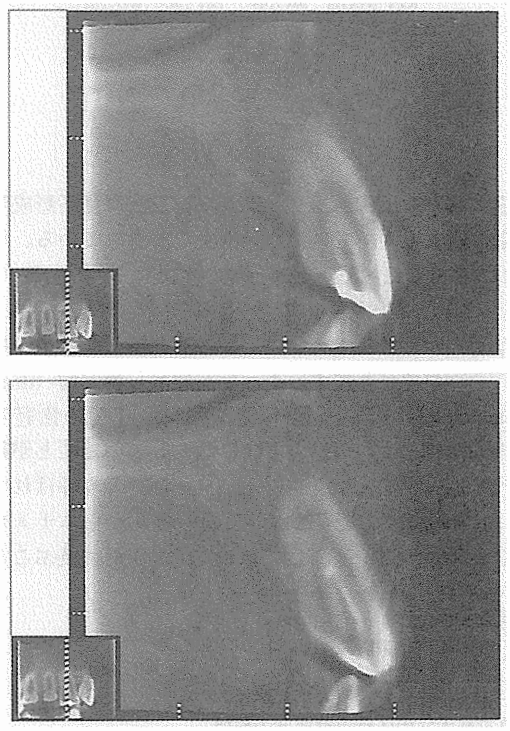

図4　3 DX®縦断像（矢状断）
側切歯歯髄腔内中央に歯冠部より根尖に至る歯牙様構造物が認められ，その内部に歯髄腔様透過像が見られる。

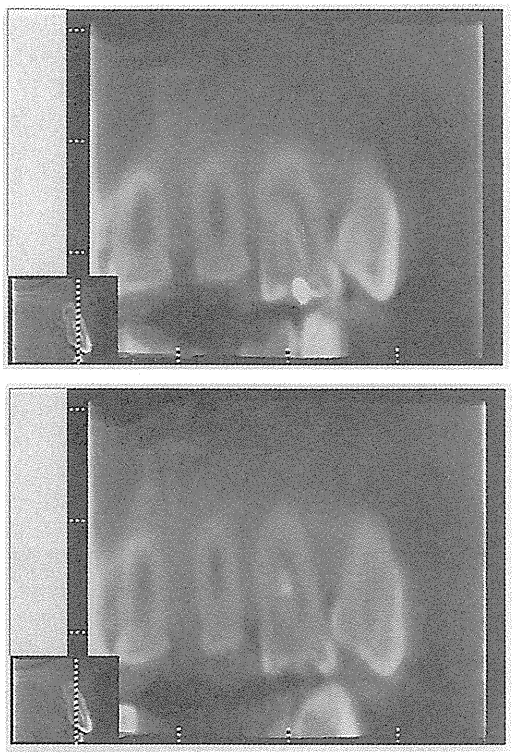

図5　3 DX®横断像（前頭断）
側切歯歯髄腔内に歯牙様構造物が認められ，その歯牙様構造物は側切歯歯髄腔の近心側にあり，さらに，周囲には側切歯歯髄腔が確認できる。

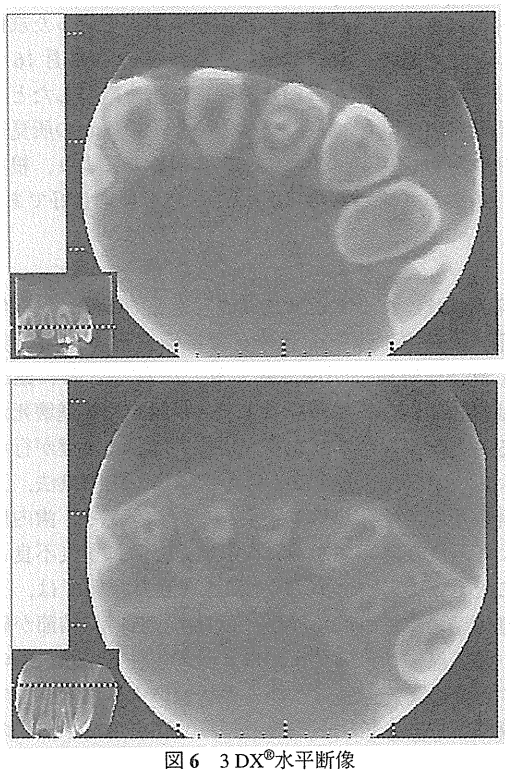

図6　3 DX®水平断像
側切歯歯髄腔内にある歯牙様構造物は円形で近心へ偏位しているのが確認できる。また根尖部の水平断像では，歯牙様構造物の根尖が側切歯の根尖と一致しておらず，側切歯歯根の根尖付近の近心側から陥入歯の根尖が歯牙の外部と交通しているのが認められる。

4．口腔内所見

上顎左側側切歯口蓋面に結節を認め，その一部に，破折を認める。

5．エックス線写真及び3 DX®所見

口内法エックス線写真より，上顎左側側切歯歯髄腔内に，歯牙様の不透過像を認める。根尖部には歯根膜腔の拡大及び骨のびまん性吸収を認める（図1）。3 DX®より，歯牙様不透過像は根尖付近まで認められるが，その根尖は側切歯の根尖と一致していない。側切歯歯根の根尖付近の近心側から陥入歯の根尖が歯の外部と交通している（図4, 5, 6）。陥入歯の根長は切縁より約19 mmである（上顎左側側切歯の根長は約21 mm）。歯牙様構造物の内部には口蓋側の歯冠部より歯髄腔様の透過像を認める。

以上の所見より本症例は陥入歯の歯髄様腔内への感染から根尖性歯周炎を惹起したものと診断した。

処置及び経過

上顎左側側切歯に口蓋側より髄室開拡を行った。3 DX®所見より陥入歯の内部には口蓋側歯冠部より歯髄腔様の透過像を認めたので，歯冠部エナメル質及び象牙質の一部を除去したところ，根管口が中央部と遠心部の二箇所に確認できた。中央部の根管からは排膿が認められたが，遠心側の根管からは鮮紅色の出血を認め切削時に痛みを訴えたため歯髄が生活していると判断し水酸化カルシウムで直接覆髄した後レジン修復を行った。排膿が見られた根管は洗浄後，開放状態にした。また顔面部腫脹，自発痛の緩解を目的に，抗生剤及び消炎鎮痛剤の処方を行った。4日後の11月20日には顔面部腫脹は緩解した。根管は腐敗臭が認められたためリーマー及びファイルにて19 mmまで拡大し，メトロニタゾール及びセファクロルの貼薬を行った。同様の処置を3日後に行ったところ腐敗臭が消失し，12月1日に#25のガッタパーチャーポイントにて根管充塡を行った（図2）。12月27日に経過を観察したところ打診痛，動揺など不快事項は生じていなかった。電気歯髄診断器にて測定をしたところ側切歯歯冠中央部では反応が見られなかったが，近遠

心部では生活反応が見られた。髄室開拡を行った部位はレジンにて緊密に封鎖した。さらに2001年2月16日および2001年12月6日の来院時に経過を観察したところ根尖部圧痛，動揺，打診痛は認めずそのほかの所見にも異常は認められず，またエックス線診査により，根尖病巣の縮小が確認できた（図3）。現在も経過良好である。

考　察

陥入歯はこれまでに発生原因，形態的観察，組織学的観察，出現率，臨床的意義などに関する多くの研究報告，及び症例報告が成されてきている[9,10]。特に臨床的には盲孔部からの齲蝕の発生や，歯髄炎や歯髄壊死が起こることが報告されており，病態に応じた治療が行われている[11]。その治療の多くは予防塡塞，歯内療法，又は外科療法を用い行われている。しかしながら，歯内療法による治療は陥入部の複雑な形態より時に予後不良となることもある[4]。今回の我々の遭遇した症例では，上顎左側側切歯口蓋面に結節が存在し，咬合時に結節が破折し，陥入部より感染が生じたと考えられる。陥入歯の存在する歯の歯冠形態は，陥入の状態により正常なものから異常な形態を示すものまで幅広く存在する。多くの場合，頬舌径が近遠心径より大きくなり，歯冠の舌側に大きな溝が確認される[12]。今回の症例においても，唇側面観には形態異常が確認できず，口蓋面に結節及び大きな溝が確認できた。通常，組織学的に陥入部は歯髄と交通していないが，石灰化が十分に行われておらず，しばしばエナメル質の欠如も確認される。陥入部には細菌及びその産生物，上皮の落屑または外来性物質が存在し，それらが歯髄感染を誘発すると報告されている[13]。

今回遭遇した陥入歯の根尖は側切歯の根尖と一致しておらず，側切歯歯根の根尖付近の近心側から歯の外部と交通していたため，その部で根尖性歯周炎が起こっていたと考えられる。さらに特筆すべきことは，治療後の電気歯髄診断器を用いた診査により側切歯固有の歯髄が生活していたことである。陥入歯の根尖が側切歯根尖と一致していないことで，陥入部からの感染が陥入部周囲の歯髄に影響を与えず，根周囲の組織にのみ影響を及ぼしたと考えられる。3型の陥入歯においてこのような現象がしばしば確認できるため[14,15]，治療時には根管形態と感染の波及状態を十分に把握した上で治療計画を立てるべきである。

陥入歯の根管より排膿がみられ，その部に感染根管治療をおこなった。しかしながらデンタルエックス線写真よりその根管形態が複雑であることが予想されたため，より詳細な情報を得るために3 DX®の撮影を行った。3

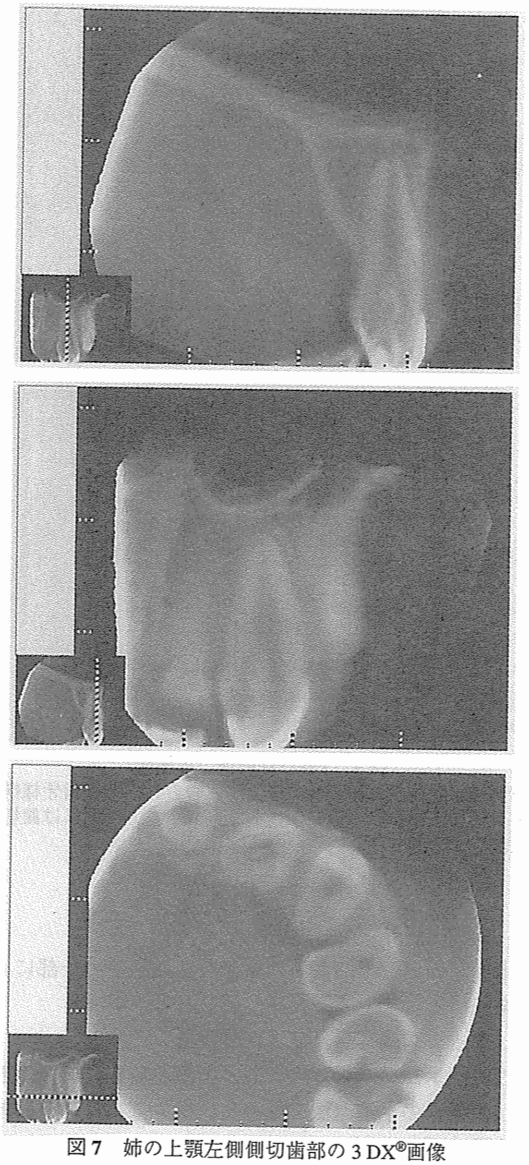

図7　姉の上顎左側側切歯部の3 DX®画像

DX®は多機能型回転式パノラマエックス線撮影装置を用いてイメージインテンシファイヤー（I. I＝光電子倍増管）を撮像系とする歯科用小照射野エックス線CTであり，この画像における解像度は現在用いられている通常のCTのなかで，最も高い解像度の機種と比較して約四倍の精度であると報告されている[8]。その結果，様々な角度から陥入歯の形態，偏位方向及び，根管長が正確に把握できたため，より確実な感染根管処置が可能となった。

一方，この患児の姉にも同部位に陥入歯が確認された（図7）。陥入歯の発生頻度は研究者によって大きく異な

るが0.04%から10%程度とされており，上顎側切歯が最も頻度が高い。またスウェーデンにおいて3020人の小児を対象に調査を行った結果，2.7%に陥入が認められ，異常の認められた小児のうち43%には親にも陥入歯が認められ，また32%には兄弟にも陥入が認められている[16]。そのため陥入歯成因に遺伝因子が関与していることが示唆されている。陥入歯はその複雑な形態により，清掃が困難であることと，歯髄感染を起こしやすいことより，陥入歯が確認された場合に本人だけでなく，兄弟または親の診査を行い，早期に予防的処置を行うことが重要であると考えられる。

結　論

上顎左側側切歯に根尖性歯周炎を惹起した陥入歯が存在する1例を経験した。

1．デンタルエックス線写真により根尖性歯周炎を有する上顎左側側切歯に3型の陥入歯を認めた。
2．根管形態が複雑であることが予想されたため，3 DX®の撮影を行い得られた情報をもとに陥入歯に歯内療法を行った。
3．陥入歯根尖と側切歯歯根根尖が一致しておらず，側切歯固有の歯髄は生活反応を示した。
4．陥入歯の複雑な根管形態の診査が3 DX®により可能になり，治療に有用であった。

本論文の要旨は第39回日本小児歯科学会大会および総会（2001年5月17日，豊中市）において発表した。

文　献

1）Schulse, C.: Developmental abnormalities of the teeth and the jaws, Edited by Gorlin, O. and Goldman, H., Thoma's Oral Pathology, Mosby Co., St. Louis, 1970, pp. 96–183.
2）Pitt Ford, H. E.: Peri-radicular inflammation related to dens invaginatus treated without damaging the dental pulp: a case report, Int. J. Pediatr. Dent., 8: 283–286, 1998.
3）Tarjan, I. and Rozsa, N.: Endodontic treatment of immature tooth with dens invaginatus: a case report, Int. J. Pediatr. Dent., 9: 53–56, 1999.
4）Ridell, K., Mejare, I. and Matsson, L.: Dens invaginatus: a retrospective study of prophylactic invagination treatment, Int. J. Pediatr. Dent., 11: 92–97, 2001.
5）Hulsmann, M.: Dens invaginatus: aetiology, classification, prevalence, diagnosis, and treatment considerations, Int. Endod. J., 30: 79–90, 1997.
6）Oehlers, F. A.: Dens invaginatus. I. Variations of the invagination process and associated anterior crown forms, Oral Surg. Oral Med. Oral Pathol., 10: 1204–1218, 1957.
7）Vajrabhaya, L.: Nonsurgical endodontic treatment of a tooth with double dens in dente, J. Endod., 15: 323–325, 1989.
8）篠田宏司他：新世紀の歯科診断と歯科治療－歯科用小照射野X線CTによる画像診断，日歯会誌，20: 6–17, 2001.
9）Kronfeld, R.: Dens in dent, J. Dent. Res., 14: 49–66, 1934.
10）Castellarin, M., Demitri, V. and Politi, M.: Endodontic, surgical and periodontal treatment of dens invaginatus, Minerva Stomatol, 50: 41–45, 2001.
11）Froner, I. C., Rocha, L. F., da, Costa, W. F., Barros, V. M. and Morello, D.: Complex treatment of dens invaginatus type III in maxillary lateral incisor, Endod. Dent. Traumatol, 15: 88–90, 1999.
12）Serrano, J.: Triple dens invaginatus in a mesiodens, Oral Surg. Oral Med. Oral Pathol., 71: 648–649, 1991.
13）Piattelli, A. and Trisi, P.: Dens invaginatus: a histological study of undemineralized material, Endod. Dent. Traumatol, 9: 191–195, 1993.
14）Ikeda, H., Yoshioka, T. and Suda, H.: Importance of clinical examination and diagnosis–a case of dens invaginatus, Oral Surg. Oral Med. Oral Pathol., 79: 88–91, 1995.
15）Kulild, J. C. and Weller, R. N.: Treatment considerations in dens invaginatus, J. Endod., 15: 381–384, 1989.
16）Grahnen, H., Lindahl, B. and Omnell, K. A.: Dens invaginatus. I. A clinical, roentgenological and genetical study of permanent upper lateral incisors, Odontologisk Revy., 10: 115–137, 1959.

Endodontical Treatment of Teeth with Dens Invaginatus Using 3 DX®: A Case Report

Arisa Sugano, Kunihiko Shimizu, Yoshinori Arai*, Kouji Shinoda* and Takahide Maeda

Department of Pediatric Dentistry, Nihon University School of Dentist at Matsudo
(Director: Prof. Takahide Maeda)
**Department of radiology, Nihon University School of Dentistry*
(Director: Prof. Kouji Shinoda)

We found a dens invaginatius radiographically derived in a ten-year, ten-month old girl who was referred to the pediatric dental clinc, Nihon University School of Dentistry at Matsudo with spontaneous pain of the maxillary left lateral incisor, and we surmisd that the dens invaginatus induced periapical periodontitis.

The patient had a fever of 38.0℃, diffuse swelling around the left nosewing and pulsating pain. The number of leukocytes was $1.2\times10^3/\mu l$ at the time of her first medical examination. The radiographic examination showed a radiopaque invaginations extending from the cingulum to the root in the affected tooth, and a periapical radiolucent lesion. Based on the above examinations, we diagnosed her having periapical periodontitis with dens invaginatus of the maxillary left lateral incisor. We conducted an examination of the tooth using 3 DX® (Morita Co.) in order to confirm the complicated morphology of the dens invaginatus before dental treatment. As a result of images from 3 DX®, we found that the part of invagination was extended from the top of the tooth crown to a distance, 19 mm into the root (tooth size was 21 mm) in the maxillary left lateral incisor. The direction of the invagination turned toward the mesial site and the apical of invagination did not correspond to the root apex of the lateral incisor. We found two holes in the root canal of the teeth when endodontic treatment was performed with the information from the 3 DX®. One root canal showed a vital response with breeding and pain, and the necrosis contents were observed from another root canal. The root canal treatment and root canal filling with the gutta-percha point therefore were performed on the necrotized root canal. The patient had no symptoms after treatment, and the maxillary left lateral incisor still had a positive response to sensitivity testing.

The 3 DX® images were useful for the diagnosis and treatment of dens invaginatus with complicated morphology.

Key words: Dens invaginatus, Dens in dente, Endodontical treatment, 3 DX®

小児歯科学雑誌　42(4) : 575–579　2004

口唇粘膜に潰瘍を引き起こした奇形を伴う上顎中切歯に3 DX™ を利用し歯内療法を行った1例

岡本春憲　宇治川玲子　松根健介
荒井清司　今村隆一*　前田隆秀

要旨：著者らは，唇顎口蓋裂の顎裂部に近接する，奇形した突起を伴う上顎中切歯の歯内療法処置を経験した。上口唇内側粘膜における潰瘍の疼痛が，奇形歯の持続的刺激により引き起こされた。奇形歯の複雑な歯髄腔形態を3 DX®（モリタ社製）を用い診査，処置を行った。

1．3 DX®画像より，唇側突起部内の歯髄腔と本来の中切歯の歯髄腔とが交通していることが確認された。
2．奇形歯の形態修正を行ったところ，唇側面からの露髄を認めたため，抜髄処置とガッタパーチャポイントによる根管充塡を複雑な歯髄腔に対して行った。
3．現在テンポラリークラウンを奇形歯に装着し，経過観察を行っている。治療後は患者に潰瘍及び疼痛が無く，良好な口腔内環境を維持している。

Key words：奇形歯，潰瘍，3 DX™，歯内療法，唇顎口蓋裂

緒　言

唇顎口蓋裂患者においては，歯数の異常，歯の大きさと形態の異常，歯の形成と萌出の遅延，歯の位置，傾斜，捻転の異常などが認められる[1]。Hellquist ら[2]は片側性唇顎口蓋裂患者172名の破裂側における永久側切歯の形態異常は49.4%，永久上顎中切歯の形態異常は54.1%認められたと報告しており，これは非破裂者における形態異常の出現率に比較すると非常に高いことを報告している[3]。唇顎口蓋裂患者の形態異常歯に対する処置の報告も認められるが，その中には異常の程度が深刻な場合はやむを得ず抜歯を行っているケースも少なくない[4]。

今回，著者らは，唇顎口蓋裂の顎裂部に近接する奇形を伴った上顎左側中切歯の突起部による，上口唇内側粘膜への持続的刺激により生じた潰瘍部の疼痛のため日常生活に支障をきたした一例を経験した。原因歯の処置にあたり，根管形態が複雑であることがデンタルフィルムで予想されたため，複雑な歯根形態の歯内療法に対し有用であることが報告されている3 DX multi image micro CT（以下3 DX™，モリタ製作所）[5]を用い，得られた情報をもとに奇形歯の歯内療法を行ったので報告する。なお，本論文の公表に際して，患児および保護者に同意を得ている。

日本大学松戸歯学部小児歯科学講座
千葉県松戸市栄町西2-870-1
（主任：前田隆秀教授）
*日本大学松戸歯学部矯正学講座
（主任：葛西一貴教授）
（2004年6月25日受付）
（2004年7月20日受理）

症　例

患児：9歳8か月男児
主訴：上顎左側中切歯唇側面の突起部分の接触による上口唇内側粘膜潰瘍部の疼痛
現病歴：7歳11か月頃より，上顎左側中切歯の萌出がみられ，形態の異常に保護者が気がついた。8歳9か月時，定期健診にて一部萌出している奇形歯にC_2程度の齲蝕を認め，コンポジットレジン修復を行った。その後，当該歯は本大学病院の矯正科にて牽引による萌出誘導を受け，露出してきた突起部との接触により，上口唇内側粘膜に潰瘍を生じた。（図1）
既往歴：
医科的既往歴：ハウスダストに対するアレルギーを認める。漏出性中耳炎を認めるが現在は完治している。
歯科的既往歴：左側唇顎口蓋裂のため，生後4か月時に口唇形成術，1歳2か月時に口蓋形成術，7歳9か月時に口蓋裂部に腸骨移植術を受けた。齲蝕治療ならびに抜歯等の歯科治療経験あり。
家族歴：家族，親戚に唇顎口蓋裂および奇形歯を有する者は認めない。

図 1　奇形した突起を伴う上顎左側中切歯と上口唇内側粘膜の潰瘍

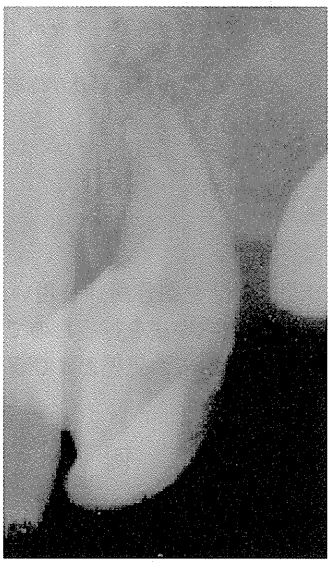

図 2　口内法エックス線写真

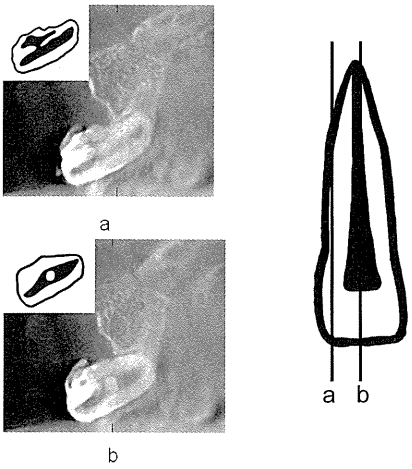

図 3　3 DX 矢状断画像と切断位置を示す模式図
a．近心側矢状断画像　b．中央部矢状断画像

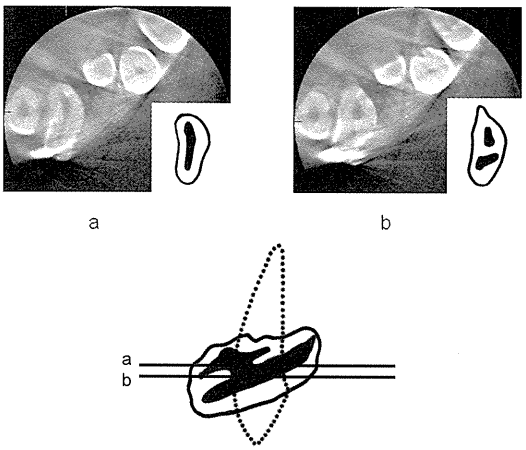

図 4　3 DX 水平断画像と切断位置を示す模式図
a．上方水平断　b．中央水平断

現症：

1）口腔内所見：上顎左側中切歯・側切歯間に顎裂の瘢痕が認められ，裂部分へは上口唇の内側粘膜が入り込んでおり，この周囲の口腔前庭は浅い。上顎左側中切歯は唇側面に突起部を持つ奇形歯であり，これにより生じた潰瘍が上口唇内側粘膜に認められた。

2）デンタルエックス線写真：歯根は近心方向に軽度に彎曲し，歯根形成は完了していた。さらに，奇形歯の歯根長は正常中切歯に比較し短かった。（図 2）

3）3 DX™ 所見：近心側矢状断画像では，唇側突起部内の歯髄腔と歯冠部歯髄腔とが交通している像を認め，中央部矢状断画像では，根管の中心部に不透過像が認められた（図 3）。水平断においては上方，つまり歯の唇側では突起部と思われる部位と歯髄腔とが交通していることが観察でき，中央水平断では，不透過像が中央部に認められた（図 4）。前額断画像では，歯が唇側傾斜しているため，根管の断層面画像が得られた。前方，つまり歯冠側では唇側突起部内の歯髄腔と歯の歯髄腔とが交通していた。さらに，中央部では歯髄腔の交通は無く，2 根管であり，後方部では 1 根管であることが確認された（図 5）。

以上の 3 DX™ 画像から，歯髄腔の複雑な形態を把握することができ，これらを用いて奇形歯に対する処置を行った。

処置および経過

浸潤麻酔下にて上顎左側中切歯唇側面の突起部分の削除及び形態修正を行ったところ，3 DX 画像から予測していた通り，唇側面より露髄を認めた。この部位からの

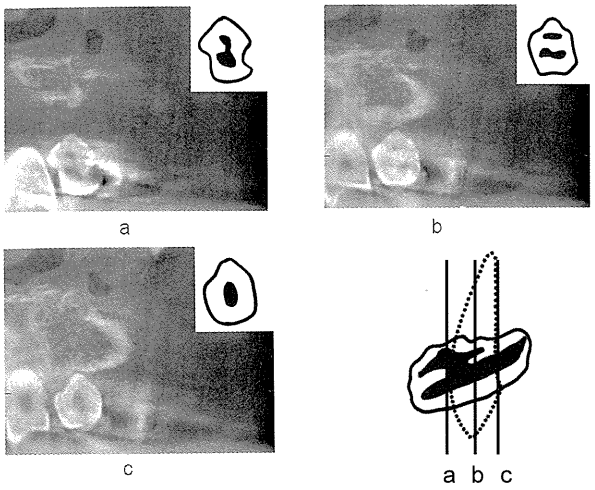

図5　3 DX 前額断画像と切断位置を示す模式図
a．前方前額断　b．中央前額断　c．後方前額断

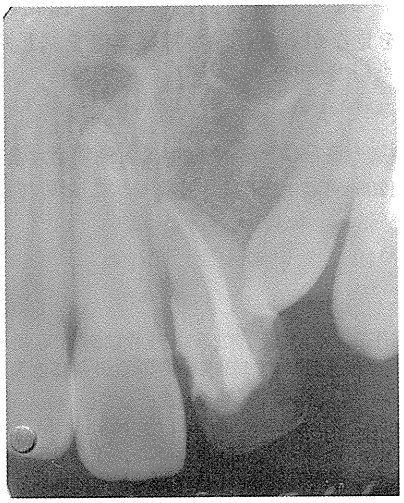

図6　根管充塡後の口内法エックス線写真

リーマー・ファイルの挿入は難しく，さらに歯冠部歯髄の残存を招く恐れがあるため舌側よりアクセスオープニング及び抜髄処置を行った。その際 3 DX 画像にて認められていた根管内の結節を削除し，複雑な根管形態を可及的に単純な根管形態とし，機械的清掃を簡便なものにした。根管貼薬は水酸化カルシウム製剤を用いコンポジットレジンにて閉鎖し，テンポラリークラウンを作成し仮着した。1 週間後，疼痛等の不快症状が認められなかったため，ガッタパーチャポイントおよびキャナルスにて根管充塡を行った。デンタルエックス線撮影より確認したところ根管充塡は良好であった（図 6）。なお，根管充塡後に被爆量を考慮し 3 DX™ 撮影を行わなかったが，今後，症状に応じ撮影を行うことも考慮している。その後，スクリューピンを植立しレジンコアにて支台歯築造および支台歯形成を行った（図 7）。現在，テンポラリークラウンを仮着し，経過を観察している。日常生活に支障をきたしていた疼痛は除去され，経過は良好である。治療前後（図 8–a, b）を比較すると明らかに上口唇内側粘膜の潰瘍及び発赤の消失が認められた。

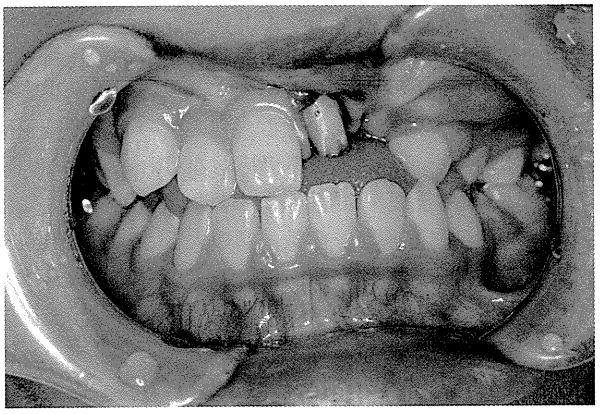

図7　支台歯築造および支台歯形成

a．治療前

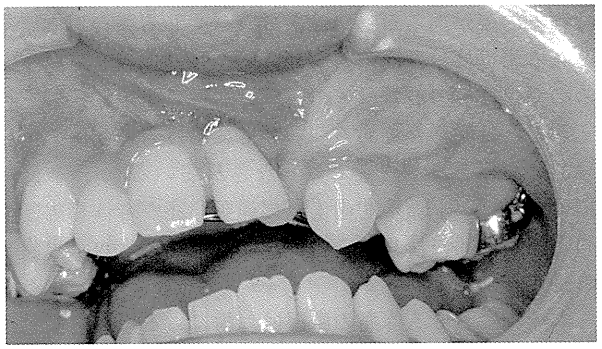

b．治療後

図8　治療前後の比較

考　察

歯の形態や歯数の異常などの発生率が唇顎口蓋裂患者

では高いことはよく知られており，このような異常は顎裂に近接する側切歯に最も多く発生することが報告されている。その他の歯でも一般集団より歯の異常発生率が高く，口唇裂・口蓋裂における各種の歯の異常は矯正治療や補綴治療を行うにあたり考慮しなければならない事項である[6]。口唇裂・口蓋裂における歯の異常は，乳歯列，永久歯列に発現し，歯数，歯の大きさ，歯の形態や形成の異常，萌出時期，萌出位置および方向の異常と多岐にわたっており，顎裂に近接する歯に最も多く発生することが報告されている[7]。

また，唇顎口蓋裂患児における顎裂に近接する上顎側切歯は，先天性欠如や同歯胚が2つに分裂して2個の歯になったように見える双生歯の発生頻度が著しく高いことも報告されている[1]。合わせて，顎裂側永久中切歯は非顎裂側中切歯よりも歯根は短く，形態異常も多く認められることも報告されている[8]。本症例においても過去の報告に認められるように顎裂に近接する中切歯の形態異常，および歯根が短いことが確認され，その歯冠部は2個の歯が一つに合わさった形態を示していた。さらに，3 DX™ における形態の検討により本症例における奇形歯は，歯冠部の形態異常を伴い，歯髄腔が2つ存在し一部が交通している像を呈していることが明らかになった。顎裂部における側切歯の欠如や過剰歯の発生には種々の説があるが，口腔上皮から生じる歯の形成原基となる歯堤は，一次口蓋の形成期にほぼ一致して発生するので，破裂の有無はその両側における歯堤に影響を与えることは明らかである。顎裂部における過剰歯の発生においてもさまざまな考察がなされている[1]が，本症例においては，上顎中切歯歯胚に過剰歯胚が合体し歯髄腔の一部が共通になり，このような形態をとった双生歯と考えられた。

本症例における疼痛の原因は，歯による口唇内側粘膜に対しての持続的な刺激によって引き起こされた潰瘍が原因であることが考えられた。口腔内における潰瘍を引き起こす原因としては齲蝕および不良補綴物による慢性的な刺激によるもの，先天歯により起こる Riga-fede などが報告している。潰瘍部の改善には，刺激を与えている原因を取り除くことが報告されており[9]，本症例においては奇形歯に対しての処置が必要と考えられた。治療にあたり，顎裂に近接する歯の抜去により保存されている場合に比べて，咬合の構築を考える上で，著しく不利となり，さらに成長期にある多くの矯正患者においては劣成長を示す上顎にとって少しでも不利にならぬよう外科的侵襲を最小限にとどめるべきと報告されている[7]ことを考慮し，より良い状態で奇形歯を保存することが必要であった。著者らは，奇形歯の保存に際し 3 DX™ を使用した。3 DX™ は少ない被曝線量で埋伏歯，根尖病巣，根分岐部病変，顎関節症およびインプラントの診断および治療に有用であり，その中でも，複雑な歯根形態の歯内療法に対し，有用であることが報告されている[5]。そこで，著者らは，本症例における奇形歯の形態修正を行うにあたり，より正確な歯髄腔の位置や形態をデンタルエックス線写真と合わせて把握し，処置中に露髄が避けられないか否かの検討および露髄時における根管治療のための情報の一つとして 3 DX™ を用いた。その結果，様々な角度より奇形歯の形態，歯根の偏位方向，根管形態および根管長を正確に把握することが可能となり，良好な根管治療を行うことが可能になった。

現在，根管処置を行い，ポスト築造後にテンポラリークラウンにて予後観察を行っているが，処置前に認められた潰瘍による疼痛も取り除かれ，良好な口腔内環境を維持している。今後は矯正治療により歯軸を改善した後，経過を見ながら最終的な補綴処置を施したいと考えている。

本論文の要旨は，第42回小児歯科学会大会および総会（2004年5月21日，福岡市）において発表した。

文　献

1）高橋庄二：口唇裂・口蓋裂患者における歯と咬合の異常，高橋庄二郎，口唇裂・口蓋裂の基礎と臨床，日本歯科評論社，東京，1996, pp. 565–575.
2）Hellquist, R., Linder-Aronson, S. Norling M, Ponten B and Stenberg T: Dental abnormalities in patient with alveolar clefts, operated upon with or without primary periosteoplasty, Euro. J. Orthod., 1: 169–180, 1979.
3）長坂信夫，小口春久，祖父江鎮雄，大野紘八郎，今村基尊：乳歯および幼若永久歯の特徴，祖父江鎮雄，長坂信夫，中田　稔：新小児歯科学，医歯薬出版株式会社，東京，2001, p. 100.
4）大山喬史：口唇裂口蓋裂とは，大山喬史，口唇口蓋裂の補綴治療，医歯薬出版株式会社，東京，1997, pp. 1–8.
5）菅野亜里早，清水邦彦，新井嘉則，篠田宏司，前田隆秀：根尖性歯周炎を惹起した嵌入歯に 3 DX®を利用し，歯内療法を行った1例，小児歯誌，40: 171–176, 2002.
6）松尾由紀子，真栁秀昭，阿部里美，戸沢加寿子，門間祐子，幸池省子：唇顎口蓋裂における乳歯及び永久歯歯胚の数の異常に関する研究，小児歯誌，25: 367–377, 1887.
7）大山紀美栄，本橋信義，黒田敬之：顎裂に近接する歯の不正とその矯正学的処置について，日口蓋誌，6: 40–49, 1981.
8）林　　薫，作田　守：矯正歯科における診断，宮崎正，口蓋裂その基礎と臨床，医歯薬出版，東京，1982, pp. 241–242.

9) 金澤正昭：先天性および後天性の異常，泉廣次，口腔外科学，学研書院，東京，1991, pp. 50–55.
10) 鈴木るり，大内　昇，加賀谷昇，向山　仁，秀島雅之，柳沢治之ら：当科における口唇口蓋裂患者の補綴治療について，日口蓋誌，17：123–135, 1992.
11) 三好作一郎，国松仁志，佐藤敦子，清水　保：永久歯列の前歯部癒合歯41例とその文献的考察，Jpn. J. Oral. Biol, 37：144–151, 1995.
12) Koji Hasimoto, Yoshinori Arai, Kazuo Iwai, Masao Araki, Shoji Kawashima and Masaaki Terakado : A comparison of a new limited cone beam computed tomography machine for dental use with a multidetector row helical CT machine, Oral Surg Oral Med Oral Pathol Oral Radiol Endod, 95 : 371–377, 2003.
13) 大畑　昇：GPのための口蓋裂知識（4）補綴処置の重要性と留意すべきこと，The Quintessence, 4：1083–1092, 1985.

A Case of Endodontic Treatment Using 3 DX™ for The Upper Central Incisor with Malformation Caused The Ulcer on Oral Mucosa of The Inner Upper Lip

Harunori Okamoto, Reiko Ujigawa, Kensuke Matsune
Kiyoshi Arai, Ryuuichi Imamura* and Takahide Maeda

Department of Pediatric Dentistry, Nihon University School of Dentistry at Matsudo
(Director : Prof. Takahide Maeda)
**Department of Orthodontic Dentistry, Nihon University School of Dentistry at Matsudo*
(Director : Prof. Kazutaka Kasai)

We experienced endodontic treatment for the upper central incisor with malformed process contiguous to the cleft plate. The sharp pain on the ulcer at the oral mucosa of the inner upper lip was caused by continuous stimulation by the malformed tooth. We conducted an examination of the malformed tooth using 3 DX™ (Morita Co.) in order to understand the complex form of the pulp chamber.

The following results were obtained.

1. From the 3 DX™ images, we confirmed that the pulp chamber in the labial process was connected to the pulp chamber of the original central incisor.
2. Pulp exposure was found in the labial process when we adjusted the crown form of the malformed tooth ; we therefore performed pulpectomy and root canal filling with the gutta-percha point on the complex form of pulp chamber.
3. We are continuing to observed progress of the malformed tooth, and inserted a temporary crown. The patient had no ulcer and sharp pain after treatment, and maintained a good oral state.

Key words : Malformed tooth, Decubitus ulser, 3 DX®, Endodontic treatment, Cleft lip and plate

Int J Oral-Med Sci 4(1):14-20, 2005

Original Article

Free Radical Study Using Electron Spin Resonance and Structural Analysis by Nuclear Magnetic Resonance of the Carisolv System

Hitomi Takeuchi,[1,3] Kiyoshi Matsushima,[1,3] Norihiro Nishiyama,[2,3] Kimiya Nemoto,[2,3] and Yasuhisa Tsujimoto[1,3]

Departments of [1]Endodontics, [2]Dental Biomaterials and [3]Research Institute of Oral Science, Nihon University School of Dentistry at Matsudo, Matsudo, Chiba 271-8587, Japan

Correspondence to :
Yasuhisa Tsujimoto
E-mail : tsuji@mascat.nihon-u.ac.jp

Abstract

In this *in vitro* study, electron spin resonance (ESR) and nuclear magnetic resonance (NMR) were used to evaluate free radical generation and chemical structural changes of amino acids in the Carisolv system. In the ESR study, hydroxyl radical (·OH), carbon radical (·C) and 5,5-dimethyl-1-pyrrolidone-(2)-oxyl-(1) (DMPO-X) were detected in the Carisolv system. ·OH was detected in a 0.25 % NaClO and 0.25% glutamic acid reaction mixture, ·OH and ·C were detected in a 0.25% lysine and 0.25% NaClO reaction mixture, and a DMPO-X like signal was detected in a 0.25% leucine and 0.25% NaClO mixture. More ·OH was detected when the Carisolv system was irradiated with plasma light than normal room light. The NMR study revealed that all the amino acids were completely degraded to smaller molecules by NaClO. These results indicate that the free radicals generated by the Carisolv system via NaClO attacked the amino acids. Then the generated ·OH in particular attacked the collagen in carious dentin and brought about degradation of the dentin structure. In addition, this mechanism was enhanced by plasma-light irradiation.

Keywords :
Carisolv, ESR, NMR, free radical

Introduction

The removal of carious dentin is an essential part of caries treatment. This has been accomplished with hand-held cutting instruments, i.e., both high- and low-speed rotary-powered cutting instruments, but many patients final this method to be unpleasant and painful, and local anesthesia is frequently needed to control pain (1, 2). Drilling can also cause deleterious thermal and pressure effects on the pulp (3, 4). The Carisolv system was developed by Ericson & others (5) to remove carious dentin by a chemo-mechanical method. This system does not cause pain because drilling is not necessary. The forerunner of the Carisolv system was originally marketed in the USA in the 1980's as Caridex. The mechanisms of action of the Carisolv and Caridex systems are very similar, but the main differences is that monoaminobutyric acid in the former has been replaced by three naturally occurring amino acids, namely lysine, leucine and glutamic acid (concentrations were not shown in the instructions for use), in the latter, and the concentration of sodium hypochlorite (0.5% NaClO) is higher in the latter. The amino acids lysine, leucine and glutamic acid, have different charges, and when chlorinated, they may interact with different moieties in the carious dentin (6). In addition, the Carisolv system contains methylcellulose to increase the viscosity and a dye agent. The efficacy of this system for caries removal *in vitro* was reported by Ericson (7). In the clinic, the Carisolv system must be used within 30 min of mixing the NaClO and amino acids because the carious dentin-removing activity of the gel declines rapidly. Twenty seconds after applying the mixture to the carious dentin, the softened dentin is gently scraped away with hand-held instruments. Previous studies on the Carisolv system provided no details about interactions between the amino acids and NaClO although Shiozawa & others (8, 9) report-

ed that free radicals were generated by the interaction between amino acids and hypochlorite. In this study, we used electron spin resonance (ESR) to identify the free radicals generated by the reactions between amino acids and NaClO, and we used nuclear magnetic resonance (NMR) to determine the chemical structures of the amino acids after they had been mixed with NaClO in an attempt to elucidate the mechanism(s) of action of the Carisolv system.

Materials and Methods

Chemicals

The Carisolv system was kindly provided by DEN'CS Co. Ltd. (Tokyo, Japan). The three amino acids used, L-glutamic acid, L-lysine and L-leucine, and NaClO were obtained from Wako Pure Chemicals Co. Ltd. (Tokyo, Japan). 5,5-dimethyl-1-pyrroline-*N*-oxide (DMPO), which is a radical-trapping agent, was obtained from Dojin Chemicals (Kumamoto, Japan). All the other chemicals used were commercially available and of analytical grade.

Free radical analysis

The amounts of free radicals generated by various mixtures of the constituents of the Carisolv system and by the system's reaction mixture itself were measured using an ESR spin-trapping method (8-10). A 20-μl aliquot of 890 mM DMPO and 200-μl aliquots of each sample mixture, i.e., NaClO and/or amino acids at various concentrations, were mixed, and the amount of free radicals generated were measured by ESR 40 s later. In addition, the effects of time, temperature and plasma-light irradiation on free radical generation by the Carisolv™ system reaction mixture were examined. The ESR spectra were recorded using a JES FA 300 (JEOL, Tokyo, Japan). The measurement conditions were as follows: microwave power, 8 mM; magnetic field, 335.4±5 mT; sweep time, 2 min; modulation frequency, 100 kHz; and time constant, 0.03 s. The quantity of each free radical was normalized relative to the standard signal intensity of a manganese oxide marker as follows: ·OH relative intensity=·OH signal intensity/Mn^{2+} marker intensity (10).

Plasma-light irradiation

The plasma-light irradiation device used was the APOLLO 95E (Dental/Medical Diagnostic Systems, Inc., USA). It uses a plasma lamp that emits light with a wavelength of 400-520 nm.

Measurement of ^{13}C NMR spectrum

An aqueous solution of NaClO 0.25% containing 20% deuterium oxide was used as the NMR solvent. The three typical α-amino acids, glutamic acid, leucine and lysine, were dissolved in this solution and allowed to stand at room temperature for 1 h, then the ^{13}C NMR spectra of the amino acids were recorded at 25 °C using a JEOL EX 270 spectrometer (Tokyo, Japan). The pulse, accumulation time and repetition time were 45°, 400 and 3.8 s, respectively, and hexamethyl-di-siloxane was used as the external reference. Control NMR spectra of the α-amino acids dissolved in 20% deuterium oxide aqueous solution were also recorded. The hexamethyl-di-siloxane (HMDSO) was used as an external reference.

Results

ESR analysis

The 5,5-dimethyl-1-pyrrolidone-(2)-oxyl-(1) (DMPO-X) was generated by the reaction between 0.5% NaClO and DMPO (Fig. 1a). The hypercoupling constants of the DMPO-X signal were analyzed and confirmed to be $A_N=0.71$ mT, $A_H=0.42$ mT which agreed well with previously reported values (11). A trace amount of ·OH was generated by the reaction between the gel of the Carisolv system and DMPO (Fig. 1b). Both the carbon radical (·C) and ·OH were detected first after the Carisolv system gel was mixed, and the amount of both radicals increased for 5 min after mixing (Fig. 1c & d). The hypercoupling constants of these signals were analyzed and found to be ·OH: $A_N=A_H=1.49$ mT, ·C: $A_N=1.61$ mT, $A_H=2.29$ mT, which also agreed with previously reported values (11). When the Carisolv™ system mixture was kept at 37 °C, the amount of both radi-

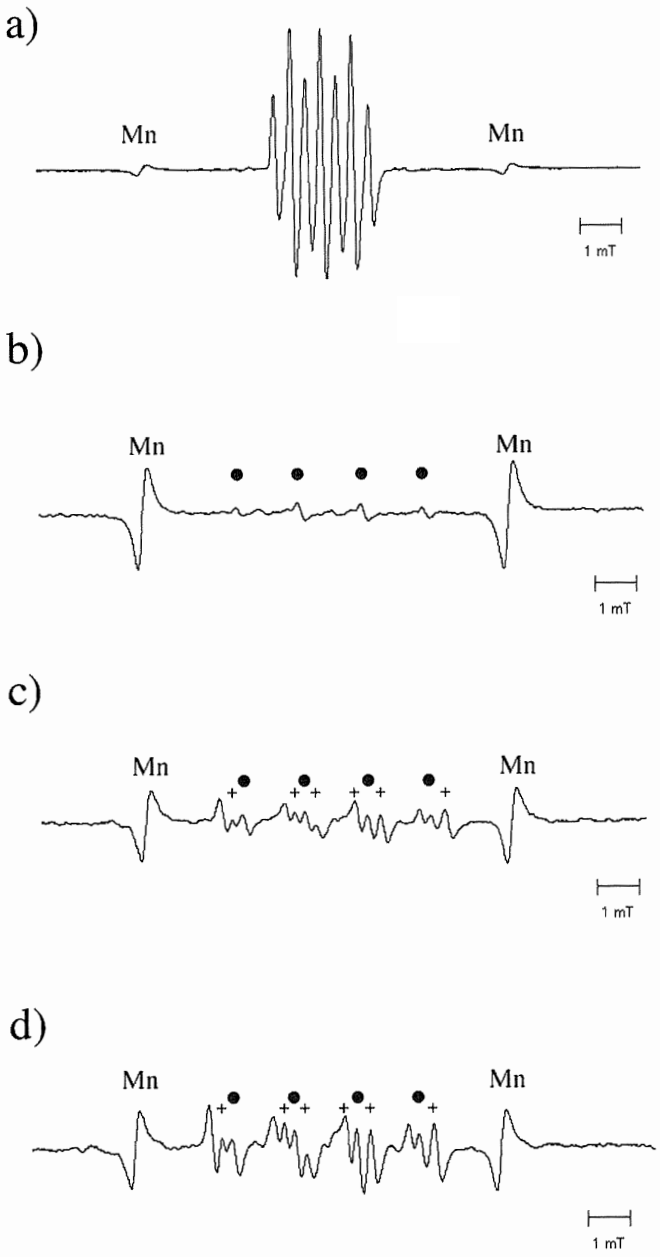

Fig. 1. Typical ESR signals. a) DMPO-X signal from the 0.5% NaClO and DMPO reaction mixture. b) A faint ·OH signal from the Carisolv™ system and DMPO reaction mixture. c) ·C and ·OH signals from the reaction between the Carisolv™ system and DMPO. d) ·C and ·OH signals 5 min after c). ●: ·OH ＋: ·C

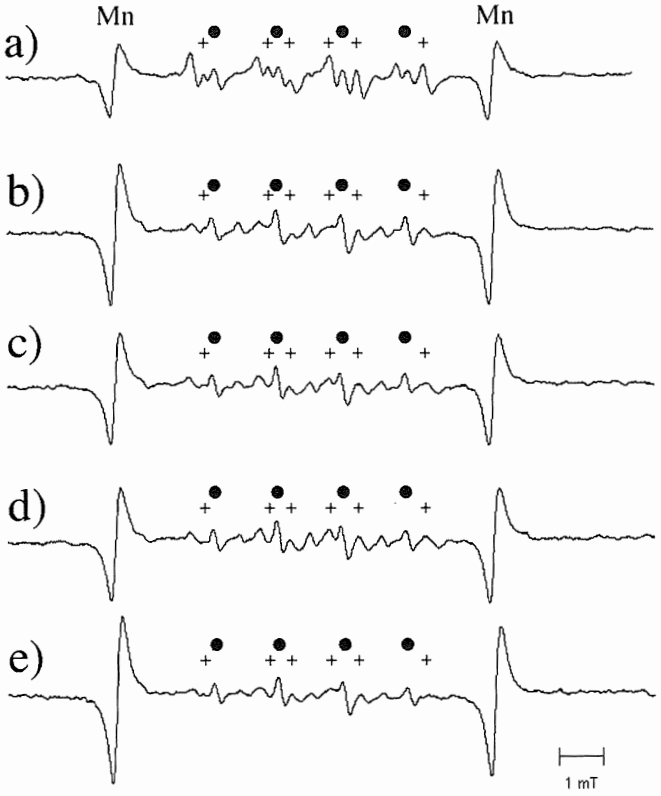

Fig. 2. Typical ESR signals generated by the Carisolv™ system reaction mixture kept at 37 °C. a) ·C and ·OH signals generated by the Carisolv™ system and DMPO reaction mixture. b) After 1 min at 37 °C. c) After 7 min at 37 °C. d) After 15 min at 37 °C. e) After 30 min at 37 °C. ●: ·OH ＋: ·C

cals generated decreased during the first minute and remained almost constant thereafter until 60 min after mixing (Fig. 2). The following radical species were detected in the amino acid and NaClO reaction mixtures: ·OH in the 0.25% NaClO and 0.25% glutamic acid reaction mixture, ·OH and ·C in the 0.25% lysine and 0.25% NaClO reaction mixture and a DMPO-X like signal in the 0.25% leucine and 0.25% NaClO mixture (Figs. 3-5). And the amounts of these radicals were increased by reaction time without DMPO-X like signal.

Plasma-light irradiation of the Carisolv™ system mixture resulted in the detection of more ·OH than was generated by the mixture exposed to normal room light (Fig. 6).

NMR analysis

The NMR peaks attributed to the carbon constituents of the amino acids were detected, which agree with previously reported values (12). When NaClO was added to the amino acids, the ^{13}C NMR peaks disappeared, and unknown peaks appeared. Typical patterns of the ^{13}C NMR peaks are shown in Figs. 7-9.

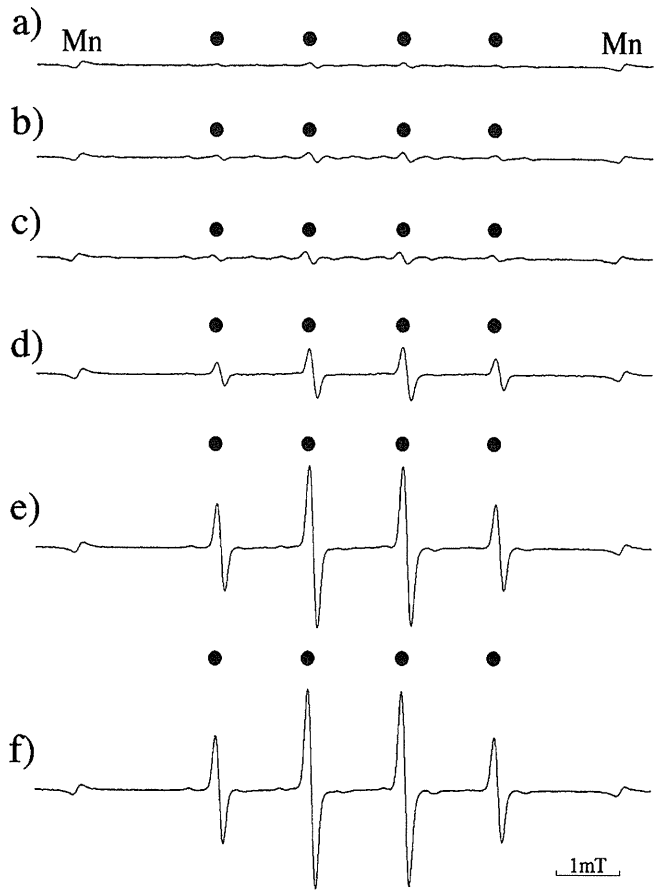

Fig. 3. Typical ESR signals generated by the NaClO and glutamic acid reaction mixtures. The generated ·OH was detected: a) 40 s, b) 3 min, c) 5 min after mixing glutamic acid and DMPO, and d) 40 s, e) 3 min, f) 5 min after mixing of glutamic acid, NaClO and DMPO. ●: ·OH

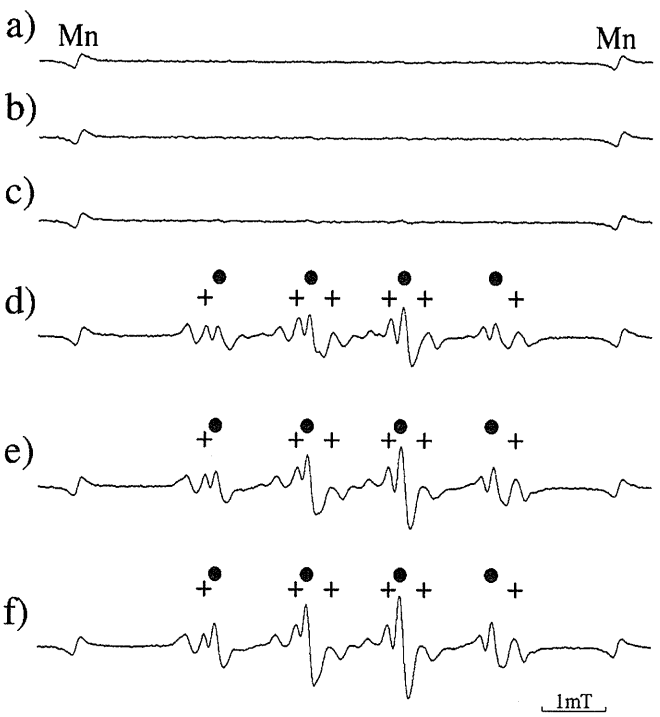

Fig. 4. Typical ESR signals generated by the NaClO and lysine reaction mixtures. a-c) No signals were generated: a) 40 s, b) 3 min, c) 5 min after mixing lysine and DMPO. d-f) ·C and ·OH signals generated by the lysine and DMPO reaction mixtures: d) 40 s, e) 3 min, f) 5 min after mixing lysine, NaClO and DMPO. ●: ·OH +: ·C

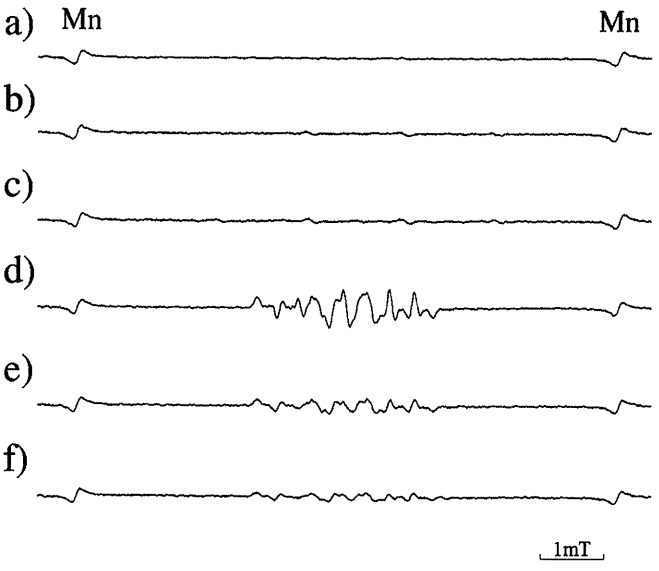

Fig. 5. Typical ESR signals generated by the NaClO and leucine reaction mixtures. a-c) No signals were generated: a) 40 s, b) 3 min, c) 5 min after mixing leucine and DMPO. d-f) DMPO-X like signals were observed and their intensities decreased with time: d) 40 s, e) 3 min, f) 5 min after mixing leucine, NaClO and DMPO.

Discussion

The Carisolv system was developed by Ericson & others (5) for the removal of carious dentin by chemo-mechanical means. The three amino acids contained in the Carisolv system are lysine, leucine and glutamic acid, the chemical structures of which are shown in Figs. 7-9. In clinical use, it takes about 10 min to remove caries with the Carisolv system (5). The operator should wait about 20-30 s after applying the mixed gel to the patient's tooth before starting to remove the carious tissue with a hand-held instrument. The Carisolv system removes caries effectively and painlessly, but its precise mechanism (s) of action and particularly the role of the three amino acid constituents have yet to be elucidated. To the best of our knowledge, no previous reports of the

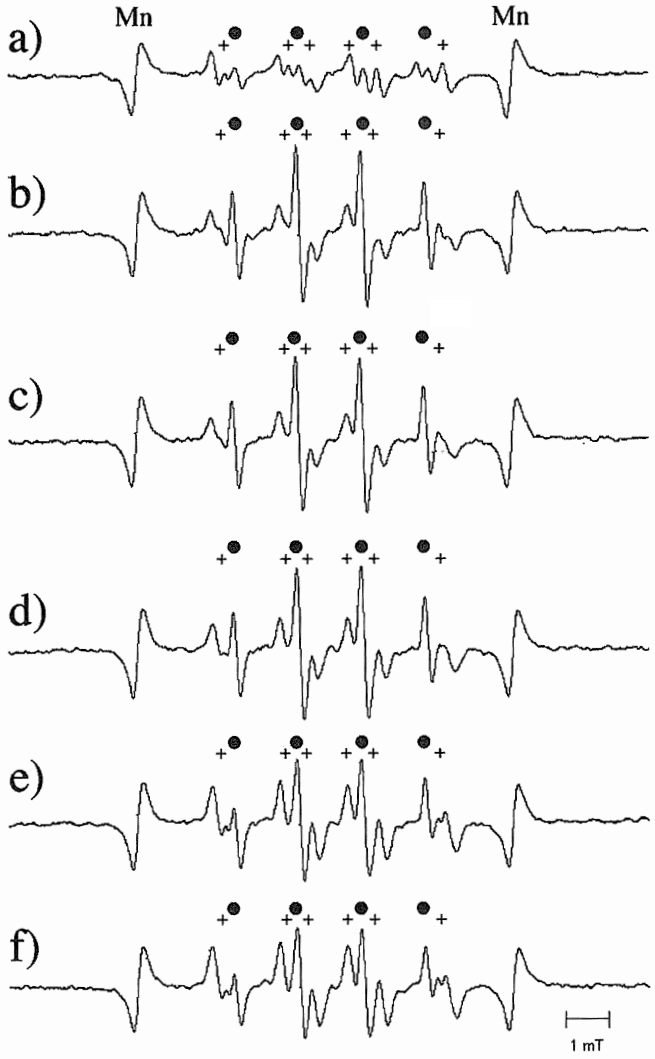

Fig. 6. Typical ESR signals when the Carisolv™ system reaction mixture was subjected to plasma light irradiation. The ·C and ·OH signals generated by the reaction between the Carisolv™ system and DMPO without plasma light irradiation are shown in a). The ·OH signal intensity increased after plasma light irradiation: b) 40 s, c) 5 min, d) 10 min, e) 30 min, f) 40 min after plasma light irradiation of the Carisolv™ reaction system for 3 s. ●: ·OH +: ·C

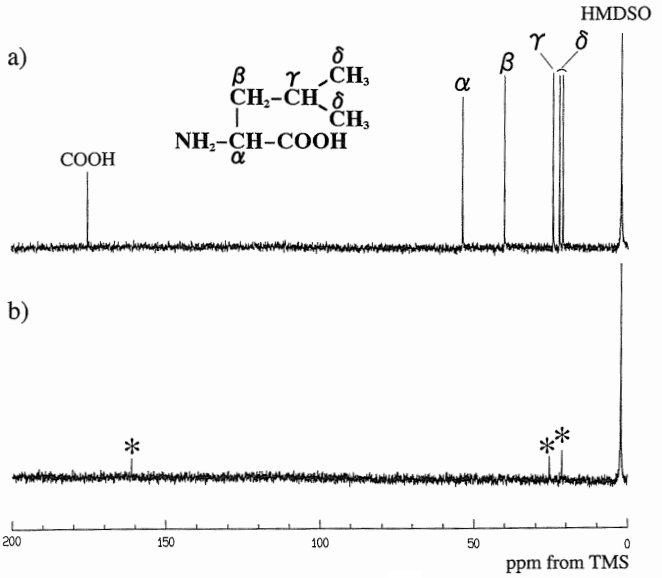

Fig. 7. Typical NMR signals of leucine. After NaClO had interacted with leucine in aqueous solution, the ^{13}C NMR peaks attributable to the carbons (a) in leucine disappeared and three unknown ^{13}C NMR peaks appeared in the NMR spectrum (b). HMDSO: control peak *: unknown by-product

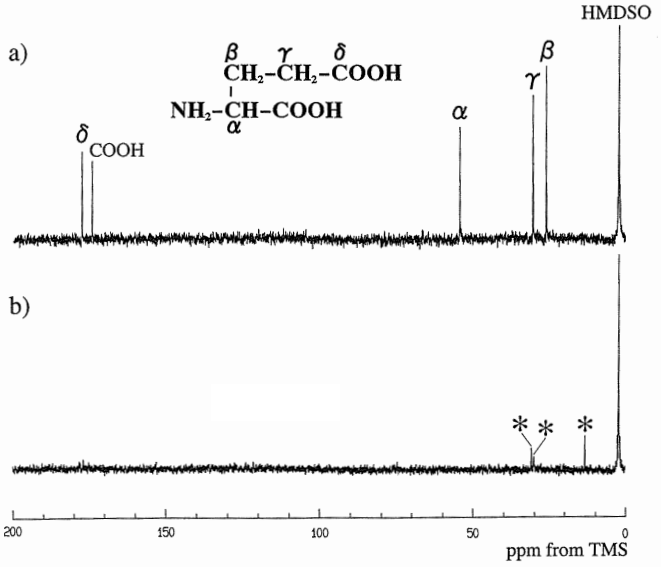

Fig. 8. Typical NMR signals of glutamic acid. After NaClO had interacted with glutamic acid in aqueous solution, the ^{13}C NMR peaks attributable to the carbons (a) in glutamic acid disappeared and three unknown ^{13}C NMR peaks appeared in the NMR spectrum (b). HMDSO: control peak *: unknown by-product

use of ESR and NMR to study free radical generation and structural analysis of the Carisolv system have been published. In our ESR study, DMPO-X was detected in 0.5 and 0.25% NaClO. Bernofsky & others (13, 14) reported that DMPO-X was generated through a secondary oxidation-reduction process during the interaction between a strong oxidizing substance and DMPO, whereas Shiozawa & others (8, 9) reported that amino acids were structurally damaged by DMPO-X. When the mixtures of amino acids and NaClO were analyzed by ESR, different radicals were detected in the reaction mixtures of NaClO and each amino acid. These results indicate

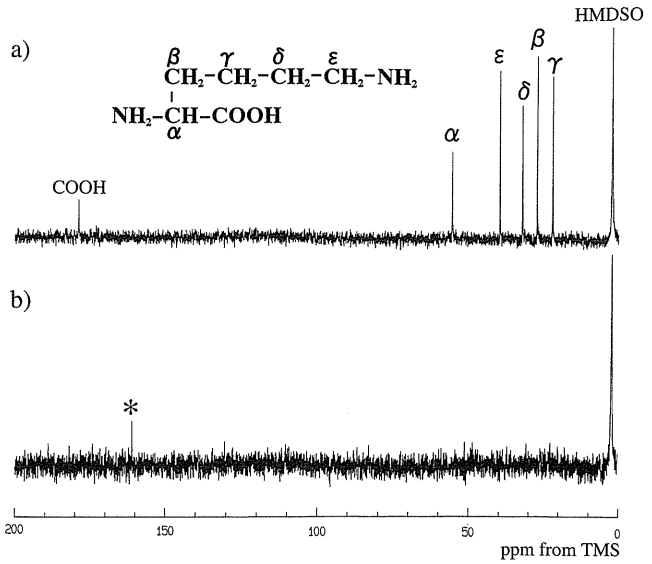

Fig. 9. Typical NMR signals of lysine. After NaClO had interacted with lysine in aqueous solution, the ^{13}C NMR peaks attributable to the carbons (a) in lysine disappeared and one unknown ^{13}C NMR peak appeared in the NMR spectrum (b). HMDSO: control peak *: unknown by-product

that a strong oxidizing substance attacked the amino acids, resulting in the generation of some free radicals. Shiozawa (15) reported that some active oxygen species were generated by a mixture of NaClO and hydrogen peroxide (H_2O_2). One explanation for this phenomenon is that NaClO will be changed to HClO in the surrounding environment, and then HClO is decomposed to ·OH and ·Cl (or Cl^-) by H_2O_2. It is well known that free radicals and active oxygen species damage cells and tissues. In particular, ·OH generated in human tissue occasionally exerts biological actions, such as inflammation, DNA damage, carcinogenesis, aging and mutation (16-18). In addition, Curran & others (19) reported that ·OH generated by Fenton's reagent degraded soluble collagen in a time- and dose-dependent manner and this degradation was inhibited by free radical scavengers. Furthermore, Moseley & others (20) reported that exposure of the proteoglycans of alveolar bone to ·OH for 24 h resulted in significant modification of the amino-acid composition with decreases in the proportion of leucine and the complete loss of proline. In our study, ·OH was generated by glutamic acid, and the reaction mixture of glutamic acid and NaClO, ·C and ·OH were generated by the lysine and NaClO reaction mixture, and a DMPO-X like signal was detected in the leucine and NaClO reaction mixture. We cannot explain why glutamic acid generated ·OH because other amino acid solutions did not generate any radicals and the origin of ·OH is unknown. In addition, our NMR analysis confirmed that the structure of the glutamic acid we used was normal. Further studies into this phenomenon are underway in our laboratory. Regarding the detection of different radicals in the different reaction mixtures, since these three amino acids have different charges, their reactivities with NaClO might differ, which may account for the different radicals detected. However, ·OH was detected in the Carisolv system, which suggests that ·OH plays an important role that enables carious dentin to be removed without drilling. Therefore, glutamic acid and lysine appear to be important components of the Carisolv system. Our NMR study showed that all three amino acids were degraded completely by NaClO, and unknown byproducts were detected. However, we could not identify the chemical structures of these byproducts, and further studies to do so are underway in our laboratory.

The results of both the ESR and NMR studies showed that the three amino acids changed their structures and generated free radicals when they were mixed with NaClO. The main radical generated by the Carisolv system was ·OH. It has been shown that ·OH generation is enhanced by light irradiation of H_2O_2 (21). In the present study, we used a plasma lamp, a device used to cure composite resin, to irradiate the Carisolv system mixture and found that more ·OH was generated than when incubated at 37 °C in normal room light without such irradiation. Therefore, plasma light irradiation of the Carisolv™ system may increase the effectiveness of this system for removing carious dentin by increasing ·OH generation.

In view of the results of our present study, we are carrying out research to develop more effective and safer chemo-mechanical methods using an ·OH generation system for the removal of carious dentin.

Acknowledgments

This study was supported by a grant from the Ministry of Education, Culture, Sports, Science and Technology to "Academic Frontier" Projects (in 2001-2005), Grant-in-aid for Exploratory Research (2004-2006), The Tsuchiya Foundation (2001) and Suzuki Memorial Grant of Nihon University School of Dentistry at Matsudo (2003).

References

1. Berggren U, Meynert G : Dental fear and avoidance : Causes, symptoms and consequences, J Am Dent Assoc, 109 : 247-251, 1984.
2. Green RM, Green A : Adult attitudes to dentistry among dental attenders in South Wales, Brit Dent J, 159 : 157-160, 1985.
3. Shovelton S : The maintenance of pulp vitality, Brit Dent J, 133 : 95-101, 1972.
4. Stanley HR, Swedlow H : Biological effects of various cutting methods in cavity preparation : The part pressure plays in pulpal response, J Am Dent Assoc : 61, 450-456, 1960.
5. Ericson D, Zimmerman M, Raber H, Gotrick B, Bornstein R, Thorell J : Clinical evaluation of efficacy and safety of a new method for chemo-mechanical removal of caries, Caries Res, 33 : 171-177, 1999.
6. Strid L, Hedward C : Patent SE 8704832, 1989.
7. Ericson D : In vitro efficacy of a new gel for chemo-mechanical caries removal, J Dent Res, 77 : SI 360 1252, 1998.
8. Shiozawa A, Ohta T, Kashima M, Tsujimoto Y, Yamazaki M : Effect of hypochlorous acid on amino acids (Report 1) The effect on glycine and arginine on free radical analysis, Jpn J Conserv Dent, 42 : 553-559, 1999. (in Japanese)
9. Shiozawa A, Ohta T, Kashima M, Takeuchi H, Tsujimoto Y, Yamazaki M : Effect of hypochlorous acid on amino acids (Report 2) Investigation of each amino acid by free radical analysis, Jpn J Conserv Dent, 42 : 560-568, 1999. (in Japanese)
10. Tsujimoto Y, Saitoh K, Kashima M, Shiozawa A, Kozuka M, Hashizume H, Kimura K, Yamazaki M, Fujii A : Effect of nonsteroidal anti-inflammatory drugs on lipid peroxidation by hydroxyl radical, Gen Pharmacol, 31 : 405-408, 1998.
11. Buettner GR : Spin trapping : ESR parameters of spin adducts, Free Radical Biol Med, 3 : 259-303, 1987.
12. Breitmaier E and Voelter W : Carbon-13 NMR spectroscopy : high-resolution methods and applications in organic chemistry and biochemistry, 415-418, 1987, New York VCH.
13. Bernofsky C, Olavesen EY, Felix CC, Kalyanaraman B : Evidence for a hydroperoxyl radical from hypochlorite-modified adenosine 5'-monophosphate (AMP), Biochem Arch, 4 : 103-107, 1988.
14. Bernofsky C, Bandara BMR & Hinojosa O () Electron spin resonance studies of the reaction of hypochlorite with 5,5-dimethyl-1-pyrroline-*N*-oxide, Free Radical Biol Med, 8 : 231-239, 1990.
15. Shiozawa A : Characterization of reactive oxygen species generated from the mixture of NaClO and H_2O_2 used as root canal irrigants, J Endodont, 26 : 11-15, 2000.
16. McCord JM : Free radicals and inflammation : Protection of synovial fluid by superoxide dismutase, Science, 185 : 529-531, 1974.
17. Kawanishi S, Hiraku Y, Murata M, Oikawa S : The role of metals in site-specific DNA damage with reference to carcinogenesis, Free Radical Biol Med, 32 : 822-832, 2002.
18. Harman D : Role of free radicals in mutation, cancer, aging, and the maintenance of life, Radiat Res, 16 : 753-763, 1962.
19. Curran SF, Amoruso MA, Goldstein BD, Berg RA : Degradation of soluble collagen by ozone or hydroxyl radical, Febs Lett, 176 : 155-160, 1984.
20. Moseley R, Waddington RJ, Embery G, Rees G : The modification of alveolar bone proteoglycans by reactive oxygen species *in vitro*, Connect Tissue Res, 37 : 13-28, 1998.
21. Kashima-Tanaka M, Tsujimoto Y, Kawamoto K, Senda N, Ito K, Yamazaki M : Generation of free radicals and/or active oxygen by lights or lasers irradiation of hydrogen peroxide or sodium hypochlorite, J Endodont, 29 : 141-143, 2003.

JOURNAL OF ENDODONTICS
Copyright © 2003 by The American Association of Endodontists
Printed in U.S.A.
VOL. 30, NO. 1, JANUARY 2004

Effects of the Hydroxyl Radical and Hydrogen Peroxide on Tooth Bleaching

Kohji Kawamoto, DDS, and Yasuhisa Tsujimoto, DDS, PhD

The mechanisms of bleaching of discolored coronal teeth using hydrogen peroxide (H_2O_2) were investigated. In a scanning–electron-microscopy study, the intertubular dentin and peritubular dentin were dissolved by high concentrations of H_2O_2, which is used for bleaching. The X-ray diffraction study showed that hydroxyapatite was not influenced by H_2O_2. In an electron–spin-resonance study, more hydroxyl radical (· OH) was detected as the H_2O_2 concentration was increased. When amino acids that are core components of dentin proteins, such as proline and alanine, were added to H_2O_2, the generation of · OH decreased, but there was no change when glycine was added. A nuclear–magnetic-resonance study showed that proline was degraded completely by H_2O_2, the structure of alanine changed slightly, and glycine was not affected by H_2O_2. It is suggested that H_2O_2 and · OH do not influence the inorganic tissue of dentin but attack the organic component of dentin. These facts suggest that · OH has the main role in tooth bleaching with H_2O_2.

Discoloration of teeth arises from decomposition of necrotic pulp tissue after death of the pulp and hemorrhage into the pulp chamber after a severe blow to the tooth. The Walking bleach method developed by Nutting and Poe in 1963 (1) involves bleaching the tooth by placing a paste of 30% (vol/vol) hydrogen peroxide (H_2O_2) and sodium perborate into the pulp chamber for a certain period. Many dentists have found this method for bleaching the coronal discoloration of teeth to be effective. It is well known that the hydroxyl radical (· OH) is generated from H_2O_2 after interaction with metal ions, light irradiation, or laser irradiation (2–4). · OH is a toxic, active form of oxygen and a free radical. · OH damages connective tissue, cell membranes, deoxyribose nucleic acid, and other tissues (5–7). In cellular membranes, the · OH is thought to attack the unsaturated fatty acid of the cellular membrane and this is followed by tissue destruction. · OH also attacks peptide chains of protein, and this induces decomposition of organic substances. The mechanism of tooth bleaching and the role of H_2O_2 are not yet clear; however, it has been suspected that the strong oxidative action of the · OH generated from H_2O_2 acts on the organic component of dentin and the pigmented materials and that this results in bleaching. We measured the · OH generated from various concentrations of H_2O_2 using the electron-spin resonance (ESR) spin-trapping method (4, 8).

The effect of H_2O_2 on the dentin wall of the root canal was observed using scanning electron microscopy (SEM). To study calcium (Ca) loss caused by treatment with H_2O_2, we measured how much dissolved Ca was released from a block of tooth immersed in H_2O_2. In addition, the structure of amino acids after treatment with H_2O_2 and · OH was determined using nuclear magnetic resonance (NMR) spectroscopy. The objectives of this study were to clarify the mechanisms by which H_2O_2 bleaches teeth and to determine which substance is responsible for the bleaching action.

MATERIALS AND METHODS

Chemicals

The reagents, H_2O_2 and EDTA, and the amino acids, L-proline, L-alanine, and glycine, were obtained from Wako Pure Chemicals (Osaka, Japan). As a spin-trapping agent, 5,5-dimethyl-1-pyrroline-*N*-oxide (DMPO, Dojin Chemicals, Kumamoto, Japan) was used. All other chemicals were obtained from local sources and were of the highest grade available.

Measurement of · OH

The amount of · OH generated at each concentration of H_2O_2 was measured using the ESR–spin-trapping method (4, 8). We also measured the amount of · OH generated in a solution containing 10% (wt/vol) amino acids in 30% (vol/vol) H_2O_2 that was incubated at 37°C for 3 weeks. The ESR spectrum was recorded with a JES FA300 (JEOL, Tokyo, Japan). The measuring conditions were: microwave power, 8.0 mW; magnetic field, 335.4 ± 5 mT; sweep time, 0.5 min; modulation frequency, 100 kHz; and time constant, 0.03 s.

SEM Observation

Four samples were obtained from the root of an extracted human tooth according to the method of Tsujimoto et al. (9). The dentin

surfaces were observed using SEM after treatment, as follows. The pulp tissue was removed using an explorer, and the canal wall was filed with a #40 K-file 30 times. The smear layer was removed with 15% (wt/vol) EDTA, pH 7.3, and then H_2O_2 was applied to the samples at various concentrations for 1, 5, and 10 days at 37°C. The samples were then dehydrated in a graded-ethanol series from 40% to 100%, and in 3-methylbutyl acetate using the critical-point drying method. The dried samples were sputter-coated with a layer of Au-Pt and observed using an S-2150 SEM (Hitachi, Tokyo, Japan) at 15 kV.

Measurement of Wet Weight of Tooth Block

The wet weights of each tooth block, before and after bleaching with H_2O_2, were measured using an R2000D electronic scale (Sartorius, Germany).

Measurement of the Amount of Dissolved Calcium

The amount of Ca dissolved from the tooth blocks that were incubated in pure water (PW) or H_2O_2 was measured using an inductively coupled, plasma atomic emission spectrometer SPS1700R (Seiko Instrument Inc., Tokyo, Japan). The measuring conditions were: power source, 1.30 kW; plasma flow (argon gas), 16.0 l/min; and modulation frequency, 27.12 kHz.

X-ray Diffraction Study of Hydroxyapatite

To evaluate the effects of H_2O_2 on the inorganic component of dentin, an X-ray diffraction study was performed. Five hundred milligrams of hydroxyapatite (HAP), kindly provided by Sangi Co. Ltd., was added to 500 ml of 30% (vol/vol) H_2O_2 for 1 week at room temperature. The HAP was then analyzed using an X-ray diffraction device, M18X HF22, and analyzer, MXP18 (Mac-Science, Tokyo, Japan), at 40 mA and 45 kV.

Observation of Tooth Discoloration

To study the bleaching effect of H_2O_2, each tooth block was immersed in 10%, 20%, or 30% H_2O_2 and then photographed. The change in color of the tooth was evaluated by eye.

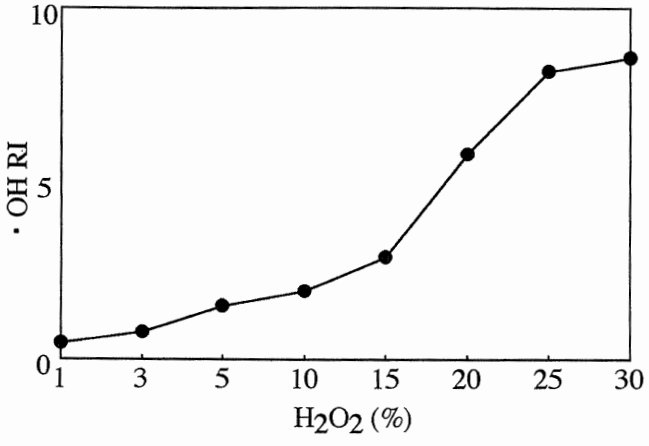

FIG . 1. The amounts of · OH generated in various concentrations of H_2O_2.

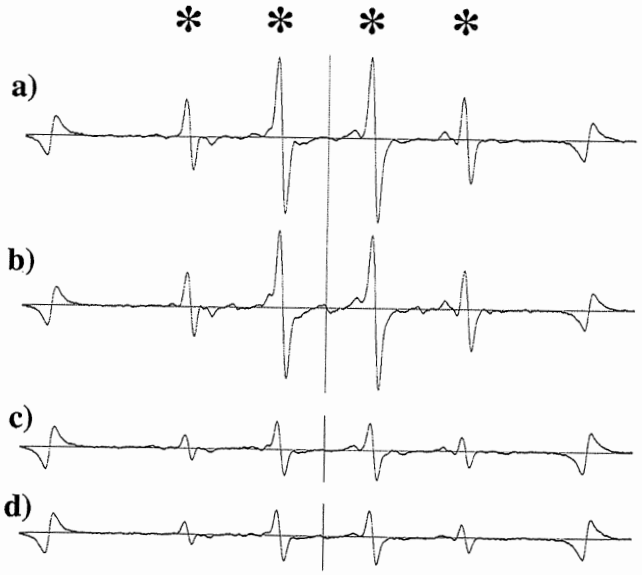

FIG 2. Typical ESR spectra from a solution of 10% (wt/vol) amino acids in 30% (vol/vol) H_2O_2 left for 3 weeks at 37°C. (*a*) Control: 30% H_2O_2; (*b*) glycine; (c) proline; (*d*) alanine.

Measurement of ^{13}C NMR Spectrum

Three amino acids that are representative of those found in teeth—proline, glycine, and alanine—were dissolved in a 30% (vol/vol) H_2O_2 solution and incubated at 37°C for 3 weeks. After this, 20% (wt/vol) deuterium oxide was added to the α–amino-acid solution. The ^{13}C NMR spectra of the amino acids were then measured at 25°C using a JEOL EX 270 spectrometer (Tokyo, Japan). The accumulation and repetition times were 400 and 3.8 s, respectively. Hexamethyl-di-siloxane was used as the external reference. Control NMR spectra of the amino acids also were observed after dissolving the α-amino acids in 20% (wt/vol) deuterium–oxide-aqueous solutions.

RESULTS

Measurement of · OH

The amount of · OH generated at each concentration of H_2O_2 are shown in Fig. 1. The hypercoupling constant of this signal was analyzed and found to be: · OH: $A_N = A_H = 1.49$ mT, which agreed with the value reported previously (10). When the amino acids were added to H_2O_2, the · OH generated was lower when proline or alanine was added but was not changed by the addition of glycine (Fig. 2).

SEM observation

Figures 3 to 5 show scanning electron micrographs of each sample. The intertubular dentin and peritubular dentin were dissolved by higher concentrations of H_2O_2 and if the H_2O_2 was applied for longer times.

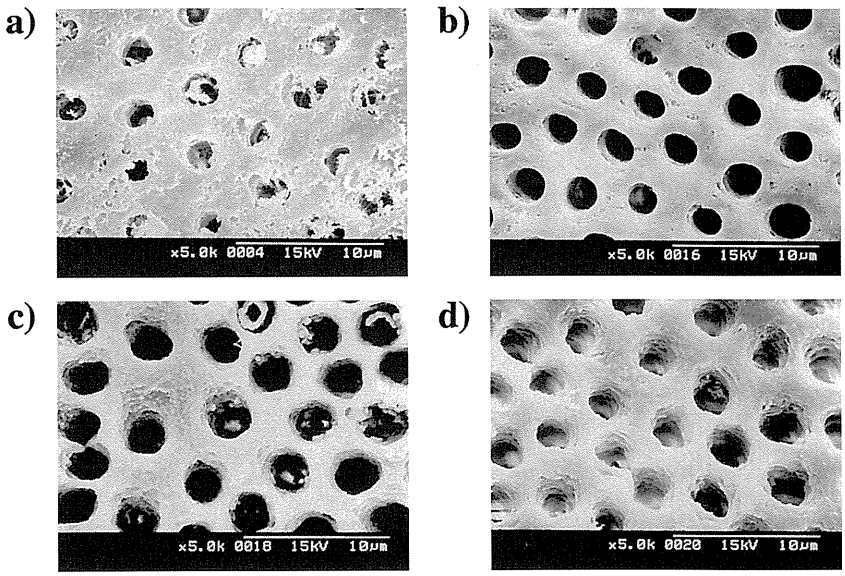

FIG 3. Typical scanning electron micrographs after treatment with 10% (vol/vol) H_2O_2. (*a*) Control: the smear layer was removed using 15% (wt/vol) EDTA. (*b*) One day after treatment with 10% (vol/vol) H_2O_2. (*c*) Five days after treatment with 10% (vol/vol) H_2O_2. (*d*) Ten days after treatment with 10% (vol/vol) H_2O_2.

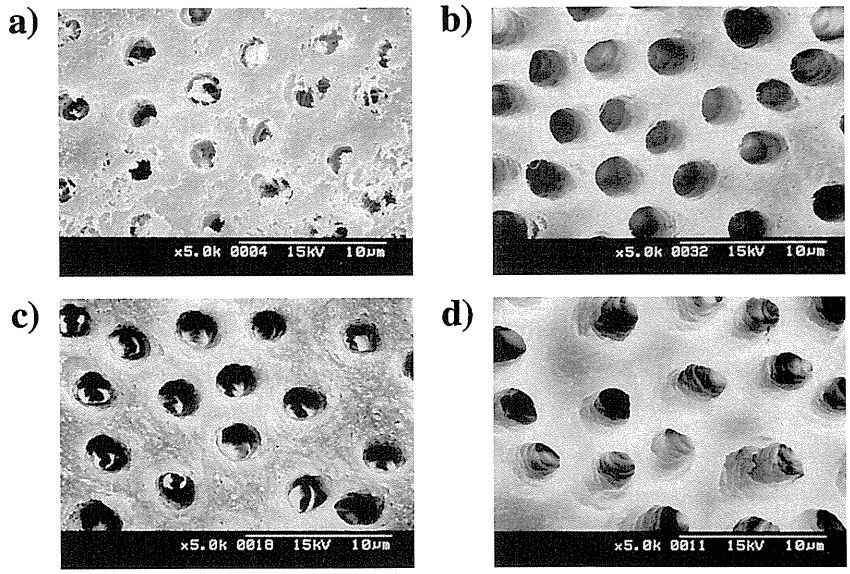

FIG 4. Typical scanning electron micrographs after treatment with 20% (vol/vol) H_2O_2. (*a*) Control: the smear layer was removed using 15% (wt/vol) EDTA. (*b*) One day after treatment with 20% (vol/vol) H_2O_2. (*c*) Five days after treatment with 20% (vol/vol) H_2O_2. (*d*) Ten days after treatment with 20% (vol/vol) H_2O_2.

Measurement of Tooth-block Wet Weight

The mean percentage wet weight of each sample ($n = 5$) is shown in Fig. 6. There was a slight decrease in wet weight observed at high concentrations of H_2O_2.

Measurement of the Amount of Dissolved Calcium

The ratio of Ca weight and the decrease in wet weight from tooth-block samples is shown in Fig. 7. The weight ratios decreased in both a time- and concentration-dependent manner; however, the amount of Ca in each sample was almost unchanged.

X-ray Diffraction Study of HAP

The peaks of HAP in the X-ray diffraction analysis are shown in Fig. 8. The coincidence pattern of peaks was obtained between nontreated HAP and HAP treated with 30% H_2O_2.

Observation of Tooth-block Color

The color of samples changed in both a concentration- and time-dependent manner (Fig. 9). There was a whitening effect in each sample. A transparent effect was obtained using 10% and 20% H_2O_2. An opaque effect was obtained using 30% H_2O_2. A

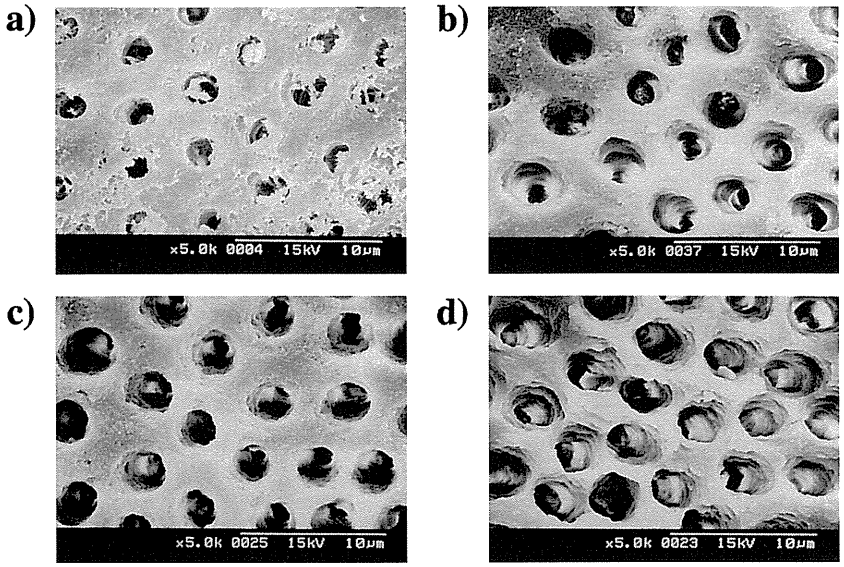

FIG 5. Typical scanning electron micrographs after treatment with 30% (vol/vol) H_2O_2. (*a*) Control: the smear layer was removed using 15% (wt/vol) EDTA. (*b*) One day after treatment with 30% (vol/vol) H_2O_2. (*c*) Five days after treatment with 30% (vol/vol) H_2O_2. (*d*) Ten days after treatment with 30% (vol/vol) H_2O_2.

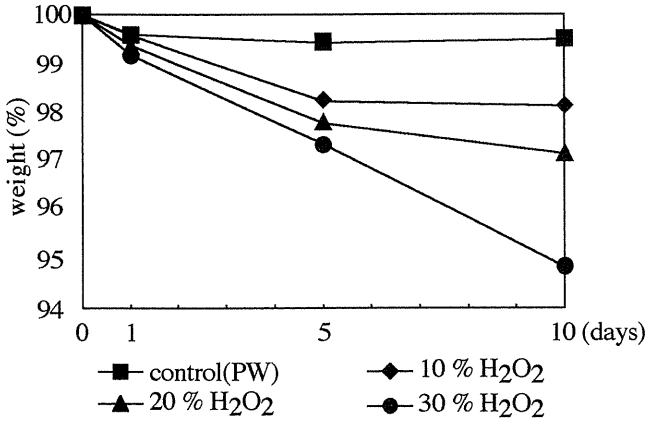

FIG 6. Mean percentage of wet weight of each sample treated with H_2O_2 (n = 5).

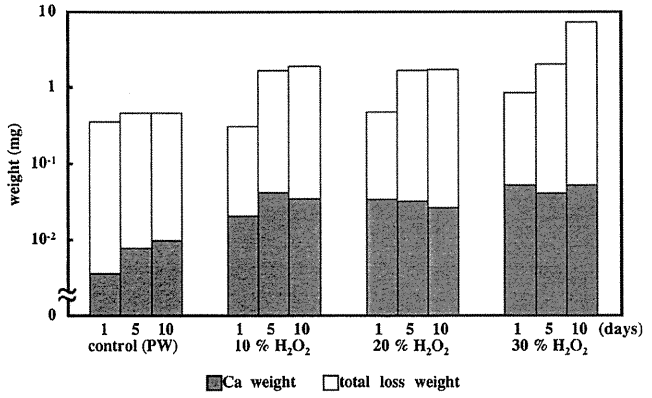

FIG 7. The ratio of Ca weight and decrease in wet weight from tooth-block samples.

clearer bleaching effect was obtained using 10% and 20% H_2O_2 than for 30% H_2O_2, in this experiment.

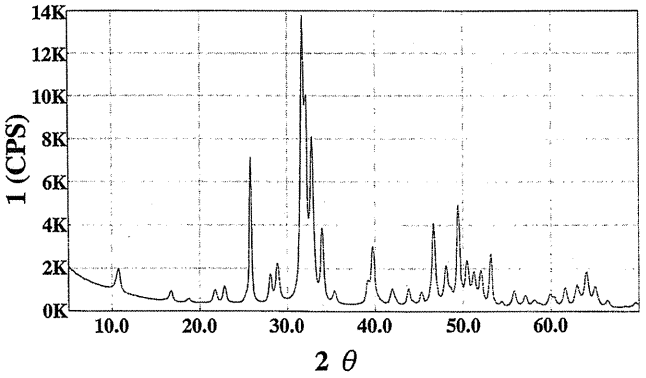

FIG 8. X-ray diffraction pattern of HAP. The peaks of HAP treated with 30% (vol/vol) H_2O_2 coincided with those of the control in the X-ray diffraction.

Measurement of ^{13}C NMR Spectrum

The NMR peaks attributable to the carbon constituents of the amino acids were detectable, and agreed with previously reported values (11). When H_2O_2 was added to the amino acids, the ^{13}C peaks of glycine did not change, but the ^{13}C peaks of proline disappeared and unknown peaks appeared. Unknown peaks appeared in the alanine solution but the ^{13}C peaks of alanine were still present (Figs. 10–12).

DISCUSSION

Generally, H_2O_2 has been used in bleaching of tooth coronal discoloration and it is an effective bleaching agent. We have reported that · OH is generated from H_2O_2 and may be important in tooth bleaching (4). We also have reported that H_2O_2 damages the structure of the tooth (12). However, the detailed mechanisms by which H_2O_2 bleaches teeth have not yet been clarified.

In the ESR study, · OH was detected and the · OH levels increased in an H_2O_2–concentration-dependent manner. Usually,

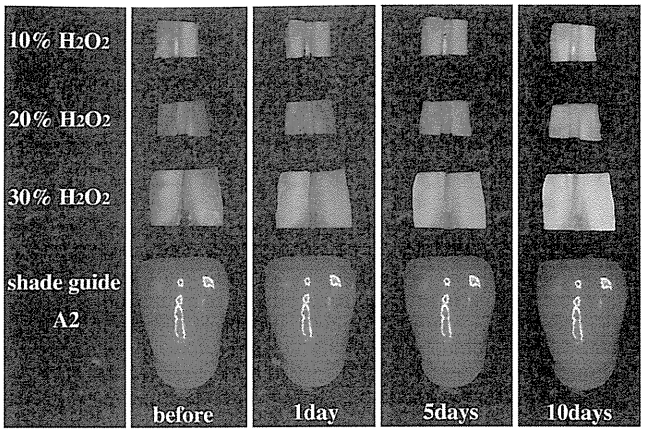

FIG 9. The change in color of the tooth block before and after treatment with 10%, 20%, or 30% (vol/vol) H_2O_2.

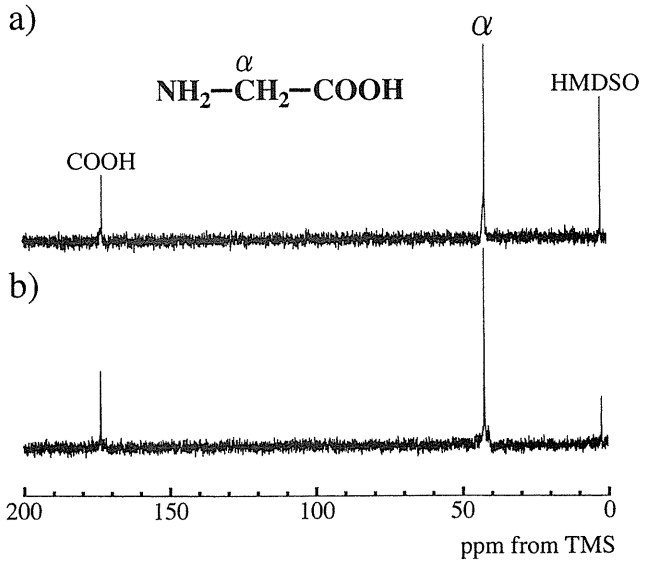

FIG 10. Typical NMR signals for glycine. After 30% (vol/vol) H_2O_2 had interacted with glycine, the ^{13}C NMR peaks attributed to the carbons in glycine (*a*) were the same ^{13}C NMR peaks that appeared in the normal glycine NMR spectrum (*b*). HMDSO = control peak; *unknown by-product.

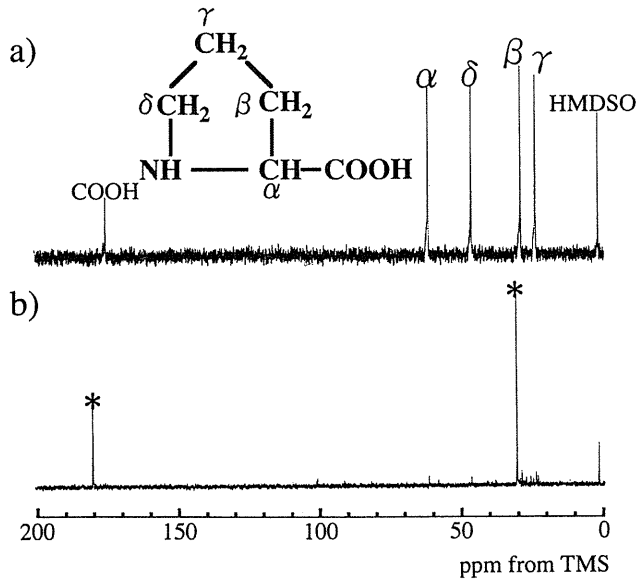

FIG 11. Typical NMR signals of proline. After 30% (vol/vol) H_2O_2 had interacted with proline, the ^{13}C NMR peaks attributed to the carbons in proline (*a*) disappeared and two unknown ^{13}C NMR peaks appeared in the NMR spectrum (*b*). HMDSO = control peak.

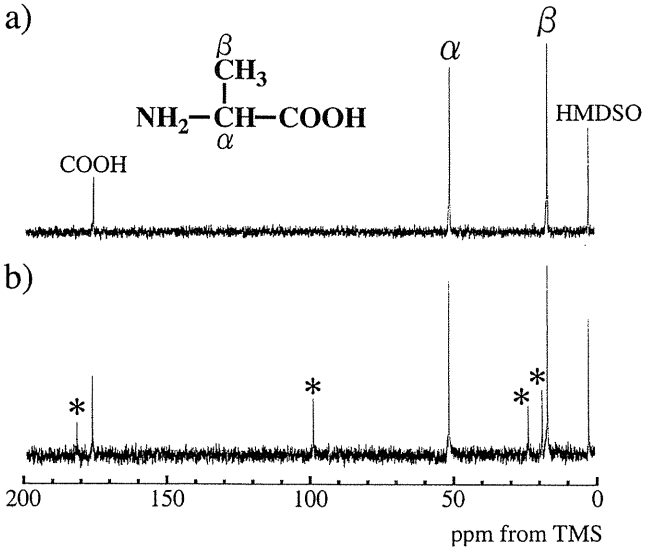

FIG 12. Typical NMR signals of alanine. After 30% (vol/vol) H_2O_2 had interacted with alanine, the ^{13}C NMR peaks attributed to the carbons in alanine (*a*) remained and four unknown ^{13}C NMR peaks appeared in the NMR spectrum (*b*). HMDSO = control peak; *unknown by-product.

commercial H_2O_2 includes a few metal ions (10^{-1} ppm level). It is well known that the Fenton reaction (13, 14) occurs in the presence of metal ions, especially Fe^{2+}. Therefore, when a chelating agent was added to each concentration of H_2O_2, the amount of · OH generated decreased linearly (data not shown).

In the SEM study, we found that a higher concentration of H_2O_2 and a longer application time increased the damage to intertubular dentin and peritubular dentin. This shows that destruction of dentin occurred as a result of H_2O_2 application. This result agrees with our previous report (12). The color of each sample changed as a result of bleaching by H_2O_2. In particular, the transparency disappeared when the tooth was treated with 30% H_2O_2. Also, the wet weight of samples was lower in those samples treated with 30% H_2O_2 than in those treated with lower concentrations of H_2O_2. However, the amounts of dissolved Ca from each sample were almost same. As the X–ray-diffraction study revealed, the structure of HAP was not changed by H_2O_2 treatment. These results showed that · OH and H_2O_2 did not damage the inorganic tissue of the tooth, but did damage other substances such as organic tissue, and that the constructive component of dentin was lost and dissolved in solution. This might be the reason that the wet weights were lower.

The structure of two amino acids that are components of the organic tissue of dentin were changed by the application of · OH and/or H_2O_2 but glycine was not changed, according to the NMR study. Proline was degraded. Glycine did not cause any alteration in the · OH signal in the ESR study; however, proline and alanine caused a reduction in the · OH signal. Proline and alanine may be more susceptible to attack by · OH, and their structure changed

with the disappearance of the · OH signal; glycine did not seem to participate in this reaction. Moseley et al. (15) reported a change in the amino-acid composition of bovine alveolar bone proteoglycans after exposure to H_2O_2 or the · OH for 24 h. When H_2O_2 concentrations were increased from 60 to 180 mM for 24 h, there was an apparent enrichment in the proportion of glycine relative to the total detectable amino acids, but proline and alanine did not change. In contrast, exposure of the alveolar bone proteoglycans to a · OH flux for 24 h resulted in significant modification to the amino acid composition with complete loss of proline, and corresponding enrichments of glycine and alanine.

Both these results and the results of our study suggest that amino acids such as proline, glycine, and alanine are not influenced by H_2O_2, but that · OH influences proline. However, the effects on alanine remain unclear, and further studies of this aspect are currently underway in our laboratory.

The results of this study suggest that H_2O_2 or · OH does not influence the inorganic component of dentin, but does influence the organic tissue. Therefore, it is thought that the bleaching effect occurs as a result of breakage of the polypeptide chain caused by the destruction of amino acids that are part of the composition of the organic substance, and that the · OH may be the main substance responsible for tooth bleaching. We are conducting further research using the organic–tissue-degradation system to develop safe and effective tooth-bleaching agents.

This study was supported by a Grant from the Ministry of Education, Culture, Sports, Science and Technology to promote 2001-Multidisciplinary Research Projects (in 2001–2005), and The Tsuchiya Foundation (2001).

The authors thank Associate Professor N. Nishiyama (Department of Dental Materials, Nihon University School of Dentistry at Matsudo) with the NMR work and for helpful comments, Professor M. Yamazaki (Department of Endodontics, Nihon University School of Dentistry at Matsudo) for critical reading of the manuscript and helpful comments, and Dr. T. Ishizaki (Central Research Center, Sangi Co. Ltd.) for the X-ray diffraction work.

Dr. Kawamoto is a graduate student, and Dr. Tsujimoto is assistant professor, Department of Endodontics, Nihon University School of Dentistry at Matsudo, Chiba, Japan.

Address requests for reprints to Dr. Yasuhisa Tsujimoto, Department of Endodontics, Nihon University School of Dentistry at Matsudo, 870-1, Sakaecho, Nishi-2, Matsudo, Chiba 271-8587, Japan.

References

1. Nutting EB, Poe GS. A new combination for bleaching teeth. J Soc Calif Dent Assoc 1963;31:289–91.
2. Halliwell B. Superoxide-dependent formation of hydroxyl radicals in the presence of iron chelates. FEBS Lett 1978;92:321–6.
3. Gutteridge JMC. Iron promoters of the Fenton reaction and lipid peroxidation can be released from haemoglobin by peroxides. FEBS Lett 1986; 201:291–5.
4. Kashima-Tanaka M, Tsujimoto Y, Kawamoto K, Senda N, Ito K, Yamazaki M. Generation of free radicals and/or active oxygen by light or laser irradiation of hydrogen peroxide or sodium hypochlorite. J Endodon 2003;29: 141–3.
5. Curran SF, Amuruso MF, Goldstein BD, Berg RA. Degradation of soluble collagen by ozone or hydroxyl radicals. FEBS Lett 1984;176:155–60.
6. Rowley DA, Halliwell B. Formation of hydroxyl radicals from hydrogen peroxide and iron salts by superoxide and ascorbate-dependent mechanisms: relevance to the pathology of rheumatoid disease. Clin Sci 1983;64: 649–53.
7. Halliwell B. Free radicals, reactive oxygen species and human disease: a critical evaluation with special reference to atherosclerosis. Br J Exp Pathol 1989;70:737–57.
8. Tanigawa T. Determination of hydroxyl radical scavenging activity by electron spin resonance. J Kyoto Pref Univ Med 1990;99:133–43.
9. Tsujimoto Y, Kozuka M, Hitotsune N, Yamazaki M. Removal capability of smear layer of root canal by NaClO and H_2O_2 mixed solution [Japanese]. J JEA 1997;18:19–24.
10. Buettner GR. Spin trapping: ESR parameters of spin adducts. Free Rad Biol Med 1987;3:259–303.
11. Breitmaier E, Volter W. Carbon-13 NMR spectroscopy: high-resolution methods and applications in organic chemistry and biochemistry. New York VCH 1987;415–8.
12. Kozuka M, Kawamoto K, Miura H, Tsujimoto Y, Yamazaki M. Effect of H_2O_2 for use of tooth bleaching to root canal dentin surface: examination of temperature and application time by SEM [Japanese]. J JEA 2001;22:16–9.
13. Cohen G, Sinet PM. Fenton reaction between ferrous-diethylenetriaminepentaacetic acid and hydrogen peroxide. FEBS Lett 1982;138:258–60.
14. Dunford HB. Free radicals in iron-containing systems. Free Rad Biol Med 1987;3:405–21.
15. Moseley R, Waddington RJ, Embery G, Rees SG. The modification of alveolar bone proteoglycans by reactive oxygen species in vitro. Connect Tissue Res 1998;37:13–28.

原　著

電子線マイクロアナライザーによる石灰化促進の可能性としてのMTAの微量成分の検討

大久保厚司[1)]　辻本恭久[2)]　三島弘幸[1,3)]　小澤幸重[1)]
[1)]日本大学松戸歯学部第2解剖学講座
[2)]日本大学松戸歯学部歯内療法学講座
[3)]高知学園短期大学保健科

Examination of trace element of Mineral Trioxide Aggregate (MTA) for the possibility of mineralization promotion by electron probe X-ray microanalyzer

OOKUBO Atsushi[1)], TSUJIMOTO Yasuhisa[2)], MISHIMA Hiroyuki[1,3)] and KOZAWA Yukishige[1)]
[1)]Department of Anatomy 2, Nihon University School of Dentistry at Matsudo
[2)]Department of Endodontics, Nihon University School of Dentistry at Matsudo
[3)]Department of Health Science, Kochi Gakuen College Health Sciences

Abstract：This research analyzed trace elements of crystal contained in powdered mineral trioxide aggregate (MTA) with SEM-EDS analysis. The results of this analysis were compared with trace elements, which have the possibility of appearing in the mineralization formation in dentine. Research has shown that some trace elements in the mineralization mechanism include Ca, P, S, Mg, Si, and Al in the root formation of dentin；include Ca, P, S, and Mg at the completed root of dentin；and Si and Al were replaced by Ca and P with the formation at the maturation of root. It is assumed that these trace elements of MTA are necessary for the mineralization process of dentine. We suppose that a vital reaction is further promoted by using these elements as a compound.

Key words：mineral trioxide aggregate (MTA), trace elements of crystal, SEM-EDS analysis
（日歯内療誌 25(3)：137～143，2004）

緒　言

1993年にTorabinejadら[1)]によってroot-end filling materialとして開発されたMineral Trioxide Aggregate (MTA) 商品名ProROOT® (Dentsply社) は，米国では1998年U. S. Food and Drug Administrationから認可されて1999年から発売されている．使用方法はMTAと蒸留水を練和硬化させ，記載されている適応症へ応用することで象牙質の石灰化を促進すると報告されている．MTAの適応症は直接覆髄[2~4)]，穿孔部の修復[5~7)]，根吸収[8,9)]，アペキシフィケーション[10~13)]，根尖孔閉鎖[14~16)]，根の垂直破折[8)]等の他材料との比較や臨床報告がされている．

MTAの主成分は3 CaO-SiO_2，2 CaO-SiO_2，3 CaO-Al_2O_2，4 CaO-Al_2O_2，Fe_2O_3，$CaSO_4$-2 H_2Oであり，製作法はこれらを焼結，粉砕し，ポルトランドセメント75%，造影剤として酸化ビスマス20%，硬化調整剤として石膏5%を混入したと記されている．

これらのMTAに含有される成分は，非コラーゲン性基質による石灰化過程でミネラルの置換に関与することを示唆させる．しかし，MTAの微量元素の成分や

受付：平成16年7月8日／受理：平成16年8月16日

MTA の全体の結晶成分

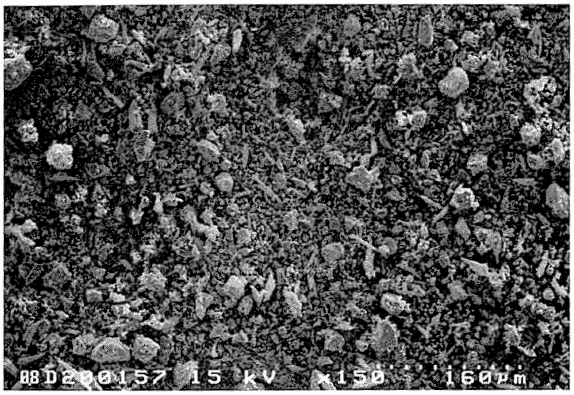

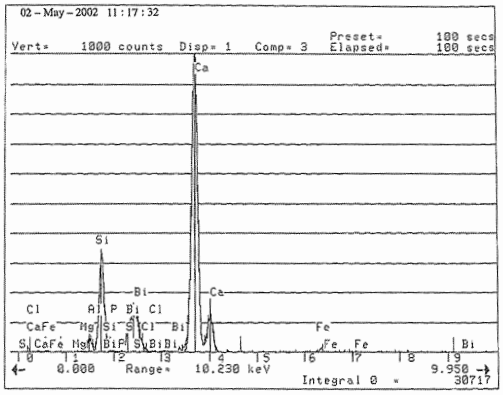

日立製-S 2700 SEM
kevex 社製・Kevex Delta Plus（Fisons）
加速電圧 15 kV 以下
02-May-2002　11：17：32, Accelerating voltage 15.0 KeV, Beam-sample incidence angle 90.0 degrees, X-ray emergence angle 35.0 degrees, X-ray-window incidence angle 0.0 degrees

Standardless EDS Analysis (XPP Quantitation)

Element & Line		K-Ratio	Weight percent	Precision 2 SIGMA	Formula	Oxide percent	NO. of CATIONS In Formula
Mg	KA	0.0031	0.55	0.10	MgO	0.91	0.0216
Al	KA	0.0065	0.97	0.11	Al_2O_3	1.03	0.0343
Si	KA	0.0466	5.92	0.19	SiO_2	12.66	0.2018
P	KA	0.0013	0.16	0.05	P_2O_5	0.37	0.0050
S	KA	0.0109	1.24	0.13	SO_3	3.10	0.0371
Cl	KA	0.0021	0.25	0.07	Cl	0.25	0.0000
Ca	KA	0.2953	32.38	0.49	CaO	71.15	0.7739
Fe	KA	0.0161	1.95	0.22	FeO	2.51	0.0334
Pb	KA	0.0000	0.00	0.00	PbO	0.00	0.0000
Bi	KA	0.0486	6.49	0.34	Bi_2O_3	7.24	0.0298
D	*		50.10				
Total						100.01	1.1368

*Determined by Stoichiometry, Number of CAT ions calculated on basis of 3 oxygen atoms.
Iterations 5, Normalization Factor：1.658
Note：K-ratio＝K-ratio X R, where R＝reference (standard) / reference (sample)

図 1　MTA 粉末の全体像（SEM 所見）

SEM 所見では MTA 粉末の全体像は 0.2～50 μ 程度のさまざまな大きさと形の結晶の集合体からなり，EDS 分析では MTA の元素は Ca，Bi，Si，Fe，S，Al，Mg，Cl，P の順に検出した．Oxide percent は CaO 71.15%，SiO_2 12.66%で合計 83.81%を占め，Bi_2O_3 が 7.24%，ほかに微量元素を SO_3 3.10%，FeO 2.51%，Al_2O_3 1.03%，MgO 0.91%，P_2O_5 0.37%，Cl 0.25%の順に検出した．

比率を記したものは少なく，精製水で練和硬化後に X 線分析された報告[17,18]では，硬化時間が長いことから硬化中に生体の体液と触れて反応することは避けられない．

そこで，本研究では象牙質やセメント質に置換する可能性があるミネラルの存在を明らかにするために，MTA 粉末の結晶構造を走査型電子顕微鏡にて観察すると同時に，エネルギー分散型 X 線分析装置にて MTA 結晶の微量元素を検出し，象牙質や象牙前質の石灰化時期における微量元素[19,20]の置換の可能性を報告する．

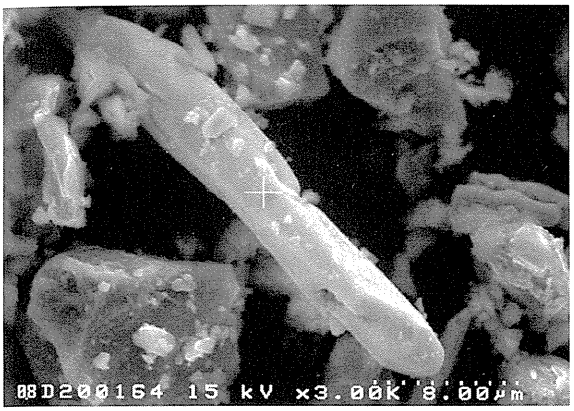

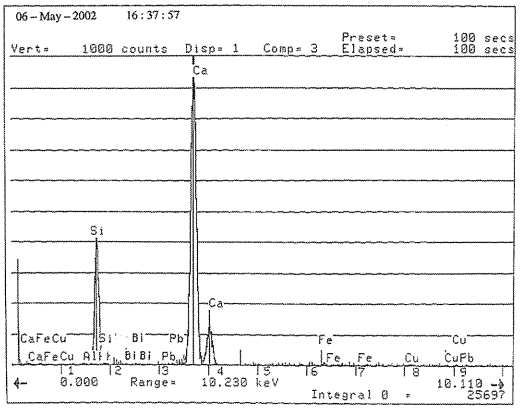

Standardless EDS Analysis (XPP Quantitation)

Element & Line		K-Ratio	Weight percent	Precision 2 SIGMA	Formula	Oxide percent	NO. of CATIONS In Formula
Al	KA	0.0016	0.24	0.07	Al_2O_3	0.45	0.0083
Si	KA	0.0576	7.39	0.24	SiO_2	15.80	0.2471
Ca	KA	0.3155	34.38	0.56	CaO	75.42	0.8047
Fe	KA	0.0127	1.54	0.25	FeO	1.99	0.0260
Bi	KA	0.0194	2.66	0.14	Bi_2O_3	2.87	0.0012
Cu	KA	0.0219	2.78	0.49	CuO	3.47	0.0410
D	*		51.07				
Total						100.00	1.1393

Normalization Factor : 1.658

図 2　MTA粉末，棒状結晶-1（SEM所見）
4.6×28 μmの棒状結晶はCaO 75.42%，SiO_2 15.80%，CuO 3.47%，Bi_2O_3 2.87%，FeO 1.99%，Al_2O_3 0.45%を検出した．

材料および方法

SEM試料台にカーボン製の両面テープの片側を接着させ，観察側にMTA粉末を一層接着させ，真空下でカーボン蒸着を60秒施した．MTA粉末試料は走査型電子顕微鏡（SEM）日立製-S 2700で倍率150～5,000倍で観察し，エネルギー分散型X線分析装置（EDS）kevex社製Kevex Delta Plus（Fisons）を用いて，加速電圧15 kV下，分析時間は100秒の条件下で，X線分析を行った．分析部位は写真にて記録し，分析データはMOにて保存した．

結　　果

SEM-EDSによる所見では，MTA粉末の全体像は0.2～50 μ程度のさまざまな大きさと形の結晶の集合体からなり，elementはCa，Bi，Si，Fe，S，Al，Mg，Cl，Pの順に検出した．Oxide percentはCaO 71.15%，SiO_2 12.66%で合計83.81%を占め，Bi_2O_3が7.24%，ほかに微量元素をSO_3 3.10%，FeO 2.51%，Al_2O_3 1.03%，MgO 0.91%，P_2O_5 0.37%，Cl 0.25%の順に検出した（図1-1，2，3）．

結晶は大きさや形状により，4.6×28 μmの棒状，4.3×42 μmの棒状，8×10 μmの菱状，0.8×1.0 μmの顆粒状の4種に大別した．

4.6×28 μmの棒状はCaO 75.42%，SiO_2 15.80%，CuO 3.47%，Bi_2O_3 2.87%，FeO 1.99%，Al_2O_3 0.45%（図2-1，2，3）．8×10 μmの菱状はCaO 73.86%，CuO 16.27%，FeO 6.94%，SiO_2 1.74%，Bi_2O_3 1.19%（図3-1，3-2，3-3）を検出した．

4.3×42 μmの棒状はBi_2O_3 71.75%，CaO 13.22%，CuO 7.45%，FeO 3.95%，SiO_2 3.63%（図4-1，2，3）であり，ビスマス金属酸化物と思われる．

0.8×1.0 μmの顆粒状はCaO 67.15%，SiO_2 11.13%，Bi_2O_3 7.90%，FeO 6.30%，Al_2O_3 5.16%，CuO 1.90%，MgO 0.36%（図5-1，2，3）を検出した．

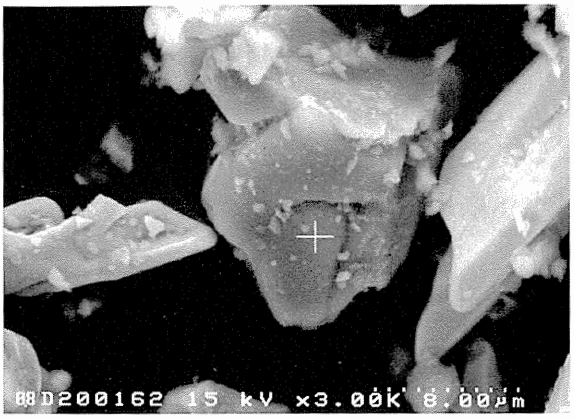

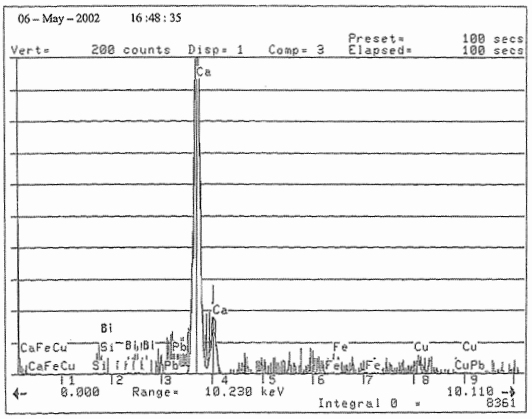

Standardless EDS Analysis (XPP Quantitation)

Element & Line		K-Ratio	Weight percent	Precision 2 SIGMA	Formula	Oxide percent	NO. of CATIONS In Formula
Si	KA	0.0060	0.01	0.22	SiO_2	1.74	0.0302
Ca	KA	0.3177	33.61	1.11	CaO	73.86	0.8735
Fe	KA	0.0461	5.39	0.79	FeO	6.94	0.1006
Cu	KA	0.1051	13.00	1.75	CuO	16.27	0.2131
Bi	KA	0.0082	1.11	0.18	Bi_2O_3	1.19	0.0056
D	*		46.08				
Total						100.00	1.2229

Normalization Factor：1.658

図 3　MTA 粉末，菱状結晶（SEM 所見）
8×10 μm の菱状結晶は CaO 73.86%，CuO 16.27%，FeO 6.94%，SiO_2 1.74%，Bi_2O_3 1.19%を検出した．

考　　察

象牙前質から象牙質への石灰化に関して Mishima ら[19]は，象牙質の成長段階によって出現する歯冠部と歯根部の微量元素の SEM-EDS 分析を行っている．歯根成長期（根未完成歯）において，象牙質の石灰化機構に必要な元素として Ca，P，S，Mg，Si，Al を検出した．髄角部では 8～22 μm の石灰化球を認め，象牙細管は 3 μm で Ca，P を，髄周象牙質では 3～20 μm の石灰化球を認め，象牙細管は 3 μm で Ca，P，Mg，Si，S の微量元素を，成長の最先端部象牙質の石灰化球は 7～51 μm，象牙細管は 1.4～2 μm で Ca，P，Mg，Al，Si，S の微量元素を認めたと報告している．そして，完成した歯根象牙質からは Ca，P，S，Mg を検出し，髄角部では 6～20 μm の石灰化球を認め，象牙細管は 3 μm で Ca，P 微量元素を，象牙質では 7～23 μm の石灰化球を認め，象牙細管は 3 μm で Ca，P，Mg の微量元素を，根中央部象牙質では 4～24 μm の石灰化球を認め，象牙細管は 2 μm で Ca，P，Mg，S の微量元素を，根尖部はコラーゲン線維の石灰化が起こり，象牙細管は 1.4～2 μm で Ca，P，Mg，S の微量元素を認め，歯根の成長と熟成に伴い Si と Al は Ca と P に置換されていると報告している．

Hohling ら[20]は，象牙前質の成長過程の石灰化微量元素をみるために，ウィスター系ラットの凍結乾燥した切歯を spurr 包埋後，400 nm に薄切りした象牙質と象牙前質を SEM-EDS で分析した．その結果，象牙質内では Ca，P の微量元素のほか，Al，Si，S，Cl，K を認め通常の象牙質値を示すが，象牙前質では Ca や P よりも Al，Si，S，Cl，K が高い数値を表したと報告している．さらに，象牙質最表層の微量元素では Al と C が高値を示し，Ca と P がほぼ同じ程度 Si，S がほぼ同量であり，少量の K を認めた．象牙前質の最表層や中央部では Al は同等に高値を示し，Si，P，S，Cl はほぼ同量であり，Ca，K は多少低い値を示した．象牙前質最表層の元素は Ca，P，S，K，Si，Al，Cl を，象牙前質に直面した部位では Ca，P がほとんどで微量元素として S，K，Si，Al が検出されたことは，成長過程の象牙質と同様に Ca と P によって置換されたためと推定している．

MTA の構成成分は，4 CaO-Al_2O_2-Fe_2O_3 を除いて

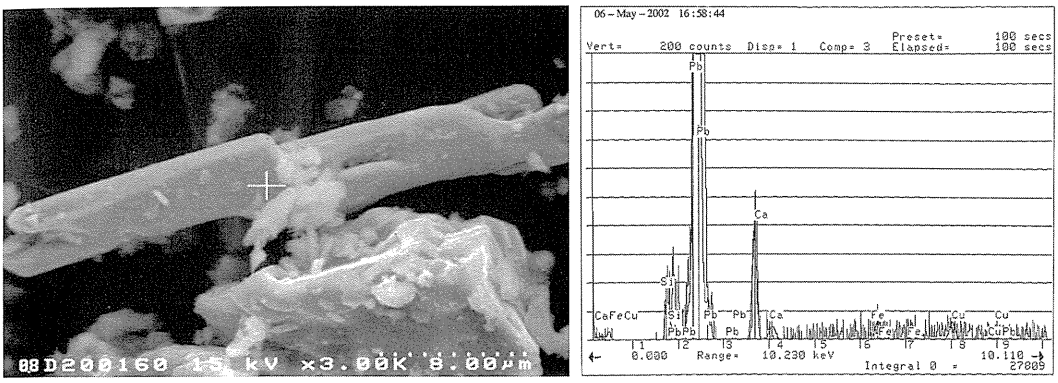

Standardless EDS Analysis (XPP Quantitation)

Element & Line		K-Ratio	Weight percent	Precision 2 SIGMA	Formula	Oxide percent	NO. of CATIONS In Formula
Si	KA	0.0148	1.70	0.23	SiO_2	3.63	0.1742
Ca	KA	0.0571	6.01	0.44	CaO	13.22	0.4323
Fe	KA	0.0333	3.07	0.50	FeO	3.95	0.1586
Cu	KA	0.0656	5.95	0.84	CuO	7.45	0.2698
Bi	KA	0.5876	66.61	0.23	Bi_2O_3	71.75	0.9263
D	*		16.66				
Total						100.00	1.9612

Normalization Factor：1.658

図 4　MTA粉末，棒状結晶-2（SEM所見）
4.3×42 μmの棒状結晶は Bi_2O_3 71.75%，CaO 13.22%，CuO 7.45%，FeO 3.95%，SiO_2 3.63%を検出した．造影剤に使用されているビスマスと思われる．

石灰化の初期に必要な微量元素である．3 CaO-SiO_2，2 CaO-SiO_2，3 CaO-Al_2O_2，$CaSO_4$-2 H_2Oは酸化カルシウム系や二酸化ケイ素系[21,22]の化合物であり，SEM-EDSでも骨置換作用をもつCaO 71.15%とSiO_2 12.66%を合計83.81%認めた．そのため，化合物は元素単体より生体で置換を行いやすくなると推測する．

象牙質の石灰化は初期にAl, P, Si, S, Cl, Ca, Cu, Zn等が検出され，後にCaやPに置換されていく機構が推定されており，MTAは中期，後期に出現するCaとSiを多く含み，ほかに微量なFe, S, Al, Mg, Clなどのミネラルが含まれているので，象牙芽細胞と石灰化象牙質の間には未石灰化の象牙前質が常に存在するように，セメント質よりもむしろ象牙前質に近い石灰化機構を補助すると考えられる．その結果，MTAに含まれるミネラルは供給源として象牙質石灰化を促進するものと推測される．

結　　論

MTAの粉末に含まれる結晶の微量成分をSEM-EDSにより分析し，象牙質もしくは象牙前質の石灰化機構時に出現する微量元素との類似性を推測した．

すなわち，SEM-EDSによるelementはCa, Bi, Si, Fe, S, Al, Mg, Cl, Pの順に検出し，象牙質初期に必要な微量元素と類似していた．また，oxide percentはCaO 71.15%，SiO_2 12.66%で合計83.81%を占めた．MTAは，置換性石灰化に適した組織環境をもたらし，これらの成分が修復象牙質反応を調節していく可能性があることが推測された．

本研究の研究費の一部は，文部科学省平成13年度学術フロンティア推進事業によった．

文　　献

1) Torabinejad M, Watson TF, Pitt Ford TR：Sealing ability of a mineral trioxide aggregate when used as a root end filling material, J Endod, 19：591-595, 1993.
2) Faraco IM Jr, Holland R：Response of the pulp of dogs to capping with mineral trioxide aggregate or a calcium hydroxide cement, Dent Traumatol, 17：163-166, 2001.
3) Tziafas D, Pantelidou O, Alvanou A et al.：The

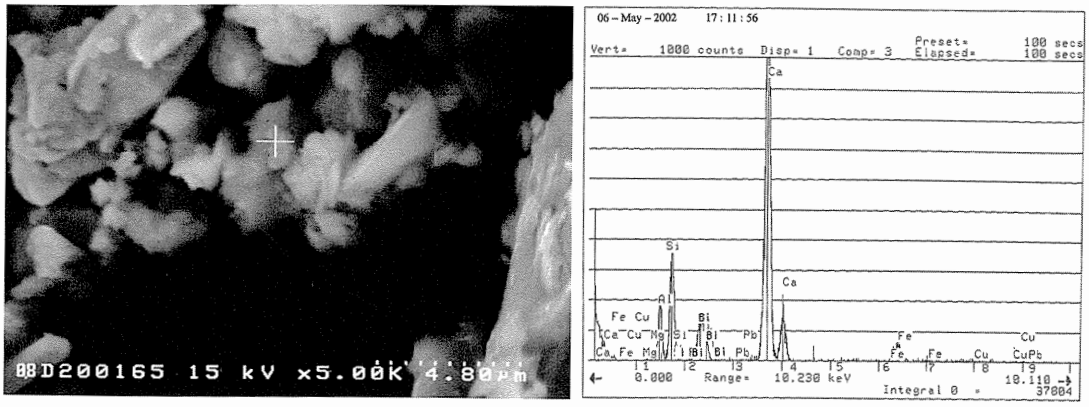

Standardless EDS Analysis (XPP Quantitation)

Element & Line		K-Ratio	Weight percent	Precision 2 SIGMA	Formula	Oxide percent	NO. of CATIONS In Formula
Mg	KA	0.0012	0.88	0.06	MgO	0.36	0.0091
Al	KA	0.0182	2.73	0.14	Al_2O_3	5.16	0.1024
Si	KA	0.0401	5.20	0.17	SiO_2	11.13	0.1874
Ca	KA	0.2815	30.56	0.44	CaO	67.15	0.7711
Fe	KA	0.0411	4.90	0.33	FeO	6.30	0.0888
Cu	KA	0.0123	1.52	0.24	CuO	1.90	0.0242
Bi	KA	0.0549	7.41	0.39	Bi_2O_3	7.90	0.0362
D	*		47.46				
Total						100.00	1.2191

Normalization Factor：1.658

図 5　MTA 粉末，顆粒状結晶（SEM 所見）
0.8×1.0 μm の顆粒状結晶は CaO 67.15%，SiO_2 11.13%，Bi_2O_3 7.90%，FeO 6.30%，Al_2O_3 5.16%，CuO 1.90%，MgO 0.36%を検出した．

dentinogenic effect of mineral trioxide aggregate (MTA) in short-term capping experiments, Int Endod J, 35：245-254, 2002.

4) 上床俊裕，吉嶺嘉人，小野真紀子ほか：MTA (Mineral Trioxide Aggregate) 応用後の初期歯髄反応に関する組織学的研究，日歯内療誌，25：63-66，2004.

5) Ford TR, Torabinejad M, McKendry DJ et al.：Use of mineral trioxide aggregate for repair of furcal perforations, Oral Surg Oral Med Oral Pathol Oral Radiol Endod, 79：756-763, 1995.

6) Daoudi MF, Saunders WP：In vitro evaluation of furcal perforation repair using mineral trioxide aggregate or resin modified glass lonomer cement with and without the use of the operating microscope, J Endod, 28：512-515, 2002.

7) Main C, Mirzayan N, Shabahang S et al.：Repair of root perforations using mineral trioxide aggregate：a long-term study, J Endod, 30：80-83, 2004.

8) Schwartz RS, Mauger M, Clement DJ et al.：Mineral trioxide aggregate：a new material for endodontics, J Am Dent Assoc, 130：967-975, 1999.

9) White C Jr, Bryant N：Combined therapy of mineral trioxide aggregate and guided tissue regeneration in the treatment of external root resorption and an associated osseous defect, J Periodontol, 73：1517-1521, 2002.

10) Steinig TH, Regan JD, Gutmann JL：The use and predictable placement of Mineral Trioxide Aggregate in one-visit apexification cases, Aust Endod J, 29：34-42, 2003.

11) Linsuwanont P：MTA apexification combined with conventional root canal retreatment, Aust Endod J, 29：45-49, 2003.

12) Lawley GR, Schindler WG, Walker WA et al.：Evaluation of ultrasonically placed MTA and fracture resistance with intracanal composite resin in a model of apexification, J Endod, 30：

167-172, 2004.
13) Kratchman SI：Perforation repair and one-step apexification procedures, Dent Clin North Am, 48：291-307, 2004.
14) Lamb EL, Loushine RJ, Weller RN et al.：Effect of root resection on the apical sealing ability of mineral trioxide aggregate, Oral Surg Oral Med Oral Pathol Oral Radiol Endod, 95：732-735, 2003.
15) Pistorius A, Willershausen B, Briseno Marroquin B：Effect of apical root-end filling materials on gingival fibroblasts, Int Endod J, 36：610-615, 2003.
16) Apaydin ES, Shabahang S, Torabinejad M：Hard-tissue healing after application of fresh or set MTA as root-end-filling material, J Endod, 30：21-24, 2004.
17) Torabinejad M, Hong CU, McDonald F et al.：Physical and chemical properties of a new root-end filling material, J Endod, 21：349-353, 1995.
18) Lee YL, Lee BS, Lin FH et al.：Effects of physiological environments on the hydration behavior of mineral trioxide aggregate, Biomaterials, 25：787-793, 2004.
19) Mishima H, Kozawa Y：SEM and EDS analysis of calcospherites in human teeth, Eur J Oral Sci, 106(suppl 1)：392-396, 1998.
20) Hohling HJ, Mishima H, Kozawa Y et al.：Microprobe analyses of the potassium-calcium distribution relationship in predentine, Sca Micro, 5：247-255, 1991.
21) Furusawa T, Mizunuma K：Osteoconductive properties and efficacy of resorbable bioactive glass as a bone-grafting material, Implant Dent, 6：93-101, 1997.
22) Cerruti M, Morterra C：Carbonate formation on bioactive glasses, Langmuir, 20：6382-6388, 2004.

著者連絡先：大久保厚司
日宇歯科・矯正歯科
〒857-1151　長崎県佐世保市日宇町
695-6　大久保第2ビル2F
TEL：0956-33-5821
FAX：0956-33-6876

原著論文

歯内療法外科処置におけるPRPの応用 歯根穿孔部封鎖およびサイナスリフトに PRP 法を実施した上顎小臼歯症例

Application of PRP in endodontics surgical treatment –The maxillary premolar case that performed PRP concentration method for root canal perforation part reconstruction and the maxillary sinus floor augmentation –

日本大学松戸歯学部第２解剖教室[1]，(社)日本歯科先端技術研究所宇部実験所[2]，
日本大学松戸歯学部歯内療法学講座[3]，高知短期大学保健科[4]

大久保 厚司[1,2]，辻本 恭久[3]，下御領 良二[2]，
岸 民祐[2]，田中 悟[2]，山田 啓二[2]，鈴木 久仁博[1]，
寒河江 登士郎[1]，三島 弘幸[1,4]，小澤 幸重[1]

Atsushi OOKUBO [1,2], Yasuhisa TSUJIMOTO [3], Ryoji SHIMOGORYO [2]
Tamisuke KISHI [2], Satoru TANAKA [2)] Keiji YAMADA [2], Kunihiro SUZUKI [1],
Toshirou SAKAE[1], Hiroyuki MISHIMA [1,4], Yukisige KOZAWA [1]

[1]Department of Anatomy [2], Nihon University School of Dentistry at MATSUDO,
[2] Japan Institute of Advanced Dentistry, [3] Department of Endodontics,
Nihon University School of Dentistry at Matsudo, [4] Kochu Gakuen College Health Sciences

Platelet Rich Plasma (PRP)は骨再生や軟組織治癒過程において通常血流の3倍量が確保できれば間葉系幹細胞に働きかけ，骨造成を高めるとされている．

本文では，歯根穿孔部より上顎洞内に突出したガッタパーチャの除去および上顎洞底粘膜挙上術後にフィルターで血小板量を確保しながら必要量の PRP を濃縮する方法を用いて抽出した PRP と多血小板血漿凝集塊(PRP clot)による骨造成と歯根穿孔部の修復おこなった症例の報告を行う．

キーワード：多血小板血漿（PRP）濃縮，多血小板血漿凝集塊，歯根穿孔部の修復，
上顎洞底粘膜挙上術

1 緒 言

上顎左側第二小臼歯(以下⌊5)に根管治療の形跡はあるが，根尖まで充分な根管充填がなされておらず，打診に反応があり，X線写真像では根尖部に僅かに根尖病変様の歯槽白線の拡大を認め，慢性根尖性歯周炎と診断し，再根管治療を試みた．しかし，ポストコアの除去後，象牙質より硬度が高いレジン系セメント剤単独で根管充填されていたため，レジン系セメントを除去中に歯根遠心彎曲部より穿孔，さらに根管閉塞時に加熱加圧ガッタパーチャが穿孔部より上顎洞

底を穿通して突出するという, 二重の偶発症が重なった.

処置としては, 骨再生や軟組織の治癒効果が期待され, 感染や遺伝子変異がない自己蛋白由来[1]による多血小板血漿 (PRP : Platelet Rich Plasma)[2-7]を埋植する方法を試みた.

2 臨床経過とPRPの応用

1) 偶発症例に対する処置

患者 : 57歳 (1941年生) 女性, 初診 : 1999年2月9日, 歯科的主訴 : 顎機能異常, 一般既往歴 : 特記事項なし, 現病歴 : 1992年頃から開口時クリック音と慢性的な第1ー第5頸椎の圧迫・緊張感と肩凝り, 時折, 片頭痛を訴える.

現症 : |5 の根管治療の不具ならびに根尖部に僅かに根尖病変様のX線透過像と歯槽白線の拡大. 歯髄反応 (-), 咬合痛 (-), 歯肉の発赤 (-), 腫脹 (-), 動揺度 (M1). また, |5のプロービング時に出血を認めプロービングデプスは頬側分岐部の1点のみ4mm, 他は3mm であり, 歯周ポケット部に歯石やセメント質の剥離は認められなかった. 本症例の上顎洞底の解剖学的形態は洞底が低く, |5 は洞底を避けて歯根は近心に傾き, 遠心根と洞底は薄い一層の外皮質骨があるだけで, さらに洞底は|56 の固形空隙下5mm程度, |67 の口蓋根根尖は上顎洞内におよぶと推測された(図 1).

当医院における臨床診断名 : 慢性根尖性歯周炎

治療経過 : 1回目 : 1999年3月18日, |5 の根管治療開始

|5 クラウンおよびメタルコアー除去し, 根管充填に使用されていたレジン系セメントを超音波にて除去中に, 遠心側から穿孔し, 上顎洞内へ突出した (図 2) . 2%NaClOを2分間作用させて止血し, 拡大顕微鏡を使い, 主根管のレジン系根管セメント単体をエンド短針, 手用ファイルと超音波ファイルの交互操作で取り除いた後, 2回目のファイル試適(図 3)を行い, 水酸化カルシウム貼薬後, 仮封した.

2回目 : 1999年3月30日, |5 の根管治療

咬合痛 (-), 誘発痛 (-), 腫脹 (-), 動揺度 (M1). ラバーダム防湿. 主根管の穿通と根管形成をおこなうが, 根尖より3mm部までで, 閉鎖. 電気的根管長測定をおこない, 水酸化カルシウム貼薬後, 仮封.

3回目 : 1999年4月9日, |5 の 根管充填

咬合痛 (-), 誘発痛 (-), 歯肉の発赤 (-), 腫脹 (-), 動揺度 (M0). ラバーダム防湿. No.35まで手用ファイルで根管形成を行い, 3% H_2O_2で洗浄後, 滅菌水で洗浄. 根管内をエンドサクションで乾燥後, 出血が無いことを確認し, T.L.C. Brasseler にて軟化させたオブチュレーションガッタで根管充填するも, ガッタパーチャが歯根遠心側から上顎洞内まで突出した(図4). 主根管を同様に根管充填し, 患者には痛みの可能性を説明する.

4回目 : 1999年4月22日, |5 の 築造, クラ

図1 1999年3月18日. 初診時のX線写真. |45と|567の歯根中央部に上顎洞底が位置し, 隔壁も存在する.

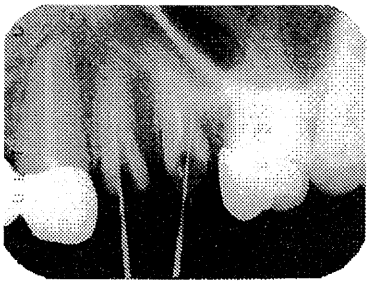

図2 1999年3月18日. コア除去後 |45はレジン系根管充填用セメント単体除去中に |5 の遠心部より上顎洞に穿孔する.

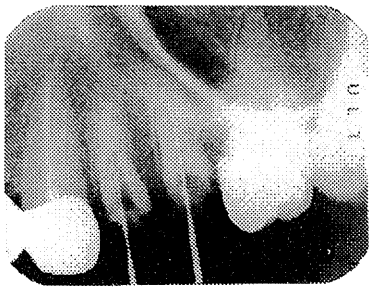

図3 1999年3月18日. レジン系根管充填用セメントを超音波と手用ファイルで取り除く.

図4 1999年4月22日. |5 の根管充填加熱ガッタパーチャが穿孔部より上顎洞内に突出し, 二重の偶発となる.

ウン形成後, テンポラリークラウンの仮着.

咬合痛 (-), 誘発痛 (-), 歯肉の発赤 (-), 腫脹 (-), 動揺度 (M0). スクリューポストとコアレジンで作製した連合コアを一度取り出し, スーパーボンドで装着.

5回目 : 1999年5月18日, |5 の 上顎洞底粘膜挙上術とガッタパーチャの摘出術.

|5 の臨床症状は咬合痛 (-), 誘発痛 (-), 歯肉の発赤 (-), 腫脹 (-), 動揺度 (M0).

ロセフィン1g を混入したソルラクト200mLを静脈内に点滴し, 上顎洞底粘膜挙上術を施行した.

(1) 上顎洞底粘膜挙上術の術式

施行部は2%キシロカインの局所麻酔下で|4部に縦切開し, |456 の頬側歯肉を歯頚部より齦境移行部まで骨膜下剥離をおこなう(図5, 6). 上顎洞底部に相当する頬側骨をNo.10ラウンドバーで洞粘膜を穿孔しないように開削し(図 7). 洞粘膜の厚さを視認的に確認する. 次に開削部位から上顎骨内部の洞粘膜の骨膜剥離を(株)ワイディエム Medicine Applicator : 点薬器ホルダーでおこない, 破骨鉗子で骨片を取り除き, この操作を必要な開削量までくり返す. 穿孔した加熱軟化性のガッタパーチャの一端は洞粘膜に付着している(図 8) ので, ピンセットで取り除くことができる. この時, 洞粘膜は必要以上に穿孔させない.

そして, その洞粘膜の下方から洞底粘膜を挙上 (図 9) し, 内部にPRP clotを詰め込み, 最期にPRPを注入する. 本症例では挙上した洞底粘膜内部に洞粘膜の補強の意味でPRP clotを埋植した. その後, PRP を

図 5

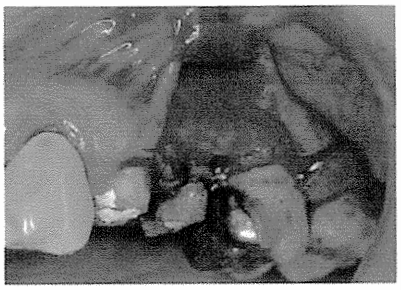

図 6

図 7

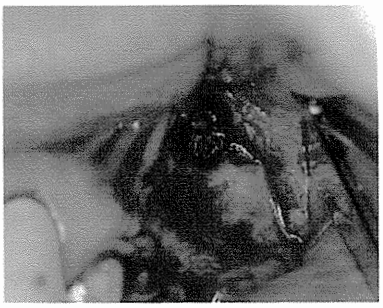

図 8

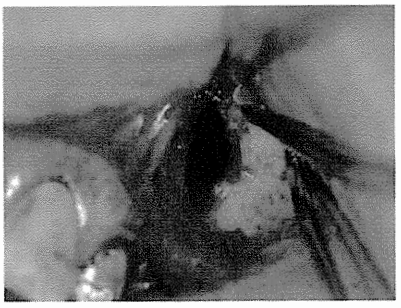

図 9

図 10-3

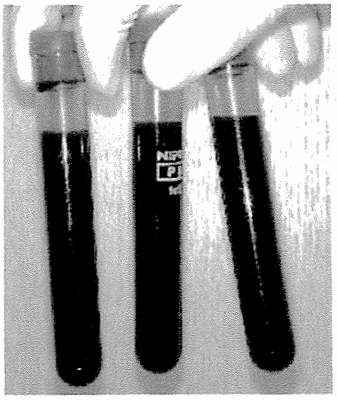

図 10-1

図 10-2

図 11-1

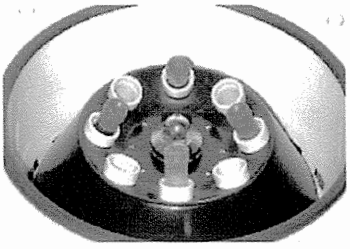

図 11-2

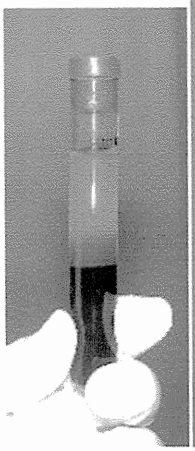

図 11-3

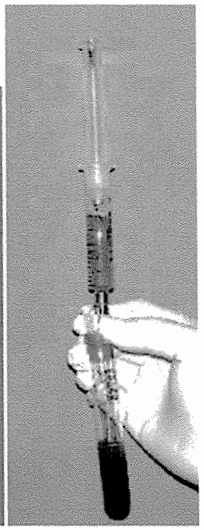

図 11-4

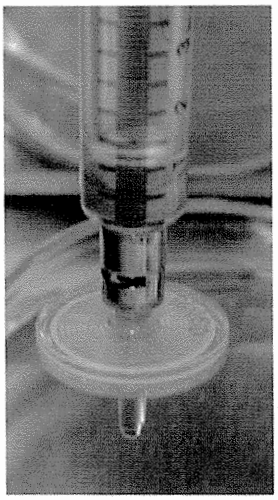

図 11-5

＜洞粘膜挙上術の手順＞
図5　初診時, 歯肉の状態
図6　頬粘膜剥離
図7　AO式サイナスリフト法に則って上顎洞粘膜に損傷を与えないように, No.10ラウンドバーで骨開削と点薬器ホルダーで粘膜剥離をおこなう.
図8　頬側骨除去後の上顎洞粘膜 と突出した加熱ガッタパーチャの終末を確認し, ピンセットで除去する.
図9　上顎洞粘底膜挙上

＜PRP clot の作製法＞
図10-1 VACUTAINER 滅菌真空ガラス採血管 10cc 用に約 8mL 静脈血を採血する(抗凝固剤は含まない). 本症例では 10cc 程度の上顎洞底挙上を予定していたので 15mL 程度の clot を必要とした.
図10-2 1000 r.p.m.で 15 分間, 遠心分離する. 各々5mL 程度の PRP clot が作製された.
図10-3 本手術に必要な約 15mL の PRP clotを作製する. PRP clot 外膜は線維性結合反応を起こし, 内部は血漿も多く含まれた状態でゲル化している. 時間経過と伴に血漿が浸透圧で排出するので 15 分以内に挙上部に埋植する.

＜PRP の抽出と濃縮方法＞
図11-1 3.8%クエン酸ナトリウム液 0.5mL を抗凝固剤として注入した VACUTAINER 滅菌真空ガラス採血管 10mL 用 に約 8mL 静脈血を採血する.
図11-2 遠心器に対角線状に採血管を置く.
PRP 作製にはなるべく新鮮な血小板の濃縮が必要であり, 1000r.p.m.(116.3g)を 15 分間遠心分離する. 1200r.p.m.(約 160g)以上では重力加速が増し, 相対遠心力が大きくなり過ぎて血小板の形態変形を認める.
図11-3 PRP と PPP を含む血漿層と白血球, 赤血球と多少の血小板を含む血球層とに分離する.
1000 r.p.m.(116.3g)を 15 分間遠心分離することで均一に全血液濃度の 3 倍近くの血小板数が血漿中に浮遊している. この回転数は遠心器で作製する場合に PRP 中に最も多く血小板が浮遊しており, 年齢, 性別, 血液比重に左右されない. これより高回転では血小板の浮遊率は低くなる.
図11-4 血漿液を滅菌ガラスシリンジ VAN 白硬注射筒 5mL を, ニプロカテラン 18G×70RB のシリンジで血球が混入しないように注入する.
図11-5 0.45μm のメッシュ状のフィルターに付け直して PPP を排出する.
PRP による成長因子の発現は全血の 3～5 倍, 血小板数が 100 万以上とされているので, 採血管 2 本を抽出したものをフィルターで濃縮すれば, 必要量の血小が得られる. また, 小手術など手術野にあわせて血漿を排出して必要量の PRP を作製することも容易にできて, 操作性が良い.
手術野に注入する場合は, 塩化カルシウムの代わりに, カーボネイトアパタイトを混入するとよい.

注入し縫合した.

サワシリン500mg ×3日, エンピナースP 6×3日, ボルタレン25mg 1T×3(疼痛時服用)を処方した.

(2) PRP clot の作成

PRP clot [8] (図10-1, 2, 3)の作製には10mLガラス採血管で8mL静脈血を採取し, 素早く1,000 r.p.m.(116.3g)で15分間遠心分離する. 血小板は空気に触れるとフィブリンにより線維性結合反応を起こし, 内部は血漿も多く含まれた状態でゲル化したものを挙上部の空間に詰め込む. 本症例では, 採血管3本分の PRP clot を埋植した.

(3) 濃縮PRPに必要量の血小板の確保

PRP中に含まれる血小板数は風邪，生理，体調不良や血液比重などの生体の生理変化や疾病の影響を受けること，遠心分離時の回転数による血小板成分の変化ならびに臨床応用で血小板数を未確認のまま埋植されていることから，臨床応用では差異[3,6]があると考える．そこで，下記の方法でPRP濃縮を調整した．

① PRPの抽出にはあらかじめ 3.8%クエン酸ナトリウウム液 0.5mL（東亜薬品工業株式会社 診断用クエン酸ナトリウム液)を抗凝固剤として注入した滅菌真空ガラス採血管10mL用 (VACUTAINER Brand Tube for Determinations Requiring serum or 10m Draw)から8mL静脈血を採血する(図11-1)．

② 井内盛栄堂社製遠心器CN-1040（ 回転数0～4,000r.p.m. 最大遠心力1,880G ）を用いて1,000r.p.m. (116.3g)で15分間遠心分離する(図11-2, 3)．

③ 血球層との境界より血漿液をガラスシリンジVAN白硬注射筒 5mL（翼工業株式会社)を滅菌して，ニプロガンマ線滅菌済みニプロカテラン針18G×70RBのシリンジで注入する(図11-4)．

④ 注入した血漿液を0.45μmのメッシュ状のフィルター（東洋濾紙 ; DISMIC 13CPO45AS)で血漿液を排出し，PRPの抽出と濃縮をおこなう．さらに，手術部位に必要量のPRPを調節する(図11-5)．

⑤ 術中に 濃縮PRPを位相差顕微鏡でカウントして全体像としてとらえ，有効な血小板数を視認的に確認し，血小板数が足らない場合はさらにPPPを排出させる(図11-6)．

⑥ ゲル化にはPRP / 1mLに対してカーボネイトアパタイト[9]を0.2g/mL量入れ，10分程経過させで凝集する．

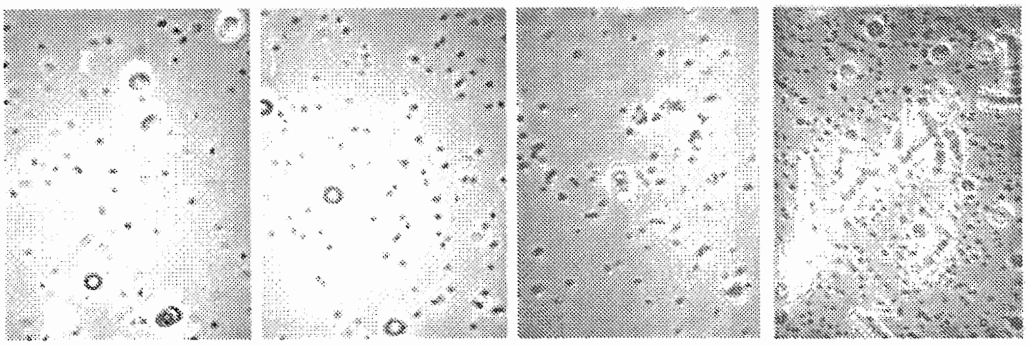

図 11-6 位相差顕微鏡によるPRP量の臨床的視認

他項目自動血球係数装置 XE-9000（ Sysmex 社)を用いてフローサイトメトリー法で測定したPRP溶液を位相差顕微鏡で観察し，臨床応用の目安とする．PRP 量が少なければ骨造成率は期待できず，ゲル化しない．全血の3倍量が必要と考えられ，PRP中の血小板数は100万を移植側に確保できれば，骨造成率は13～20%増加すると考える．

6回目 : 1999年5月19日, 手術野の洗浄
⏌5 は特記事項無し, 鼻出血無し. 手術部は歯肉の発赤 (+), 腫脹 (+), 疼痛(-). アクリノール洗浄.
7回目 : 1999年5月22日, 手術野の洗浄
⏌5 は特記事項無し, 手術部は歯肉の発赤 (-), 腫脹 (+), 疼痛(-). アクリノール洗浄.
6回目 : 1999年5月29日 ⏌5 は特記事項無し, 手術部は, 歯肉の発赤 (-), 腫脹 (-), 疼痛(-). ヒビテン, 3% H_2O_2洗浄後, 抜糸. ガッタパーチャ除去後のデンタル写真(図-12).

2) 経過症例に観るPRP応用の硬組織再建結果

1999年10月22日, 特記すべき臨床症状なし. ポーセレンクラウン装着.
2000年9月26日, 術後16カ月のデンタル写真(図13).
2001年4月11日, 術後23カ月, 特記すべき臨床症状なし. ⏌5 の 上顎洞底粘膜挙上術とガッタパーチャの摘出術部はオルソパントも所見では上顎洞底粘膜挙上術後の正常な骨造成状態が観られ, 穿孔部の暗影も無い.

2003年4月18日, 術後47カ月, 特記すべき臨床症状なし. ⏌5 の 上顎洞底粘膜挙上術とガッタパーチャの摘出術部はオルソパントも所見では上顎洞底粘膜挙上術後の正常な骨造成状態が観られ, 穿孔部の暗影も無く安定した状態を保つ. また, 主訴である顎関節機能異常も観られず, 良好な経過をたどる.

以下はオルソパノラマ所見で経過を観る(図14-1, 2, 3, 4).

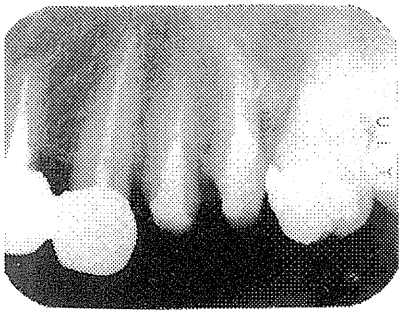

図12 1999年5月18日. ⏌5 のガッタパーチャ除去と将来の口腔インプラントの可能性も考慮して, PRP clot とPRPによる上顎洞底挙上術を施行する.

図13 2000年9月26日. 16ヶ月経過, ⏌5 穿孔部と上顎洞底挙上部は良好に経過する. 歯槽骨部の再生を認め, 歯周ポケットは2mmと正常範囲である.

3 考 察

1. PRPの効果について

PRP 中の血小板から放出される蛋白として, 細胞質中に数十個存在するα顆粒から少なくとも骨形成に関与する蛋白・成長因子を放出[4-7, 10]する.

Danesh-Meyer ら[2] はヒトにおいて骨置換材とPRP併用によるサイナスリフトの組織学的評価ではPRPによる特別な効果はないとしており, 下御領ら[3]も動物実験においてインプラント周囲

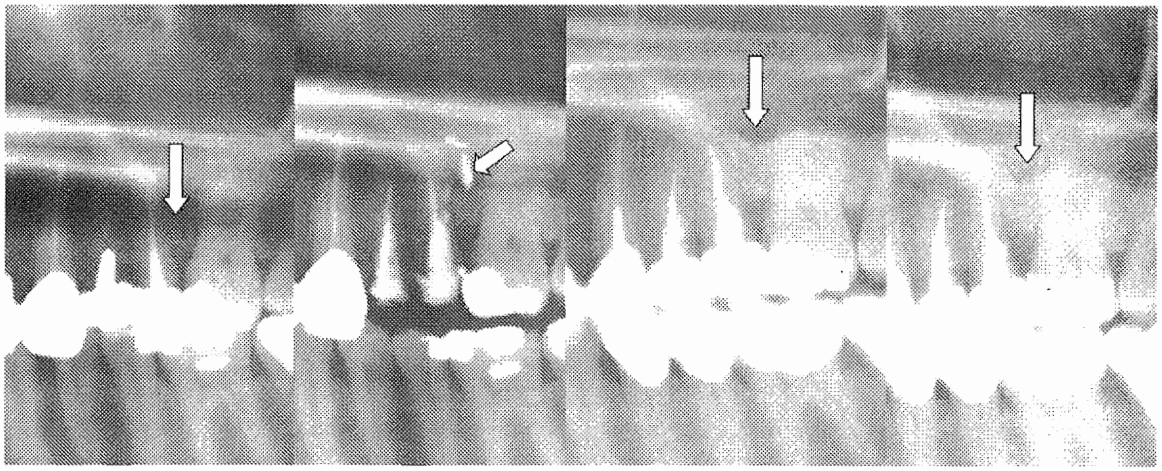

図14－1　図14－2　図14－3　図14－4

＜上顎洞粘膜挙上術後の骨造成＞

図 14-1　1999. 3.11.
上顎洞底は|56 歯頚部付近まで介入している.

図 14-2　1999. 5.18.
|5 の歯根の遠心部より, 加熱軟化型ガッタパーチャの上顎洞内への穿孔. 洞底が低く, 根中央部におよぶ. また, 歯槽骨頂も吸収をみる.

図 14-3　2001.4.11.
上顎洞底は|56 歯頚部付近まで介入している.

図 14-4 2003,4.1.　約 4 年後の経過観察.
|5 の穿孔部の歯槽硬線の肥厚もなく, 上顎洞底挙上術後の骨造成も良好な経過を観察する.

組織過不足部にPRPと自家骨併用によるGBRを施行した研究では無細胞の移植材へのPRPの効果は疑問視し, PRP併用群とPRP未使用群での有為差を得なかったと報告している. しかし, Marxら[6]は移植部には全血の3倍量の血小板濃縮を必要とし, 移植部にPRPが埋植された群は74.0%±11%, 移植部にPRPが埋植されなかった群は55.1%±8% (p = 0.005)の骨造成率であったと報告している. また, Tischler[11]も正常血流の3倍量とその数は1,1000,000 /μL に濃縮が必要であるとしている.

PRP に含まれている骨形成因子として期待されるのはトランスフォーミング成長因子β (Transforming Growth Factor β / TGFβ) [10]は線維芽細胞や平滑筋細胞に働き, PDGF の産生促進や軟骨細胞促進, 炎症性単核球の遊走促進に働く, コラーゲンやフィブロネクチンなどの EMC 構成蛋白質の産生を促進, 細胞外マトリックスの産生を促進, 増殖因子, サイトカインの産生抑制, アポトーシスの促進, ステロイドの生産制御, 免疫グロブリンのクラス変換. 総合作用として血管新生制御, 免疫抑制, 骨リモデリング

に関与するBMP類やその発現の引き金となるアクチビンはTGF-βスパーファミリーの一種である.

血小板由来成長因子(Platelet-derived growth factor / PDGF)[10]は間葉系細胞に対し遊走・増殖刺激活性する. インシュリン様成長因子(Insulin-like Growth Factor / IGF-1)[10]は成長ホルモン依存性に骨発育させるソマトメジンCであり, インスリン様の代謝作用をもち, 骨組織をはじめとする多くの細胞の増殖・分化やアポトーシスの抑制に関与する.

PRP凝集の利点として術式が簡便, 自己組織応用のため安全, フィブリンによる付着力, 弾力に富む, 歯根表面への生物学的適応性が高い, 成長因子を含む, 血管新生作用, 骨伝導能, 止血作用, 白血球が高濃度に含まれるため抗感染作用, 創傷治癒効果が得られる等が考えられる. しかし, TGF-βとPDGFはインターロイキン1, 6, 8と同様に炎症性サイトカインにも分類されているので正常組織に応用すれば骨形成に進むが, 炎症組織では拡炎する可能性があるので不良肉芽は完全な除去が必要である.

X線による経過観察では上顎洞底挙上部の骨造成だけでなく, 穿孔部の根周囲組織は炎症の拡炎や歯槽白線の肥厚もなく良好に経過している. Kawase T, ら[8]の歯根膜と造骨細胞の細胞培養で細胞外基質生産の考察に, PRPが放出する成長因子と結合するフィブリノーゲンが歯周組織の創傷癒合を効果的に促進する可能性があるという報告と同様に, 骨組織や根周囲組織の修復にPRPが関与した可能性を示唆させる.

4 結 論

自己採血から得られるフィルターを用いたPRP凝集法は感染や遺伝子変異の心配がなく, 価格面で非常に安価に抽出可能で, 移植部に必要量の血小板の供給が可能である. 本偶発症例では予後不良の場合に口腔インプラントの必要性も考慮してこの手法をおこなった. しかし, 上顎洞底粘膜挙上術を施行して, 4年の良好な経過を観察するが, この施行法からPRP凝集とPRP clotは創傷治癒の初期段階の働きと引き続く骨再生や根周囲組織の治癒効果の手助けをした可能性が示唆される.

また, 本偶発症例を通じて, 根管充填にはレジン系セメント単体で根管充填せずに, 正規の方法に則ったガッタパーチャによる側方加圧充填を根尖孔まで到達させることが重要であり, 再治療をおこなうことも前提としてレジン系セメントは象牙質より硬度が低い物性に変える必要性があると考える.

謝辞

本研究の研究費の一部は、文部科学省平成13年度学術フロンティア推進事業によった.

参考文献

1) 村上広樹, 大久保厚司, 田中 悟, 他. 生体由来材料の取扱いについて. 日歯先技研誌 2003;9(4):195－200.
2) Danesh-Meyer MJ, Filstein MR, Shanaman R . Histological evaluation of sinus augmentation using platelet rich plasma (PRP): a case series. J Int Acad Periodontol 2001;3:48－56.
3) 下御領 良二, 大久保 厚司, 田中 悟. PRP と自家骨併用によるGBRについての組織学的研究. 日歯先技研誌 2004;10:71－73.
4) 大久保厚司, 下御領良二, 山根 進 他. グローバルエンドドンテックス, 日本歯内療法学会編 - PRP の臨床的確認と歯根端切除術への応用, クインテッセンス 2004:81－86.
5) Marx RE. Platelet-rich plasma (PRP): what is PRP and what is not PRP? Implant Dent. 2001;10:225－228.
6) Marx RE, Carlson ER, Eichstaedt RM, et.al. Platelet-rich plasma: Growth factor enhancement for bone grafts. Oral Surg Oral Med Oral Pathol Oral Radiol Endod 1998;85:638－646.
7) Marx RE, Garg AK. A novel aid to elevation of the sinus membrane for the sinus lift procedure. Implant Dent 2002;11:268－271.
8) Kawase T, Okuda K, Wolff LF, Yoshie H. Platelet-rich plasma-derived fibrin clot formation stimulates collagen synthesis in periodontal ligament and osteoblastic cells in vitro. J Periodontol 2003;74:858－864.
9) T. Sakae, A. Ookubo, Racquel Z. LeGeros, et.al. Bone Formation Induced by Several Carbonate. - and Fluoride-Containing Apatite Implanted in Dog Mandible. Bioceramics. 2003;15:395－398.
10) 宮園浩平, 管村和夫/編. サイトカイン・増殖因子. 第 3 章増殖因子, 第 4 章 TGF-β スーパーファミリィ. 羊土社, 2000. p.80－163.
11) Michael T. Platelet Rich Plasma - Utilizing antilogous growth factors for dental surgery to enhance bone and soft tissue grafts. New York State Dental Journal 2002:3.

連絡先
大久保 厚司
〒857-1151 長崎県佐世保市日宇町 695-6
大久保第 2 ビル 2F 日宇歯科・矯正歯科
Tel 0956-33-5821, Fax 0956-33-6876

尚, PRP の抽出器具に関しては テクノ鈴田
Tel 0956-28-4365 まで

(Received August 23, 2004/
Accepted September 28, 2004)

原著論文(臨床系・研究症例)

Application of PRP in endodontics surgical treatment - The maxillary premolar case that performed PRP concentration method for root canal perforation part reconstraction and the maxillary sinus floor augmentation -

Atsushi OOKUBO [1,2], Yasuhisa TSUJIMOTO [3], Ryoji SHIMOGORYO [2], Tamisuke KISHI [2], Satoru TANAKA [2], Keiji YAMADA [2], Kunihiro SUZUKI [1], Toshirou SAKAE[1], Hiroyuki MISHIMA [1,4], Yukisige KOZAWA [1]

[1]Department of Anatomy 2, Nihon University School of Dentistry at MATSUDO, [2] Japan Institute of Advanced Dentistry, [3] Department of Endodontics, Nihon University School of Dentistry at Matsudo, [4] Kochu Gakuen College Health Sciences

If Platelet Rich Plasma (PRP) can guarantee the quantity of 3 times that the normal blood flow in bone regeneration and soft tissue healing process, it is assumed that it approaches the mesenchymal stem cell, and raises the osteogenesis. We removed prominent gutta-percha in the maxillary sinus for part of the root perforation and did the operation of the maxillary sinus floor augmentation.

We reports the case that the new bone created by PRP which is extracted making use of the method of concentrating PRP of the necessary quantity and PRP clot while guaranteeing the blood platelet quantity with the filter and the part of root perforation repaired.

Key Words: Platelet Rich Plasma (PRP)concentration , PRP clot, repair of root perforation, the maxillary sinus floor augmentation

原　著

Mineral Trioxide Aggregateに根管洗浄液を作用させた後の表面の変化（第1報）

川島　正　小塚昌宏　三浦　浩　川本幸司　大久保厚司*
石井信之**　石崎　勉***　辻本恭久
日本大学松戸歯学部歯内療法学講座
*日本大学松戸歯学部第II解剖学講座
**神奈川歯科大学口腔治療学講座
***株式会社サンギ

Changes of the surface of MTA by root canal irrigants (Part 1)

KAWASHIMA Tadashi, KOZUKA Masahiro, MIURA Hiroshi, KAWAMOTO Kohji, OOKUBO Atsushi*, TANI-ISHII Nobuyuki**, ISHIZAKI Tsutomu*** and TSUJIMOTO Yasuhisa
Department of Endodontics, Nihon University School of Dentistry at Matsudo
*Department of Anatomy II, Nihon University School of Dentistry at Matsudo
**Department of Operative Dentistry and Endodontics, Kanagawa Dental College
***Central Research Center, Sangi Co. Ltd.

Abstract：This study investigated the effects of root canal irrigants on the surface of mineral trioxide aggregate (MTA) by using a scanning electron microscope (SEM) and elemental analyzer.

The SEM observation of the control samples revealed crystals growing in various shapes and sizes as the treatment progressed. In the H_2O_2 treatment group, numerous triangular crystals were observed after 1 week and these grew into cubic crystals after 2 weeks. Small amorphous crystals were observed among other crystals after 3 weeks. In the NaClO treated samples, numerous square type crystals were observed on the surface of all samples. In the EDTA treatment group, rounded crystals grew as the treatment progressed.

We assume the crystals will form with silicate oxide or tricalcium in NaClO, Bi oxide will change to Bi compound in H_2O_2, and ferrous oxide will change to ferrous compound by chelating action in EDTA.

In the elemental analysis of H_2O, H_2O_2 and NaClO treatment groups, Ca was high rate, but in the EDTA treatment group, Bi was high rate.

Key words：mineral trioxide aggregate (MTA), root canal irrigants, SEM, element analysis
（日歯内療誌 26(1)：14～18，2005）

緒　言

根管治療の日常臨床では根管系が解剖学的に複雑であったり，術者の技術の未熟さから，思いがけないところを切削したり，穿孔し取り返しのつかない医原性疾患を引き起こし，最悪の場合，抜歯になることがある．穿孔部を修復するに際してもさまざまな方法や薬剤，材料があるが，従来の方法ではアマルガム，セメント，接着性レジン等を用いて行われてきている．しかし，症例によっては予後不良の場合があり，穿孔部を完全に封鎖し，治癒を促進する薬剤はなかった．1993年，米国ロマリンダ大学 Trabinejad 教授によって開発された Mineral Trioxide Aggregate（以下 MTA

受付：平成16年7月8日／受理：平成16年9月30日

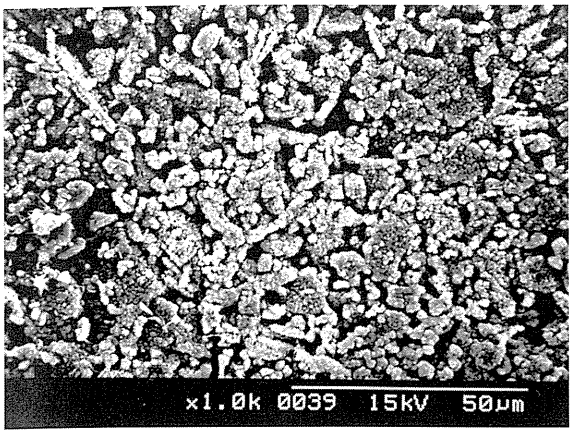

図 1 H_2O 作用群（コントロール，×1,000）の SEM 像

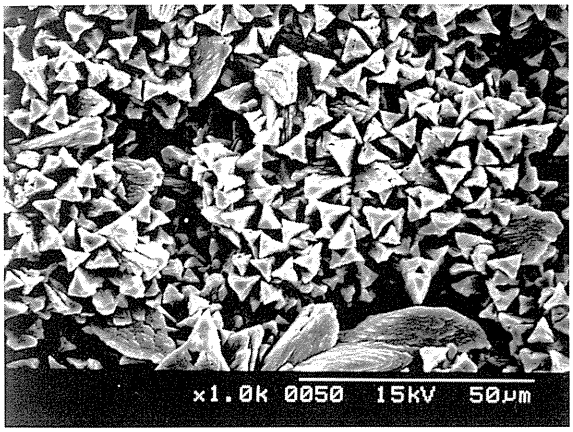

図 2 H_2O_2作用群（×1,000）の SEM 像

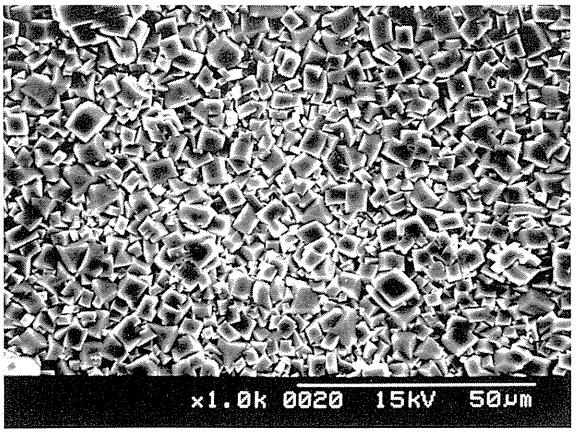

図 3 NaClO 作用群（×1,000）の SEM 像

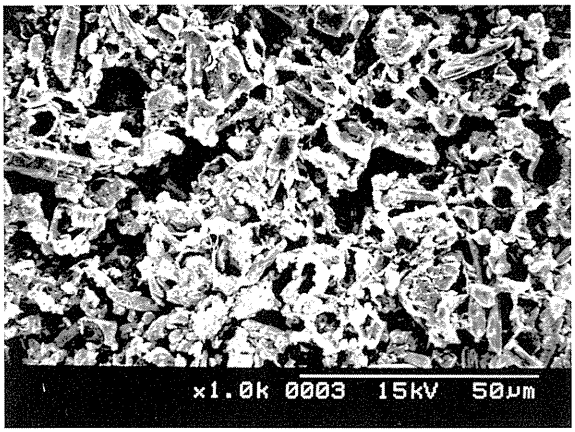

図 4 EDTA 作用群（×1,000）の SEM 像

と略す）は，穿孔や内部吸収の処置，逆根管充塡，覆髄等に用いられ，穿孔部の閉鎖性や治癒促進に有効性があると近年，注目されている[1~8]．MTA のこれまでの報告をみると，硬化までに時間がかかるが Super-EBA と同様の硬さになるには 21 日後であるという[9]．しかし，結晶構造の変化を電子顕微鏡写真で報告したものはまだない．MTA による穿孔部の修復部分に根管洗浄剤や漂白剤等が長時間作用した場合，これらの薬剤によって MTA 表面が化学的な変化を引き起こすことが想像される．そこで本研究は，MTA に臨床で使用されている各種根管洗浄液を作用させた場合，表面表層にどのような変化や影響がみられるかを走査型電子顕微鏡（以下 SEM と略す）で観察し，さらに表面の元素分析を行うことを目的として行った．

材料および方法

MTA は DENTSPLY　TULSA　DENTAL 社製 PRO ROOT™を用いた．MTA はメーカーの指示通り練和し，2 枚のガラス練板の間に圧接し，直径約 1 cm，厚さ約 1 mm に調整し試料とした．実験には練和後 72 時間，室温で湿度 100%下に放置したものを用いた．試料を 3% H_2O_2，5% NaClO，15% EDTA，各溶液 2 mL 中に室温で湿度 100%下に 1 週間静置して浸漬した．コントロールは H_2O に浸漬した．試料をシリンジを用いて 10 mL の精製水で洗浄後，24 時間室温にて自然乾燥した．その後 Au-Pt 真空蒸着を行い，日立社製 SEM S-2150 を用い，加速電圧 15 kV の条件下で観察を行った．

表面の元素分析は，日立社製 S-2380 N 走査型電子顕微鏡，堀場社製 EMAX-5770 W を用い，加速電圧 20 kV の条件下で MTA の成分中に含まれる Al，Si，S，Ca，Fe，Bi の各元素について面分析を行った．

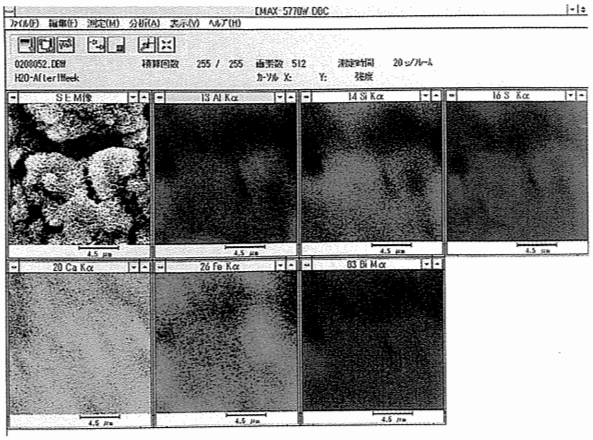

図 5　H_2O（コントロール）作用群の面分析結果

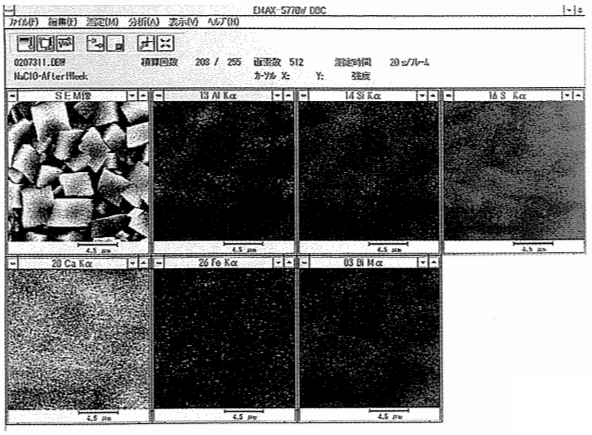

図 7　NaClO 作用群の面分析結果

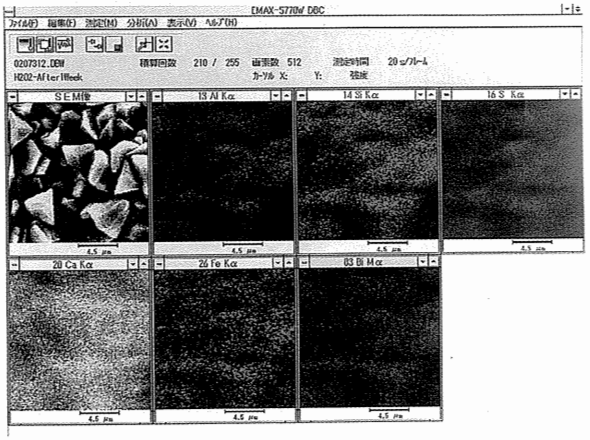

図 6　H_2O_2作用群の面分析結果

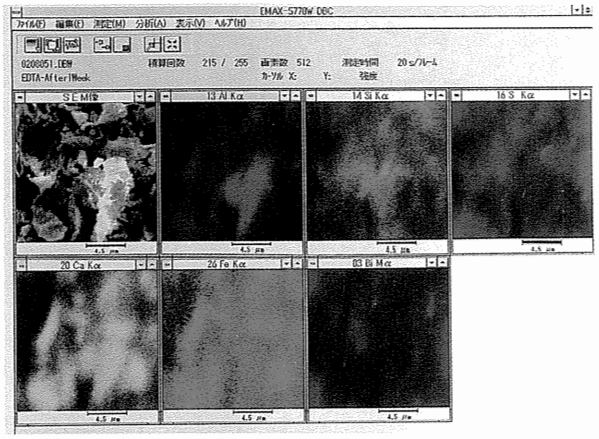

図 8　EDTA 作用群の面分析結果

表 1　H_2O 作用群（コントロール）の試料表面の面分析結果

H_2O	重量濃度（%）
Al	3.91
Si	14.78
S	4.73
Ca	64.29
Fe	8.44
Bi	3.85

表 2　H_2O_2作用群の試料表面の面分析結果

H_2O_2	重量濃度（%）
Al	0.98
Si	1.88
S	3.37
Ca	93.68
Fe	0.09
Bi	0

表 3　NaClO の作用群の試料表面の面分析結果

NaClO	重量濃度（%）
Al	0.38
Si	0.6
S	1.54
Ca	97.48
Fe	0
Bi	0

表 4　EDTA 作用群の試料表面の面分析結果

EDTA	重量濃度（%）
Al	9.39
Si	12.99
S	1.97
Ca	25.97
Fe	14.96
Bi	34.72

結　　果

1．SEM 所見

H_2O 作用群（コントロール）では，丸い粒子状の構造がいくつか互いに癒合して表面を覆っているのが観察された（図 1）．

H_2O_2作用群では，約 5〜10 μm の矢じり様三角形の結晶が観察された（図 2）．

NaClO 作用群の SEM 像では，約 3〜5 μm の板状(立方体状)構造物で表面が覆われているのが観察された（図 3）．

EDTA 作用群の SEM 像ではところどころに間隙を認め，不定形の構造物同士が融合している像がみられ，針状結晶構造物が観察された（図 4）．

2．元素分析

1）H_2O 作用群（コントロール）

本試料の表面には多孔性の粒子が確認できた．その元素分析の結果において（図 5），分析したすべての元素が一様に分布しているのが確認できた．いずれの元素も，試料表面の板状構造物に一様に分布していることが確認された．面分析結果においては，Ca の積算強度が最も高かった（表 1）．

2）H_2O_2作用群

矢じり様三角結晶の元素分析の結果において，分析対象したすべての元素が全体に確認された（図 6）．面分析結果において，Ca の分布範囲が広いことから，Ca 積算強度が高かった（表 2）．

3）NaClO 作用群

面分析画像に示したように，いずれの元素も試料表面の板状（あるいは立方体状）構造物に一様に分布しているのが確認された（図 7）．

同一部位の面分析結果においては，Ca の積算強度が最も高かった（表 3）．

4）EDTA 作用群

面分析画像により，すべての元素については，ほぼ一様な分布が確認された（図 8）．同一部位の面分析結果において Bi の積算強度が最も高かった（表 4）．

考　　察

MTA は，これまでの報告から良好な臨床成績が得られ[10]，また安定した物質であると思われているが，本実験において，各種洗浄液によって MTA の表面がさまざまな影響を受けることがわかった．MTA は，水硬性セメントとしてはケイ酸カルシウムを主成分とするポルトランドセメントであり，硬化反応はこれらに水を加えてペースト状にすると直ちに水和反応が始まり，まず凝結が起こって流動性が失われ，その後ケイ酸カルシウム水和物ゲルを生じて硬化する．ほかの成分に SiO_2, Al_2O_3, FeO, MgO, Bi_2O_3等があると報告[10]されている．主な成分のなかでそれぞれの化合物の性質を調べてみると，水に溶解するものは CaO_3, FeO 等で，水に溶解しないものは Bi_2O_3，Al_2O_3で，酸に溶解するものは CaO_3，Bi_2O_3，FeO 等であり，アルカリに溶解するものは SiO_3，Al_2O_3等である．したがって，コントロールでは Ca が水に溶解し，元素分析に示されるように表面に析出したものと思われる．MTA の表面に結晶様構造物が「析出」または「成長」しているが，今回の実験ではどちらかわからないため，「析出」を用いた．アルカリ性である NaClO 作用群でみられた結晶は，Si の化合物か Al の水酸化化合物が析出，沈着した可能性があるが，元素分析の結果から Ca の化合物が析出したものと推測される．弱酸性である H_2O_2 作用群の場合ビスマスの化合物が析出，沈着する可能性があるが元素分析の結果，やはり Ca の化合物が析出したものと推測される．EDTA 作用群では，キレート反応を考えると Al や微量の Fe の化合物が析出，沈着したものと推測されるが，元素分析の結果から，Bi の化合物が析出したものと思われる．MTA の詳しい成分分析は大久保ら[11]の論文に掲載されている．今後，さらに 2，3 週間後の変化を調べ，検討するつもりである．

結　　論

1．MTA 表面に 1 週間，各種根管洗浄剤を作用させるとさまざまな形態の構造物が観察された．

2．MTA 表面の構造物を元素分析すると，H_2O, H_2O_2, NaClO 作用後において Ca が，EDTA 作用後では Bi が多く分析された．

なお，この研究の一部は，文部科学省平成 13 年度学術フロンティア推進事業および平成 15 年度日本大学松戸歯学部鈴木研究費（03-1011，03-1014）の一部を使用して行われた．

文　　献

1) Torabinejad M, Watson TF, Pitt Ford TR：The sealing ability of a mineral trioxide aggregate as a retrograde root filling material, J Endod, 19：591-595, 1993.
2) Torabinejad M, Hong CU, Pitt Ford TR：Physical properties of a new root end filling materials, J Endod, 21：349-352, 1995.

3) Torabinejad M, Falah Rastegar A, Kettering JD et al.：Bacterial leakage of mineral trioxide aggregate as a root end filling material, J Endod, 21：109-112, 1995.
4) Torabinejad M, Higa RK, Mckendry DJ et al.：Effects of blood contamination of dye leakage of root end filling materials, J Endod, 20：159-163, 1994.
5) Torabinejad M, Wilder Smith P, Pitt Ford TR：Comparative investigation of marginal adaptation of mineral trioxide aggregate and other commonly used root end filling materials, J Endod, 21：295-299, 1995.
6) Torabinejad M, Hong CU, Pitt Ford TR et al.：Antibacterial effects of some root endofilling materials, J Endod, 21：403-406, 1995.
7) Torabinejad M, Hong CU, Pitt Ford TR et al.：Cytotoxicity of four root canal end filling materials, J Endod, 21：489-492, 1995.
8) Torabinejad M, Hong CU, Pitt Ford TR：Tissue reaction to implanted SuperEBA and mineral trioxide aggregate in the mandibles of guinea pigs：A preliminary report, J Endod, 21：569-571, 1995.
9) Torabinejad M, Hong CU, McDonald F et al.：Physical chemical properties of a new Root-End filling material, J Endod, 21：349-353, 1995.
10) 辻本恭久：MINERAL TRIOXIDE AGGREGATE のこれまでの研究結果と臨床応用，日本歯科先端技術研究所学術会誌，18(3)：112-117，2002.
11) 大久保厚司，辻本恭久，三島弘幸ほか：電子線マイクロアナライザーによる石灰化促進の可能性としての MTA の微量成分の検討，日歯内療誌，25：137-143，2004.

著者連絡先：川島　正
日本大学松戸歯学部歯内療法学講座
〒271-8587　千葉県松戸市栄町西2-870-1

Biol. Pharm. Bull. **27**(6) 831—834 (2004)

Dentin Is Dissolved by High Concentrations of L-Ascorbic Acid 2-[3,4-Dihydro-2,5,7,8-tetramethyl-2-(4,8,12-trimethyltridecyl)-2*H*-1-benzopyran-6-yl-hydrogen Phosphate] Potassium Salt with or without Hydrogen Peroxide

Masahiro KOZUKA and Yasuhisa TSUJIMOTO*

Research Institute of Oral Science, Department of Endodontics, Nihon University School of Dentistry at Matsudo; 870–1 Sakaecho, Nishi-2, Matsudo, Chiba 271–8587, Japan. Received October 27, 2003; accepted February 17, 2004

L-Ascorbic acid 2-[3,4-dihydro-2,5,7,8-tetramethyl-2-(4,8,12-trimethyltridecyl)-2*H*-1-benzopyran-6-yl-hydrogen phosphate] potassium salt (EPC-K_1) is a conjugate of vitamin C and vitamin E that is water-soluble and stable at room temperature. EPC-K_1 has been developed as a hydroxyl radical (·OH) scavenger and antioxidant. In a previous tooth whitening experiment, it was accidentally found that tooth (dentin) blocks were dissolved by EPC-K_1 with H_2O_2. In the current study, high concentrations of EPC-K_1 (2.5, 25 mM) with 3% H_2O_2 dissolved and caused the collapse of dentin blocks. Similar concentrations of EPC-K_1 without 3% H_2O_2, however, dissolved the dentin blocks without collapse over a 3-week period. In these cases, a ·OH-like signal was detected using an ESR spin-trapping method. The volume of calcium in solution (including the dentin block) increased on the addition of EPC-K_1 in a concentration-dependent manner. In addition, the calcium : phosphorus ratio changed from 2 : 1 in sound dentin to 1 : 2 in the collapsed dentin block. High concentrations of EPC-K_1 are therefore considered to have calcium chelating and dentin dissolving activity. The dentin dissolving activity was enhanced when EPC-K_1 was used with H_2O_2. EPC-K_1 had no protective effect when used in tooth whitening with H_2O_2.

Key words dentin; hydroxyl radical; ESR

In a previous study, it was reported[1,2] that hydroxyl radicals (·OH) generated *via* hydrogen peroxide (H_2O_2) were responsible for tooth whitening. However, the detailed mechanism(s) of tooth whitening have not yet been elucidated. It is well known that ·OH are scavenged by ·OH scavengers such as methanol, dimethyl sulfoxide (DMSO) and L-ascorbic acid 2-[3,4-dihydro-2,5,7,8-tetramethyl-2-(4,8,12-trimethyltridecyl)-2*H*-1-benzopyran-6-yl-hydrogen phosphate] potassium salt (EPC-K_1).[3—11] EPC-K_1, a conjugate of vitamin C and vitamin E that is water-soluble and stable at room temperature, was developed as a ·OH scavenger and antioxidant agent by Senju Pharmaceuticals (Osaka, Japan).

In the tooth whitening pilot study, we used EPC-K_1 to investigate the relationship between whitening effect and ·OH. At that time we accidentally found that the tooth (dentin) blocks were dissolved by H_2O_2 with EPC-K_1. EPC-K_1 has been developed as an antioxidant for the living body. There is a huge problem if EPC-K_1 is able to dissolve dentin blocks, because tooth components are almost the same as bone. If damage to organic and/or inorganic components occurs with EPC-K_1, the components of the human body will become unbalanced.

The aim of the current study is to examine the effects of EPC-K_1 with and without H_2O_2 on dentin blocks over time.

MATERIALS AND METHODS

Chemicals EPC-K_1 was kindly provided by Senju Pharmaceuticals (Osaka, Japan). 5,5-Dimethyl-1-pyrroline-*N*-oxide (DMPO), which is used as a trapping agent for free radicals, was obtained from Dojin Chemicals (Kumamoto, Japan). Ethylenediamine-*N*,*N*,*N*′,*N*′-tetraacetic acid (EDTA), used as an irrigant for the removal of a smear layer, was obtained from Dojin Chemicals (Kumamoto, Japan). H_2O_2 which is used as a tooth whitening agent, and ethanol and DMSO, which are used as ·OH scavengers, were obtained from Wako Pure Chemical Industries, Ltd., (Osaka, Japan).

Dentin Blocks The dentin blocks were prepared as described by Tsujimoto *et al.*[12] Four blocks were obtained from the root of an extracted human single cone tooth. The pulp and smear layers were removed by file, then 15% EDTA was applied on the dentin wall for 2 min. The sample was washed with pure water (PW) and blot dried with Kimwipe (Kimberly-Clark Co. Ltd., Japan) paper. The sample was then weighed. Three blocks were used for each examination.

Free Radical Measurement The ESR spin-trapping method[11,13,14] was used to measure free radical generation from each solution. The final concentration of DMPO in 200 μl of the reaction mixture was adjusted to 89.0 mM for this experiment. The ESR spectra were measured using a JES FA 300 (JEOL, Tokyo, Japan). The measurement conditions were as follows: microwave power, 8 mW; magnetic field, 335.0±5 mT; sweep time, 2 min; modulation frequency, 100 kHz; and time constant, 0.03 s.

Calcium Volume Measurement The calcium volumes of each solution around the dentin blocks were measured over time using an inductively coupled plasma atomic emission spectrometer (SPS 1700R; Seiko Instrument Inc., Tokyo, Japan). The measurement conditions were as follows: modulation frequency, 27.12 MHz; microwave power, 1.30 kW; plasma flow (argon gas), 16.0 l/min.

Changes in pH The pH of each solution was measured using an ISFET pH Meter KS723 (Shindengen Electric Manufacturing Co., Ltd., Tokyo, Japan).

Wet Tooth Block Weight The wet tooth block weight was measured using a R2000D electric scale (Sartorious, Germany).

* To whom correspondence should be addressed. e-mail: tsuji@mascat.nihon-u.ac.jp

© 2004 Pharmaceutical Society of Japan

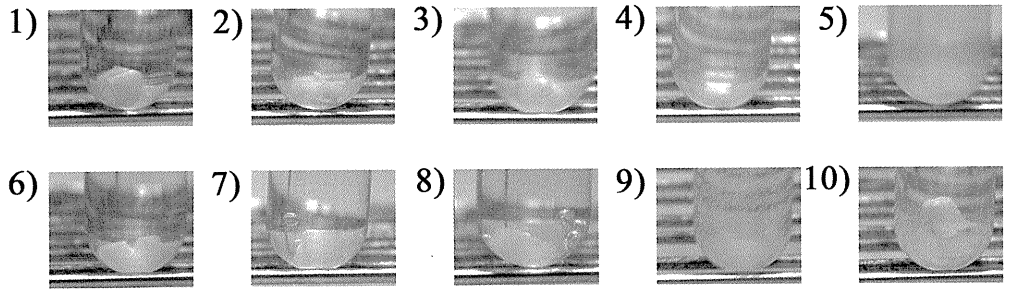

Fig. 1. The Conditions in Each Solution Including Dentin Block

(1) PW, (2) 0.025 mM EPC-K_1, (3) 0.25 mM EPC-K_1, (4) 2.5 mM EPC-K_1, (5) 25 mM EPC-K_1, (6) 3% H_2O_2, (7) 3% H_2O_2 with 0.025 mM EPC-K_1, (8) 3% H_2O_2 with 0.25 mM EPC-K_1, (9) 3% H_2O_2 with 2.5 mM EPC-K_1, (10) 3% H_2O_2 with 25 mM EPC-K_1.

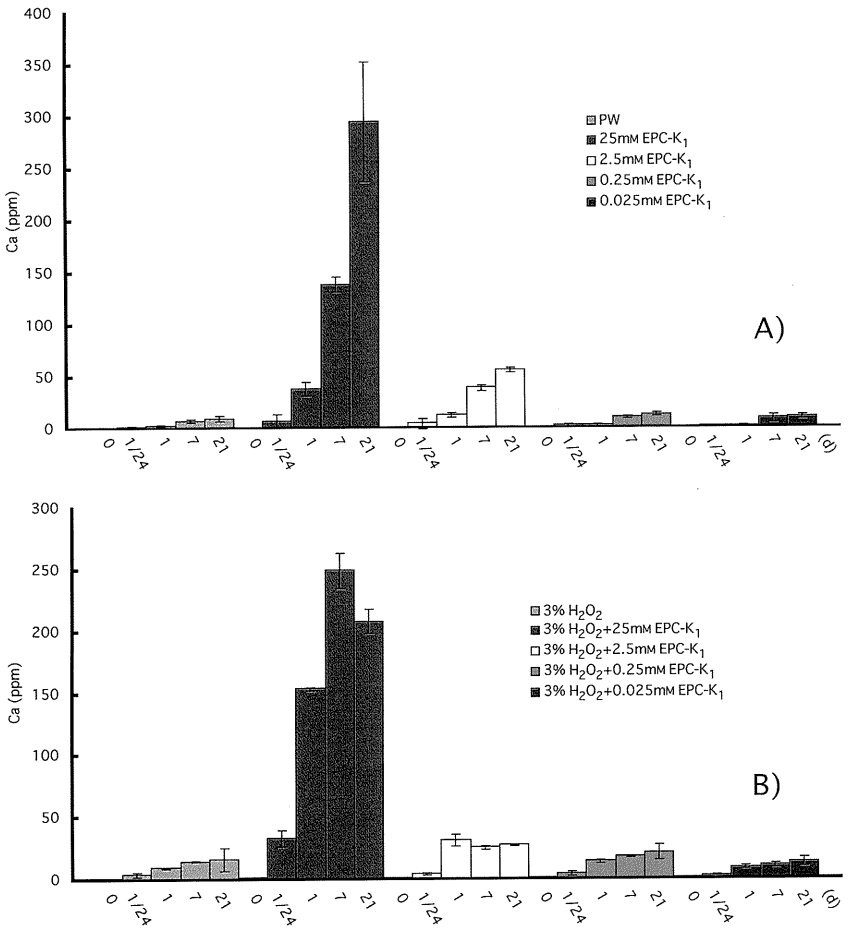

Fig. 2. Relationship between Each Solution and Calcium Volume

(A) Calcium volume in PW with/without each concentration of EPC-K_1. (B) Calcium volume in H_2O_2 with/without each concentration of EPC-K_1.

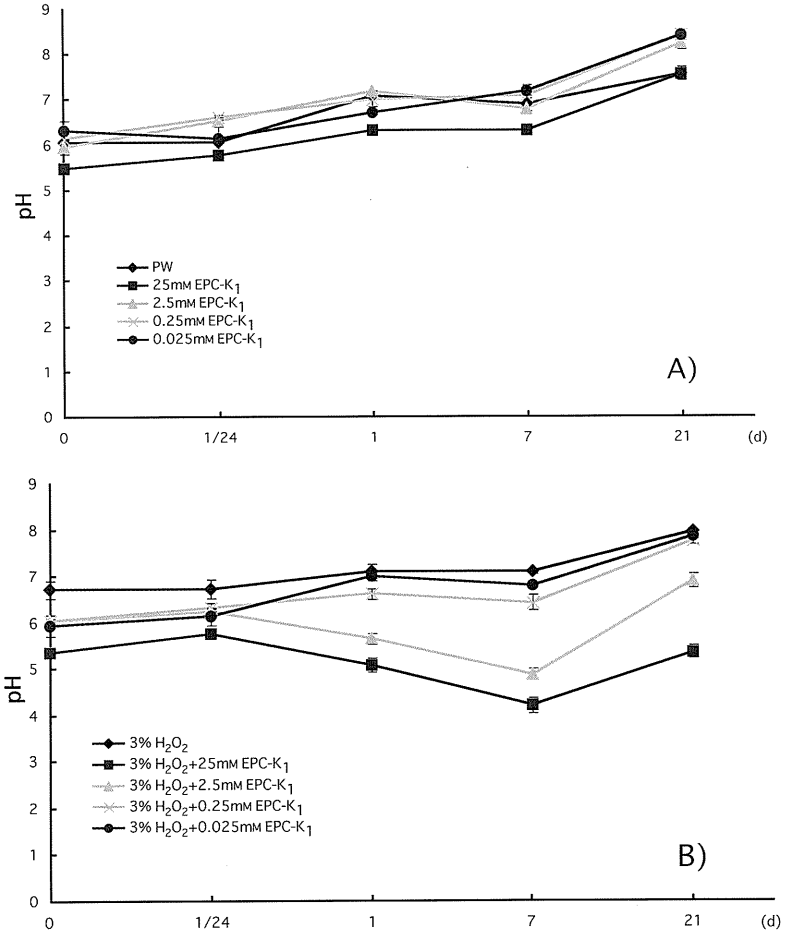

Fig. 3. Changes in pH

(A) PW with/without each concentration of EPC-K_1. (B) H_2O_2 with/without each concentration of EPC-K_1.

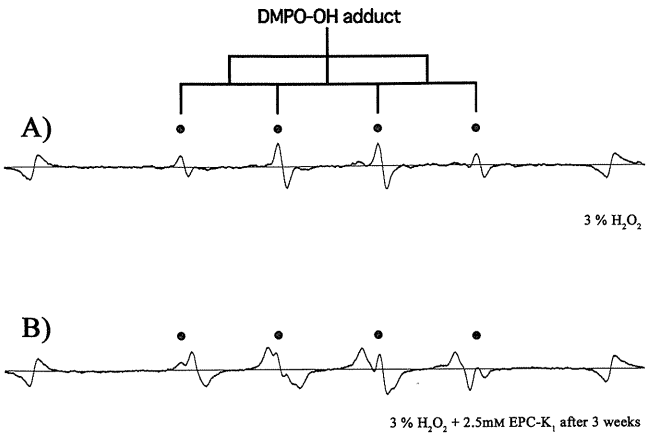

Fig. 4. Typical ESR Signal

(A) ·OH signal from 3% H_2O_2. (B) ·OH-like signal from 3% H_2O_2 with 2.5 mM EPC-K_1.

RESULTS

State of the Dentin Blocks The typical state of the dentin blocks in each solution after 3 weeks is shown in Fig. 1 (results at 1 and 2 weeks not shown). The dentin blocks and solutions in PW and EPC-K_1 showed little change after 3 weeks; however, the color of the solutions in 2.5 and 25 mM EPC-K_1 changed to milk-white. The color of the dentin blocks became white after 3 weeks in 3% H_2O_2 and 3% H_2O_2 with EPC-K_1. However, after 3 weeks in 3% H_2O_2 with 2.5 and 25 mM EPC-K_1 the dentin blocks had collapsed. An exceptional amount of collapse was observed in 3% H_2O_2 with 25 mM EPC-K_1 after 3 weeks.

Calcium Volume of the Solutions The calcium volume in the solutions is shown in Figs. 2A and B. Calcium volume increased after the addition of EPC-K_1 in a concentration-dependent manner. An exceptional amount of calcium was detected after the addition of 25 mM EPC-K_1.

Changes in pH The change in pH of each solution (including the dentin block) is shown in Fig. 3. In the case of EPC-K_1, the pH of the solution (approximately pH 6) increased gradually after mixing. After 3 weeks, the pH was approximately 8 (Fig. 3A). The pH of the solution was approximately 6 after mixing with 3% H_2O_2 and differing concentrations of EPC-K_1. The pH increased to pH 7—8 in 3% H_2O_2, 3% H_2O_2 with 0.025 mM and 0.25 mM EPC-K_1. However, in 3% H_2O_2 with 2.5 and 25 mM EPC-K_1 the pH decreased to pH 4—5 at 1 week and then increased to pH 6 after 3 weeks (Fig. 3B).

Wet Dentin Block Weight The wet dentin block weight showed little change except when 3% H_2O_2 was used with 25 mM EPC-K_1 for 3 weeks. This happened because the dentin block collapsed (data not shown).

Analysis of Collapsed Dentin Blocks The calcium: phosphorus ratio of the collapsed tooth block was measured using an inductively coupled plasma atomic emission spectrometer (SPS 1700R; Seiko Instrument Inc., Tokyo, Japan). The calcium : phosphorus ratio was found to be 1 : 2 in 3% H_2O_2 with 25 mM EPC-K_1.

Free Radical Measurement Generated free radicals were measured using an ESR spin-trapping method.[11,13,14] ·OH were detected from 3% H_2O_2 (Fig. 4), and a carbon center radical (·C) was detected when ethanol or DMSO was added to 3% H_2O_2 (data not shown). This means that free ·OH was produced followed by conversion to the DMPO-C-center.[15] ·OH was not detected with every concentration of EPC-K_1, however ·OH-like signals were observed at 3 weeks with high concentrations of EPC-K_1 (2.5, 25 mM) (Fig. 4). ·OH-like signals were also detected at 3 weeks in H_2O_2 solutions with 2.5 and 25 mM EPC-K_1. Higher ·OH-like signals were detected with 2.5 and 25 mM EPC-K_1 with H_2O_2 than without H_2O_2.

DISCUSSION

EPC-K_1 is composed of vitamin C and vitamin E joined by a phosphodiester linkage. EPC-K_1 has been reported to have potent ·OH scavenging activity, anti-lipid peroxidation activity,[10] and can chelate iron and copper.[11] In addition, Kuribayashi *et al.*[16] suggested that EPC-K_1 might be useful in the treatment of ischemia-reperfusion. It was thought that EPC-K_1 could be used to treat the inflammation of dental pulp and gingiva, and in tooth replantation and transplantation. It has not been reported what kind of effect EPC-K_1 has on the tooth component. As mentioned above, we found accidentally that EPC-K_1 dissolved dentin during the tooth whitening experiment. It is therefore very important to clarify the effects of EPC-K_1 before it is applied clinically.

The results of the current study show that high concentrations of EPC-K_1 (2.5, 25 mM) with 3% H_2O_2 dissolved and caused the collapse of dentin blocks. When the pH of the solution was measured, it was found to be pH 5—6 for 24 h, then decreased to pH 4—5 in the first week, and then rose after 3 weeks to pH 5.5—7.

High concentrations of EPC-K_1 (2.5, 25 mM) without 3% H_2O_2, on the other hand, dissolved the dentin blocks without causing a collapse. In this case, the initial pH was approximately 6 and then increased gradually to pH 8 after 3 weeks.

The ·OH was generated from H_2O_2 *via* Fenton reaction[17,18] because of H_2O_2 generally includes a small volume of metal in the manufacture process. In this experiment, the EPC-K_1 concentrations ranged from 0.025—25 mM. This was because the ·OH generated from 3% H_2O_2 was completely eliminated by the addition of 0.025—25 mM EPC-K_1 in a preliminary study (data not shown). The pH experiment is an important aspect because teeth are dissolved by acidic solutions such as phosphoric acid, which is used as a tooth etching agent. The pH was not dependent on dentin being dissolved by EPC-K_1; the pH decreased to pH 4—5 in the first week and then rose to pH 5.5—7 after 3 weeks when high concentrations of EPC-K_1 with H_2O_2 were used. This observation is difficult to explain, although it is suggested that the dissolving of dentin by EPC-K_1 is enhanced by H_2O_2. A further study to clarify this issue is currently underway.

In a previous tooth whitening study,[2] the ·OH generated from H_2O_2 degraded the amino acids that make up organic matter, although the structure of hydroxyl apatite, like the inorganic material in dentin, did not change after application of H_2O_2. The weight of the dentin block decreased after application of H_2O_2, but the calcium volume did not change. It has been suggested that the ·OH generated from H_2O_2 degraded the organic matter of dentin, and then destroyed its structure. In this study, a ·OH-like signal was detected with 2.5 and

25 mM EPC-K_1 with and without H_2O_2. In addition, dentin bleaching (whitening) by the ·OH generated from H_2O_2 was not prevented by the addition of EPC-K_1, a ·OH scavenger. There have been no reports on free radical generation from EPC-K_1 solutions, and it is unknown how ·OH-like radicals are produced. There is no evidence that the ·OH-like signal influences the dissolving of dentin, and this phenomenon therefore requires clarification in a further study.

In sound dentin, the calcium : phosphorus ratio is usually 2 : 1, but in this study the calcium : phosphorus ratio was 1 : 2 in the collapsed tooth blocks treated with 25 mM EPC-K_1 with 3% H_2O_2. It is suggested that EPC-K_1 not only chelates iron and copper, as reported previously,[10,11] but can also chelate calcium.

From the results of this study, it is suggested that H_2O_2 generates ·OH which attack an organic material, such as dental collagen, and that the calcium component of dentin was lost over time by the chelating activity of EPC-K_1. It is therefore evident that high concentrations of EPC-K_1 should not be used for long periods of time during tooth replantation, treatment of periapical lesions, tooth transplants and implants. This is because the alveolar bone might be damaged by EPC-K_1. High concentrations of EPC-K_1 for protection against bone resorption and/or the chelation of calcium from bone or teeth should be used with caution.

Acknowledgements We thank Dr. T. Ishizaki (Central Research Center, Sangi Co. Ltd.) for the calcium volume measurement work. This study was supported by a Grant from the Ministry of Education, Culture, Sports, Science and Technology to promote 2001-Multidisciplinary Research Projects (in 2001—2005), and from The Tsuchiya Foundation (2001).

REFERENCES

1) Tsujimoto Y., Kozuka M., Shiozawa A., Kashima M., Kawamoto K., Miura H., Saitoh K., Matsushima K., Yamazaki M., *Jpn. J. Conserv. Dent.*, **43**, 10—15 (2000).
2) Kawamoto K., Tsujimoto Y., *J. Endodon.*, **30**, 45—50 (2004).
3) Mori A., Edamatsu R., Kohno M., Ohmori S., *Neuroscience*, **15**, 371—376 (1989).
4) Shiozawa A., Kimura K., Hashizume H., Tsujimoto Y., Yamazaki M., *Jpn. J. Conserv. Dent.*, **39**, 1171—1177 (1996).
5) Miura T., Tsujimoto Y., *Nihon Univ. J. Oral Sci.*, **23**, 103—110 (1997).
6) Yamamoto H., Kimura K., Tsujimoto Y., Yamazaki M., *Jpn. J. Conserv. Dent.*, **40**, 1247—1254 (1997).
7) Yamamoto H., *Nihon Univ. J. Oral Sci.*, **24**, 29—37 (1998).
8) Noda Y., Anzai K., Mori A., Kohno M., Shinmei M., Packer L., *Biochem. Mol. Biol. Int.*, **42**, 35—44 (1997).
9) Tsujimoto Y., Saitoh K., Kashima M., Shiozawa A., Kozuka M., Hashizume H., Kimura K., Yamazaki M., Fujii A., *Gen. Pharmacol.*, **31**, 405—408 (1998).
10) Anzai K., Mira Y., Ueda J., Ozawa T., Noda Y., Mori A., Packer L., *Research Commun. Biochem. Cell Mol. Biol.*, **2**, 129—138 (1998).
11) Tomita T., Kashima M., Tsujimoto Y., *Chem. Pharm. Bull.*, **48**, 330—333 (2000).
12) Tsujimoto Y., Kozuka M., Hitotsune N., Yamazaki M., *J. Jpn. Endo. Assoc.*, **18**, 19—24 (1997).
13) Tanigawa T., *J. Kyoto Pref. Univ. Med.*, **99**, 133—143 (1990).
14) Kohno M., Yamada M., Mitsuta K., Mizuta K., Yoshikawa T., *Bull. Chem. Soc. Jpn.*, **64**, 1447—1453 (1991).
15) Finkelstein E., Rosen G. M., Rauckman E. J., *J. Am. Chem. Soc.*, **102**, 4994 (1980).
16) Kuribayashi Y., Yoshida K., Sakaue T., Okumura A., *Arzneim.-Forsch./Drug Res.*, **42**, 1072—1074 (1992).
17) Cohen G., Sinet P. M., *FEBS Lett.*, **138**, 258—260 (1982).
18) Dunford H. B., *Free Rad. Biol. Med.*, **3**, 405—421 (1987).